The determination of infrared optical constants of some liquids and thin-film solids

Catlow, Brendan

THE DETERMINATION OF INFRARED OPTICAL CONSTANTS OF SOME LIQUIDS AND THIN-FILM SOLIDS

A Thesis submitted to

The University of Durham

by

Brendan Catlow, B.Sc. (Hons.)

(Hatfield College)

for the Degree of Doctor of Philosophy

November 1986

DECLARATION

The work described in this thesis was carried out by me in the Chemistry department of the University of Durham, between September 1983 and October 1986. I declare that this work has not been accepted in substance for any degree, and is not being concurrently submitted in candidature for any other degree. The work is original except where indicated by reference.

Signed .....Brendan Callow.....

.....
(Supervisor)

date: .....26th November 1986.

Acknowledgements

My sincere thanks are due to Dr. Jack Yarwood for his support and guidance throughout the work involved with this thesis. His enthusiasm and dedication have been a constant source of inspiration.

Thanks are also due to Ches Pacynko who gave up much of his time in introducing me to the practicalities of far infrared spectroscopy; to Rob Green and Terry Harrison for their much-valued technical assistance; to François Guillaume, Peter Lux and Gerald Davies for helpful and stimulating discussions over many a pint of beer; and to all the above-mentioned, together with Rosemary Sides and Richard Buchner, who have made the three years of my Ph.D. such an enjoyable time.

Special mention should be made of Bob Brown, who died this year. His contribution to this work, and to the work of many before me, has been invaluable. His knowledge and personality have been a great asset to the department and he will be sadly missed.

The work of Chris Jones and Gerald Davies in preparing the Langmuir - Blodggett films studied in this work is gratefully acknowledged.

Finally, my thanks go to Loretta Hardman; first of all for her patience when it seemed I was more interested in the computer than her, and also for her painstaking efforts in labelling the diagrams in this thesis.

TO

MUM AND DAD

THE DETERMINATION OF INFRARED OPTICAL CONSTANTS OF SOME LIQUIDS AND THIN-FILM SOLIDS

BRENDAN CATLOW

ABSTRACT

Fourier transform infrared techniques have been applied in order to determine the optical constants of several liquid and thin-film solid systems over infrared frequencies. In the far infrared region, dispersive interferometry has been employed leading to the derivation of both real and imaginary parts of the complex refractive index in one experiment. As an extension to this, a method has been devised for the analysis of 'full interferograms' involving multiple internal reflections that inevitably arise for normal transmission through thin parallel specimens. A program has been written which constrcts a theoretical complex insertion loss for the system under study and then performs an iteration on estimated values for absorption coefficient and refractive index. Results are presented for several liquids analysed using this technique.

The bandshapes of pure acetonitrile and benzene have been studied in the far infrared region of the spectrum. This was as a consequence of claims in the literature [83,84] that discernable structure in such bandshapes indicated the presence of long-ranged order in molecular liquids. Bandshapes have been produced using both non-dispersive and dispersive transmission, and spectra from both experiments have been averaged. These are presented together with the standard deviation on the mean. It is concluded that there is no evidence for real structure above the level of the noise in the spectra.

The collision-induced spectrum of iodine in benzene has been studied in the far infrared region. Subsequent analysis has been done in both the frequency domain and the time domain in order to examine the nature of the intermolecular interactions and the time evolution of the relaxation processes. Experimental intensity and second moment data have been found to agree well with those predicted by a theory based only on classical electrostatic forces of attraction. Spectra have been modelled using two approaches for solving the generalised Langevin equation. The fits were found to be reasonable and the fitted parameters have been used to study the interactions involved in the system.

A mid infrared study of Langmuir-Blodgett films has been undertaken, involving layers of ω-tricosenoic acid on a silicon substrate. Anomalies in the carbonyl intensities for the first few layers have been attributed to the partially polarised nature of the incident radiation, and have been used to study the orientation of the fatty acid molecules relative to the substrate surface.

A variable temperature cryostat with sample-holder has been interfaced with a Beckmann FS720 interferometer. This has been used to measure the optical constants of several solids over a limited frequency range in the far infrared.

CONTENTS

CHAPTER 1

1. FOURIER TRANSFORM INFRARED SPECTROSCOPY

1.1 Introduction

Fourier transform methods were first introduced to the field of infrared spectroscopy for use in the long wavelength region (> 25μm) which, because of the inherently weak sources available, is difficult to study by the more traditional dispersive methods. With recent improvements in computing capabilities and engineering, the particular advantages of the Fourier transform approach (see section 1.2) have now been extended to the mid-infrared region. The theory of Fourier transform spectroscopy has been dealt with extensively in the literature [1 - 3] so only the basic principles of the technique will be outlined here.

1.1.1 The Mathematical concepts

A vast amount of work has been done on the theory of Fourier transforms [1,4] so only relevant details that will be drawn upon in later chapters are included here.

1.1.1a. The Fourier Transform

Fourier's integral basically states that

$$f(x) = \int_{-\infty}^{\infty}\left[\int_{-\infty}^{\infty} f(x)\exp(-i2\pi\omega x)dx\right]\exp(i2\pi\omega x)d\omega \qquad (1.1)$$

from which, denoting ξ as the Fourier transform operator, we say that if

$$\xi\{f(x)\} = \int_{-\infty}^{\infty} f(x)\exp(-i2\pi\omega x)\ dx \qquad (1.2)$$

then the inverse Fourier transform

$$\xi^{-1}\{f(x)\} = \int_{-\infty}^{\infty}\xi\{f(x)\}\exp(i2\pi\omega x)dx \qquad (1.3)$$

The conditions under which a function may have a Fourier transform are [4]:

(i) The integral of f(x) exists for $-\infty < x < \infty$.

(ii) Any discontinuities in f(x) are finite.

In the physical world these conditions are violated if there is infinite energy, for example a sine wave existing for $-\infty < t < \infty$ represents infinite energy at a single frequency and hence contradicts the second condition. Although such a periodic function has no Fourier transform it is considered to have a line spectrum (figure 1.1). This will be shown later to have important consequences in the analysis of interferograms.

Fig. 1.1

Fourier Transform Pairs

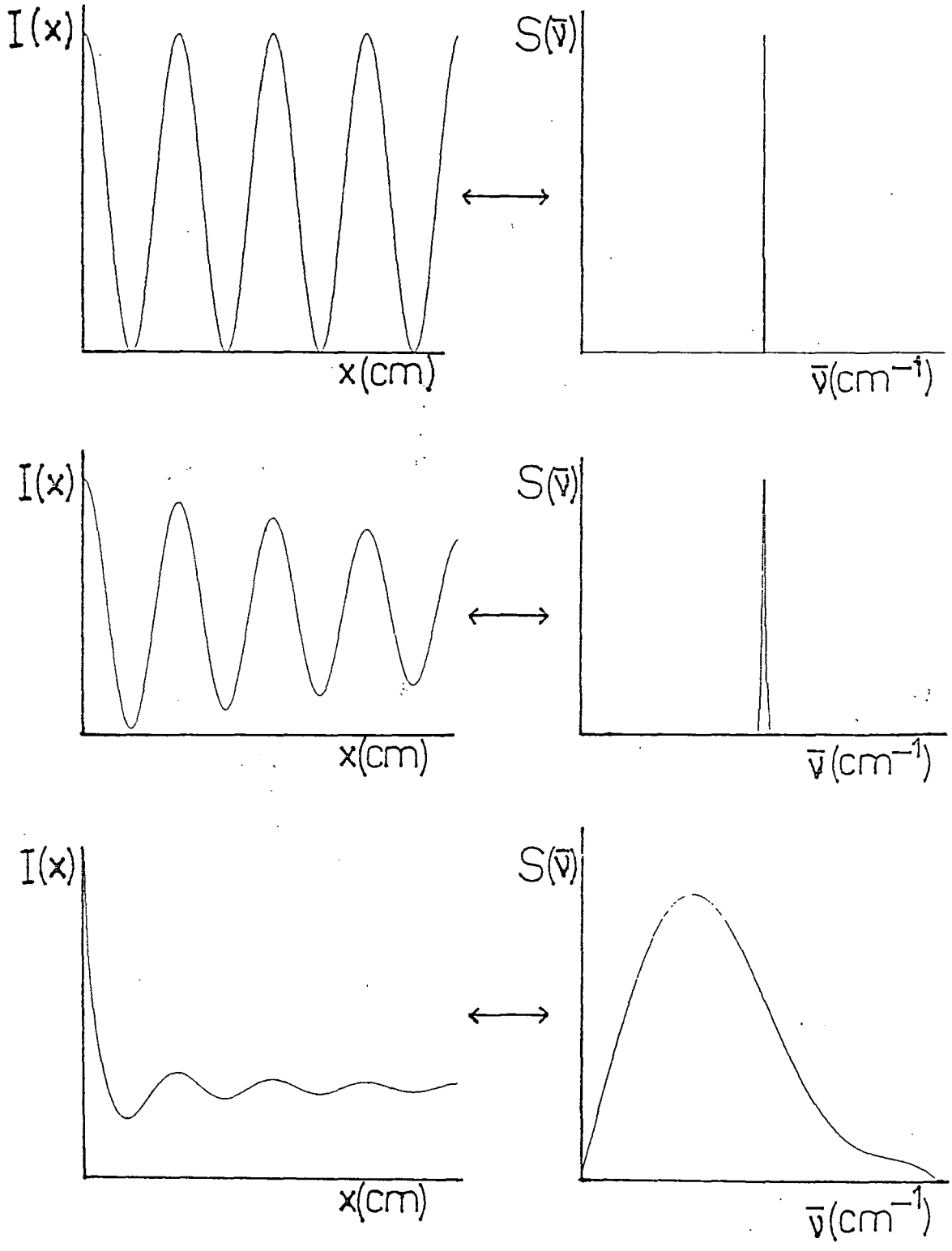

Fig. 1.2

Convolution Theory

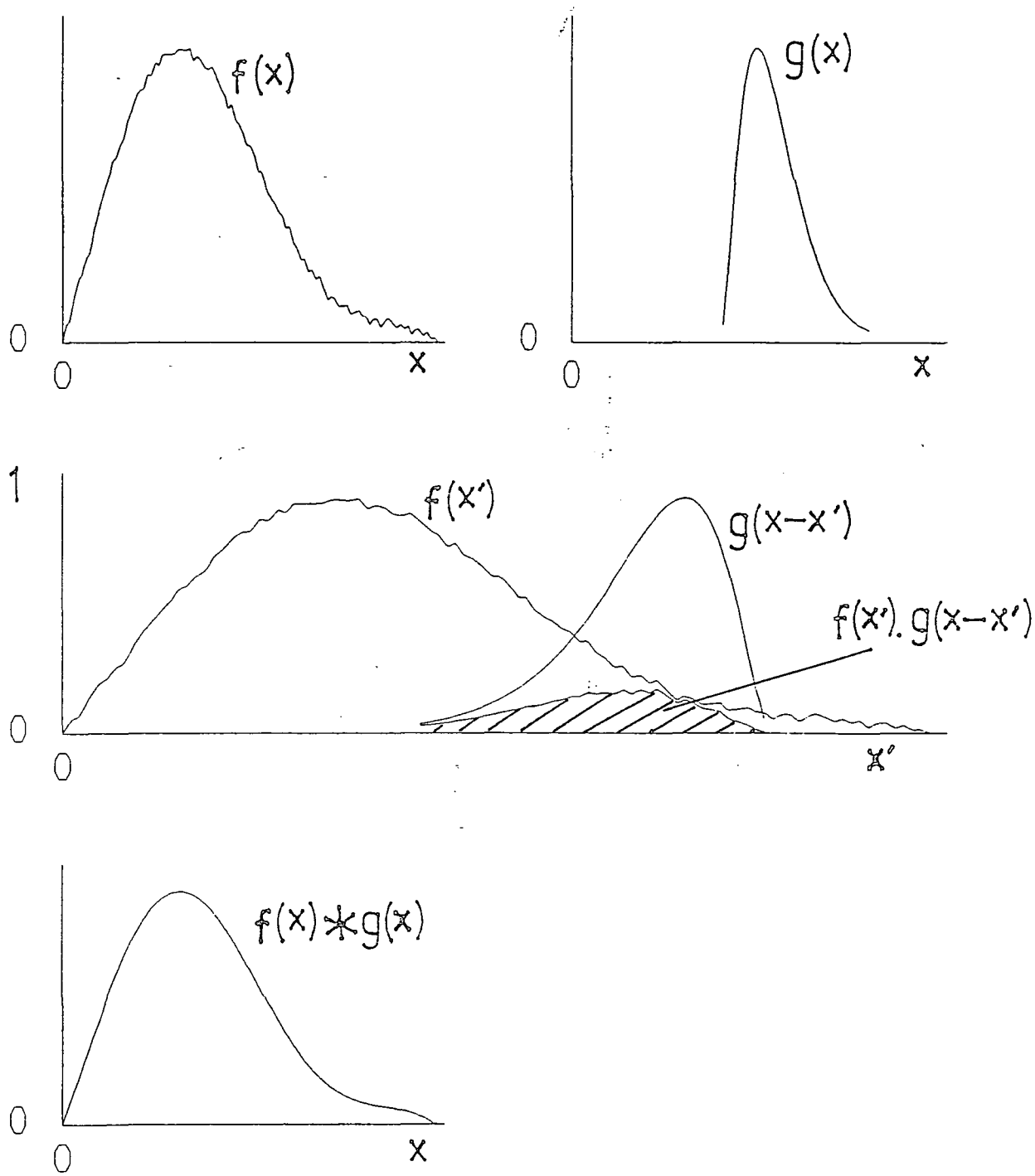

1.1.1b. Convolution Theorem

The convolution of two functions, written $f(x) * g(x)$, is defined as

$$f(x) * g(x) = \int_{-\infty}^{\infty} f(x')g(x-x')\,dx' \qquad (1.4)$$

and is a function of x. Thus if we have functions f(x) and g(x) as shown in figure (1.2), x' represents a shift along the x axis and the convolution is the area under the curve $f(x').g(x-x')$ for all values of x. One of the effects of convolution is that of smoothing the function f(x).

It can be shown [4] that the Fourier transform of the convolution of f(x) and g(x) is identical to the product of the Fourier transforms of f(x) and g(x).
i.e.

$$\xi\{f(x) * g(x)\} = \xi\{f(x)\}.\xi\{g(x)\} \qquad (1.5)$$

A special case of the convolution theorem is the autocorrelation theorem which states

$$\xi\{f(x) * f(x+x')\} = |\xi\{f(x)\}|^2 \qquad (1.6)$$

Note that for complex f(x) the autocorrelation is always real. In words, autocorrelating a function

corresponds to squaring its transform.

1.1.1c The Causality Principle

This universal law of physics basically prohibits any response to an impulse preceding the impulse itself. The response function [1], R(t), must then be zero for all $t < 0$ and may be finite for all $t > 0$ and is thus a one-sided, and therefore asymmetric, function. This asymmetry in the time variable must produce a corresponding asymmetry in the frequency variable [5]. The causality principle and its consequences will be drawn upon later in this thesis when the relationship between the real and imaginary parts of the complex quantities that we measure is considered.

1.1.2 Basic Principles of Interferometry

A number of interferometric techniques have been developed [6 - 8] in order to study the infrared region by Fourier methods. The basic principles and equations involved are, however, very similar and will be described here for a simple Michelson interferometer (figure 1.3).

A parallel beam of polychromatic light is directed on to a beamsplitter orientated at 45° to the direction of the beam. The beamsplitter material (see section 1.3.1b) is such that it is, ideally, 50% reflecting and 50% transmitting over the frequency range of interest. The two

Fig. 1.3

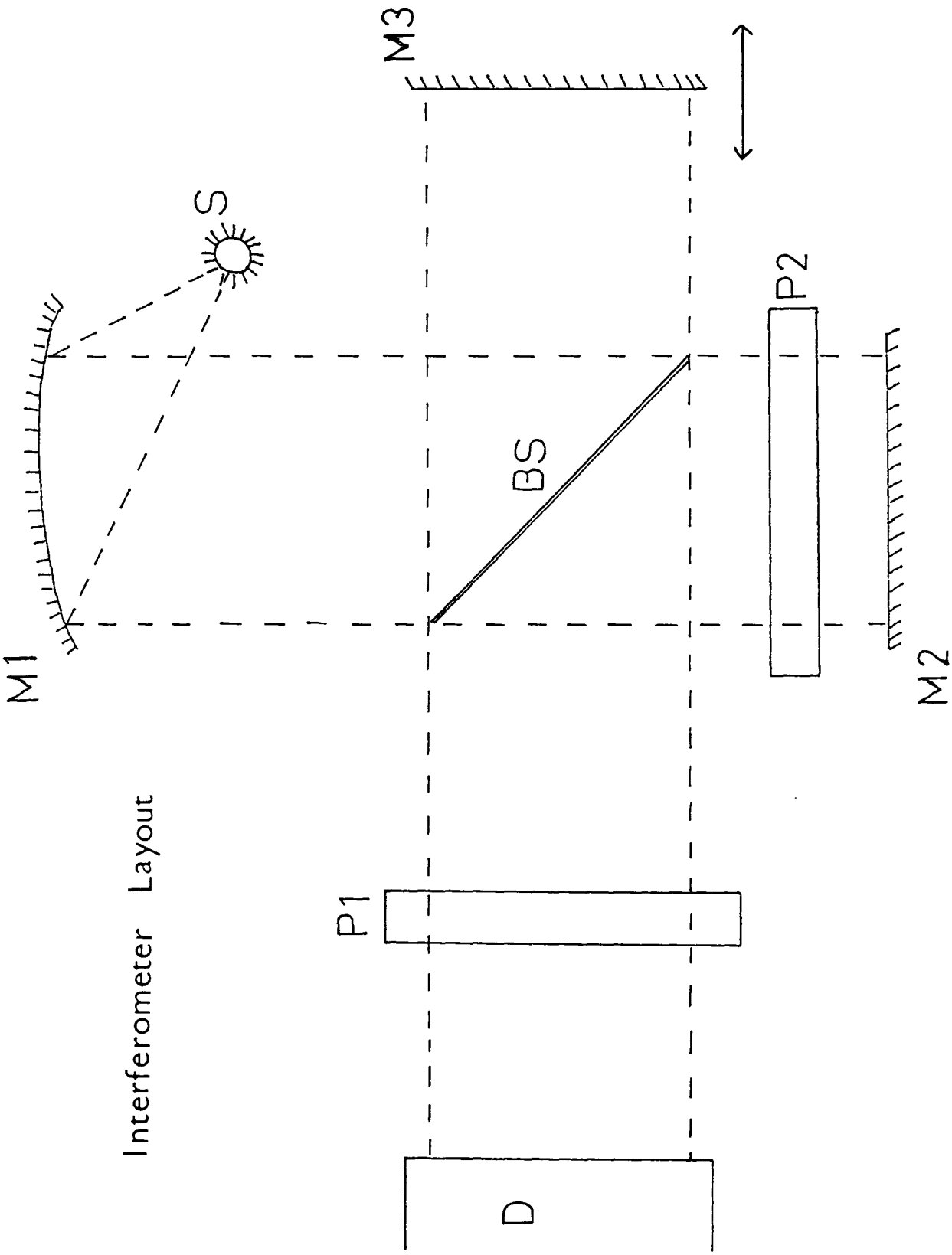

Interferometer Layout

identical beams thus produced then travel in mutually perpendicular directions and are reflected back on themselves by the mirrors M2 and M3 so that they are recombined on meeting the beamsplitter again. Half of the original beam will be returned to the source and the other half will proceed to the detector. As the mirror M3 is displaced from its position of zero path difference, whereby M2 and M3 are equidistant from the beamsplitter, the recombined beams will interfere with one another constructively or destructively to produce an interference pattern which is a function of this displacement and of the frequencies present.

Experiments involving two sample positions, P1 and P2, will be described corresponding to non-dispersive and dispersive interferometry respectively.

For monochromatic radiation, the intensity at the detector will be given by

$$I(x) = \hat{S}(\nu_o)\left[1 + \exp(i2\pi\bar{\nu}_o x)\right] \qquad (1.7)$$

where $\bar{\nu}$ is the frequency in wavenumbers and x the path difference of the two beams. $\hat{S}$ is related to the amplitude of the radiation which arrives at the beamsplitter with phase delay $2\pi\bar{\nu}x$. If we consider that the source spectrum consists of several monochromatic lines then the total intensity can be regarded as a simple Fourier series,

$$I(x) = \sum_i \hat{S}_i(\bar{\nu}) + \sum_i \hat{S}_i(\bar{\nu})\exp(i2\pi\bar{\nu}_i x) \qquad (1.8)$$

For the more realistic case of a continuous spectral distribution we must sum over all frequencies and

$$I(x) = \int_0^\infty \hat{S}(\bar{\nu})d\bar{\nu} + \int_0^\infty \hat{S}(\bar{\nu})\exp(i2\pi\bar{\nu}x)\, d\bar{\nu} \qquad (1.9)$$

Note that at zero path difference, x = 0 and equation (1.9) reduces to

$$I_o = 2\int_0^\infty \hat{S}(\bar{\nu})d\bar{\nu} \qquad (1.10)$$

and

$$I'(x) = I(x) - I_o/2 = \int_0^\infty \hat{S}(\bar{\nu})\exp(i2\pi\bar{\nu}x)d\bar{\nu} \qquad (1.11)$$

This is a Fourier integral which may be transformed (equation 1.2) to obtain the spectrum, $\hat{S}(\bar{\nu})$, according to

$$\hat{S}(\bar{\nu}) = \int_0^\infty I'(x)\exp(-i2\pi\bar{\nu}x)dx \qquad (1.12)$$

The post-transformation handling of data depends on sample position and will be considered separately for non-dispersive and dispersive interferograms.

1.1.3 Non-Dispersive Transmission

When the sample is probed after the beams have been recombined the interferogram should be, for an amplitude

modulated signal, totally symmetric and an even function. This requires the imaginary part of equation 1.12 to be zero, and the cosine transform can be written as

$$p(\bar{\nu}) = \int_{-\infty}^{\infty} I'(x)\cos(2\pi\bar{\nu}x)\, dx \qquad (1.13)$$

For phase modulated interferograms, the function is now odd and therefore the cosine spectrum is zero. It must then be described in terms of its sine transform

$$q(\bar{\nu}) = \int_{-\infty}^{\infty} I'(x)\sin(2\pi\bar{\nu}x)\, dx \qquad (1.14)$$

In practice the interferogram cannot be expressed wholly in terms of either one of its sine or cosine transforms alone because asymmetry is introduced into it by factors such as: misalignment of the interferometer; imperfect sampling of the interferogram; temperature and pressure gradients within the interferometer. Two methods of eliminating such asymmetry have been employed in this work:

(a) Performing a convolution (equation 1.4) of the two halves of an interferogram either side of zero path position. This is equivalent to taking the modulus of the complex Fourier transform [1]

$$\mathrm{mod}\{\hat{S}(\nu)\} = \left[p(\bar{\nu})^2 + q(\bar{\nu})^2\right]^{\frac{1}{2}} \qquad (1.15)$$

and renders the interferogram virtually symmetric so that the complex integral may be replaced by the cosine transform. In this work, both the real and imaginary parts of the complex Fourier transform are extracted and used in equation 1.15.

(b) Performing a phase correction on the interferograms according to the procedure of Forman, Steele and Vanasse [9].

Asymmetry in the interferogram is equivalent to a frequency dependent phase error, $\phi(\bar{\nu})$, in the observed interferogram. For a double-sided interferogram we can include this in equation (1.12) according to

$$\hat{S}(\bar{\nu}) = \int_0^\infty I'(x)\exp\{-i\left[2\pi\bar{\nu}x + \phi(\bar{\nu})\right]\}\,dx \tag{1.16}$$

and, as $\exp\phi(\nu)$ is independent of x, we can take it outside the integral to give

$$\hat{S}'(\bar{\nu}) = \hat{S}(\bar{\nu})\exp\left[i\phi(\bar{\nu})\right] = \int_0^\infty I'(x)\exp(-i2\pi\bar{\nu}x)\,dx \tag{1.17}$$

where $\hat{S}(\bar{\nu})$ is the true and $\hat{S}'(\bar{\nu})$ the observed spectrum, and they are related by

$$\hat{S}(\bar{\nu}) = \hat{S}'(\bar{\nu})\exp\left[-i\phi(\bar{\nu})\right] \tag{1.18}$$

Thus it can be seen that I'(x) can be obtained through the convolution of the Fourier transforms of $\hat{S}'(\bar{\nu})$ and $\exp[-i\phi(\bar{\nu})]$

$$I'(x) = \xi\{\hat{S}(\bar{\nu})\} * \xi\{\exp\left[-i\phi(\bar{\nu})\right]\} \qquad (1.19)$$

where $\phi(\bar{\nu})$ can be determined through

$$\phi(\bar{\nu}) = \arctan\left\{\frac{q(\bar{\nu})}{p(\bar{\nu})}\right\} \qquad (1.20)$$

As $\phi(\bar{\nu})$ is a slowly varying function of frequency it can be described accurately using only the central part of the interferogram, usually about 16 points either side of zero path position. This is transformed and apodised to produce the phase correction function which is then convolved with the original interferogram, thereby eliminating all imaginary terms (see section 1.1) by performing what is in effect an auto-correlation.

Several advantages are to be gained through using a single-sided interferogram, namely:

- scanning and computation times are halved
- computer memory requirements are halved
- maximum resolving power is obtained for a given mirror drive.

Since the convolution is performed with only the central part of the asymmetric interferogram little extra noise is introduced since this is the region with greatest signal to noise ratio. The procedure is well illustrated when it is applied to phase modulated interferograms which are primarily odd functions. After correction they take on

Phase Correction

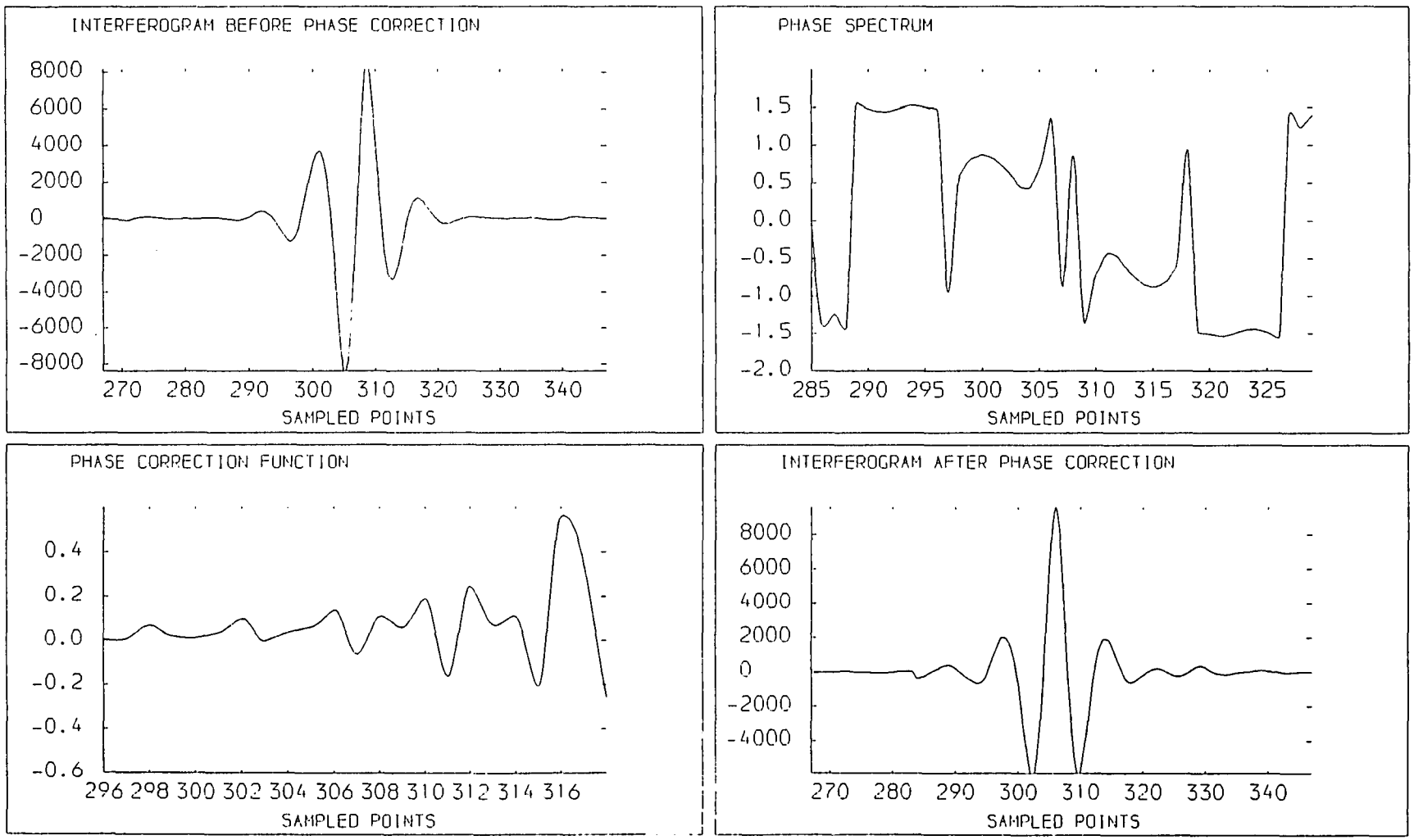

Fig. 1.4

the appearance of amplitude modulated interferograms which are even functions (figure 1.4).

The power reaching the detector is given by equation 1.15 and this contains information about all the components of the system as well as the sample. In order to eliminate this extraneous information it is necessary to perform a ratio which leaves us with the transmission, $T(\bar{\nu})$, of the sample

$$T(\bar{\nu}) = \frac{\text{mod}\{\hat{S}^S(\bar{\nu})\}}{\text{mod}\{S^B(\bar{\nu})\}} = \frac{I}{I_o} \tag{1.21}$$

where superscripts S and B refer to sample and background respectively.

The Beer-Lambert law can then be used to yield the absorption coefficient, $\alpha(\bar{\nu})$.

$$\alpha(\bar{\nu}) = \frac{1}{c\ell} \ln\left[\frac{1}{T(\bar{\nu})}\right] \tag{1.22}$$

where ℓ is the pathlength of sample and c, where required, is the concentration.

1.1.4 Dispersive Interferometry

The introduction of a sample into one arm of the interferometer produces a phase delay in one of the beams which will be a function of optical thickness, ℓ, and refractive index $n(\bar{\nu})$, of the sample

$$\phi(\bar{\nu}) = 4\pi\bar{\nu}\ell n(\bar{\nu}) \qquad (1.23)$$

Thus, from the phase-change and attenuation of the beam it is possible to determine both absorption coefficient and refractive index through one experiment. Since we now need to analyse the phase, which manifests itself as an asymmetry in the interferogram we need both cosine and sine transforms (equatins 1.13 and 1.14), and the phase is given by

$$\phi(\bar{\nu}) = \arctan\left[\frac{q(\bar{\nu})}{p(\bar{\nu})}\right] \qquad (1.24)$$

We can again obtain the absorption coefficient using equation 1.22, allowing for the fact that only half the light reaching the detector has interacted with the sample, and the refractive index can be derived through the difference in phase. These processes will be described in greater detail in the next chapter.

1.2 Advantages of Fourier Transform Spectroscopy

1.2.1 Multiplex advantage

A traditional dispersive instrument scans each frequency element individually. If N spectral elements are scanned in a time T, then each element will be oberved for a time T/N and the signal-to-noise ratio will be proportional to $(T/N)^{\frac{1}{2}}$. In the case of an interferometer, all the frequency elements are observed simultaneously and the

signal-to-noise ratio is proportional to $T^{\frac{1}{2}}$ so there is a substantial improvement with respect to the time taken to record a spectrum. This advantage was foreseen by Felgett [10,11] who coined the name of multiplex spectrometry.

1.2.2 Throughput advantage

Jacquinot [12] pointed out that an interferometer allows a larger area of radiation to be incident on the sample than does a conventional instrument, since there is no need for a slit. Resolution is increased using an interferometer by moving the mirror through larger distances, and the time taken to record a spectrum is proportional to the inverse of the resolution required. For a grating spectrometer the time to record a spectrum is inversely proportional to the square of the width of the slit, so for higher resolutions the interferometer is progressively much faster than the grating spectrometer.

1.3 Practical Use of the Interferometer

All the effort involved in producing a spectrum from an interferometer is geared towards maximising the signal-to-noise-ratio over the frequency range of interest. The following sections will examine the considerations necessary to increase the efficiency of interferometric measurements.

1.3.1 Choosing the frequency range

For a given resolution and signal-to-noise ratio it is quicker both to record and analyse an interferogram recorded over a narrow frequency range than a large one. It is often therefore advantageous to filter off any unwanted radiation and this has important consequences for the way in which an interferogram is sampled.

1.3.1a Sampling the interferograms

In a practical situation two major adjustments have to be made to equation 1.12. The interferogram is scanned over a finite distance and sampled at discrete intervals of path difference, Δx. Thus the integration of a continuous function over an infinite range of path difference must in effect be replaced by the summation over a limited range of regularly spaced values of the function $I(x)$.

$$\hat{S}(\nu) = \sum_{x=-\ell}^{\ell} I'(x)\exp(i2\pi\bar{\nu}x) \qquad (1.25)$$

The restriction of pathlength, governed by the physical limitation on travel of the mirror-drive, will confer a finite resolution in the computed spectrum (section 1.3.4). The choice of Δx, the sampling interval, should be such that

all the frequencies arriving at the detector can be described using as few points as possible. If Δx is too small then superfluous information is collected and time is consequently wasted. If Δx is too large then the solution to equation 1.25 is ambiguous and lower frequencies may be envisaged as passing through the points so that a real feature can be reflected at lower frequencies. This phenomenon is called aliasing and can be avoided if the highest frequency present in the interferogram is sampled at least twice per wavelength. Thus the sampling interval is restricted to

$$\Delta x \leq \frac{1}{2\bar{\nu}_{max}} \qquad (1.26)$$

and $\bar{\nu}_{max}$ can be chosen by use of a filter or series of filters which totally eliminate higher frequencies. Thus with a filter of high frequency cut-off $200cm^{-1}$ a sampling interval of $20\mu m$ could be used since this gives an aliasing frequency of $250cm^{-1}$.

1.3.1b <u>The Beamsplitter</u>

The beamsplitter material used throughout this work was Mylar (polyethylene tetraphthalate). This material has the desired reflectivity and only weak absorption features over the far infrared frequency range. Since the beamsplitter

Fig. 1.5

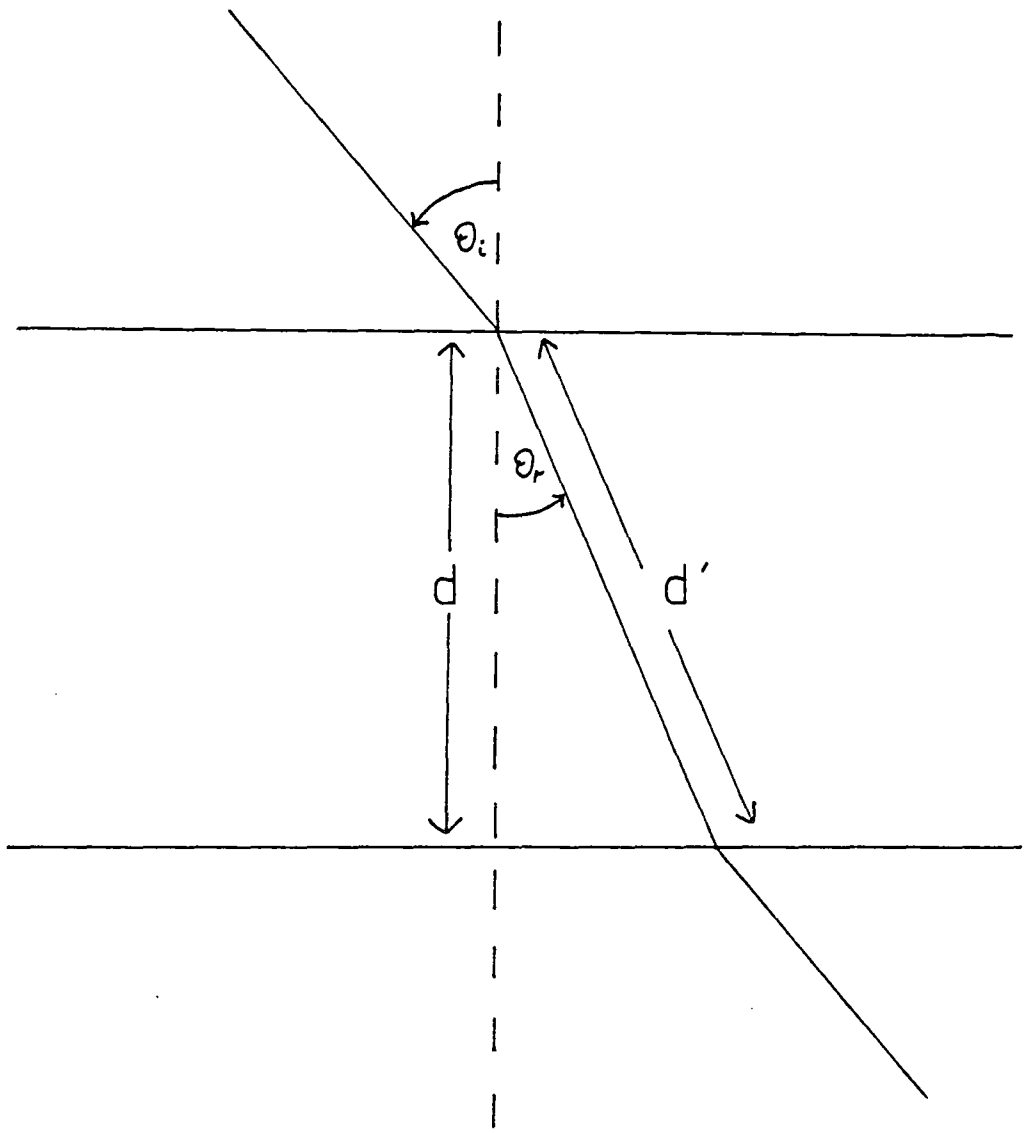

Beamsplitter Geometry

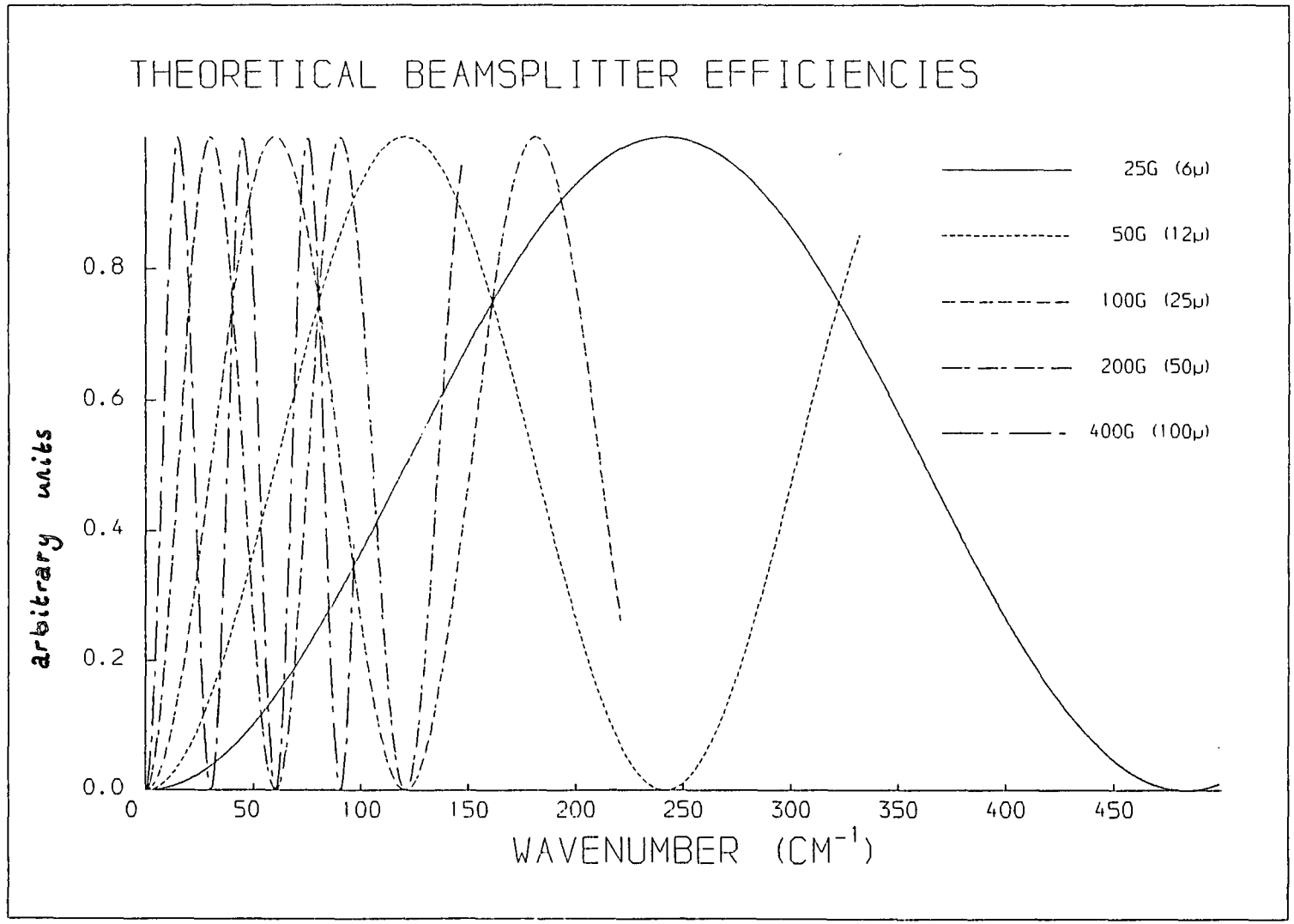
THEORETICAL BEAMSPLITTER EFFICIENCIES
arbitrary units
0.0
0.2
0.4
0.6
0.8
0
50
100
150
200
250
300
350
400
450
WAVENUMBER (CM-1)
25G (6μ)
50G (12μ)
100G (25μ)
200G (50μ)
400G (100μ)

Fig. 1.6

is, of necessity, a thin parallel film it gives rise to channel spectra due to internal reflections of the beam. Successive minima are separated in frequency by an amount $\Delta\bar{\nu}$ where

$$\Delta\bar{\nu} = 1 / 4d' \qquad (1.27)$$

d' being the optical thickness which, from figure 1.5, is related to actual thickness by

$$d' = d / \cos\theta_r \qquad (1.28)$$

with θ_r the angle of refraction derived from Snell's law,

$$n = \sin\theta_i / \sin\theta_r \qquad (1.29)$$

Mylar has a refractive index of about 1.8 [13] and the angle of incidence, θ_i, is 45°. Thus from equations 1.27 to 1.29 it is evident that changing the beamsplitter thickness will change the positions of these minima and it is therefore possible to maximise the efficiency of an interferometer over a selected frequency range, as illustrated in figure 1.6. It is interesting to note that because the beamsplitter orientation is close to the Brewster angle [14] the outgoing beam will be partially polarised.

1.3.1c Modulation of the signal

There are basically two types of modulation in general

use. Amplitude modulation is achieved by rotating a three bladed chopper in front of the source and, as such, results in half the beam being lost. For the majority of the work in this thesis phase modulation [15,16] has been employed. This is achieved by applying a sinusoidal jitter to the stationary mirror so that a periodic displacement is imposed on the path difference of the two beams. With this technique there is no blocking of the beam, and the power reaching the detector should, as a result, be twice that for an amplitude modulated beam (figure 1.7).

From equation 1.11 it can be seen that there is a constant term in the interferogram function equal to $\frac{1}{2}I_o$ which, for an amplitude modulated interferogram, must be subtracted before the interferogram is analysed. As a phase modulated interferogram is actually the derivative of this function, the constant term disappears and the shapes of amplitude and phase modulated interferograms are different (figure 1.8).

Phase modulation imposes an amplitude dependent Bessel function on the instrument profile, and by using different modulation currents it is possible to bias the instrument profile obtained with a particular beamsplitter to higher or lower wavenumbers. This is illustrated in figure 1.9 for a 175μm beamsplitter. The flexibility afforded through using phase modulation is particularly useful when high energy is required at low wavenumbers, although the Bessel functions which are imposed on the spectrum by the jittering mirror

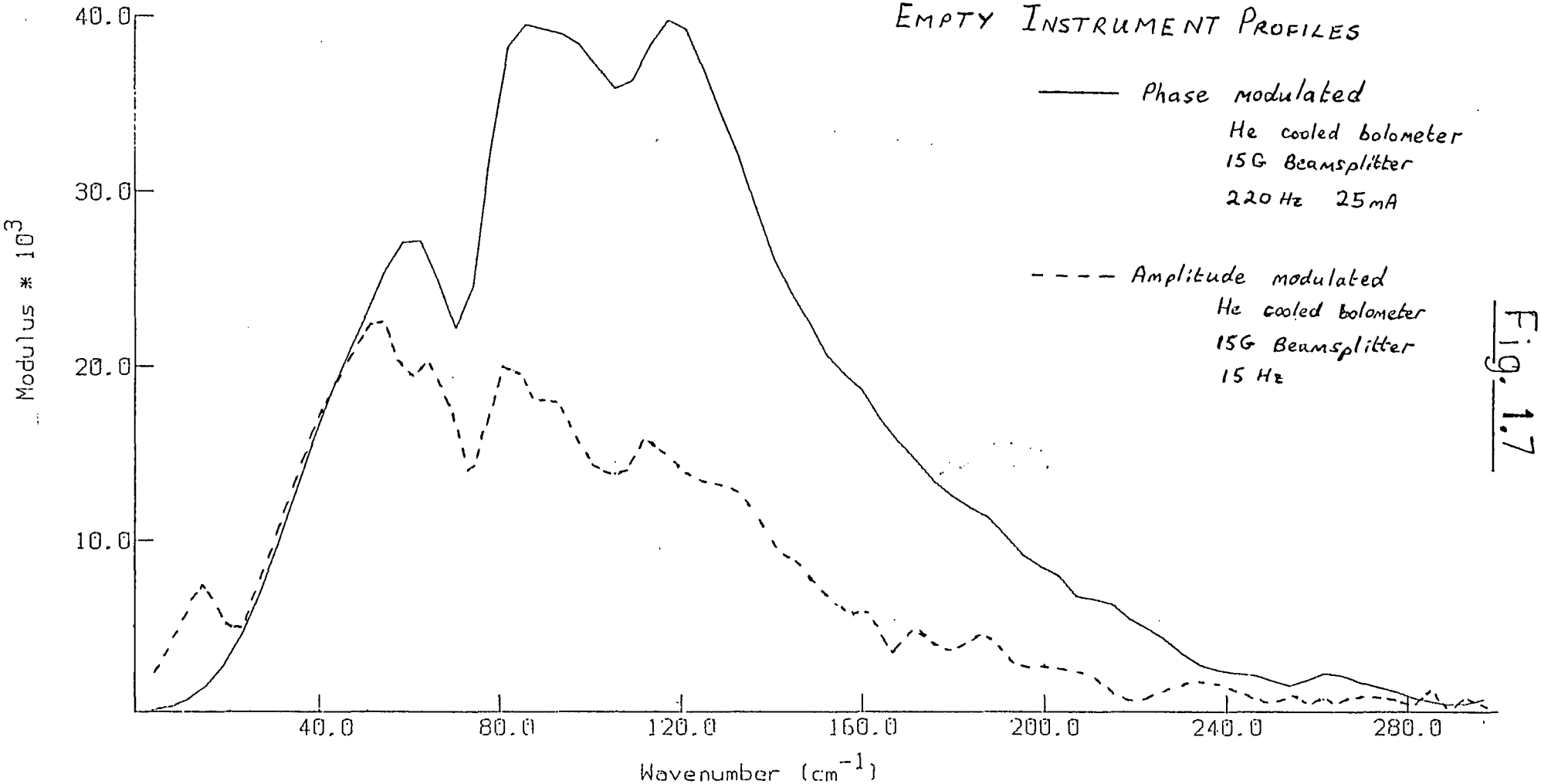
EMPTY INSTRUMENT PROFILES
Phase modulated
He cooled bolometer
15G Beamsplitter
220 Hz 25mA
Amplitude modulated
He cooled bolometer
15G Beamsplitter
15 Hz
Modulus * 10^3
40.0
30.0
20.0
10.0
40.0
80.0
120.0
160.0
200.0
240.0
280.0
Wavenumber (cm^-1)

Fig. 1.7

Fig. 1.8

Phase modulated

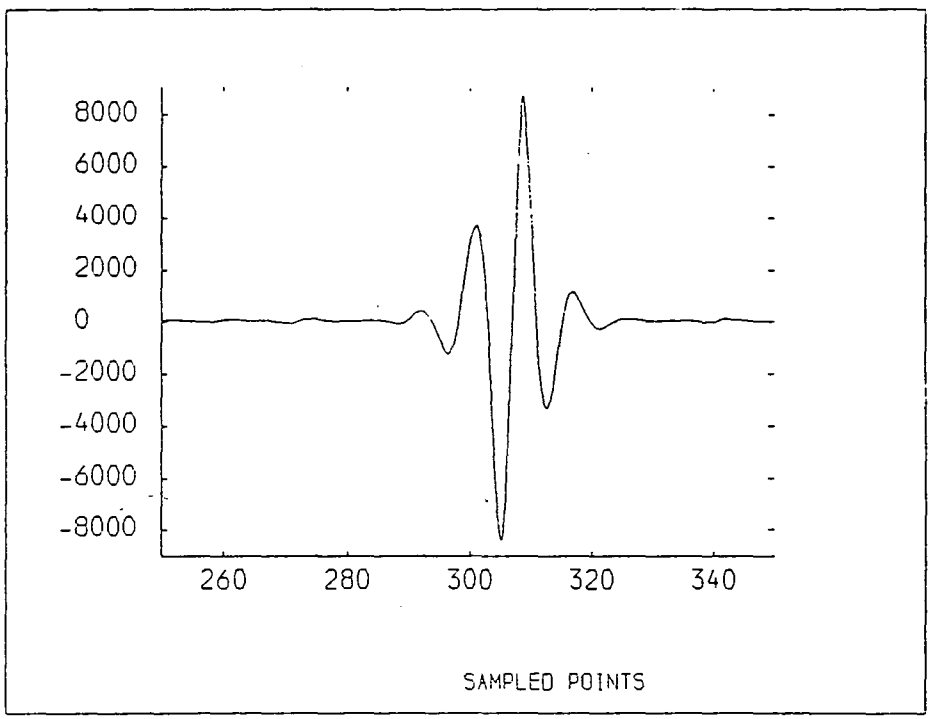

Amplitude modulated

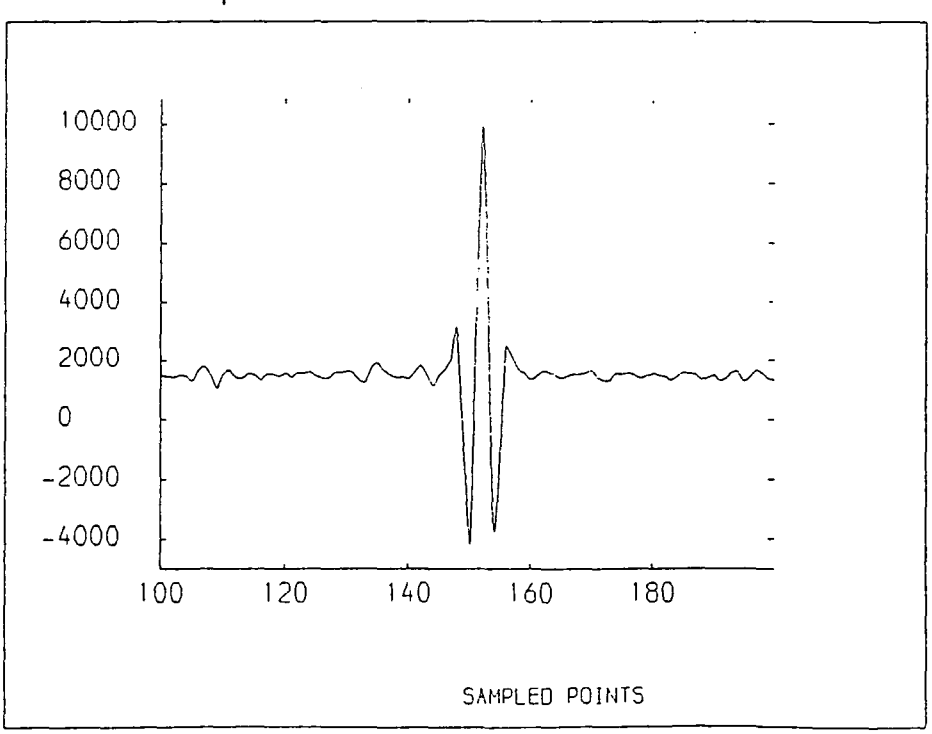

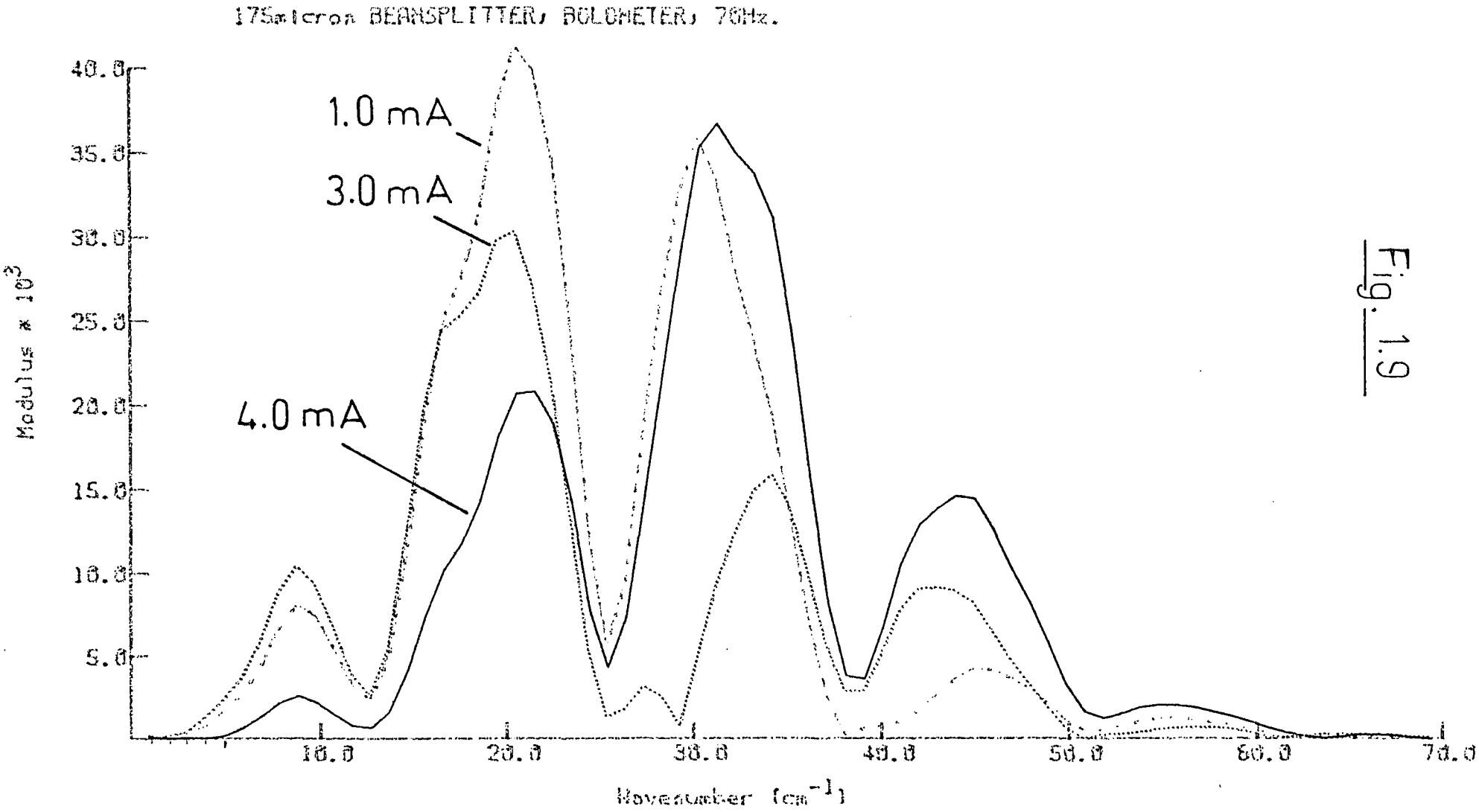
175micron BEAMSPLITTER, BOLOMETER, 70Hz.
1.0 mA
3.0 mA
4.0 mA
Modulus * 10^3
40.0
35.0
30.0
25.0
20.0
15.0
10.0
5.0
10.0
20.0
30.0
40.0
50.0
60.0
70.0
Wavenumber (cm^-1)

Fig. 19

can cause problems because they can have minima at low frequencies.

1.3.2 Dynamic Range

Amplifier noise at a given gain setting is independent of the amount of signal it receives. Similarly the analogue-to-digital converter has a limit in accuracy independent of signal level. It follows that to maximise the efficiency of the recording electronics it is important to fill the dynamic range as much as possible. Careful selection of preamplifier and lock-in amplifier settings is necessary to match the maximum value of the interferogram with the top of the dynamic range.

For an amplitude modulated interferogram the constant part of the function discussed in the previous section occupies up to half of the dynamic range but can be significantly reduced using a zero-offset on the lock-in amplifier. If, however, the two beams are not equivalent, equation 1.11 does not apply and the constant part of the interferogram can be significantly larger than the signal. In cases such as this the zero-offset available may be insufficient. Such a situation can arise if the aperture in one arm is different from the other or through having the sample in one arm during a dispersive experiment.

This problem has been overcome through generating a constant signal modulated at the same frequency as the

experimental signal and subtracting the two using the lock-in aplifier in the A-B mode (see section 3.1.2).

Such problems, of course, do not exist using phase modulation which is thus especially preferred in a dispersive instrument.

1.3.3 Apodisation

The noise in an interferogram is fairly constant with respect to path difference but the signal is concentrated at and around zero path difference. Thus signal-to-noise becomes progressively poorer at path differences away from the zero position. An ideal interferogram should reach zero intensity at infinite path difference, but since in a real situation interferograms are truncated they are inevitably non-zero at their extremities, and this leads to distortion of the computed spectrum (figure 1.10).

Apodisation is a process whereby the interferogram is convolved with a function which reduces it gradually to zero at the limit of travel, thus effectively smoothing the spectrum. Throughout this work an apodisation function of the form $\cos^2\theta$ has been used, where θ varies from 0 at zero path difference to $\pi/2$ at the end of the interferogram.

1.3.4 Resolution

The resolution depends on the path difference, x,

Fig. 1.10

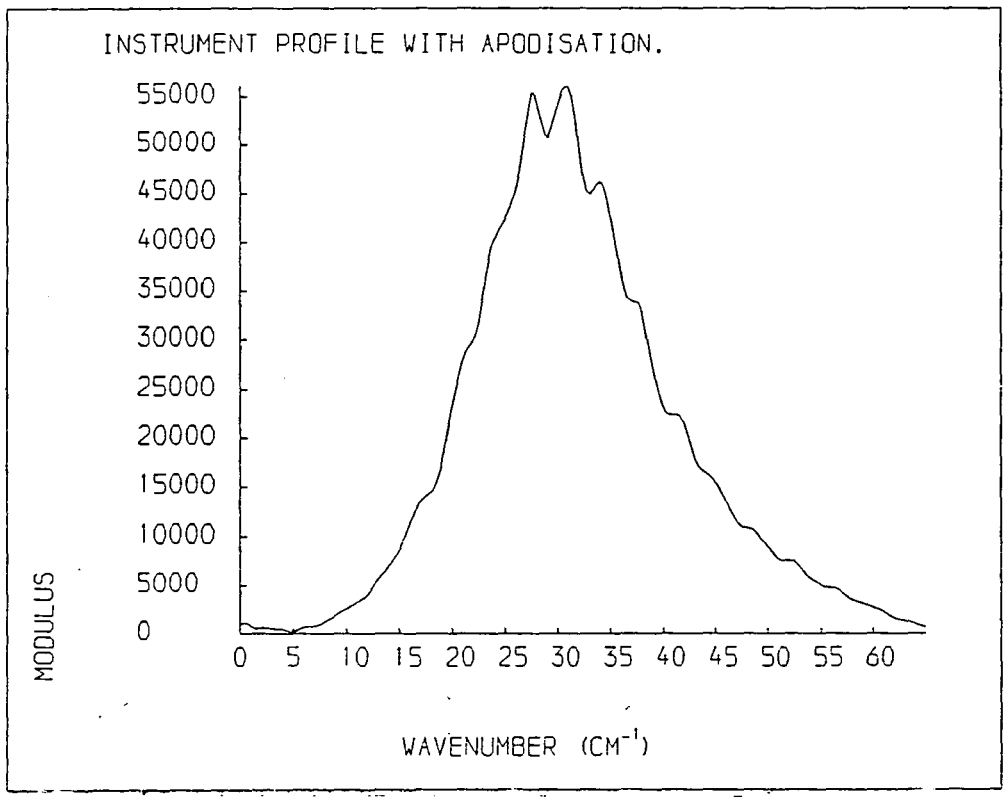
INSTRUMENT PROFILE WITH APODISATION.
55000
50000
45000
40000
35000
30000
25000
20000
15000
10000
5000
0
MODULUS
0 5 10 15 20 25 30 35 40 45 50 55 60
WAVENUMBER (CM-1)

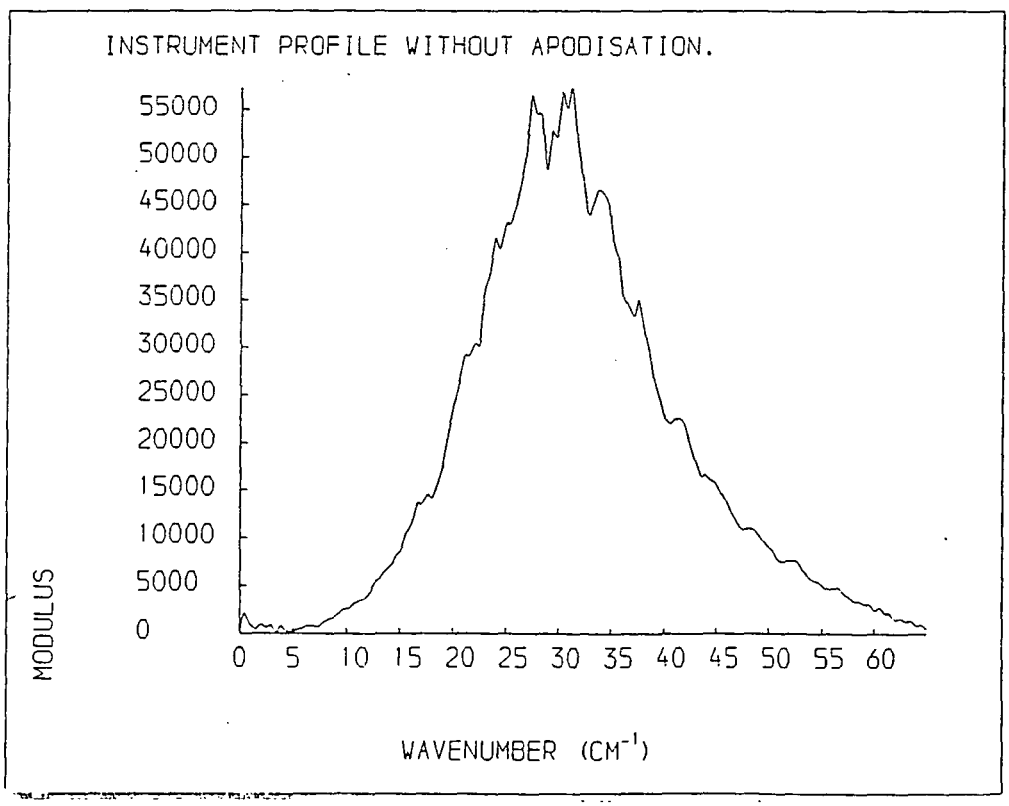
INSTRUMENT PROFILE WITHOUT APODISATION.
55000
50000
45000
40000
35000
30000
25000
20000
15000
10000
5000
0
MODULUS
0 5 10 15 20 25 30 35 40 45 50 55 60
WAVENUMBER (CM-1)

scanned on one side of zero path difference according to

$$R \sim 1 / x \tag{1.30}$$

Apodisation, however, has the effect of approximately halving the resolution obtained, so scanning a path difference of 5mm from zero path difference will give an effective resolution of approximately $4cm^{-1}$.

Figures 1.11 to 1.14 illustrate the effect of increasing the resolution on a spectrum of water vapour recorded between 10 and 45 cm^{-1}. For comparison, table 1.1 lists rotational lines that have been assigned in the literature [17,18].

Lines 8 and 9 are separated by approximately 0.5 cm^{-1}, and with a spectral resolution of 1 cm^{-1} these two lines can clearly not be distinguished from one another. Doubling the resolution to $0.5cm^{-1}$ is enough to recognise that there are two discrete bands and to resolve line 10. Increasing the resolution further improves the appearance of the spectrum and confirms the integrity of the individual lines. It is worth noting that increasing the resolution also has the effect of increasing the noise in the spectrum. This is because the signal generally decreases with increasing path difference, so that the further from zero path difference the data is recorded, the higher is the relative contribution of noise.

$$S/N \propto 1 / \sqrt{L} \tag{1.31}$$

Table 1.1

rotatinal lines for water vapour [17, 18]

	$\bar{\nu}$ (cm^{-1})	relative strength
1.	14·94	w
2.	18·58	m
3.	20·70	w
4.	25·08	s
5.	30·56	w
6.	32·37	w
7.	32·95	s
8.	36·60	s
9.	37·13	s
10.	37·92	w
11.	38·47	s
12.	38·79	s
13.	40·28	s
14.	40·99	s

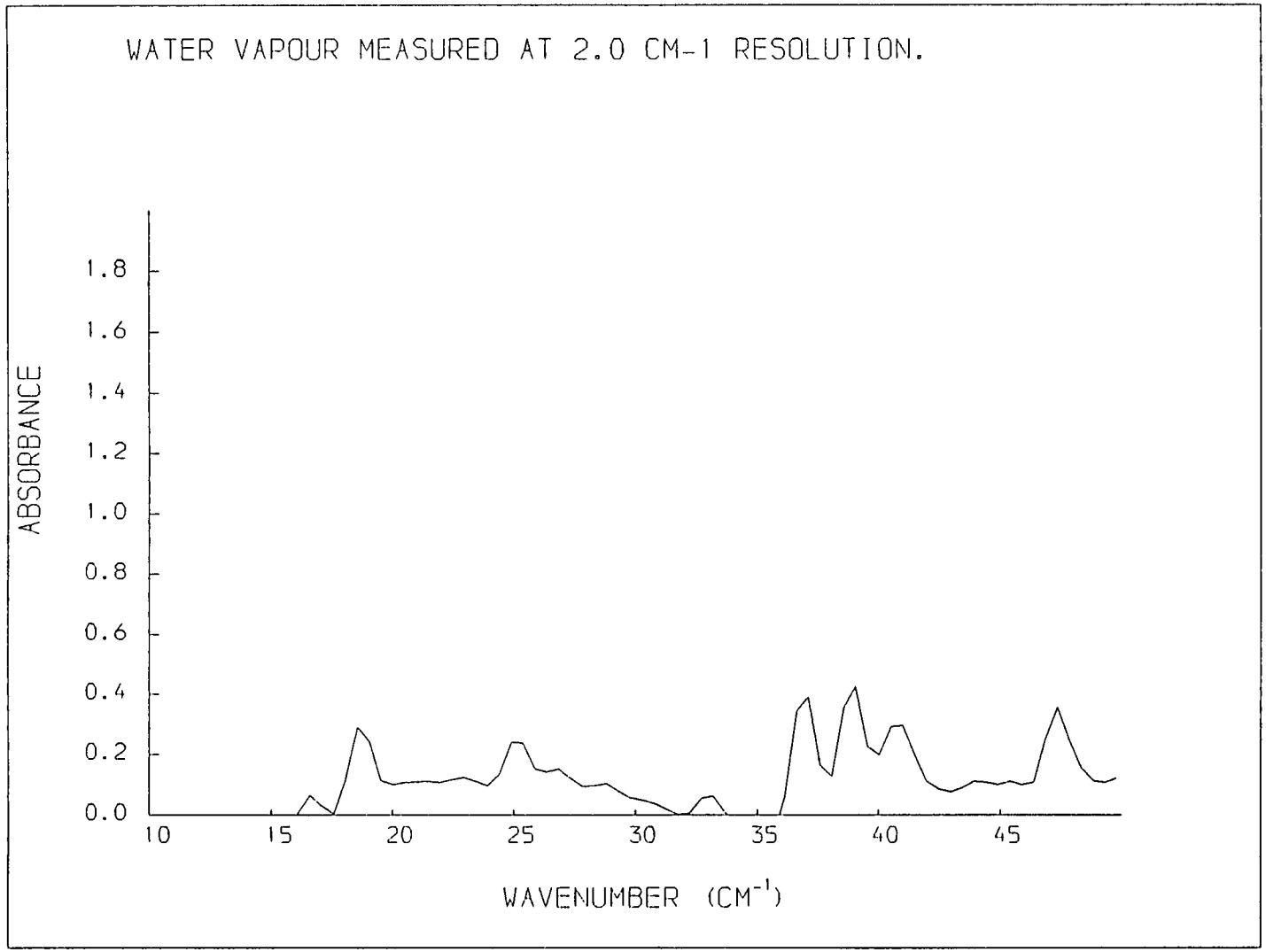
WATER VAPOUR MEASURED AT 2.0 CM-1 RESOLUTION.
ABSORBANCE
1.8
1.6
1.4
1.2
1.0
0.8
0.6
0.4
0.2
0.0
10
15
20
25
30
35
40
45
WAVENUMBER (CM-1)

Fig. 1.11

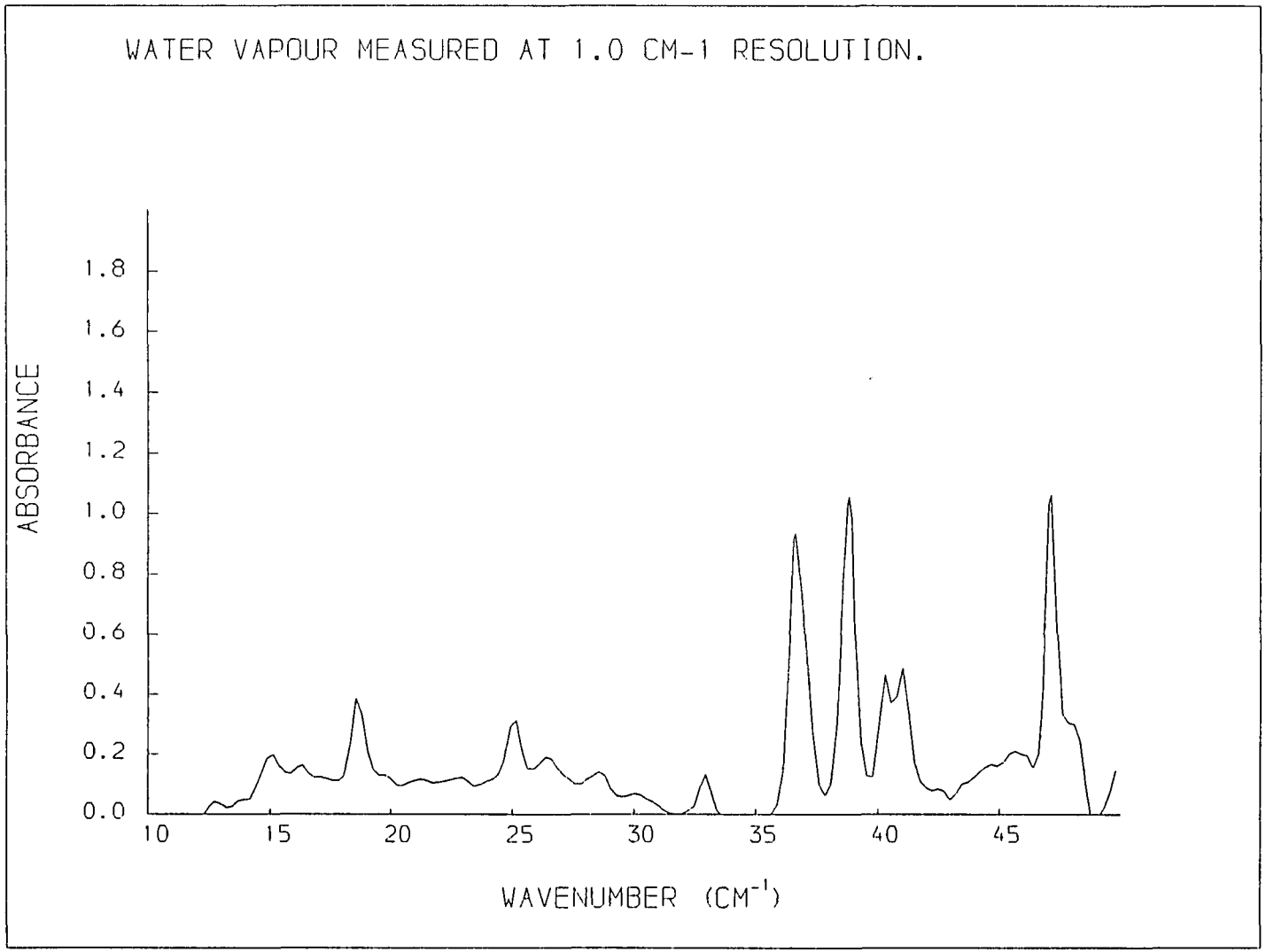
WATER VAPOUR MEASURED AT 1.0 CM-1 RESOLUTION.
ABSORBANCE
1.8
1.6
1.4
1.2
1.0
0.8
0.6
0.4
0.2
0.0
10
15
20
25
30
35
40
45
WAVENUMBER (CM-1)

Fig. 1.12

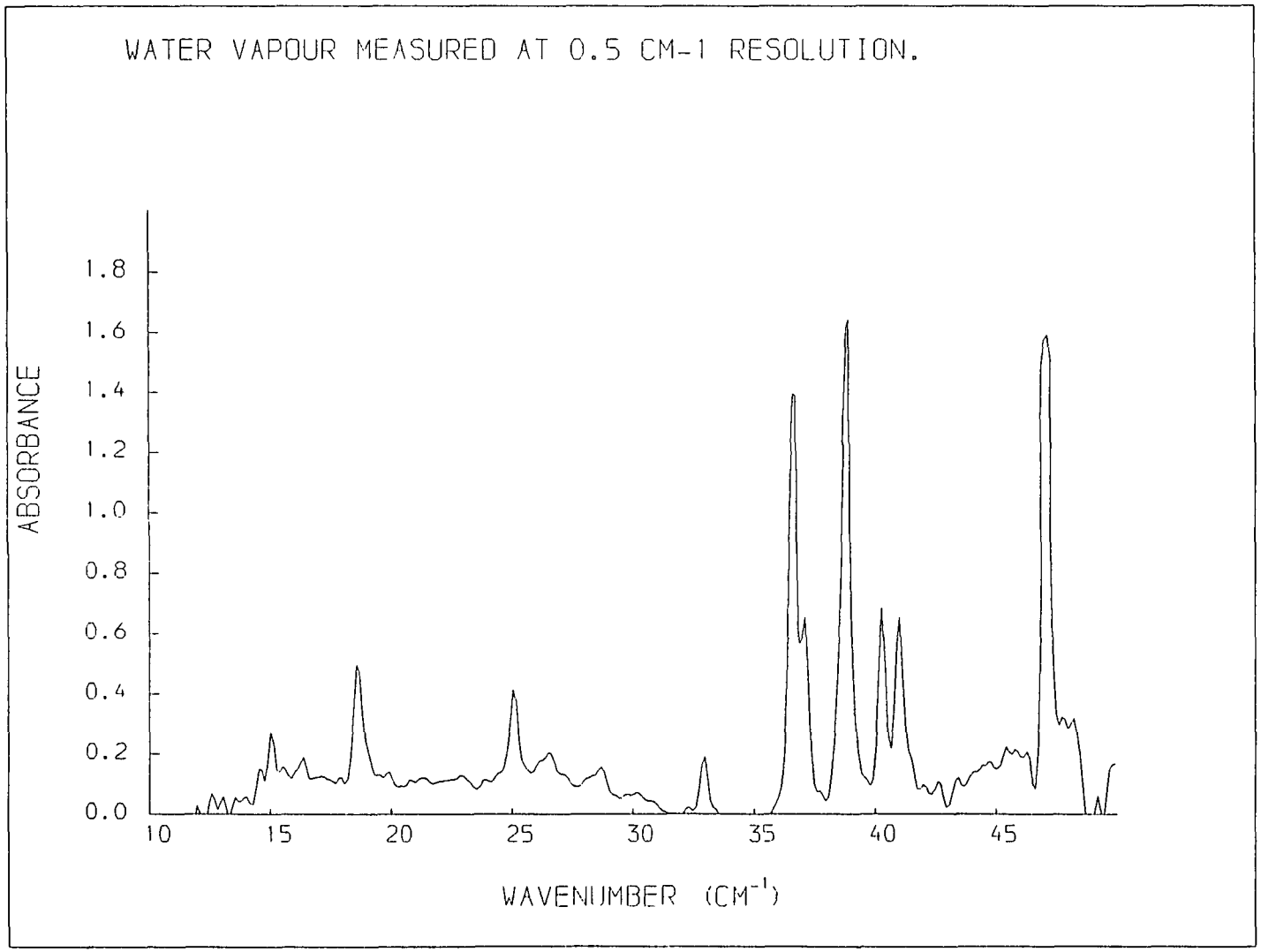
WATER VAPOUR MEASURED AT 0.5 CM-1 RESOLUTION.
ABSORBANCE
1.8
1.6
1.4
1.2
1.0
0.8
0.6
0.4
0.2
0.0
10
15
20
25
30
35
40
45
WAVENUMBER (CM-1)

Fig. 1.13

Fig. 1.14

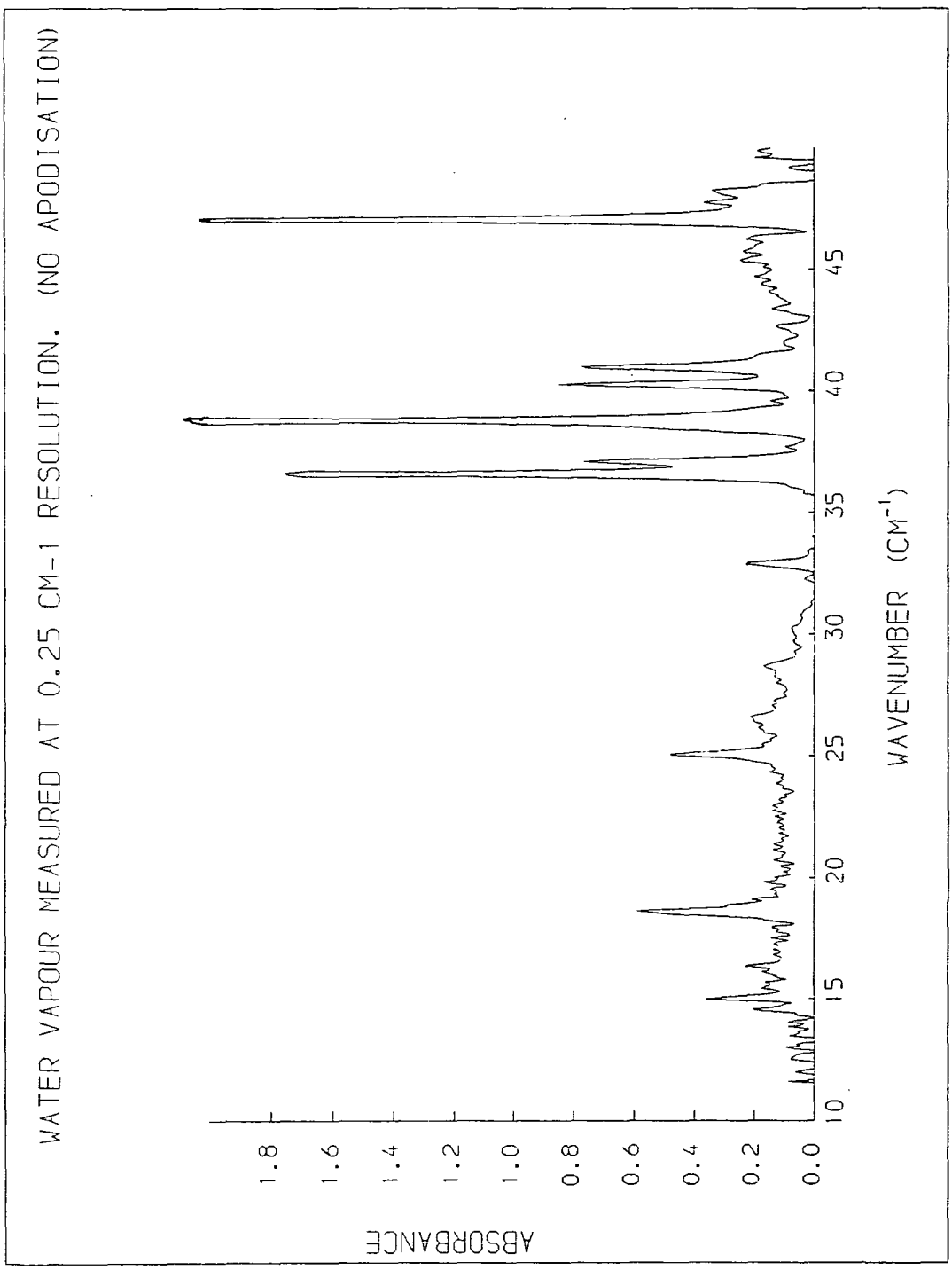
WATER VAPOUR MEASURED AT 0.25 CM-1 RESOLUTION. (NO APODISATION)
ABSORBANCE
0.0
0.2
0.4
0.6
0.8
1.0
1.2
1.4
1.6
1.8
10
15
20
25
30
35
40
45
WAVENUMBER (CM-1)

where L = total displacement.

Also, when the band half-width is comparable to the spectral resolution it is important to have good resolution if quantitative intensity measurements are required.

1.3.5 Noise in the interferogram

Most of the preceeding sections are concerned in some way with increasing the signal to noise ratio in a spectrum. There are, however, more direct ways of reducing the noise in an interferogram. Lock-in amplifiers are capable of integrating a signal over a period of time which is controlled by a time constant. A high time constant means that more noise can be averaged out, since it is random, but the scanning time must be slower. In general, interferograms are scanned at two or three times the inverse time constant.

Another method, which is effectively the same, is to record several interferograms and average them, a process known as 'catting'. The signal to noise improvement is then proportional to the square root of the number of averaged interferograms. Catting can be performed in the interferogram or in the spectrum.

The types of noise which must be dealt with in Fourier transform spectroscopy can be conveniently categorised into two groups: additive and multiplicative noise. Additive noise maintains a fairly constant level independently of the

amount of signal being detected. Multiplicative noise increases with the signal and so is at its largest when the signal is at a maximum. The multiplexing advantage of interferometers does not apply for multiplicative noise. Examples of sources of additive noise are those caused by the detector and associated recording electronics and those arising from erratic fluctuations in the reference modulating system. Multiplicative noise can be caused by fluctuations in the intensity of the radiation caused by, for example, an unstable source.

The most important source of noise for far infrared work is usually that from the detector, which is additive. The experimental interferogram is then

$$I'(x) = I(x) + \varepsilon(x) \tag{1.32}$$

For single sided, phase modulated interferograms the spectrum is given by [1]

$$S'(\bar{\nu}) = S(\bar{\nu}) + N(\bar{\nu}) = 2\int_0^\infty \left[I(x) + \varepsilon(x)\right] \sin(2\pi\bar{\nu}x)\, dx \tag{1.33}$$

since the Fourier transform is a linear-process [4]. Thus the noise in the spectrum is the sine transformation of the noise in the interferogram and is additive to the spectral intensity.

The situation is more complicated for double-sided interferograms since the modulus is obtained by a non-linear

process. If sine and cosine transforms are given by

$$p(\bar{\nu}) = p'(\bar{\nu}) + N(\bar{\nu}) \tag{1.34}$$

$$q(\bar{\nu}) = q'(\bar{\nu}) + M(\bar{\nu}) \tag{1.35}$$

then the modulus is

$$\text{mod}\{S(\bar{\nu})\} = \Big[p'(\bar{\nu})^2 + q'(\bar{\nu})^2 + 2p'(\bar{\nu})N(\bar{\nu}) + 2q'(\bar{\nu})M(\bar{\nu}) + N^2(\bar{\nu}) + M^2(\bar{\nu}) \Big]^{\frac{1}{2}} \tag{1.36}$$

and the average values of $N^2(\bar{\nu})$ and $M^2(\bar{\nu})$ are non-zero so that, even if there were no signal, mod $\{\hat{S}(\bar{\nu})\} > 0$. When ratioing two modulus spectra over regions of low transmissivity this can lead to large systematic errors.

CHAPTER 2

DETERMINATION OF INFRARED OPTICAL CONSTANTS

2.1 Introduction

The propagation of any electromagnetic wave through an isotropic medium can be described using Maxwell's equations involving the complex electric field vector, $\hat{E}$ [19,20].

$$\nabla^2\hat{E} = \frac{\hat{\varepsilon}\hat{\mu}}{c^2}\frac{\partial^2 E}{\partial t^2} + \frac{4\pi\hat{\mu}\hat{\sigma}}{c^2}\frac{\partial E}{\partial t} \qquad (2.1)$$

were $\hat{\varepsilon}$ is the complex permittivity, $\hat{\sigma}$ the complex conductivity and $\hat{\mu}$ the complex permeability (which is unity for non-magnetic materials and, as such, shall be ignored throughout this work). For a dielectric medium the conductivity is zero.

Through solving equation 2.1 it can be shown [19] that the phase velocity, $\hat{c}'$, of propagation through a medium is given by

$$\hat{c}' = c / \sqrt{\hat{\varepsilon}} \qquad (2.2)$$

and from the definition of refractive index the important relationship

$$\hat{n} = \hat{c}' / c = \sqrt{\hat{\varepsilon}} \qquad (2.3)$$

is derived.

Considering the real and imaginary parts of $\hat{n}$ and $\hat{\varepsilon}$ as a function of frequency introduces four optical constants which are used extensively for the description of observed spectral properties

$$\hat{n}(\bar{\nu}) = n(\bar{\nu}) + i\kappa(\bar{\nu}) \tag{2.4}$$

$$\hat{\varepsilon}(\bar{\nu}) = \varepsilon'(\bar{\nu}) + i\varepsilon''(\bar{\nu}) \tag{2.5}$$

n is the real refractive index and κ the absorption index which is often converted to the absorption coefficient introduced in equation 1.22

$$\alpha(\bar{\nu}) = 4\pi\bar{\nu}\kappa(\bar{\nu}) \tag{2.6}$$

ε' is the real permittivity and describes the capacitance of the medium. ε'' is the dielectric loss and relates to the rate at which the electric field loses energy to the medium. If the limiting permittivities at low and high frequencies are denoted by ε_o and ε_∞ respectively, ε' and ε'' can be expressed (see section 4.2.1) in terms of a relaxation time, τ

$$\varepsilon'(\omega) = \varepsilon_\infty + \frac{\varepsilon_o - \varepsilon_\infty}{1 + \omega^2\tau^2} \tag{2.7}$$

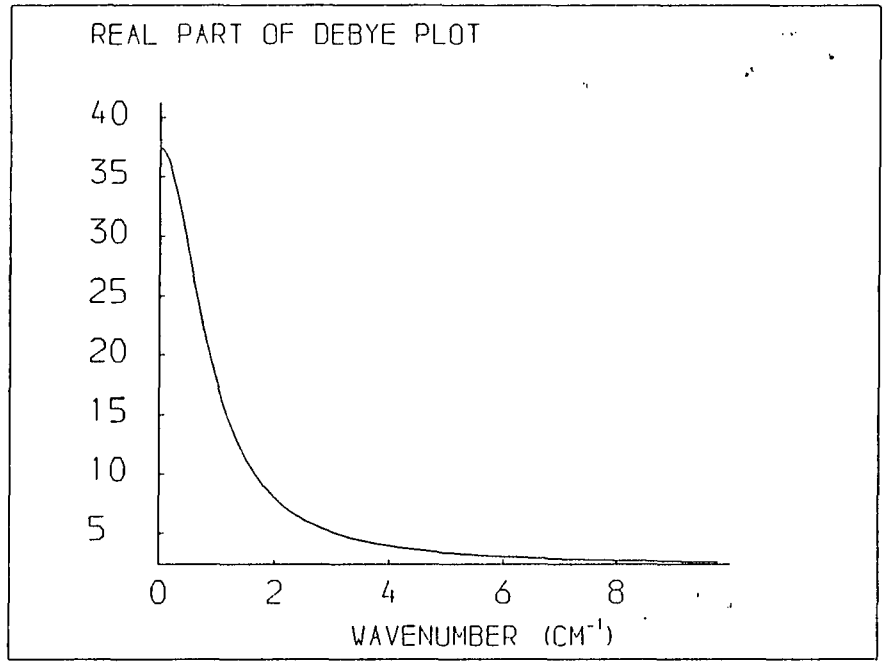
REAL PART OF DEBYE PLOT
40
35
30
25
20
15
10
5
0
2
4
6
8
WAVENUMBER (CM-1)

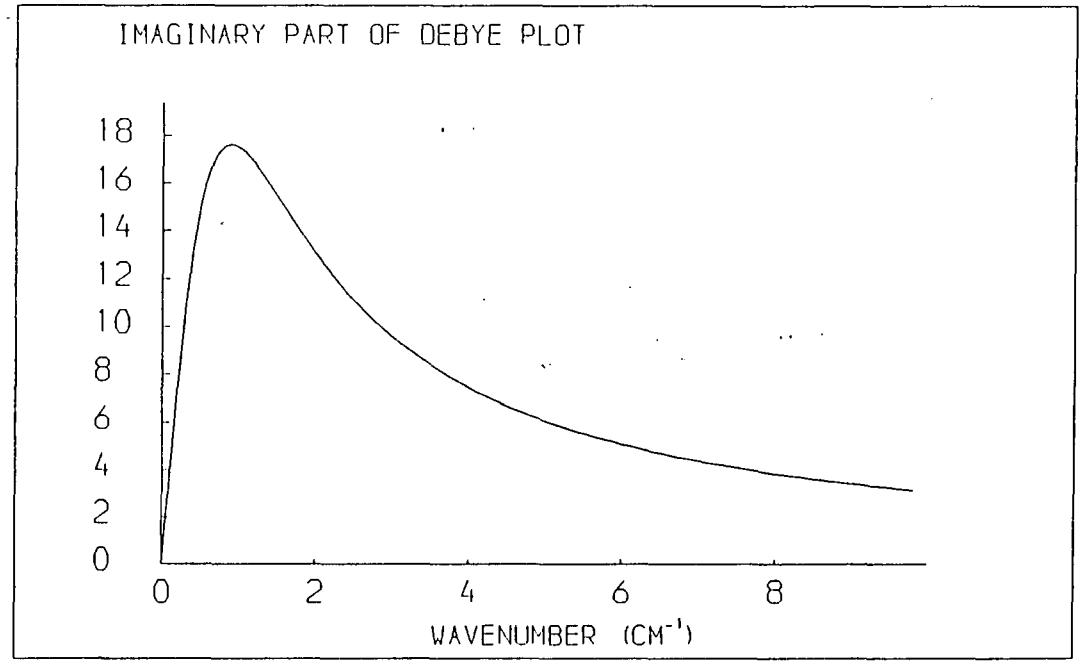
IMAGINARY PART OF DEBYE PLOT
18
16
14
12
10
8
6
4
2
0
0
2
4
6
8
WAVENUMBER (CM-1)

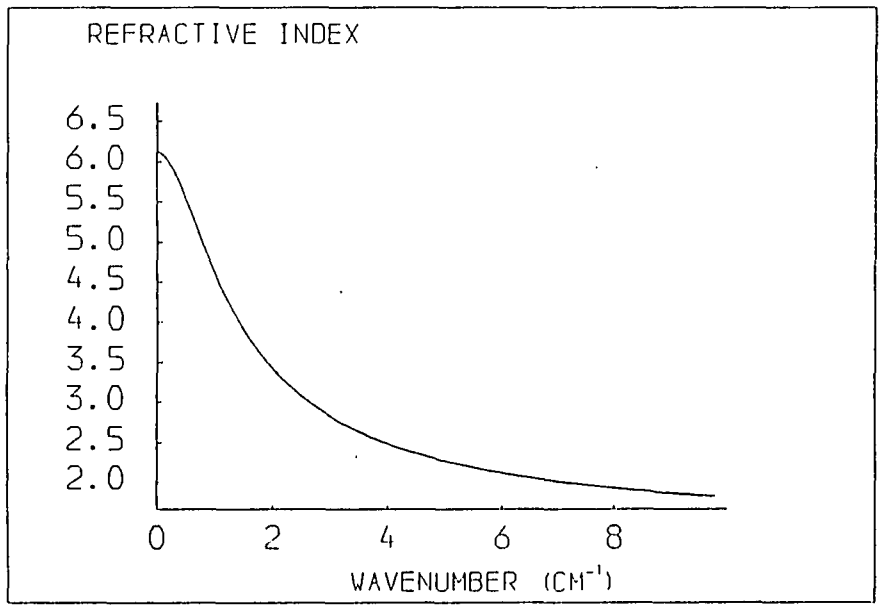
REFRACTIVE INDEX
6.5
6.0
5.5
5.0
4.5
4.0
3.5
3.0
2.5
2.0
0
2
4
6
8
WAVENUMBER (CM-1)

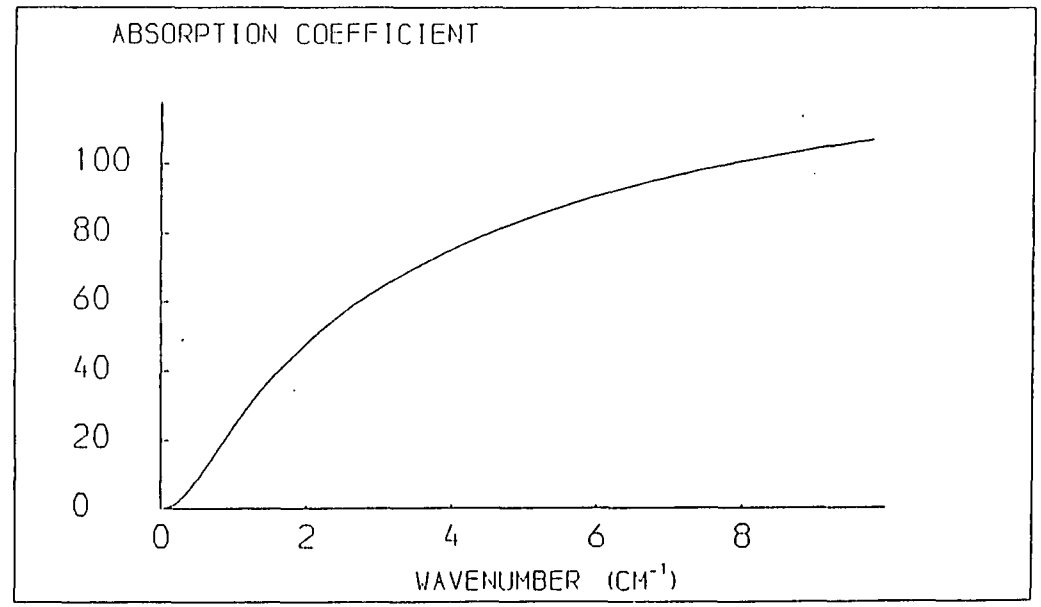
ABSORPTION COEFFICIENT
100
80
60
40
20
0
0
2
4
6
8
WAVENUMBER (CM-1)

Fig. 2.1

$$\varepsilon''(\omega) = \frac{(\varepsilon_o - \varepsilon_\infty)\omega\tau}{1 + \omega^2\tau^2} \tag{2.8}$$

where ω is angular frequency. These identities are called the Debye equations and ignore any inertial terms in the equations of motion and assume an exponential relaxation process. They are illustrated in figure 2.1.

It is useful when comparing microwave and infrared experiments to be able to interconvert $\hat{n}$ and $\hat{\varepsilon}$ data, and this is readily done using the following equations, [21,22]

$$\varepsilon'(\bar{\nu}) = n^2(\bar{\nu}) - \kappa^2(\bar{\nu}) \tag{2.9}$$

$$\varepsilon''(\bar{\nu}) = 2n(\bar{\nu})\kappa(\bar{\nu}) \tag{2.10}$$

$$n^2(\bar{\nu}) = \tfrac{1}{2}\left\{\left[\varepsilon'(\bar{\nu})^2 + \varepsilon''(\bar{\nu})^2\right]^{\frac{1}{2}} + \varepsilon'\right\} \tag{2.11}$$

$$\kappa^2(\bar{\nu}) = \tfrac{1}{2}\left\{\left[\varepsilon'(\bar{\nu})^2 + \varepsilon''(\bar{\nu})^2\right]^{\frac{1}{2}} - \varepsilon'\right\} \tag{2.12}$$

For conducting materials the second term in equation 2.1 is non zero and the conductivity, $\sigma(\bar{\nu})$, can be related to the other optical constants according to [23]

$$\sigma(\bar{\nu}) = \frac{n(\bar{\nu})\alpha(\bar{\nu})}{4\pi} \tag{2.13}$$

Thus, through the experimental determination of $\hat{n}(\bar{\nu})$ it is possible to determine all the other optical constants

required. The remainder of this chapter is devoted to describing different procedures for obtaining the real and imaginary parts of the complex refractive index.

2.2 Transmission methods

2.2.1 Measurement of Absorption Coefficient

These correspond to placing the sample at position P1 in figure 1.3. The absorption coefficient can then be calculated by use of equation 1.22. If the ratio I/I_o in equation 1.21 corresponds to sample versus no sample in the beam then the computed absorption coefficient will be incorrect due to reflection losses at the interfaces. As these reflection losses depend only on the difference in refractive index across an interface they can be eliminated by ratioing two samples of different thickness. The thickness, ℓ, in equation 1.22 must then be replaced by the difference in sample thicknesses.

An inaccurate knowledge of sample thickness leads to the main source of systematic error in the computed absorption coefficient, and this becomes critically important for lossy samples where very small pathlengths are required. Sample thickness was determined either by averaging several readings using a micrometer or by examining channel fringes in a mid-infrared spectrum using

equation 2.15, described in the next section.

2.2.2 Measurement of Refrative Index

2.2.2a By channel Spectra

Channel fringes in the computed spectrum arise through multiple reflections within the sample. Figure 2.2 illustrates the effect of a single internal reflection within a sample of pathlength d and average refractive index $\bar{n}$. The reflected beam suffers a path-difference displacement of

$$\delta = 4 \bar{n} d \tag{2.14}$$

and a subsidiary interferogram appears at this distance away from zero path position, much reduced in intensity because it has travelled further through the sample. Successive internal reflections will be correspondingly less intense.

Transformation of such an interferogram results in a power spectrum which contains sinusoidal oscillations which are separated by [20]

$$\bar{\nu}_1 - \bar{\nu}_2 = k / 2\bar{n}d \tag{2.15}$$

where k is the number of maxima between $\bar{\nu}_1$ and $\bar{\nu}_2$.

These methods of determining n by transmission can only give an average refractive index which is not frequency dependent since they ignore the phase shifts that occur on

Fig. 2.2

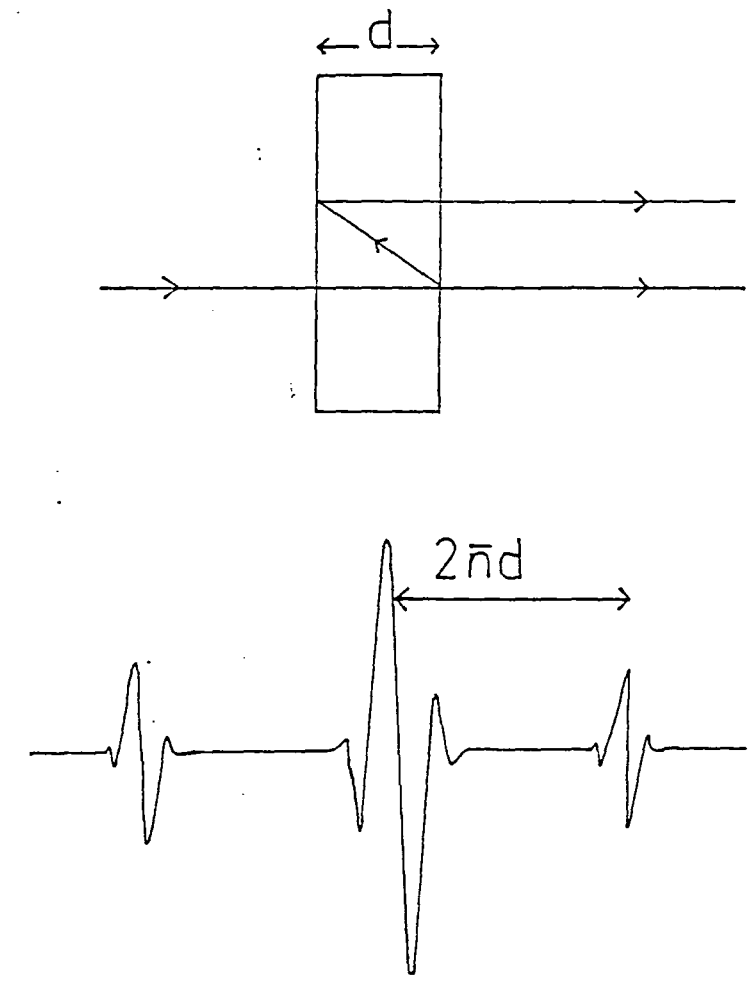

reflection. There is also a difficulty involved in locating the precise frequency of the maximum points on the channel spectrum unless high resolution is used.

2.2.2b By Kramers-Krönig Analysis

It was discussed in section 1.1.1c how the Causality principle led to R(t) being asymmetric and equal to zero for $t < 0$. Any such one-sided function may be considered as a sum of its odd and even parts, i.e.

$$R(t) = R_e(t) + R_o(t) \tag{2.16}$$

and since $R(t) = 0$ for $t < 0$, then

$$R_e(-t) = - R_o(-t) \tag{2.17}$$

Now, from the definition of odd and even functions:

$$R_e(t) = R_e(-t); \; R_o(t) = -R_o(-t), \tag{2.18}$$

then the odd and even parts of the function are related according to

$$R_o(t) = R_e(t) \; \mathrm{sgn}(t) \tag{2.19}$$

where the signum function, sgn(t), is defined as in figure

Fig. 2.3

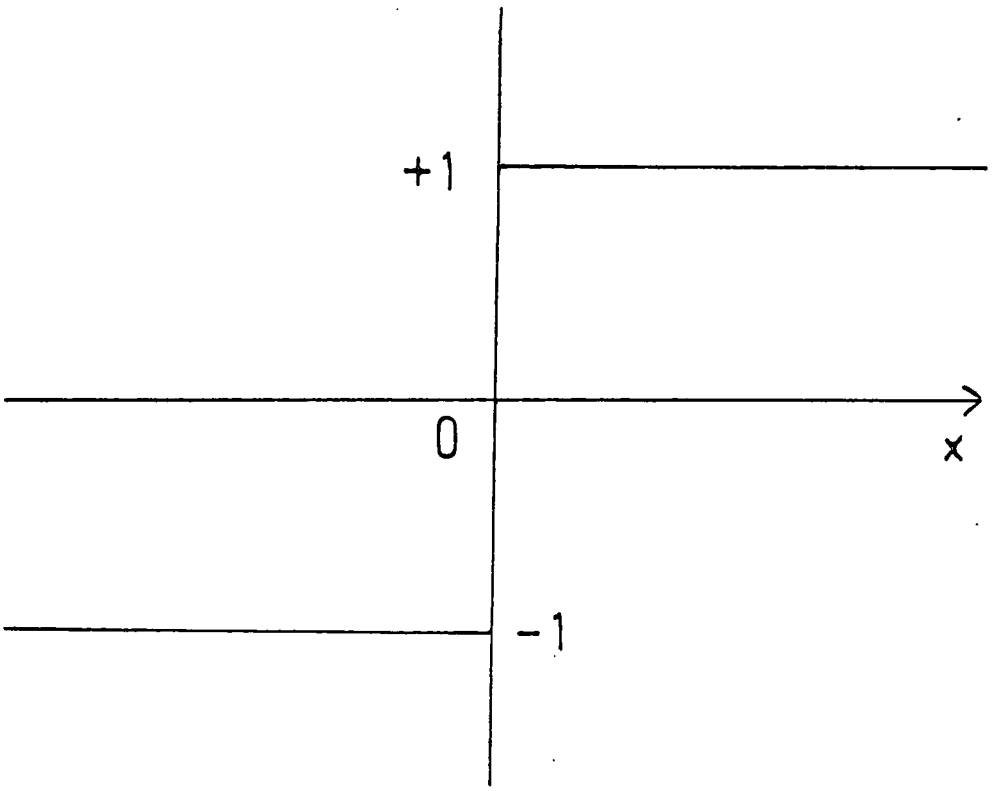

The signum function

$$\operatorname{sgn}(x) = 1 \quad \text{for } x > 0$$

$$\operatorname{sgn}(x) = -1 \quad \text{for } x < 0$$

2.3.

Fourier transforming R(t) in order to get to the frequency domain gives a transfer function [1],

$$\hat{T}(\bar{\nu}) = \int_{-\infty}^{\infty} R(t)\,\mathrm{expi}2\pi\bar{\nu}t\,dt \tag{2.20}$$

which, from equation 2.16 can be expressed as

$$\hat{T}(\bar{\nu}) = T'(\bar{\nu}) + iT''(\bar{\nu}) = \int_{-\infty}^{\infty} Re(t)\cos 2\pi\bar{\nu}t\,dt + i\int_{-\infty}^{\infty} R_o(t)\sin 2\pi\bar{\nu}t\,dt \tag{2.21}$$

and substituting in equation 2.19 gives

$$T'(\bar{\nu}) = \int_{-\infty}^{\infty} R_o(t)\ \mathrm{sgn}(t)\ \cos 2\pi\bar{\nu}t\,dt \tag{2.22}$$

and

$$T''(\bar{\nu}) = \int_{-\infty}^{\infty} Re(t)\ \mathrm{sgn}(t)\ \sin 2\pi\bar{\nu}t\,dt$$

$$= -i\ \mathrm{sgn}(t) \int_{-\infty}^{\infty} Re(t)\ \mathrm{expi}2\pi\bar{\nu}t\,dt \tag{2.23}$$

since

$$\int_{-\infty}^{\infty} \cos x = 0\ . \tag{2.24}$$

Now the inverse Fourier transform of sgn(t) is shown trivially through equation 1.2 to be $-i/(\pi\bar{\nu})$, so equation 2.23 can be written as a product of Fourier transforms

$$T''(\nu) = \xi\{-1/\pi\bar{\nu}\}.\xi\{T'(\bar{\nu})\} \tag{2.25}$$

and hence from equation 1.5

$$T''(\bar{\nu}) = \xi\{(-1/\pi\bar{\nu}) * T'(\bar{\nu})\} \tag{2.26}$$

Applying convolution theorem to this by use of equation 1.4 gives the general Kramers-Krönig relation

$$T''(\bar{\nu}) = \frac{-P}{\pi}\int_{-\infty}^{\infty} \frac{T'(\bar{\nu})}{\bar{\nu}' - \bar{\nu}}\, d\bar{\nu} \tag{2.27}$$

where P means the principal value and allows for the singularity at $\bar{\nu} = \bar{\nu}'$.

In the same way it cn be shown that

$$T'(\bar{\nu}) = \frac{P}{\pi}\int_{-\infty}^{\infty} \frac{T''(\bar{\nu})}{\bar{\nu}' - \bar{\nu}}\, d\bar{\nu} \tag{2.28}$$

By inspection, equations 2.27 and 2.28 conform to the definition of a Hilbert transform [1] , and we say that T' and T" are Hilbert transforms of one another

$$H\{f(x)\} = \frac{1}{\pi}\int_{-\infty}^{\infty} \frac{f(x')}{x' - x}\, dx' \tag{2.29}$$

A Hilbert transform does not alter the amplitude of a function but alters the phase by $\pi/2$. Thus, two consecutive Hilbert transforms alter the phase by π and we have

$$H\{H\{f(x)\}\} = -f(x) \tag{2.30}$$

These properties are illustrated in figure 2.4 where it can be seen that an even function is converted to an odd function, and vice versa.

Fig. 2.4

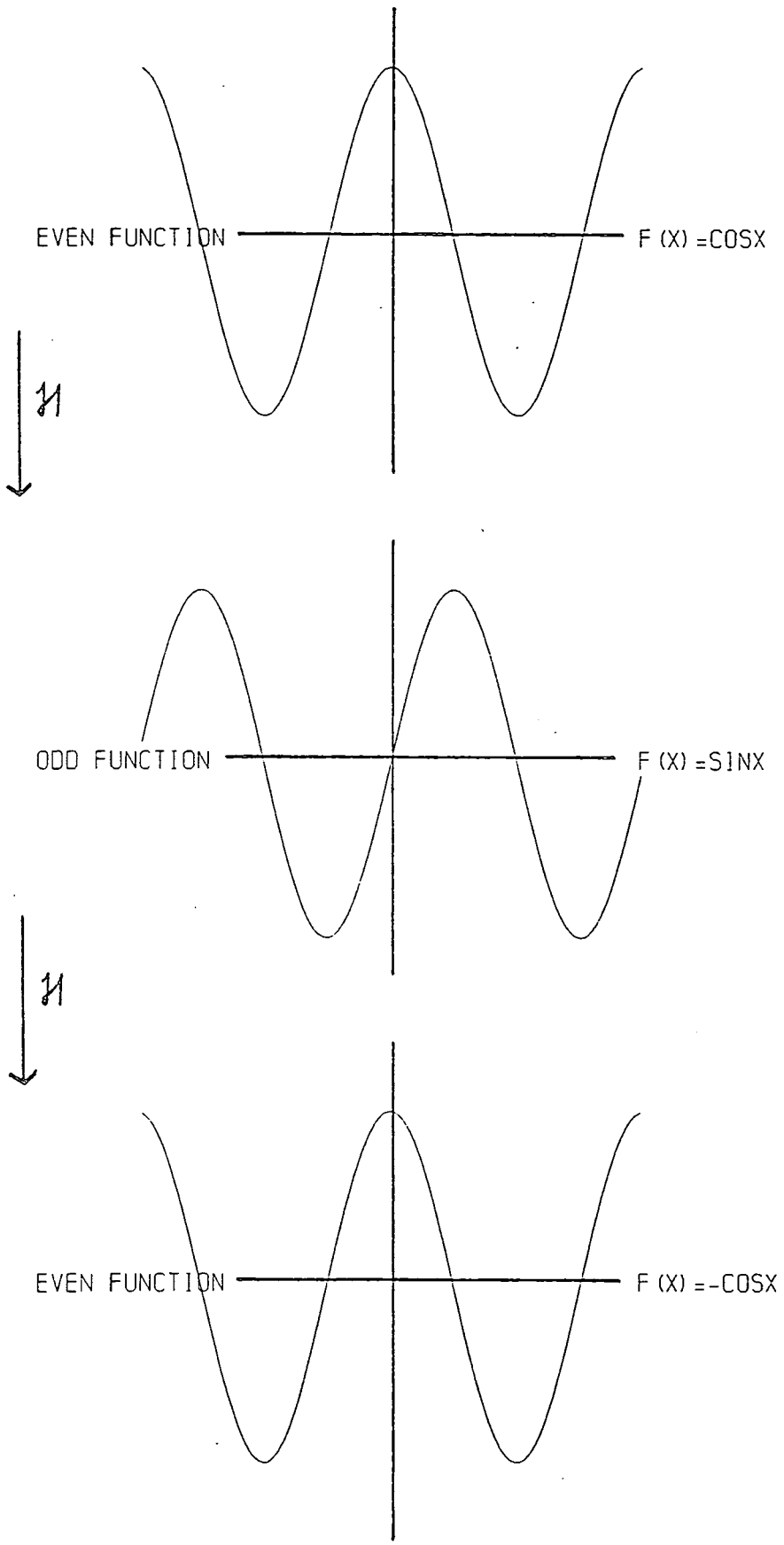
EVEN FUNCTION
F (X) =COSX
ODD FUNCTION
F (X) =SINX
EVEN FUNCTION
F (X) =-COSX

Fig. 2.5

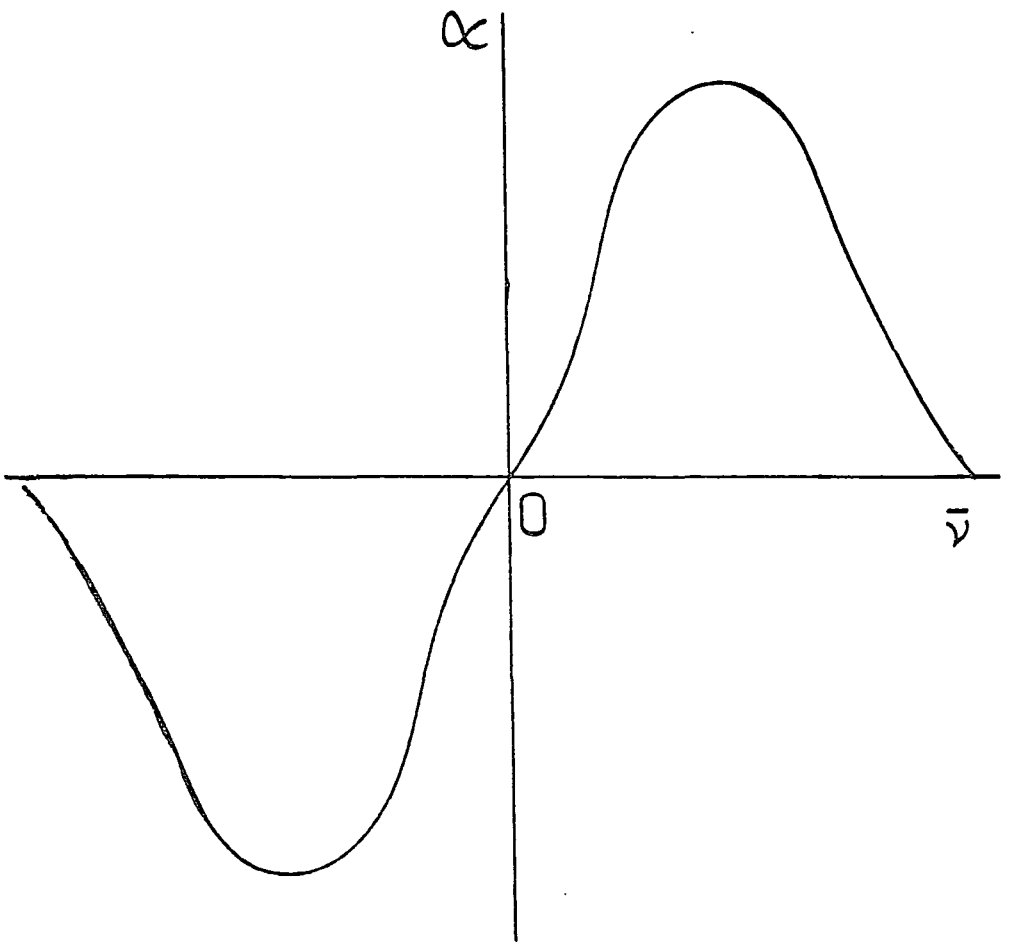

Further symmetry arguments [5] can be used to alleviate the difficulty of having negative frequencies in equations 2.27 and 2.28, and replacing our transfer function by $\hat{n}(\bar{\nu})$ leads to the familiar relationship

$$n(\bar{\nu}) - n_{\infty} = \frac{c}{2\pi^2} P \int_0^{\infty} \frac{\alpha(\bar{\nu}')}{\bar{\nu}'^2 - \bar{\nu}^2} d\bar{\nu} \qquad (2.31)$$

where n_{∞} has been introduced to allow for the fact that the right hand side of the equation is zero at infinite frequency.

In practical terms, to derive refractive index from absorption coefficient data, it is necessary to perform a Hilbert transformation of a full band symmetrical about zero frequency. Since $\alpha(\bar{\nu})$ is an odd function this requires setting up an array as illustrated in figure 2.5. This is then Fourier transformed and multiplied by the sigum function according to equation 2.25. The value for n_{∞} may be ascertained experimentally in a dispersive measurement at some high frequency.

2.3 Dispersive Methods

Placing the sample in one arm of the interferometer enables both the absorption coefficient and the frequency dependent refractive index to be obtained simultaneously [22]. Using two different thicknesses of sample, the absorption coefficient can be calculated through equation

1.22 and the refractive index through subtracting the phase spectra calculated in equation 1.24 and adding on a 'fringe shift' term, FS, to take into account the difference in optical thickness between the two samples [24,25] (figure 2.6)

$$n(\bar{\nu}) = \frac{\phi^S(\bar{\nu}) - \phi^B(\bar{\nu})}{4\pi\bar{\nu}\,(d^S - d^B)} + \frac{FS}{(d^S - d^B)} \qquad 2.32$$

$$FS = (MS^S - MS^B) + (ZPD^S - ZPD^B)\,\frac{SI}{2} \qquad 2.33$$

where MS is the position of the mirror at the start of recording the interferogram, ZPD is the mirror position at zero path difference and SI is the sampling interval. The superscripts S and B refer to sample and background, and all parameters are in centimetres.

It is important to note the exact mirror position at the start of recording each interferogram, as the phase shifts involved are of the order of a few microns. The mirror positions ZPD^S and ZPD^B are taken as the nearest sampled points to zero path difference following the procedure of Birch et al. [24].

The foregoing discussion is a somewhat simplified approach to dispersive analysis and cannot be applied to more complicated situations, where reflection terms do not

Fig. 2.6

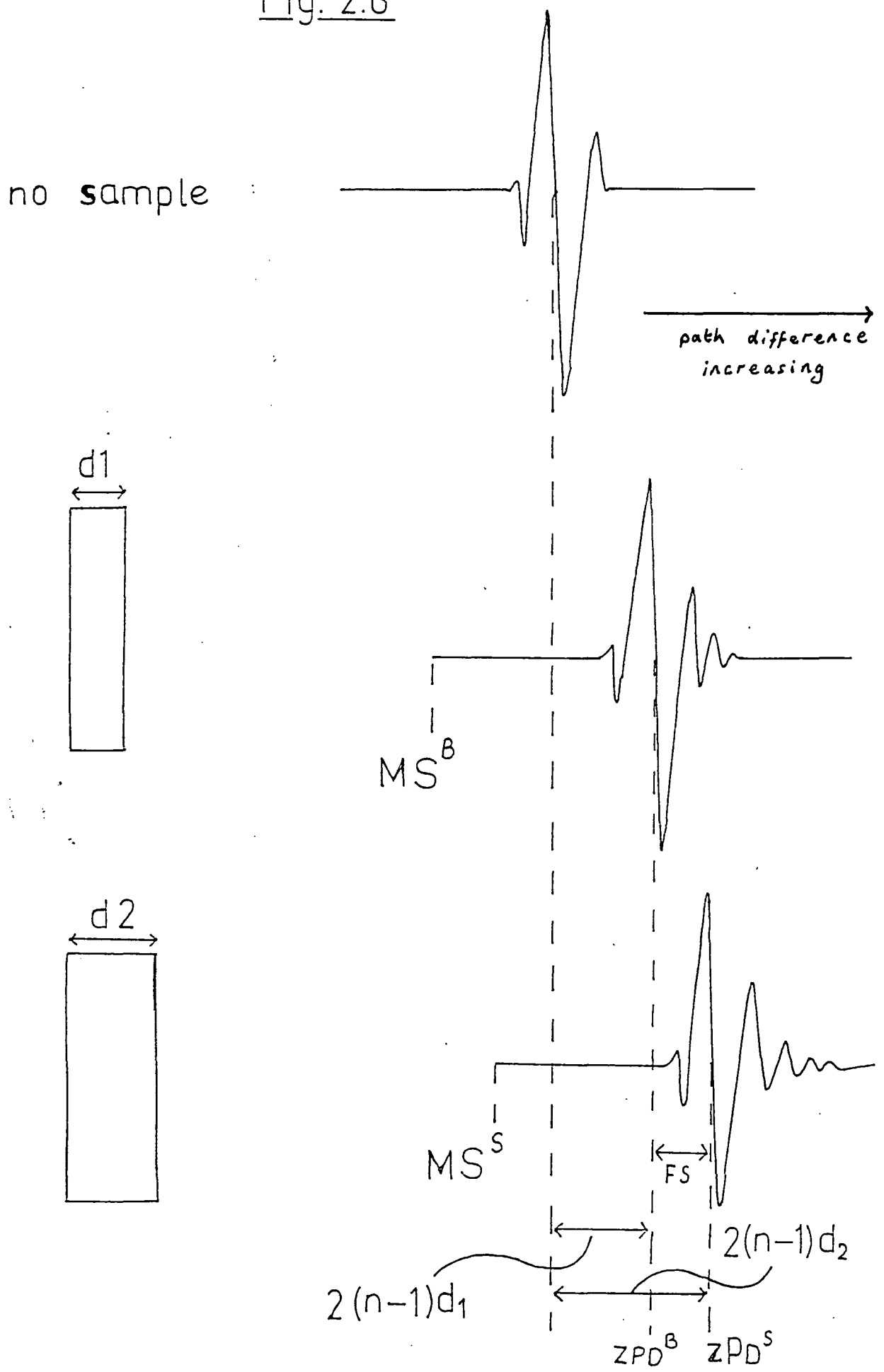
no sample
path difference increasing
d1
d2
MS^B
MS^S
FS
2(n−1)d2
2(n−1)d1
ZPD^B
ZPD^S

cancel, and which require a full knowledge of the relevant Fresnel coefficients.

2.4 The Complex Insertion Loss

The experimentally determined entity for dispersive work shall be referred to as the complex insertion loss and defined as [24,26]

$$\hat{L}\ (\bar{\nu}) = L\ (\bar{\nu})\ \exp\left[i\phi(\bar{\nu})\right] = \frac{F\{\ I_S(x)\}}{F\{\ I_B(x)\}} \tag{2.34}$$

where $L(\bar{\nu})$ is the ratio of sample and background modulus spectra and $\phi(\bar{\nu})$ is now the difference in phase spectra. The complex insertion loss can be determined theoretically by building up the Fresnel coefficients for transmission and reflection at an interface, and propagation through a medium, into an expression involving the optical constants. The coefficients for adjacent mediums x and y, in the general case, are as follows [22,27]

$$\hat{r}_{xy}^{\perp} = \frac{\hat{n}_x \cos\hat{\theta}_x - \hat{n}_y \cos\hat{\theta}_y}{\hat{n}_x \cos\hat{\theta}_x + \hat{n}_y \cos\hat{\theta}_y} \tag{2.35}$$

$$\hat{r}_{xy}^{/\!/} = \frac{\hat{n}_x \cos\hat{\theta}_y - \hat{n}_y \cos\hat{\theta}_x}{\hat{n}_x \cos\hat{\theta}_y + \hat{n}_y \cos\hat{\theta}_x} \tag{2.36}$$

$$\hat{t}^{\perp}_{xy} = \frac{2\,\hat{n}_x \cos\hat{\theta}_x}{\hat{n}_x \cos\hat{\theta}_x + \hat{n}_y \cos\hat{\theta}_y} \tag{2.37}$$

$$\hat{t}^{/\!/}_{xy} = \frac{2\hat{n}_x \cos\hat{\theta}_x}{\hat{n}_x \cos\hat{\theta}_y + \hat{n}_y \cos\hat{\theta}_x} \tag{2.38}$$

where $\hat{\theta}_x$ and $\hat{\theta}_y$ are angles of incidence and refraction respectively, r is the reflection coefficient and t the transmission coefficient. For normal incidence these equations reduce to

$$\hat{r}_{xy} = \frac{\hat{n}_x - \hat{n}_y}{\hat{n}_x + \hat{n}_y} \tag{2.39}$$

$$t_{xy} = \frac{2\hat{n}_x}{\hat{n}_x + \hat{n}_y} \tag{2.40}$$

The term for propagaion is given by

$$\hat{\mathbf{a}}_x = \exp\,(i2\pi\hat{n}\,\bar{\nu}d) \tag{2.41}$$

Thus for reflection through a parallel sample, medium 1, placed in one arm of an interferometer between media 0 and 2, the reflected beam may be described according to figure 2.7 and the complex insertion loss for two thicknesses of sample is then

$$\hat{L}(\bar{\nu}) = \frac{\left[\hat{a}^2_o \;\; \hat{a}^2_1 \;\; \hat{t}_{01} \;\; \hat{t}_{10} \;\; \hat{r}_{12}\right]^S}{\left[\hat{a}^2_o \;\; \hat{a}^2_1 \;\; \hat{t}_{01} \;\; \hat{t}_{10} \;\; \hat{r}_{12}\right]^B} \tag{2.42}$$

and since the term $\hat{a}^2_o\;\hat{t}_{01}\,\hat{t}_{10}\,\hat{r}_{12}$ will be identical for sample and background, it can be cancelled and we have

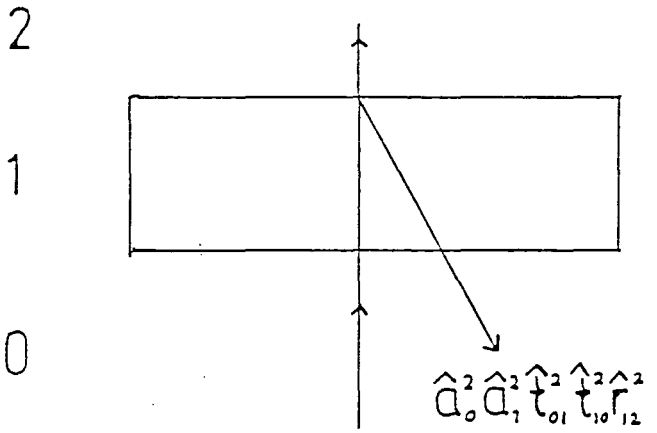
2
1
0
$\hat{a}_0^2 \hat{a}_1^2 \hat{t}_{01}^2 \hat{t}_{10}^2 \hat{r}_{12}^2$

Fig. 2.7

Fig. 2.8

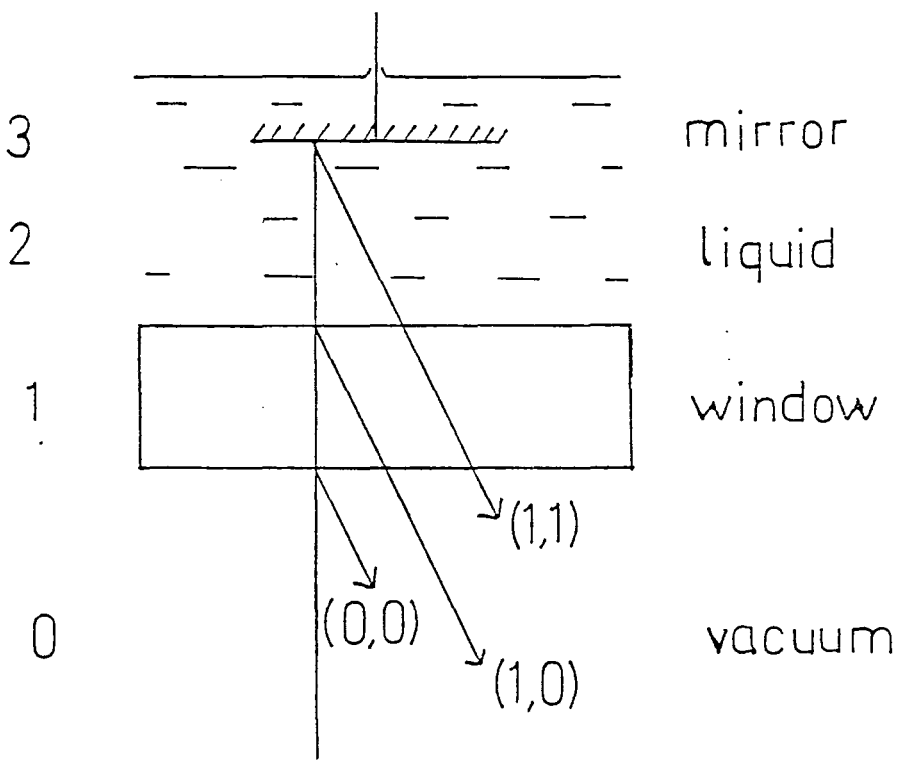
3
2
1
0
mirror
liquid
window
vacuum
(1,1)
(0,0)
(1,0)

$$\hat{L}(\bar{\nu}) = \frac{\left[\hat{a}_1^2\right]^S}{\left[\hat{a}_1^2\right]^B} = \exp\left[i2\pi\hat{n}\bar{\nu}(d^S - d^B) \right] \tag{2.43}$$

$$\therefore \quad \hat{L}(\bar{\nu}) = \exp\left[(d^S - d^B)\,\alpha_1 \right] \exp\left[i4\pi\bar{\nu}\,(d^S - d^B) n_1 \right] \tag{2.44}$$

and equating this expression with equation 2.34 results in

$$L(\bar{\nu}) = \exp\left[- (d^S - d^B)\alpha_1 \right] \tag{2.45}$$

and

$$\phi(\bar{\nu}) = 4\pi\bar{\nu}(d^S - d^B)\, n_1 \tag{2.46}$$

which are equivalent to equations 1.22 and 2.32 if we include the fringe shift term in equation 2.46.

2.4.1 Application to Dispersive Transmission

2.4.1a The liquid Cell

It is clear from equation 2.42 that by ratioing two pathlengths of sample many of the Fresnel coefficients will cancel out. This fact is utilised when operating the variable-thickness cell [28] illustrated schematically in figure 2.8. The liquid sample is gravity held on a silicon window and the mirror, which takes the place of the fixed mirror M2 in figure 1.3, can be immersed in the liquid at any fixed pathlength by micrometer control. The beam from

the interferometer enters from below the silicon window and is reflected back on itself at each interface. Following the notation at Honijk et al. [29] , the reflection at the front surface of the silicon window shall be referred to as the (0,0) reflection; the reflection from the back surface as the (1,0) reflection; the reflection from the mirror as the (1,1) reflection.

The signatures in the interferogram associated with these reflections are shown in figure 2.9. It is interesting to note from these that there is a change in phase of 180° between a reflection from a medium of high refractive index to one of a lower refractive index and from a medium of low refractive index to one of a higher refractive index.

In a dispersive transmission experiment, the (1,1) signature for both pathlengths is compared. This gives a complex insertion loss of

$$\hat{L}(\tilde{\nu}) = \frac{\left[\hat{a}_0^2\ \hat{a}_1^2\ \hat{a}_2^2\ \hat{t}_{01}\ \hat{t}_{10}\ \hat{t}_{12}\ \hat{t}_{21}\ \hat{r}_{23}\right]^S}{\left[\hat{a}_0^2\ \hat{a}_1^2\ \hat{a}_2^2\ \hat{t}_{01}\ \hat{t}_{10}\ \hat{t}_{12}\ \hat{t}_{21}\ \hat{r}_{23}\right]^B} \qquad (2.47)$$

but since only $\hat{a}_2$ changes with increasing liquid pathlength this simplifies to (cf equation 2.43)

$$\hat{L}(\nu) = \frac{\left[\hat{a}_2^2\right]^S}{\left[\hat{a}_2^2\right]^B} \qquad (2.48)$$

and hence no knowledge of the window material optical constants is required.

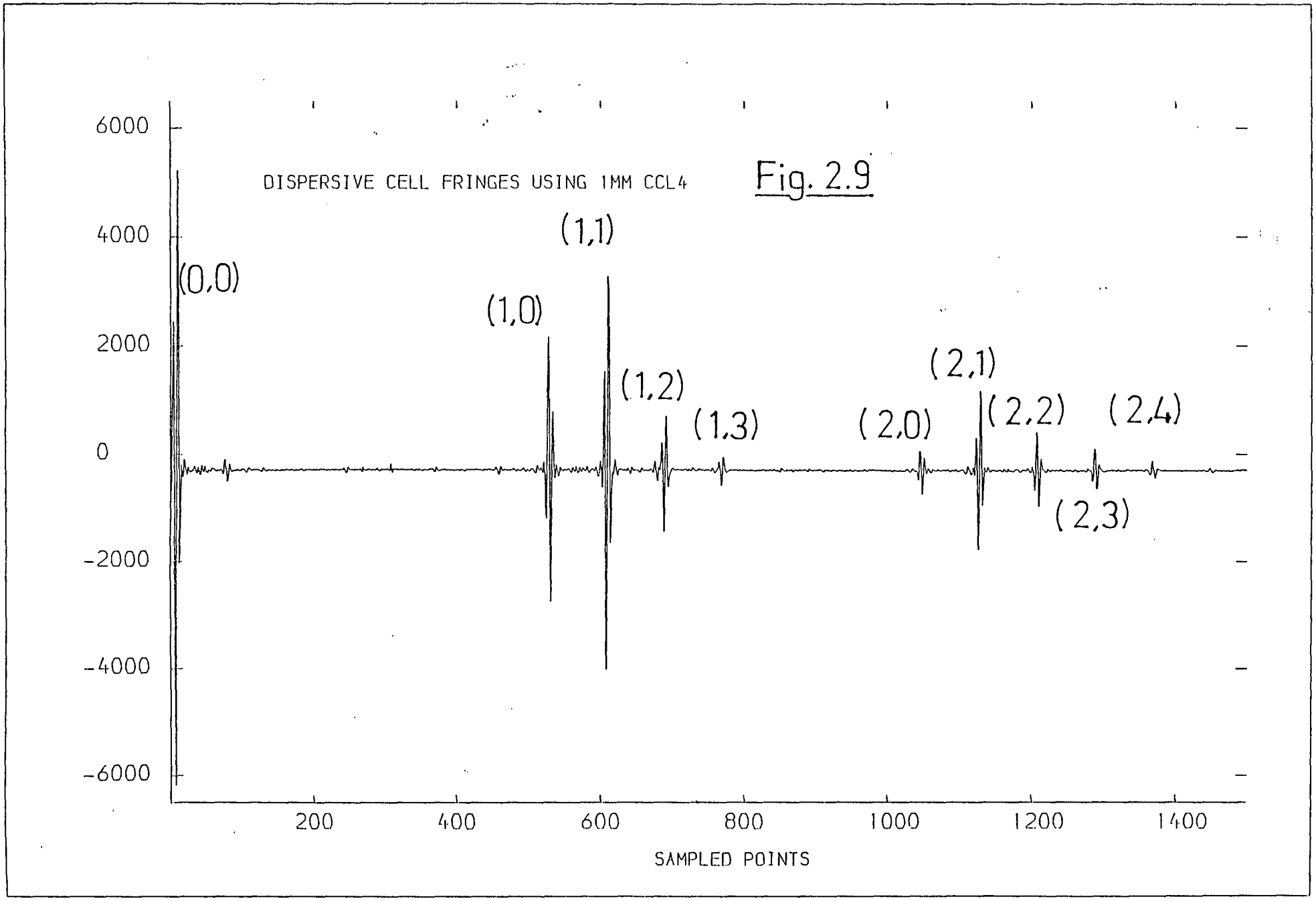
DISPERSIVE CELL FRINGES USING 1MM CCL4
Fig. 2.9
6000
4000
2000
0
-2000
-4000
-6000
(0,0)
(1,0)
(1,1)
(1,2)
(1,3)
(2,0)
(2,1)
(2,2)
(2,3)
(2,4)
200
400
600
800
1000
1200
1400
SAMPLED POINTS

Fig. 2.10

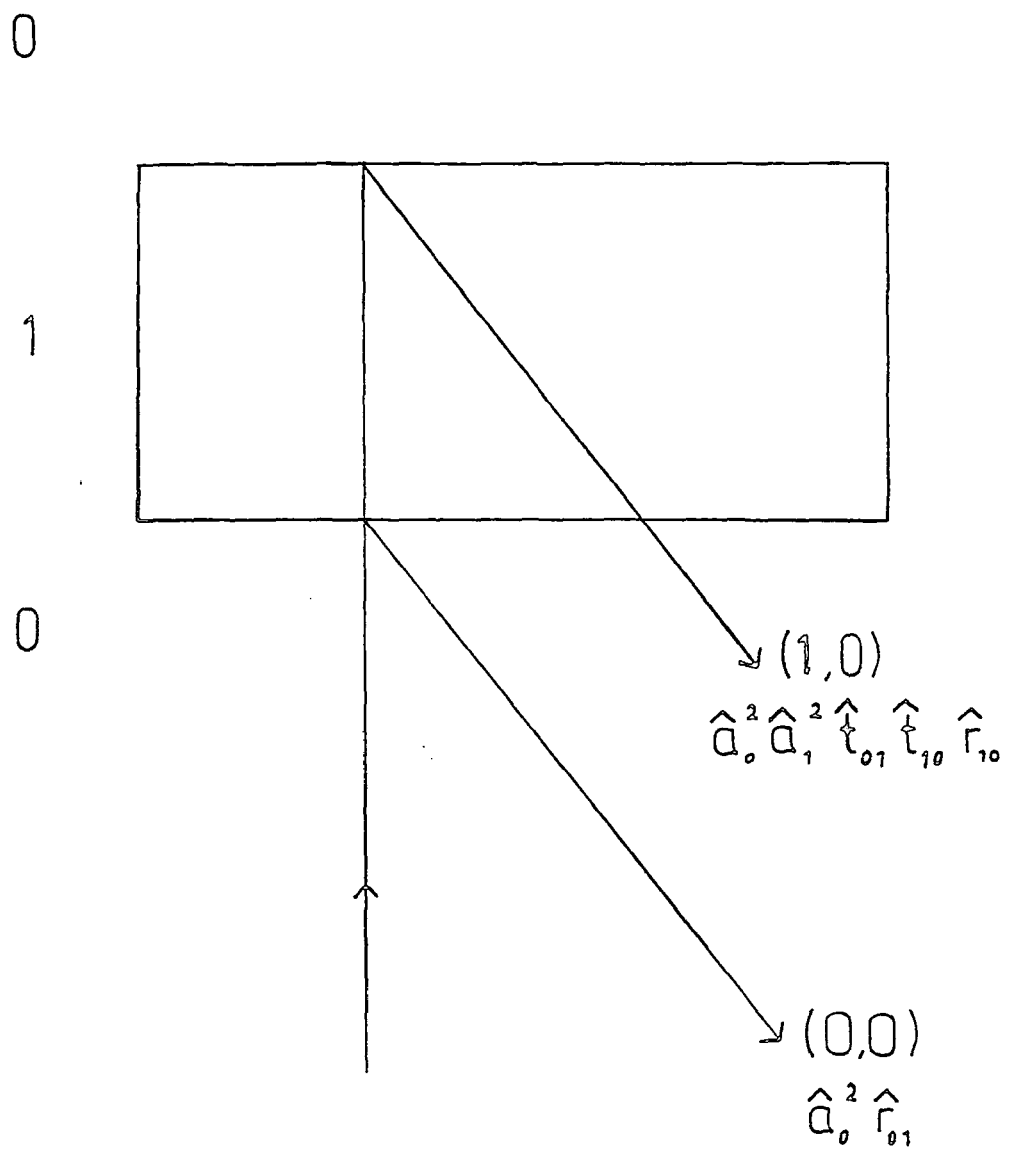

2.4.1b Free standing solid

The analysis of a free-standing parallel sample illustrated in section 2.3 requires two thicknesses of sample and, as a consequence, involves interfering with the interferometer during the course of an experiment through changing samples, with the associated problems of ensuring both samples are placed in identical positions. With a knowledge of the theoretical complex insertion loss, however, the optical constants may be extracted by comparing the (0,0) and (1,0) reflections shown in figure 2.10 where medium 0 is vacuum or air, for which

$$\hat{n}_o = 1 + 0i \tag{2.49}$$

If $\hat{n}_o$ is substituted into the equation for the complex insertion loss for this situation,

$$\hat{L}(\bar{\nu}) = \frac{\hat{a}_1^2 \hat{t}_{01} \hat{t}_{10} \hat{r}_{10}}{\hat{r}_{01}} , \tag{2.50}$$

we have

$$\hat{L}(\bar{\nu}) = \frac{-\hat{a}_1^2 4\hat{n}_1}{(1 + \hat{n}_1)^2} = \hat{a}_1^2 \left[1 - \left(\frac{\hat{n}_1 - 1}{\hat{n}_1 + 1}\right)^2\right] \tag{2.51}$$

Then through equations 2.34 and 2.41,

$$\alpha(\bar{\nu}) = \frac{1}{d} \ell n(1 - R / T) \tag{2.52}$$

where

$$R = \left(\frac{n_1 - 1}{n_1 + 1}\right)^2 \tag{2.53}$$

and T is the transmission defined in equation 1.21. The refractive index is calculated from the phase in the usual way according to equation 2.32.

2.4.2 Application to dispersive reflection

The liquid cell described in section 2.4.1a is limited in that it is very difficult to achieve pathlengths of less than several hundred microns because of surface tension effects, so that highly absorbing liquids cannot be studied by transmission.

Fortunately, highly absorbing liquids produce a large phase shift in the beam on reflection, and this can be used to advantage, giving the optical constants of the sample with little attenuation of the beam. Thus, if the optical constants of the window are known, the (1,0) reflection in figure 2.8 is sufficient to yield n and α of the liquid [30]. The window optical constants are found according to section 2.4.1b. The background in this case is the (0,0) fringe, so the complex insertion loss is

$$\hat{L}(\bar{\nu}) = \frac{\hat{t}_{01}\hat{t}_{10}\hat{a}_1^2\hat{r}_{12}}{\hat{r}_{01}} = \frac{\hat{a}_1^2(1-\hat{r}_{01}^2)\hat{r}_{12}}{\hat{r}_{01}} \qquad (2.54)$$

where $\hat{r}_{12}$ contains the information we require through $\hat{n}_2$, and $\hat{L}(\bar{\nu})$ is what is measured experimentally. Rearranging gives

$$\hat{n}_2 = \hat{n}_1\left[\frac{\hat{a}_1^2\,(1-\hat{r}_{o1}^2) - \hat{L}(\bar{\nu})\,\hat{r}_{o1}}{\hat{a}_1^2\,(1-\hat{r}_{o1}^2) + \hat{L}(\bar{\nu})\,\hat{r}_{o1}}\right] \tag{2.55}$$

The full procedure then involves recording the (0,0) and (1,0) signatures as part of the same interferogram, for the empty cell, with sufficient points either side of both to obtain the resolution required. After having inroduced the liquid, the (0,0) and (1,0) signatures are recorded again from the same starting point. The (1,0) signature will be shifted due to the phase changes caused by inroduction of the liquid. The (0,0) signature, however, is not affected and can be used as a point of reference through the fringe-shift term which is taken as the distance between the (0,0) and (1,0) signatures.

The thickness of the silicon window used was 0.3039cm so the distance in mirror travel between the (0,0) and (1,0) signatures, $\bar{n}d$, is approximately 1.04cm which imposes a limit in resolution on the spectra of $1cm^{-1}$ maximum. In practice this limit was taken as $2cm^{-1}$ to ensure that structure associated with one signature did not overlap with the wings of the other.

It is impossible to produce reasonable liquid spectra by this method without first being able to obtain accurate window optical constants. Some data obtained in this work are presented in figure 2.11 and compared with data recorded by Birch [31] for silicon of a similar resistivity, in table 2.1. It can be seen that the two sets of data agree quite well.

Fig. 2.11

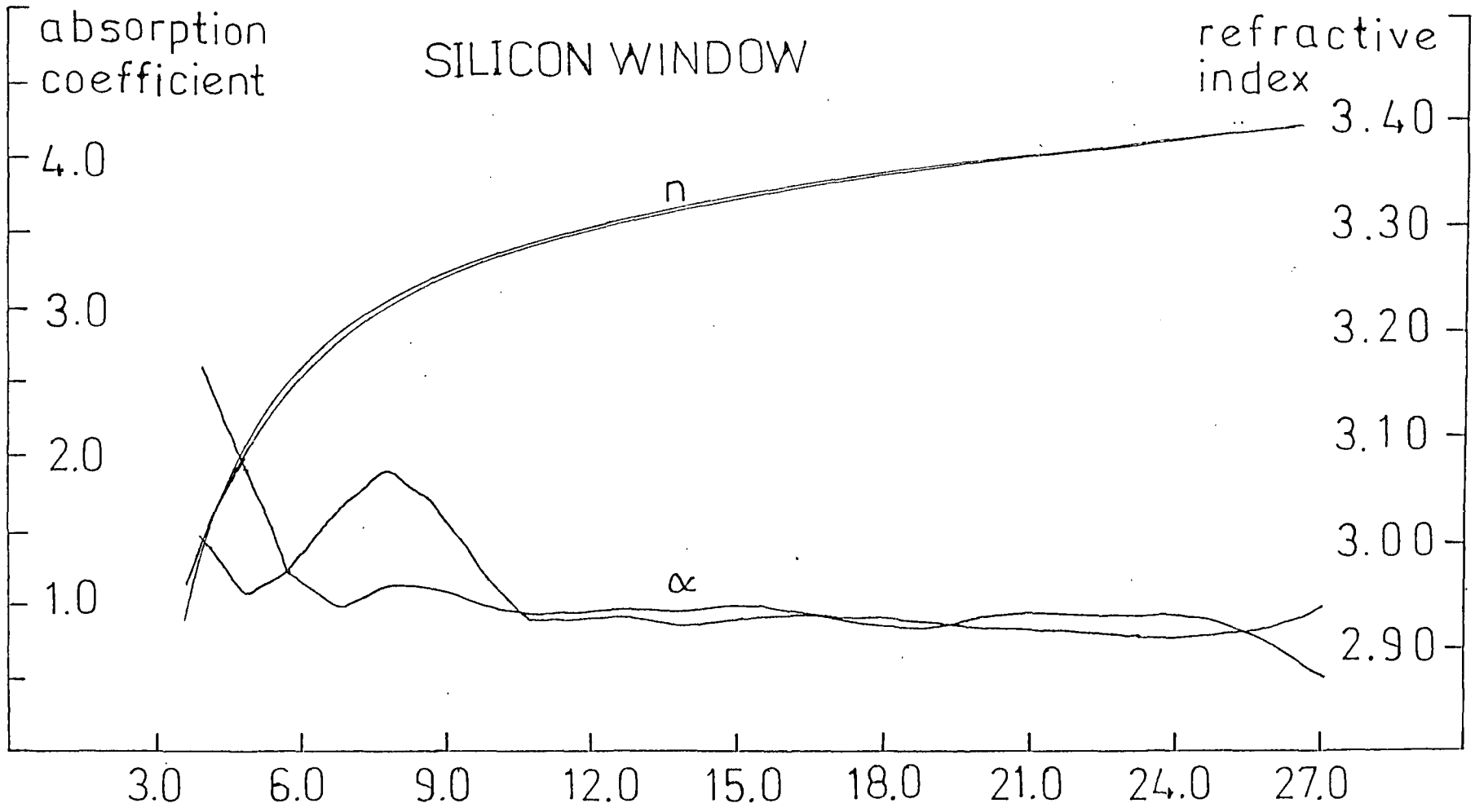
absorption coefficient
SILICON WINDOW
refractive index
4.0
3.0
2.0
1.0
3.40
3.30
3.20
3.10
3.00
2.90
n
α
3.0
6.0
9.0
12.0
15.0
18.0
21.0
24.0
27.0

Table 2.1

Wavenumber (cm^{-1})	Refractive index (this work) 298K	Refractive index (this work) 290K *	Refractive index (Birch [31]) 290K
30	3.415	3.413	3.412
50	3.416	3.414	3.413
80	3.417	3.415	3.413
100	3.417	3.415	3.414

* corrected from 298K data using a temperature coefficient for n of $2.0 \times 10^{-4} K$ [31]

Silicon window refractive index

2.4.3 Errors involved with Dispersive Work

The major source of errors involved in dispersive as compared with non-dispersive work arise through phase instability of the instrument. Since the crucial measurement is of a small phase change due to the presence of sample in one arm of the interferometer, this is more critical for reflection than for transmission.

Temperature variations in the interferometer cause their own phase shifts so it is essential to maintain a steady temperature throughout the duration of the experiment and to ensure that the two arms of the interferometer are held at as close a temperature as is practically possible. Fluctuations in temperature between the two arms, and as a function of time, can lead to serious systematic errors in the computed optical constants.

In order to overcome these problems, water was circulated around the two arms of the interferometer from a thermostatted bath. However, the stepping motor on the instrument causes problems due to heating of the moving-mirror arm and this is best overcome by isolating it from the rest of the arm by means of a non-conducting spacer. The temperature variation throughout individual experiments, measured near to the silicon window, was found to be typically within 0.2°C which would suggest that the measured window refractive index would be accurate to within

10^{-5}. However, the temperature difference between the two arms was often of the order of 1° C and this is expected to produce larger errors.

Large phase errors occur if the sample is introduced at a temperature different from that of the window : a difference of approximately four degrees causing a shift in zero path difference of up to a sampling interval. Therefore, samples were placed in the water-bath before being introduced to the liquid cell.

The phase instability in an instrument can be described in terms of the drift of zero path difference with respect to time. It is assumed that this will be a uni-directional, slowly varying, approximately linear function of time. This would hold for phase changes due to the gradual warming of the stepper-motor or to natural changes in the environmental temperature. Figure 2.12 shows the change in the (0,0) signature phase spectrum as a function of time. The total drift in an experiment, then, can be reduced simply by increasing the speed of recording an inerferogram. This cannot be done indefinitely, however, because it would lead to unacceptably poor signal-to-noise levels in the spectra.

The phase errors caused by the drift in zero path difference will produce a distortion in the fringe shift term which can be corrected for it we can estimate the rate of drift throughout the experiment.

Two methods have been employed to measure this drift. The simplest is to sit on one lobe of the (1,0) signature

Fig. 2.12

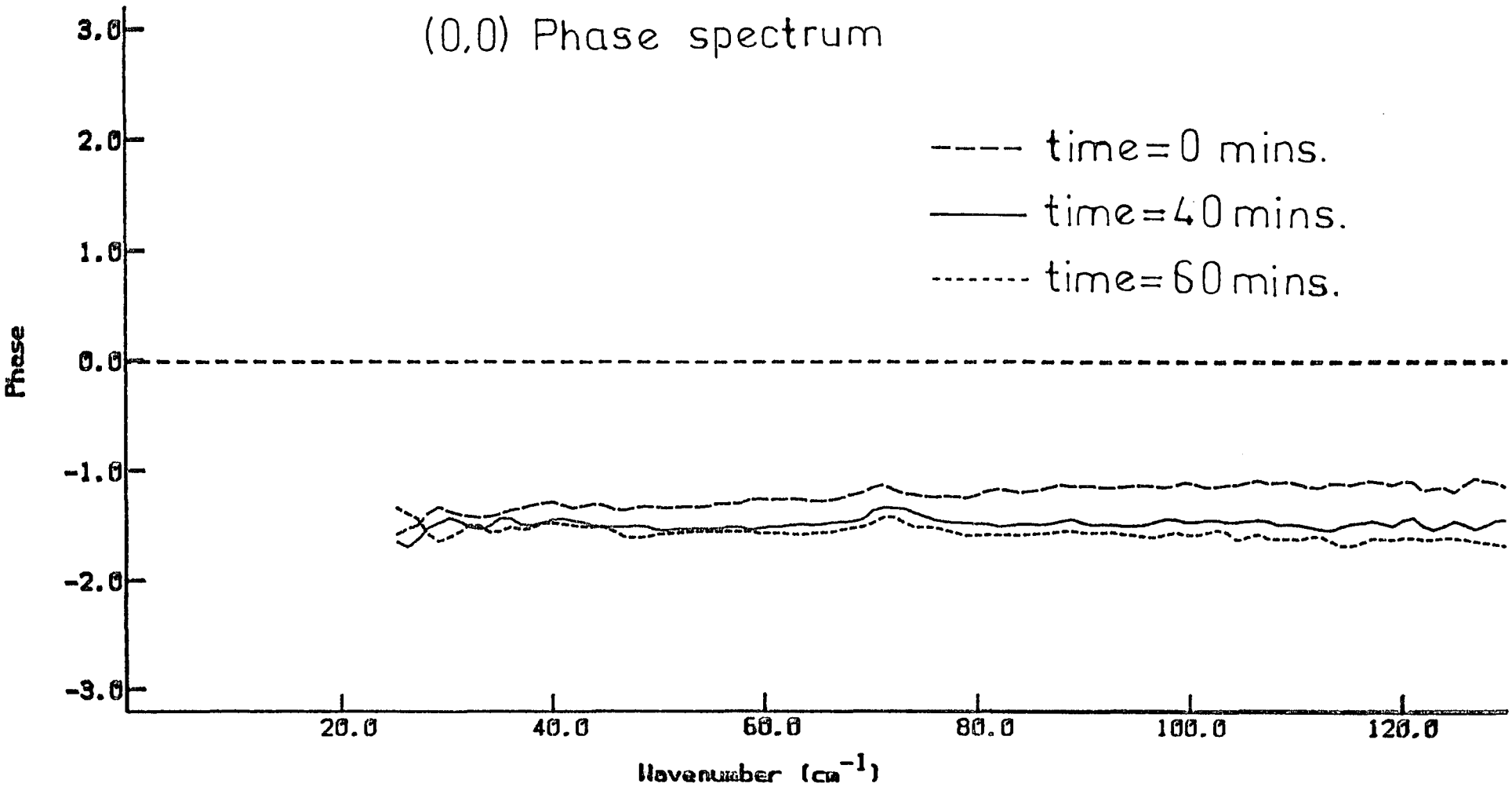
(0,0) Phase spectrum
time=0 mins.
time=40 mins.
time=60 mins.
Phase
3.0
2.0
1.0
0.0
-1.0
-2.0
-3.0
20.0
40.0
60.0
80.0
100.0
120.0
Wavenumber (cm^{-1})

for a period of time comparable to the duration of the experiment. Then by moving the mirror to find again the peak intensity, it is possible to estimate the rate at which zero path difference is shifting.

A more quantitative method is achieved by comparing the (0,0) fringes of sample and background for a reflection experiment (or (1,0) fringes for a transmission experiment) (figure 2.13). Since the (0,0) fringe is unchanged with the addition of sample it should occur at the same position of mirror travel. Any change in position then is due entirely to instrument instability and, furthermore, this change is a direct measure of the drift in the signal between recordings of the two (0,0) zero path differences, and consequently a good approximation of the drift occurring during the background run. To perform a similar correction for the sample run, a further (0,0) fringe must be recorded immediately after the experiment so that the (0,0) fringes of sample run and this reference run can be compared. From the diagram, x-x' is a measure of the phase drift, and can be determined knowing the voltages at the sampled points either side of zero path difference for sample and background.

From simple geometry we have

$$\tan\theta = \frac{D + d}{SI} = \frac{D' + d'}{SI} \qquad (2.56)$$

Fig. 2.13

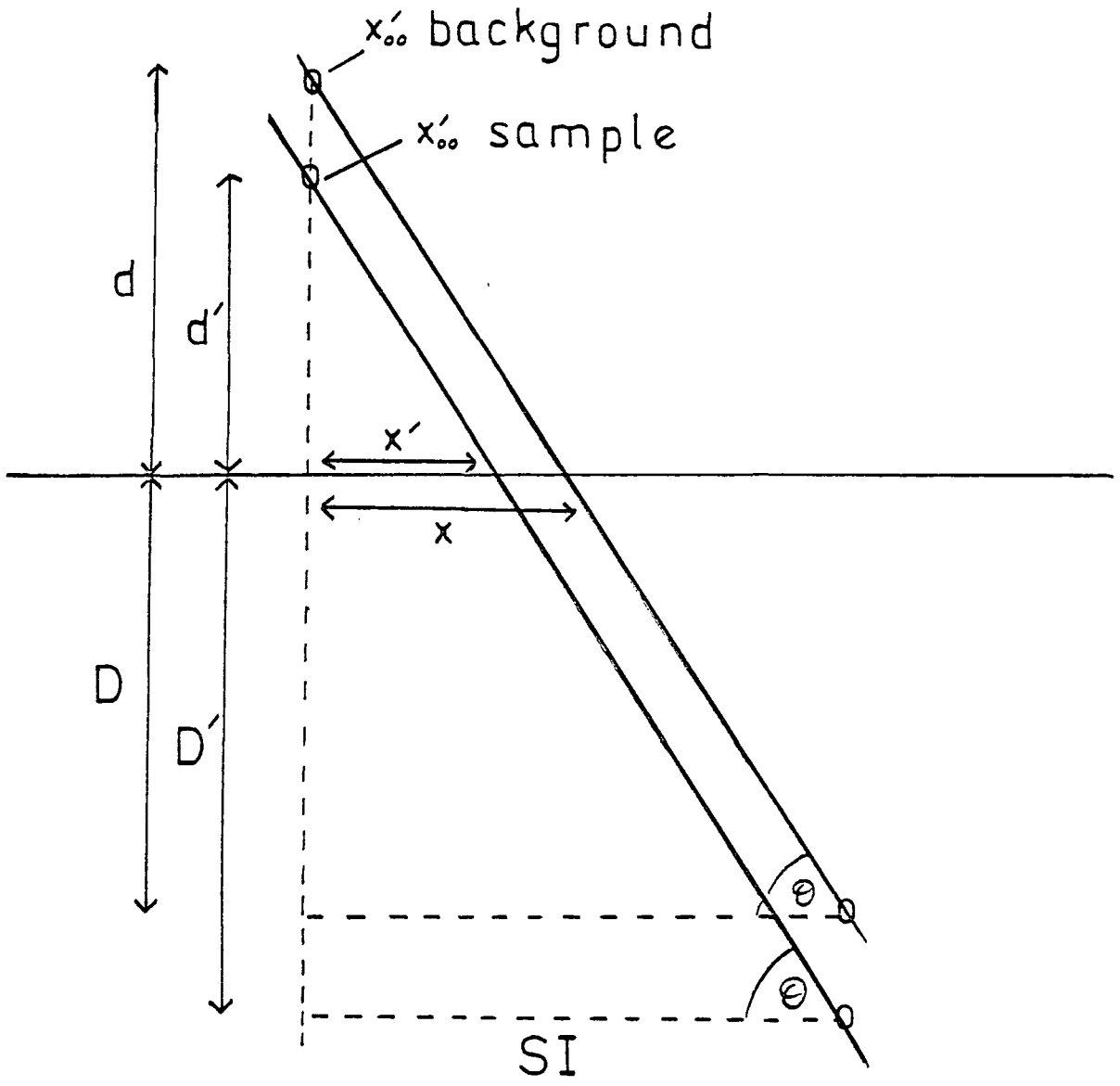

central portion of (0,0)

interferograms.

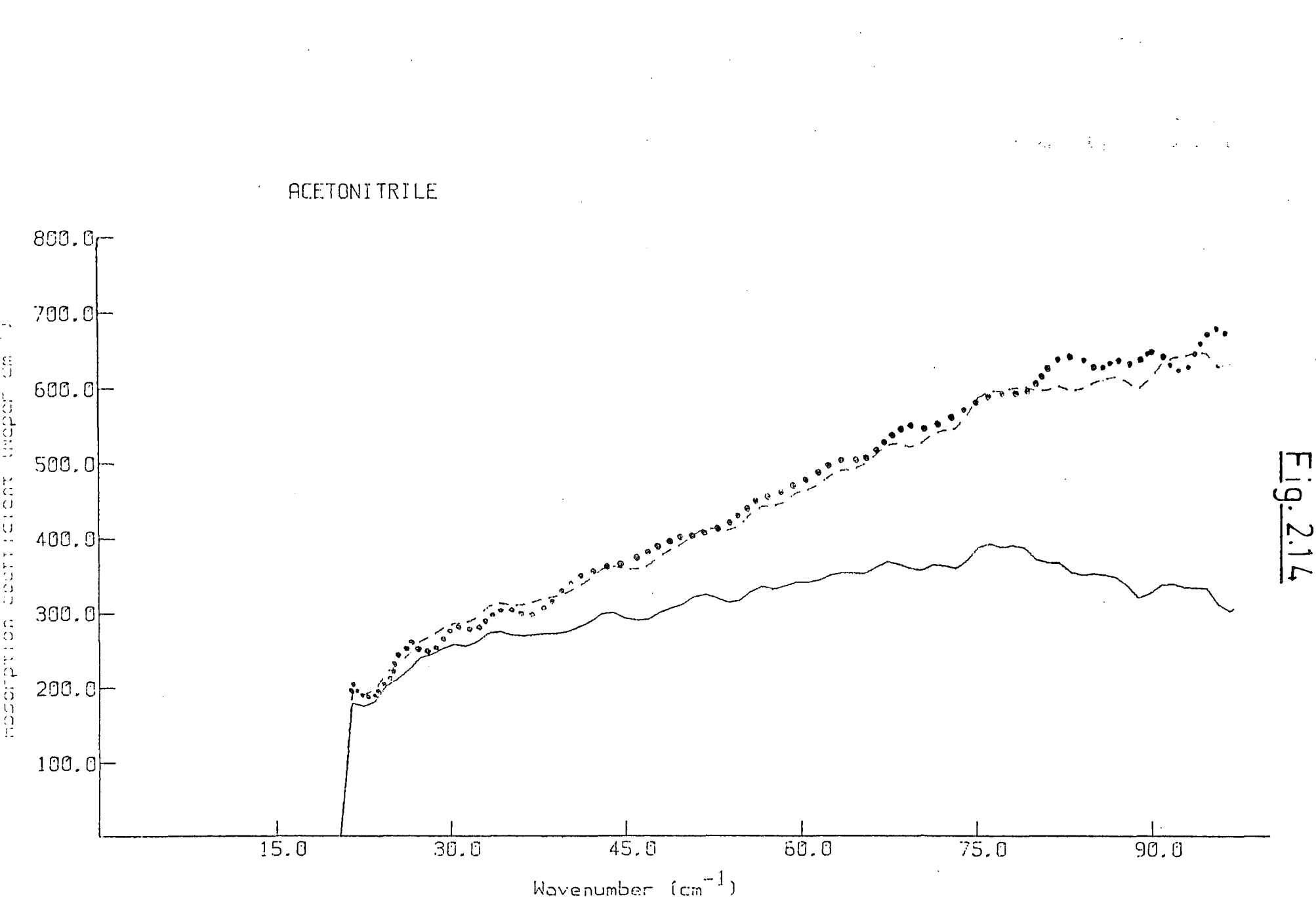
ACETONITRILE
800.0
700.0
600.0
500.0
400.0
300.0
200.0
100.0
15.0
30.0
45.0
60.0
75.0
90.0
Wavenumber (cm^{-1})

Fig. 2.14

$$x = \frac{d}{\tan\theta} \quad ; \quad x' = \frac{d'}{\tan\theta} \tag{2.57}$$

Equation 2.33 must now be corrected to

$$FS = (MS^S - MS^B) + \{(ZPD^S - ZPD^B) + (x - x')\}\ SI\ /\ 2 \tag{2.58}$$

When the drift is more than half a sampling interval then the sample and background (0,0) signatures may be transformed about a different point along the mirror drive. This must be allowed for in equation 2.58 by adding or subtracting a whole sampling interval.

The effectiveness of this procedure is illustrated in figure 2.14 for the low-wavenumber wing of the far infrred acetonitrile absorption. The dotted curve is for a spectrum which required no phase correction since the (0,0) fringe was unchanged between sample and background. The full line is another spectrum recorded when there was considerable drift of zero path difference between background and sample. When this is corrected for using equation 2.58 the broken curve is produced.

For both dispersive and non-dispersive work the whole instrument is evacuated since water vapour has a significant far infrared absorption. Small residual amounts of vapour remaining in the interferometer are not usually important since they should be cancelled when a ratio is done. For dispersive work, however, this is not always the case. Consider the situation where two (1,1) signatures are being compared for different pathlengths of liquid. If there is structure due to water vapour in the interferogram

associated with the (1,0) signature, this will not be ratioed out in the final spectrum since the relative path difference between the (1,0) and (1,1) signatures has changed. It is therefore particularly important to maintain a good vacuum for dispersive work, and a pressure of approximately 0.1 Torr was found to be generally sufficient.

Systematic errors are introduced if the instrument is misaligned. A comprehensive description of alignment procedure is detailed by O'Neill [32].

2.4.4 The Full Interferogram method

In a normal dispersive transmission experiment the resolution is limited by how far the mirror can be moved away from the (1,1) signature before reaching structure associated with another signature. As we move to more absorbing materials, the pathlengths we are able to use become progressively smaller in order to maintain an acceptable level of transmission, and the resolution can be reduced drastically; so much so that very highly absorbing materials are almost impossible to measure accurately by this technique.

Editing out of unwanted signatures is unsatisfactory since it is likely to result in the loss of valuable information and, possibly, the retention of structure from the wings of the unwanted signature. If, however, these spurious signatures are retained, transformation of the full

interferogram results in the expected oscillations in the phase and modulus data which prevent the determination of the optical constants. Examples are shown in figures 2.15 and 2.16. These oscillations do not cancel out when the modulus spectra from two sample thicknesses are ratioed against one another, since the interference fringes will occur at different positions of path difference. A smaller pathlength of sample leads to (1,1) signatures which are closer together and, consequently, oscillations in the modulus spectrum which are broader. Compare figures 2.15 and 2.16.

If we can use, in our analysis, an expression that allows for all the signatures due to internal reflections, it would be possible to record and transform complicated full interferograms and derive optical constants without having to edit the interferograms and without restriction on the resolution obtainable.

Such an expression may be derived using Fresnel's equations as in section 2.4 but developing the method further to include multiple reflections. Consider a thin film on a substrate where medium 2 is of much smaller pathlength than media 0 and 1. We can then envisage reflections in accordance with figure 2.17, and the complex insertion loss is now given by a summation.

$$\hat{L}(\bar{\nu}) = \frac{\left[\hat{a}_0^4 \hat{a}_1^2 \hat{t}_{01}\hat{t}_{10}\hat{t}_{12}\hat{t}_{21}\hat{t}_{02}\hat{t}_{20}\hat{r}_{03}\sum_i (\hat{a}_2^{2i}\hat{r}_{20}^{i-1}\hat{r}_{21}^{i-1})\right]^S}{\left[\hat{a}_0^4 \hat{a}_1^2 \hat{t}_{01}\hat{t}_{10}\hat{t}_{12}\hat{t}_{21}\hat{t}_{02}\hat{t}_{20}\hat{r}_{03}\sum_i (\hat{a}_2^{2i}\hat{r}_{20}^{i-1}\hat{r}_{21}^{i-1})\right]^B} \qquad (2.59)$$

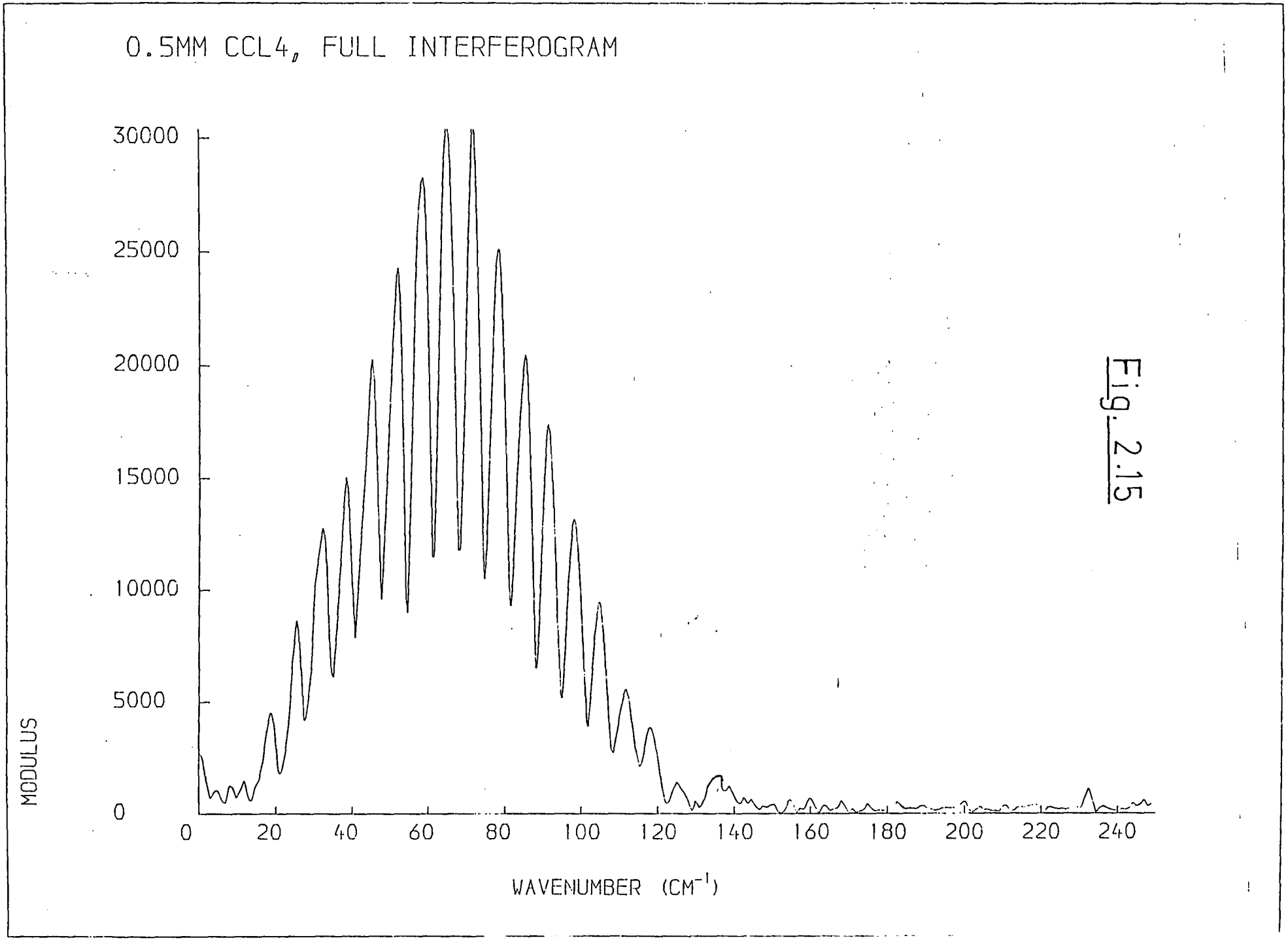
0.5MM CCL4, FULL INTERFEROGRAM
30000
25000
20000
15000
10000
5000
0
MODULUS
0
20
40
60
80
100
120
140
160
180
200
220
240
WAVENUMBER (CM-1)

Fig. 2.15

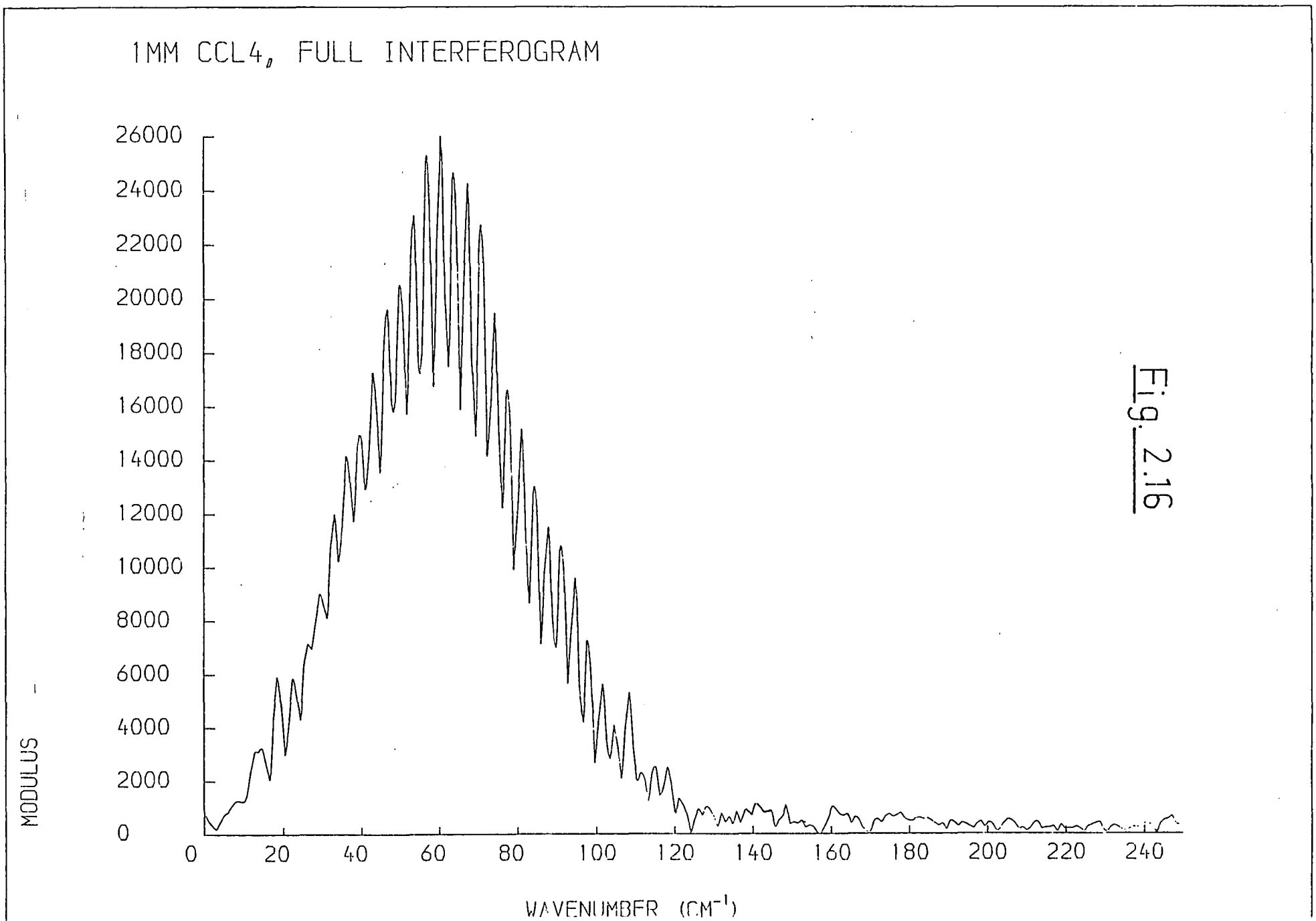
1MM CCL4, FULL INTERFEROGRAM
MODULUS
26000
24000
22000
20000
18000
16000
14000
12000
10000
8000
6000
4000
2000
0
0
20
40
60
80
100
120
140
160
180
200
220
240
WAVENUMBER (CM-1)

Fig. 2.16

Fig. 2.17.

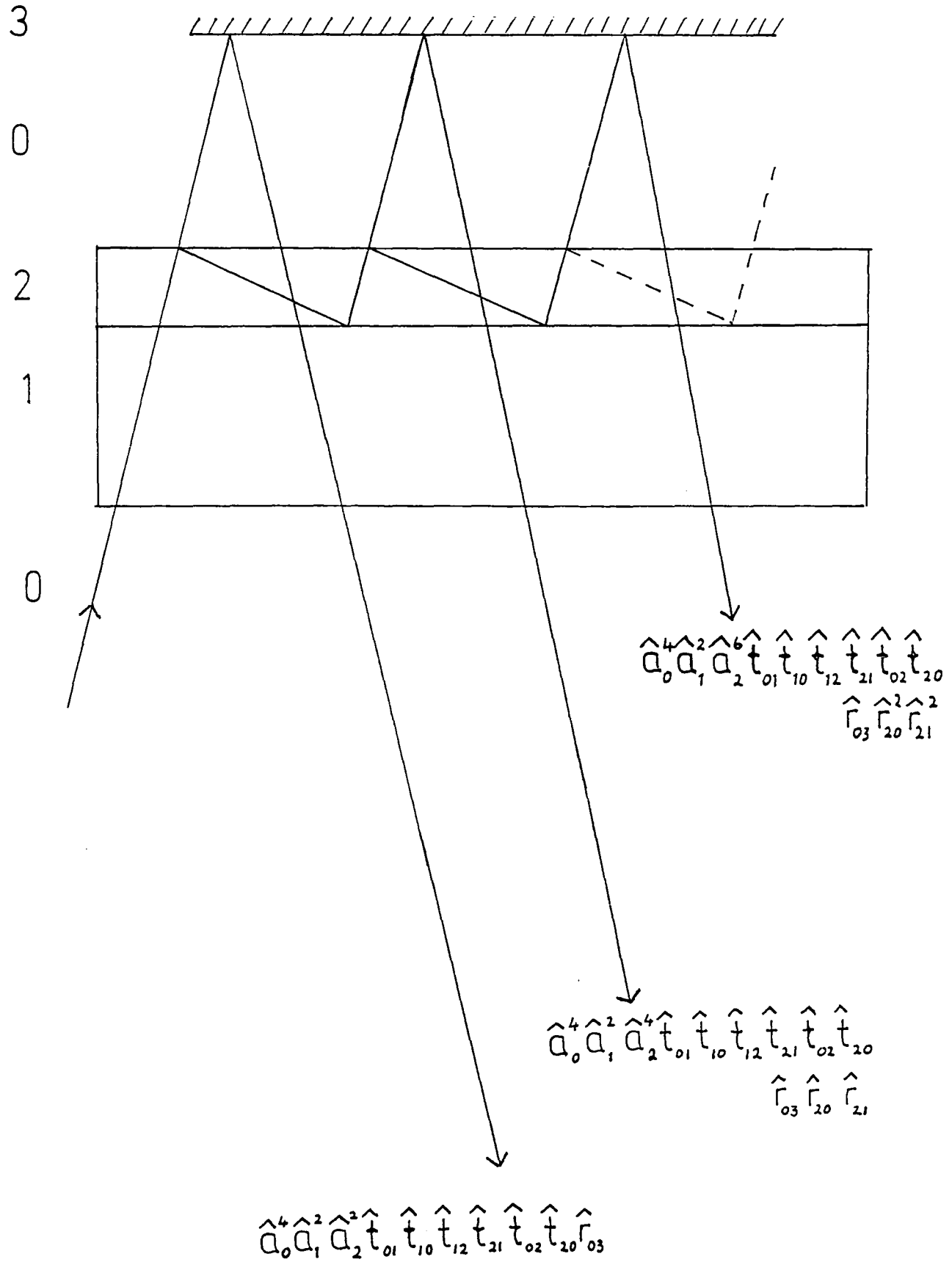
3
0
2
1
0
$\hat{a}_0^4\hat{a}_1^2\hat{a}_2^6\hat{t}_{01}\hat{t}_{10}\hat{t}_{12}\hat{t}_{21}\hat{t}_{02}\hat{t}_{20}$
$\hat{r}_{03}\hat{r}_{20}^2\hat{r}_{21}^2$
$\hat{a}_0^4\hat{a}_1^2\hat{a}_2^4\hat{t}_{01}\hat{t}_{10}\hat{t}_{12}\hat{t}_{21}\hat{t}_{02}\hat{t}_{20}$
$\hat{r}_{03}\hat{r}_{20}\hat{r}_{21}$
$\hat{a}_0^4\hat{a}_1^2\hat{a}_2^2\hat{t}_{01}\hat{t}_{10}\hat{t}_{12}\hat{t}_{21}\hat{t}_{02}\hat{t}_{20}\hat{r}_{03}$

where S and B are for two pathlengths of thin film. All terms outside the summation will be unaffected by a change in film thickness and therefore cancel when ratioed. From hereon this constructed complex insertion loss will be called the theoretical complex insertion loss to differentiate it from the experimental complex insertion loss defined in equation 2.34. For the thin film on a substrate we now have

$$\hat{L}^{Th}(\nu) = \frac{\left[\sum_i \left(\hat{a}_2^{2i}\ \hat{r}_{20}^{i-1}\ \hat{r}_{21}^{i-1}\right)\right]^S}{\left[\sum_i \left(\hat{a}_2^{2i}\ \hat{r}_{20}^{i-1}\ \hat{r}_{21}^{i-1}\right)\right]^B} \qquad (2.60)$$

This equation cannot be solved directly for n and α, and it is necessary to perform an iteration on estimated values of the optical constants. Accurate estimates may be obtained from the low resolution spectrum obtained by analysing the first signature only i.e. setting i = 1 in the summation of equation 2.60. Note that by this method it is first necessary to know the optical constants of the substrate.

The iteration procedure adopted in this work was the secant method illustrated in figure 2.18 which, in its usual form, is

$$\hat{n}_3 = \hat{n}_2 + \frac{(\hat{n}_1 - \hat{n}_2)(\hat{L} - \hat{L}_2^{Th})}{\hat{L}_1^{Th} - \hat{L}_2^{Th}} \qquad (2.61)$$

Fig. 2.18

The Secant Method

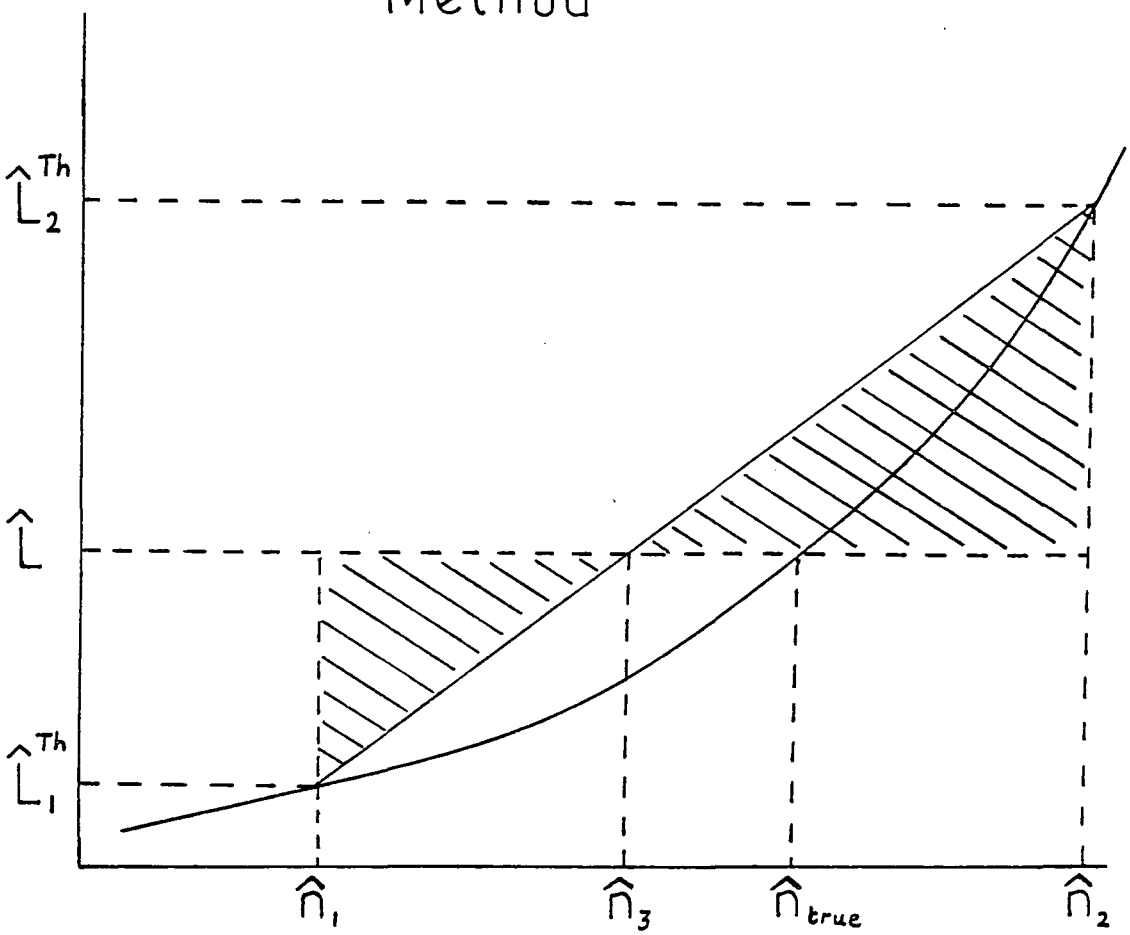

Plot of $\hat{L}(\hat{n})$ at one frequency.

Shaded triangles are similar

$$\therefore \quad \frac{\hat{n}_2 - \hat{n}_3}{\hat{n}_3 - \hat{n}_1} = \frac{\hat{L}_2 - \hat{L}}{\hat{L} - \hat{L}_1}$$

Fig. 2.19

Full interferogram method

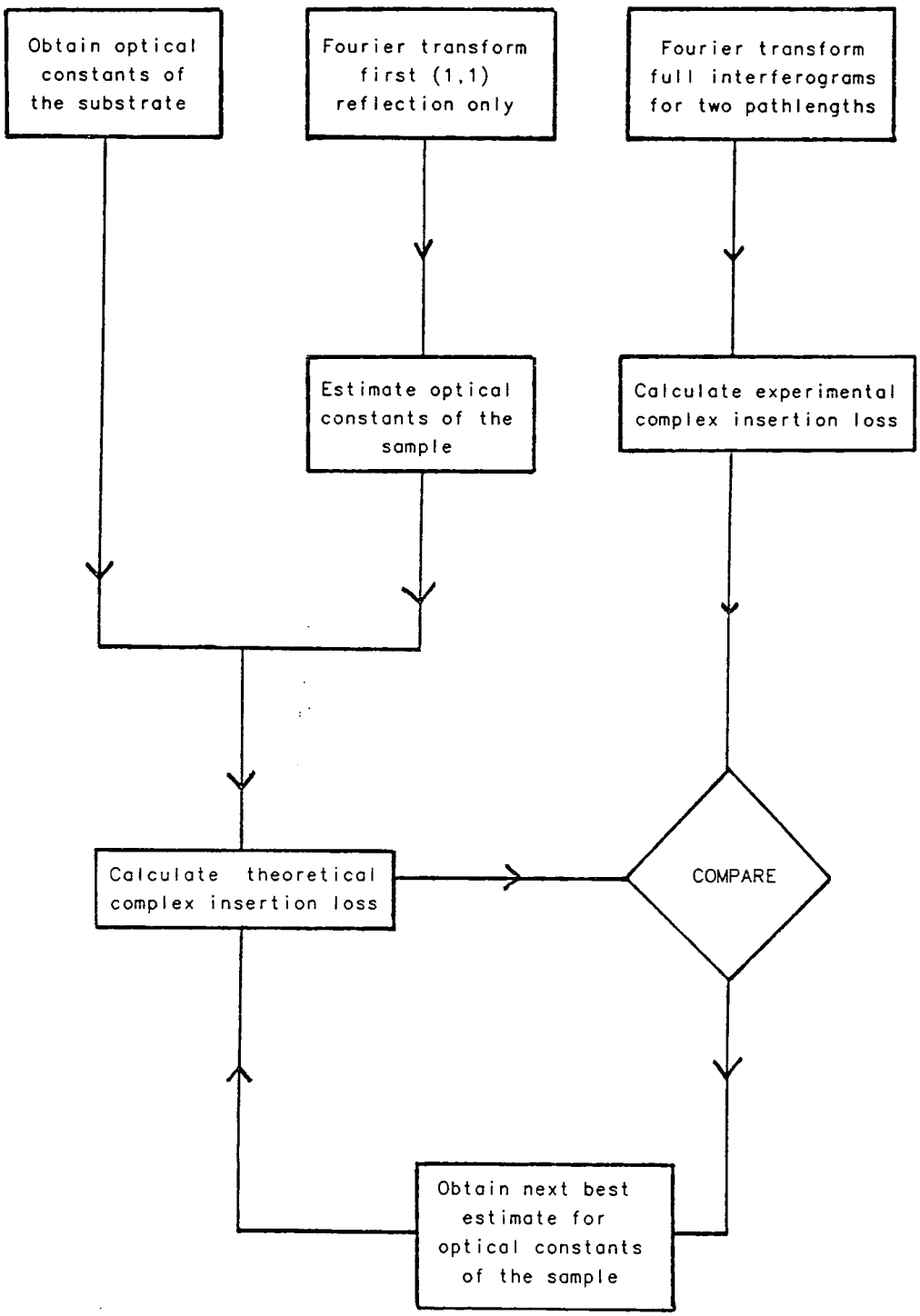

where $\hat{n}_1$ is the first guess, $\hat{n}_2$ is set at a value slightly removed from $\hat{n}_1$, and $\hat{n}_3$ is the next best estimate. This form of the secant equation, however, was found to introduce errors in the final value of $\hat{n}$ through subtractive cancellation, because as the solution is approached $\hat{L}_1^{th}$ is very close to $\hat{L}_2^{th}$ and $\hat{n}_1$ is very close to $\hat{n}_2$. The iteration was better behaved when equation 2.61 was altered by dividing the second term throughout by $\hat{L}_2$ to give [33]

$$\hat{n}_3 = \hat{n}_2 + \frac{(\hat{n}_1 - \hat{n}_2)(\hat{L} / \hat{L}_2^{Th} - 1)}{\hat{L}_1 / \hat{L}_2^{Th} - 1} \qquad (2.62)$$

As a further precaution all calculations were performed in double precision. The procedure, in full, is outlined in figure 2.19, and the program is listed in Appendix IV.

In general, the secant method has several disadvantages. It is not always guaranteed to converge and it is important to start with a fairly good estimate of the optical constants. Also, the successive iterative steps do not necessarily enclose the root and may oscillate either side of the root without further convergence. In such a case it is necessary to lower the required accuracy which is governed by the value of $\hat{L}(\bar{\nu}) - \hat{L}^{th}(\bar{\nu})$. In practice, the method is sufficient to provide accurate iterations providing estimates are arrived at experimentally from low resolution runs and the accuracy required is not too stringent.

The effect of demanding different stringencies on the

accuracy of the iteration was probed using artificial data derived using the Debye equations, 2.7 and 2.8, in conjunction with equations 2.11 and 2.13. This data was used to create a complex insertion loss, for a supposed multiple-reflection system, which was fed into the iterative procedure in place of the experimental insertion loss. The results are illustrated in figure 2.20. Higher demands on the accuracy resulted in the procedure failing to converge. It is estimated from this that the limit in accuracy for n and α is set at a maximum of 10^{-5} and 10^{-2} respectively for a noise-free system.

It is important to note that apodisation of the full interferogram would cause systematic errors in the computed optical constants because the relative intensities of the signatures would be changed and would therefore contribute differently to the experimental insertion loss as compared to the theoretical insertion loss. Hence all results presented in this thesis computed through analysis of the full interferogram involve no apodisation of the interferogram.

A command macro called FULLINT has been set up on the main frame computer which performs a complete full interferogram analysis on the inputted liquid cell raw interferogram data for sample, background and substrate. The sample and background interferograms are transformed, without apodisation, to give their sine and cosine spectra. The substrate interferogram should consist of (0,0) and

Fig. 2.20

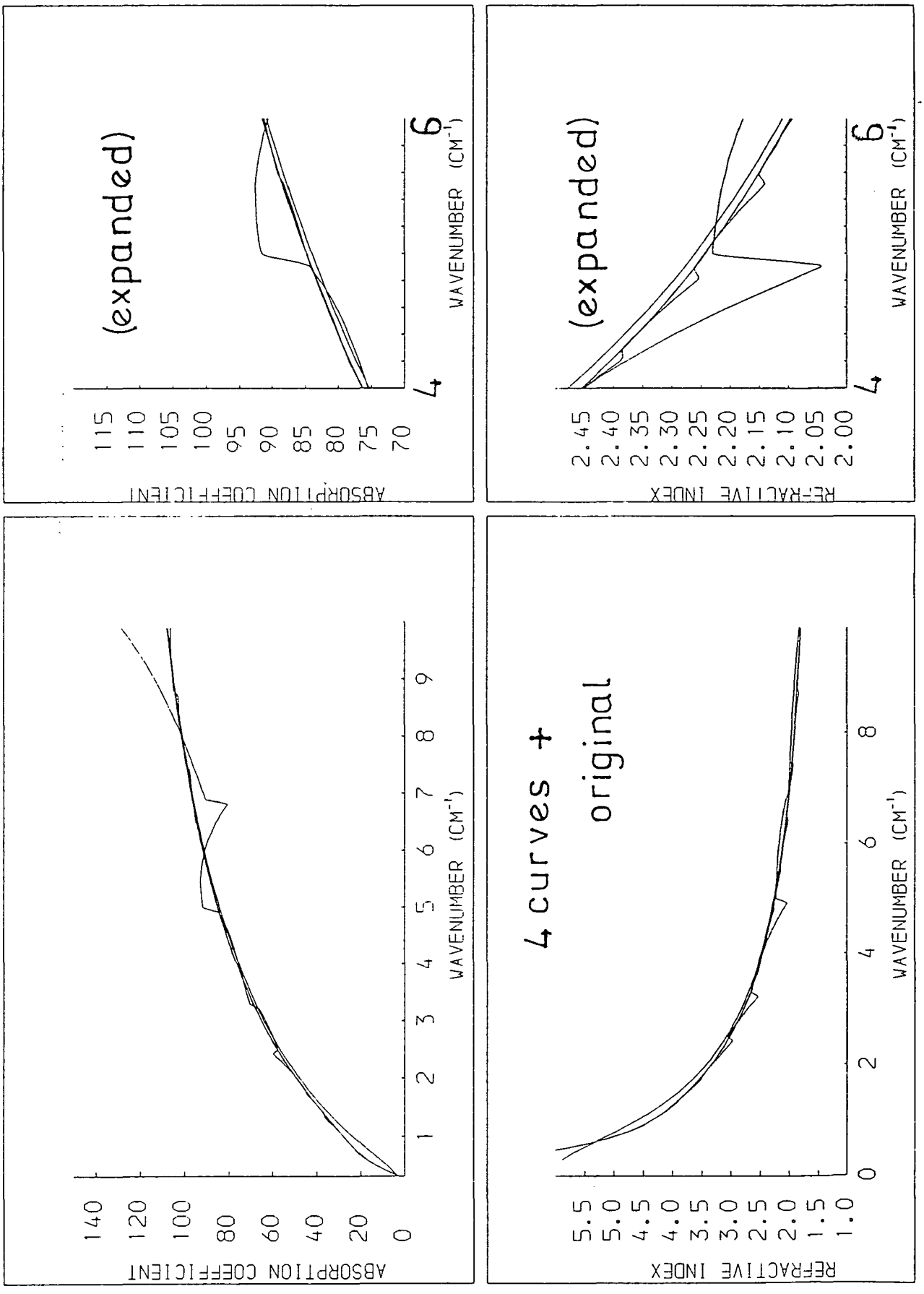
accuracy in $\hat{L}$ from .01 to .00001
(expanded)
ABSORPTION COEFFICIENT
WAVENUMBER (CM^{-1})
(expanded)
REFRACTIVE INDEX
WAVENUMBER (CM^{-1})
ABSORPTION COEFFICIENT
WAVENUMBER (CM^{-1})
4 curves + original
REFRACTIVE INDEX
WAVENUMBER (CM^{-1})

(1,0) signatures. These are apodised and transformed to give modulus and phase spectra which are subsequently used to compute the optical constants of the substrate as in section 2.4.1b.

The transformed data is read in, by the main program FLINT, together with the parameters necessary for the analysis. In describing these parameters, they will be split up into two types: fixed parameters which are invarient for a particular experiment; variable parameters which may be tailored to suit the iterative procedure.

(i) Fixed parameters

These are the liquid pathlengths, the gain factor and the mirror start positions. The liquid pathlengths are used to calculate the effective liquid pathlength, d, needed for evaluating the propagation coefficients (equation 2.41) required to compute the theoretical complex insertion loss in equation 2.60. The gain factor is the gain setting for the sample interferogram divided by the gain setting for the background interferogram. The mirror start positions must be noted accurately so that a fringe shift term may be calculated using equation 2.33.

(ii) Variable parameters

These are the accuracies required in the calculated real and imaginary parts of the complex insertion loss, the increment required in determining the next value of the guess in the iterative routine, and the number of fringes to be included in the analysis.

The accuracy of the theoretical complex insertion loss is measured as the difference between it and the experimental complex insertion loss. This accuracy will obviously be limited by the amount of noise in the experimental data. It is necessary to try the full procedure using different values for the required accuracy to discover the smallest value of $L^{th}(\bar{\nu}) - L(\bar{\nu})$ which can be achieved without the iteration failing to converge.

The increment parameter, I, is used to obtain the next value of the guess, $\hat{n}_2$, in the following way:

$$\hat{n}_2 = \hat{n}_1 + I\hat{n}_1 \qquad (2.63)$$

where $\hat{n}_1$ and $\hat{n}_2$ are the same as for equation 2.62. Its value depends on the general shape of $\hat{n}$. With reference to figure 2.18, if $\hat{n}$ is very steep then I must be large in order to ensure that $\hat{n}_\ell$ lies between $\hat{n}_1$ and $\hat{n}_2$. If I is too large, however, the guess $\hat{n}_2$ will be too far away from $\hat{n}_\ell$, the true value, and the iteration may fail. The aim should be to choose a value for I so that $\hat{n}_2$ is sufficiently close to $\hat{n}_\ell$ for the steepest gradient in $\hat{n}$. Again, trial and error is probably the best approach.

The number of fringes to be included in the construction of $L^{th}(\bar{\nu})$ may be chosen independently for sample and background. These are normally taken as being the number of fringes that can be discerned in the interferograms above the noise level, although it is not always clear how to define 'discernable'! In practice, the

inclusion of an extra fringe which has an intensity comparable to the noise level makes little difference to the final computed spectrum.

The validity of the procedure was demonstrated using the dispersive liquid cell with liquids whose optical constants were either well known or determined through a normal dispersive transmission experiment for comparison. Refractive index and absorption coefficient data are presented for carbon tetrachloride, figures 2.21 and 2.22; benzene, figures 2.23 and 2.24; benzonitrile-carbon tetrachloride mixtures, figures 2.25 and 2.26. The results were found to compare well with previous studies [28,34,25] .

Fig 2.21

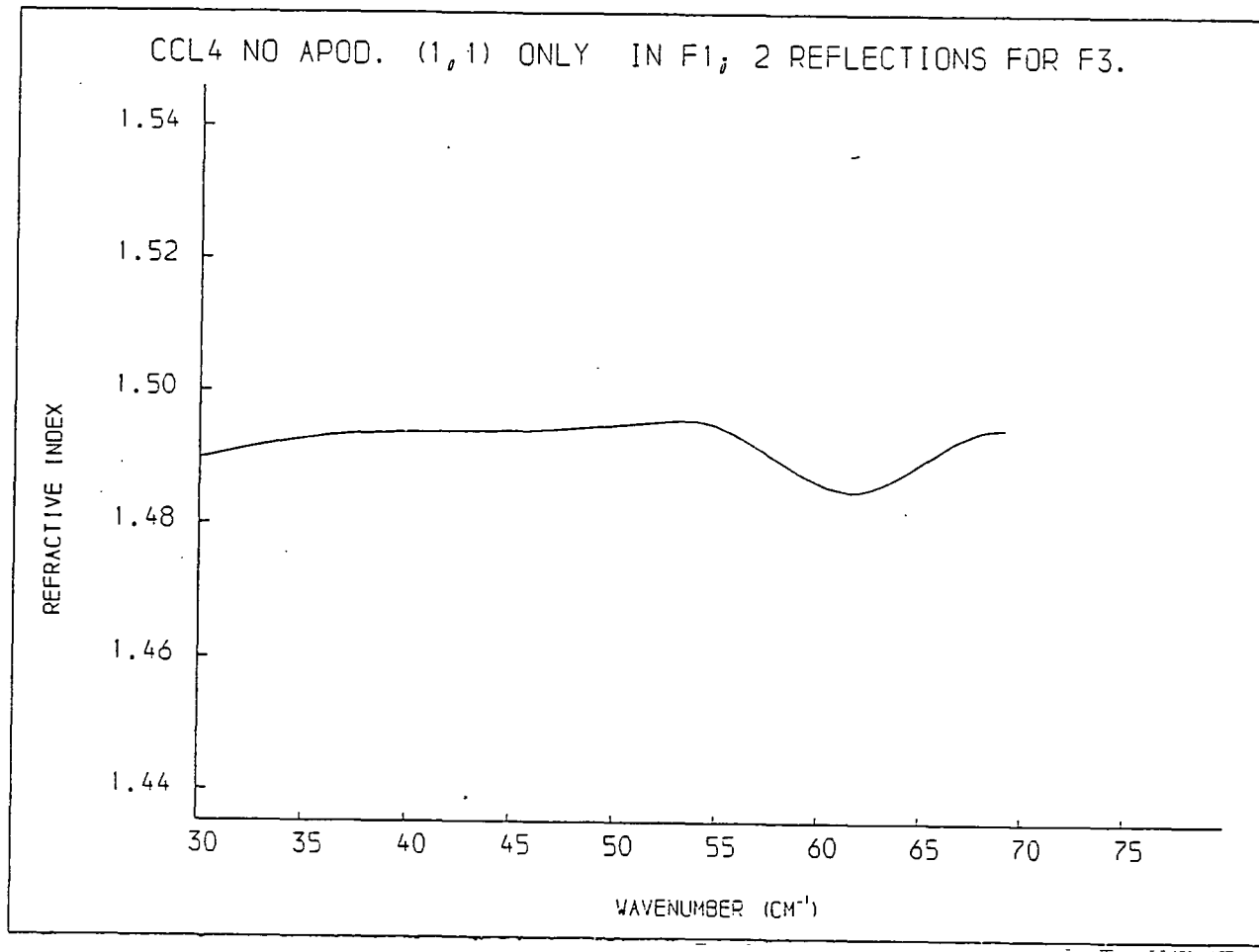

Fig. 2.22

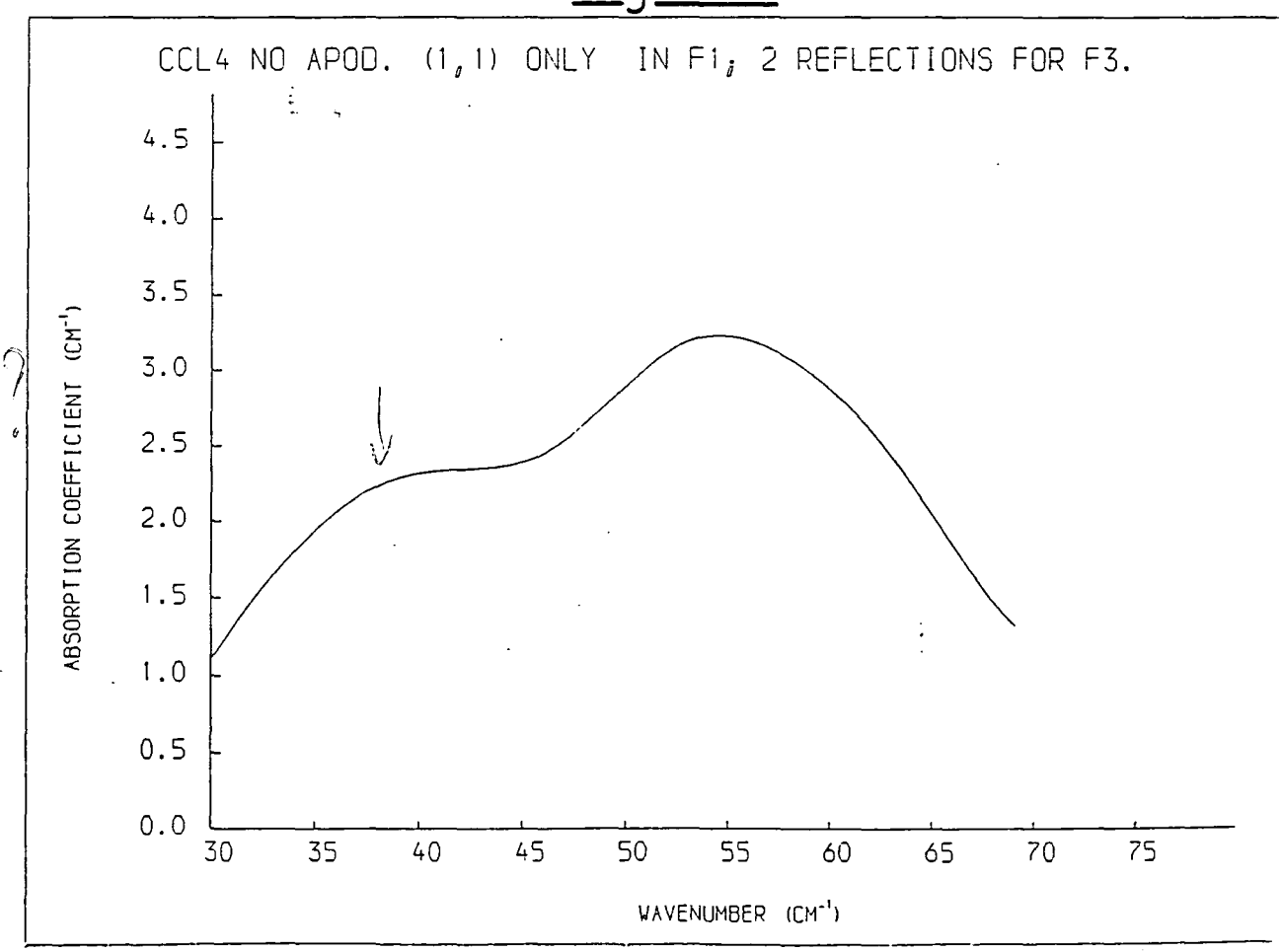

Fig. 2.23

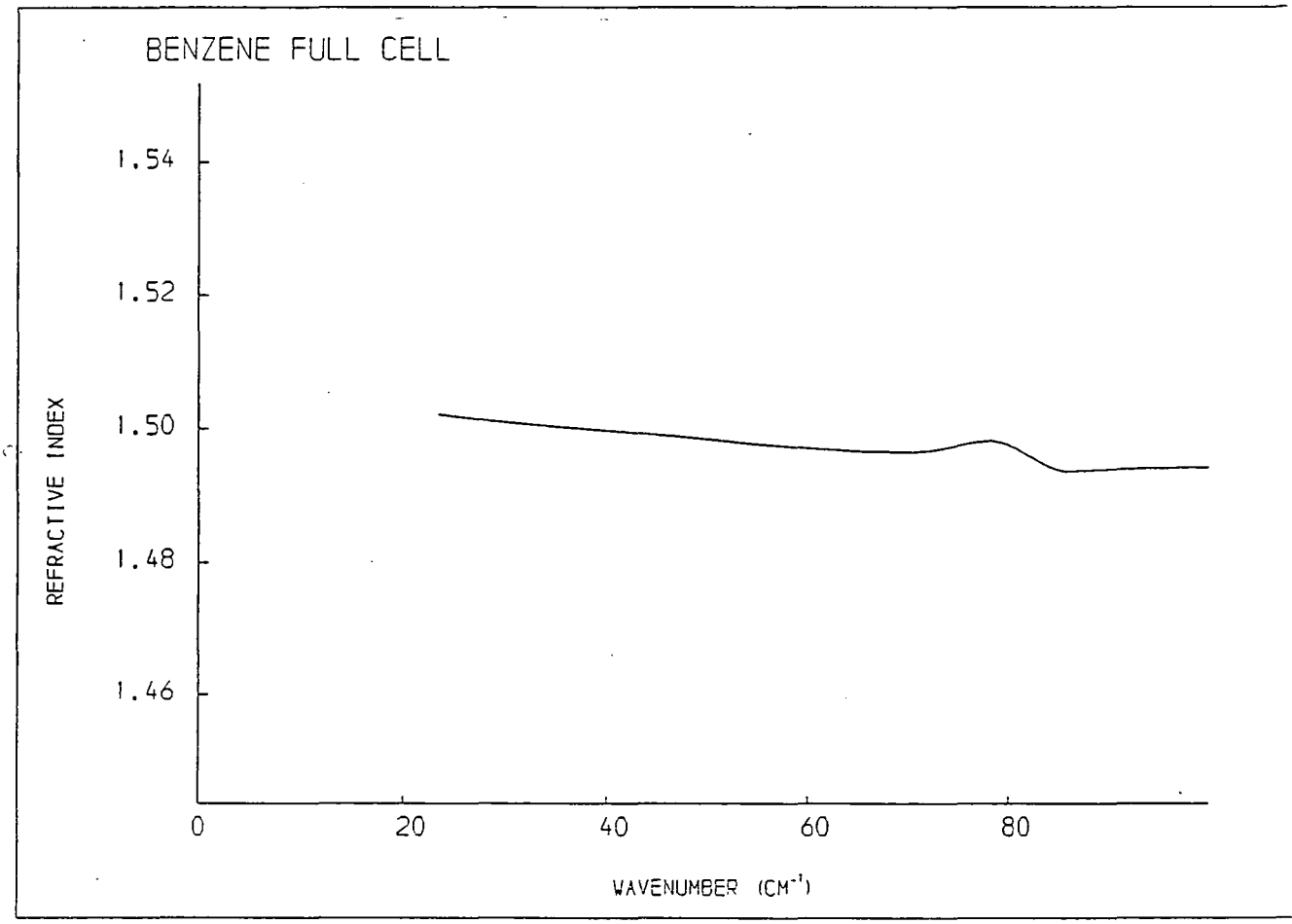

Fig. 2.24

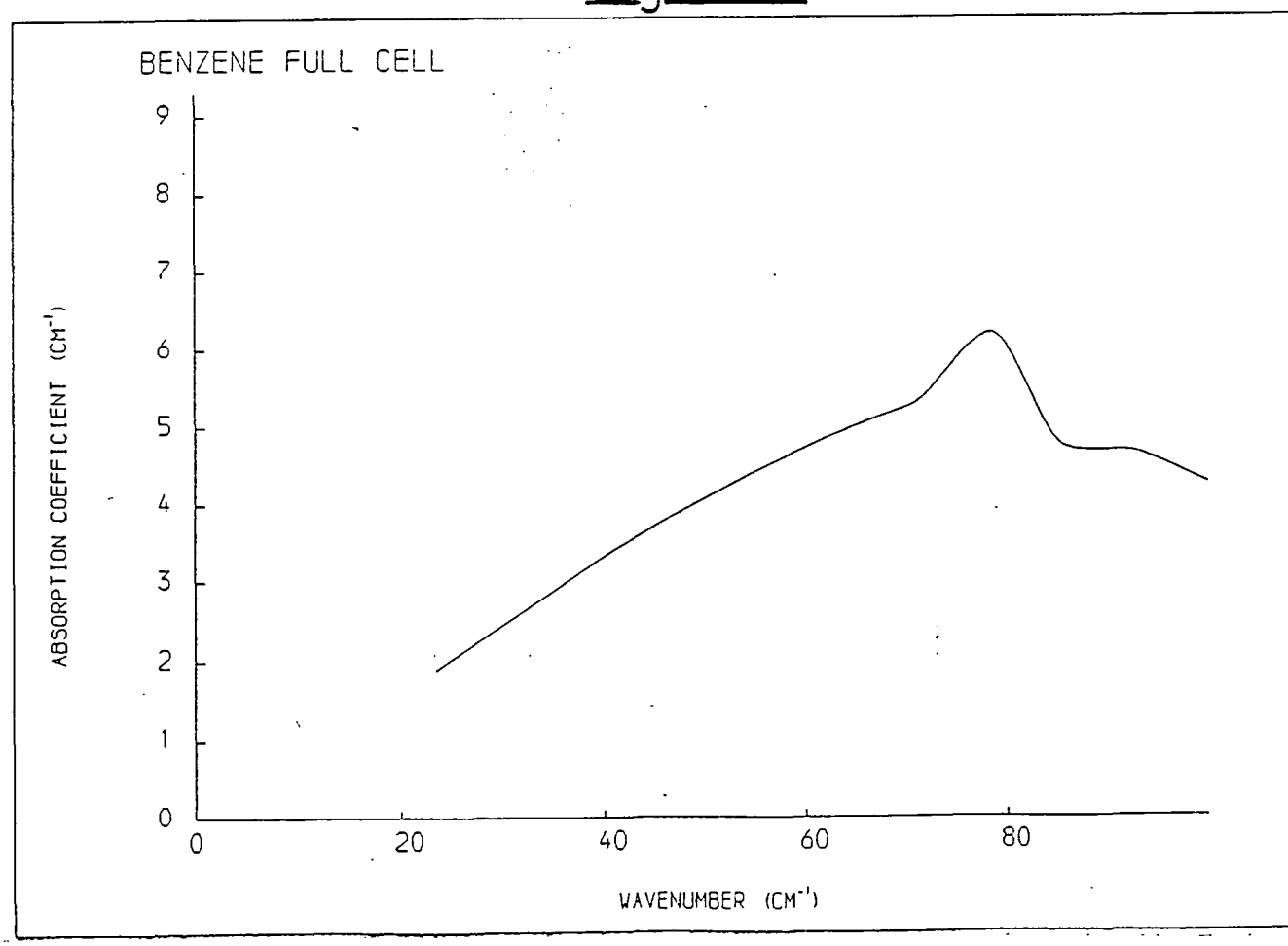

Fig. 2.25

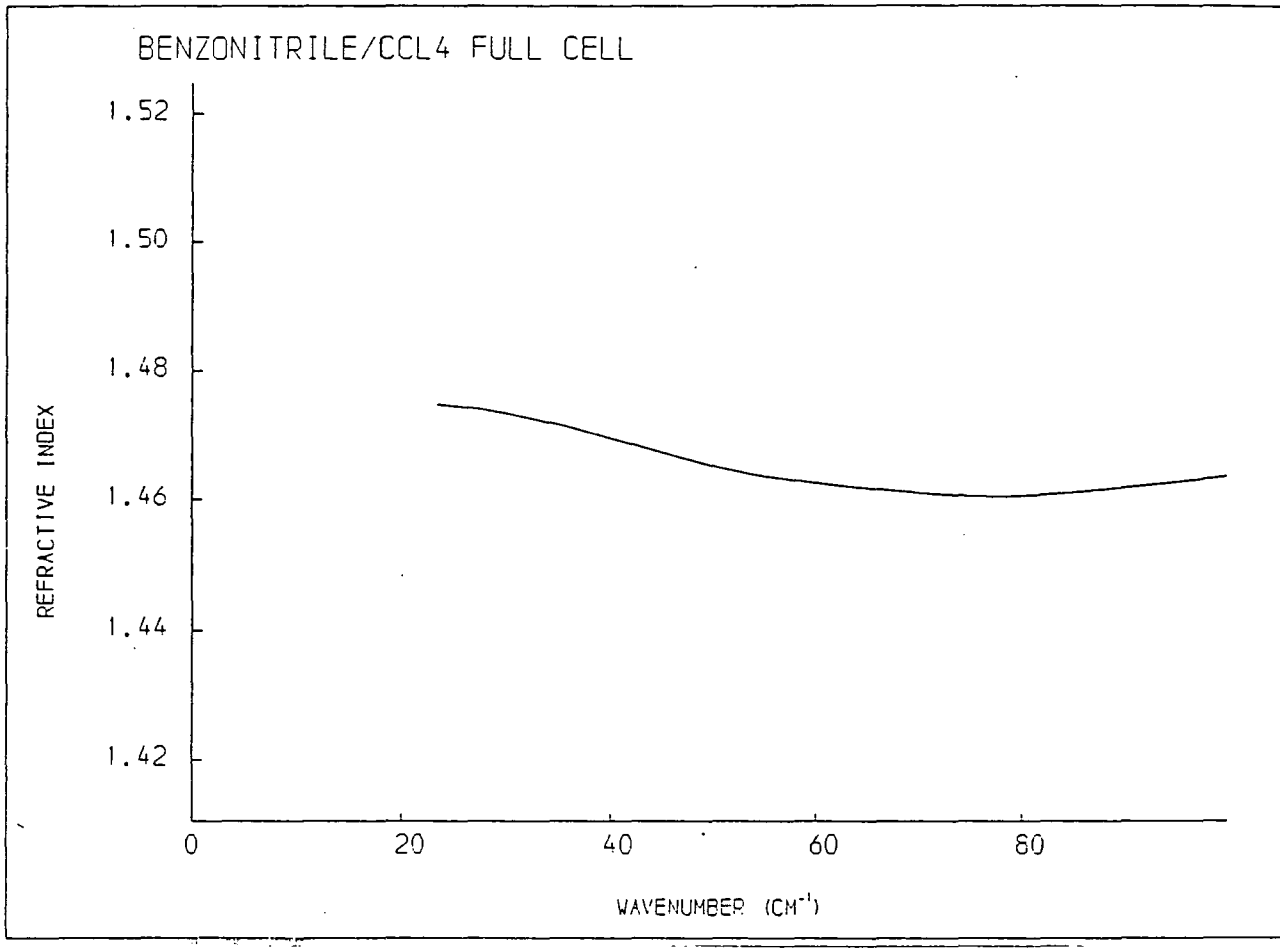

Fig. 2.26

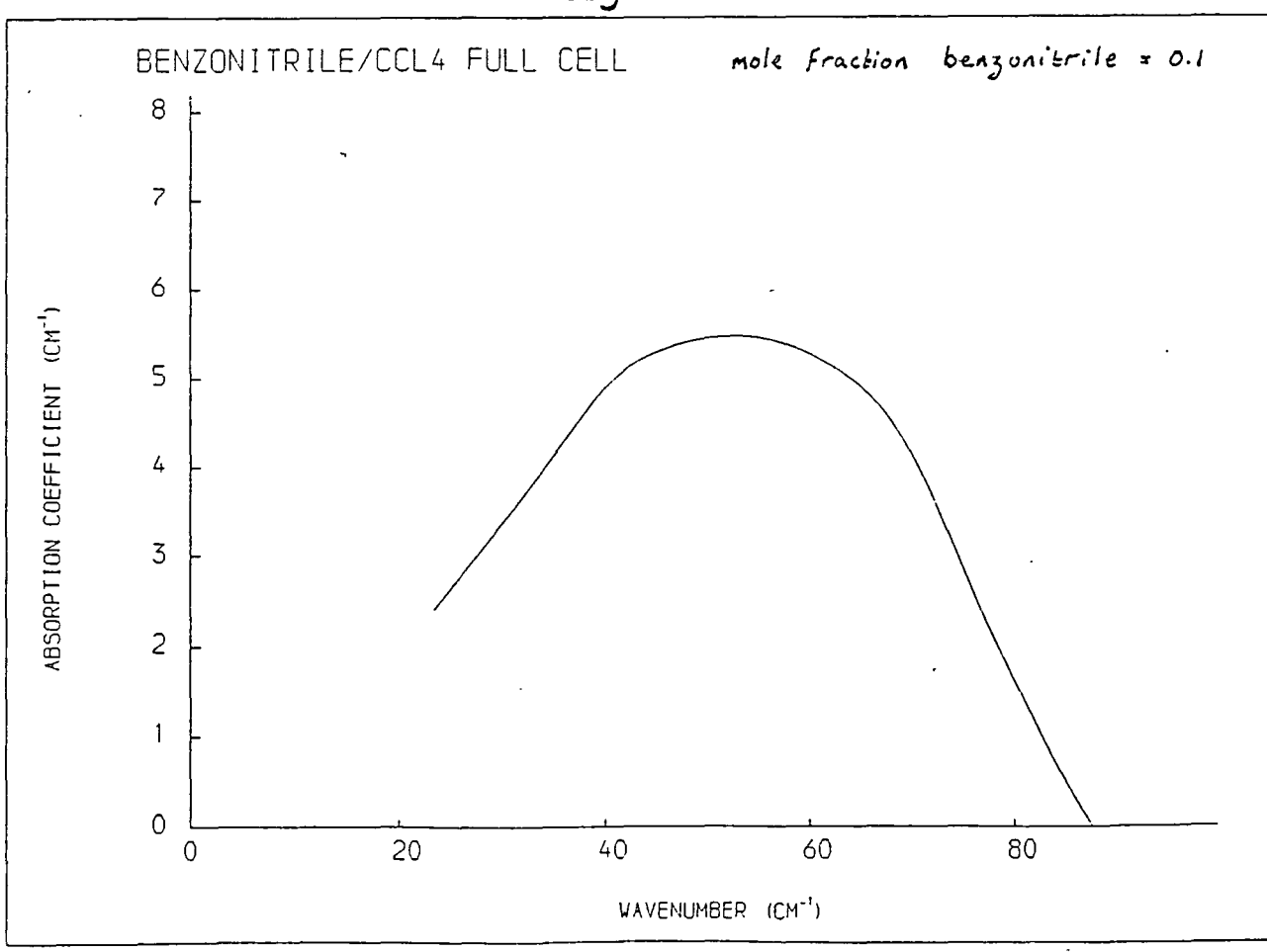

CHAPTER 3

INSTRUMENTATION

3.1 For Far Infrared

Two adapted Beckmann FS720 Michelson interferometers have been used to collect all the far infrared data presented in this thesis. The main adaptations are to the stationery arms of the instruments, one of which has been adapted to take a special liquid dispersive cell and the other, as part of this work, to take an Oxford Instruments Ltd. variable temperature cryostat by means of which solid samples may be studied between 4.2K and 300K.

3.1.1 Description of Interferometer with Dispersive Liquid Cell

The liquid cell has been described briefly in section 2.4.1a and extensively elsewhere [28,32]. The instrument may be used in non-dispersive mode simply by replacing the silicon window of the cell with a flat, stainless steel mirror. The diameter of the aperture is 50mm so that its area is considerably less than that of the original 70mm Beckmann mirrors, and signal throughput can be expected to be correspondingly poorer. The aperture is matched in the

other arm by a similar sized mirror attached to a stepping-motor driven micrometer drive. Such a drive is essential for dispersive measurements where the position of path difference must be known accurately. A certain amount of 'slack' is inherent in the stepping motor and it is imortant to take this up using the 'inch' control on the stepping motor controller before starting to record an interferogram. If the spindle connecting the motor to the micrometer is not straight then the torque will change relative to mirror position and the stepping intervals will vary with path difference, leading to frequency shifts in the computed spectrum. This can be checked by recording a modulus spectrum for (0,0) and (1,0) fringes with the silicon window in place and comparing the frequency position of the polythene peak. Figure 3.1 shows such a case resulting from a slightly bent spindle.

Phase modulation is achieved in this interferometer by means of a mirror attached to a ling vibrator in the stationary arm. The mirror is placed at 45° to the horizontal so that light is reflected vertically upwards through the liquid cell. The jitter is controlled by means of a power oscillator so that the frequency and amplitude of vibration can be varied. The frequency should be tuned to match the attributes of the detector that is used. A Golay detector operates better with a frequency of between 11 and 15Hz, whereas the efficiency of the helium-cooled germanium bolometer improves using frequencies of up to an order of

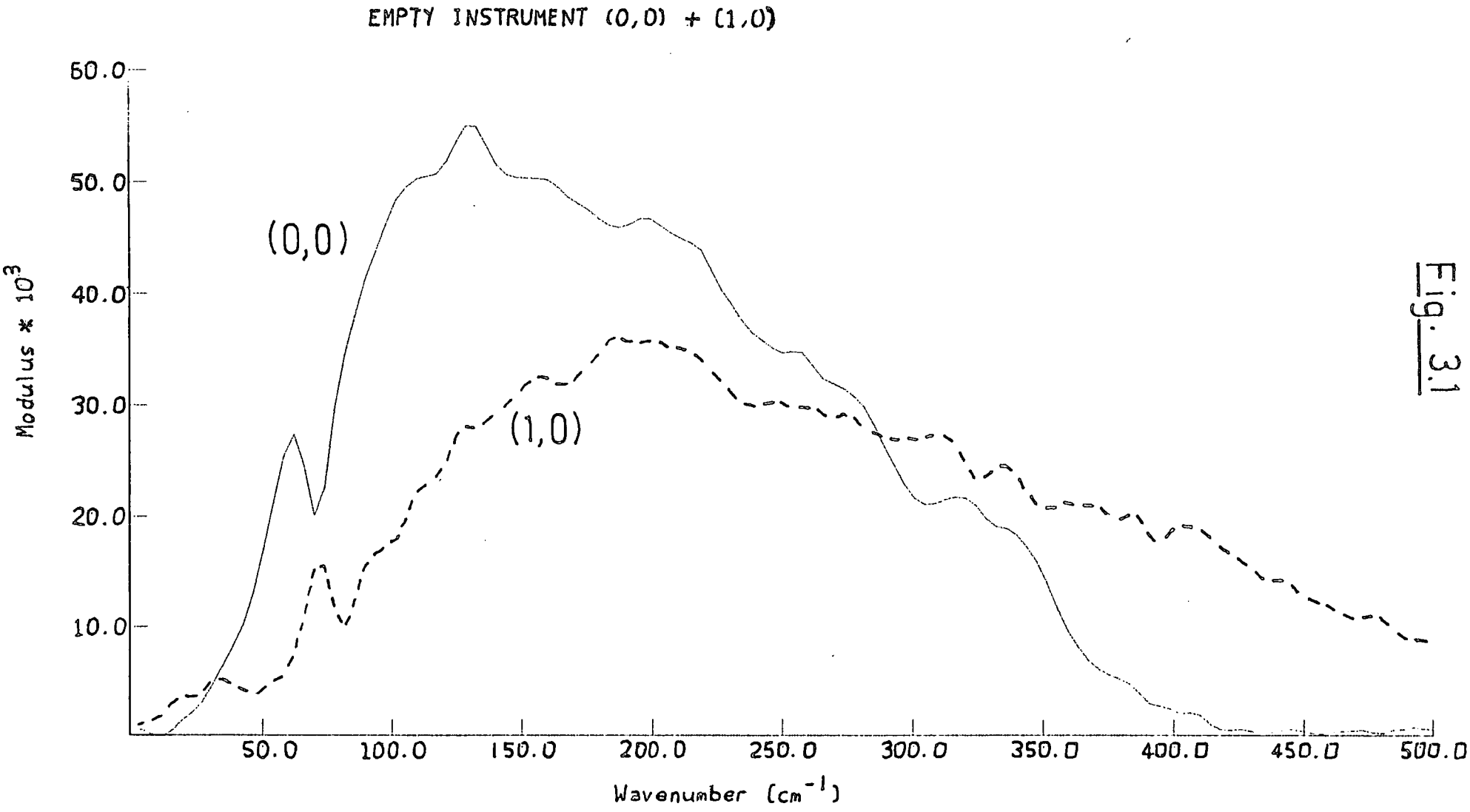
EMPTY INSTRUMENT (0,0) + (1,0)
60.0
50.0
40.0
30.0
20.0
10.0
Modulus * 10^3
(0,0)
(1,0)
50.0
100.0
150.0
200.0
250.0
300.0
350.0
400.0
450.0
500.0
Wavenumber (cm^-1)

Fig. 3.1

LAYOUT of INTERFEROMER ELECTRONICS I

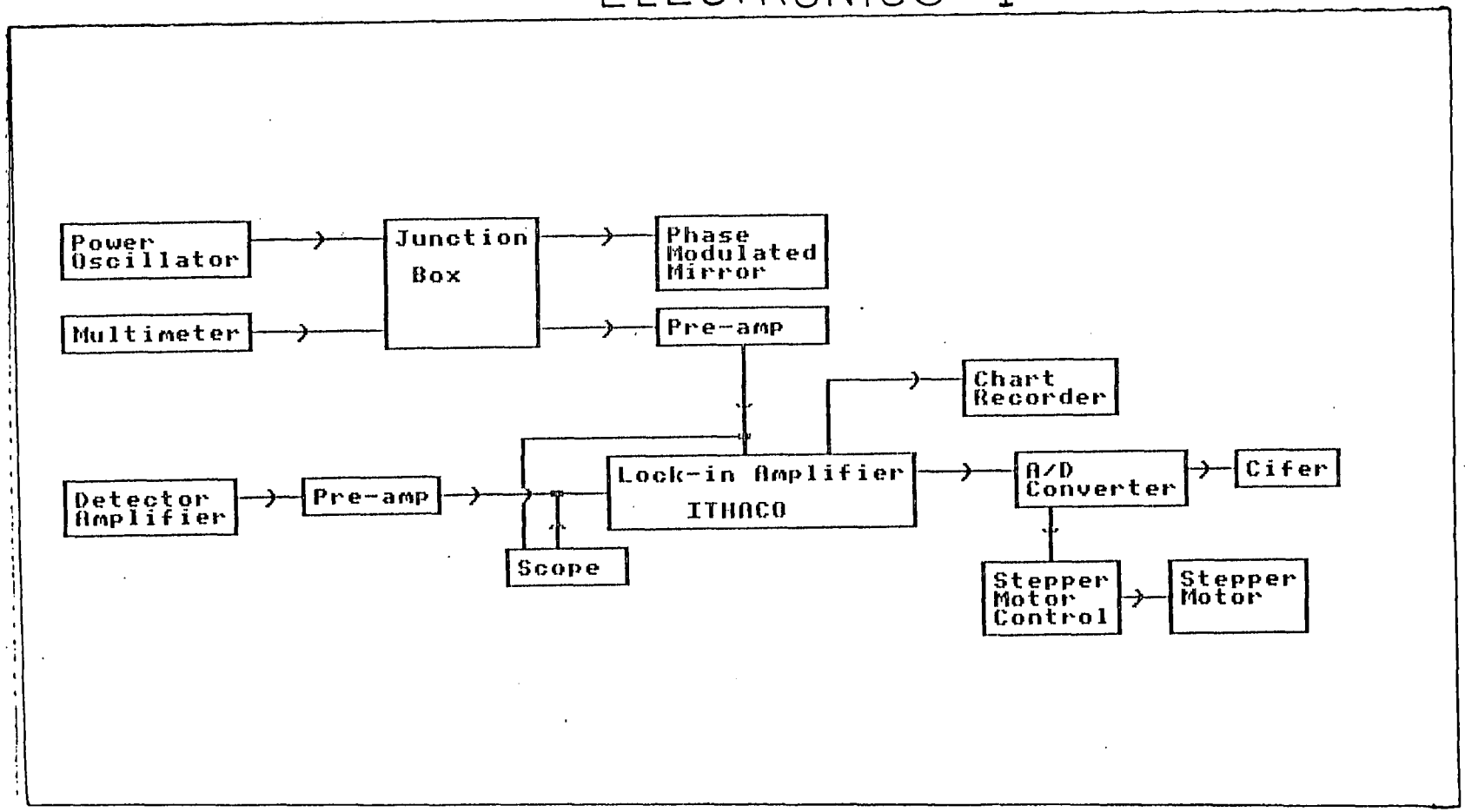

Fig. 3.2

magnitude higher than this, though care should be taken to avoid multiples of 50Hz where mains interference can be a problem. A modulation frequency of 70Hz was found to be suitable for most cases.

The wave-form from the phase modulator is fed into the reference channel of an Ithaco lock-in amplifier. The signal from the detector is fed into a pre-amplifier before the lock-in amplifier so that a wider range of sensitivities can be accessed and the full dynamic range of the analogue-to-digital converter achieved. A Cifer microcomputer is dedicated to the interferometer for collection and analysis of data.

The layout of electronic peripherals to the interferometer is shown in figure 3.2.

3.1.2 Description of Interferometer with Cryostat

The stationary arm of this interferometer has been adapted such that a variable temperature sample holder in an Oxford instruments MD5 cryostat can be interfaced with it. The MD5 cryostat includes a base section, which allows optical access to the sample, as used by Birch et al. [36]. Amplitude modulation, by means of a three-bladed rotor, is employed at a fixed frequency of 15Hz so the original Beckmann mirror is retained. The sample is held vertically so the mirror is simply displaced from its original position to the far side of the cryostat.

The original continuous scan Mori mirror drive has been replaced with a stepping motor for the same reasons as discussed in section 3.1.1. This mirror has a diameter of 60mm, but the aperture of the sample holder is of only 40mm diameter. This means that the area of one is over twice the area of the other and a significant component of the beam reflected from one arm does not interfere with light from the second. As a consequence of this the constant term, $I_o/2$, in equation 1.11 is much larger than normal and fills most of the dynamic range. The situation is worsened, for the same reasons, when an absorbing sample is introduced into one arm. The difference in aperture may be corrected for by placing an iris or similar aperture in the second arm, but a large problem still remains when using lossy samples. A solution to this difficulty was found by generating a signal, modulated at the same frequency as the real signal, and using this to subtract the constant component of the real signal. The ac, square-wave signal from the modulating chopper was converted to a dc signal of the same frequency and fed into the second signal channel of the lock-in amplifier which was then operated in A-B mode. Figure 3.3 illustrates this procedure.

Since, when using phase-modulation we actually look at the derivative of the signal, then the constant term disappears and there is no need to offset the signal to fill the dynamic range. It would therefore be of considerable advantage in the future to introduce phase modulation to

Fig. 3.3

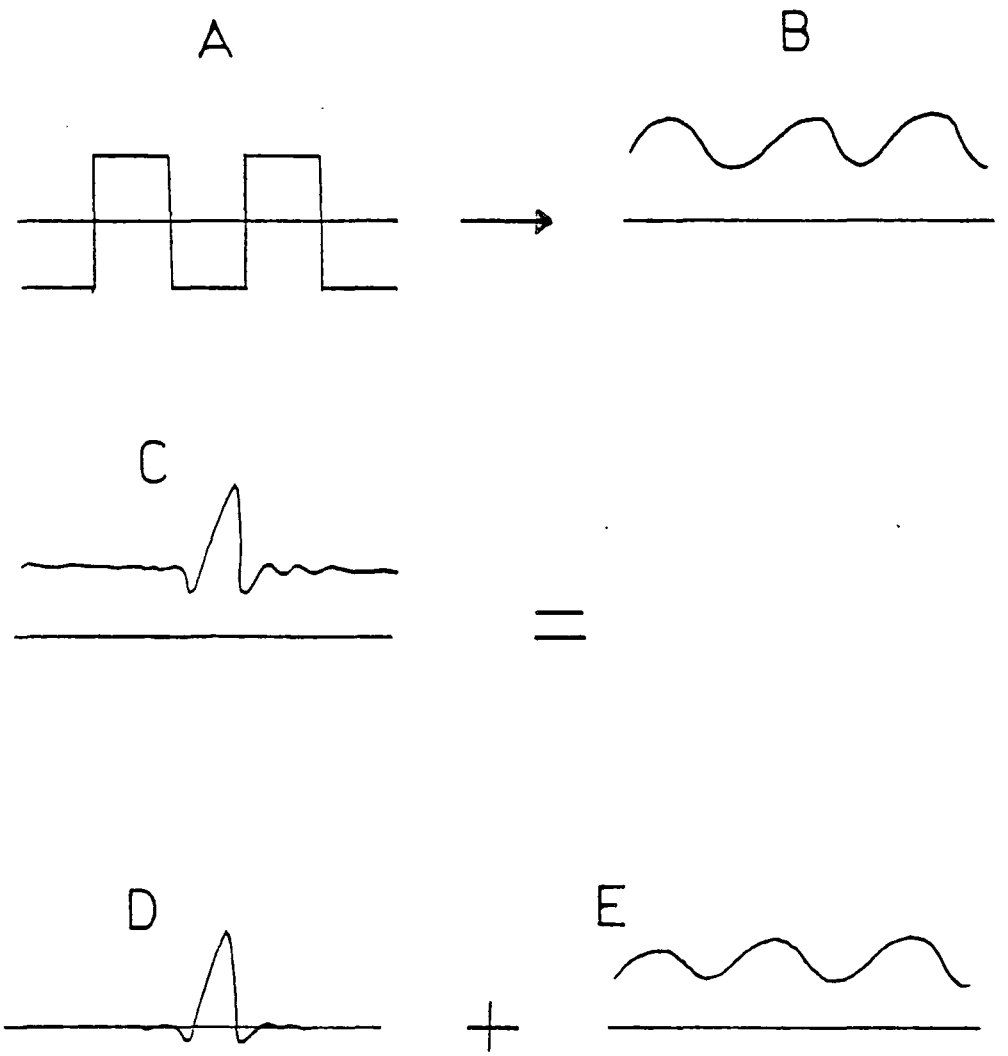

$$E \equiv B$$

$$\therefore \; D = C - B$$

Fig. 3.4

Layout of interferometer electronics II

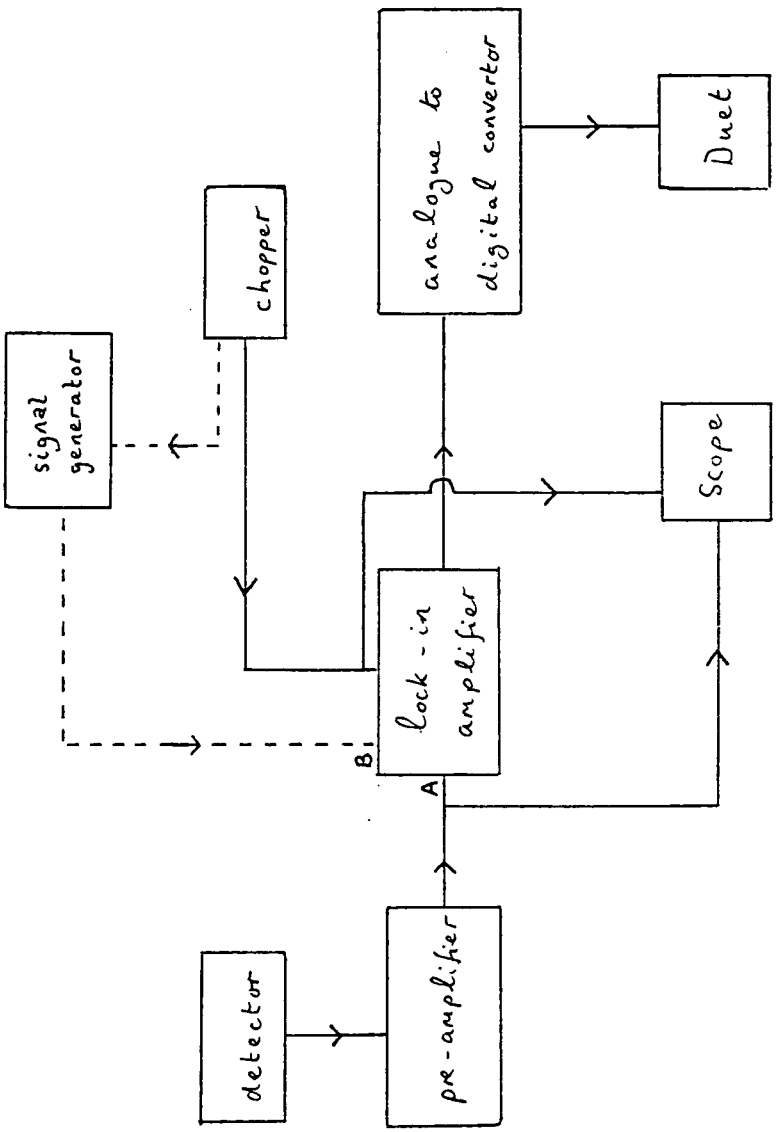

this system.

The data collection and analysis is performed by a Duet microcomputer with a graphics terminal. The general layout of the interferometer system is illustrated in figure 3.4.

3.1.3 The MD5 Cryostat with Variable Temperature Insert

A diagram of the cryostat and insert is drawn in figure 3.5. The cryostat consists of two baths, one intended for liquid helium and the other one for liquid nitrogen. The helium bath is thermally linked to the sample space via a heat exchanger; helium is supplied to this by means of a needle valve located on the top flange. The sample is top loaded and cooled by a static column of helium gas. Two identical mounting positions are provided on the sample holder and both of these can be placed in the path of the beam by vertical movement of the holder so that sample and background runs can be made with minimal disturbance to the system. A thermocouple has been positioned on the sample holder to measure the temperature of the sample.

The temperature of the sample can be varied between 4.2K and 300K by means of a heater and thermal resistance sensor situated in the heat exchanger. These are controlled by an Oxford Instruments Ltd. 3120 temperature controller. The measured temprature is compared with a required temperature and an error signal is generated which is proportional to the difference.

Fig. 3.5

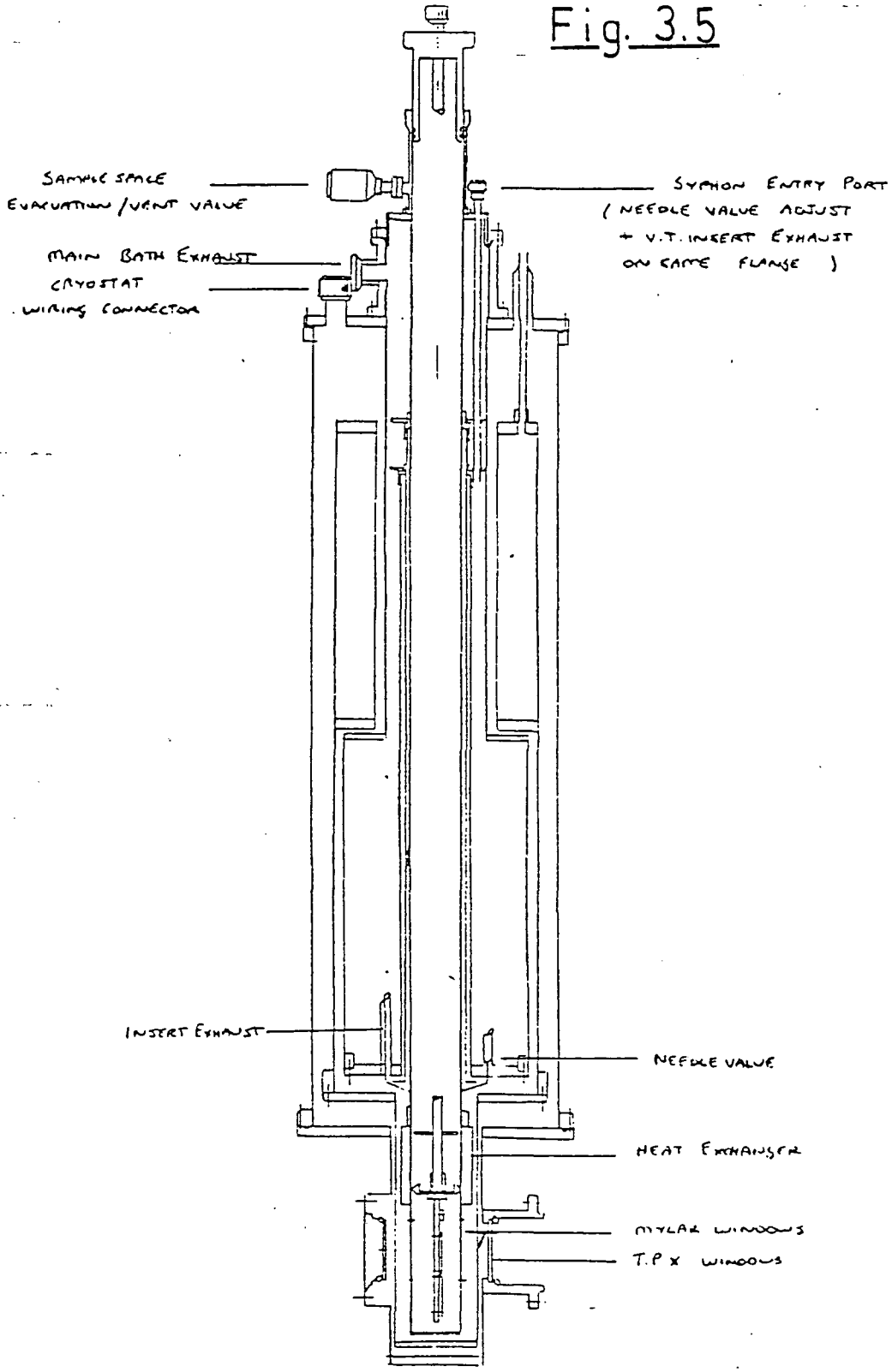

Sketch of Special MD5 - VT Insert

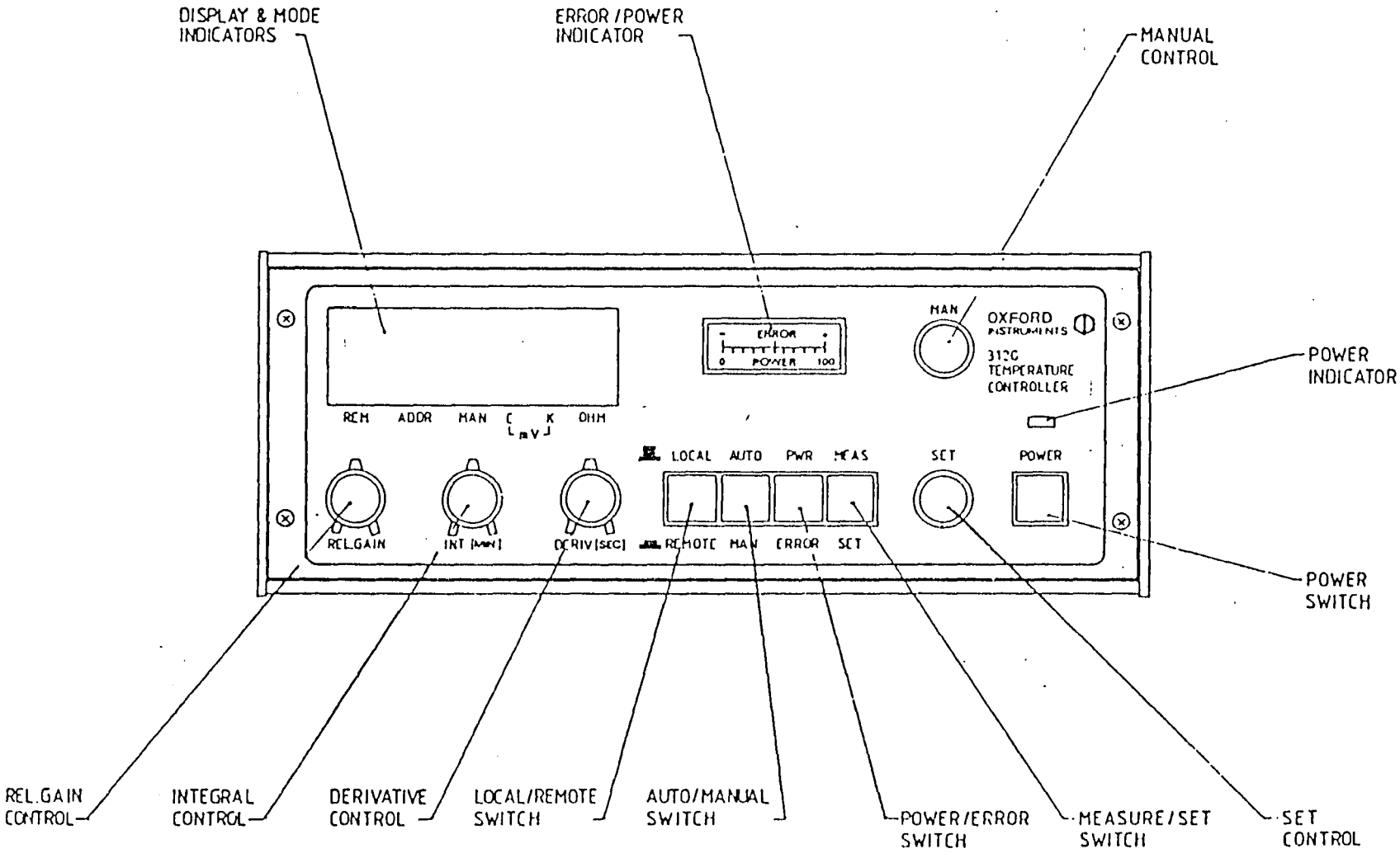

Fig. 3.6

TEMPERATURE CONTROLLER

The controller output to the heater then depends on:

(i) the magnitude of the error,

(ii) the integral with respect to time of the error,

(iii) the derivative with respect to time of the error.

The coefficients of all three can be varied in order to obtain a steady temperature. It is important to note that the measured temperature is that of the heat exchanger, not of the sample. The sample temperature should be read using the thermocouple in the sample holder. A diagram of the controller is provided in figure 3.6.

Before filling the cryostat with cryogens, the vacuum space should be pumped to better than 10^{-6} torr. If using liquid helium, the inner bath should first be cooled with liquid nitrogen which is blown out using gaseous helium after several hours standing. For temperatures above 70K liquid nitrogen may be used in the inner bath.

The cryostat was supplied with a total of six windows. The vacuum space of the cryostat ($< 10^{-6}$ torr) was isolated from the vacuum space of the interferometer ($\sim 10^{-2}$ torr) via two TPX windows.

Two Mylar windows formed part of the radiation shield and a further two were fitted over the apertures in the sample compartment. The Mylar windows on the radiation shield were subsequently removed to improve signal throughput. A lot of signal is still lost, however, through reflection and absorption by the remaining windows and, since the windows are present in only one arm of the

interferometer, they cause considerable dispersion. Such dispersion does not affect the experimental results, however, since we are looking at the difference in phase change for sample and background. Example interferograms are presented in figure 3.7 to illustrate the degree of dispersion produced by the windows and give some idea of the intensity loss that can be expected through the presence of the windows. The percentage loss figures are calculated using Fresnel's equations.

The thickness of the Mylar windows is 100μm and they produce an interference fringe in the interferogram, marked with an arrow in figure 3.7. This has the effect of modulating the spectrum and effectively means that the energy is restricted to the frequency range below approximately $60cm^{-1}$.

The performance of the cryostat and interferometer has been tested using materials whose optical constants are well known in the far infrared: teflon [37,38]; perspex [37,39]; polythene [36,37,39]. The far infrared spectrum of the conducting polymer polyacetylene [40,41] was also studied and compared with results obtained with the same cryostat at the National Physical Laboratory.

The optical constants of teflon and perspex are presented in figures 3.8 and 3.9 respectively. They were measured at room temperature. The absorption levels of the two polymers are very similar, and both rise slightly to higher frequencies. These spectra are the result of only

Fig. 3.7

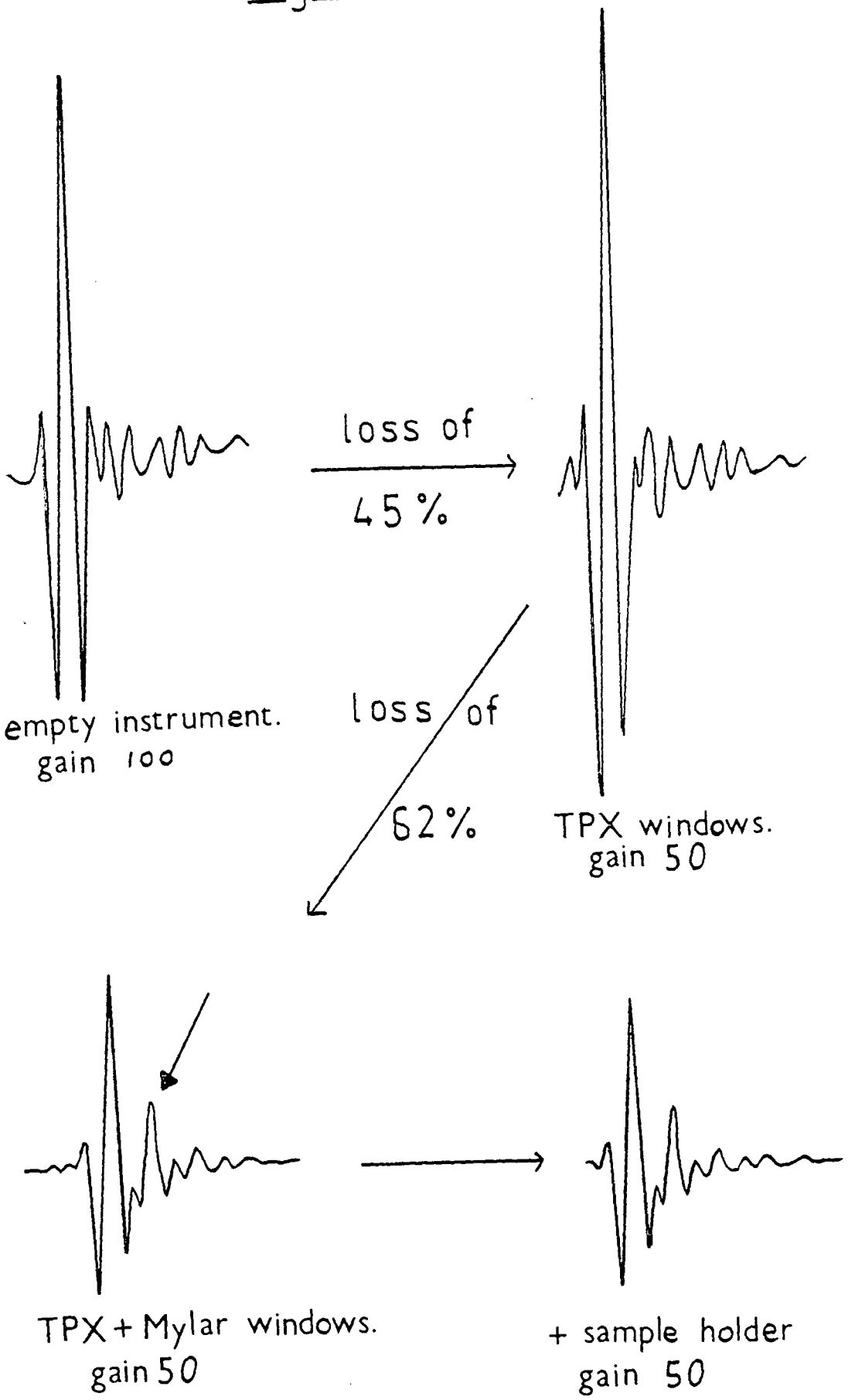
loss of
45 %
empty instrument.
gain 100
loss of
62 %
TPX windows.
gain 50
TPX + Mylar windows.
gain 50
+ sample holder
gain 50

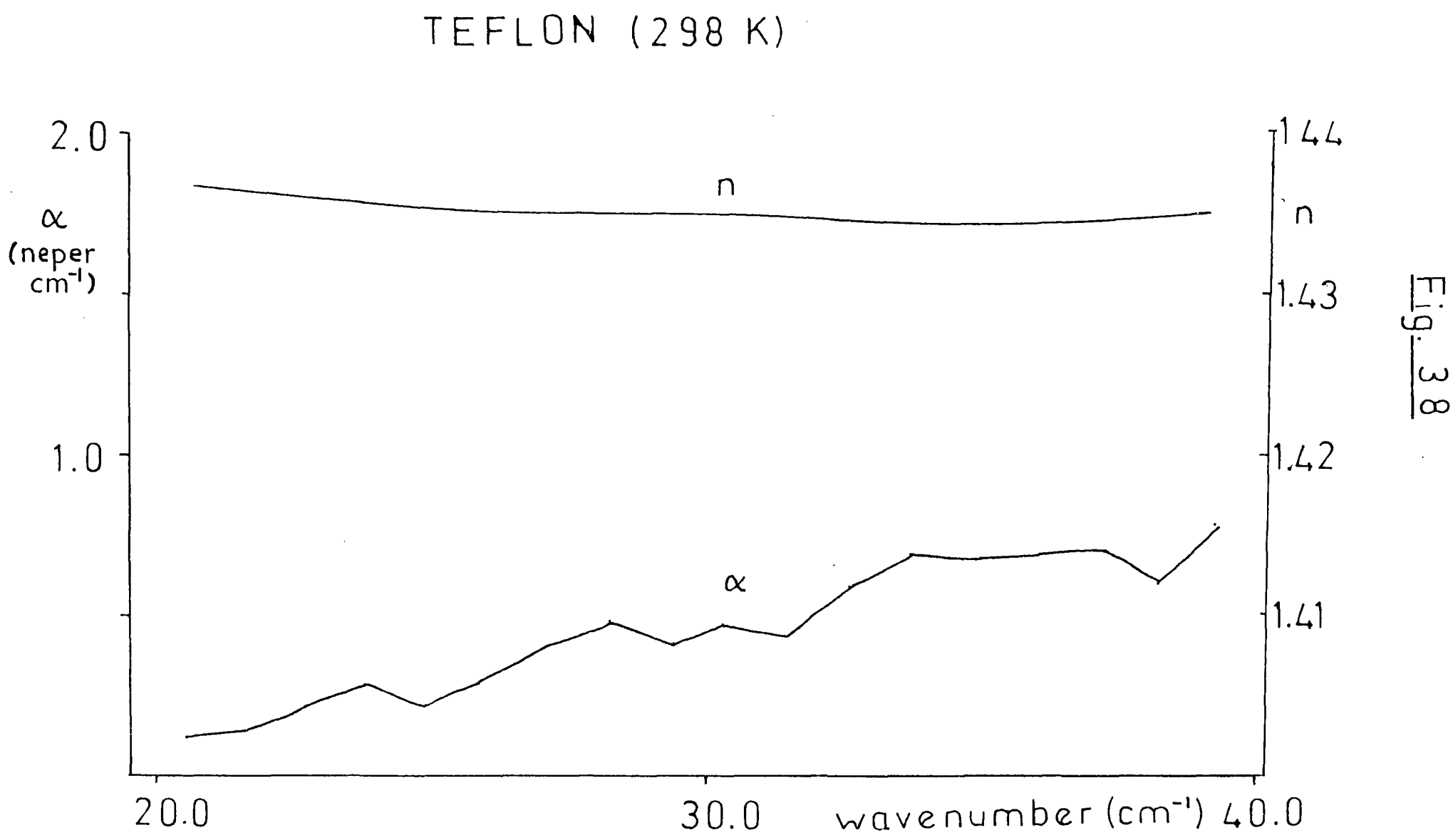
TEFLON (298 K)
2.0
α
(neper
cm⁻¹)
1.0
n
α
1.44
n
1.43
1.42
1.41
20.0
30.0
wavenumber (cm⁻¹)
40.0

Fig. 38

Fig. 3.9

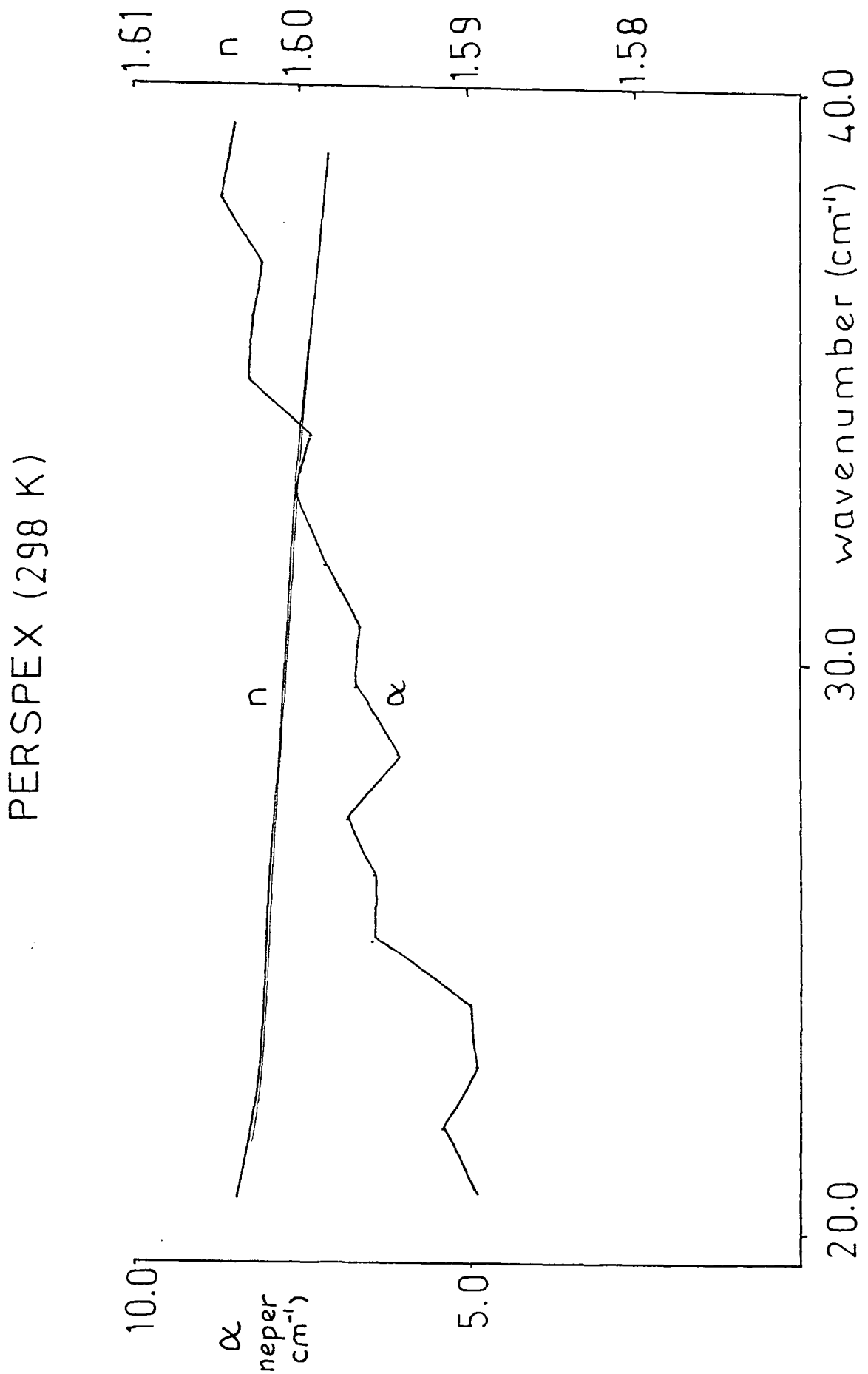
PERSPEX (298 K)
1.61
n
1.60
1.59
1.58
n
α
10.0
α (neper cm⁻¹)
5.0
20.0
30.0
wavenumber (cm⁻¹)
40.0

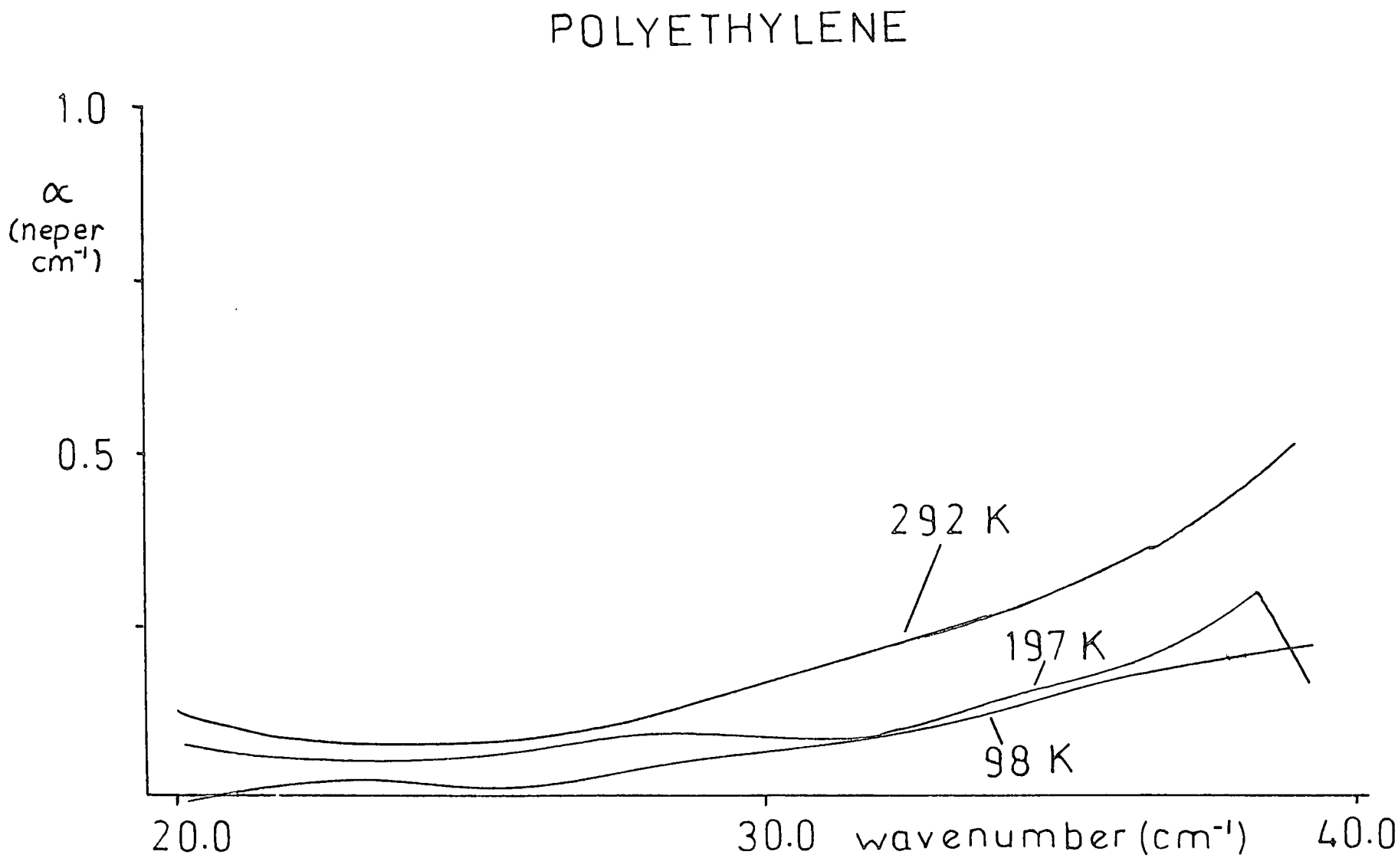
POLYETHYLENE
1.0
α
(neper
cm⁻¹)
0.5
292 K
197 K
98 K
20.0
30.0
wavenumber (cm⁻¹)
40.0

Fig. 3.10

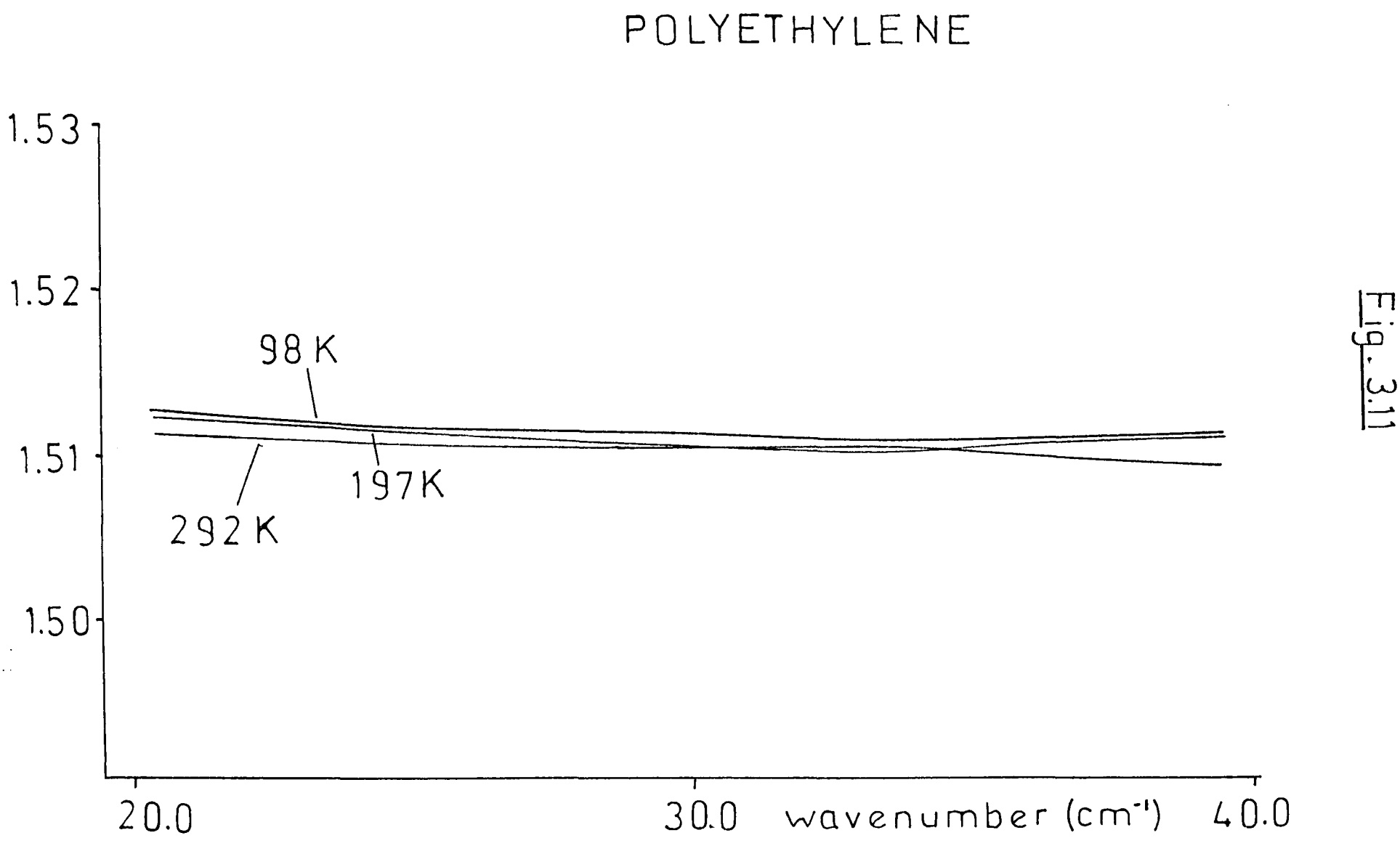
POLYETHYLENE
1.53
1.52
1.51
1.50
98 K
197K
292 K
20.0
30.0
wavenumber (cm⁻¹)
40.0

Fig. 3.11

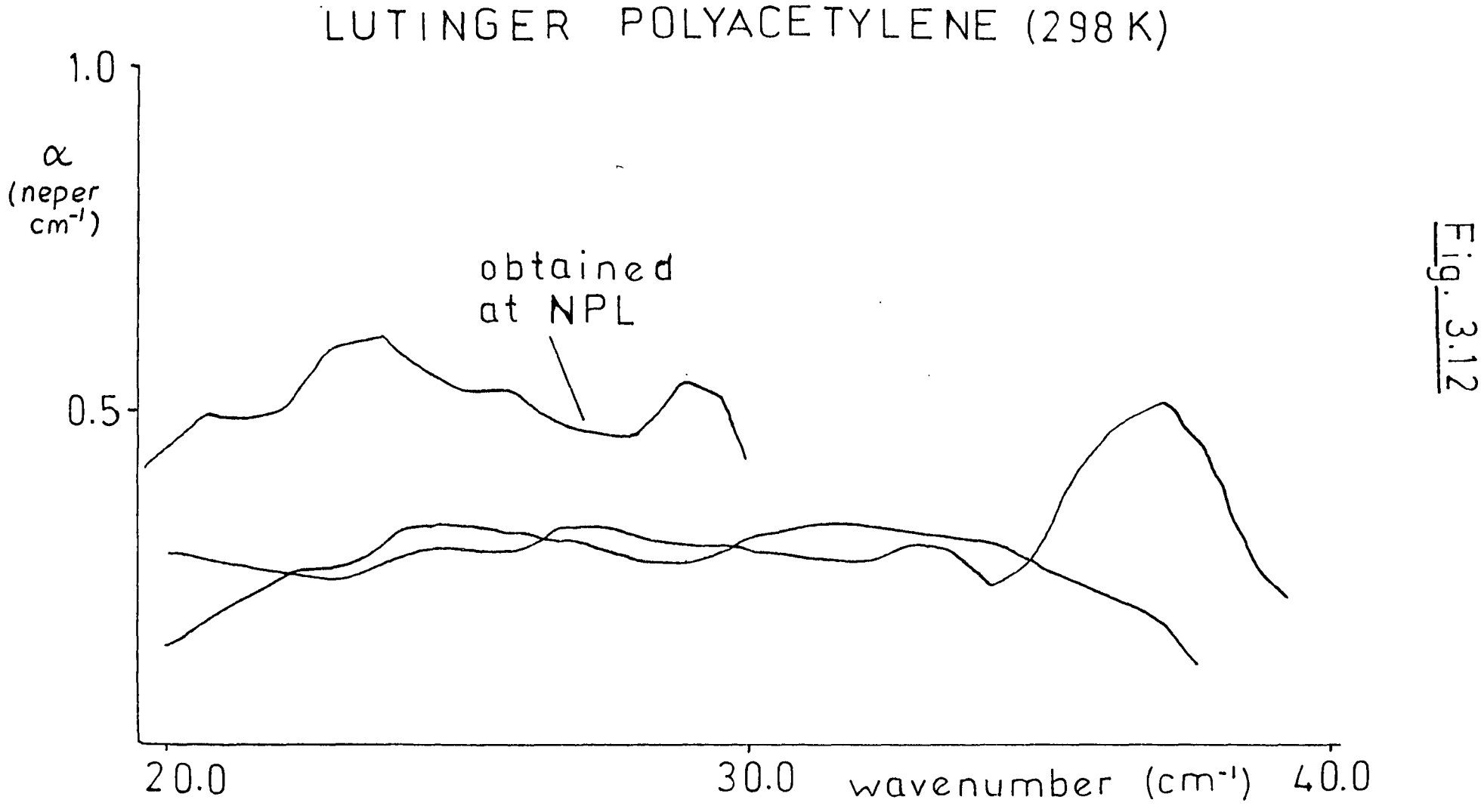
LUTINGER POLYACETYLENE (298 K)
1.0
α
(neper
cm⁻¹)
0.5
obtained
at NPL
20.0
30.0
wavenumber (cm⁻¹)
40.0

Fig. 3.12

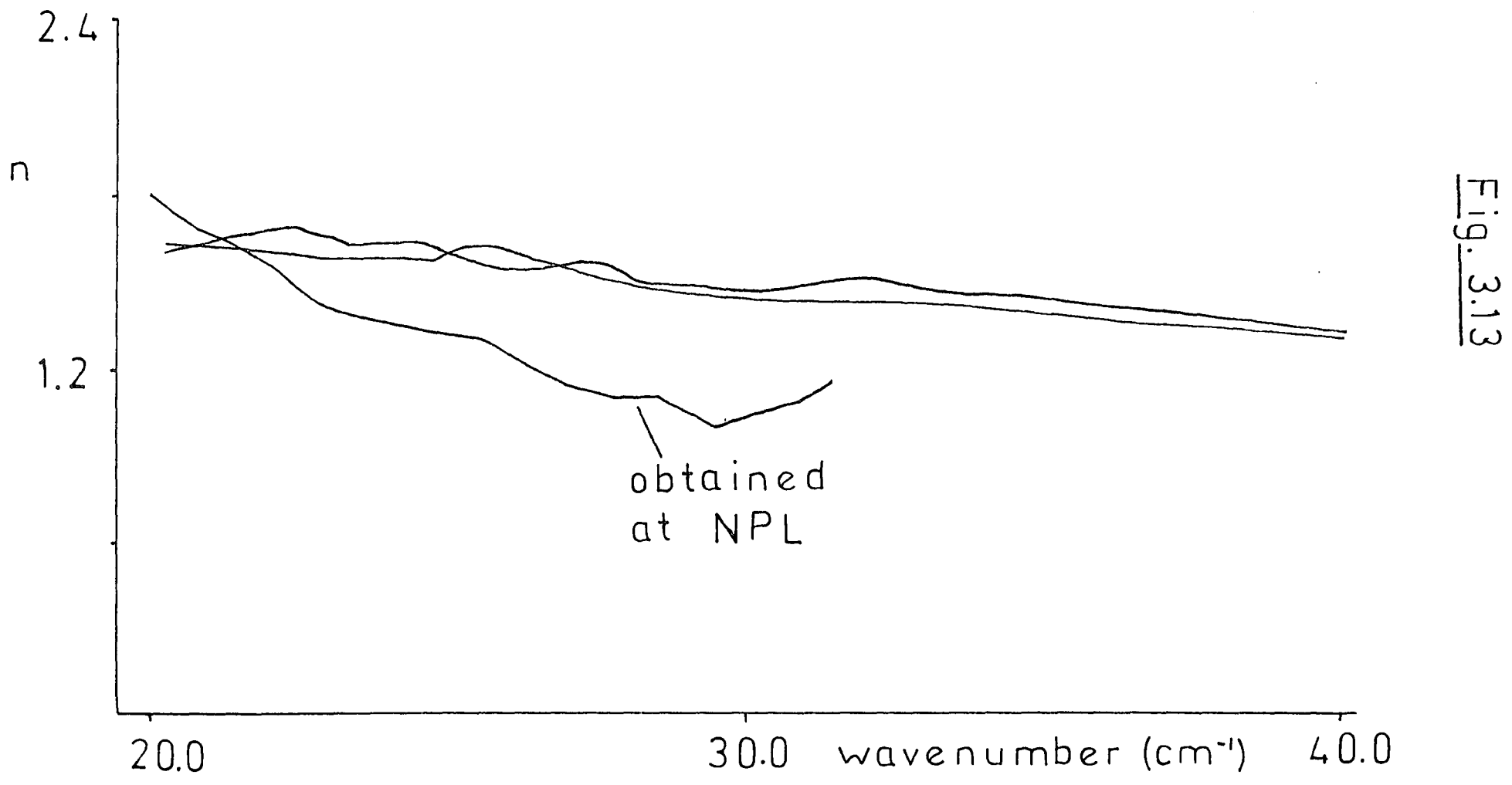
LUTINGER POLYACETYLENE (298 K)
2.4
n
1.2
obtained
at NPL
20.0
30.0
wavenumber (cm⁻¹)
40.0

Fig. 3.13

one experimental run and not an average of several as presented elsewhere [36]. The absorption coefficient is thus fairly noisy, but the overall level agrees with previous studies [36]. The refractive indices differ slightly with those quoted in the literature [36] and this is probably due to inaccuracies in measuring the specimen thickness.

The optical constants for polythene as a function of temperature are shown in figures 3.10 and 3.11. The absorption coefficient at room temperature is of the same order of magnitude as the other polymers measured, but rises more gradually at higher frequencies. It is difficult to compare absolute absorption levels with those derived elsewhere [36,37,39] because the levels can vary with the manufacuring process. The absorption coefficient is sensitive to the presence of plasticizers and anti-oxidants added to the polymer [36].

With decreasing temperature, the refractive index increases due to thermal-contraction of the polymer leading to an increase in density [39]. The absorption coefficient shows a decrease with temperature as found elsewhere [39].

3.1.4 Detectors

Two types of detector have been used throughout this work: IR50 Golay detectors and a helium cooled germanium bolometer supplied by Oxford Instruments Ltd. Golay

detectors are pneumatic in operation; a gas filled bladder expands when heated by the infrared radiation, and the expansion is monitored by a photodiode. As such, the Golay detector is sensitive to external vibrations and temperature variations, and the output signal is liable to be noisy. A diamond-windowed Golay detector is necessary for work above $120cm^{-1}$, but below this a quartz windowed detector is sufficient.

The germanium bolometer houses a single antimony doped crystal of germanium. The antimony gives rise to donor levels close to the conduction band of germanium. Electrons from the donor levels are excited by far infrared radiation into the conduction band and change the resistivity of the crystal. The signal outputted by the detector is directly related to the resistivity and is free from mechanical noise. The efficiency of the bolometer in terms of signal-to-noise is much greater than that of the Golay detector.

The bolometer is much more sensitive at lower temperatures and its efficiency increases dramatically as the temperature is lowered from 4.2K to 1.6K by pumping on the helium. Typically, an increase in signal of approximately 600 was realised on lowering the temperature.

3.2 For Mid Infrared

The work in the mid-infrared region presented in this

thesis between 1200 and 4000 cm^{-1} was done using a Nicolet 60SX Fourier transform infrared spectrometer. The layout of the optical bench is illustrated in figure 3.14. This is a rapid-scanning instrument and any number of interferograms may be accumulated and averaged before transforming. Since it is a single-beam interferometer, interferograms must be recorded for sample and background and a ratio performed in the frequency domain. A dedicated microcomputer is linked to the optical bench for data collection and analysis. A more comprehensive description of the instrument is given by Lux [42].

Fig. 3.14

60SX—Infrared Spectrometer Optics

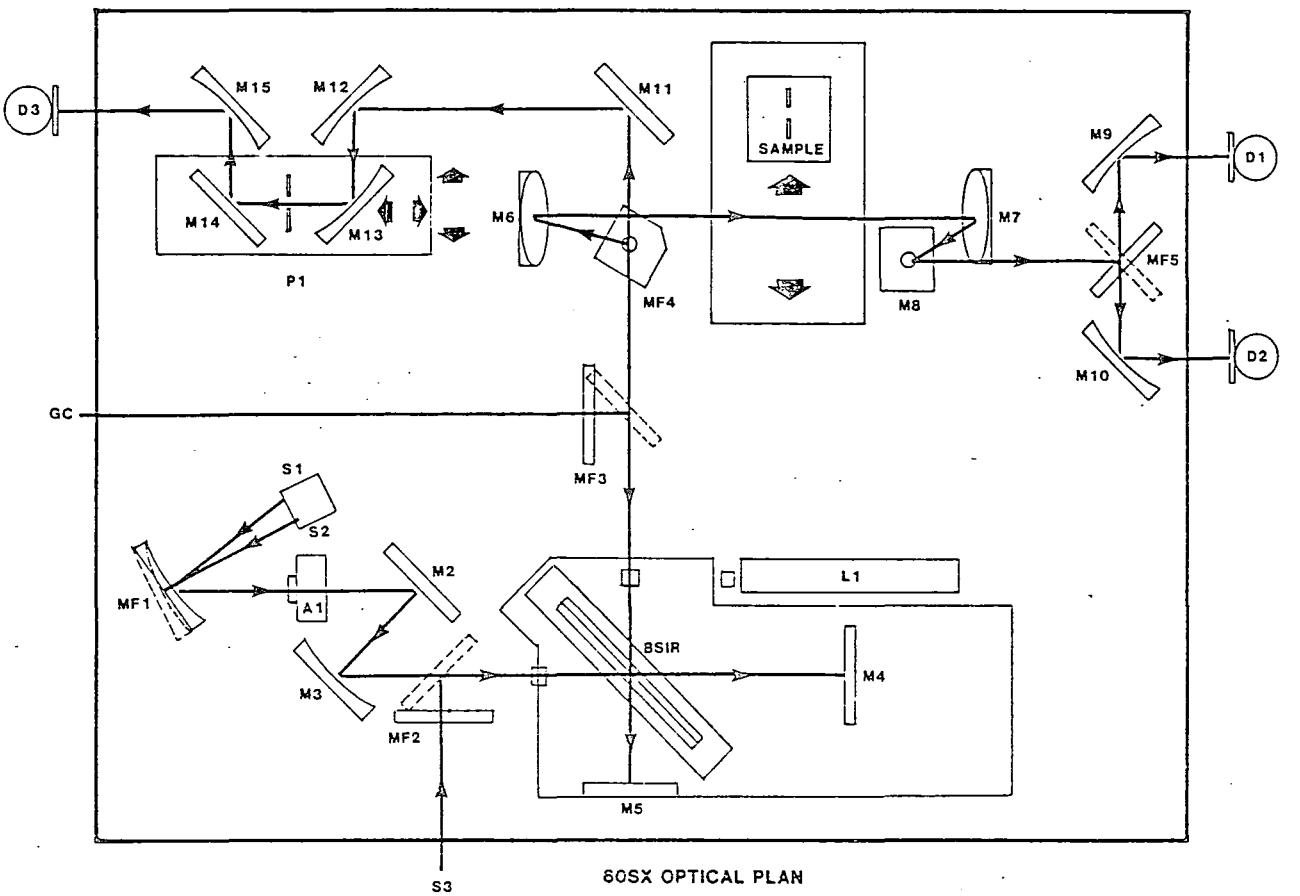

S1	Standard Globar source
S2	Standard tungsten-halogen source
S3	Optional source
MF1	Computer-controlled source selection mirror 208 mm EFL
A1	Computer-controlled aperture
M2	Flat mirror
M3	Collimating off-axis parabolic mirror 208 mm EFL
MF2	Moving flat mirror to external source
BSIR	Infrared/laser reference beamsplitter
M4	Interferometer moving mirror
M5	Interferometer fixed mirror
MF3	Moving flat mirror to GC accessory
L1	Reference laser
MF4	Moving flat mirror to micro beam
M6	Sample focusing mirror, off-axis parabola 237 mm EFL
M7	Sample collection mirror, off-axis parabola 237 mm EFL
M8	Flat mirror
MF5	2-position computer controlled detector selection flat mirror
M9, M10	Detector condensing mirror, off-axis parabola 64 mm EFL
D1, D2, D3	Pre-aligned detector positions
M11	Flat mirror
M12	Micro beam condensing mirror, off-axis parabola 64 mm EFL
M13	Z-axis micro-beam computer-controlled focusing mirror, off-axis parabola 64 mm EFL
M14	X-axis micro-beam computer-controlled mirror flat
M15	Detector condensed mirror, off-axis parabola 64 mm EFL

CHAPTER 4

THEORY OF LIQUID DYNAMICS

4.1 Introduction

The study of liquid dynamics can be used as an effective tool to examine the intermolecular forces that exist between individual molecules in a fluid. These forces are weak compared with say intramolecular forces and give rise to absorption in the far infrared and microwave regions of the spectrum. They correspond to rotational and translational motions of individual molecules, as well as what can be considered as oscillations of a molecule in the 'liquid lattice' formed by its neighbours (libration). This can be compared to the lattice vibrations seen for a solid crystal in the same region, but the 'lattice' for a liquid is not static but in a state of continuous rapid change.

A given molecule, then, may be considered to be oscillating in a van der Waals' force field which is changing rapidly as the environment of the molecule is undergoing change. The molecular reorientational events occurring in the liquid, depending strongly on intermolecular interactions and the separation between molecules, will be affected to a great extent by this rapid perturbation of the molecular environment.

The molecular processes alluded to here occur on a pico-second time scale and, as such, are well suited to study by microwave and far infrared spectroscopies. Absorption in the far infrared region describes the fast modulation of the intermolecular forces whereas the microwave absorption reflects the slower processes.

4.1.1 The Far Infrared Profile of Liquids

A typical far infrared profile for a polar or non-polar liquid, figure 4.1, is broad and featurless, as compared to the corresponding bands for a gas or a crystal which show considerable spectral structure. This is a consequence of the different molecular environments for the three phases. A solid crystal consists of molecules which are, in the perfect case, in identical environments. As each molecule is in the same potential well they all absorb at the same limited number of frequencies. A gas molecule exists in relative isolation with only occasional collisions with other molecules and discrete rotational bands can be observed, e.g. figure 1.15. A liquid, however, consists of molecules in a state of continuous collision occurring on a time scale which is small in comparison to the rotational time and a given molecule is unable to rotate freely.

The positions of the molecules in a liquid and the collisions between them are random and each molecule has a unique environment. As intermolecular interactions are

greatly dependent on distance, each molecule will be subject to a unique set of forces and, in the liquid as a whole, there will be a large number of librational frequencies. These may be considered as merging together to form a featureless band. Since the quantised spectral structure is not discernable it is appropriate to use classical equations of motion to describe the dynamics of a liquid system.

The infrared selection rules require that only motions that produce a change in the magnitude or direction of the dipole moment relative to the normal coordinates may contribute to the infrared spectrum. From this we would expect only rotation of polar molecules to produce a spectrum in the far infrared region. This, however, is obviously not the case since many non-polar molecules such as carbon tetrachloride [43,44], benzene [45,46] , carbon disulphide [44,46,47] and others [48-51] show significant absorption. This may be explained by considering the presence of fluctuating induced dipoles caused by collisions with other molecules and will thus be referred to as the collision-induced effect.

Since this effect can be observed for non-polar molecules, it should be expected that the profile for a polar liquid will have a contribution from a collision-induced part as well as the reorientational part allowed by the selection rules.

4.1.2 Interpretation of Far Infrared Liquid Profiles

Far infrared spectra are usually measured experimentally using equation 1.22 to give the absorption coefficient, $\alpha(\bar{\nu})$. The spectra may also be described by the spectral density or absorption cross-section, $I(\bar{\nu})$, and the two are related by [52],

$$I(\bar{\nu}) = \frac{3\hbar n(\bar{\nu})\alpha(\bar{\nu})}{4\pi^3\rho^2 V\bar{\nu}\left[1 - \exp(-hc\bar{\nu}/kT)\right]} \tag{4.1}$$

where V is the volume and ρ the number density. The factor $[1 - \exp(\frac{-hc\bar{\nu}}{kT})]$ accounts for induced emission from the sample which is important at low frequencies because the energies of transitions which give rise to absorption are comparable to kT. The absorption cross-section can also be related to the correlation function of the total dipole moment density, M_T, according to the real part of

$$I(\bar{\nu}) = c\int_{-\infty}^{\infty} \langle M_T(t) \cdot M_T(0)\rangle \exp(-i2\pi\bar{\nu}ct)\, dt \tag{4.2}$$

That is, the correlation function denoted by

$$c(t) = \langle M_T(t) \cdot M_T(0)\rangle \tag{4.3}$$

is the Fourier transform of the absorption cross section. The correlation function may be normalised according to

$$c(t) = \frac{\langle M_T(t) \cdot M_T(0)\rangle}{\langle |M_T(0)|^2\rangle} \tag{4.4}$$

The angular brackets refer to an ensemble average over all molecules in the system. Following Madden et al. [53,54] a polar liquid is considered to possess a total dipole

moment density made up of a reorientational part, ${}^{O}M_T(t)$, and an interaction induced part, ${}^{I}M_T(t)$. The induced part depends critically on the relative positions and orientations of the molecules in the fluid and is the only contribution to the total dipole moment density in fluids lacking permanent dipoles. For liquids possessing a dipole moment there will be an induced effect from the polar molecules themselves on one another, and this will contribute to ${}^{I}M_T$. Cross terms may also be significant since there will be some correlation between the reorientational and induced parts. Thus the total dipole moment density for a polar liquid can be written as [54]

$$M_T(t) = (1 + G_T)\, {}^{O}M_T(t) + \Delta M_T(t) \tag{4.5}$$

where

$$G_T = \frac{\langle {}^{O}M_T(0) \cdot {}^{I}M_T(0) \rangle}{\langle {}^{O}M_T(0) \cdot {}^{O}M_T(0) \rangle} \tag{4.6}$$

and

$$\Delta M_T(t) = {}^{I}M_T(t) - G_T\, {}^{O}M_T(t) \tag{4.7}$$

When the permanent moments are in a configuration giving rise to the value of ${}^{O}M_T$, then $G_T\, {}^{O}M_T(t)$ is the average value of the induced moments and ΔM_T results from the fluctuations of the molecules about this configuration.

The correlation function is now given by

$$\begin{aligned} \langle M_T(t) \cdot M_T(0) \rangle &= (1 + G_T)^2 \langle {}^{O}M_T(t) \cdot {}^{O}M_T(0) \rangle \\ &+ 2(1 + G_T) \langle \Delta M_T(t) \cdot {}^{O}M_T(0) \rangle \\ &+ \langle \Delta M_T(t) \cdot \Delta M_T(0) \rangle \end{aligned} \tag{4.8}$$

where the first term on the right hand side is the reorientational part and the other two terms are the collision induced parts. The relative contributions of each term in equation 4.8 to the correlation function have been estimated by computer simulation of liquid acetonitrile [53,54].

A means of studying interaction-induced dynamic processes in dense fluid systems which has been widely adopted [46,47,55-57] is by studying spectra which are 'forbidden' in the isolated molecule approximation. These spectra have been obtained by various techniques including far infrared [44,45,48], vibrational infrared [58] and light-scattering [59,60]. The spectra may be thought of as representing three types of processes, although the divisions are arbitrary:

(a) Long-time fluctuations which manifest themselves in the low frequency absorptions and represent the diffusional motion of molecules between different potential wells in the liquid. This is a relatively slow process since it requires a certain activation energy to lift the molecule out of the potential well;

(b) Medium-time fluctuations represent large amplitude displacements, within the same potential well, which sense the well shape and hence acquire a resonant character;

(c) Short-time fluctuations appear in the high frequency part of the spectrum and are due to the displacement of

molecules over distances so short that the long-ranged intermolecular potential does not perceptibly change. These short-time processes are important because they occur so frequently and affect the short range forces of repulsion or attraction.

The remainder of this chapter is devoted to describing methods of far infrared band shape analysis, and those pertinent to collison-induced spectra will be applied to the iodine-benzene system in chapter 6.

4.2 Models for Far Infrared Lineshapes Based on the Langevin Equation

The Langevin equation provides the basis for many models applied to liquid dynamics. It was originally applied to describe translational Brownian motion in liquids [61] and is, in its most basic form

$$M\dot{v}(t) = mcv + \kappa(t) \tag{4.9}$$

This equation has been used together with approximations and with addition of terms to include inertial effects in many models to describe molecular motions in liquids.

4.2.1 The Debye Model

Debye used the Langevin equation to describe the

dynamics of polar molecules on a long timescale. The Brownian motion of the original Langevin equation is treated as a random torque on the molecules and short range forces between molecules are ignored, such that only collisional interactions are considered. Also he assumed the total absence of inertial effects, which is equivalent to assuming instantaneous acceleration. Considering that the torque on a molecule, produced by the applied field, is resisted by collisions with its neighbours through a coefficient of friction, β, then this torque may be written

$$m = \beta \frac{d\omega}{dt} \tag{4.10}$$

where ω is the angular velocity of rotation. Inserting the torque into the Langevin equation then gives

$$\frac{d\omega(t)}{dt} = -\beta\omega(t) + \Gamma(t) \tag{4.11}$$

where the first term on the right accounts for the retardation to rotation due to the viscosity of the medium and the second term is the randomly varying force due to impacts of the surrounding molecules through Brownian motion. The Debye relaxation time, τ_D, given by

$$\beta \alpha \tau_D^{-1} \tag{4.12}$$

describes the frictional properties of a particular system. The solution to this equation, derived by Debye, can be written, combining equations 2.7 and 2.8

$$\frac{\hat{\varepsilon}(\omega) - \varepsilon_\infty}{\varepsilon_o - \varepsilon_\infty} = \frac{1}{1 - i\omega\tau_D} \tag{4.13}$$

and the relaxation time for a spherical molecule is related to the macroscopic viscosity, η, by [62]

$$\tau_D = \frac{4\pi\eta a^3}{kT} \tag{4.14}$$

The Debye model works well at long times and fits experimental microwave data well [63]. However, at high frequencies equation 2.8 approaches

$$\varepsilon''(\omega) \quad \alpha \quad \omega^{-1} \tag{4.15}$$

and since from equations 2.6 and 2.10

$$\alpha(\omega) = \frac{\omega\varepsilon''(\omega)}{cn(\omega)} \tag{4.16}$$

and n is approximately constant at high frequency we can derive

$$\alpha_\infty = \frac{\varepsilon_o - \varepsilon_\infty}{\varepsilon_\infty^{\frac{1}{2}} c\tau_D} \tag{4.17}$$

and α is predicted to reach a limiting high frequency, the so-called Debye plateau, figure 4.2. This is obviously not in agreement with experiment since all polar liquids eventually recover transparency (Figure 4.1).

4.2.2 Inertia corrected Debye Models

The basic Debye model can be corrected so that it does predict a fall off to zero intensity at high frequencies by including inertial terms in the expression for the torque

$$M = \frac{\beta d\omega}{dt} + \frac{I d\omega}{dt} \tag{4.18}$$

Fig. 4.2

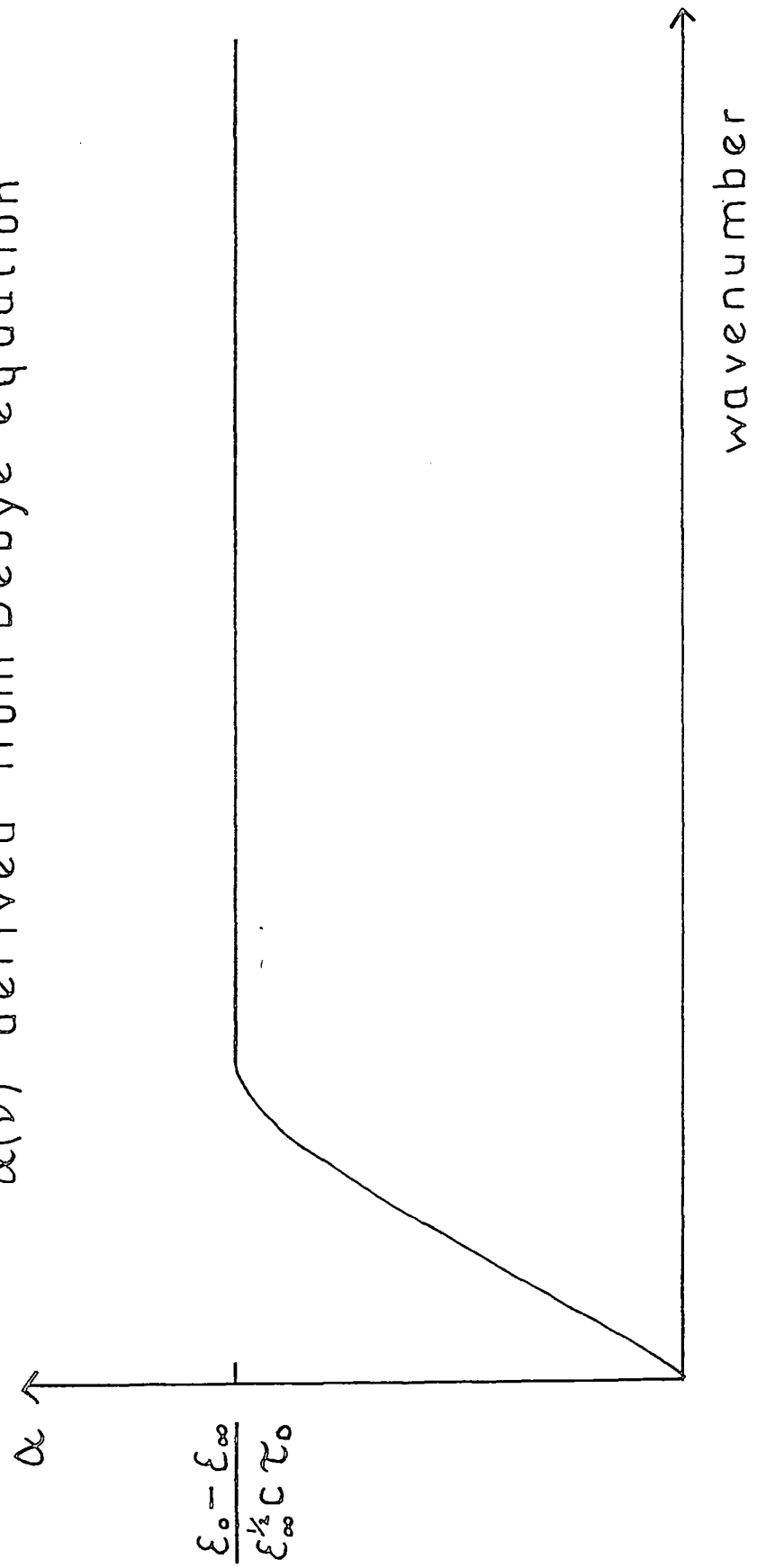
α(ν̄) derived from Debye equation
α
$\frac{\varepsilon_0 - \varepsilon_\infty}{\varepsilon_\infty^{1/2} c \tau_0}$
wavenumber

where I is the relevant moment of inertia. The resulting Langevin equation cannot be solved analytically but solutions have been approximated by Rocard [64]

$$\frac{\hat{\varepsilon} - \varepsilon_\infty}{\varepsilon_o - \varepsilon_\infty} = \frac{1}{(1 - i\omega\tau_D)(1 - i\tau_F)} \tag{4.19}$$

and Powles [65]

$$\frac{\hat{\varepsilon} - \varepsilon_\infty}{\varepsilon_o - \varepsilon_\infty} = \frac{1}{(1 - i\omega\tau_D - (1-\lambda)i\omega\tau_F - \tau_F\tau_D\omega^2)} \tag{4.20}$$

where τ_F is called the friction time. λ may be set to zero, in which case the Rocard equation is derived, or to unity to yield

$$\frac{\hat{\varepsilon} - \varepsilon_\infty}{\varepsilon_o - \varepsilon_\infty} = \frac{1}{(1 - i\omega\tau_D - \tau_F\tau_D\omega^2)} \tag{4.21}$$

Although these models eliminate the Debye plateau they still do not account for all of the absorption [5]. The excess absorption which is not accounted for by the relaxation of the orientational polarisation is referred to as the Poley absorption band from the worker who first predicted its presence [66]. Since for non-polar liquids there is no Debye process, only the Poley band is observed [67].

For Polar molecules the Poley absorption has been attributed to a librating molecule in a non-static cage made up of neighbouring molecules [68,69]. This 'itinerant oscillator' concept has been applied and extended in several subsequent models [70-74].

4.2.3 Memory function formalism

In the Debye equation and its extensions the coefficient of friction, β, does not vary with time. A more realistic model is obtained by introducing a time dependent frictional term into the Langevin equation via the memory function, $K(t)$ [75], and allowing molecular collisions to occur on a finite time scale. A more generalised form of the Langevin equation is now [76]

$$\frac{d\omega(t)}{dt} = -\int_0^t K(t-\tau)\omega(\tau)\,d\tau + \Gamma(t) \qquad (4.22)$$

The fluctuation-dissipation theorem [77] states that the memory function is the correlation function of the random torque on a molecule, i.e.

$$K(t) = \frac{\langle \Gamma(0) \cdot \Gamma(t) \rangle}{\langle \omega(0) \cdot \omega(0) \rangle} \qquad (4.23)$$

Taking the ensemble average of the variables in equation 4.22 with their value at zero frequency leads to

$$\frac{d}{dt}\langle \omega(0) \cdot \omega(t) \rangle = -\int_0^t K(t-\tau)\langle \omega(0).\omega(\tau) \rangle d\tau + \langle \omega(0).\Gamma(t) \rangle \qquad (4.24)$$

and since there is no correlation between Γ and ω we have

$$\langle \omega(0) \cdot \Gamma(t) \rangle = 0 \qquad (4.25)$$

Experimentally, we are interested in the rotational correlation function defined as [78].

$$c(t) = \langle \mu(0) \cdot \mu(t) \rangle = \frac{3\hbar c}{4\pi^2} \int_{-\infty}^{\infty} \exp(i\omega t) \frac{I(\omega)}{\omega(1-\exp(-\hbar\omega/kT))}\, d\omega \qquad (4.26)$$

where μ is a unit vector along which the dipole or induced-dipole lies and $I(\omega)$ is the absorption cross section per molecule. So replacing variables in equation 4.24 gives us

$$\frac{d}{dt} \langle \mu(0) \cdot \mu(t) \rangle = -\int_0^t K(t - \tau) \langle \mu(0) \cdot \mu(t) \rangle \, d\tau \qquad (4.27)$$

and hence

$$\frac{d\, c(t)}{dt} = -\int_0^t K_o(t - \tau)\, c(\tau)\, d\tau \qquad (4.28)$$

4.2.4 The Mori Continued Fraction

The memory functions, K_n, introduced in the previous section are defined so as to follow a series of Volterra equations [48]

$$\frac{\partial K_{n-1}(t)}{\partial t} = -\int_0^t K_n(t - \tau)\, K_{n-1}(\tau)\, d\tau \qquad (4.29)$$

$$n = 1, 2, 3 \ldots\ldots N$$

Through Laplace transformations, defined as

$$\hat{f}(p) = L\{f(x)\} = \int_0^\infty f(x) \exp(-px)\, dx \,, \qquad (4.30)$$

where $p = -i\omega$, Mori derived [76]

$$\hat{c}(p) = \cfrac{c(0)}{p + K_o(p)} = \cfrac{c(0)}{p + \cfrac{K_o(0)}{p + K_1(p)}} = \ldots\ldots \qquad (4.31)$$

This series must be truncated by approximating K_N to some function, e.g. [43]

$$K_1(t) = K_1(0) \exp(-\gamma t) \tag{4.32}$$

so that

$$K_1(p) = K_1(0) / (p + \gamma) \tag{4.33}$$

This is then substituted into equation 4.31 to give $\hat{c}(p)$ from which the real part of the complex spectral function $\hat{c}(i\omega)$ may be derived through inverse Laplace transformation

$$\mathrm{Re}\ \hat{c}(i\omega) = \frac{K_0(0)\ K_1(0)\ \gamma}{\gamma^2\left[K_0(0)-\omega^2\right]^2 + \omega^2\{\omega^2-\left[K_0(0)+K_1(0)\right]\}^2} \tag{4.34}$$

Now since

$$\alpha(\omega) = \frac{(\varepsilon_o - \varepsilon_\infty)\ \omega^2}{cn(\omega)}\ \mathrm{Re}\left[\hat{c}(i\omega)\right] \tag{4.35}$$

the second order truncation of the Mori continued fraction leads to a potential model for the absorption index in terms of three parameters, γ, $K_o(0)$ and $K_1(0)$. γ is the inverse torque relaxation time with units of s^{-1}. The relative magnitudes of $K_o(0)$ and $K_1(0)$ can be estimated if it is assumed that $c(t)$ is an even function of time and can be expressed as [79]

$$c(t) = \sum_{n=o}^{\infty} a_n \frac{t^{2n}}{(2n)!} \tag{4.36}$$

It follows [43,75] from equation 4.31 that

$$K_i(t) = \sum_{n=o}^{\infty} i_{k_n} \frac{t^{2n}}{(2n)!} \tag{4.37}$$

and

$$K_N(0) = {}^{o}k_n = -a_{N+1} - \sum_{n=1}^{N} {}^{o}k_{N-n}\, a_n \tag{4.38}$$

so that we have

$$K_o(0) = -a_1 \tag{4.39}$$

$$K_1(0) = a_1 - a_2/a_1 \tag{4.40}$$

and so on.

The a_i can then be related to the spectral moments according to [43,47]

$$a_1 = \frac{-4c^2}{(\varepsilon_o - \varepsilon_\infty)} \int_o^\infty \alpha(\bar{\nu})\, d\bar{\nu} \tag{4.41}$$

$$a_2 = \frac{16\pi^2 c^4}{(\varepsilon_o - \varepsilon_\infty)} \int_o^\infty \bar{\nu}^2 \alpha(\bar{\nu})\, d\bar{\nu} \tag{4.42}$$

Thus $K_o(0)$ is related to the second moment and $K_1(0)$ to the intermolecular mean square torque through the fourth spectral moment. The mean square torque is the derivative of the intermolecular potential, so values of $K_1(0)$ can give an indication of the gradient of this potential [80].

4.2.5 The Oxtoby Model

This approach [73] describes the liquid by a simple cell model. The translational intermolecular dynamics are treated using a generalised Langevin equation. The cell model [81] consists of a molecule moving in a uniform

spherical cell formed by the solvent molecules. The potential energy between the molecule and its surroundings is assumed to be an isotropic potential and independent of orientation, and includes contributions from electrostatic and induced interactions and repulsive forces, as well as those arising from charge-transfer. The cell potential, V_c, as a function of the displacement, R, of the molecule from the centre of the cell, in terms of the pair potential V(r) is

$$V_c(R) = \frac{N}{2} \int_0^{\pi} \sin\theta \; V\left(R^2 + r_c^2 - 2Rr_c \cos\theta\right)^{\frac{1}{2}} d\theta \qquad (4.43)$$

where N is the number of solvent molecules forming the surface of the sphere of radius r_c, and θ an angle that describes the location of solvent molecules on the cell walls. The distance between the component parts of the complex is

$$r = r_c - R. \qquad (4.44)$$

It is anticipated that weak complexes will exhibit a broad, shallow minimum in the potential near the centre of the cell and oscillate rapidly between different solvent molecules. This situation is the interaction induced limit. For a strong complex, however, the molecule will be preferentially bound to one of the solvent molecules making up the sphere and the minimum will be displaced from the

Fig. 4.3

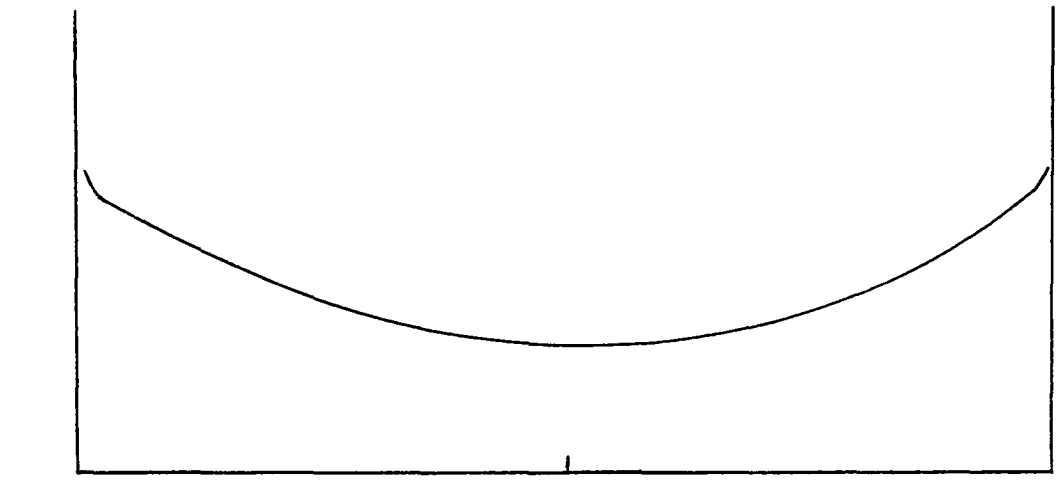

$R = r_c$ $R = 0$ $R = r_c$

weak complex

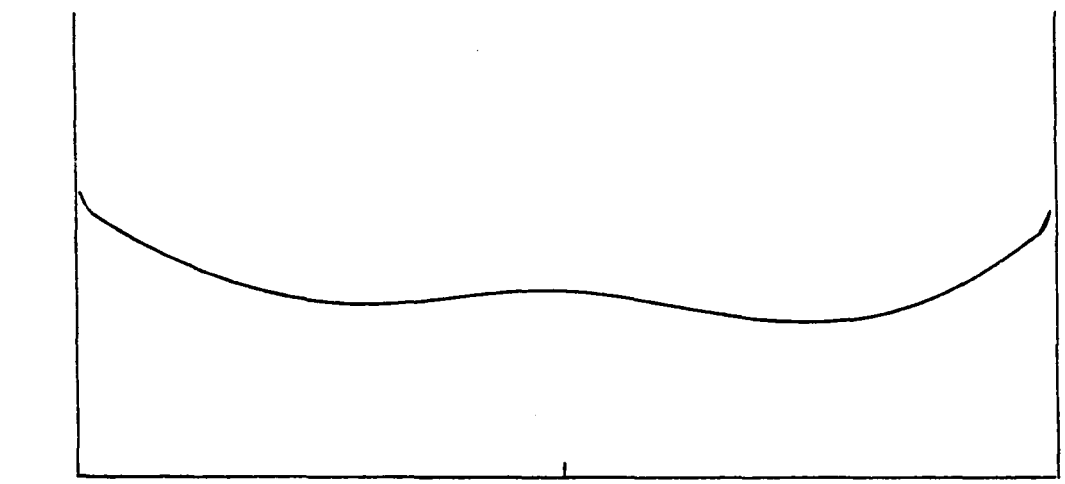

$R = r_c$ $R = 0$ $R = r_c$

strong complex

centre. These limits are illustrated in Figure 4.3.

The cell model dipole moment, $\vec{\mu}_c(R)$, is an average value for the dipole moment of the complex over all positions on the spherical shell, i.e.

$$\vec{\mu}_c(R) = \frac{N}{4\pi} \int_0^{2\pi} \int_0^{\pi} \vec{\mu}(R - r(\theta,\psi)) \sin\theta \, d\psi \, d\theta \qquad (4.45)$$

where $\mu(r) = rm(r)$; m is the charge.

Using the expressions for cell potential and cell dipole moment a function, $\vec{R}(t)$, can be obtained which describes the ensemble average of correlations in the cell dynamics. In the particular model used a simple linear dependence of $\vec{\mu}$ on $\vec{R}$ is assumed.

A dynamical variable, A_1, is introduced which is related to R(t) via the reduced mass, μ_R.

$$A_1 = \mu_R \, R(t) \qquad (4.46)$$

Describing the system by this variable only leads to a simple exponential decay for the correlation function; a situation comparable to the Debye treatment. Two more variables are introduced by taking the first and second time derivatives of A_1

$$A_2 = \dot{A}_1 \quad ; \quad A_3 = \dot{A}_2 \qquad (4.47)$$

such that A_2 is now a momentum and A_3 a force. A_2 accounts for inertial effects and A_3 accounts for anharmonicities in the cell potential, $V_c(R)$, since the cell is not static but fluctuates.

Denoting by ρ the momentum term taken from A_2, writing

δF for the forces in the average cell potential other than those arising through simple harmonic motion, and introducing a damping coefficient α, Oxtoby [73] uses three variables to describe the absorption cross section:

$$\omega_o^2 = \frac{\langle \rho^2 \rangle}{\mu_R^2 \langle R^2 \rangle} \tag{4.48}$$

$$\omega_1^4 = \frac{\langle \delta F^2 \rangle}{\mu_R^2 \langle R^2 \rangle} \tag{4.49}$$

$$\gamma = \alpha \; / \; \omega_1^4 \tag{4.50}$$

$$I(\omega) = \frac{2\omega_1^4 \; / \; (\gamma \omega_o^4)}{\left[1 - \frac{\omega^2}{\omega_o^2}\right]^2 + \frac{\omega^2}{\gamma^2}\left[\frac{\omega^2}{\omega_o^2} - \frac{\omega_o^4}{\omega^4} - 1\right]^2} \tag{4.51}$$

and this is related to absorption coefficient by

$$\alpha(\omega) = \frac{2\omega(1 - \exp(-\beta\hbar\omega))}{\beta\hbar(1 + \exp(-\beta\hbar\omega))} \; I(\omega) \tag{4.52}$$

ω_o is the average harmonic frequency of the cell and γ is a relaxation time. For strong complexes we can expect relatively weak fluctuations so that δF is negligible and hence $\omega_1 < \omega_o$. Plots of $\alpha(\bar{\nu})$ for various values of the three parameters are presented in Figure 4.4.

Fig. 4.4

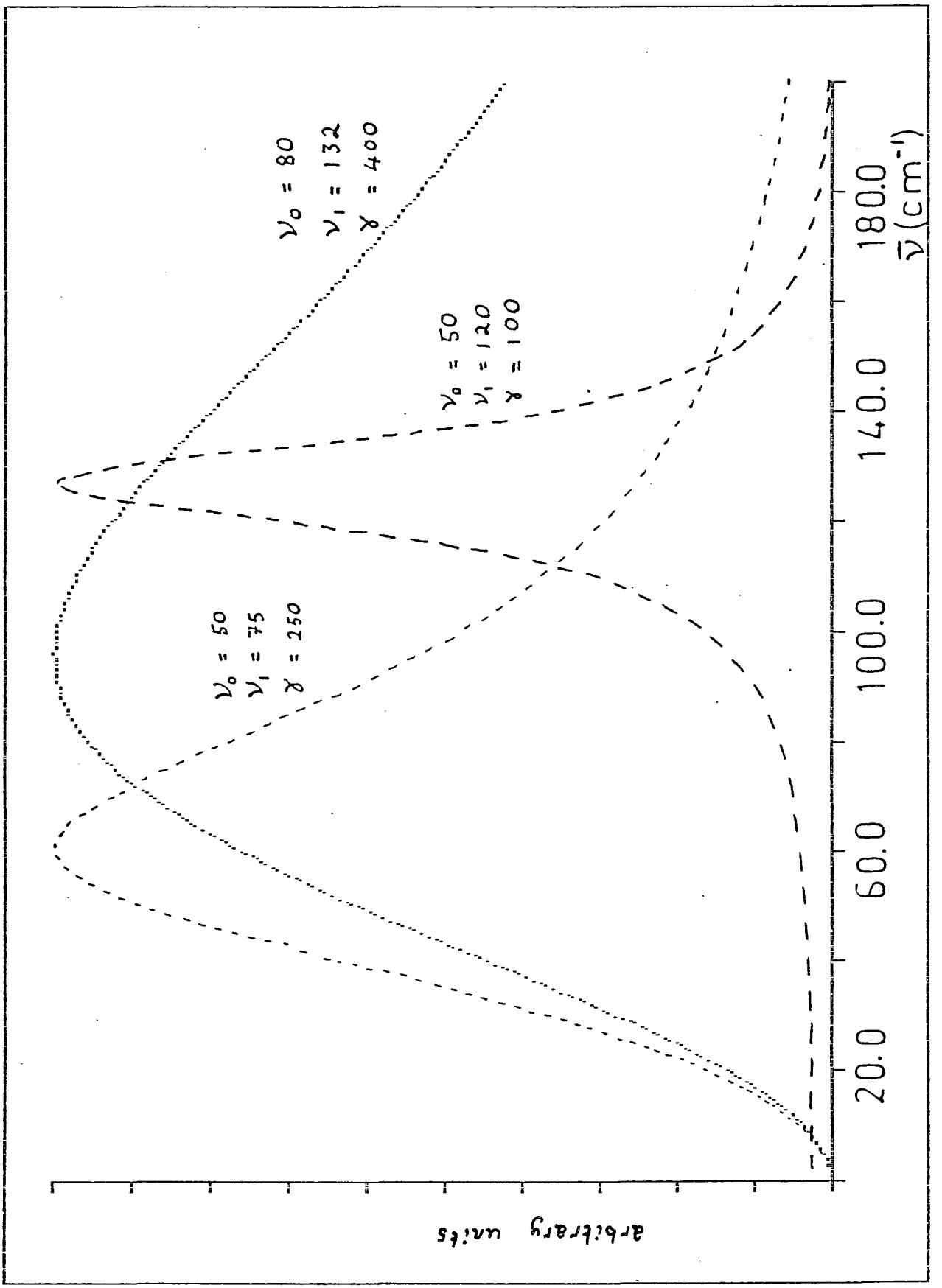
$\nu_0 = 80$
$\nu_1 = 132$
$\gamma = 400$
$\nu_0 = 50$
$\nu_1 = 120$
$\gamma = 100$
$\nu_0 = 50$
$\nu_1 = 75$
$\gamma = 250$
20.0
60.0
100.0
140.0
180.0
$\bar{\nu}$ (cm^{-1})
arbitrary units

4.3 Band Shape Analysis by Multipole Expansion

Classically, the total dipole moment can be expressed as a sum of the various types of molecular interactions contributing to it. These forces are classified as: coulombic, induction and dispersive, and are described in table 4.1. For collision induced infrared studies the lowest order multipole of importance will be the quadrupole and the lowest order induced multipole will be the induced dipole. Thus for induced interactions between molecules with large quadrupole moments and dipole polarisabilities the quadrupole-induced dipole moment will be the dominant contribution to the correlation function, though higher order interactions may also play a part.

The origin of the higher multipole moments can be pictured by considering the potential at position P of two point charges, e_1 and e_2 in Figure 4.5. In terms of polar coordinates P is described by modulus R and argument θ. The charges are located at positions Z_1 and Z_2 from the origin O. Using the cosine rule it is trivial to show that r_i^2 is given by $R^2 - 2RZ_i\text{Cos}\theta + Z_i^2$ so that the potential at P is

$$\phi = \frac{e_1}{r_1} + \frac{e_2}{r_2} = e_1(R^2 - 2RZ_1\cos\theta + Z_1^2)^{-\frac{1}{2}} + e_2(R^2 - 2RZ_2\cos\theta + Z_2^2)^{-\frac{1}{2}} \qquad (4.53)$$

Now if R is greater than Z_1 and Z_2, a binomial expansion leads to

Table 4.1

Type of force	Interaction
coulombic	multipole - multipole
induction	multipole - induced multipole
dispersive	induced multipole-induced multipole

Fig. 4.5

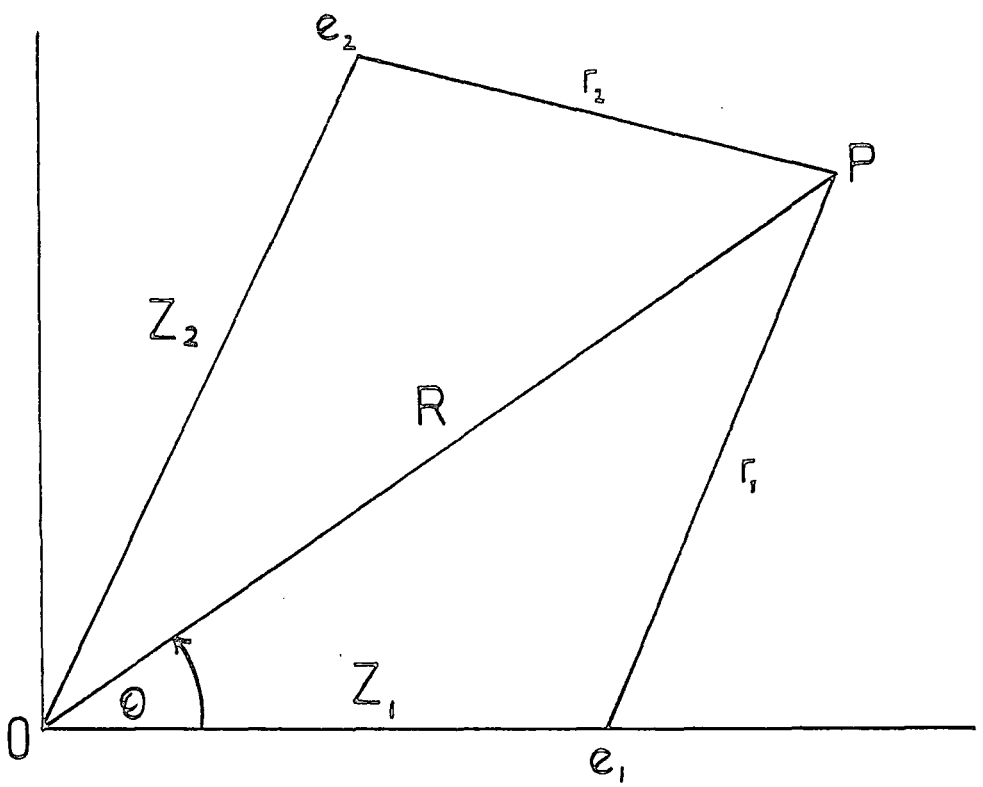

$$\phi = \frac{e_1 + e_2}{R} + \frac{(e_1 z_1 + e_2 z_2)\cos\theta}{R^2} + \frac{(e_1 z_1^2 + e_2 z_2^2)(3\cos^2\theta - 1)}{2R^3} +$$

$$\ldots\ldots\ldots + (e_1 z_1^n + e_2 z_2^n)\frac{P_n(\cos\theta)}{2R^{n+1}} \qquad (4.54)$$

where $e_1 + e_2$ is the charge, $(e_1 z_1^2 + e_2 z_2^2)$ the dipole, and successive terms yield the quadrupole and higher moments. It is now clear that the higher moments are increasingly short-ranged.

The actual situation is, of course, not quite so simple and the moments ought to be described tensorially so that a distribution of charges may be considered in the presence of an external field produced by distant charges.

Cox and Madden [46,47] have incorporated all the relevant physical effects pertaining to interaction-induced phenomena within such a multipole expansion of the total dipole moment, assuming that the interaction induced moments do not involve electron overlap.

Thus for a molecule i at position r_i in an electric field F(r) and a field gradient F'(r) the component of the total dipole moment in a particular direction α is given as

$$m_\alpha^i = \mu_\alpha^i + \alpha_{\alpha\beta}^i F_\beta(r_i) + \tfrac{1}{2}\beta_{\alpha\beta\gamma}^i F_\beta(r_i)F_\gamma(r_i) + \underline{1}A_{\alpha,\beta\gamma}^i F'_{\beta\gamma}(r_i) + \ldots. \qquad (4.55)$$
$$3$$

where

$$\mu_\alpha^i = e_i r_{i_\alpha} \qquad (4.56)$$

is the permanent dipole moment component and e_i the element of charge at the point r_i. $\alpha^i_{\alpha\beta}$ and $A^i_{\alpha,\beta\gamma}$ are components of the dipole and quadrupole polarisabilities respectively, and $\beta^i_{\alpha\beta\gamma}$ is a component of the first hyperpolarisability. The subscripts α, β and γ are vector components of laboratory axes and can represent any of the cartesian coordinates x, y or z. A repeated subscript implies a summation over all three cartesian coordinates [82].

Equation 4.55 is strictly an infinite series involving terms for the dipole, quadrupole, octopole, hexadecapole and higher moments. However, only the leading terms that are necessary to describe observable phenomena are retained.

For non-dipolar molecules in the presence of an incident electromagnetic radiation of frequency $\bar{\nu}_L$ with an associated electric field E^L, the field and field gradient are given by equations 4.57 and 4.58 respectively.

$$F_\alpha(r_i) = E_\alpha^L(r_i) + \sum_{j\neq i} T^2(r_{ij})_{\alpha\beta}\, \alpha^j_{\beta\delta}\, E_\delta^L(r_{ij}) - \frac{1}{3}\sum_{j\neq i} T^3(r_{ij})_{\alpha\beta\gamma}\, \theta^j_{\beta\gamma} - \frac{1}{3}\sum_{j\neq i} T^3(r_{ij})_{\alpha\beta\varepsilon}\, A^j_{\beta\varepsilon,\delta}\, E_\delta^L(r_{ij}) \qquad (4.57)$$

$$F'_{\alpha\beta}(r_i) = \sum_{j\neq i} T^3(r_{ij})_{\alpha\beta\varepsilon}\, \alpha^j_{\varepsilon\delta}\, E_\delta^L(r_j) \qquad (4.58)$$

where θ^i is the quadrupole moment of molecule i and the

interaction tensors, $T^n(r_{ij})$, are given by

$$T^n(r_{ij})_{\alpha,\beta\ldots n} = \frac{1}{4\pi\varepsilon_o} \nabla_\alpha \nabla_\beta \ldots \nabla_n \frac{1}{|r_{ij}|} \quad . \tag{4.59}$$

r_{ij} is now the intermolecular vector connecting the centres of molecules i and j. Combining expressions 4.55 to 4.58 in order to derive the moment responsible for a collision-induced far infrared absorption leaves us with [46]

$$m_\alpha{}^i = \frac{1}{3} \sum_{j\neq i} \alpha_{\alpha\beta}{}^i \, T^3(r_{ij})_{\beta\varepsilon\phi} \, \theta_{\varepsilon\phi}{}^j \quad , \tag{4.60}$$

the quadrupole-induced dipole moment. This is the expression applicable to experimental work described in this thesis, but the multipole expansion may also be applied to infrared vibrational modes and to bandshapes derived from light-scattering experiments [46,47].

Equation 4.60 implies that a moment is induced on molecule i by the quadrupole moment of surrounding molecules. If values of α^i and θ^j can be found, then inserting equation 4.60 into 4.4 gives a model for the correlation function.

CHAPTER 5

INVESTIGATION OF THE DETAILED SPECTRAL PROFILE OF LIQUID ACETONITRILE AND LIQUID BENZENE

5.1 Introduction

The far infrared profile for molecular liquids was described in section 4.1.1 as being broad and featureless, due to the fact that individual molecules are colliding on a timescale which is fast compared to the speed of rotation, and the quantised rotational levels are broadened out. However, publications have appeared in the literature [83,84] which claim to present spectra of acetontrile showing discrete features superimposed on the normal absorption band. It was claimed further [85] by the same worker that such spectral structure could be seen in other molecular liquids, including benzene.

The spectral detail was attributed to strong co-operative reorientation of molecular aggregates in the liquid. Their observation in the far infrared spectrum would require such clusters of molecules to have a lifetime of greater than a few picoseconds, a phenomenon which is not accounted for by current models of the microscopic dynamics of the liquid state at temperatures far from the triple point. If the discrete spectral features were found to be

reproducible, then their existence would have far-reaching effects in the field of liquid dynamics, and attempts to obtain single-particle properties would be severely complicated.

The work presented in this chapter is part of an effort to produce independent, high resolution measurements of acetonitrile [86] and benzene in an attempt to ascertain whether the proposed structure is real or, in particular, what limits can be placed on the confidence level of discerning possible real structure above the level of the noise.

Acetonitrile, with a dipole moment of 3.9D, has a very high peak absorption coefficient, α_{max} = 600 neper cm^{-1}, which means that the transmitted light, even at small pathlengths, is low, (figure 5.18). Consequently the signal-to-noise ratio is poor, and is at its worst at the band centre where the more pronounced structure is said to occur.

Two strategies were adopted to investigate the band profiles. The first was to repeat the transmission work of Evans [83,84] at higher resolution than the 4 cm^{-1} he quotes. Then to average several spectra in order to reduce the noise component and provide some means of assessing statistically the validity of attributing observed structure to a real cause. Secondly, spectra for acetonitrile were recorded by dispersive reflection, a technique which is susceptible to entirely different sources of error than

those for transmission. Thus it is more feasible to have confidence in the presence of any discrete features found to be common to both experiments than to one in isolation. An advantage of dispersive reflection in this case is that the detected signal levels are higher since the radiation does not have to traverse a lossy medium.

5.2 Experimental Details

The acetonitrile was obtained from BDH Chemicals Ltd. and the benzene from Aldrich Chemical Company Ltd. Both liquids were spectroscopic grade and were dried over a molecular sieve before use, without further purification. Unless otherwise stated, the temperature of the liquid was controlled to 298 $\pm$ 2K.

Spectra were recorded using both Golay detectors and the cooled germanium bolometer. The bolometer was much preferred because its high signal-to-noise efficiency meant that interferograms could be recorded at a much faster rate. Thus for transmission work there was less risk of losing liquid sample before having recorded all the data, and for dispersive work the difference in phase drift between sample and background runs was considerably less.

Evans asserts that stucture arising from the supposed composite nature of the spectrum of acetonitrile is observable on the low frequency side of the absorption band; the high frequency side he describes as being very smooth

[83,84] . Since there are advantages to be gained through studying a limited frequency range (see section 1.3.1), it was decided to concentrate our measurements of acetonitrile on the low frequency side of maximum absorption (30-100 cm^{-1}).

5.2.1 Transmission Experiments

All results by transmission were obtained by ratioing two pathlengths of liquid contained in a liquid cell consisting of a spacer held between two optically transparent windows. For experiments with acetonitrile, silicon windows were used since there have been suggestions [84] that because polymeric materials are triboelectric they may cause alignment of polar molecules in the liquid which are close to the windows. This would be important for the case of acetonitrile since, because of its high absorption characteristics, very small pathlengths must be used. spectra of acetonitrile presented here were obtained using PTFE spacers of between 6μm and 25μm.

The silicon windows are not ideal for such an experiment because they have a high coefficient of reflection and hence much of the radiation is lost. There would of course, be a problem with channel spectra due to the windows, but these were specially wedged to eliminate the possibility (figure 5.2). Another problem with using silicon is that it is optically opaque in the visible

region, thus making it difficult to be confident that no air-bubbles have been introduced with the liquid. Great care was taken in loading the cell to avoid introducing bubbles, and the intensities of the resulting spectra were compared with those obtained from dispersive reflection, figure 5.19. The presence of an air bubble in the cell is expected to cause a very noticeable drop in intensity.

Much larger pathlengths have been employed for benzene since its peak absorption coefficient, figure 5.6, is considerably less than that of acetonitrile. Thus polyethylene spacers have been used to create pathlengths varying from 1.0mm to 10.0mm and the liquid has been held between polyethylene windows.

Since the absorption coefficient depends on inverse pathlength, the errors transmitted to it via errors in the measured pathlength will be much greater for very small pathlengths. Thus the spectrum of acetonitrile is much more prone to systematic errors than is the spectrum of benzene. All pathlengths were taken as an average of several measurements of the spacers with a micrometer, but with spacers used for acetonitrile an additional measurement was performed using the channel spectra of the empty cell in the mid infrared according to equation 2.15, e.g. figure 5.1.

The error in absorption coefficient due to inacurate knowledge of the pathlength is between $\pm$ 5 and 10 percent for acetonitrile and approximately $\pm$ 2 percent for benzene.

Difficulties were encountered, for experiments on

Fig. 5.1

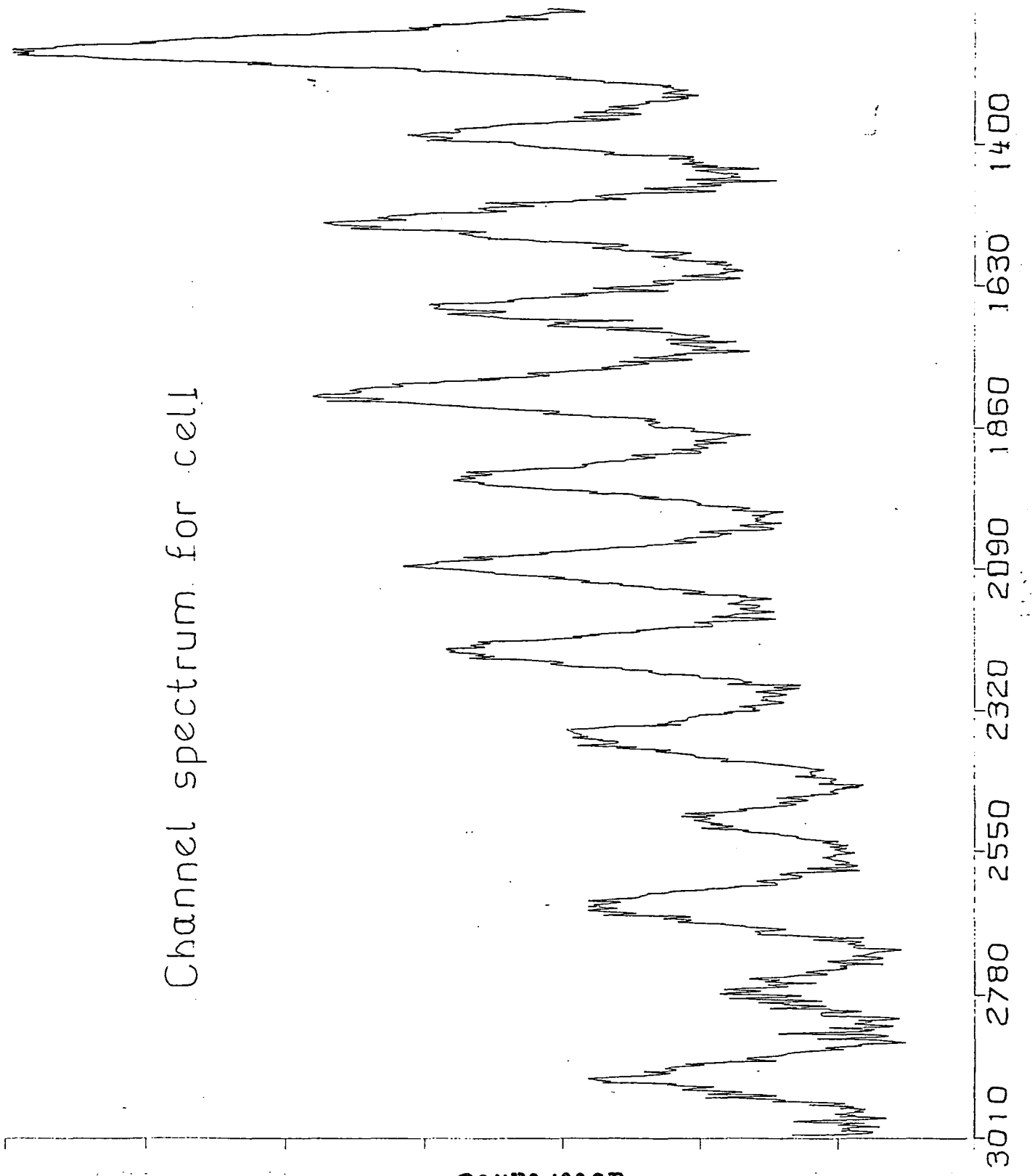
Channel spectrum for cell
absorbance
3010
2780
2550
2320
2090
1860
1630
1400

Fig. 5.2

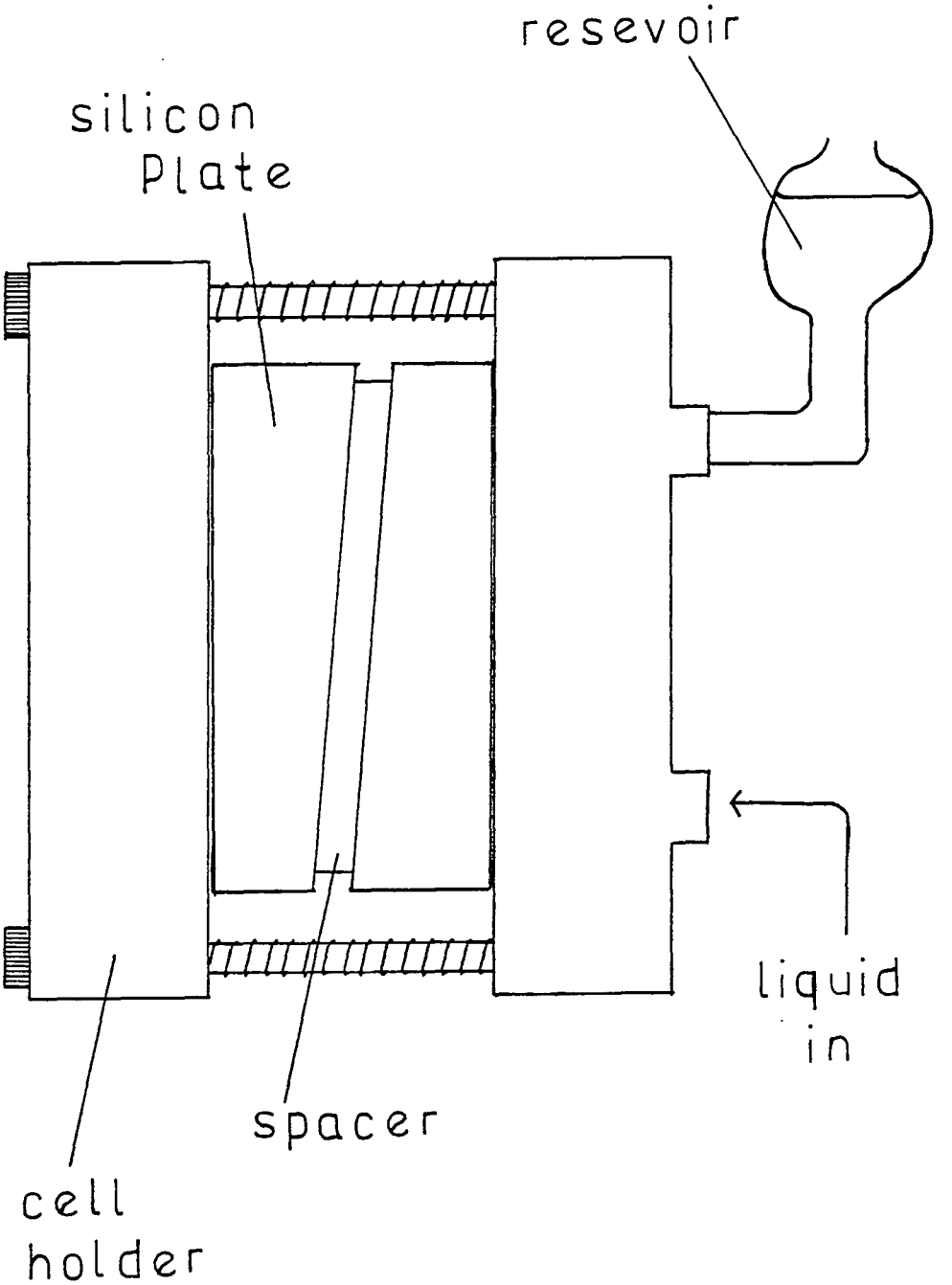

acetonitrile, with loss of sample from the cell during the course of an experiment. Liquid evaporating from the outer edges of the cell was being replaced by liquid from the bulk of the cell. This loss was found to be serious over the timescale of recording an interferogram; typically thirty minutes. The loss of liquid was countered by placing a reservoir at the upper-most entry port, which was filled by forcing the liquid through the cell from the lower entry-port, to form a continuous column of liquid between cell and reservoir (see figure 5.2). This procedure worked well, but the intensity of the signature at zero path difference was checked immediately before and after each experiment to ensure that no liquid had been lost.

Interferograms have been recorded as both double-sided and single-sided; the single-sided ones being preferred for high resolution (> 2 cm^{-1}) work since the time of recording an interferogram is halved.

5.2.2 Dispersive Experiments

Benzene spectra were obtained by transmission in the dispersive liquid cell. Pathlengths of between 1.0mm and 5.0mm were used. In order to obtain a high resolution spectrum it was necessary to employ the full interferogram method (section 2.4.4) since signatures due to multiple reflections in the liquid were inevitably present.

Due to the very small pathlengths required for

transmission experiments on acetonitrile, a reflection experiment was used to study this liquid (section 2.4.2). High resolution experiments were not performed due to the proximity of the (1,0) and (0,0) signatures of the liquid cell as discussed in section 2.4.4. Thus spectra by reflection are presented here at a resolution of 4 cm^{-1}.

In all experiments the interferometer was maintained at a steady temperature by a flow of water round the instrument from a bath. All samples were introduced to the liquid cell at the same temperature of the bath.

Great care was taken over alignment of the instrument and of the liquid cell, particularly for dispersive transmission work.

5.3 Results and Discussion

Figure 5.3 shows the full acetonitrile far infrared absorption band at a resolution of 2 cm^{-1}, obtained by ratioing pathlengths of 28μm and 13μm by transmission. Three spectra were recorded using the same cells to show the reproducibility of the measurement. These spectra compare well with those obtained by Evans [83,84] in terms of the overall shape and the frequency of maxmum absorption, but the level of absorption obtained consistently throughout this work is approximately twice that quoted by Evans.

This is probably due to uncertainties in determining the effective pathlength. Polymeric windows, as used by

Evans, are notoriously bad for achieving uniform layers of sample at small pathlengths since they are non-rigid. Two acetonitrile spectra were recorded by transmission using polythene windows and they are presented in figures 5.4 and 5.5. The maximum absorption value is approximately 30% less than that achieved using the rigid silicon windows.

The level of absorption for those spectra obtained with silicon windows is in good agreement with previous measurements [86] and with simulation studies calculated by Edwards and Madden [54].

Figure 5.6 shows spectra of benzene recorded by transmission with a resolution of 2 cm^{-1}.

Four spectra are presented here to show the level of reproducibility obtained. All are derived from ratioing pathlengths of 5.0 mm and 2.5 mm. The shape and intensity agree well with data in the literature [43] and these spectra are, as expected, much less noisy than the acetonitrile spectra. There is no evidence for any discrete features comparable to those resolved by Evans.

It is, however, much more difficult to conclude from the individual spectrum of acetonitrile whether it supports the existence of any real structure. Figures 5.7 and 5.8 show the averages of fifteen and twenty spectra respectively, at 2 cm^{-1} resolution for the low frequency side of the absorption band, all obtained by transmission. Spectra in figure 5.7 were obtained using the bolometer; those in figure 5.8 using a Golay detector. Both sets of

data are plotted together with their standard deviation on the mean

$$\sigma_m = \frac{1}{\sqrt{n}} \sqrt{\frac{\Sigma(x_i - \bar{x})^2}{n - 1}} \qquad (5.1)$$

to two standard deviations. Although the spectra do apparently show structure superimposed on the absorption profile, this is within the standard deviation of the data and, furthermore, does not correspond in position to the structure reported by Evans [83,84]. Thus with the present signal-to-noise ratio it is not possible to assign structure in the spectrum to real discrete features at this resolution. That is, if there <u>were</u> real features with intensity greater than the upper-bounds implied by figures 5.5 and 5.6, they must be regularly spaced in frequency and separated by less than 2 cm^{-1}.

It has also been suggested by Evans [85] that in order to observe the proposed features in spectra of acetonitrile and benzene, much bigger pathlengths than those employed to record spectra in figures 5.3 - 5.8 are required. Figures 5.9 - 5.11 illustrate the effect of increasing the effective pathlength of sample on the spectrum of benzene at 8°C. Figure 5.12 shows how the transmission through the instrument is affected by the different pathlengths employed. As transmission decreases, the signal-to-noise level suffers a corresponding decrease and the spectra derived from using longer pathlengths are seen to be noisier. This is because the noise remains relatively

unaffected by changes in pathlength, whereas the signal is reduced according to Beer's law (equation 1.22). Thus it is important to be careful about assigning what appear to be weak features superimposed on the band profile at transmission levels where the noise is expected to be of the same order of magnitude. At a pathlength of 6 mm, Beer's law predicts a transmission of only about 3% at the band maximum.

The spectrum in figure 5.11 of 10 mm versus 5 mm benzene does show structure similar to that reported by Evans [85] , but this does not correspond to his in terms of frequency position and was found to be non-reproducible. Thus the features must be due to random noise in the spectrum.

Increasing the resolution of the benzene spectrum to 1 cm^{-1} (figure 5.13) only has the effect of increasing the general noise level and does not resolve structure resembling that proposed by Evans [83-85]. The spectra were recorded at 8°C because any discrete features correponding to the proposed molecular aggregates [83,84] are expected to be more pronounced at lower temperatures where the lifetime of such aggregates would be longer. Spectra of benzene at higher temperatures are presented in figure 5.14. The expected line broadening with increasing temperature can be clearly seen.

Spectra of acetonitrile in polythene cells at room temperature are presented in figures 5.15 and 5.17 as a

function of pathlength. Polythene windows were used here to give a wider range of possible pathlengths. The large reflection losses incurred using silicon limits the range of larger pathlengths that can be used. Figure 5.18 shows the transmission through the instrument for pathlengths of acetonitrile in polythene cells. The same comments apply as for the benzene results.

Results of dispersive reflection measurements on acetonitrile give spectra in good agreement with those obtained by transmission. Figure 5.19 shows the full absorption band measured by this technique and figure 5.20 the corresponding refractive index. The low frequency side of the band is shown in figure 5.21 for absorption coefficient and figure 5.22 for refractive index. A high resolution spectrum of benzene in dispersive transmission mode using the full interferogram method is presented in figures 2.23 and 2.24 in terms of its absorption coefficient and refractive index respectively. These measurements confirm conclusions drawn from the non-dispersive experiments and show no evidence for discrete features in the band profiles at the given resolution.

The interferograms produced by Evans are qualitatively different from those produced for this work, in that they are highly structured in the wings. Such structure corresponds to the proposed discrete features in the spectral domain. Dispersive experiments present the opportunity to distinguish between noise and structure due

to sample in the interferogram since, because of the principle of causality, information arising from the presence of sample in one arm of the interferometer occurs on one side of zero path difference only. A typical interferogram is presented in figure 5.23 where it can be seen that the wings of the interferograms on each side are similar.

5.4 Conclusions

The far infrared absorption profiles of acetonitrile and benzene have been studied in order to test the reproducibility of the discrete spectral features observed by Evans [83-85]. This has been done at higher resolution and by averaging spectra of acetonitrile to quantify the confidence level of attributing any structure to real features. No features were observed that were comparable to those reported by Evans, and none that were above the level whereby they could be attributed to noise.

A corroborative study of the same liquids by dispersive Fourier transform spectroscopy again revealed no evidence for the existence of features superimposed on the normal profile. It is concluded that, if such spectral features do exist, they cannot be resolved at the present signal-to-noise ratios and with a resolution of less than 2 cm^{-1}.

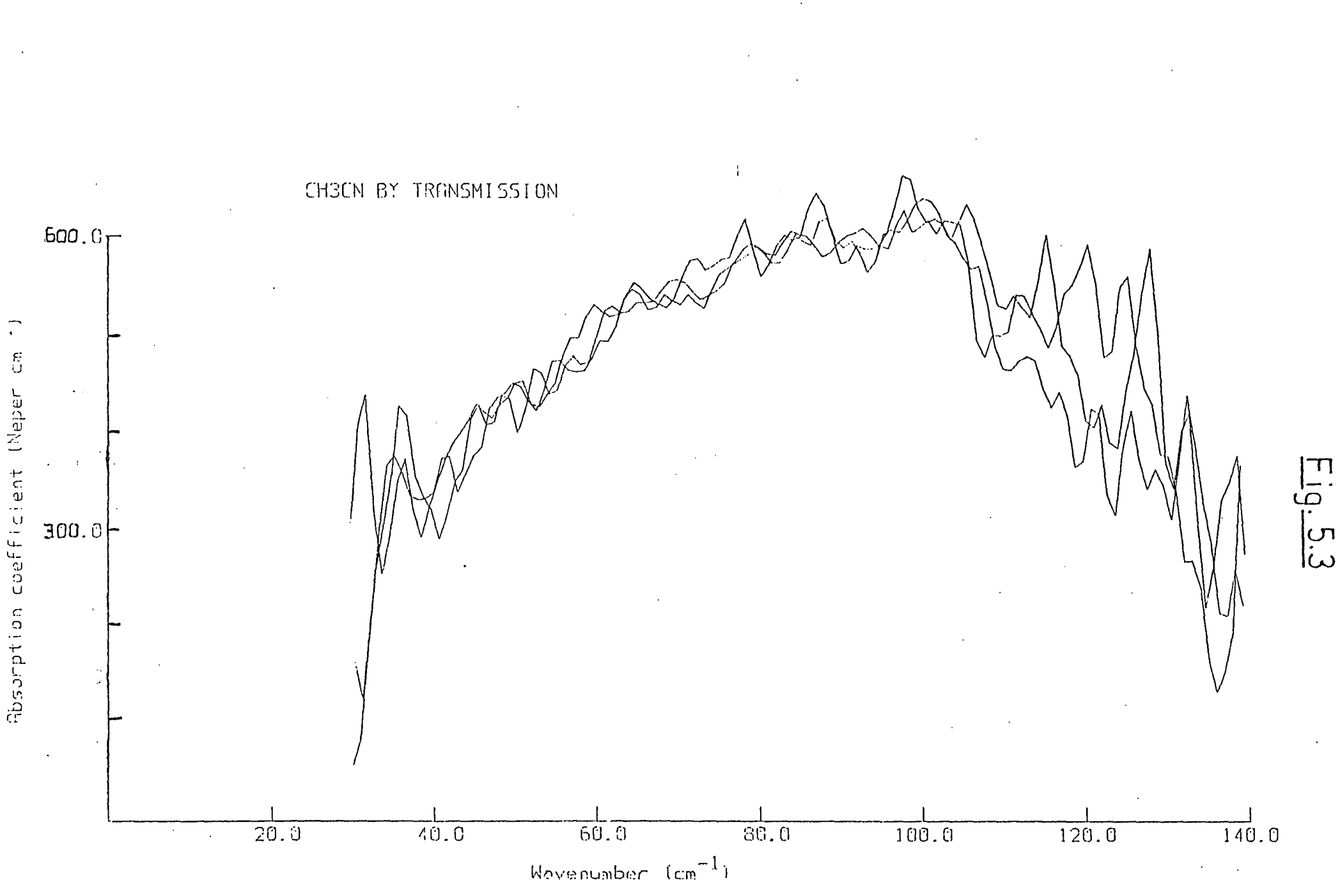
CH3CN BY TRANSMISSION
600.0
300.0
Absorption coefficient (Neper cm⁻¹)
20.0
40.0
60.0
80.0
100.0
120.0
140.0
Wavenumber (cm⁻¹)

Fig. 5.3

RATIO 0.05/0.025mm FOR ACETONITRILE IN POLYTHENE WINDOWS CELL

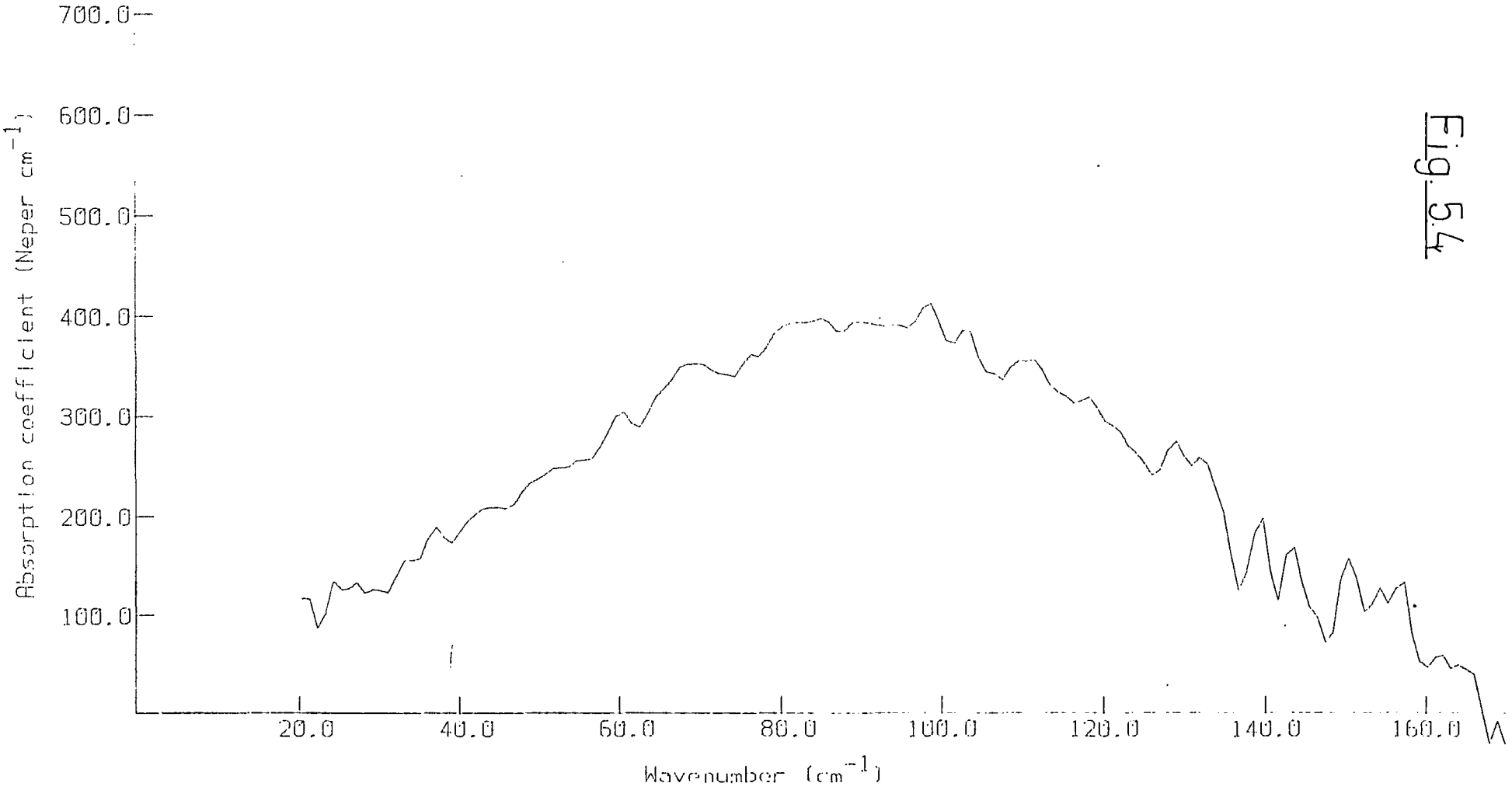

Fig 5.4

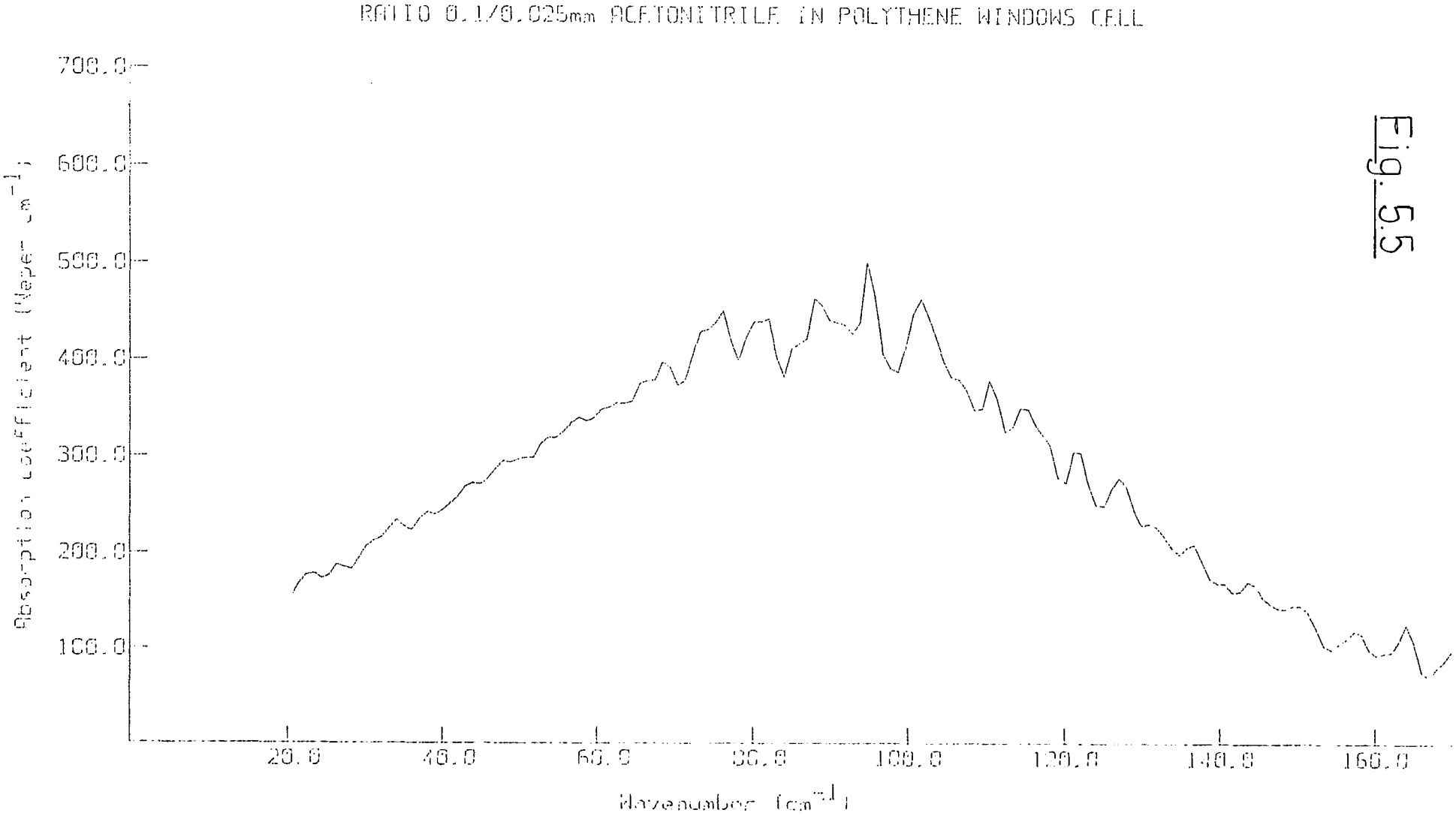
RATIO 0.1/0.025mm ACETONITRILE IN POLYTHENE WINDOWS CELL
700.0
600.0
500.0
400.0
300.0
200.0
100.0
20.0
40.0
60.0
80.0
100.0
120.0
140.0
160.0

Fig. 55

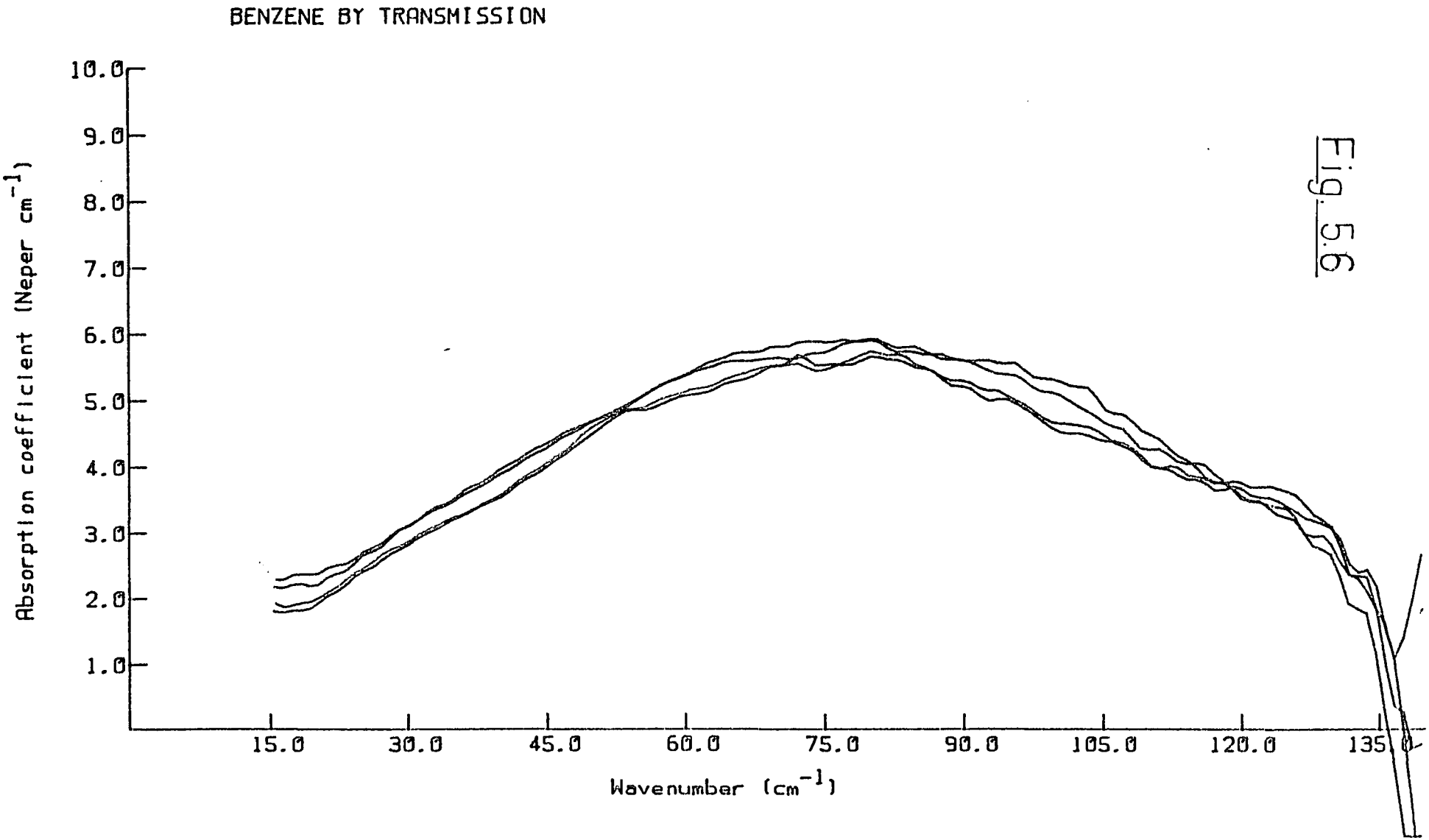
BENZENE BY TRANSMISSION
Absorption coefficient (Neper cm^{-1})
10.0
9.0
8.0
7.0
6.0
5.0
4.0
3.0
2.0
1.0
15.0
30.0
45.0
60.0
75.0
90.0
105.0
120.0
135.0
Wavenumber (cm^{-1})

Fig. 5.6

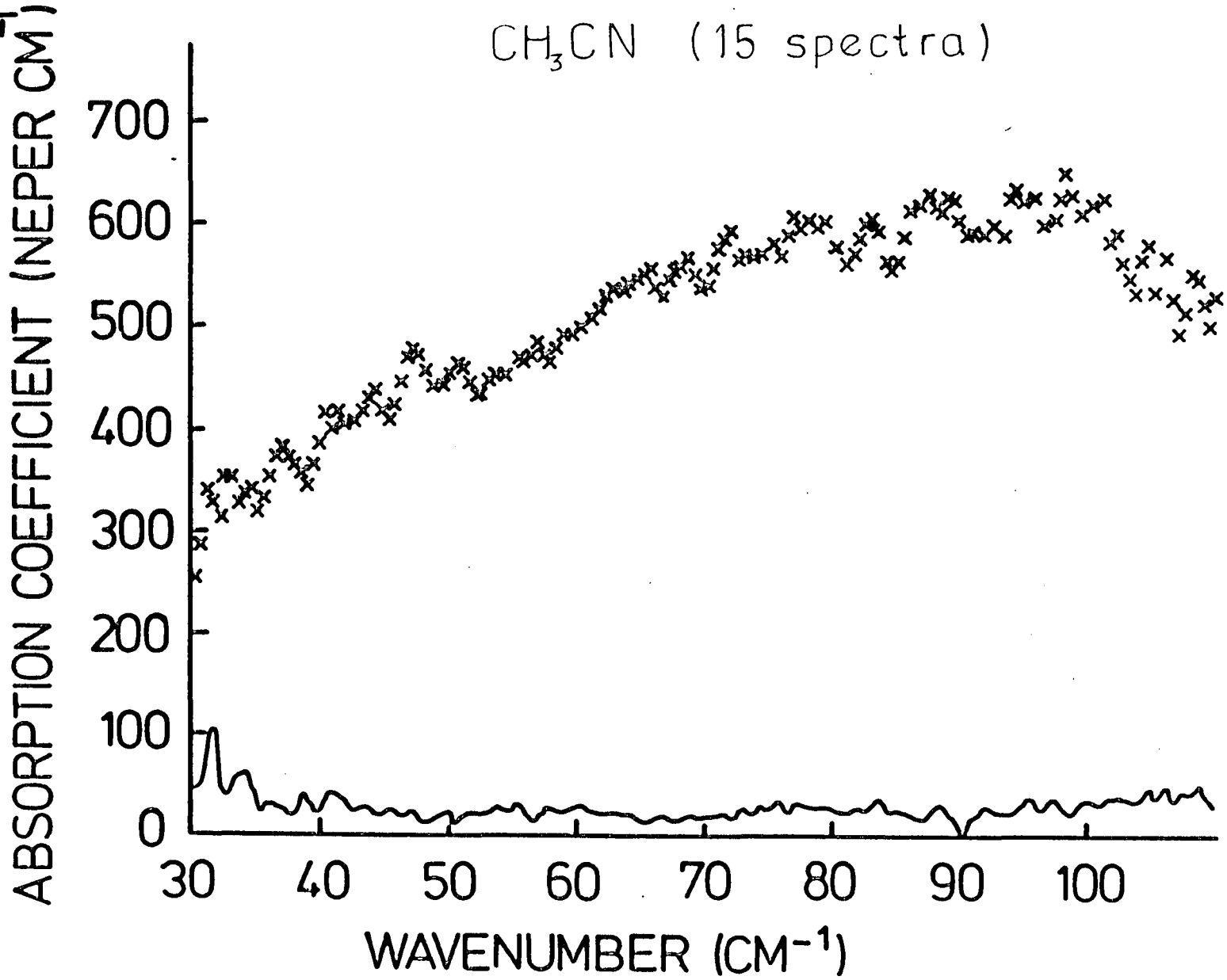
CH3CN (15 spectra)
ABSORPTION COEFFICIENT (NEPER CM-1)
700
600
500
400
300
200
100
0
30
40
50
60
70
80
90
100
WAVENUMBER (CM-1)

Fig. 5.7

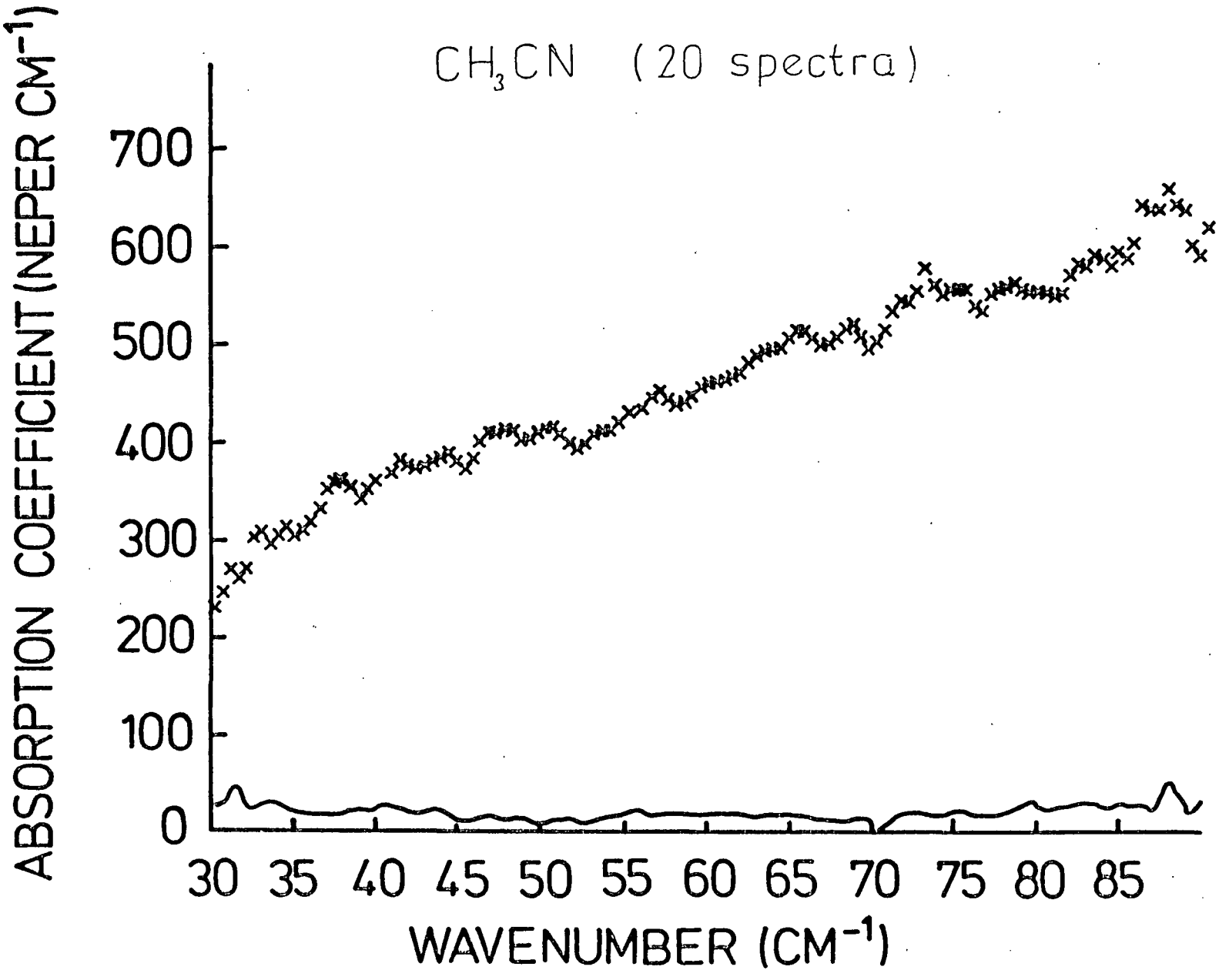
CH3CN (20 spectra)
ABSORPTION COEFFICIENT (NEPER CM-1)
700
600
500
400
300
200
100
0
30 35 40 45 50 55 60 65 70 75 80 85
WAVENUMBER (CM-1)

Fig. 5.8

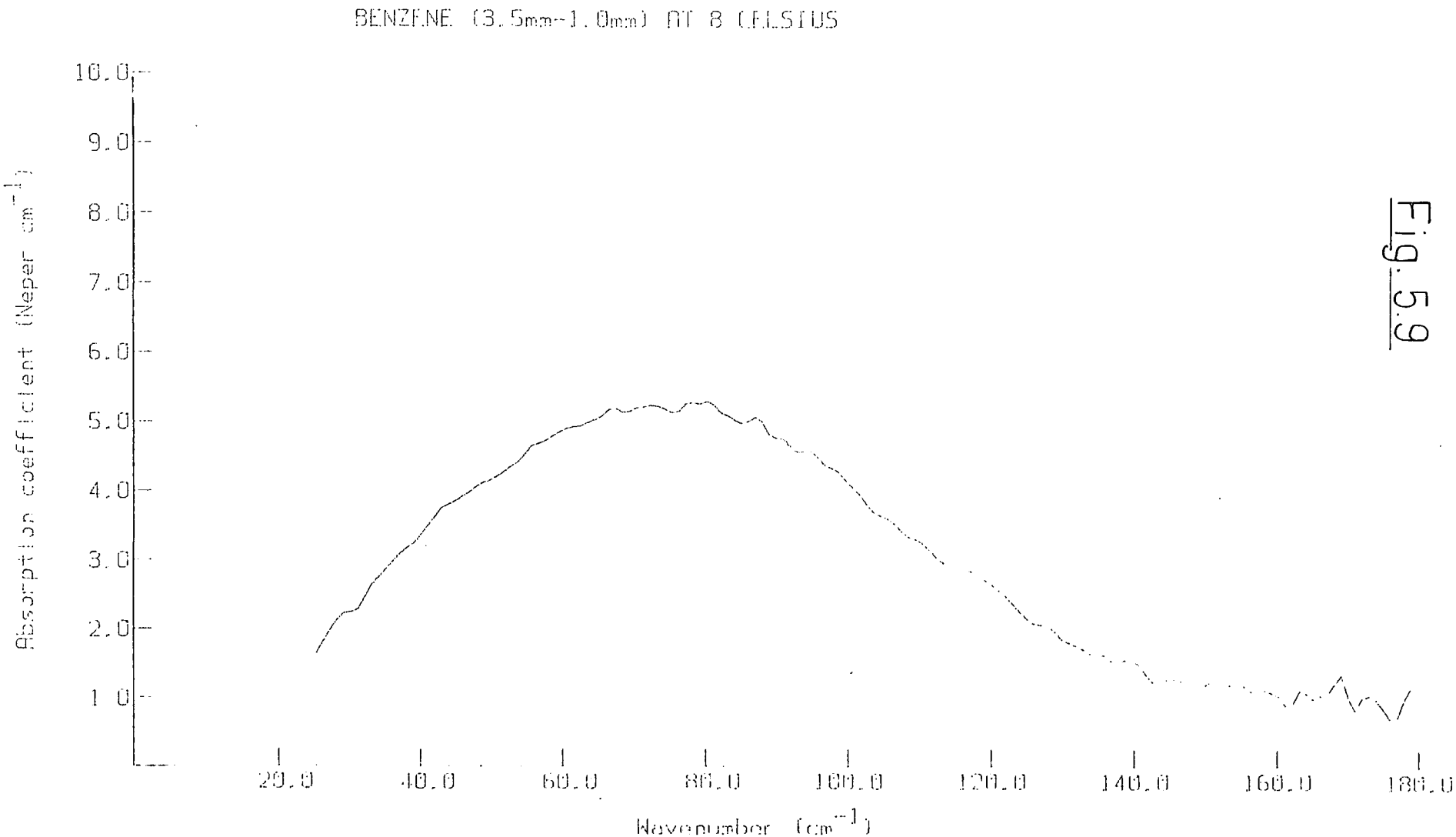
BENZENE (3.5mm-1.0mm) AT 8 CELSIUS
Absorption coefficient (Neper cm^{-1})
10.0
9.0
8.0
7.0
6.0
5.0
4.0
3.0
2.0
1.0
20.0
40.0
60.0
80.0
100.0
120.0
140.0
160.0
180.0
Wavenumber (cm^{-1})

Fig 5.9

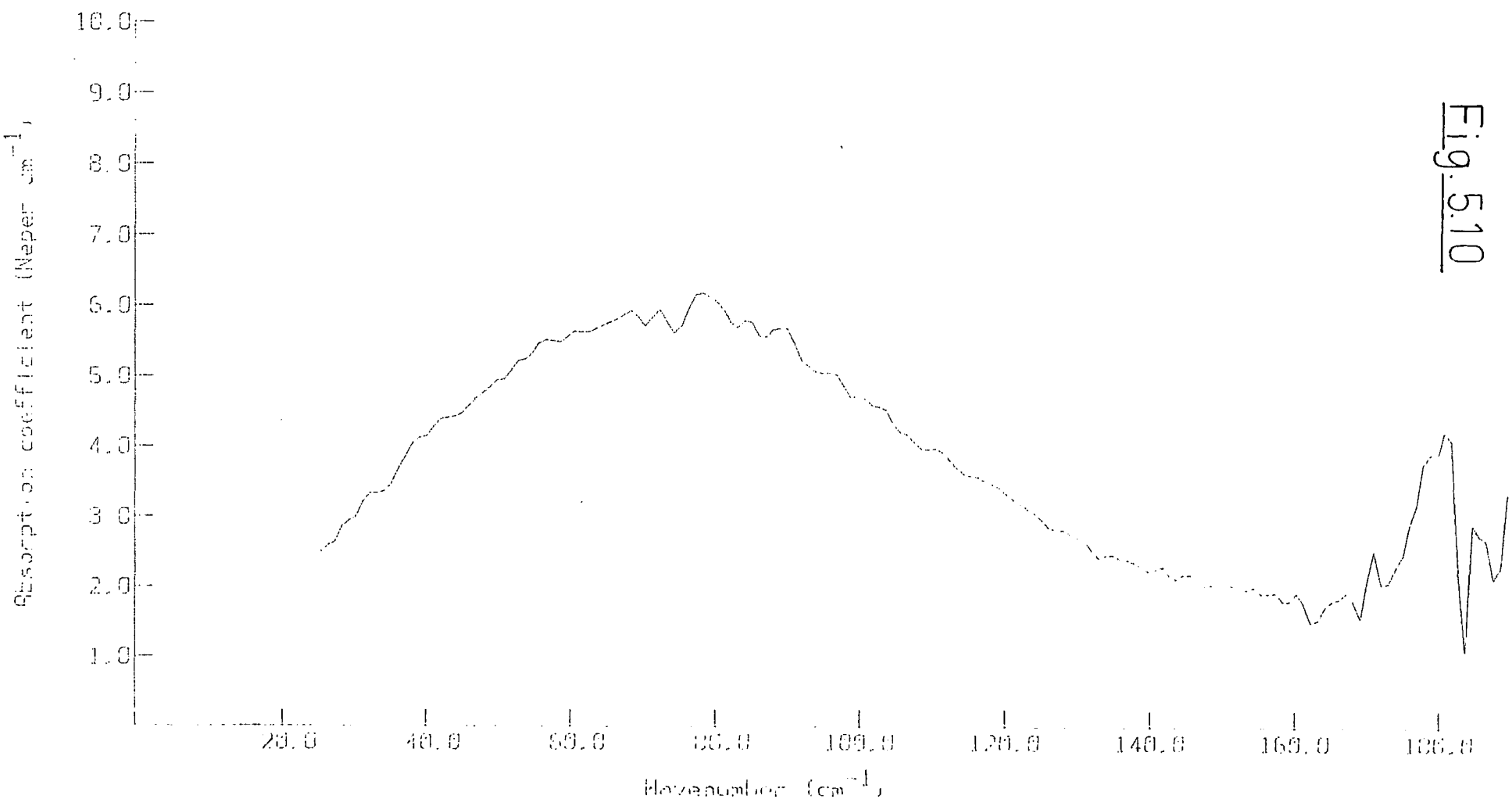
BENZENE (2.5mm-5.0mm) AT 8 CELSIUS
10.0
9.0
8.0
7.0
6.0
5.0
4.0
3.0
2.0
1.0
20.0
40.0
60.0
80.0
100.0
120.0
140.0
160.0
180.0

Fig. 5.10

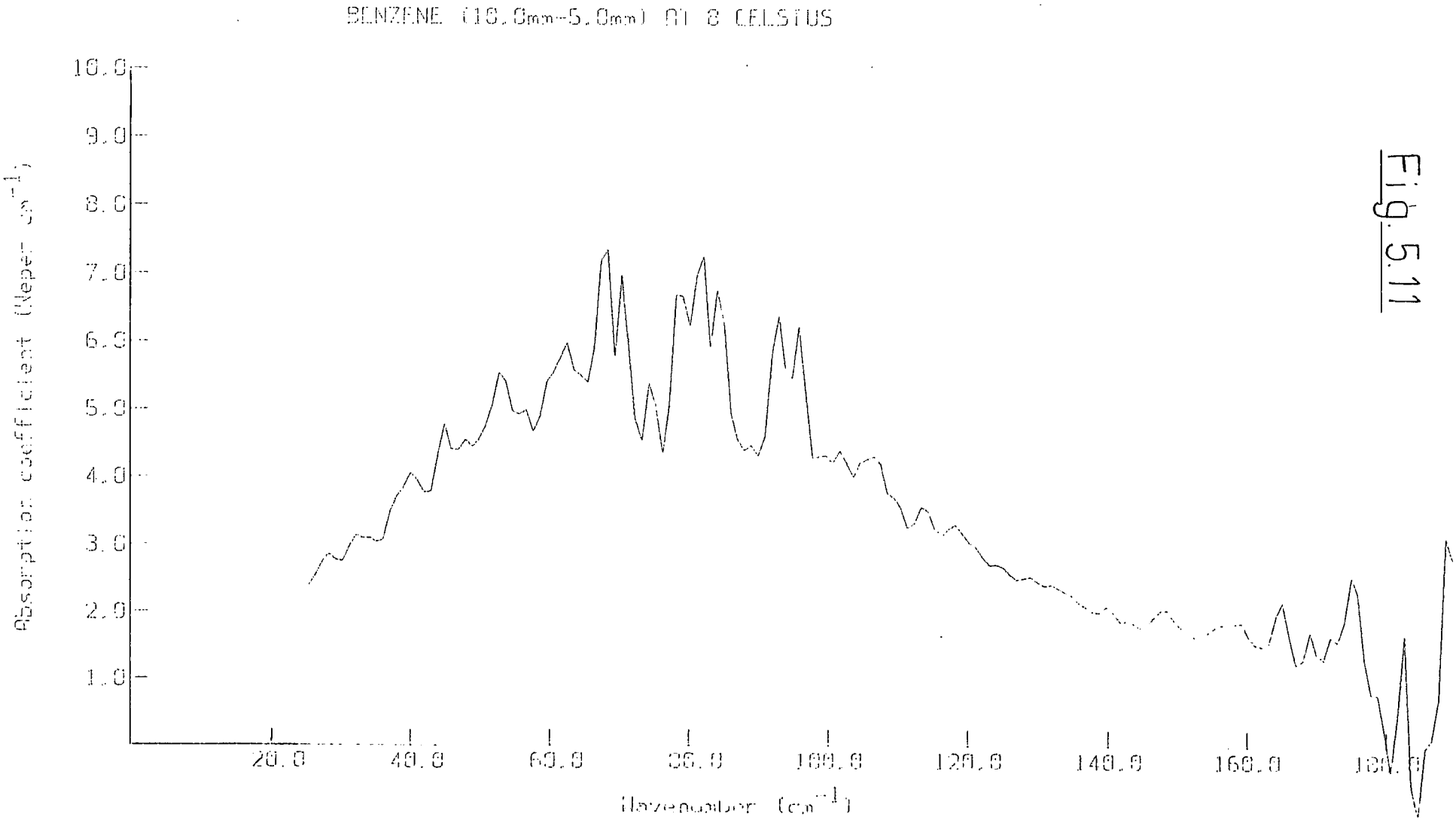
BENZENE (10.0mm-5.0mm) AT 0 CELSIUS
Absorption coefficient (Neper cm^{-1})
10.0
9.0
8.0
7.0
6.0
5.0
4.0
3.0
2.0
1.0
20.0
40.0
60.0
80.0
100.0
120.0
140.0
160.0
180.0
Wavenumber (cm^{-1})

Fig. 5.11

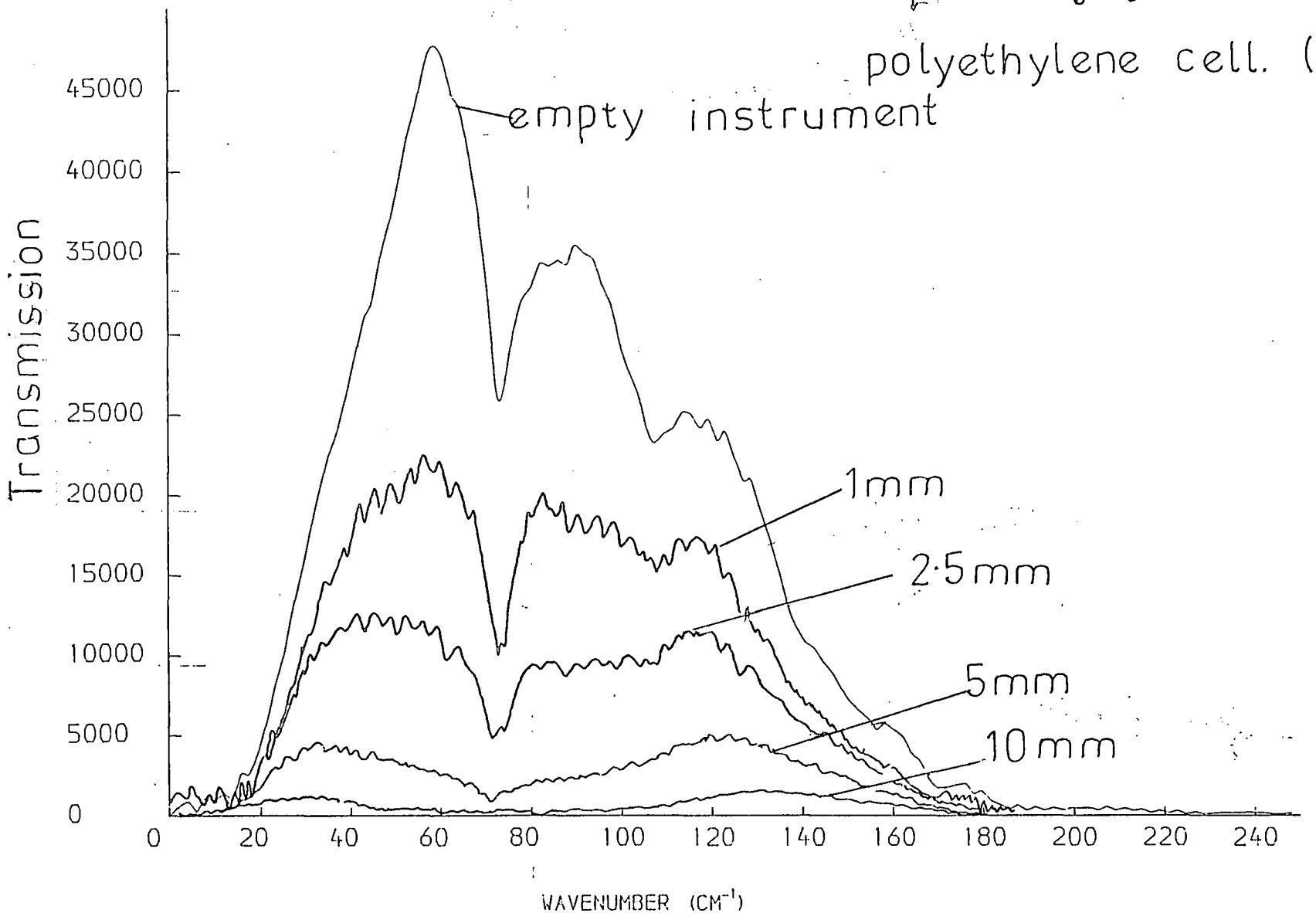
Transmission of liquid C_6H_6 in a polyethylene cell. (8°C)
empty instrument
1mm
2·5mm
5mm
10mm
Transmission
45000
40000
35000
30000
25000
20000
15000
10000
5000
0
0
20
40
60
80
100
120
140
160
180
200
220
240
WAVENUMBER (CM^{-1})

Fig. 5.12

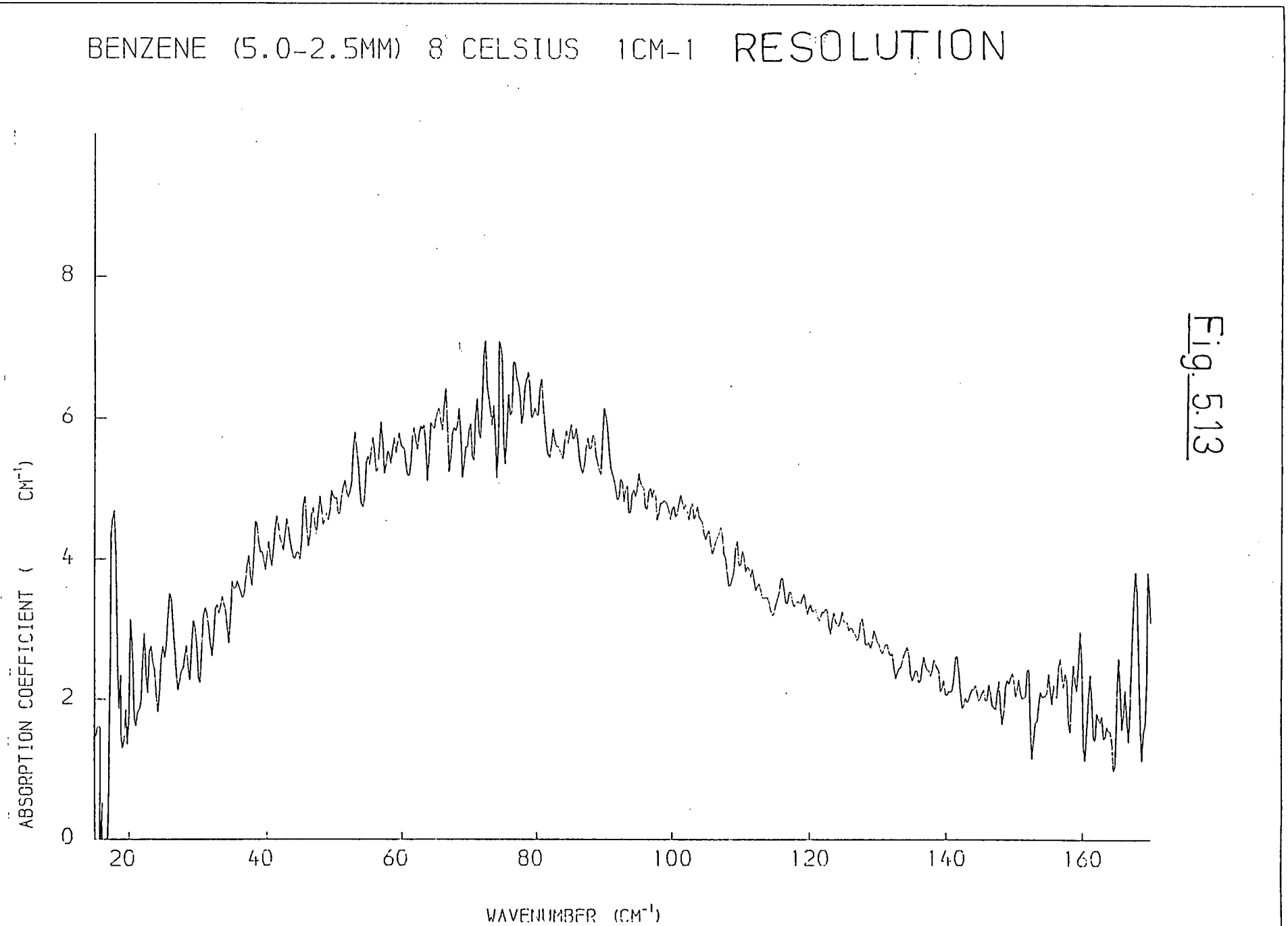
BENZENE (5.0-2.5MM) 8 CELSIUS 1CM-1 RESOLUTION
ABSORPTION COEFFICIENT (CM-1)
0
2
4
6
8
20
40
60
80
100
120
140
160
WAVENUMBER (CM-1)

Fig. 5.13

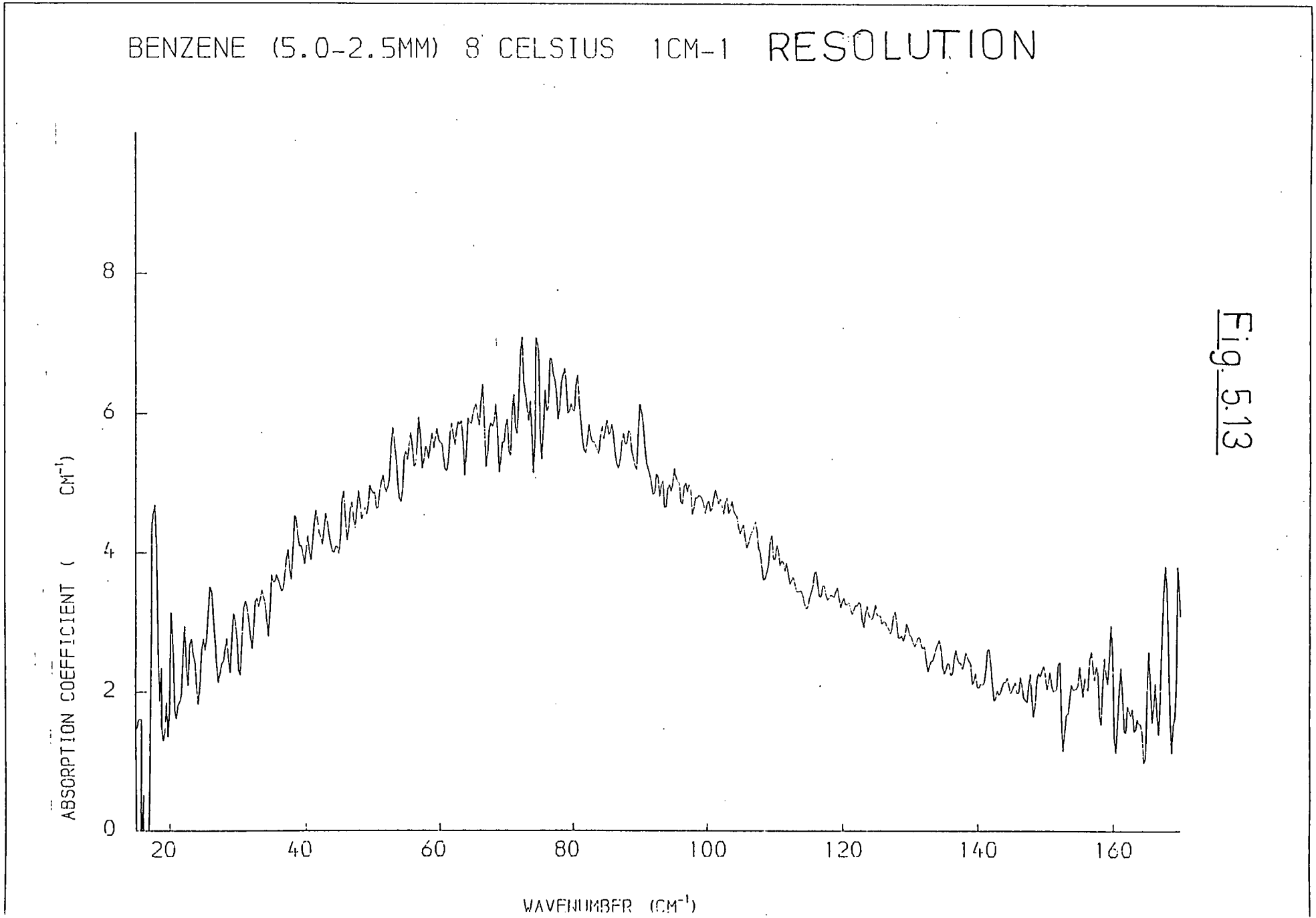
BENZENE (5.0-2.5MM) 8 CELSIUS 1CM-1 RESOLUTION
ABSORPTION COEFFICIENT (CM-1)
0
2
4
6
8
20
40
60
80
100
120
140
160
WAVENUMBER (CM-1)

Fig. 5.13

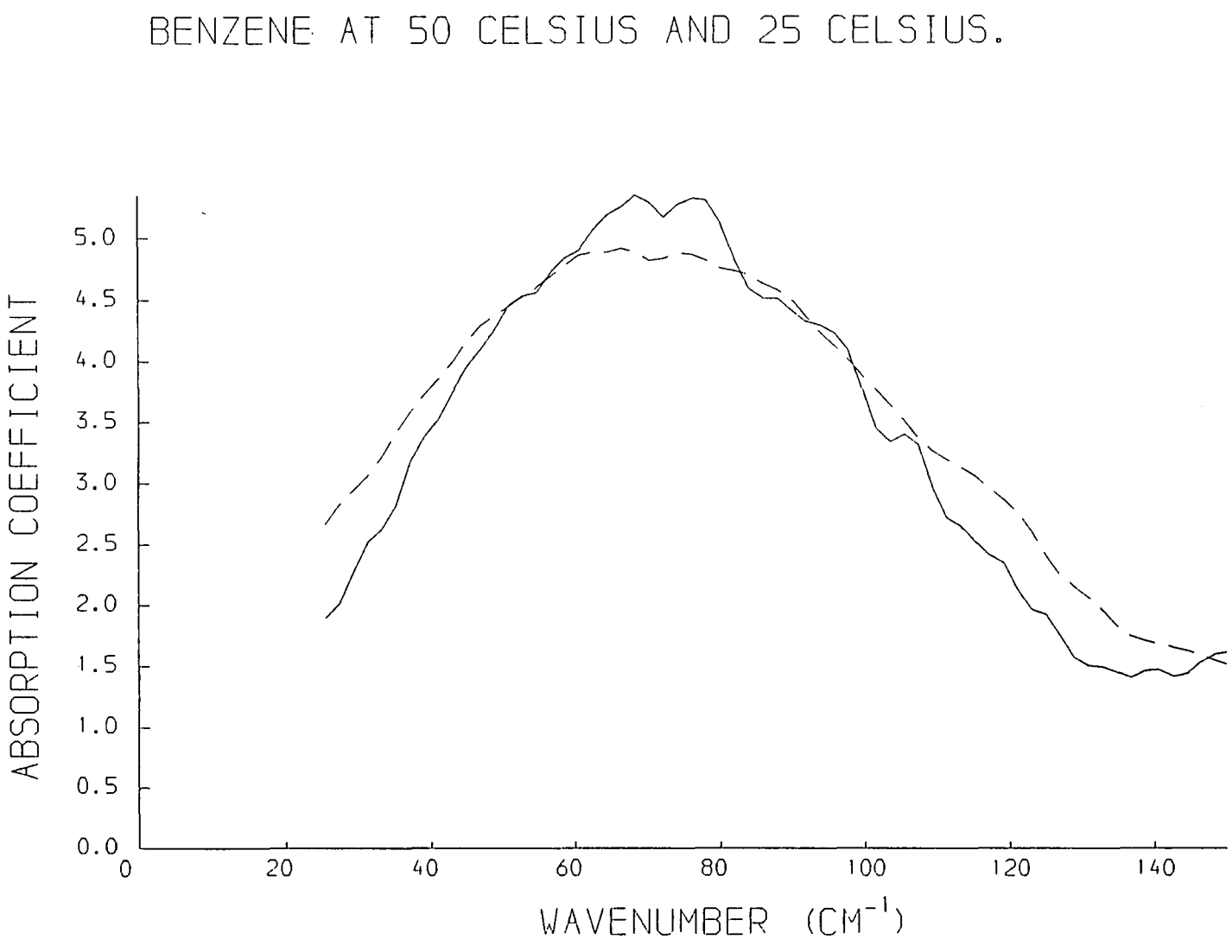
BENZENE AT 50 CELSIUS AND 25 CELSIUS.
ABSORPTION COEFFICIENT
5.0
4.5
4.0
3.5
3.0
2.5
2.0
1.5
1.0
0.5
0.0
0
20
40
60
80
100
120
140
WAVENUMBER (CM^{-1})

Fig. 5.14

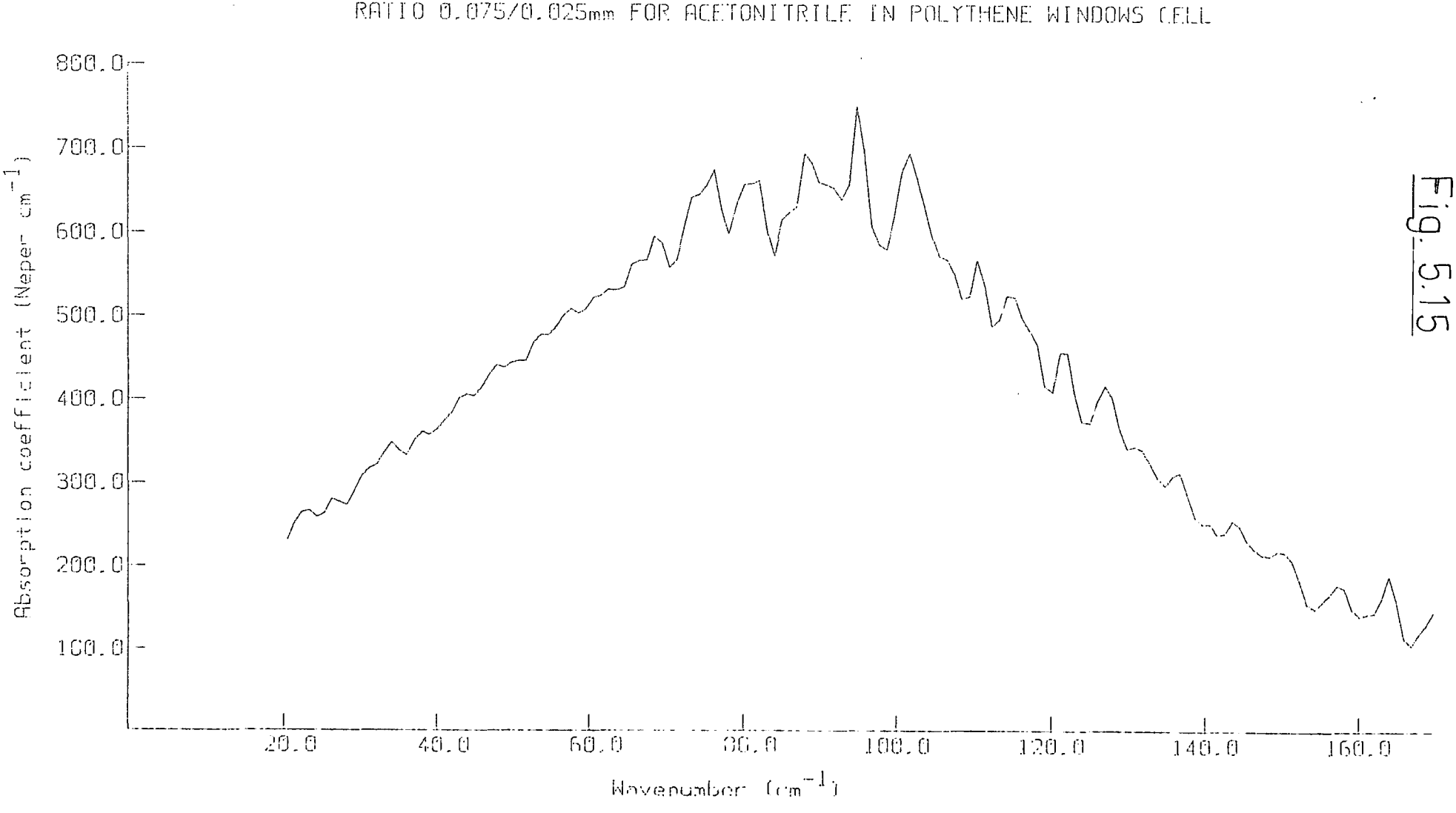
RATIO 0.075/0.025mm FOR ACETONITRILE IN POLYTHENE WINDOWS CELL
Absorption coefficient (Neper cm^{-1})
800.0
700.0
600.0
500.0
400.0
300.0
200.0
100.0
20.0
40.0
60.0
80.0
100.0
120.0
140.0
160.0
Wavenumber (cm^{-1})

Fig. 5.15

Gain = 5 (100μm), 50 (25μ

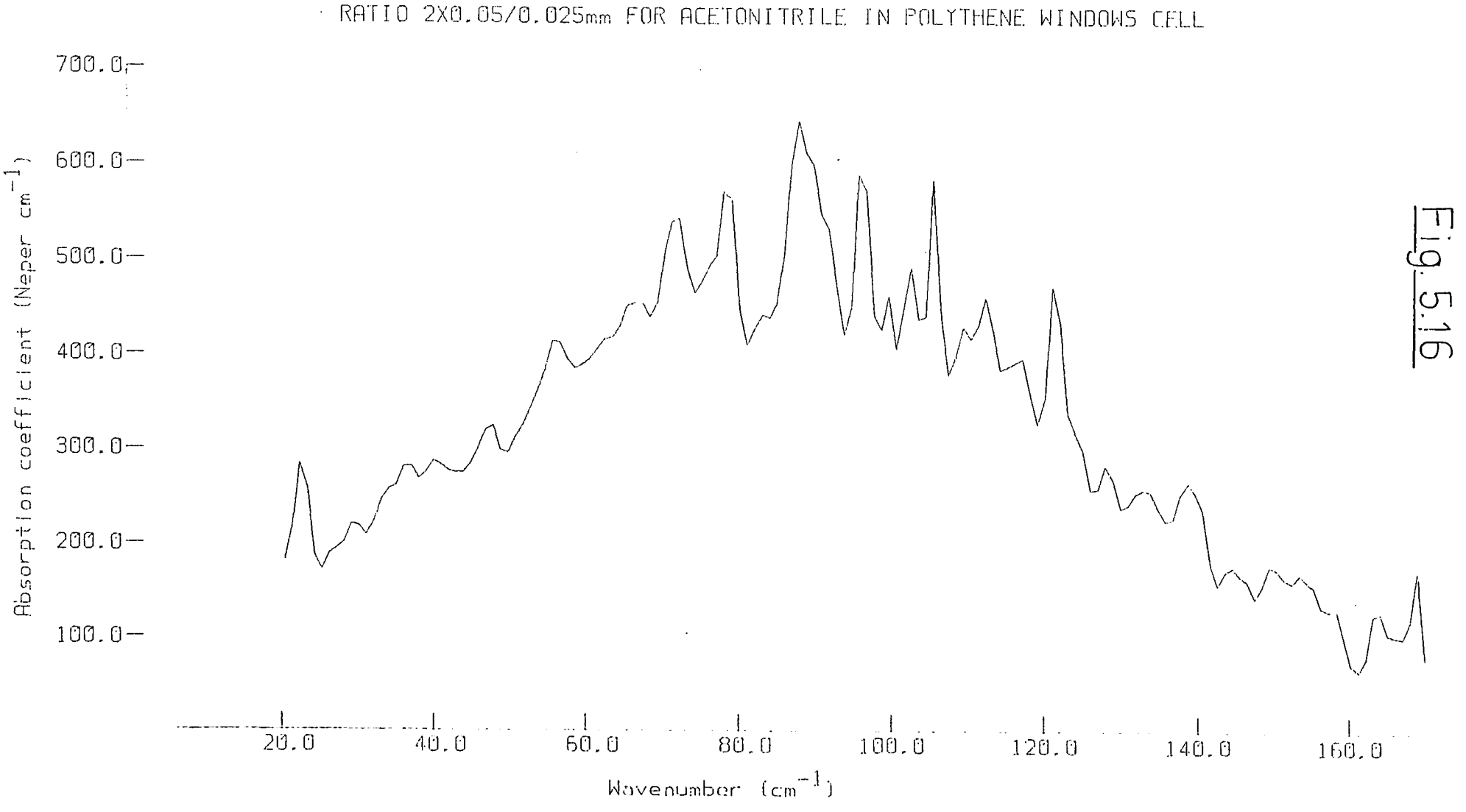

Fig. 5.16

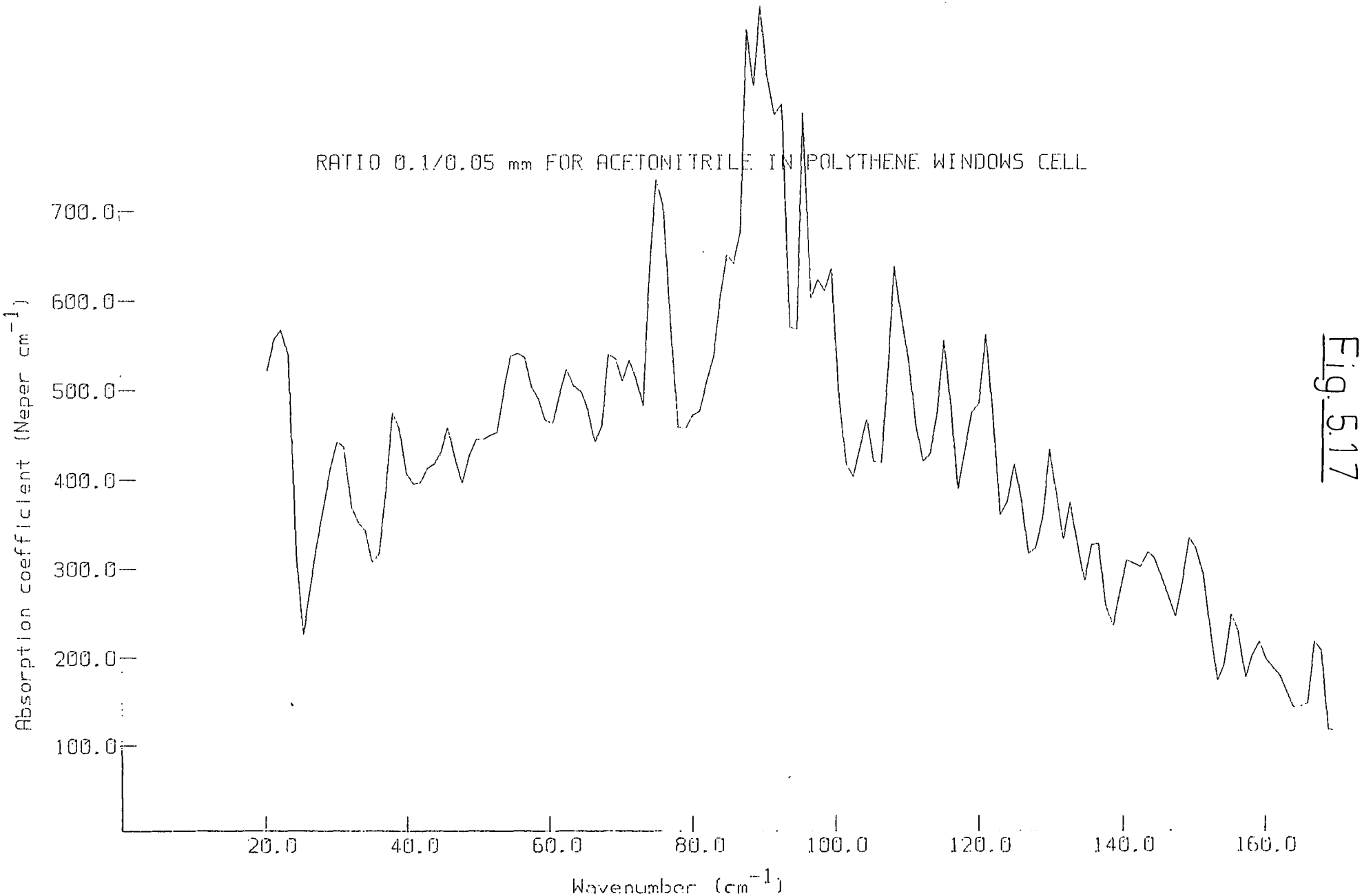
RATIO 0.1/0.05 mm FOR ACETONITRILE IN POLYTHENE WINDOWS CELL
Absorption coefficient (Neper cm^{-1})
700.0
600.0
500.0
400.0
300.0
200.0
100.0
20.0
40.0
60.0
80.0
100.0
120.0
140.0
160.0
Wavenumber (cm^{-1})

Fig. 5.17

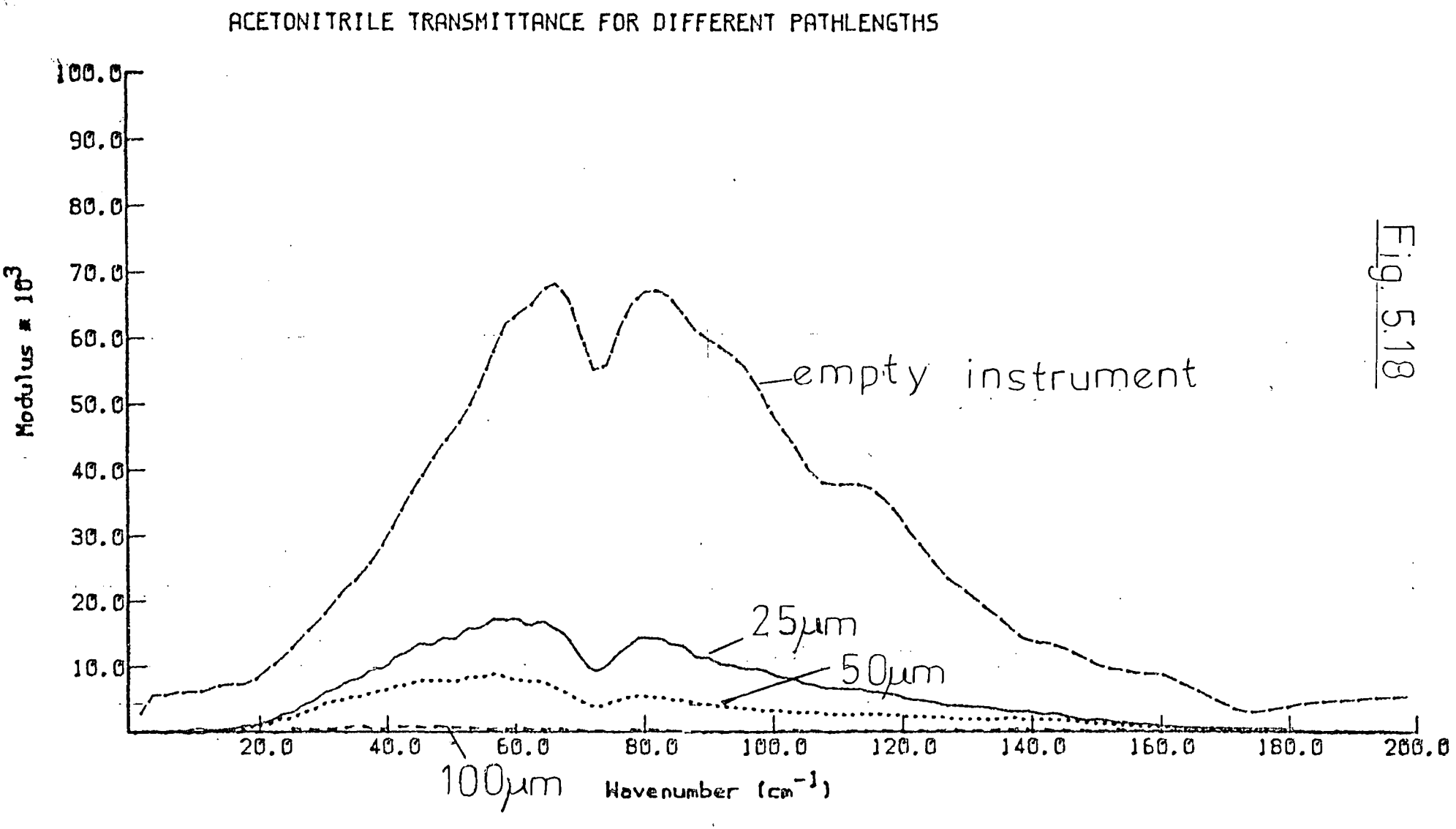
ACETONITRILE TRANSMITTANCE FOR DIFFERENT PATHLENGTHS
Modulus x 10^3
100.0
90.0
80.0
70.0
60.0
50.0
40.0
30.0
20.0
10.0
empty instrument
25μm
50μm
100μm
20.0
40.0
60.0
80.0
100.0
120.0
140.0
160.0
180.0
200.0
Wavenumber (cm^-1)

Fig. 5.18

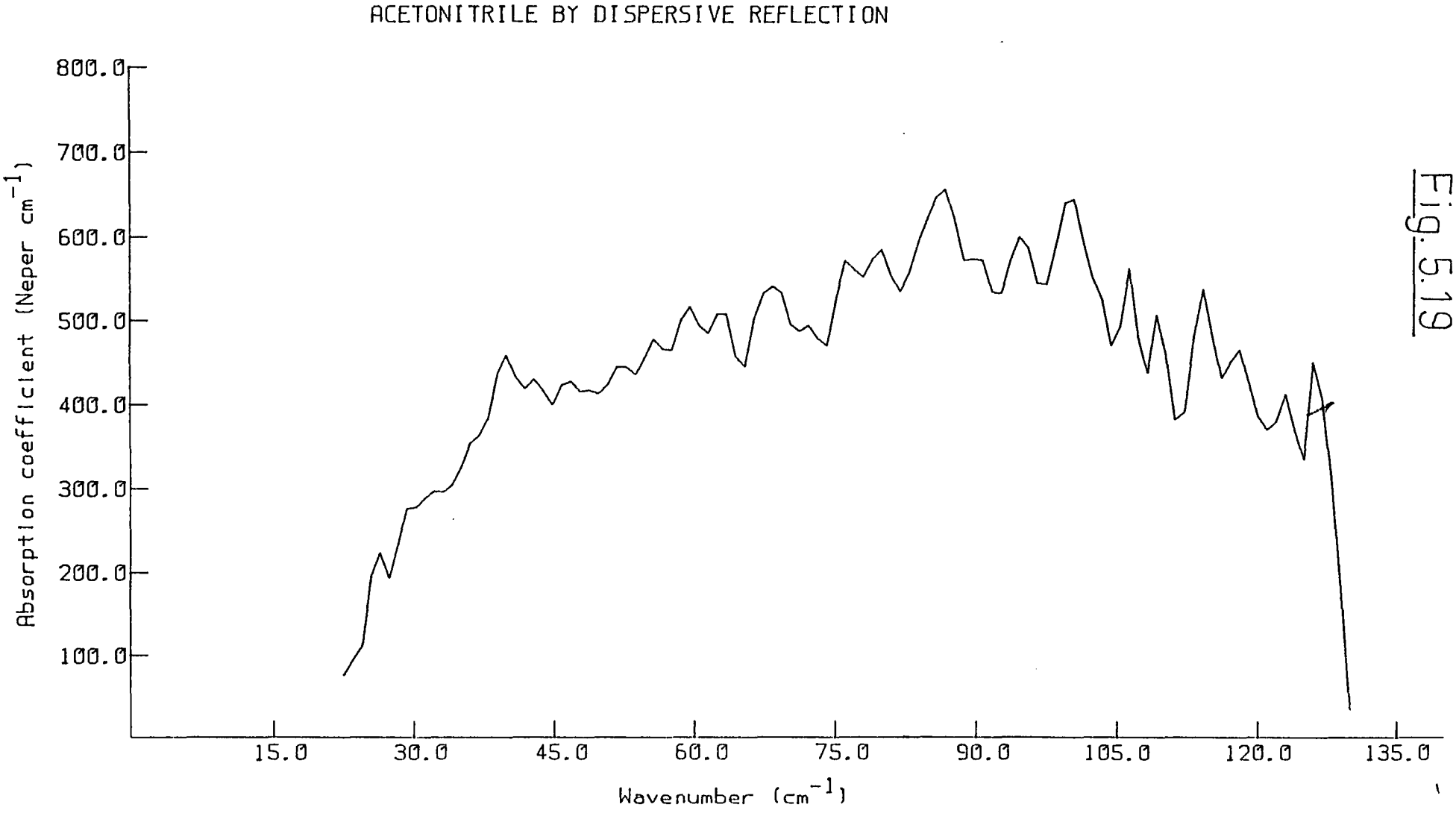
ACETONITRILE BY DISPERSIVE REFLECTION
Absorption coefficient (Neper cm^{-1})
800.0
700.0
600.0
500.0
400.0
300.0
200.0
100.0
15.0
30.0
45.0
60.0
75.0
90.0
105.0
120.0
135.0
Wavenumber (cm^{-1})

Fig. 5.16

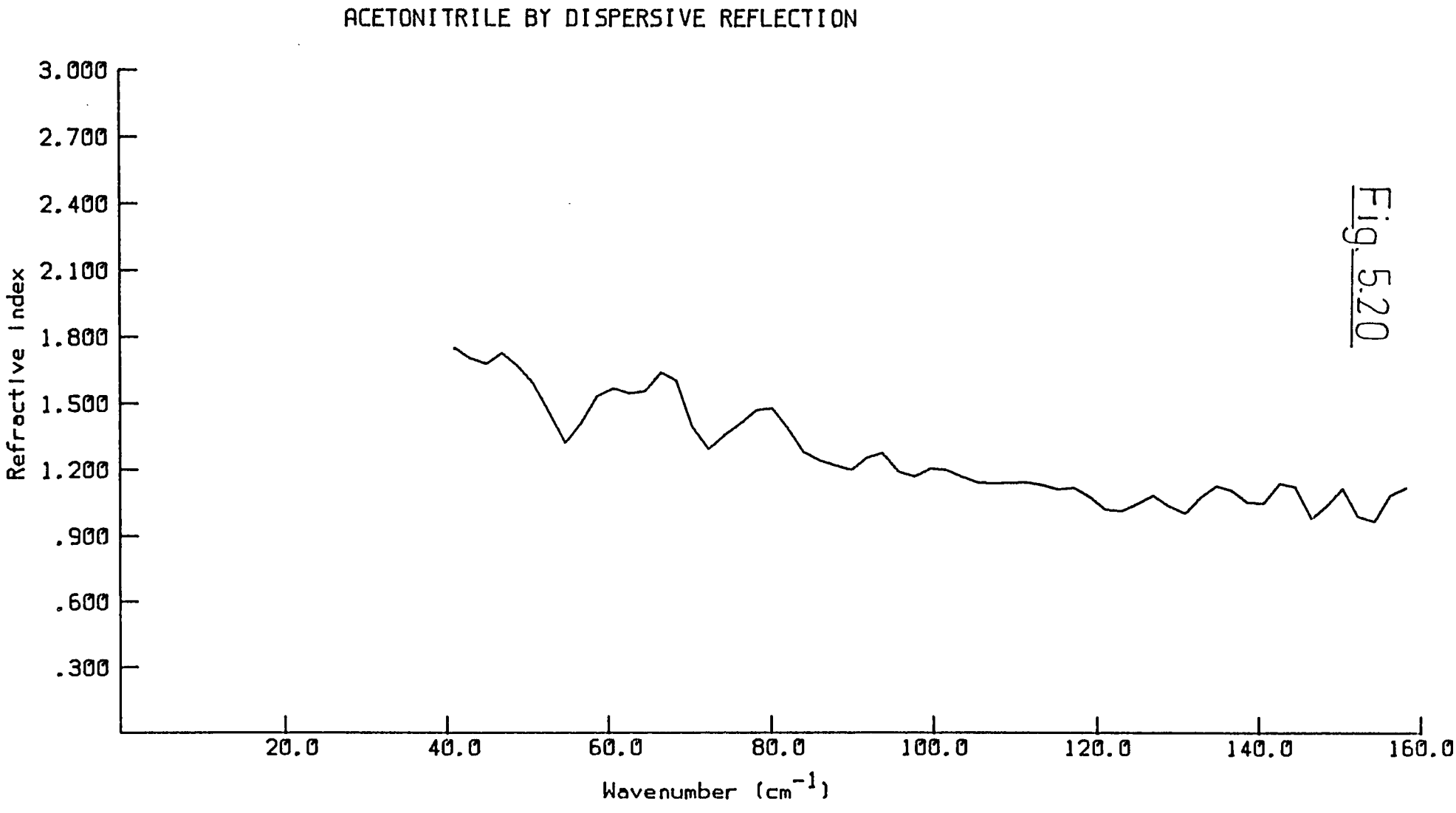
ACETONITRILE BY DISPERSIVE REFLECTION
Refractive Index
3.000
2.700
2.400
2.100
1.800
1.500
1.200
.900
.600
.300
20.0
40.0
60.0
80.0
100.0
120.0
140.0
160.0
Wavenumber (cm-1)

Fig. 5.20

LOW - WAVENUMBER SIDE OF THE FIR ABSORPTION PEAK OF ACETONITRILE.

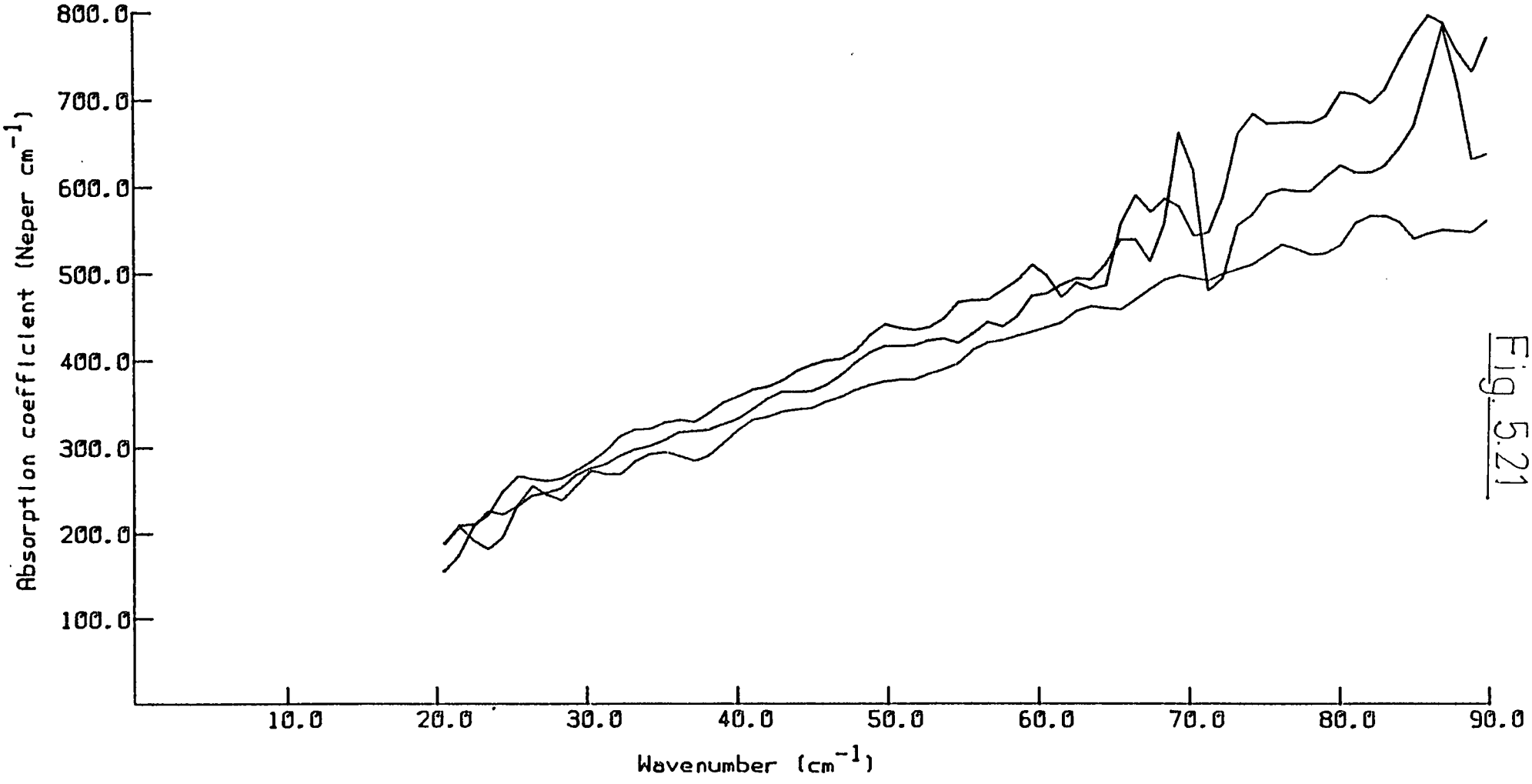

Fig. 5.21

REFRACTIVE INDEX FOR ACETONITRILE FROM DISPERSIVE REFLECTION MEASUREMENTS.

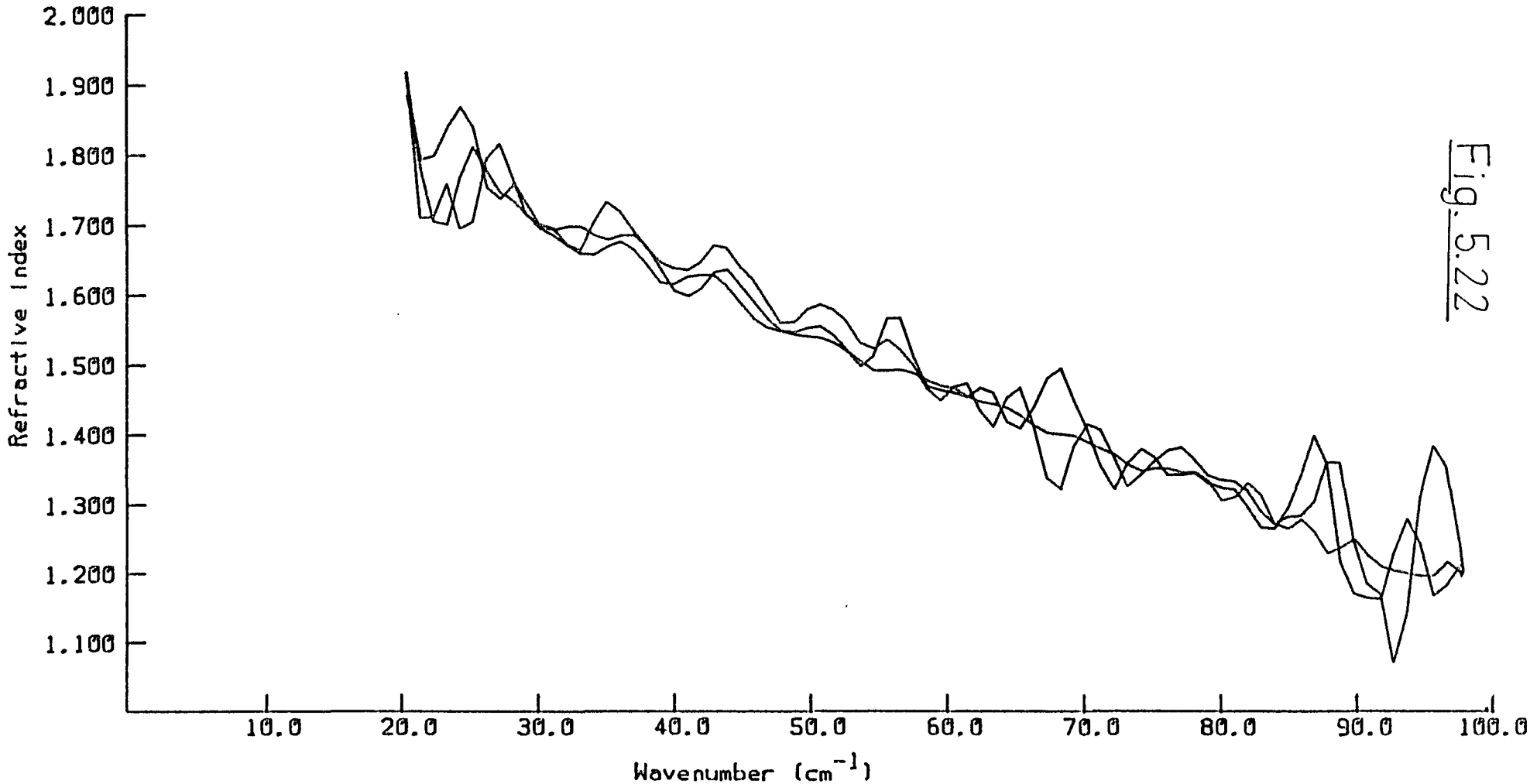

Fig. 5.22

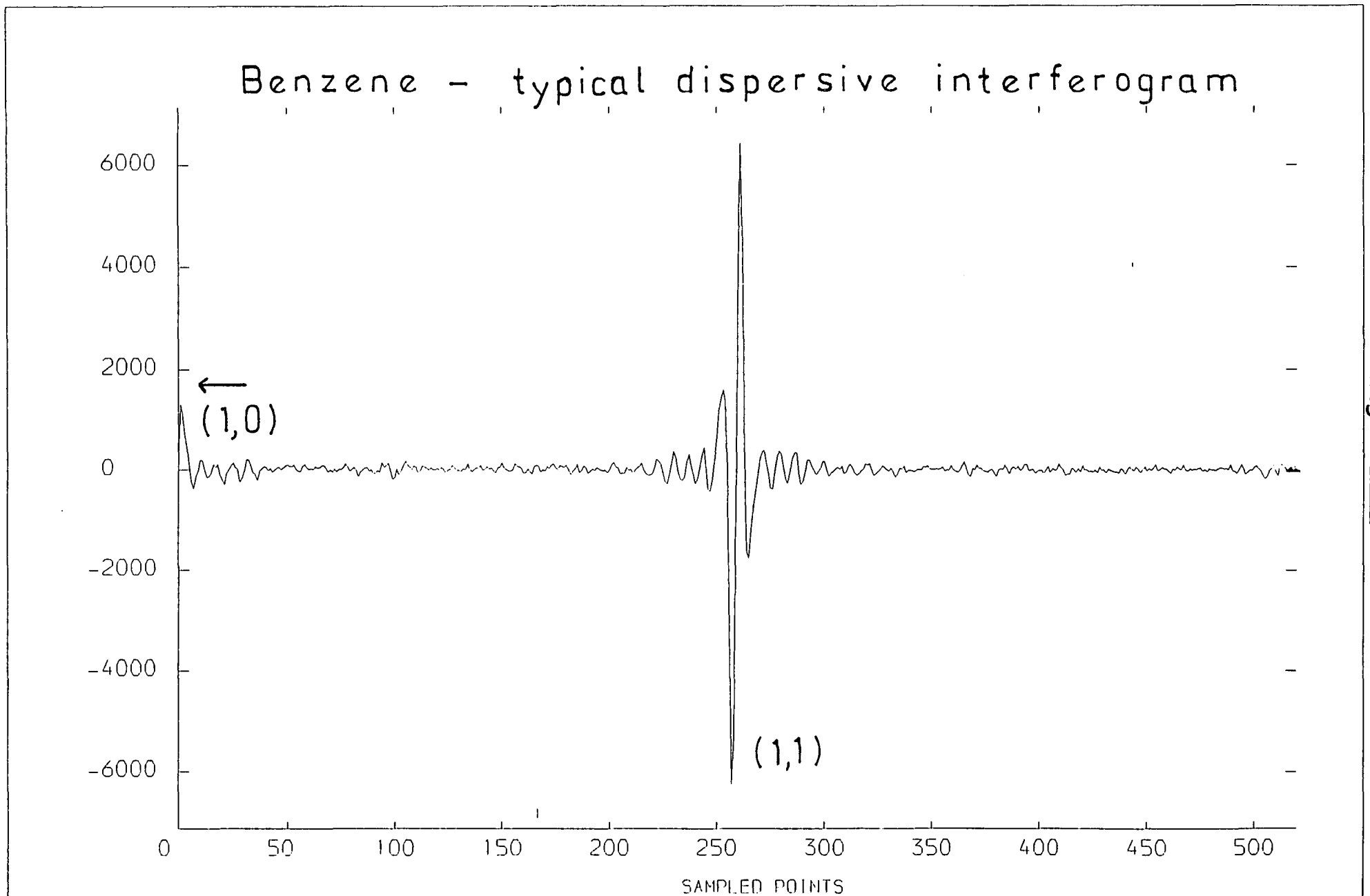
Benzene – typical dispersive interferogram
6000
4000
2000
0
-2000
-4000
-6000
(1,0)
(1,1)
0
50
100
150
200
250
300
350
400
450
500
SAMPLED POINTS

Fig. 5.23

CHAPTER 6

FAR INFRARED COLLISION-INDUCED STUDY OF IODINE IN BENZENE

6.1 Introduction

Following the discussion in section 4.1.2, the elucidation of intermolecular forces in dense liquid phases is best approached through the study of collision-induced effects. The much-studied iodine-benzene system [58,88-92] is thought to be, at best, a weak complex, although the possibility exists that charge-transfer effects could be of some importance (see next section).

The full treatment of collision-induced effects is very complicated, such that it is difficult to find meaningful points of contact between the theories and experimental results from individual spectroscopies. It is now realised [55,93] that a concerted effort must be made to study as many of the collision-induced spectra as possible for a particular system and understand the interrrelationships between them, in order to provide the maximum information for application of the theories. Thus, in this work, it was proposed to study the far infrared band of iodine in benzene and compare the results with those obtained from studies of the ν_1 infrared iodine stretching band [58,92] and the

corresponding Raman band [92].

Also, it is believed that the application, and subsequent comparison, of different theories to the same experimental results will prove enlightening for the interpretation of these molecular interactions. Two basic approaches have been adopted in this work. The first is from deduced analytical expressions for the band shapes and intensities, as discussed in section 4.3. The problem with this approach lies in the difficulty of obtaining some of the physical properties required; for instance the polarisability and quadrupole derivatives. Also, the inclusion of effects due to many body interactions is unclear [94]. The second approach is to use approximate solutions to the generalised Langevin equation for roto-translational motion in order to model the observed band shapes. Two such approaches are described in sections 4.2.4 and 4.2.5. The main difficulty with these approaches is in relating the model parameters to physically meaningful concepts.

6.1.1 Molecular Complexes

A molecular complex is usually taken as meaning an association between two molecules which is stronger than that normally expected through van der Waals forces alone [95]. This (non-rigorous) definition includes very weak molecular attraction where there is essentially no overlap

between the wavefunctions of the interacting pair, through to much stronger 'activated complexes' which may form part of a reaction pathway. Hydrogen-bonded complexes form a special, much-studied group encompassed within this definition [96,97]. A comprehensive review of the molecular complexes and the spectroscopic techniques applied to the elucidation of the intermolecular forces particular to them, is given in a book edited by Yarwood [95].

As part of an attempt to provide a basic theory for describing such complexes, without resorting to complicated quantum-mechanical computations with their own set of aproximations, Mulliken developed a resonance-structure theory [98-101] which expressed the ground-state wavefunction of the complex in the first approximation as a sum of a no-bond and a dative contribution,

$$\psi_N \sim a\psi_o(D,A) + b\psi_1(D^+ - A^-) \qquad (6.1)$$

with D the potential donor and A the potential acceptor. a and b are weighting coefficients. The corresponding excited state is then

$$\psi_v \sim a'\psi_1(D^+ - A^-) - b'\psi_o(D,A) \qquad (6.2)$$

where

$$a \simeq a' \qquad \text{and} \qquad b \simeq b' \qquad (6.3)$$

$\psi_o(D,A)$ involves classical intermolecular interactions such as coulombic or polarisation interactions and dispersion

forces. The $\psi_1(D^+-A^-)$ wavefunction is for complete transfer of an electron from the highest occupied orbital of D to the lowest unoccupied orbital of A. The coefficient b is expected to be much smaller than a. The stabilisation expected from the mixing of ψ_o with ψ_1 is known as the charge-transfer energy and may play a part in the formation of a stable complex.

ψ_N^2 is a probability distribution, and normalisation leads to

$$\int\psi_N^2\,d\tau = a^2\int\psi_o^2(D,A)d\tau + b^2\int\psi_1^2(D^+-A^-)d\tau + 2ab\int\psi_o\psi_1 d\tau = 1 \quad (6.4)$$

Since ψ_o and ψ_1 are both normalised, and writing $S_{o1}=\int\psi_o\psi_o d\tau$ for the overlap integral, we have

$$\int\psi_N^2\,d\tau = a^2 + b^2 + 2abS_{o1} = 1 \quad (6.5)$$

Then assuming that the overlap term is apportioned evenly between the no-bond and dative parts of ψ_N, we can define fractional contributions

$$F_{on} = a^2 + abSo_1 \quad \text{(no-bond)} \quad (6.6)$$

$$F_{1n} = b^2 + abSo_1 \quad \text{(dative)} \quad (6.7)$$

The fractional contributions may be estimated from measured dipole moments assuming $\vec{\mu}_o = 0$,

$$\vec{\mu}_N / \vec{\mu}_1 \simeq b^2 + abS_{o1} \quad (6.8)$$

or from force constants derived from infrared band shifts

$$\Delta k / k \simeq b^2 + abS_{o1} \qquad (6.9)$$

The energy diagram in figure 6.1 shows schematically the processes involved in this theory. At infinite separation, the energy difference between the ground and excited states is due to the ionisation energy of the donor molecule, I_D, and the electron affinity of the acceptor molecule, E_A. G_o and G_1 are classical forces, G_1 being the coulombic attraction between D^+ and A^-, G_o is the energy involved in bringing D and A together and can be attractive or repulsive depending on the particular molecules. Note that if G_o is net attractive there will be stabilisation without the need for any charge transfer stabilisation.

Further quantum mechanical stabilisation arises from mixing of the wavefunctions ψ_1 and ψ_2 and requires a quantum mechanical treatment, through variation theory. Equations 6.1 and 6.2 are of the form

$$\psi = c_o\psi_o + c_1\psi_1 \qquad (6.10)$$

and, as ψ is an eigenfunction, the relevant Hamiltonian can be applied,

$$\hat{H}\psi = E\psi \qquad (6.11)$$

The expectation value of the energy is given by variation theory as

$$E = \frac{\langle\psi^*|\hat{H}|\psi\rangle}{\langle\psi^*|\psi\rangle} \qquad (6.12)$$

Fig. 6.1

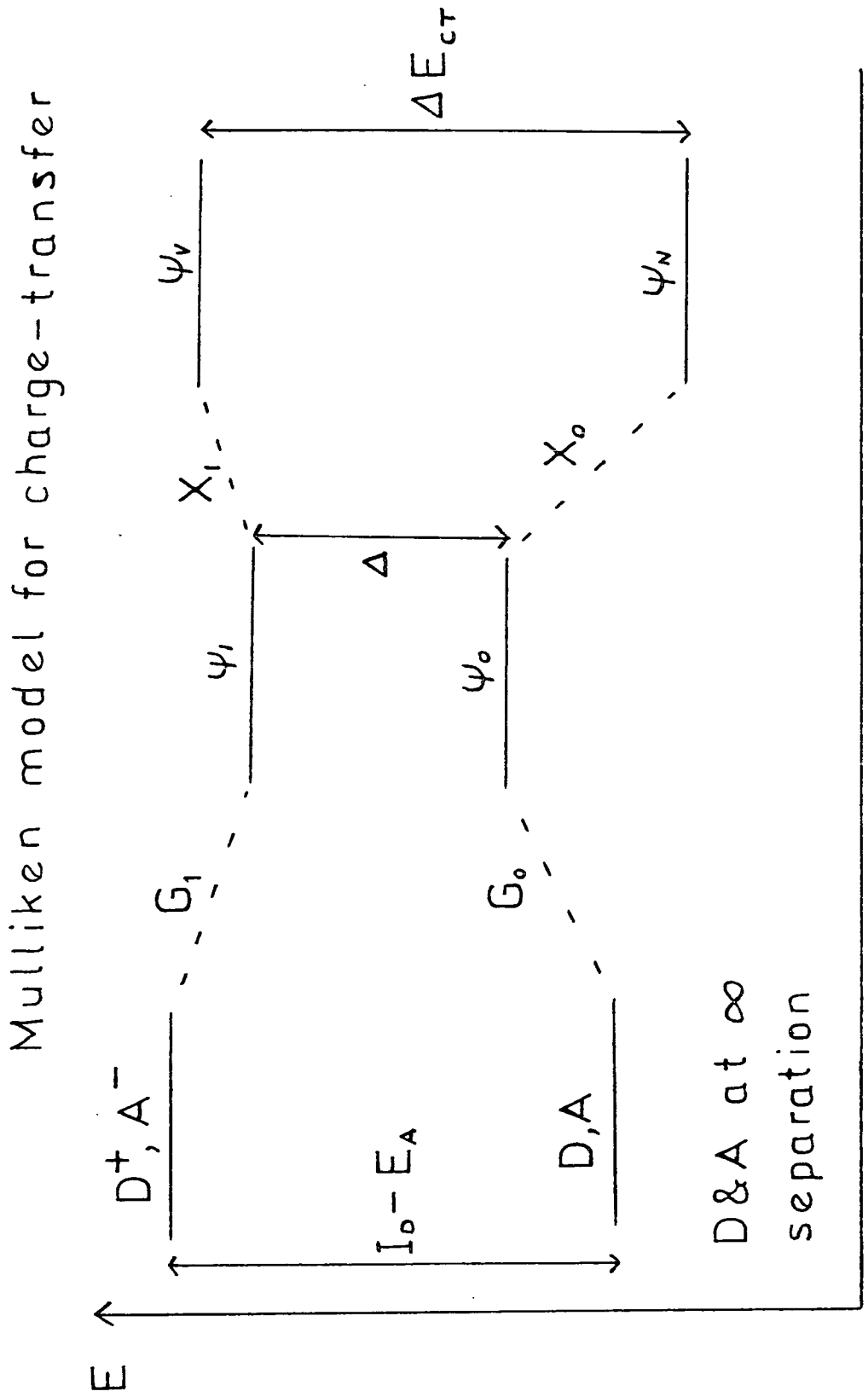
Mulliken model for charge-transfer
E
D&A at ∞ separation
D,A
D+, A−
G0
G1
X0
X1
ψ0
ψ1
ψN
ψV
Δ
ΔECT
I0 − EA

where the integrals are over all space. Equation 6.12 can then be solved to give values for the energies of the ψ_N and ψ_V states. This theory has the advantage of being simple and easily visualised. It yields the value of the energy transitions expected and enables the weight of dative contribution to be arrived at experimentally. Some of the integrals needed to solve equation 6.12, however, are difficult to estimate and the theory does not work well for strong complexes. The theory is thought to over-exaggerate the amount of charge transfer [96,102] because classical electrostatic forces are expected to have similar effects on the frequencies and force constants of molecules in the ground state as does charge transfer.

The separation of the different contributions is non-trivial. Much confusion has arisen in the literature because of this problem [95]. It is necessary, therefore, to consider all electrostatic effects, including those due to coulombic, induction, dispersion and repulsion before assigning observations to charge-transfer effects. Hanna [103,104] examined the possibility that frequency shifts and intensity changes observed in the spectra of complexes could be attributed to electrostatic effects alone. He showed further that quadrupole-induced dipole effects were likely to be important to systems such as iodine-benzene since this is the highest order electrostatic attractive force applicable to the system (see section 4.3).

A number of approaches concerned with the electrostatic

attraction between molecules in a liquid have been dealt with in chapter four of this thesis.

6.1.2 The Iodine-Benzene System

The iodine-benzene system is classed as an $a_{\sigma} \Leftarrow b_{\pi}$ complex [95]. It is a weak complex, with an equilibrium constant of ~ 0.18 l mole^{-1} [90].

The fraction of dative structure, measured through changes in force constant on complexation, has been reported as being as low as 0.02 [88]. This, in itself, does not rule out the possibility of significant charge-transfer contribution to the spectra, since a small F_{1N} can lead to large intensity changes [95]. Thermodynamic data reported in the literature [90] have supported the proposed weak-nature of this complex.

Halogens in benzene and other solvents have been studied using ultra-violet [90], infrared [58,88,91,92,102,105] and Raman [92,106-108] specroscopies. The far infrared spectrum of iodine in benzene, as studied in this work, consists of two bands and is presented in figure 6.2, with solvent absorption removed. The higher frequency band, centred at aproximately 205 cm^{-1} is the intramolecular stretching frequency, ν_{I-I}, of the iodine molecule. The low frequency band is much broader and is centred around 80 cm^{-1}. This is due to rotations and translations of the iodine molecule, as discussed in section

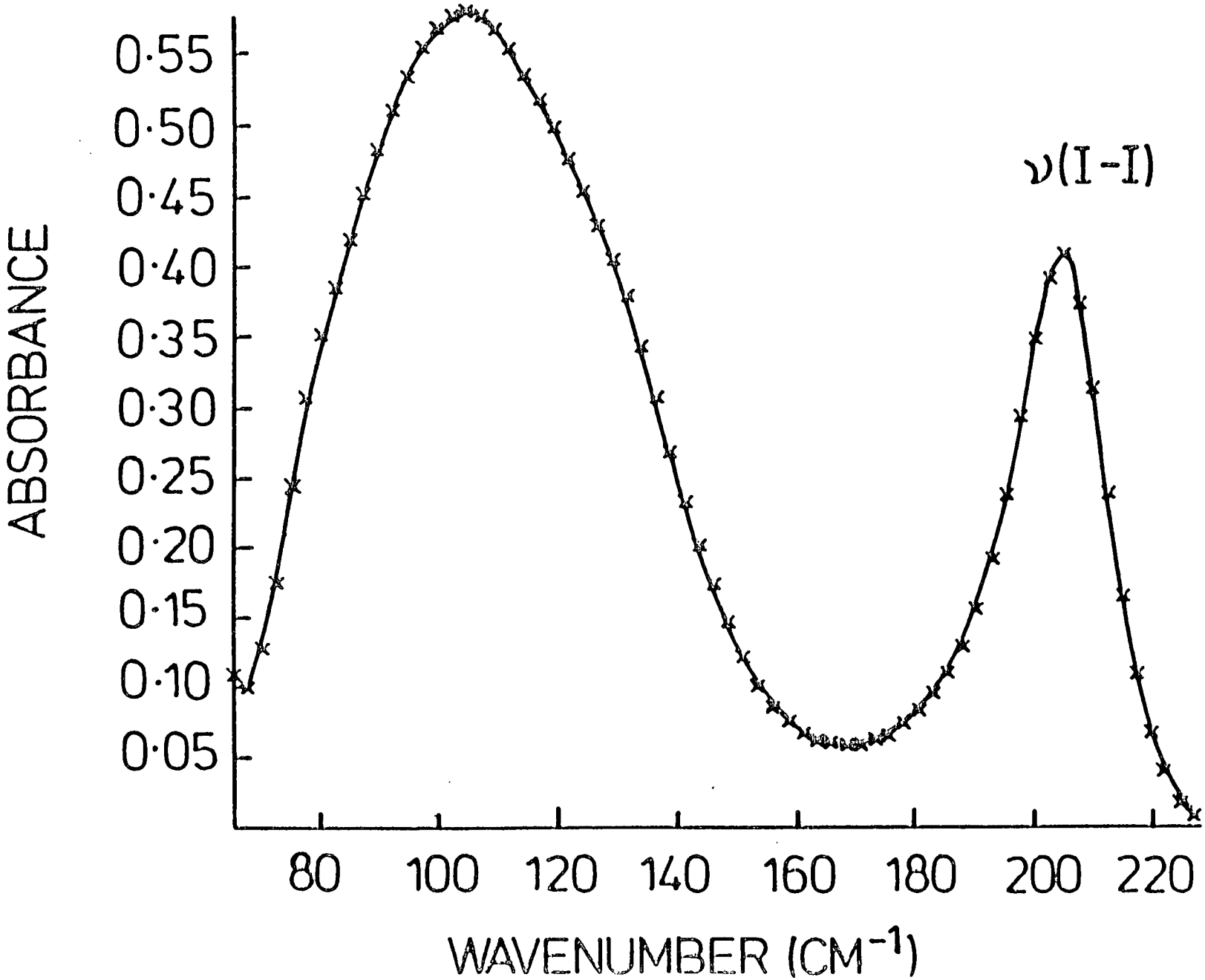
ABSORBANCE
0·55
0·50
0·45
0·40
0·35
0·30
0·25
0·20
0·15
0·10
0·05
ν(I-I)
80
100
120
140
160
180
200
220
WAVENUMBER (CM⁻¹)

Fig. 6.2

4.1 and not, as originally thought [109] from an intermolecular vibration of the complex.

The free iodine molecule does not have an infrared spectrum since it lacks a permanent dipole. Both the bands observed in the far infrared spectrum then arise solely from a collision-induced effect. If a complex is formed with benzene then an equilibrium will exist between 'complexed' and 'non-complexed' iodine molecules, and the intermolecular interactions will be different for the two cases. The spectrum is then expected to be composed of a collision-induced contribution from 'complexed' iodine molecules, and a collision-induced contribution from 'non-complexed' iodine molecules.

However, if the lifetime of the complex is very short ($< 10^{-12}$s) then, even if such an equilibrium exists, it could not be observed in the frequency region corresponding to far infrared. Thus, evidence for complex formation at high frequencies [90] does not necessarily mean that similar evidence will be observed at far infrared frequencies. At these far infrared frequencies an average of molecular orientations over a much longer time scale is seen. For the stronger benzene-ICl complex a doublet is observed in the allowed interhalogen far infrared vibrational band [95], corresponding to 'complexed' and 'non-complexed' ICl.

A recent Raman study [110] has examined the iodine stretching vibration in methylated benzene derivatives. In Raman spectroscopy, the free iodine molecule does, of

course, have an allowed spectrum. For mesitylene, two bands were observed which were attributed to 'complexed' and 'non-complexed' iodine at 200cm^{-1} and 210cm^{-1} respectively. As the number of methyl groups was reduced, and therefore the complex weakened, the two bands were seen to coalesce until only one band remained for iodine in benzene.

The solubility of iodine in benzene was found to be low, the maximum concentration used in this work being $\sim$ 0.25 moles l^{-1}. This means that iodine molecules are essentially isolated from other iodine molecules and interactions between them can be ignored. The far infrared spectrum is then composed of the following contributions:

(1) benzene-benzene interaction

(2) iodine-benzene interaction.

Contribution (1) can be eliminated to a large degree by ratioing solutions of iodine in benzene against the same pathlength of benzene.

Since iodine also possesses a significant quadrupole moment and benzene a high polarisability, contribution (2) is expected to consist of two parts: an interaction induced spectrum of iodine and a spectrum of benzene induced by interaction with iodine, both of which arise from a quadrupole induced dipole mechanism.

The correlation function can be expressed as a sum of two-body, three-body, and higher terms; the single-body term does not exist for collision induced infrared systems. The higher terms are successively less important.

$$c(t) = \sum_{ij} M_{ij}(t).M_{ij}(0) + \sum_{ijj'} M_{ij}(t).M_{ij'}(0) \qquad (6.13)$$

2-body 3-body

where M is the total dipole moment (see chapter 4).

The lineshape theory discussed in the next section will only be used to describe two-body contributions which are of considerably more importance than the 3-body contributions. Nevertheless, the effect of the three-body term on the lineshape can be judged by dilution with an inert solvent, such as hexane, since this will reduce the three body term.

The physical parameters for iodine and benzene molecules which are required for the interpretation of experimental results presented in this chapter are listed in table 6.1.

6.1.3 Comparison with Similar Systems

The iodine-benzene system is a relatively complicated one to study in the far infrared region since interactions are modulated by both translational and rotational motions. Other systems giving rise to a collision-induced absorption by a quadrupole induced dipole mechanism, but posessing negligible rotational-translational coupling, have been reported in the literature. They include studies on H_2 and D_2 liquids in liquified noble gases [111,112] and low density liquid nitrogen [113-115].

TABLE 6.1

	Polarisability (10^{-24} cm^3)	Quadrupole moment (10^{-26} e.s.u.)	Moment of inertia (10^{-40} g cm^2)	Reference
Iodine	11	2.8	749	[92]
Benzene	10.6	4.5	147	[92]

For cases such as these, the correlation function may be expressed as a product of a translational part and a rotational part which can be obtained from light scattering experiments

$$c(t) = c_{trans}(t) \langle P_2 [\cos \phi(t)] \rangle \qquad (6.14)$$

Thus, the absorption cross-section, $I(\bar{\nu})$, is a convolution of the rotational and translational contributions. The translational part of the spectrum is seen to narrow as the density is increased [111,113,11] and this has been attributed to the fact that the molecules are held close together for longer periods of time by the surrounding molecules and the relaxation times are consequently longer.

The three-body contribution to the spectrum was found to be of the same order of magnitude as the two body contribution for liquid nitrogen [114]. With increasing density the level of absorption in all these systems falls [112,113] due to cancellation between many body terms [116]. This leads to severe complications when intensity data are used to judge the importance of many body correlations.

6.1.4 Lineshape Analysis Applied to the Iodine-benzene system

The effects of the multipoles discussed in section 4.3 on interactions depend strongly on intermolecular separation

and they are modulated to a large degree by molecular vibrations, rotations and translations. As such, they offer an important means of studying intermolecular potentials for weak interactions such as those studied here.

If it is assumed, for simplicity, that the anisotropy in the polarisabilities of iodine and benzene can be ignored, then the polarisability tensor in equation 4.47 can be replaced by the mean polarisability.

$$\alpha_{\alpha\beta} \equiv \overleftrightarrow{\alpha} = \alpha\overleftrightarrow{I} \tag{6.15}$$

where $\leftarrow\rightarrow$ denotes a tensor quantity and $\overleftrightarrow{I}$ is the unit tensor. The moment responsible for the far infrared collision-induced absorption is then

$$m^i = \frac{1}{3} \sum_{i \neq j} \alpha^i \overleftrightarrow{I}\, T^3(r_{ij})\, \overleftrightarrow{\theta}^j \tag{6.16}$$

This is quite a major simplification since the assumption of isotropic polarisabilities for this system is invalid.

The far infrared bands occur in a region of the spectrum where there are no vibrational features for benzene. Thus, the molecule is approximated as a rigid entity, and we have

$$\alpha_{Bz} = \alpha^o_{Bz} \qquad \text{and} \qquad \overleftrightarrow{\theta}_{Bz} = \overleftrightarrow{\theta}^o_{Bz} \tag{6.17}$$

where o refers to equilibrium properties.

For small vibrational displacements of the iodine molecule, α_{I2} and $\overleftrightarrow{\theta}_{I2}$ may be expressed by the leading terms of the Taylor expansion in normal coordinate q as

$$\alpha_{I_2} = \alpha^{o}_{I_2} + \left(\frac{\partial \alpha}{\partial q}\right)_{q=o} q \qquad (6.18)$$

and

$$\overleftrightarrow{\theta}_{I_2} = \overleftrightarrow{\theta}_{I_2} + \left(\frac{\partial \overleftrightarrow{\theta}}{\partial q}\right)_{q=o} q \qquad (6.19)$$

Assuming no orientational correlation between benzene-benzene molecules and benzene-iodine molecules, and that there is no coupling between translational, rotational and vibrational degrees of freedom, Lascombe and Besnard [92] have deduced a correlation function of the form

$$c(t) = A(t) + B(t) \; < q(t) . \; q(o) > \qquad (6.20)$$

were $<q(t)q(o)>$ is the vibrational correlation function of the ν_{I_2} vibrational mode. The A(t) term models the low frequency band and the B(t) term models the higher frequency ν_{I_1} band.

A(t) is given by [92]

$$\begin{aligned} A(t) = {} & \frac{2}{15} N_I N_B \{(\alpha_I \eta_B)^2 < P_2[\cos \theta_B (t)] > + (\alpha_B \eta_I)^2 < P_2[\cos \phi_I (t)] >\} \\ & x \; < T^{(3)}\left[r_{BI}(t)\right] : T^{(3)}\left[r_{BI}(o)\right] > \\ & + \frac{2}{15} N_I N_B (N_B - 1) \; (\alpha_B \eta_I)^2 < P_2\left[\cos \theta_i (t)\right] > \\ & x \; < T^{(3)}\left[r_{B'I}(t)\right] : \underset{B \neq B'}{T^{(3)}}\left[r_{BI}(o)\right] > \end{aligned} \qquad (6.21)$$

where the first term describes the rotational correlation function and the second term describes the two body relative translational correlational function. The last two terms are for the three body contribution. Experimental data [92] have been analysed using equation 6.20 with the iodine vibrational profile, $\langle q(t)q(o)\rangle$ estimated from Raman experiments, and using a three parameter Mori fit (section 4.2.4) for the induced profiles. It was found [92] that the correlation functions associated with the different induced profiles used for the high and low frequency bands differed by about an order of magnitude, suggesting that the rotational behaviour of the benzene and iodine molecules is very different, in contradiction to Raman observations [92].

It was thus concluded that the two bands reflect different temporal aspects of the correlation function; the low frequency band profile describing the very fast fluctuations of the cage of benzene molecules around the iodine molecule, and the higher frequency band profile providing information not only about the vibrational and rotational behaviour of the molecules but also about the mutual diffusion of iodine and benzene molecules.

The correlation function for the low frequency band can be related to the spectral moments defined as

$$M_n = \int_{-\infty}^{\infty} \omega^n \; I(\omega) \; d\omega \qquad (6.22)$$

by [52]

$$M_{2n} = (-1)^n \; \langle c''(t) \rangle_{t\simeq o} \qquad (6.23)$$

where c"(t) is the second time derivative of the correlation function.

Ignoring the three body contributions and assuming an isotropic potential between iodine and benzene molecules, the zeroth and second moments are given by [92]

$$M_o = 12\, N_I\, N_B \{ (\alpha_I \eta_B)^2 + (\alpha_B \eta_I)^2 \} < r_{BI}^{-8} > \qquad (6.24)$$

and

$$M_2 = 12 N_I\, N_B \{ (\alpha_I \eta_B)^2 \frac{6kT}{I_B} + (\alpha_B \eta_I)^2 \frac{6kT}{I_I} < r_{BI}^{-8} >$$

$$+ 336 N_I\, N_B \{ (\alpha_I \eta_B)^2 + (\alpha_B \eta_I)^2 \} \frac{kT}{M_{BI}} < r_{BI}^{-10} > \qquad (6.25)$$

respectively. N_i represents numbers of molecules and M_{BI} is the reduced mass of the pair. I_i is the principal moment of inertia along the main symmetry axis of each molecule. η_i is the quadrupolar constant derived from $\overleftrightarrow{\theta}_i(t)$ according to the expression [92]

$$< \overleftrightarrow{\theta}(t)\ \overleftrightarrow{\theta}(o) > = 6\eta^2 <P_2 [\cos \phi\ (t)]> \qquad (6.26)$$

where $P_2[\cos\phi(t)]$ is the second order Legendre polynomial ($P_2(x) = \frac{1}{2}(3x^2-1)$) and ϕ the angle of reorientation of the unit vector directed along the main symmetry axis of the molecule.

The moments can, of course, be derived experimentally

according to

$$M_o = \int_{-\infty}^{\infty} I(\bar{\nu})\, d\bar{\nu} \qquad (6.27)$$

$$M_2 = \int_{-\infty}^{\infty} I(\bar{\nu})\, \bar{\nu}^2\, d\bar{\nu} \qquad (6.28)$$

where $I(\bar{\nu})$ is as defined in equation 4.1.

6.2 Experimental Details

Benzene and hexane were purchased from the Aldrich Chemical Co. Ltd. and were 'Spectrophotometric' grade. The solvents were dried over molecular sieves but otherwise used without further purification. The iodine was obtained from BDH Chemicals Ltd. Solutions were prepared using weighed amounts of iodine in graduated flasks immediately prior to use. The liquid helium bolometer described in section 3.1.4 has been used to collect all the data recorded in this chapter.

6.2.1 By Transmission

Cells were used with polythene windows throughout. Pathlengths of between 0.2cm and 1.5cm were employed, using polythene spacers, depending on the concentrations being

studied. Pathlengths were measured as described in section 5.2.1.

In order to obtain the full low-frequency far infrared band it was necessary to record two different portions in separate experiments in order to achieve a good signal to noise ratio throughout. The instrumental profiles for the two experiments are illustrated in figures 6.3 and 6.4. The higher frequency profile was recorded using a 25μm beamsplitter and shows reasonable energy throughput between about $20cm^{-1}$ to $140cm^{-1}$. The low frequency profile was recorded using a 175μm beamsplitter and was used to provide sufficient throughput between about $3cm^{-1}$ to 20 cm^{-1}, leaving however, a gap in the $12cm^{-1}$ region due to the first interference minimum (section 1.3.1b) of the beamsplitter channel spectrum. In most cases this gap has been filled in using data obtained with a 100μm beamsplitter. It is particularly pleasing that, on the whole, data collected in different regions fitted together very well. Data from different regions were joined together by a least squares interpolation routine from the National Algorithms Group (NAG) library, E04FDF. However actual experimental data will be shown where possible.

Despite the fact that the signal is attenuated very little by the samples due to the low absorption coefficient of both iodine and the two solvents used, it is nevertheless difficult to achieve good signal-to-noise ratio for the bands since a ratio is required of two modulus spectra which

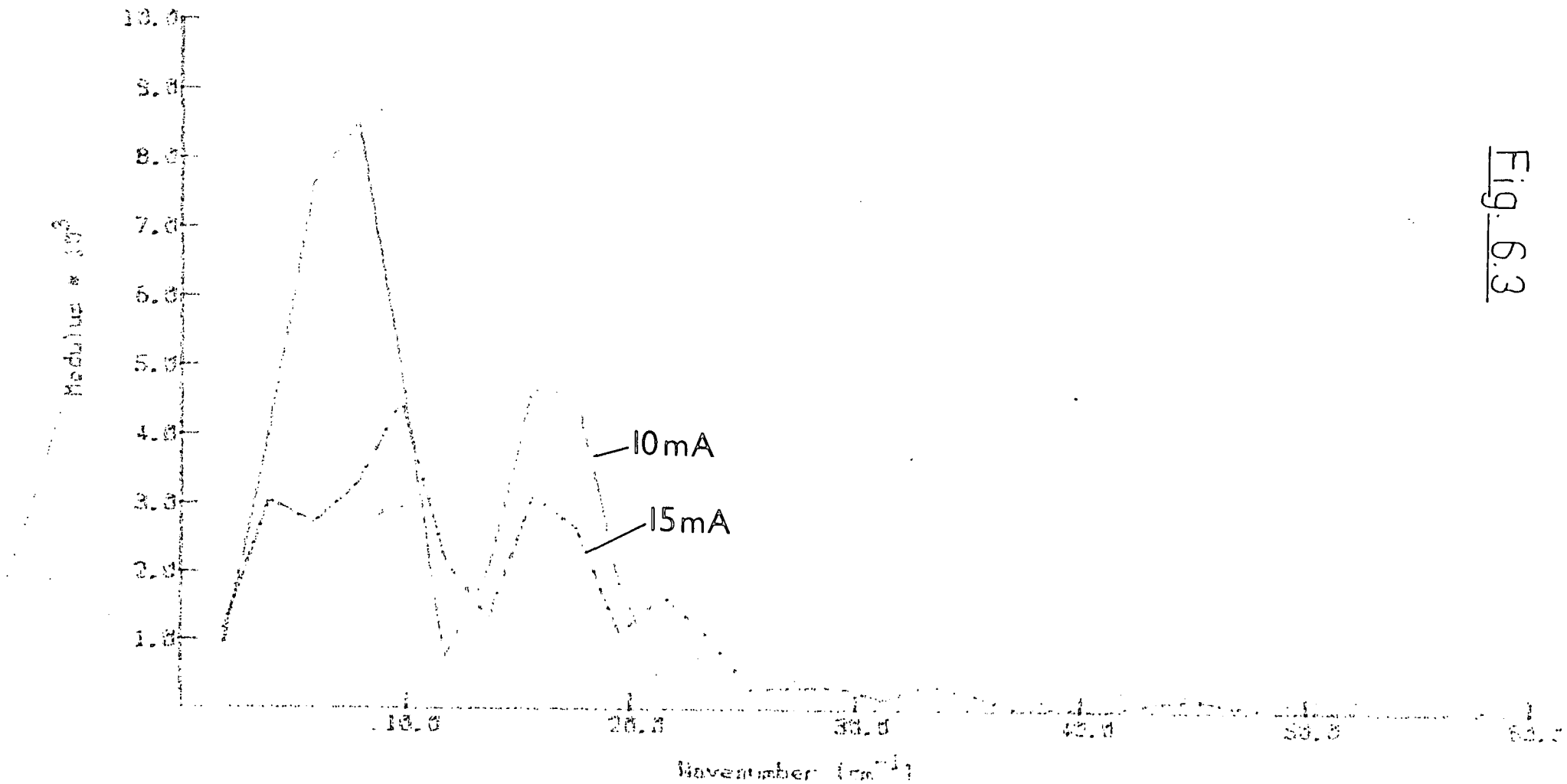
178micron BEAMSPLITTER, HCL, 74Hz.
10.0
9.0
8.0
7.0
6.0
5.0
4.0
3.0
2.0
1.0
Modulus * 10^3
10mA
15mA
10.0
20.0
30.0
40.0
50.0
60.0
Wavenumber (cm^-1)

Fig. 6.3

25μm Beamsplitter.

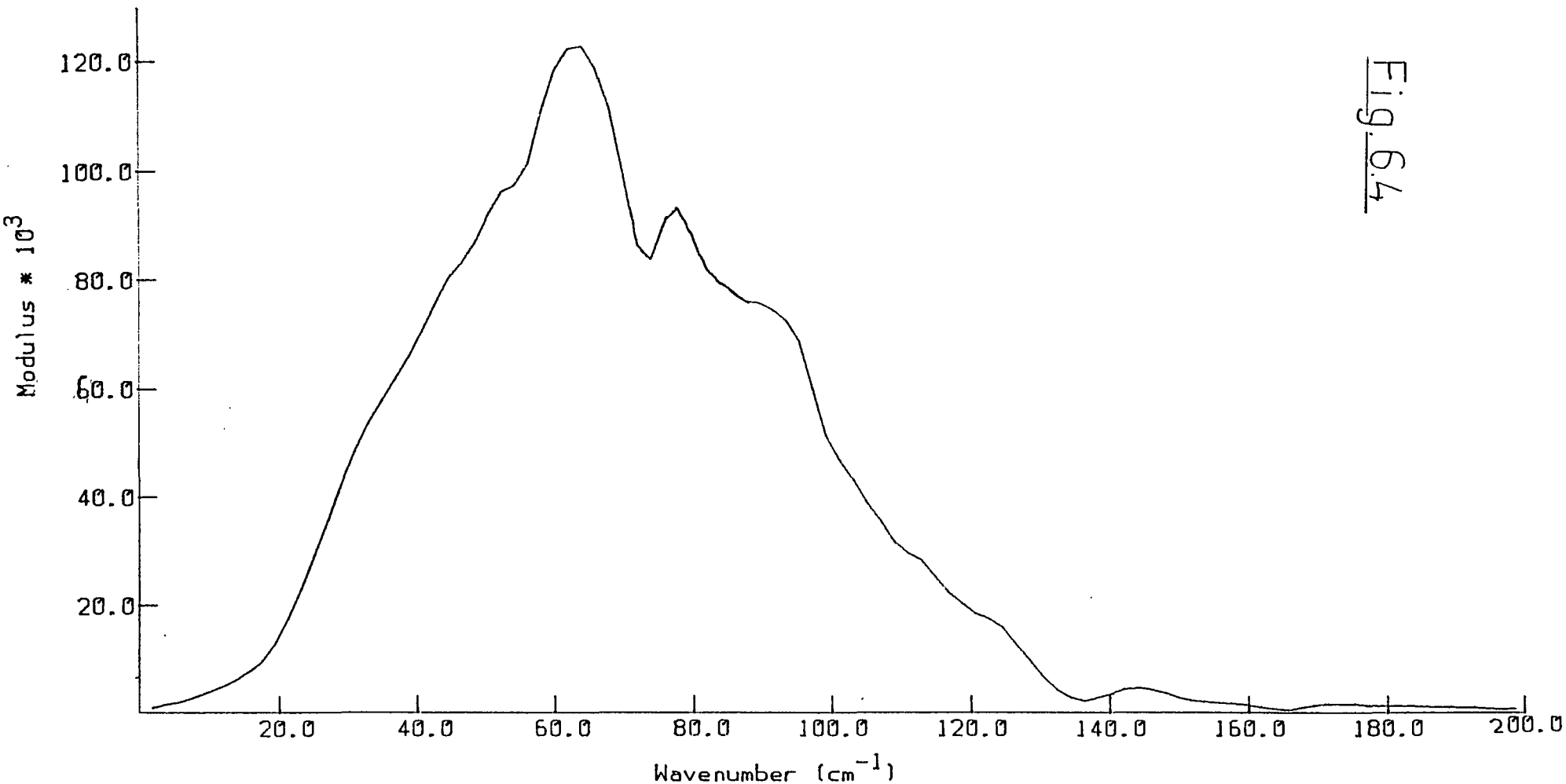

Fig 6.4

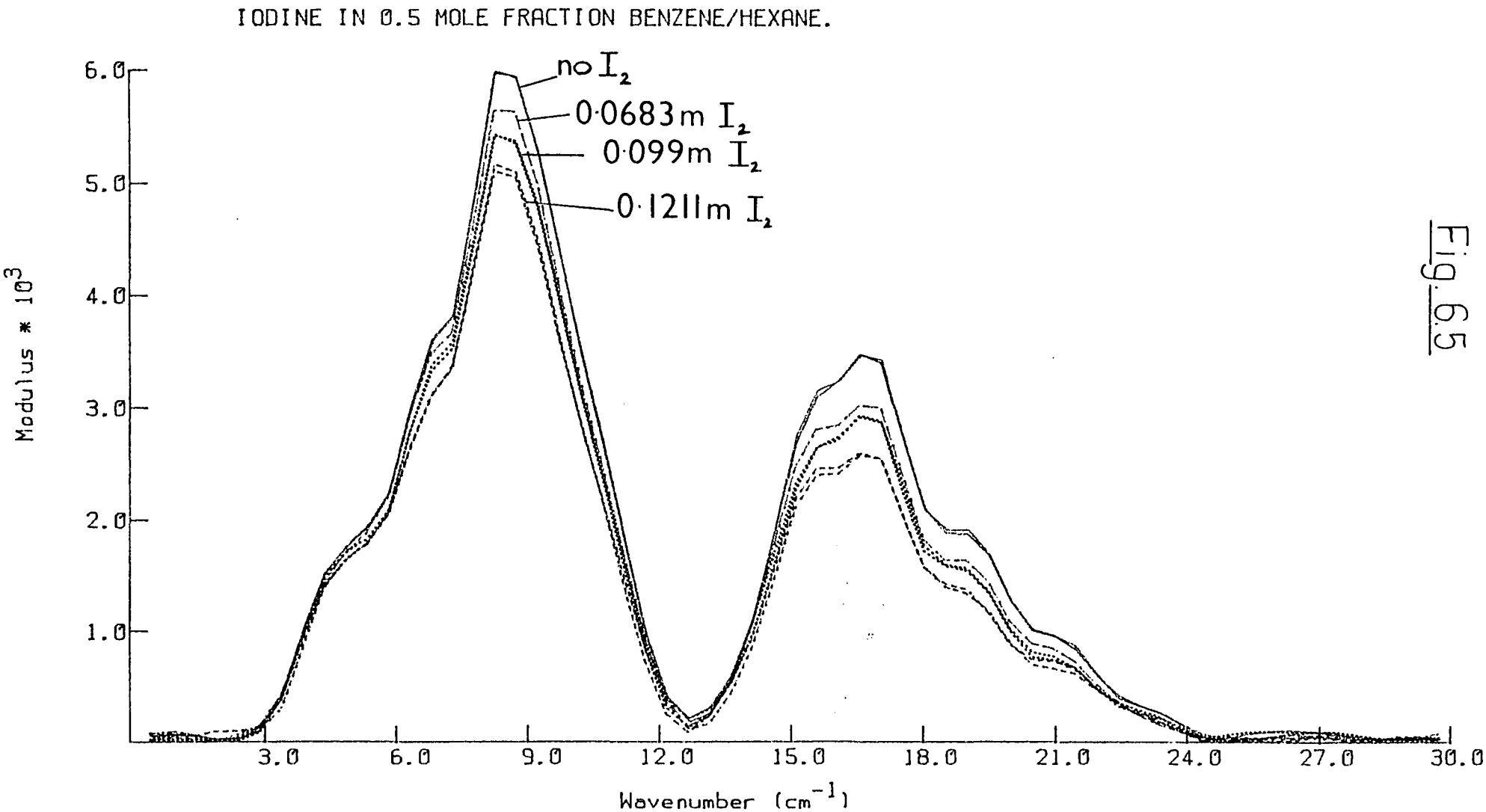
IODINE IN 0.5 MOLE FRACTION BENZENE/HEXANE.
no I_2
0·0683m I_2
0·099m I_2
0·1211m I_2
Modulus * 10^3
6.0
5.0
4.0
3.0
2.0
1.0
3.0
6.0
9.0
12.0
15.0
18.0
21.0
24.0
27.0
30.0
Wavenumber (cm^{-1})

Fig.6.5

are very similar in intensity (see for example, figure 6.5). Thus, although both modulus spectra have very good signal to noise ratio, the difference between them is expected to be much poorer. This problem becomes more critical as the concentration of iodine is reduced and eventually a limiting concentration is reached where the iodine absorption is below that which can be seen above the noise level. The lowest concentration of iodine in bezene used in this work was 0.06M so that the concentration range ran from 0.06M to 0.20M. Since the solubility of iodine in hexane is extremely low, the concentration range of iodine in a 0.5 mole fraction of benzene in hexane ran from 0.07 to 0.12M.

Two experimental procedures were adopted for deriving optical constants:

(a) ratioing a cell filled with iodine/solvent against the same pathlength of solvent;

(b) ratioing a cell filled with iodine/solvent against a different pathlength of iodine/solvent.

Thus, if we assume that procedure (b) yields a spectrum composed of the induced interactions:

(i) benzene perturbed by benzene

(ii) iodine perturbed by benzene

(iii) benzene perturbed by iodine

and procedure (a) a spectrum composed of induced interactions (ii) and (iii) then if a solvent spectrum is subtracted from (b) it should be equivalent to (a).

This is illustrated in figures 6.6 to 6.8 and is valid

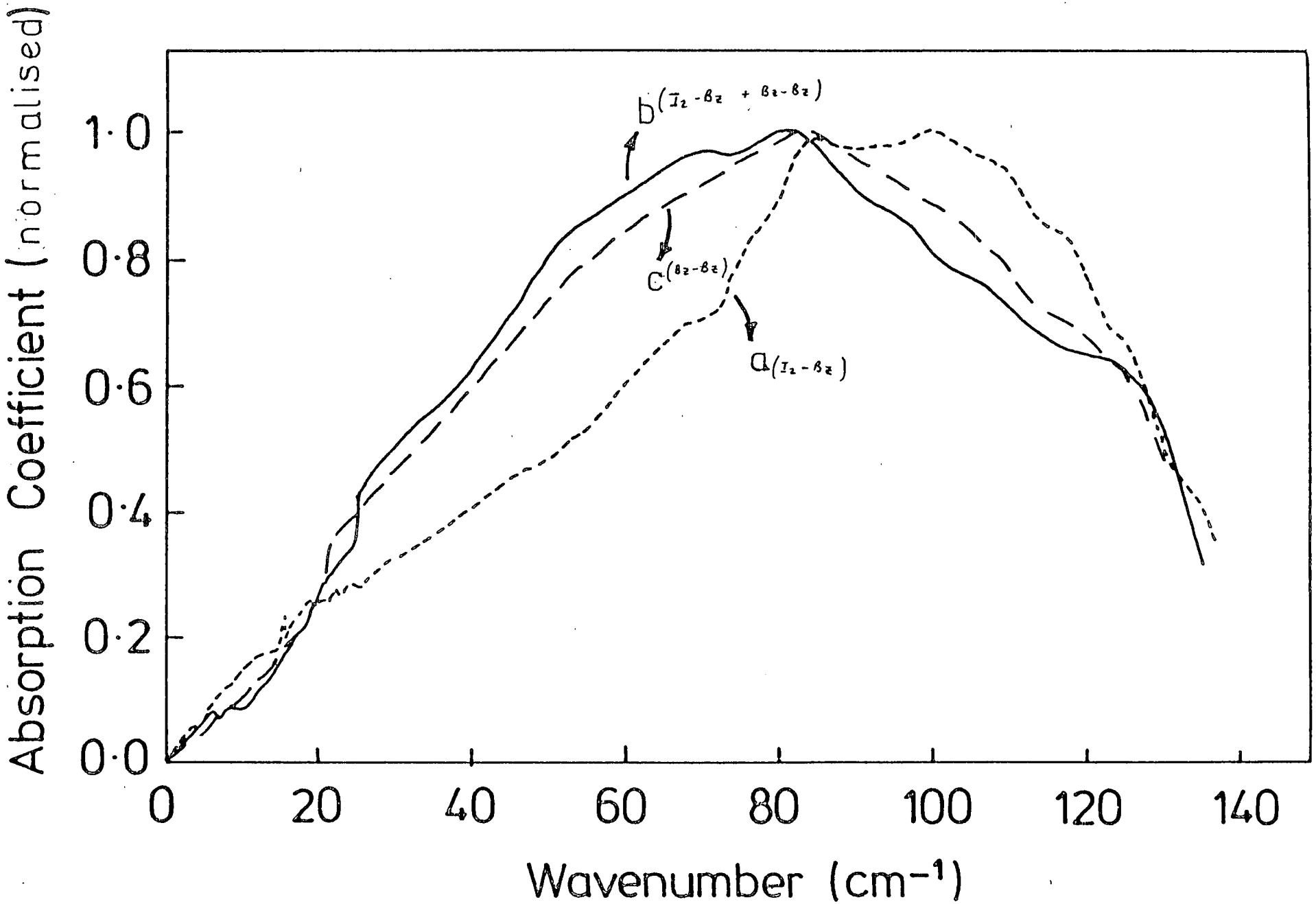
Absorption Coefficient (normalised)
1·0
0·8
0·6
0·4
0·2
0·0
0
20
40
60
80
100
120
140
Wavenumber (cm⁻¹)
b (I₂ - B₂ + B₂ - B₂)
c (B₂ - B₂)
a (I₂ - B₂)

Fig. 6.6

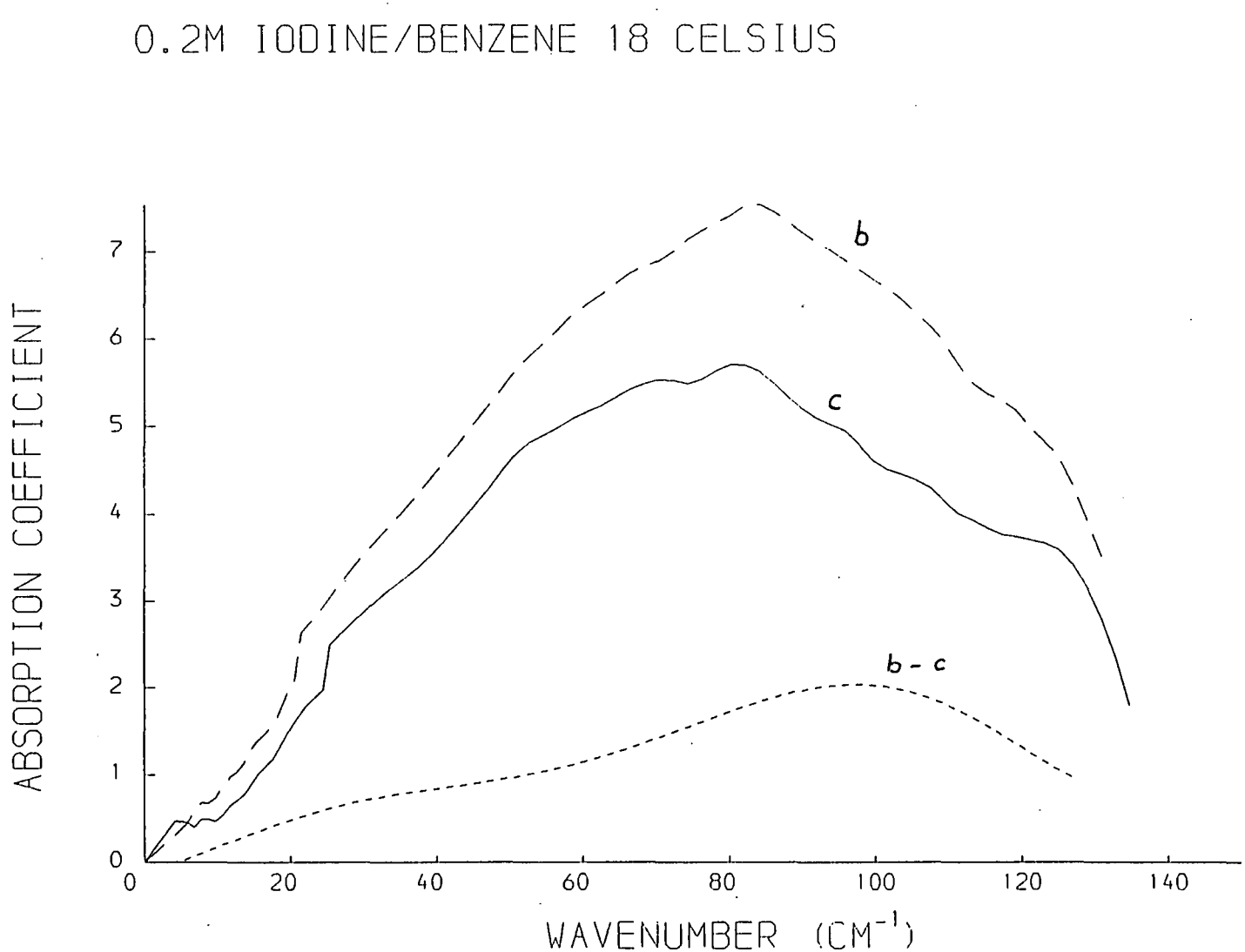
0.2M IODINE/BENZENE 18 CELSIUS
ABSORPTION COEFFICIENT
WAVENUMBER (CM⁻¹)
b
c
b - c
0
1
2
3
4
5
6
7
0
20
40
60
80
100
120
140

Fig. 9.7

0.2M IODINE/BENZENE; 18 CELSIUS.

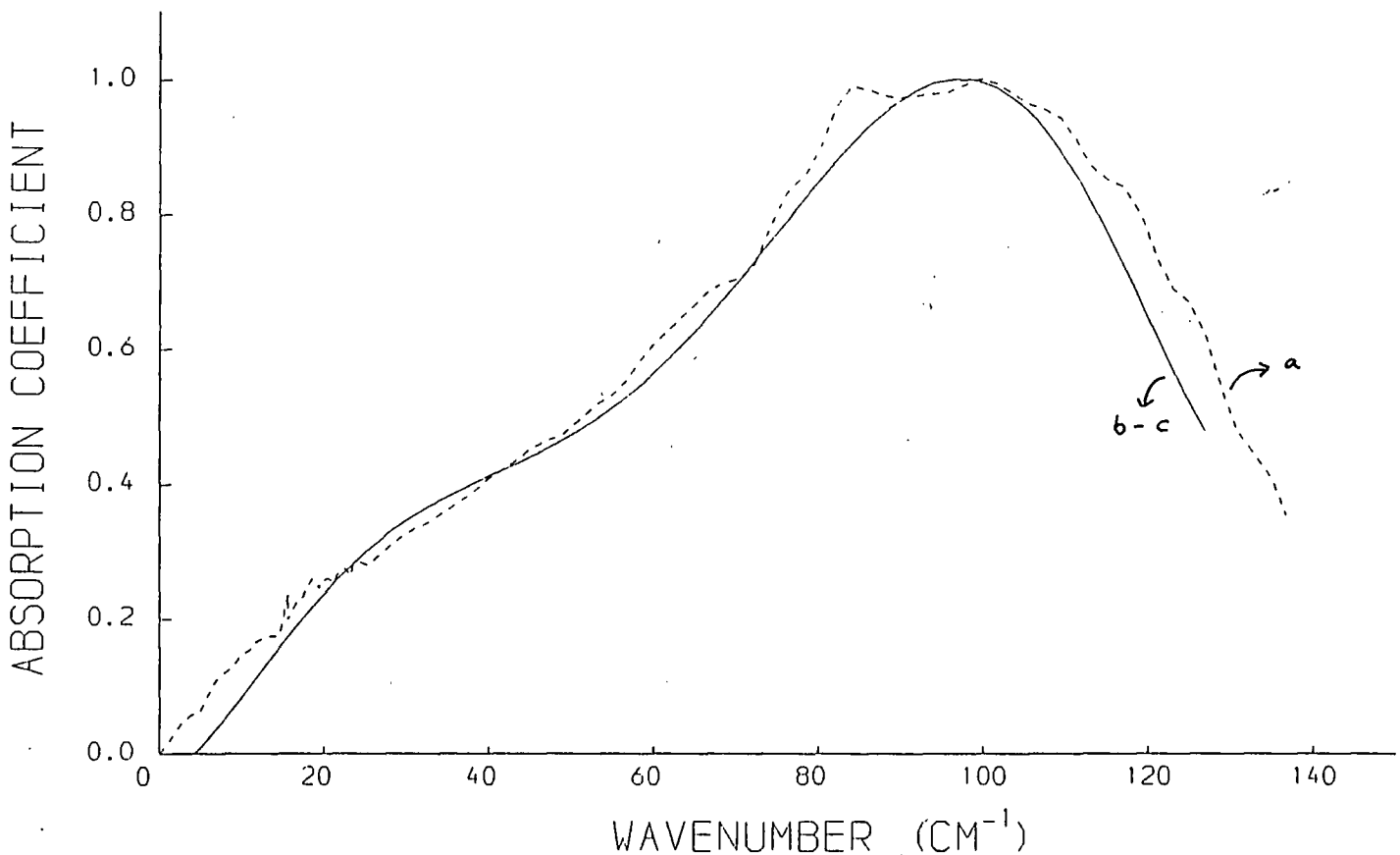

Fig. 6.8

within the experimental error. It is obviously much easier to adopt procedure (a), but this is not possible for dispersive work in our liquid cell, as discussed in the next section. Thus, by a simple subtraction it is possible to compare data recorded by transmission and dispersive experiments.

6.2.2 By dispersive Transmission

Experiments were performed on solutions of iodine in benzene by dispersive transmission in order to obtain the refractive index $n(\bar{\nu})$ which is required through equation 4.1 for most of the band-shape analysis that has been done. Spectra were recorded specifically at low wavenumbers where $n(\bar{\nu})$ is varying significantly.

Optical constants were obtained through recording two different pathlengths of the solution in the liquid cell, equivalent to procedure (b) in the preceeding section. Procedure (a) was not possible since the denominator in equation 2.32 (p.32) would vanish since $d_S - d_B = 0$. Instead, a spectrum of pure benzene was subtracted from the solution spectrum so that the refractive index obtained is due to the same interactions as the absorption coefficient obtained through procedure (a) in section 6.2.1. The subtraction was done using permittivities according to the procedure of O'Neill [32].

$$\varepsilon'_a\ (\bar{\nu}) = 1 + (\varepsilon'_b - 1)\ (\bar{\nu}) - \{\ (\varepsilon'_s - 1)\ C_s\ \}\ (\bar{\nu}) \qquad (6.29)$$

where subscripts a and b refer to the experimental procedure, and s to the pure solvent. C_s is the concentration of solvent.

Where necessary, the refractive index was extended over the whole frequency range of the band by Kramers-Krönig analysis (section 2.2.2b) using the program HTRAN.

All dispersive transmission experiments were performed at 18 $\pm$ 1°C, the temperature being controlled as described in section 5.2.2.

Data obtained by dispersive transmission is much poorer than that obtained by normal transmission at very low wavenumbers (< $10cm^{-1}$) so it was not possible to obtain reliable refractive index data below about $8cm^{-1}$. This is due probably to the fact that the silicon window absorption coefficient rises in this low frequency range where the energy throughput was, in any case, quite low.

6.3 Results

The reproducibility of a 0.2M solution of iodine in benzene is illustrated in figure 6.52.

Figure 6.6 compares the band profiles obtained for iodine in benzene by procedures a and b described in section 6.2.1. Spectrum a is for the iodine-benzene interactions

alone; spectrum b for iodine-benzene plus benzene-benzene interactions; and spectrum c is a spectrum of pure benzene. All spectra are normalised to the same value to facilitate comparison of the shape. Figure 6.7 shows the spectrum obtained by procedure b compared with a spectrum of pure benzene, and the result of subtracting one from another, which is expected to be equivalent to the spectrum obtained through procedure a. These are compared in figure 6.8 after normalisation to the same level to correct for systematic errors, including the fact that the concentration of solvent is different between the solution and the pure benzene. The most important feature to note is that the shape of the two spectra are the same so that we can be confident that they reflect the same induced phenomena. Thus from using two different experimental procedures it can be verified that the low frequency shoulders in the spectral profiles in *e.g.* figure 6.11 are real.

For the case of an 0.2M iodine solution in benzene, our data have been combined with microwave data of Kettle and Price [91] to provide the full absorption band which is necessary to give a true correlation functon [117].

6.3.1 Comparison with Beer's Law

The Beer's law dependence of the iodine concentration was examined using equation 1.22 and the results for benzene as solvent is shown in figure 6.9 for spectra as a function

of concentration and figure 6.10 for spectra corrected for concentration. Spectrum A is 0.2M; B 0.16M; C 0.13M and D 0.06M. Figures 6.11 and 6.12 show the same results for the full band. Spectrum A is 0.2M; B 0.16M and C 0.06M. Beer's law is clearly obeyed and this is expected if the induced spectra arise from benzene-iodine interactions since the benzene concentration is, in effect, constant at these low iodine concentrations..

The Beer's law dependence of iodine in a 0.5 mole fraction of benzene in hexane is illustrated in figures 6.13 and 6.14. The inaccuracies in the measurements are lower than for the iodine in benzene case, since the iodine concentration is necessarily lower, but Beer's law still seems to be obeyed. The corresponding full bands are shown in figures 6.13a and 6.14a.

6.3.2 Temperature Dependence

The low frequency wing of the I_2 in benzene band was examined as a function of temperature between 7° and 60° celsius, but no changes in the shape or intensity were observable, as shown in figure 6.15.

6.3.3 Kramers-Krönig Analysis

The effectiveness of the Kramers-Krönig procedure is illustrated in figure 6.16 for a 0.2M iodine solution in

benzene at 291K. The solid line is the Hilbert transform of the measured absorption index and the crosses are experimental refractive index data obtained through dispersive transmission. Figures 6.17 to 6.22 show the experimental absorption coefficient and the dielectric loss, permittivity and refractive indeces calculated through a Kramers-Krönig analysis of data obtained for iodine in benzene and benzene/hexane.

The level of the refractive index curve calculated from Hilbert transformation of the absorption index was set by determining experimentally the refractive index at a frequency of about $100cm^{-1}$. The value of this calculated refractive index at zero frequency was then used to determine an ε_o value for the sample through equation 2.3. Similarly a value for ε_∞ was arrived at for high frequencies. These values are presented in table 6.2.

6.3.4 Correlation functions

Correlation functions were calculated by Fourier transforming the experimental spectral density, $I(\bar{\nu})$, according to equation 4.2 , using the program FIRFT3. They are presented in figures 6.23 to 6.37.

6.3.5 Oxtoby Fits

Fitting to the Oxtoby model was done using the program

OXTOBYFIT, incorporating a NAG routine called E04FDF, to find the least squares fit using the parameters ω_o, ω_1 and γ described in section 4.2.5. The fits are presented alongside the experimental data in figures 6.38 to 6.44, and the parameters are listed in table 6.3. All the parameters are weighted by I/2kT to render them dimensionless.

6.3.6 Mori Fits

Fitting to the Mori model was performed using the program NEWFITF3 with a least squares NAG routine, E04FDF. The fits and the experimental data are presented in figures 6.45 to 6.50, and the parameters are listed, together with the Oxtoby model parameters, in table 6.3.

6.4 Discussion

6.4.1 General Shape of the Bands

Figure 6.6 compares the shapes of the three bands of interest for the iodine-benzene system, all normalised to the same intensity for purposes of comparison. Spectrum c is for pure benzene, spectrum b is that for iodine-benzene plus benzene-benzene interactions, and spectrum c is that for iodine-benzene interactions alone. It is clear from this comparison that the spectrum due to benzene-benzene interactions is centred around a lower frequency than is the

Table 6.2

SPECTRAL MOMENTS

	ε_0	ε_∞	$\frac{M_2}{M_0}$	M_0 ($cm^2 l\ mol^{-1}$)	M_2	$\frac{M_4}{M_0} \times 10^5$
Pure Benzene			3.6	69	248	0.26
0.2M Iodine/benzene (vs. Iodine/benzene)	2.3177	2.6739	3.8	424	1624	0.27
0.2M Iodine/benzene (vs. benzene)	1.0131	1.0048	3.2	103	327	0.25
0.16M Iodine/benzene (vs. benzene)	1.0069	1.0010	4.0	85	342	0.33
0.06M Iodine/benzene (vs. benzene)	1.0009	1.0004	10.6	27	286	0.99
0.12M Iodine in benzene/hexane	1.0043	1.0009	2.5	8	20	0.15
0.10M Iodine in benzene/hexane	1.0059	1.0006	1.2	13	16	0.08

Table 6.3

MODEL FITTING PARAMETERS

	MORI APPROACH			OXTOBY APPROACH				
	γ	$K_0(0)$	$K_1(0)$	γ	ω_0	ω_1	ω_1/ω_0	γ/ω_0
Pure Benzene	13.9	20.6	114.9	174.5	52.8	80.3	1.53	3.28
0.2M Iodine/benzene (vs. Iodine/benzene)	12.1	20.7	105.2	141.9	51.8	77.2	1.49	2.73
0.2M Iodine/benzene (vs. benzene)	10.4	19.0	121.2	97.9	54.0	75.3	1.39	1.81
0.16M Iodine/benzene (vs. benzene)	9.3	22.0	107.1	92.0	46.6	72.0	1.55	1.97
0.06M Iodine/benzene (vs. benzene)	8.9	37.5	95.7	89.5	47.3	73.5	1.55	1.89
0.12M Iodine in benzene/hexane	6.7	12.1	75.2	93.6	49.2	68.2	1.39	1.90
0.10M Iodine in benzene/hexane	8.0	7.3	99.3	100.5	53.3	72.5	1.36	1.89

TABLE 6.4

RELAXATION TIMES

	Short time (psec)	Long time (psec)
pure benzene	0.5	
0.2M I_2/benz (vs. I_2/benz)	0.4	6
0.2M I_2/benz	0.7	6 ?
0.16M I_2/benz	0.4	
0.06M I_2/benz	0.1	
0.12M I_2/benz/hex	0.6	
0.10M I_2/benz/hex	4	
0.07M I_2/benz/hex	-	

Fig. 6.9

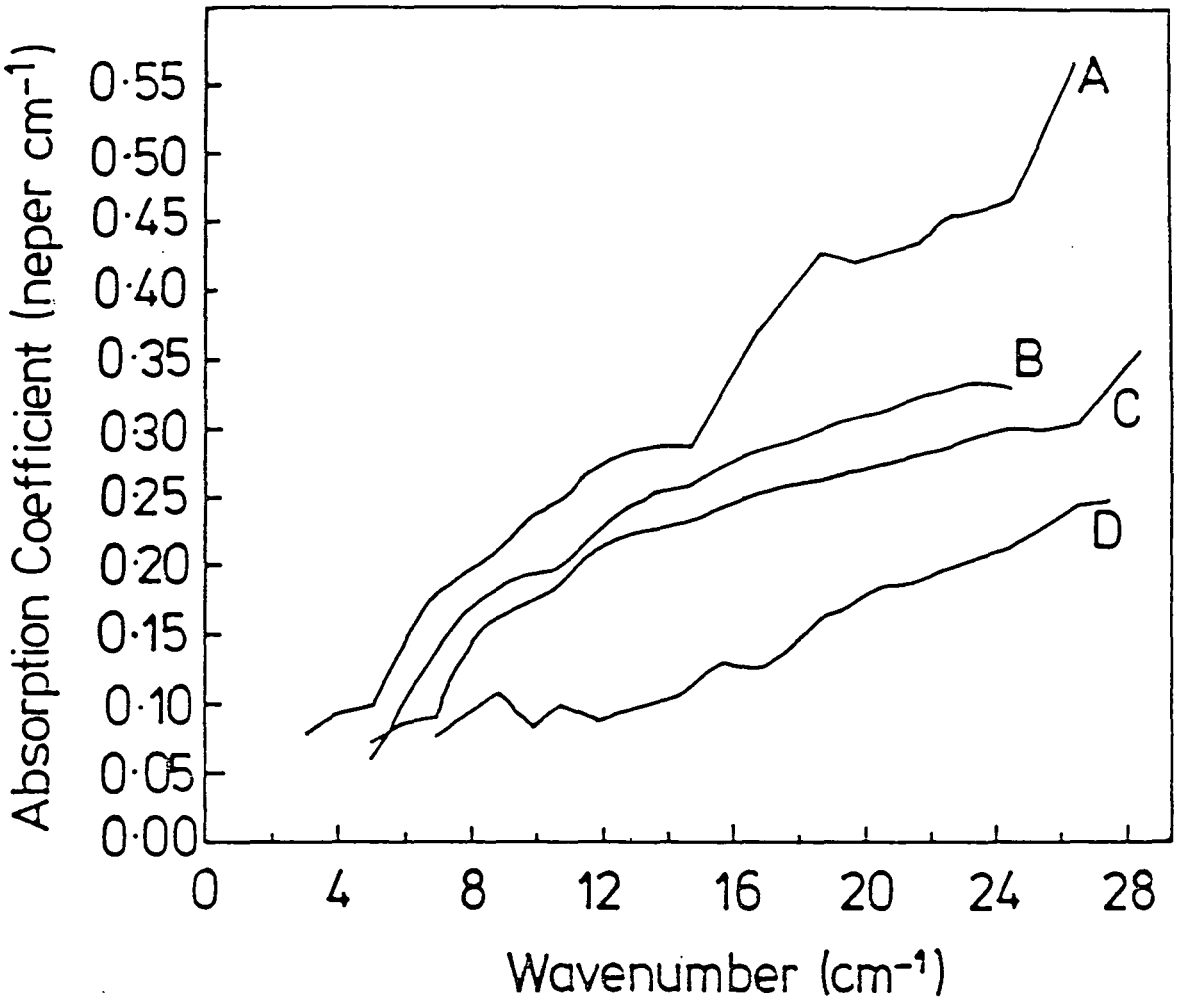

Fig. 6.10

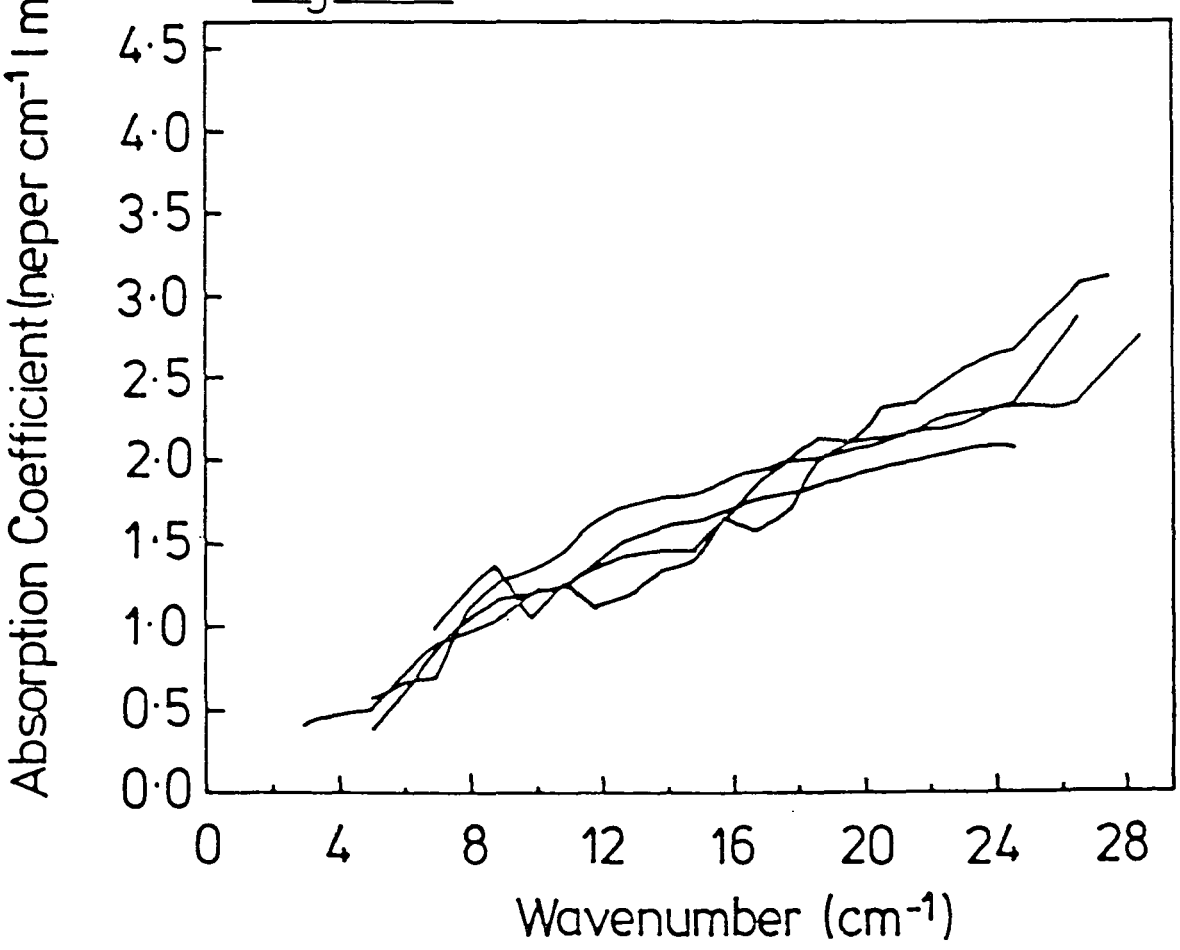

Fig. 6.11

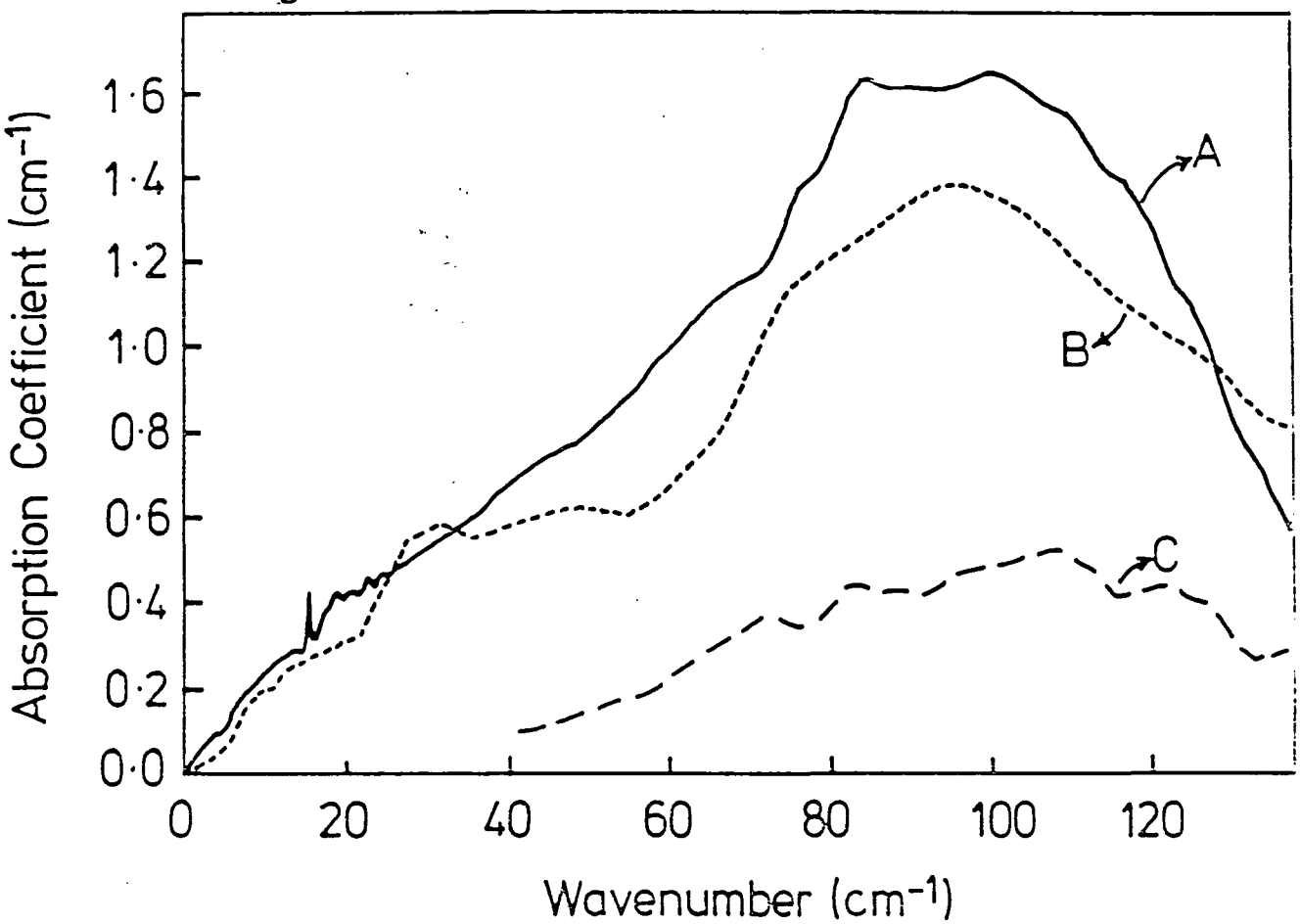

Fig. 6.12

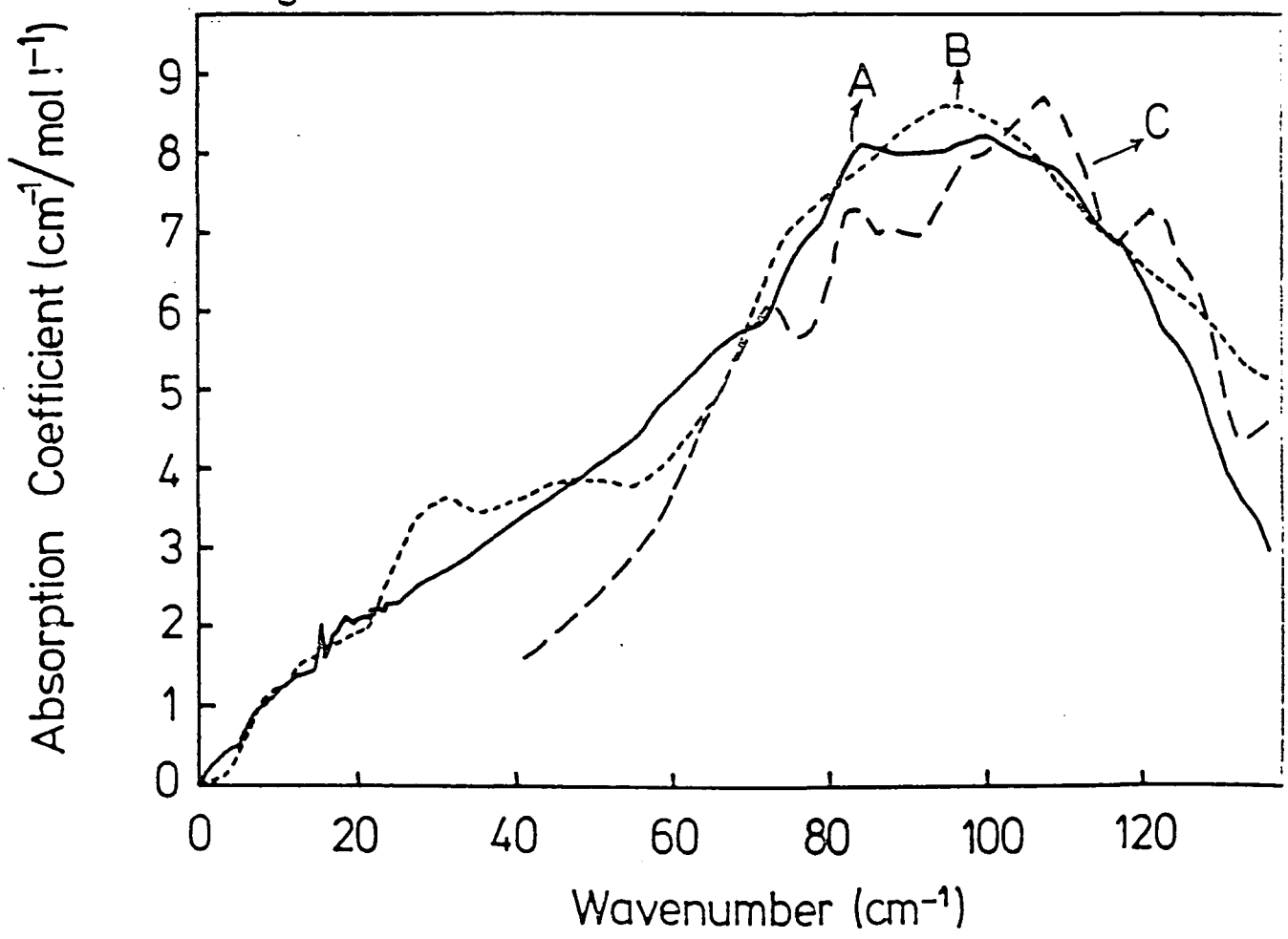

Fig. 6.13

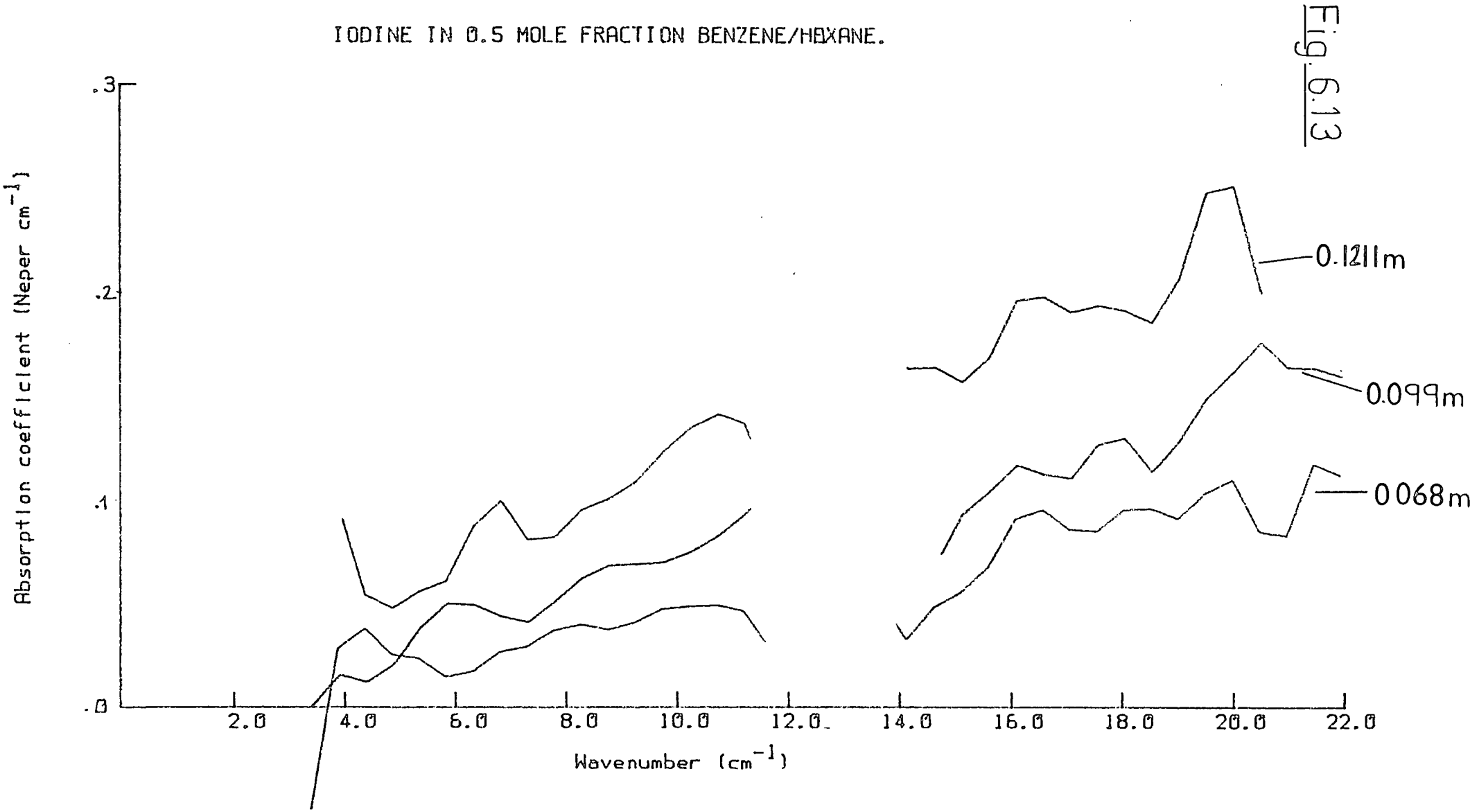
IODINE IN 0.5 MOLE FRACTION BENZENE/HEXANE.
Absorption coefficient (Neper cm^{-1})
.3
.2
.1
.0
2.0
4.0
6.0
8.0
10.0
12.0
14.0
16.0
18.0
20.0
22.0
Wavenumber (cm^{-1})
0.1211m
0.099m
0.068m

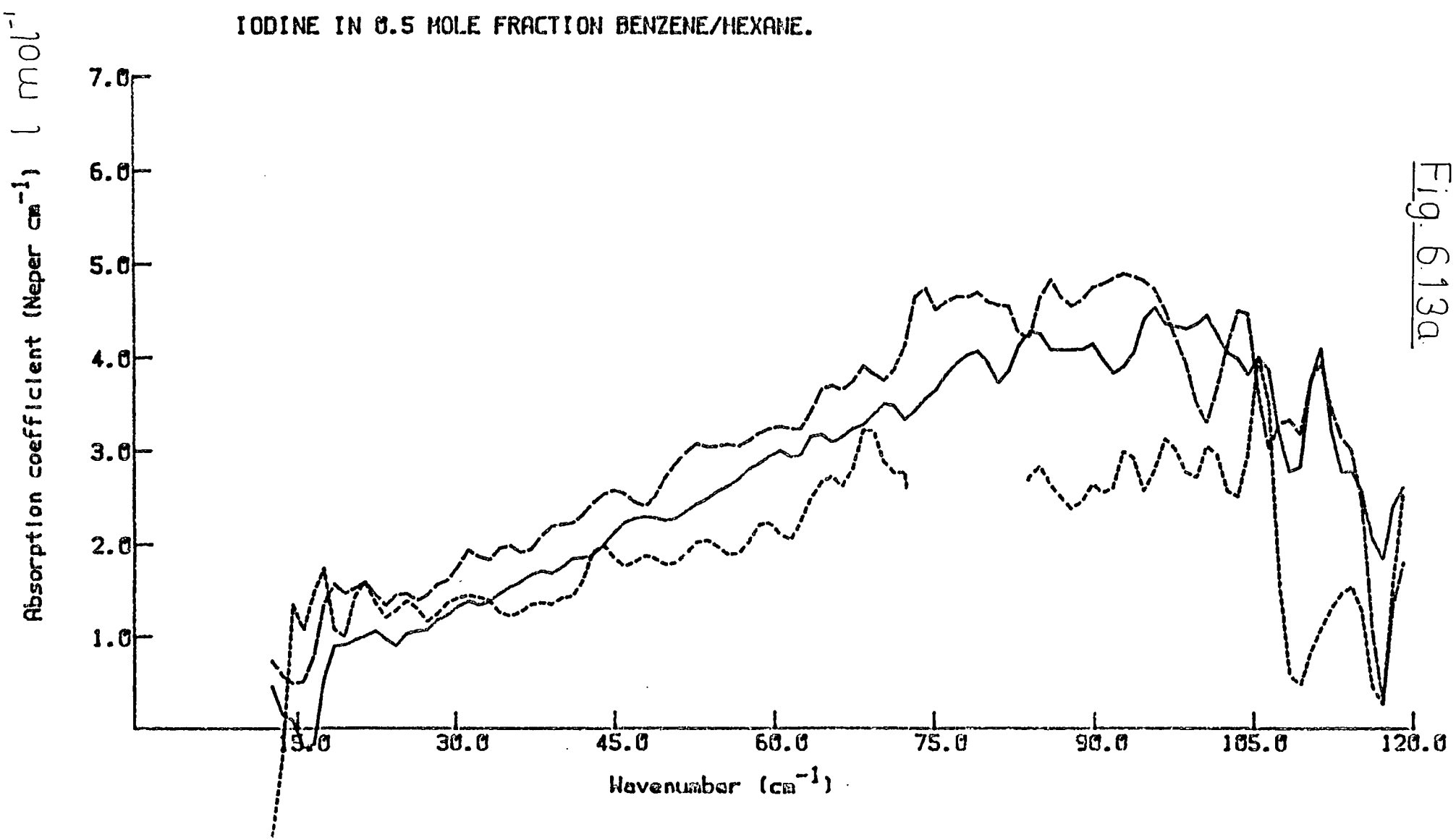
IODINE IN 0.5 MOLE FRACTION BENZENE/HEXANE.
Absorption coefficient (Neper cm^{-1}) (mol^{-1}
7.0
6.0
5.0
4.0
3.0
2.0
1.0
15.0
30.0
45.0
60.0
75.0
90.0
105.0
120.0
Wavenumber (cm^{-1})

Fig. 6.13a

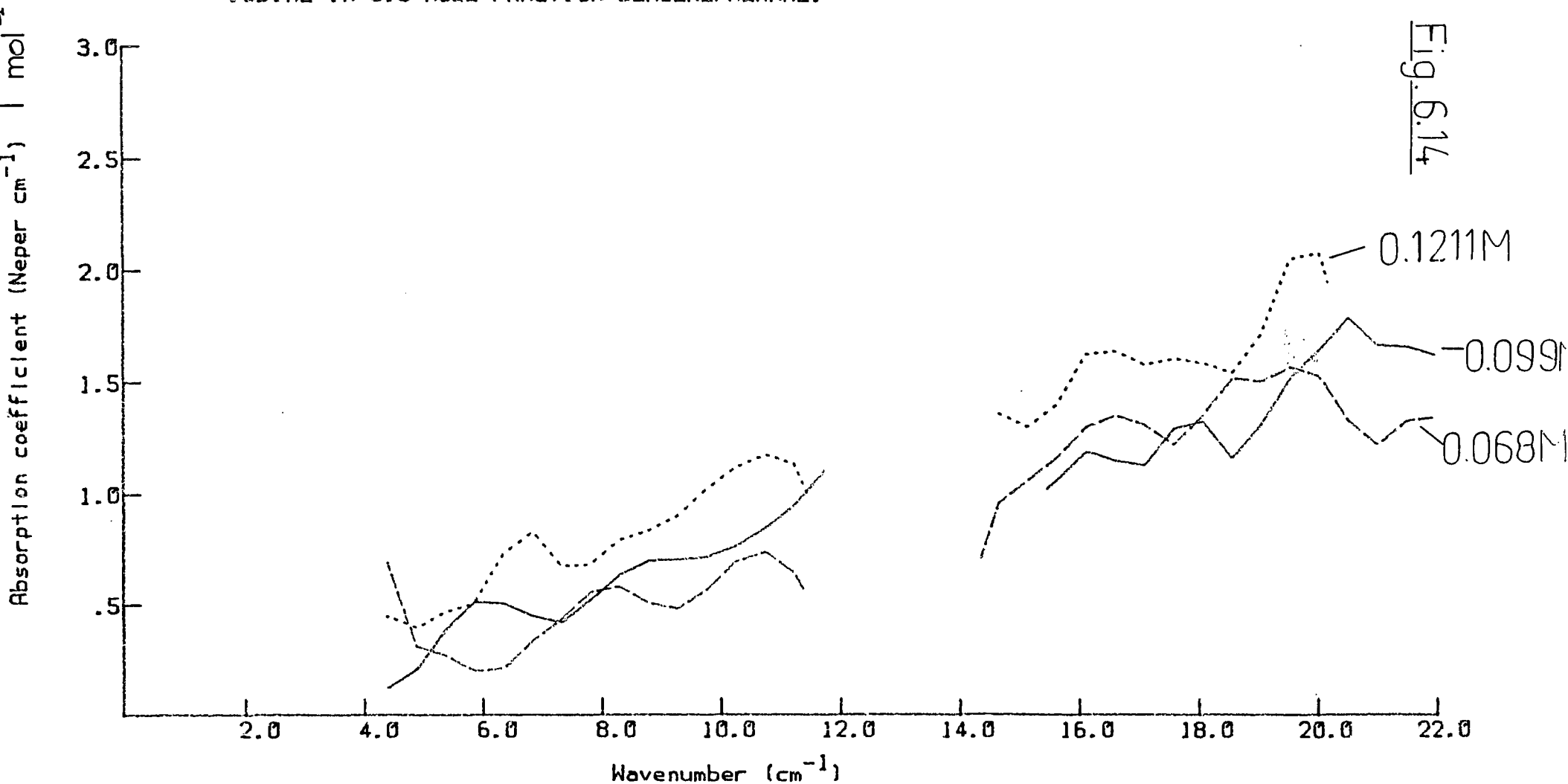
IODINE IN 0.5 MOLE FRACTION BENZENE/HEXANE.
Absorption coefficient (Neper cm^{-1}) | mol^{-1}
3.0
2.5
2.0
1.5
1.0
.5
2.0
4.0
6.0
8.0
10.0
12.0
14.0
16.0
18.0
20.0
22.0
Wavenumber (cm^{-1})
0.1211M
0.099
0.068M

Fig. 6.14

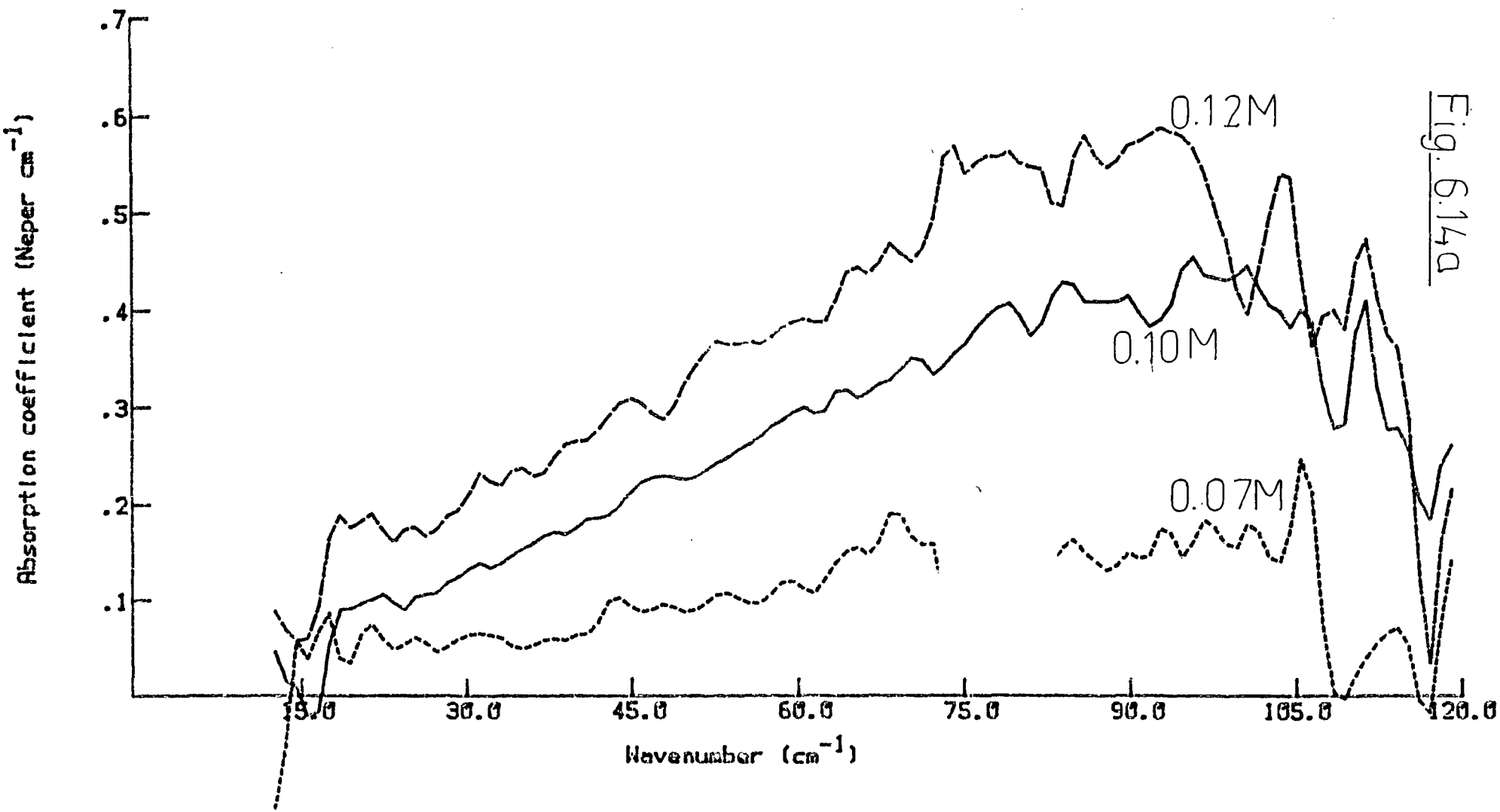
IODINE IN 0.5 MOLE FRACTION BENZENE/HEXANE.
Absorption coefficient (Neper cm^{-1})
.7
.6
.5
.4
.3
.2
.1
0.12M
0.10M
0.07M
15.0
30.0
45.0
60.0
75.0
90.0
105.0
120.0
Wavenumber (cm^{-1})

Fig. 6.14a

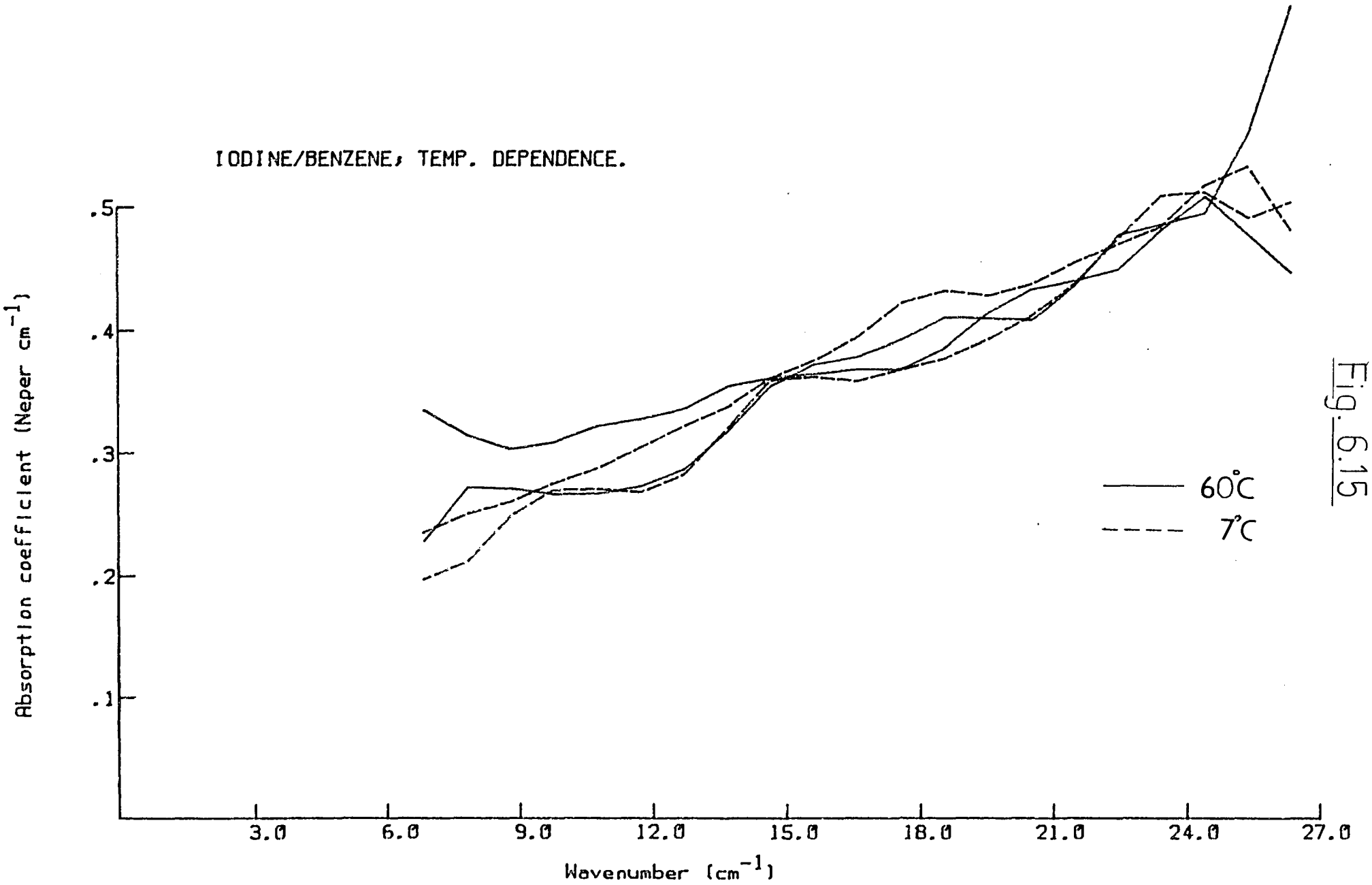
IODINE/BENZENE; TEMP. DEPENDENCE.
Absorption coefficient (Neper cm^{-1})
.5
.4
.3
.2
.1
3.0
6.0
9.0
12.0
15.0
18.0
21.0
24.0
27.0
Wavenumber (cm^{-1})
60°C
7°C

Fig. 6.15

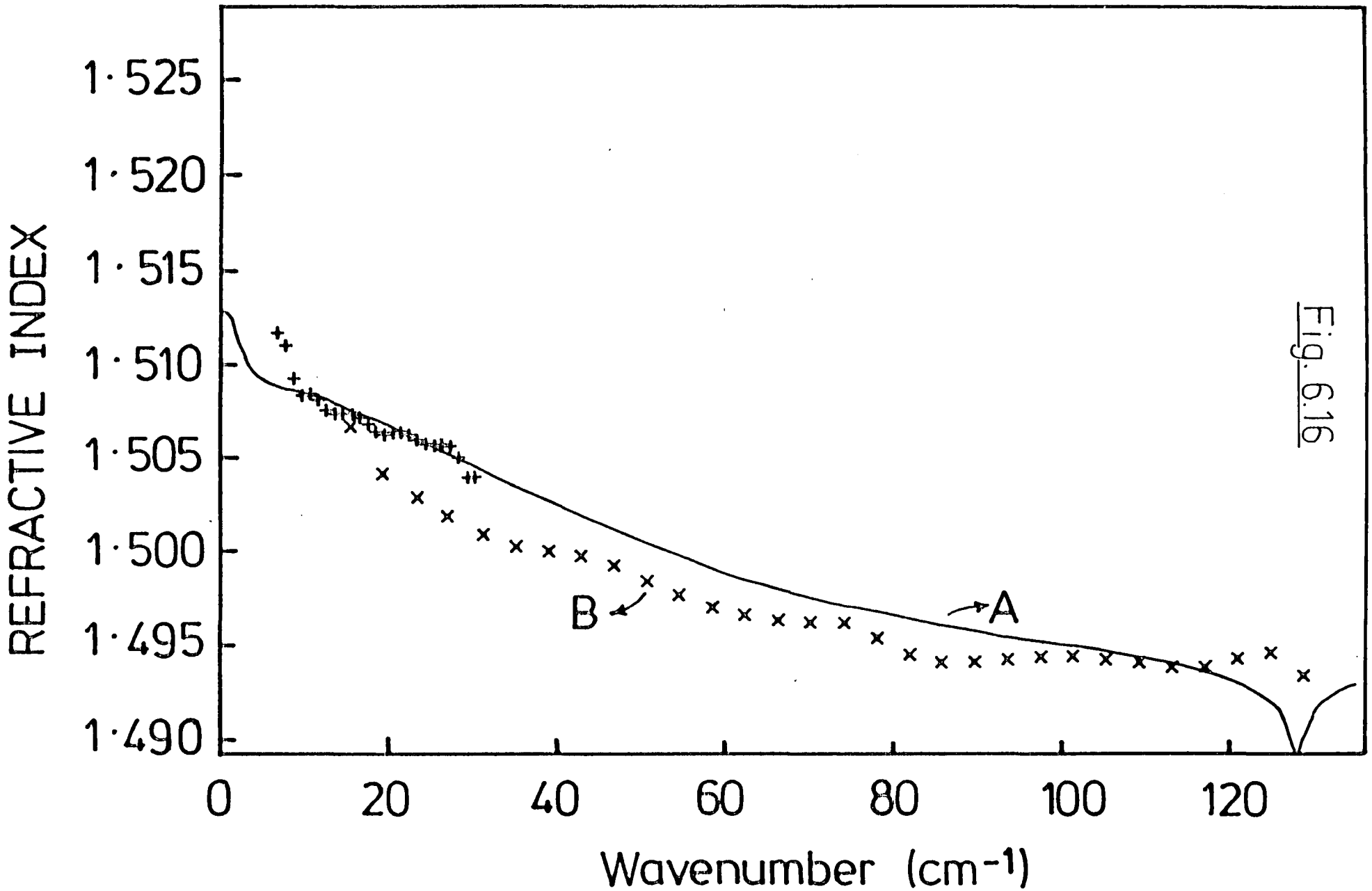
REFRACTIVE INDEX
1·525
1·520
1·515
1·510
1·505
1·500
1·495
1·490
0
20
40
60
80
100
120
Wavenumber (cm⁻¹)
A
B

Fig. 6.16

0·2M Iodine / benzene

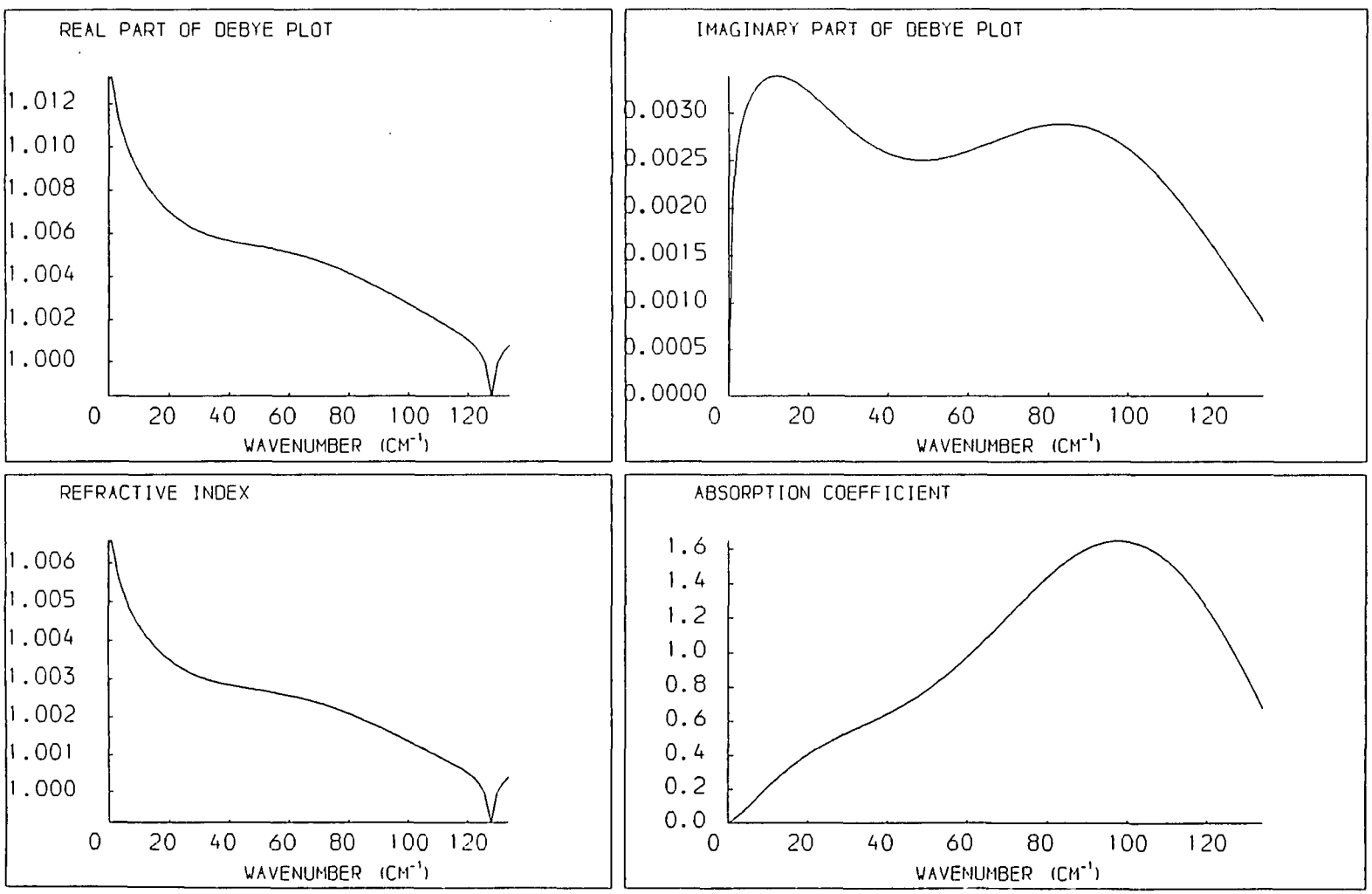

Fig. 9.17

0·16M Iodine / benzene

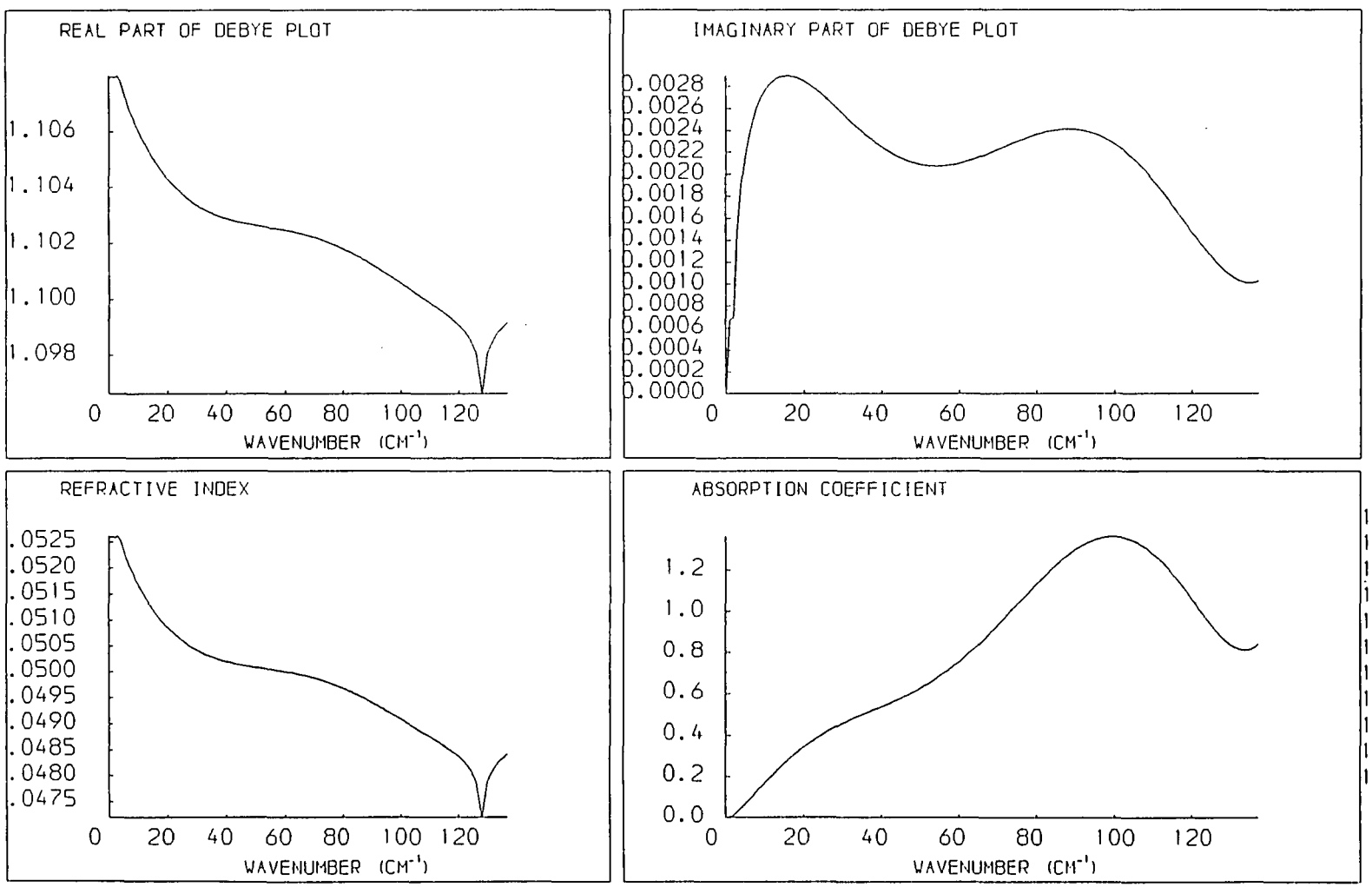

Fig. 6.18

0.06M Iodine / benzene

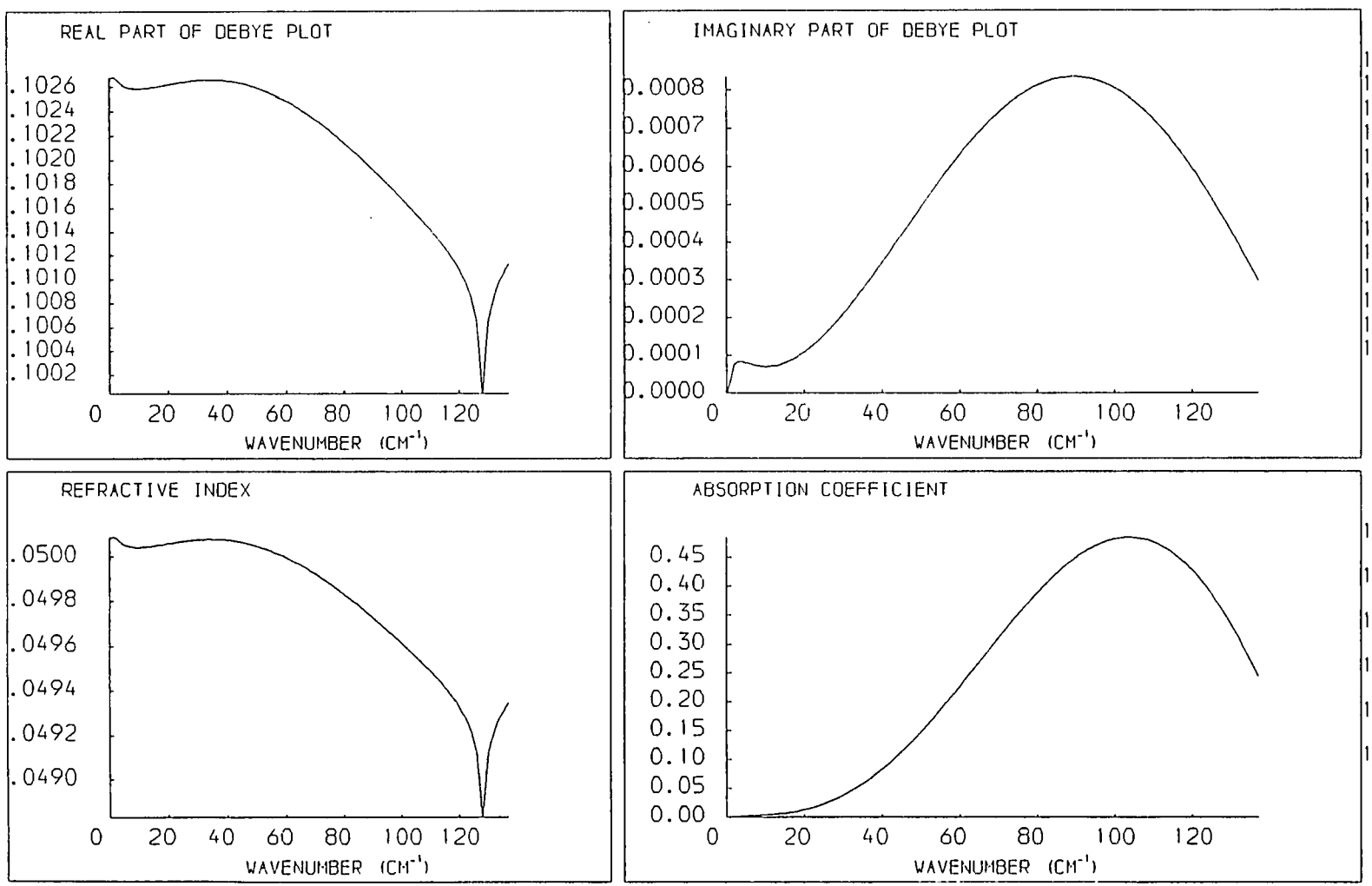

Fig. 6.19

0.12M Iodine/benzene/hexane.

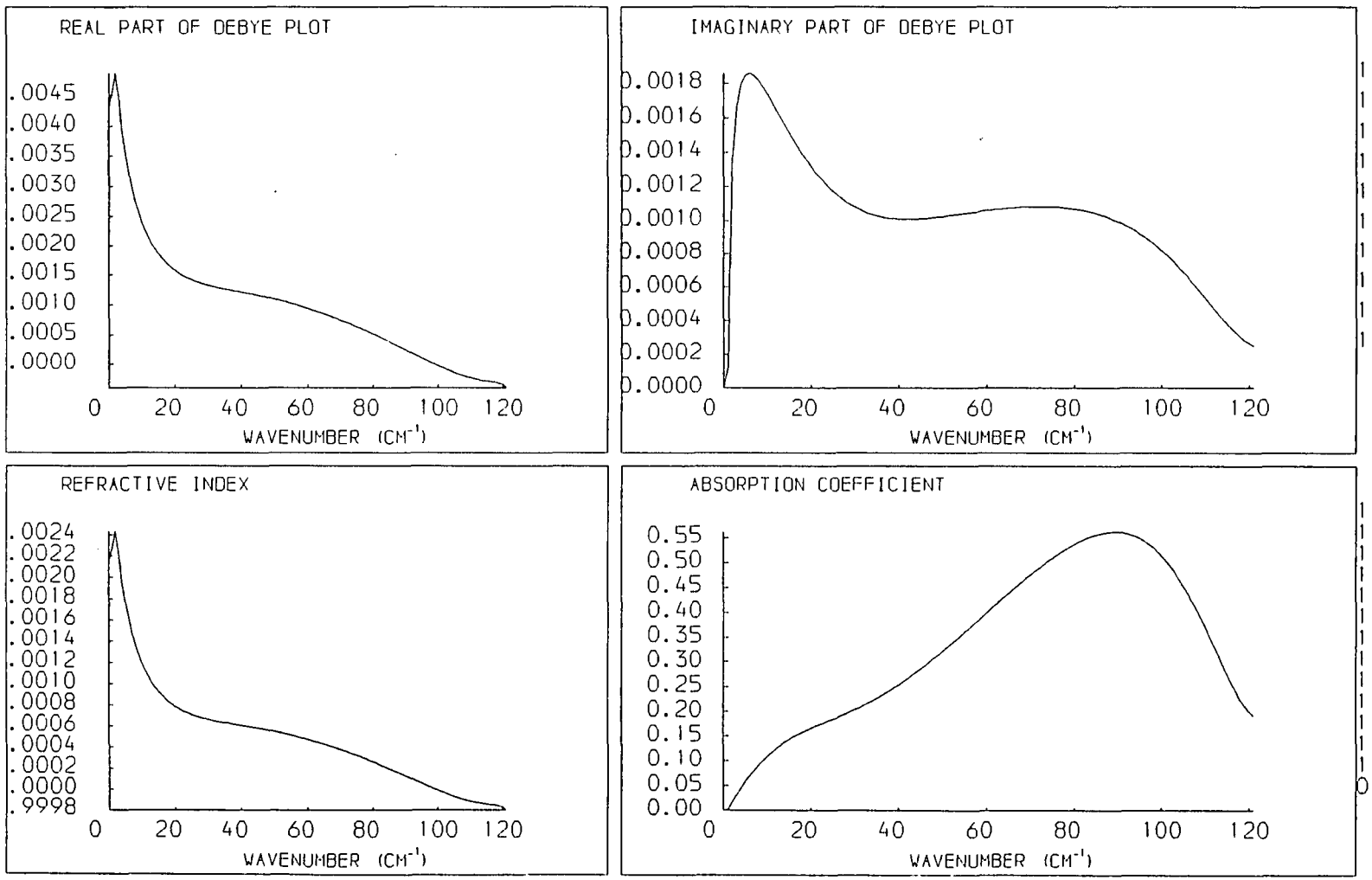

Fig. 6.20

0.10M Iodine/benzene/hexane

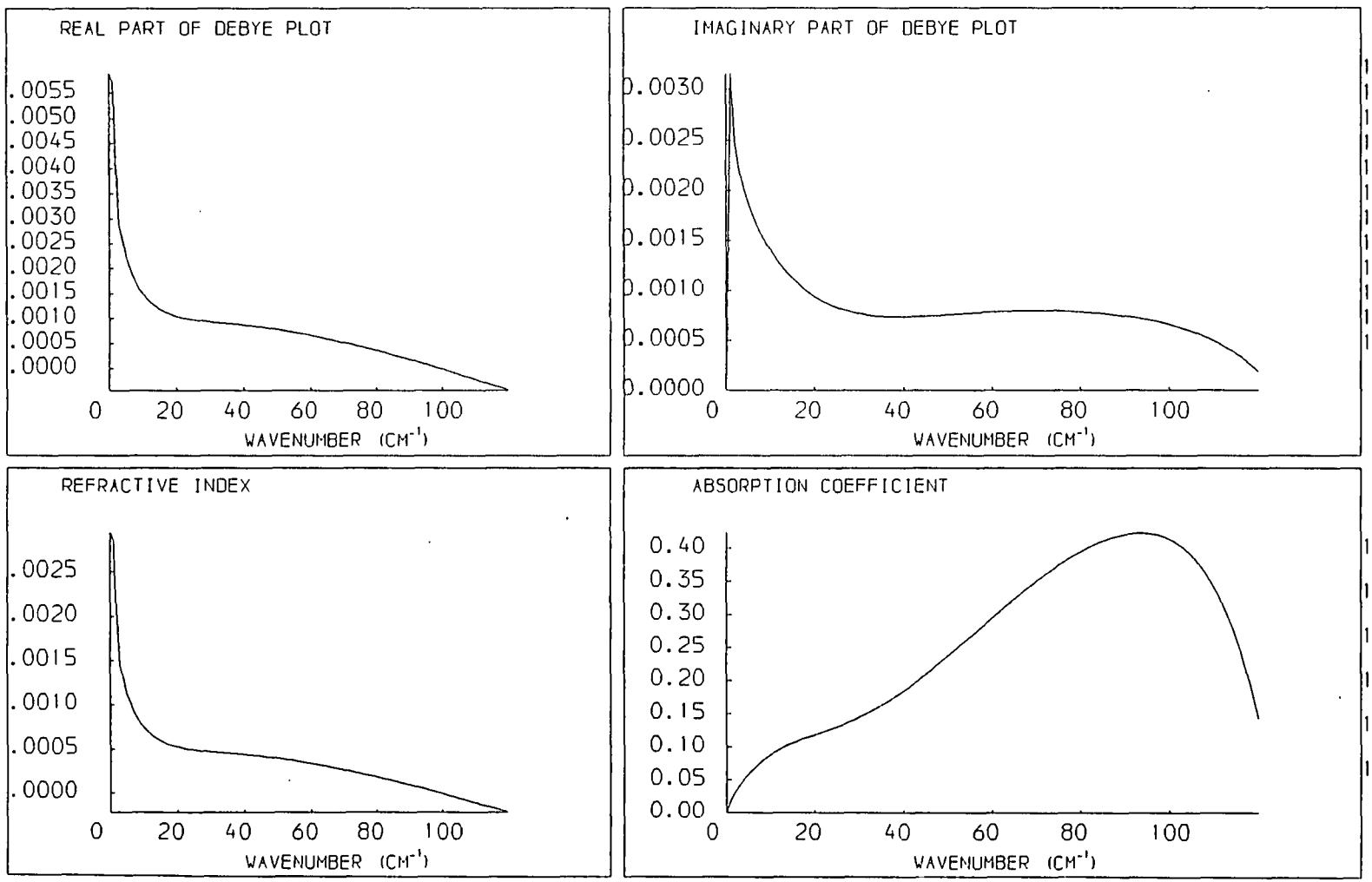

Fig. 6.21

0.07M Iodine/ benzene/ hexane

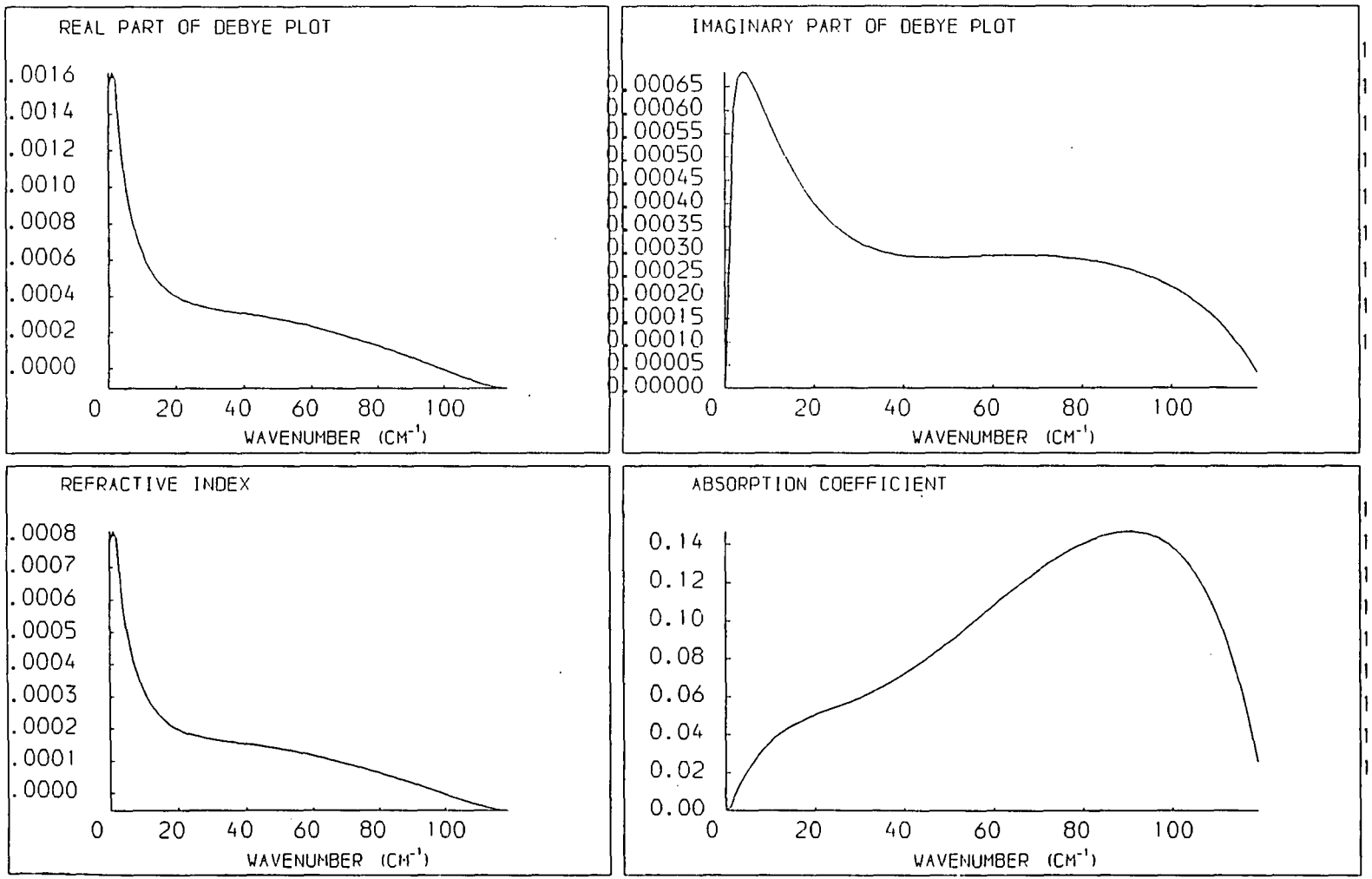

Fig. 6.22

Fig. 6.23

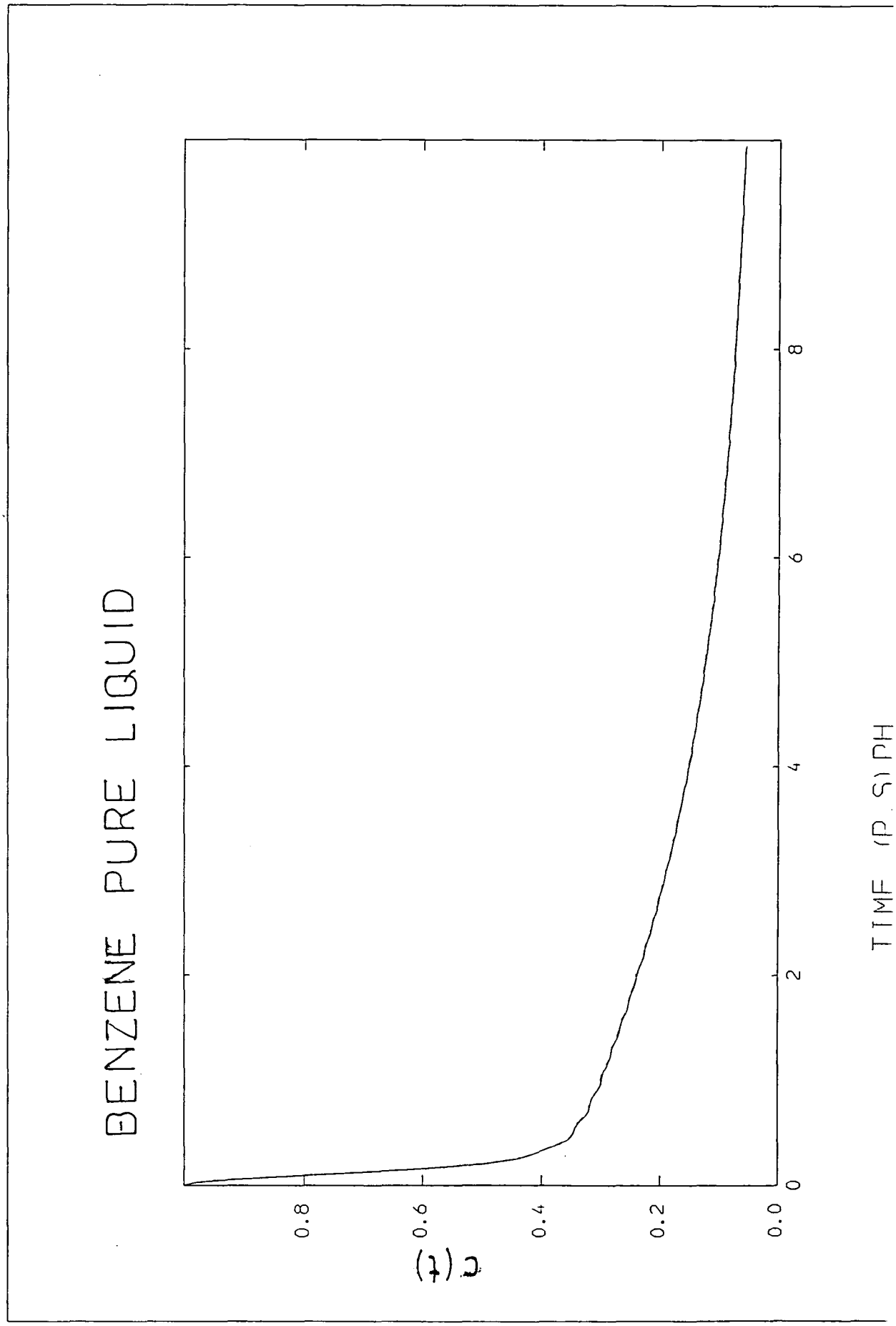

Fig. 6.24

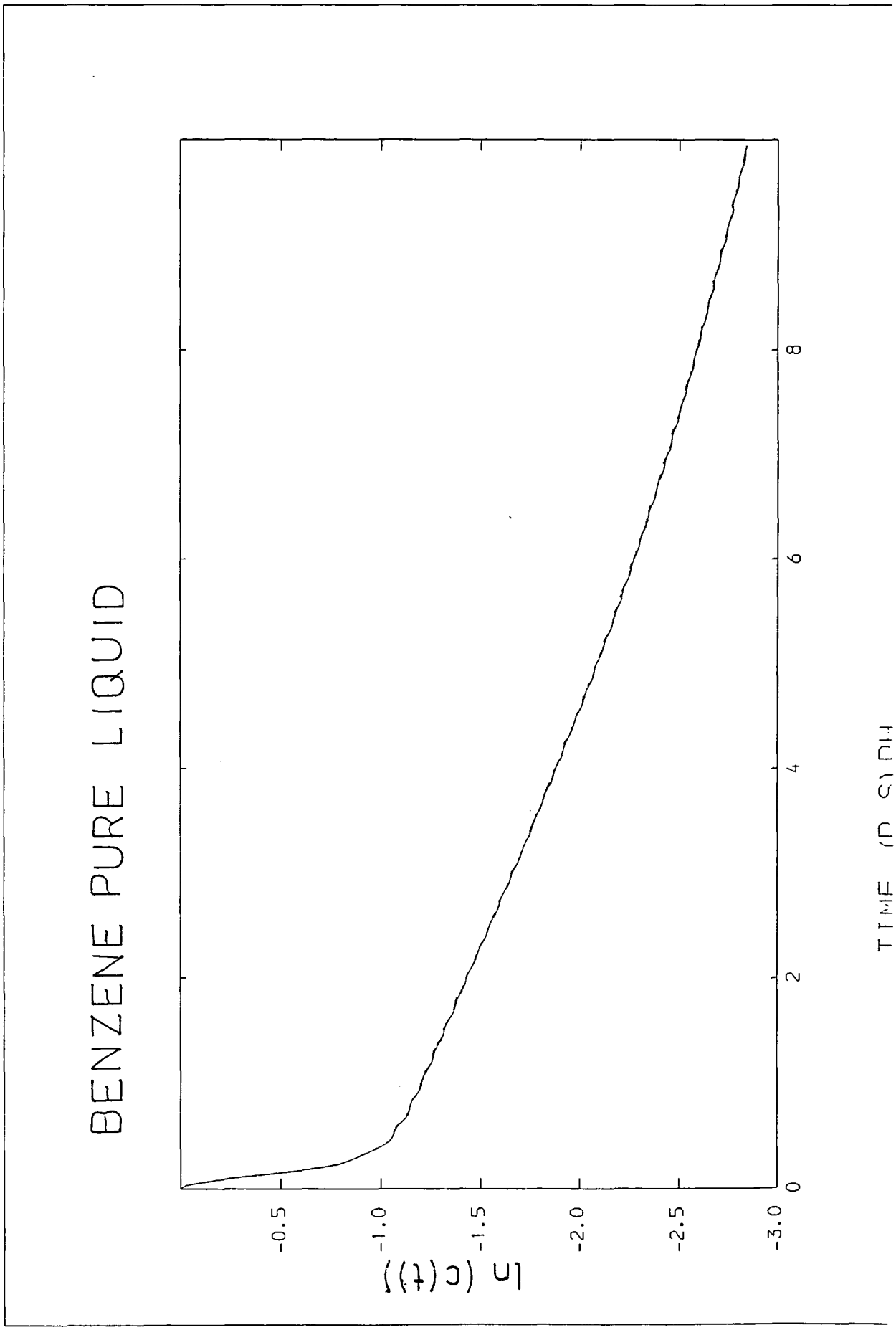

Fig. 6.25

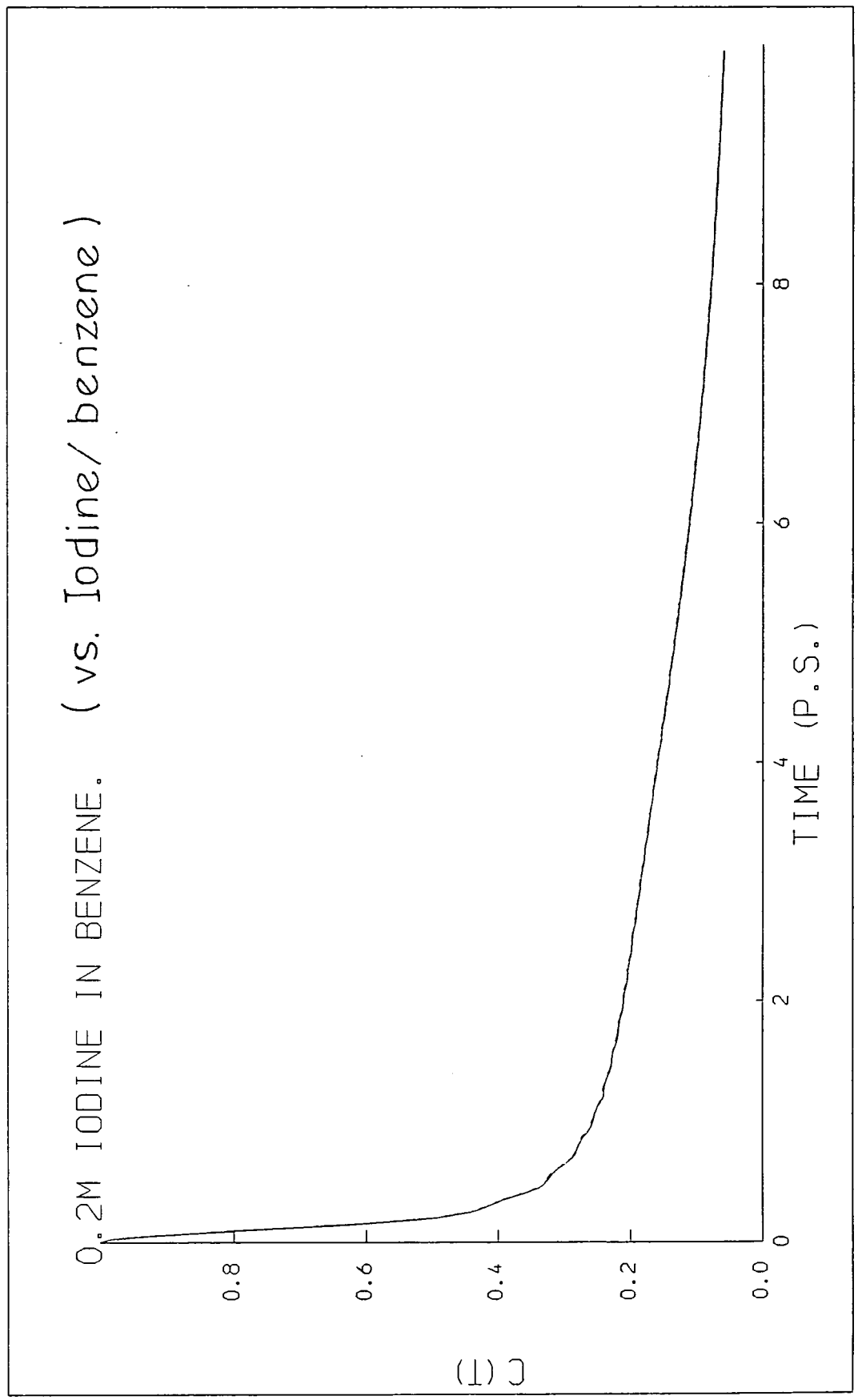
0.2M IODINE IN BENZENE. (vs. Iodine/ benzene)
C (T)
0.0
0.2
0.4
0.6
0.8
0
2
4
6
8
TIME (P.S.)

Fig. 6.26

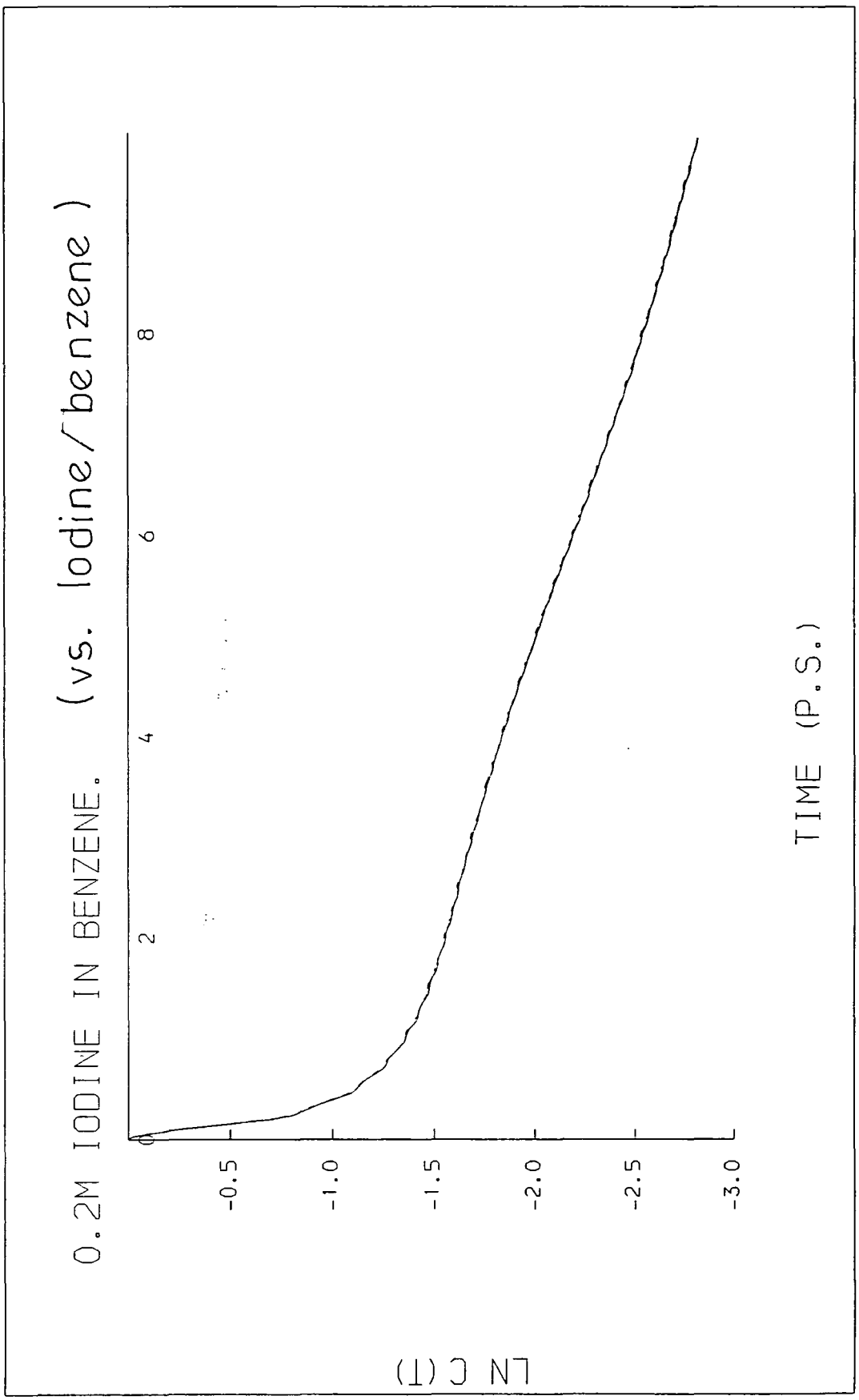
0.2M IODINE IN BENZENE. (vs. Iodine/benzene)
LN C (T)
TIME (P.S.)
0
2
4
6
8
-0.5
-1.0
-1.5
-2.0
-2.5
-3.0

Fig. 6.27

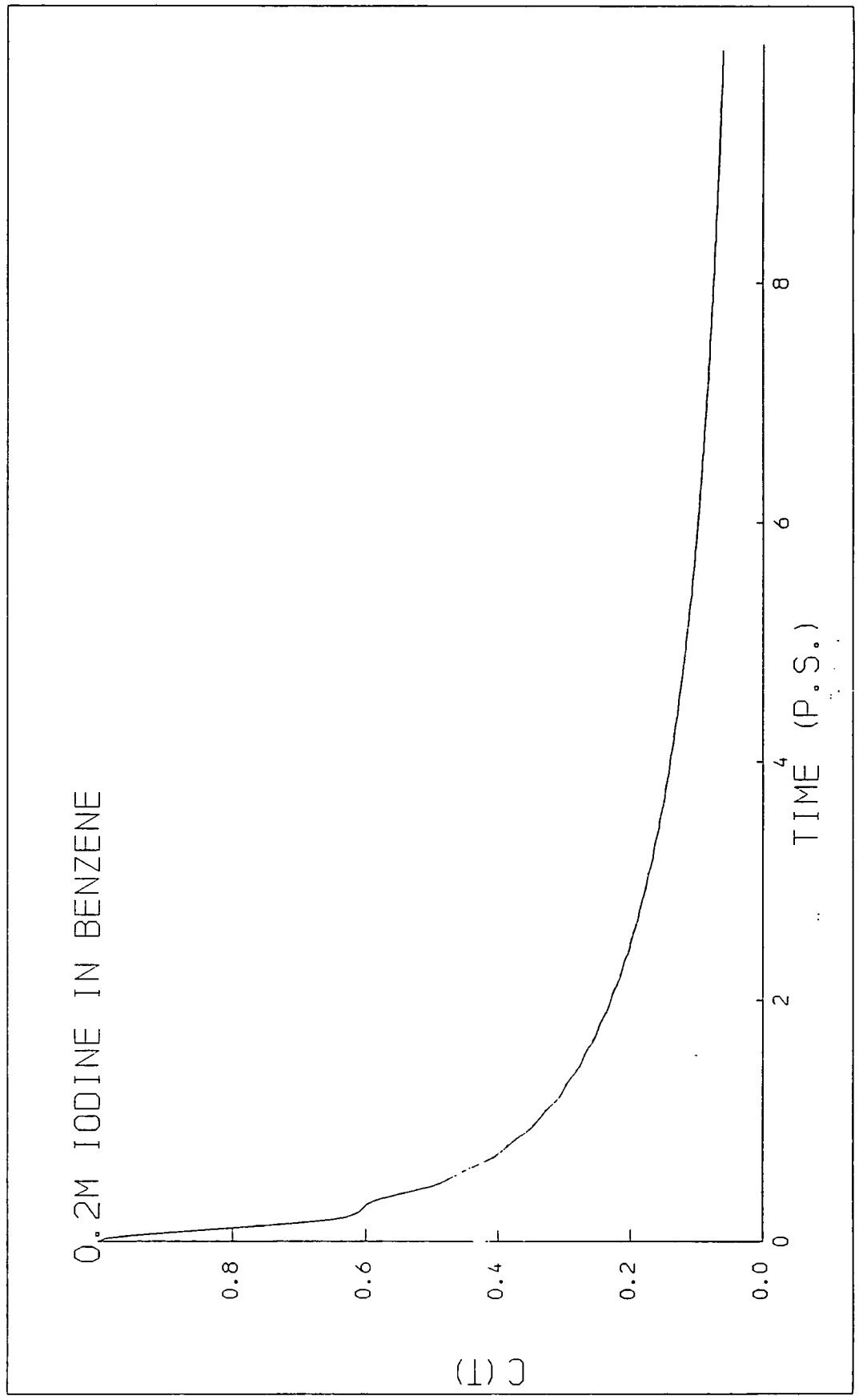

Fig. 6.28

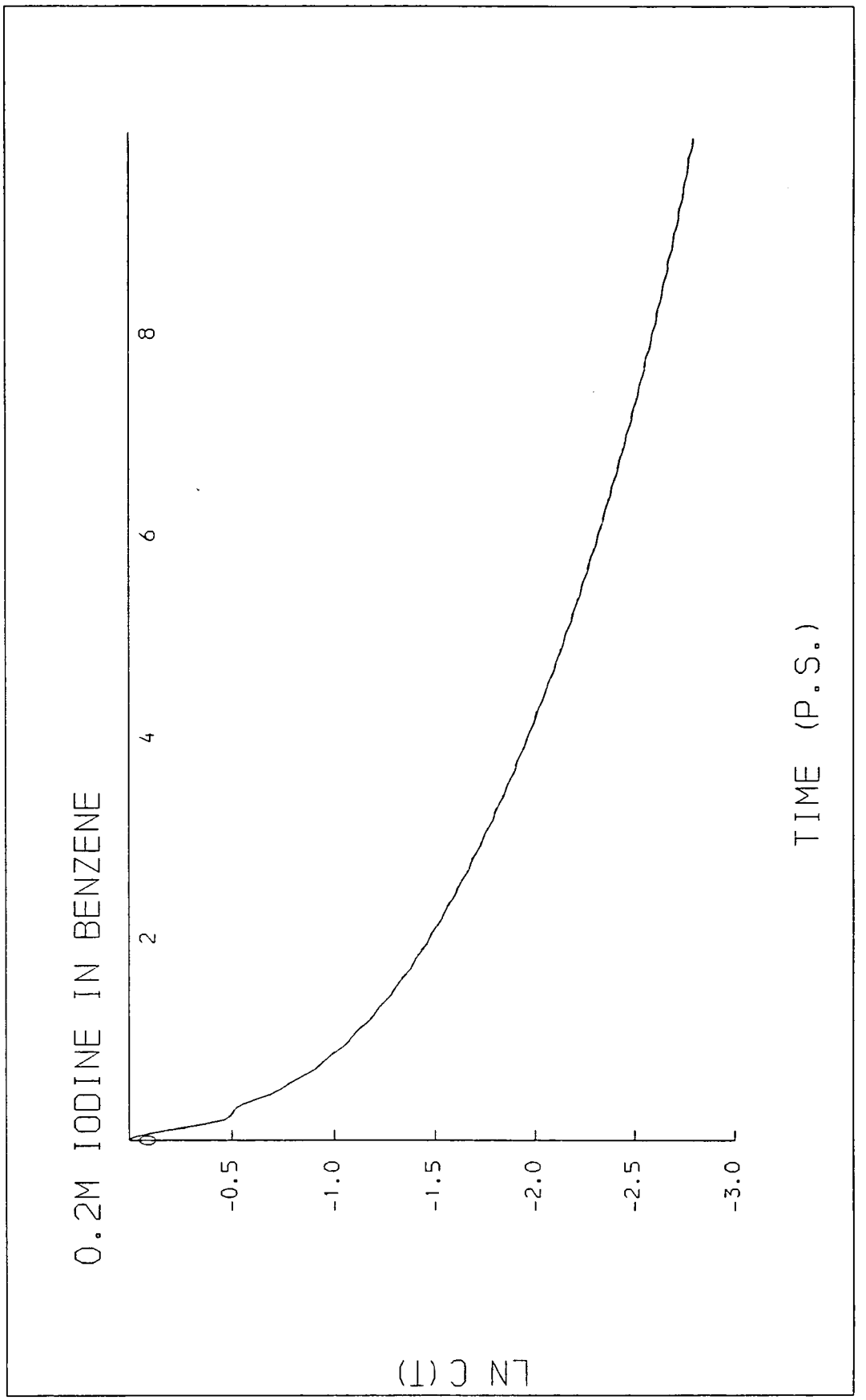

Fig. 6.29

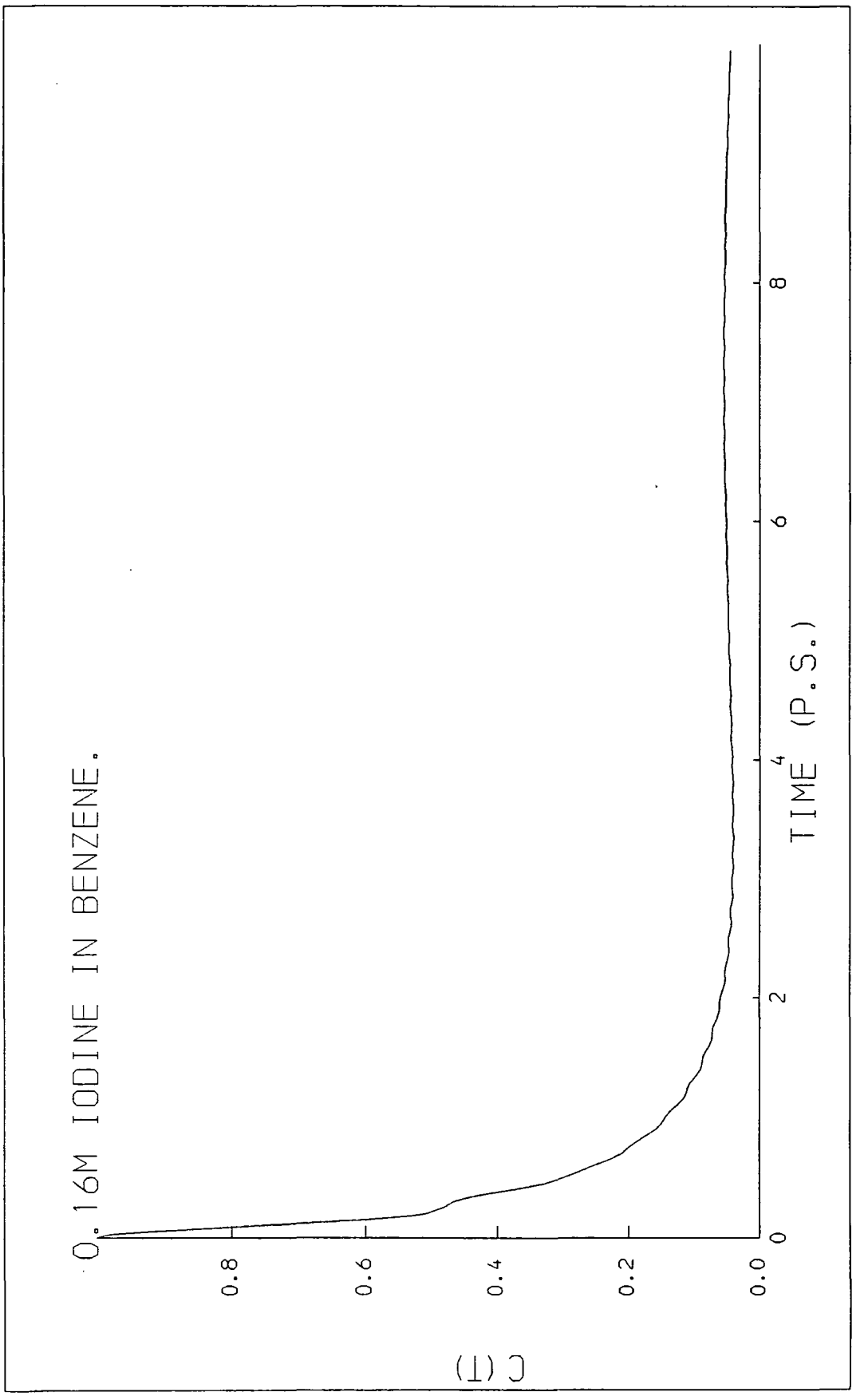

Fig.6.30

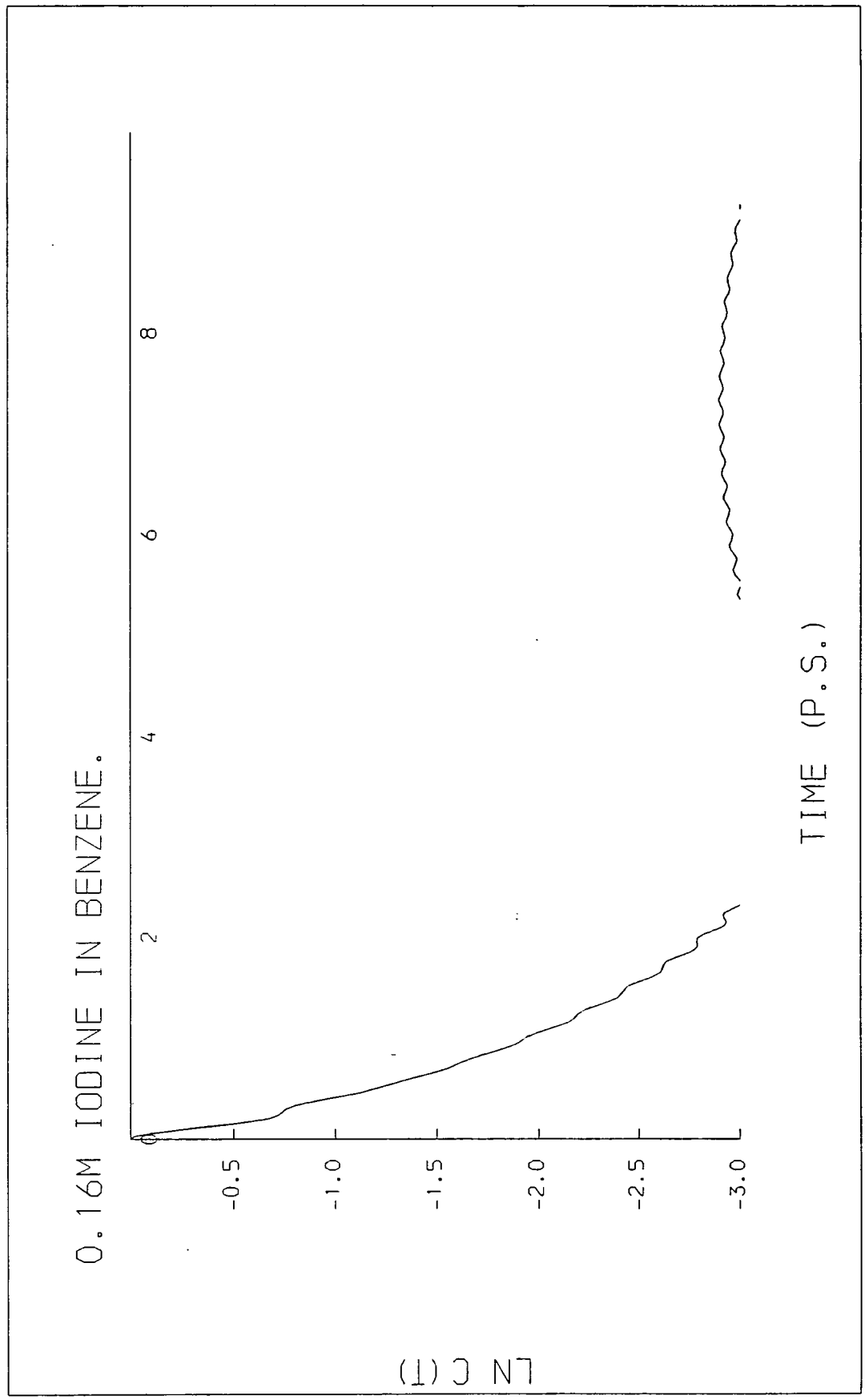

Fig. 6.31

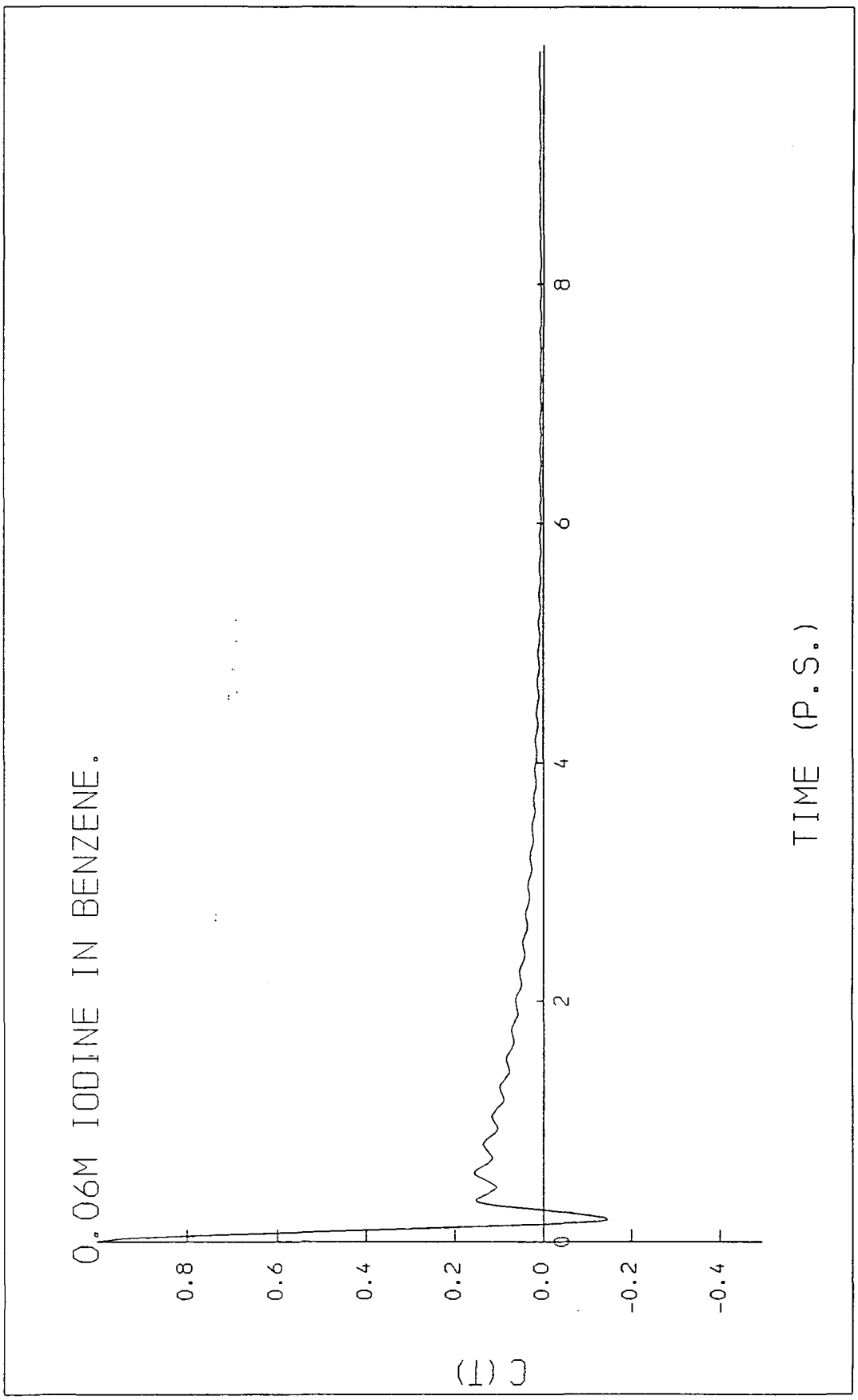

Fig. 6.32

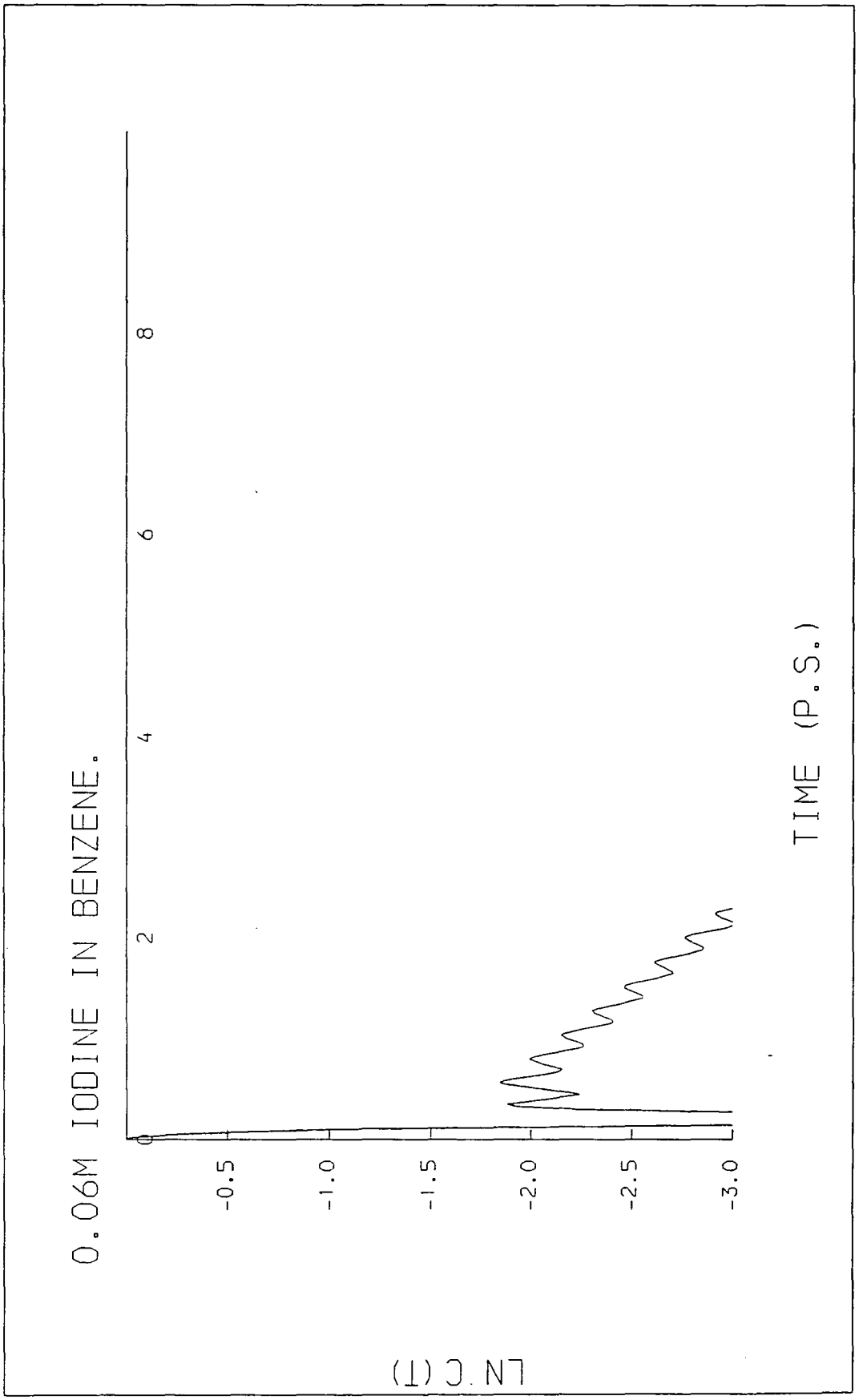

Fig. 6.33

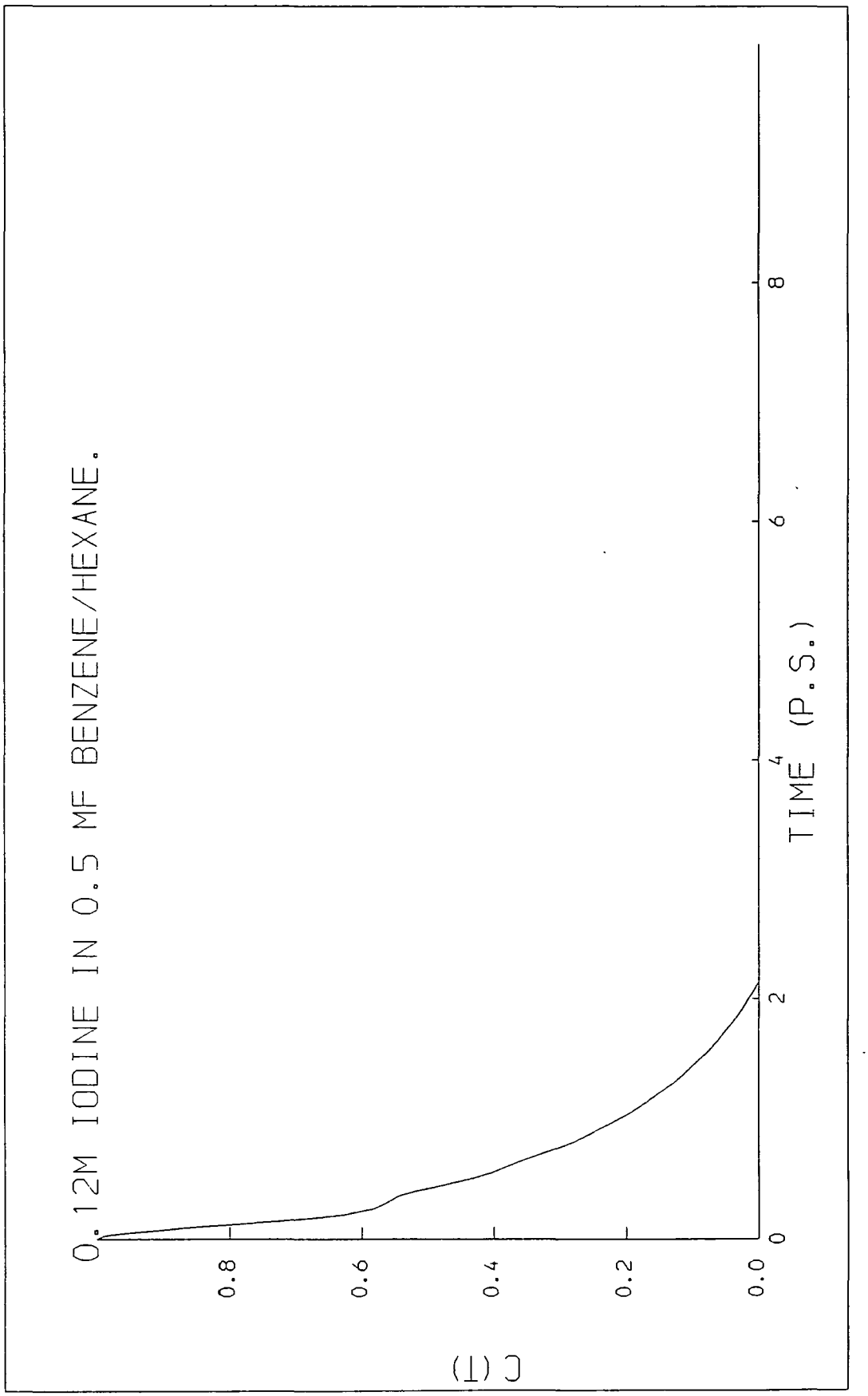
0.12M IODINE IN 0.5 MF BENZENE/HEXANE.
C (T)
0.0
0.2
0.4
0.6
0.8
0
2
4
6
8
TIME (P.S.)

Fig. 6.34

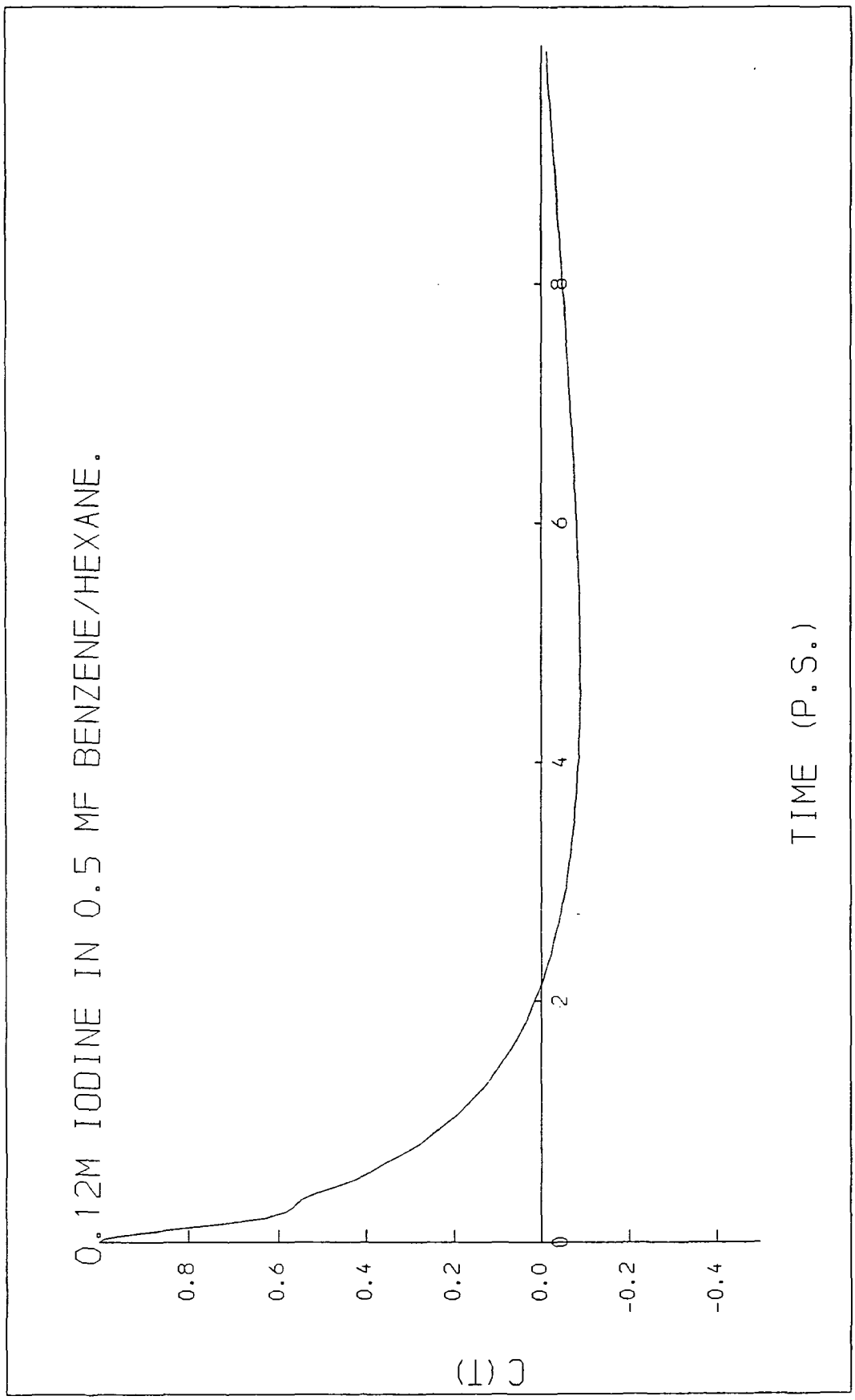
0.12M IODINE IN 0.5 MF BENZENE/HEXANE.
C (T)
0.8
0.6
0.4
0.2
0.0
-0.2
-0.4
0
2
4
6
8
TIME (P.S.)

Fig. 6.35

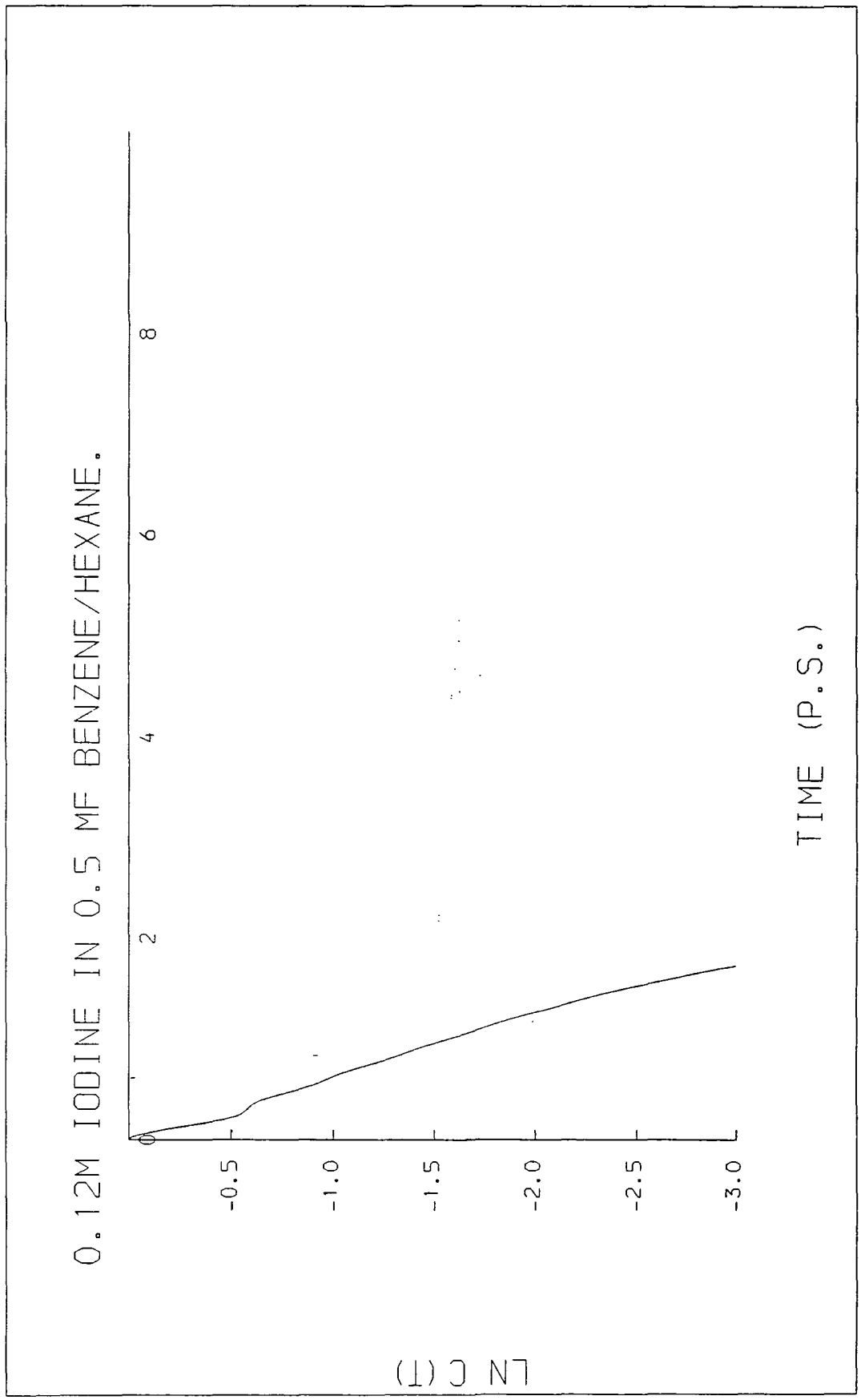
0.12M IODINE IN 0.5 MF BENZENE/HEXANE.
LN C (T)
TIME (P.S.)
0
2
4
6
8
-0.5
-1.0
-1.5
-2.0
-2.5
-3.0

Fig. 6.36

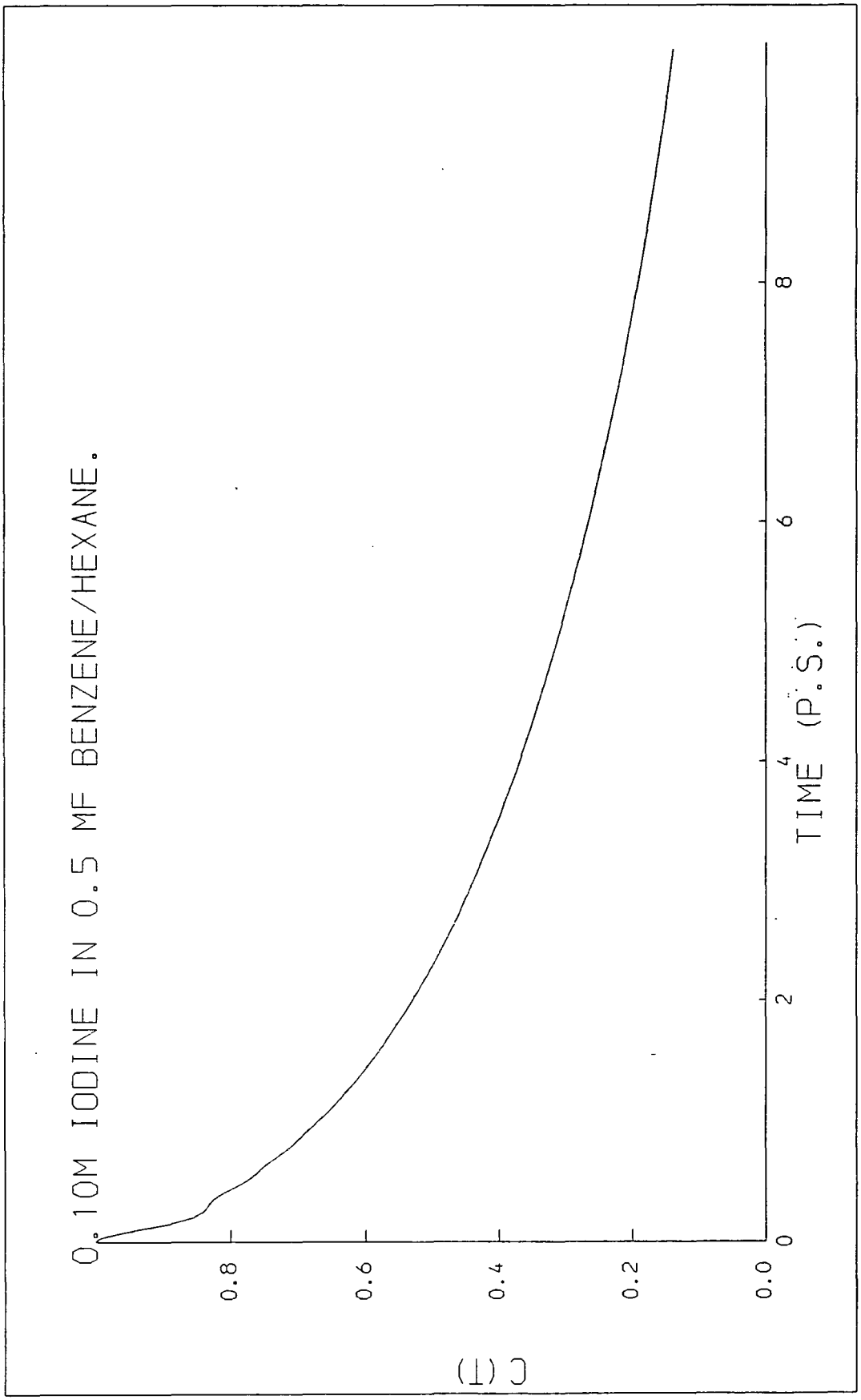
0.10M IODINE IN 0.5 MF BENZENE/HEXANE.
C (I)
0.0
0.2
0.4
0.6
0.8
0
2
4
6
8
TIME (P.S.)

Fig. 6.37

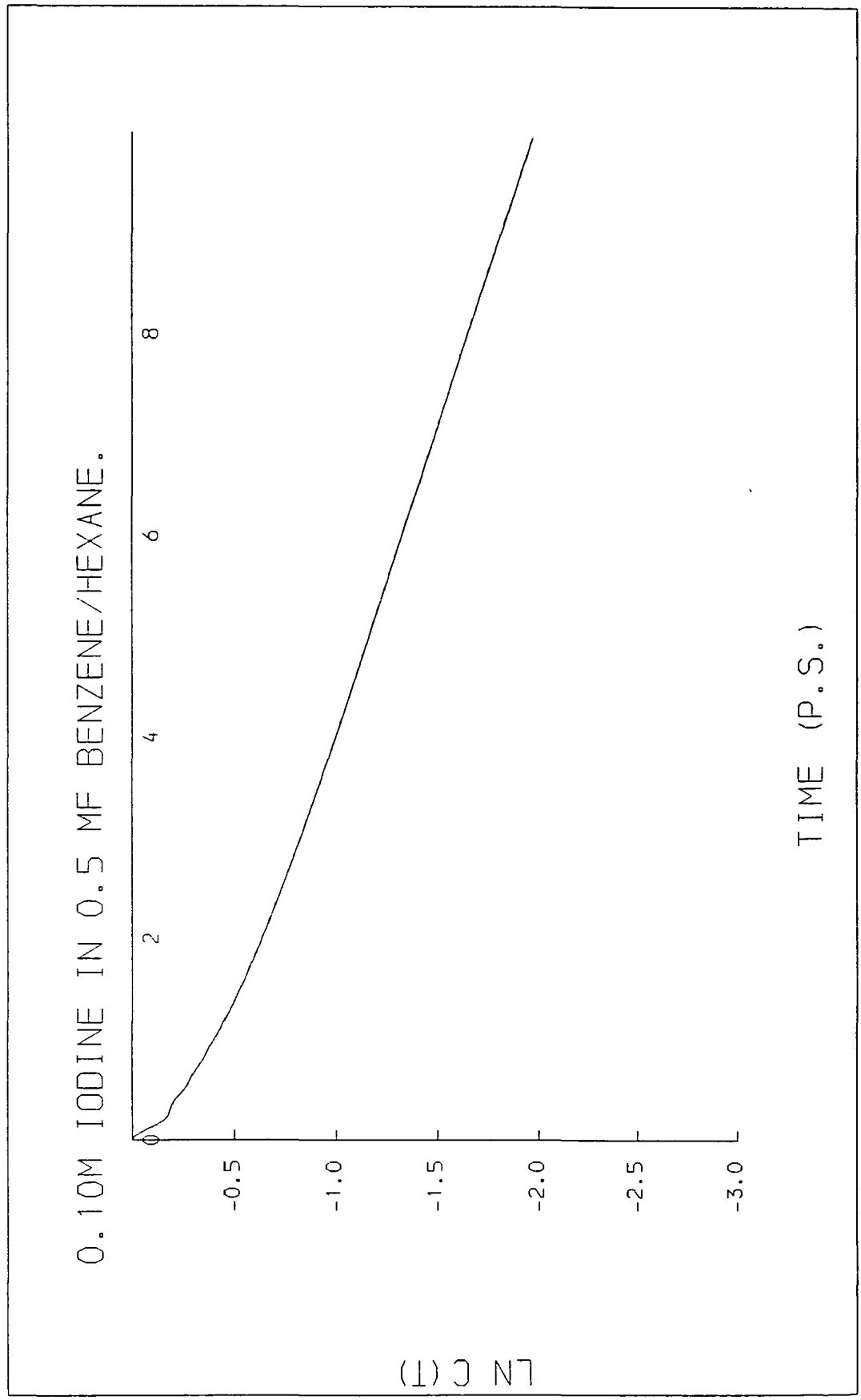
0.10M IODINE IN 0.5 MF BENZENE/HEXANE.
LN C (T)
TIME (P.S.)
0
2
4
6
8
-0.5
-1.0
-1.5
-2.0
-2.5
-3.0

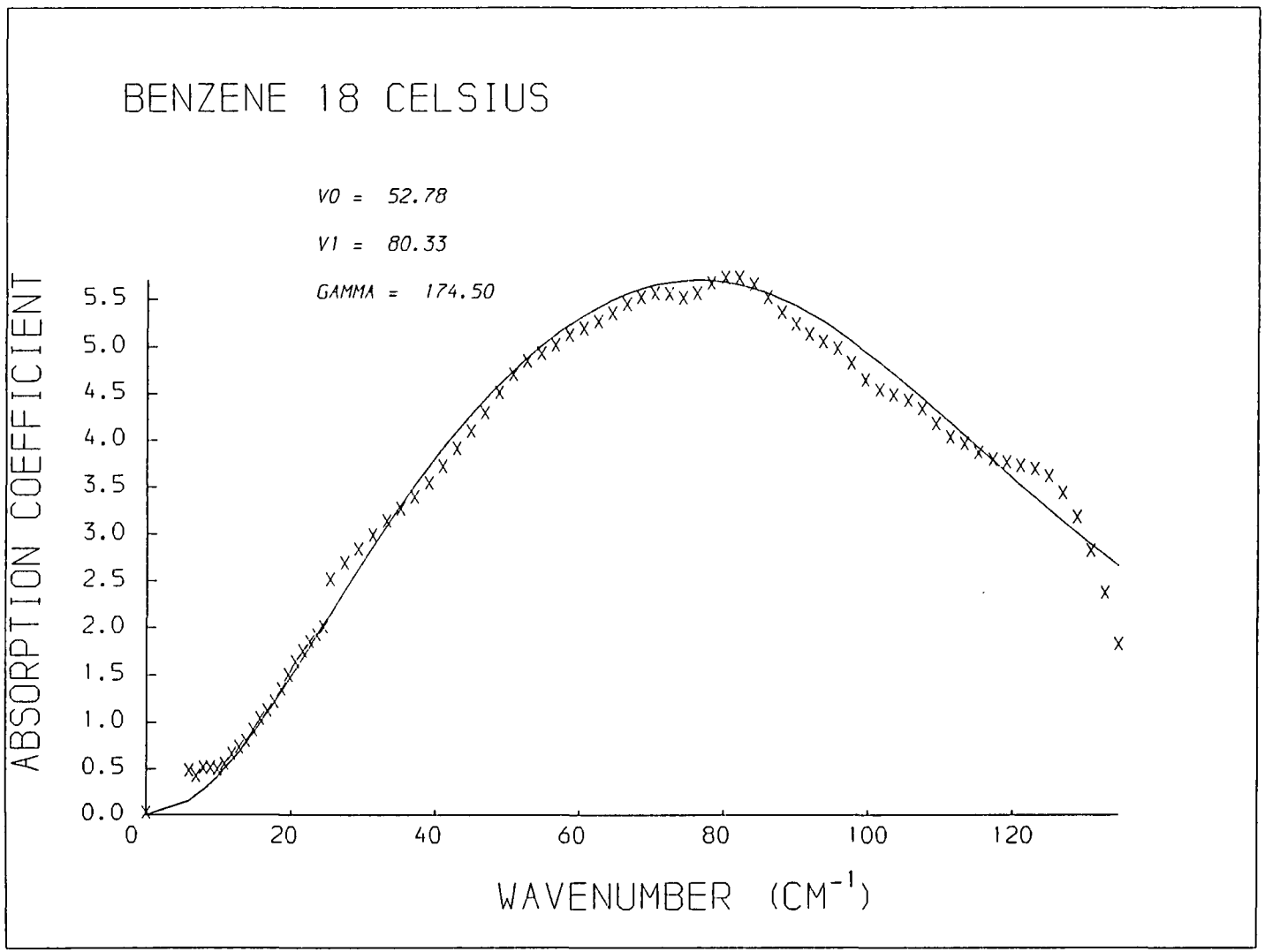
BENZENE 18 CELSIUS
V0 = 52.78
V1 = 80.33
GAMMA = 174.50
ABSORPTION COEFFICIENT
5.5
5.0
4.5
4.0
3.5
3.0
2.5
2.0
1.5
1.0
0.5
0.0
0
20
40
60
80
100
120
WAVENUMBER (CM-1)

Fig. 6.38

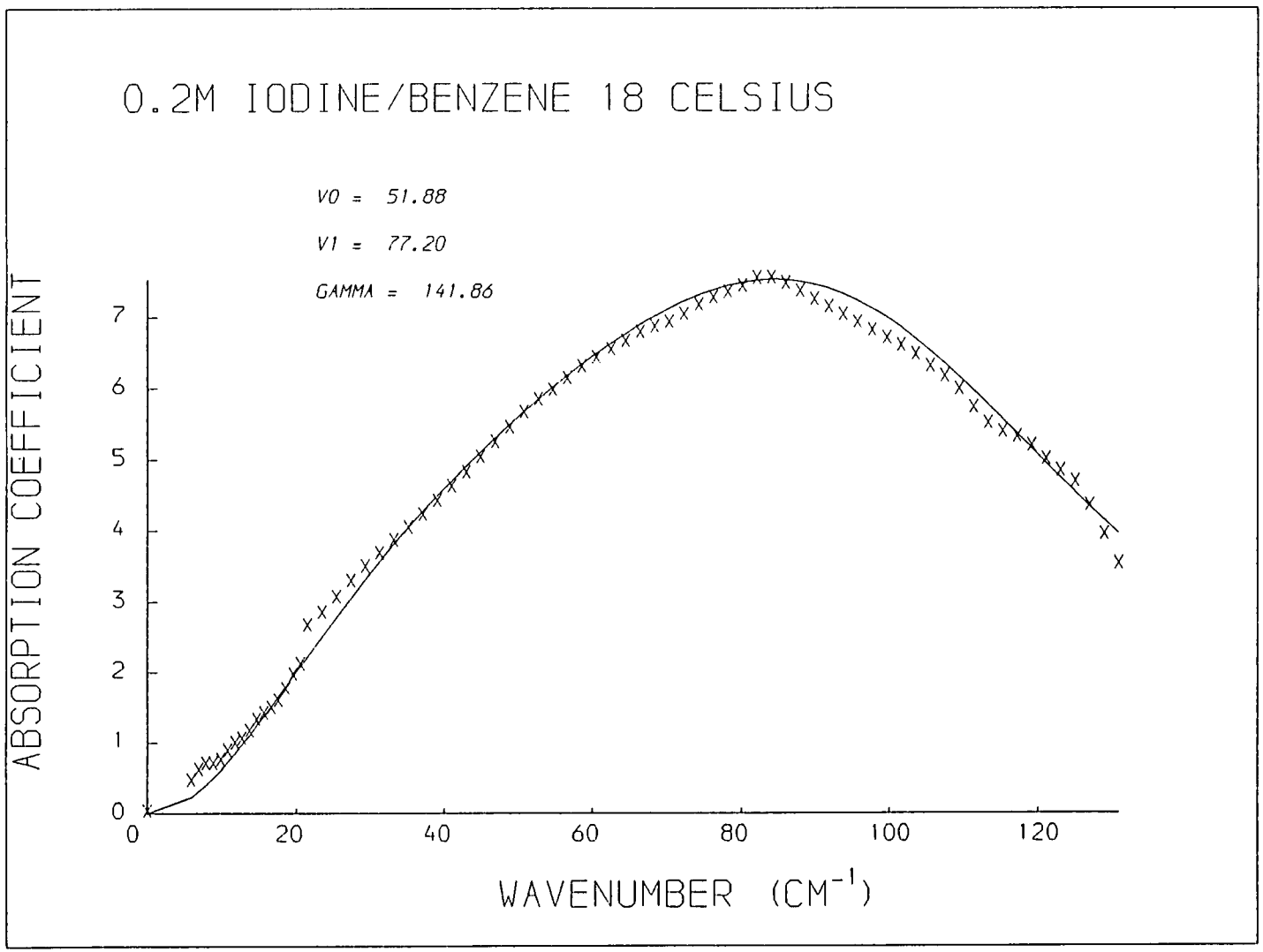
0.2M IODINE/BENZENE 18 CELSIUS
V0 = 51.88
V1 = 77.20
GAMMA = 141.86
ABSORPTION COEFFICIENT
0
1
2
3
4
5
6
7
0
20
40
60
80
100
120
WAVENUMBER (CM-1)

Fig. 6.39

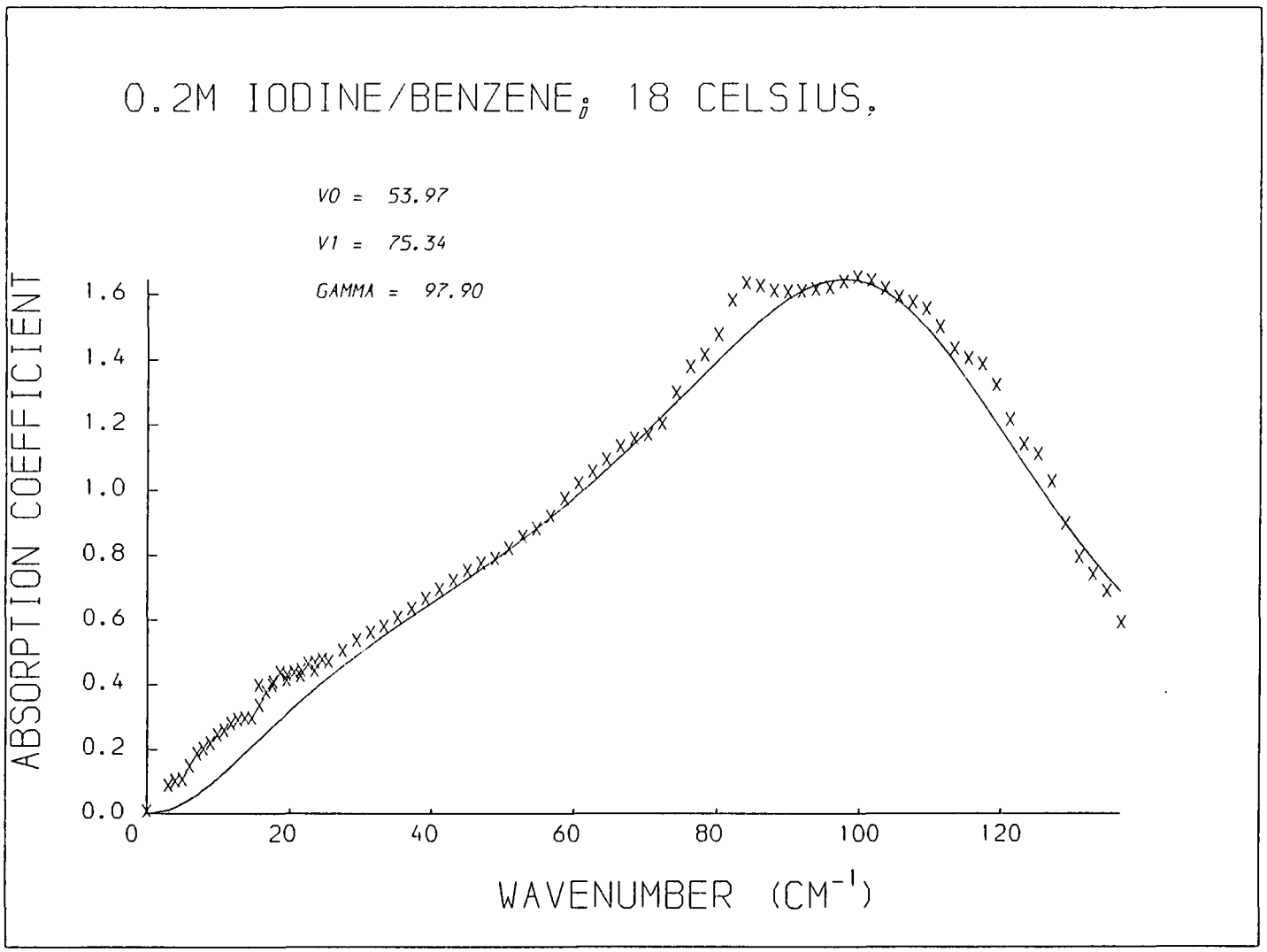
0.2M IODINE/BENZENE, 18 CELSIUS.
V0 = 53.97
V1 = 75.34
GAMMA = 97.90
ABSORPTION COEFFICIENT
1.6
1.4
1.2
1.0
0.8
0.6
0.4
0.2
0.0
0
20
40
60
80
100
120
WAVENUMBER (CM^{-1})

Fig. 6.40

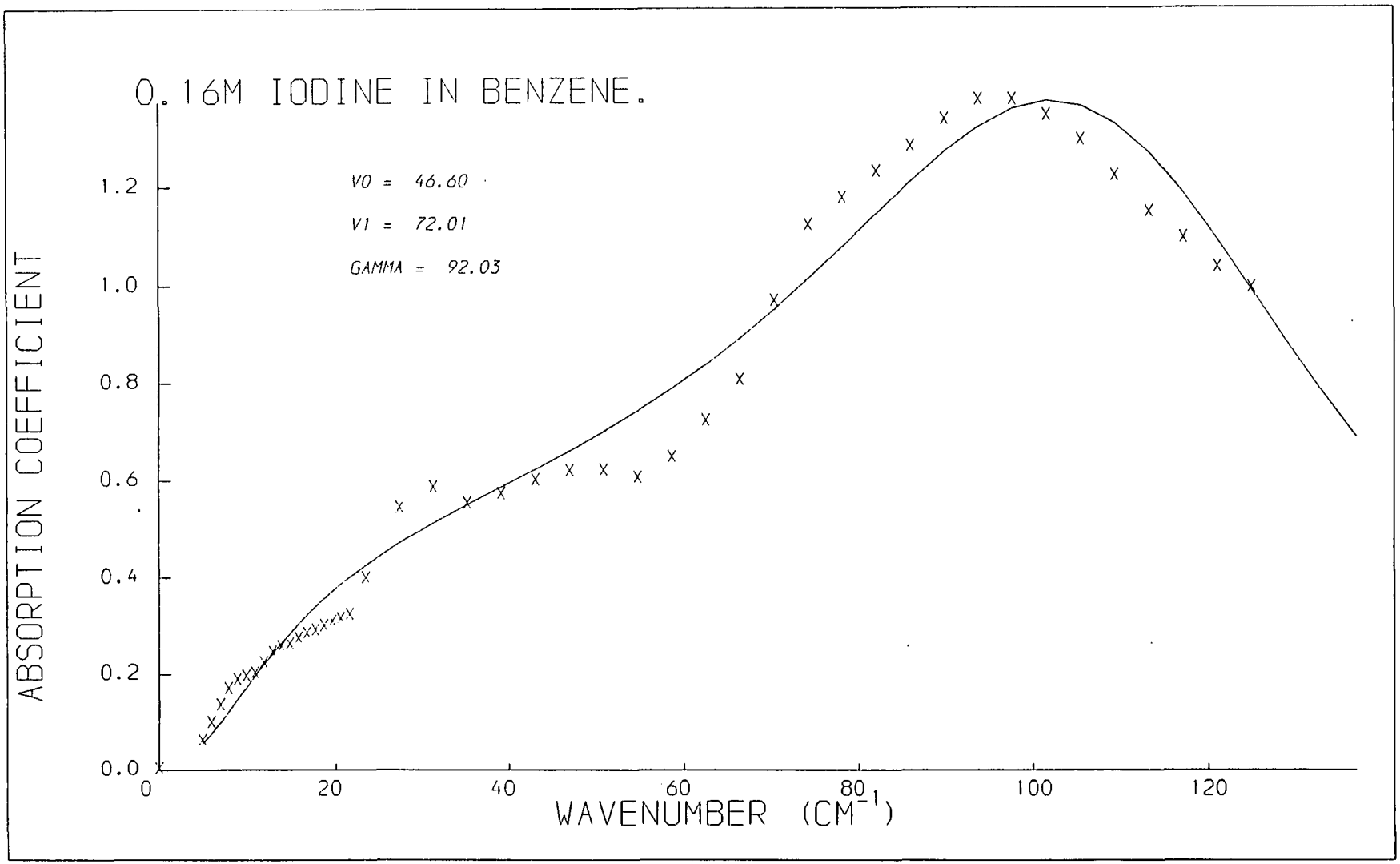
0.16M IODINE IN BENZENE.
V0 = 46.60
V1 = 72.01
GAMMA = 92.03
ABSORPTION COEFFICIENT
0.0
0.2
0.4
0.6
0.8
1.0
1.2
0
20
40
60
80
100
120
WAVENUMBER (CM-1)

Fig. 6.41

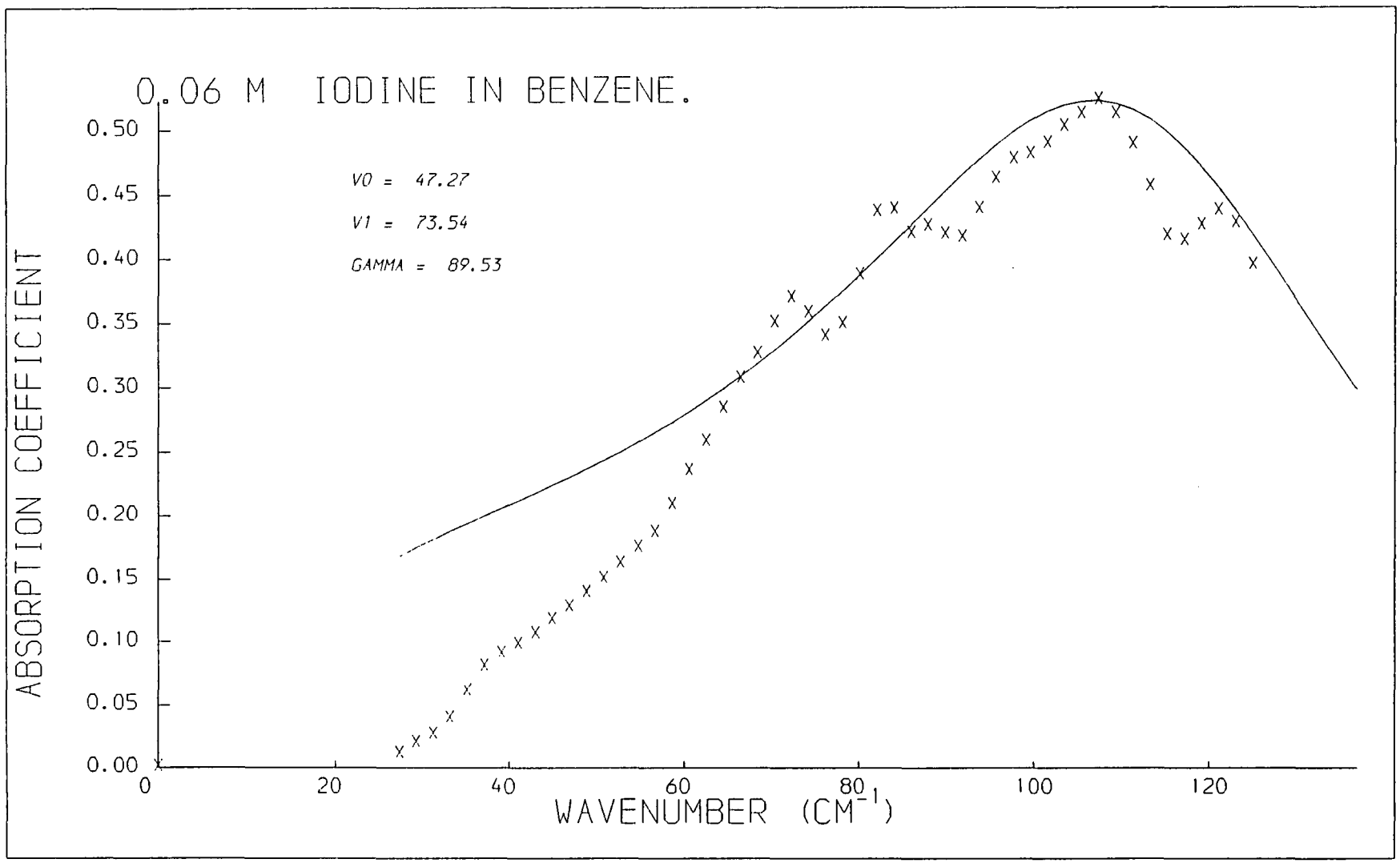
0.06 M IODINE IN BENZENE.
V0 = 47.27
V1 = 73.54
GAMMA = 89.53
ABSORPTION COEFFICIENT
0.00
0.05
0.10
0.15
0.20
0.25
0.30
0.35
0.40
0.45
0.50
0
20
40
60
80
100
120
WAVENUMBER (CM-1)

Fig. 6.42

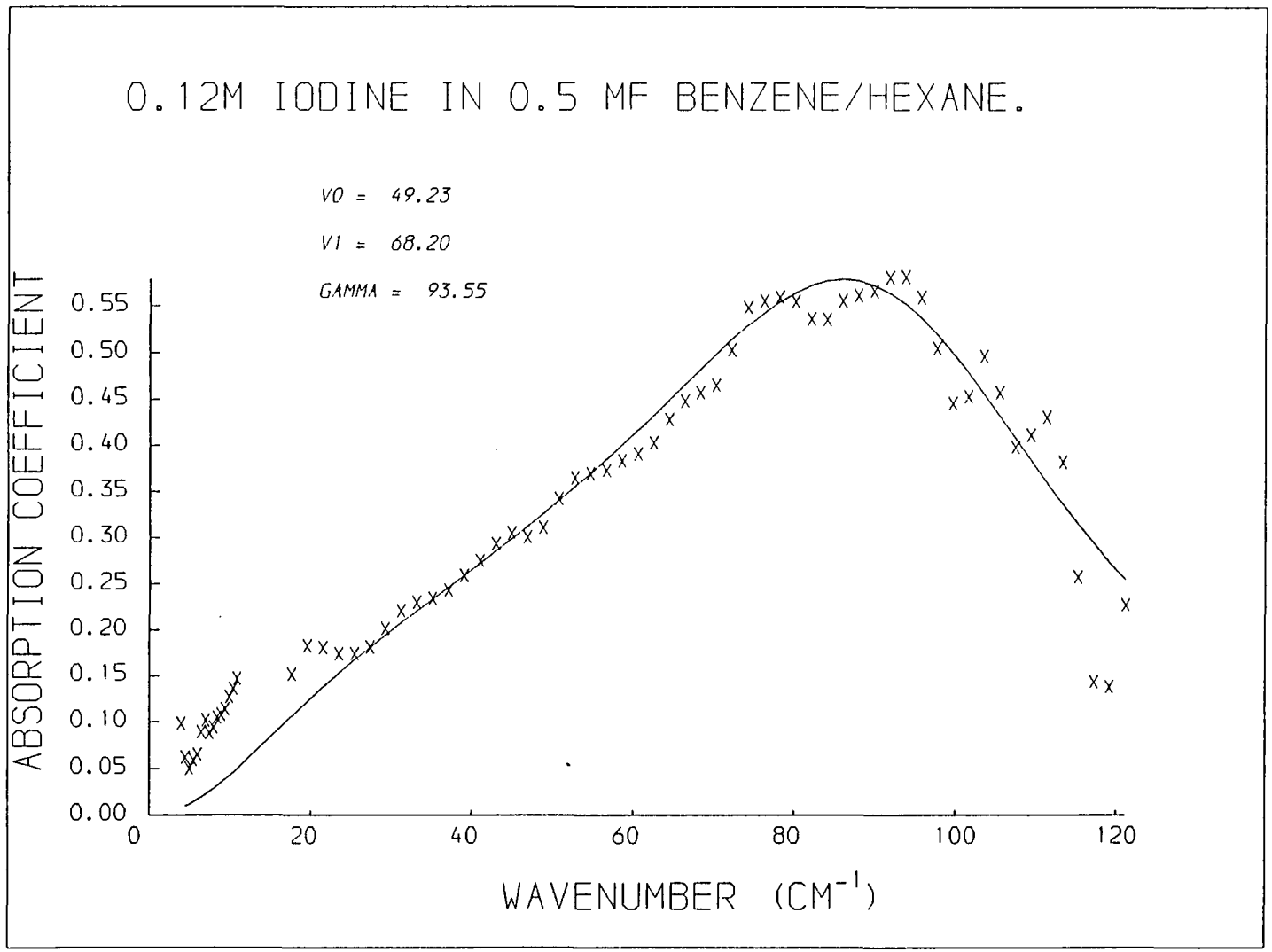
0.12M IODINE IN 0.5 MF BENZENE/HEXANE.
V0 = 49.23
V1 = 68.20
GAMMA = 93.55
ABSORPTION COEFFICIENT
0.55
0.50
0.45
0.40
0.35
0.30
0.25
0.20
0.15
0.10
0.05
0.00
0
20
40
60
80
100
120
WAVENUMBER (CM-1)

Fig. 6.43

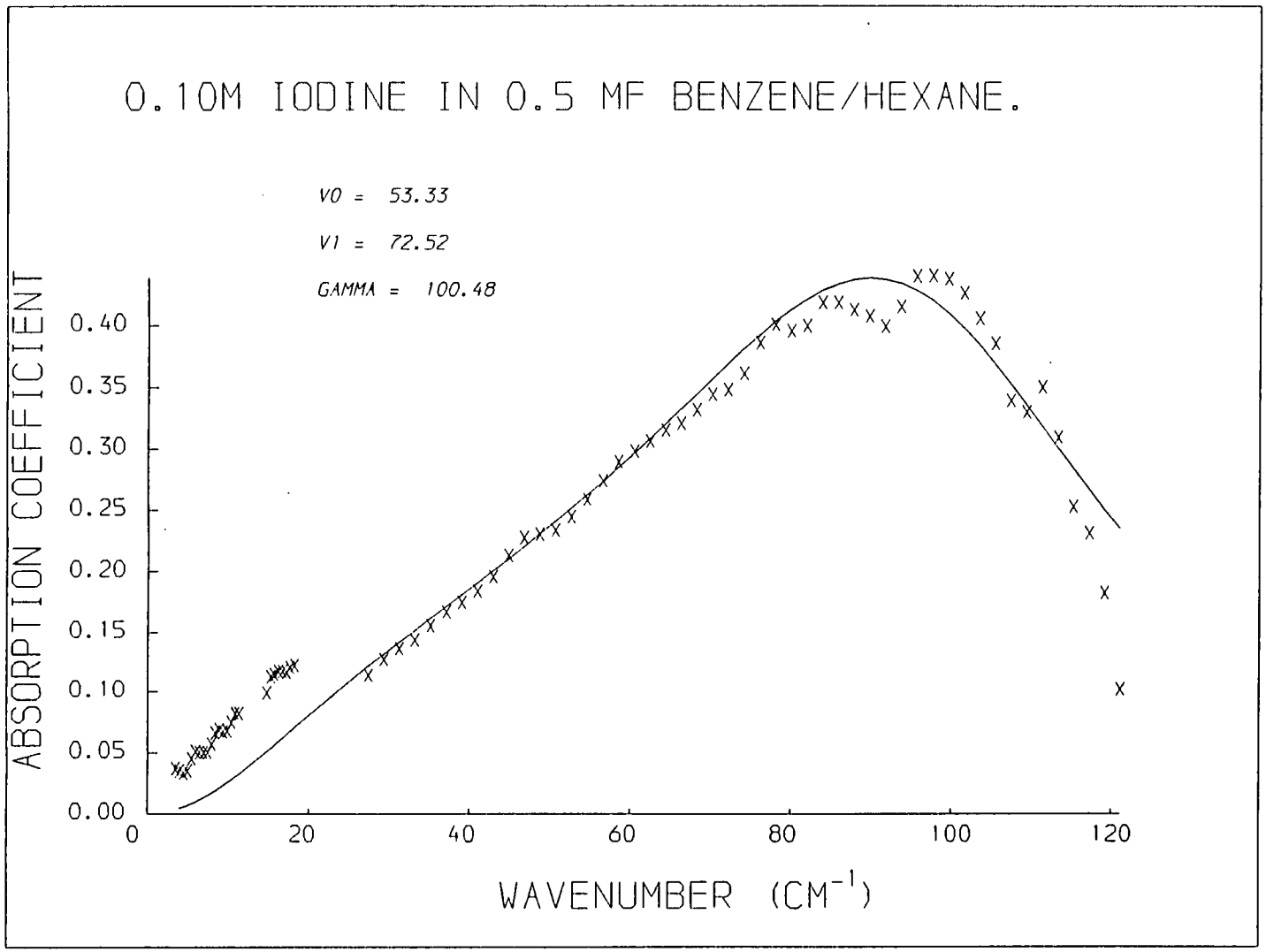
0.10M IODINE IN 0.5 MF BENZENE/HEXANE.
V0 = 53.33
V1 = 72.52
GAMMA = 100.48
ABSORPTION COEFFICIENT
0.00
0.05
0.10
0.15
0.20
0.25
0.30
0.35
0.40
0
20
40
60
80
100
120
WAVENUMBER (CM-1)

Fig. 6.7.4

Fig. 6.45

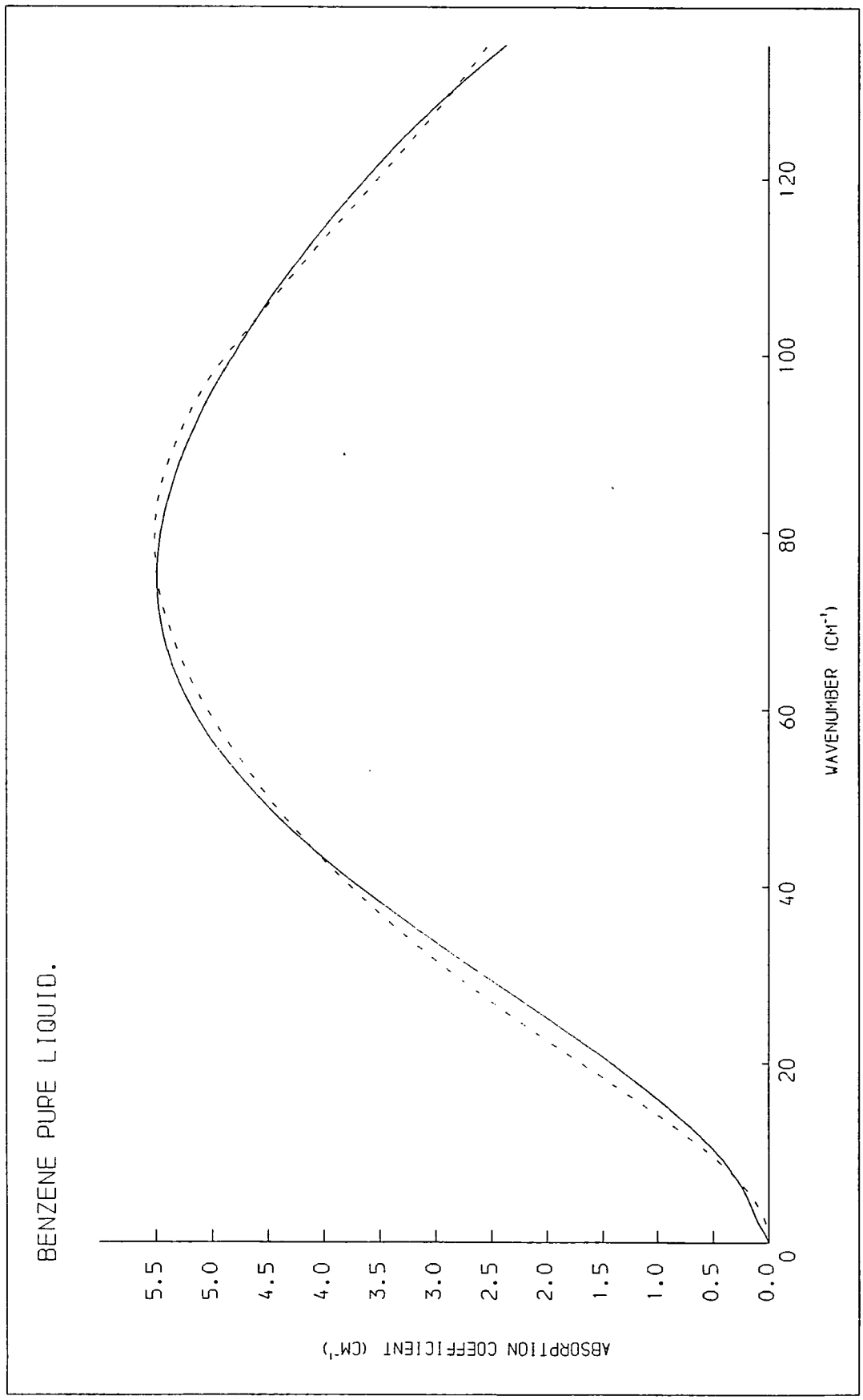
BENZENE PURE LIQUID.
ABSORPTION COEFFICIENT (CM⁻¹)
0.0
0.5
1.0
1.5
2.0
2.5
3.0
3.5
4.0
4.5
5.0
5.5
0
20
40
60
80
100
120
WAVENUMBER (CM⁻¹)

Fig. 6.46

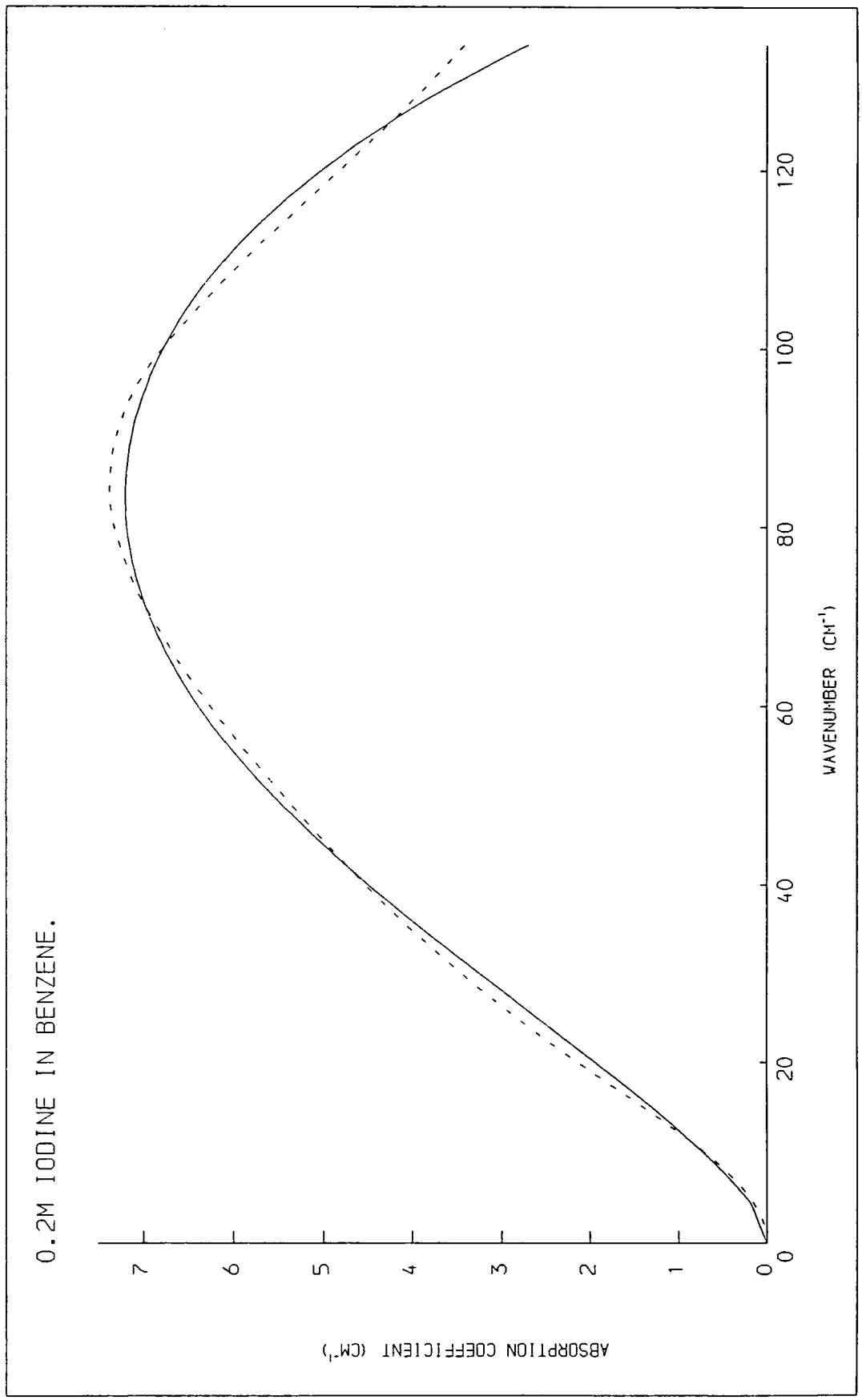
0.2M IODINE IN BENZENE.
ABSORPTION COEFFICIENT (CM⁻¹)
WAVENUMBER (CM⁻¹)
0
1
2
3
4
5
6
7
0
20
40
60
80
100
120

Fig. 6.47

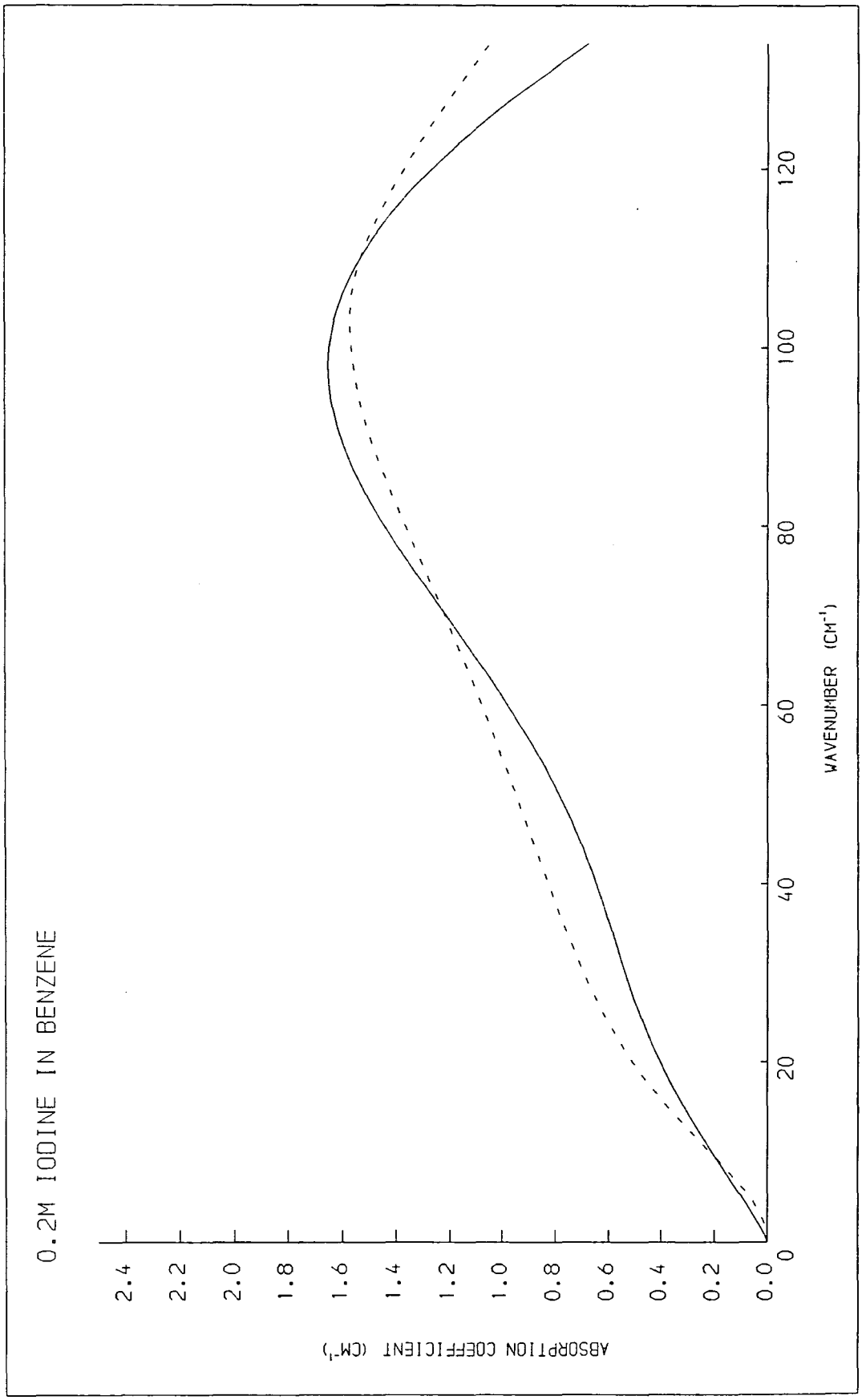
0.2M IODINE IN BENZENE
ABSORPTION COEFFICIENT (CM⁻¹)
WAVENUMBER (CM⁻¹)
0.0
0.2
0.4
0.6
0.8
1.0
1.2
1.4
1.6
1.8
2.0
2.2
2.4
0
20
40
60
80
100
120

Fig. 6.48

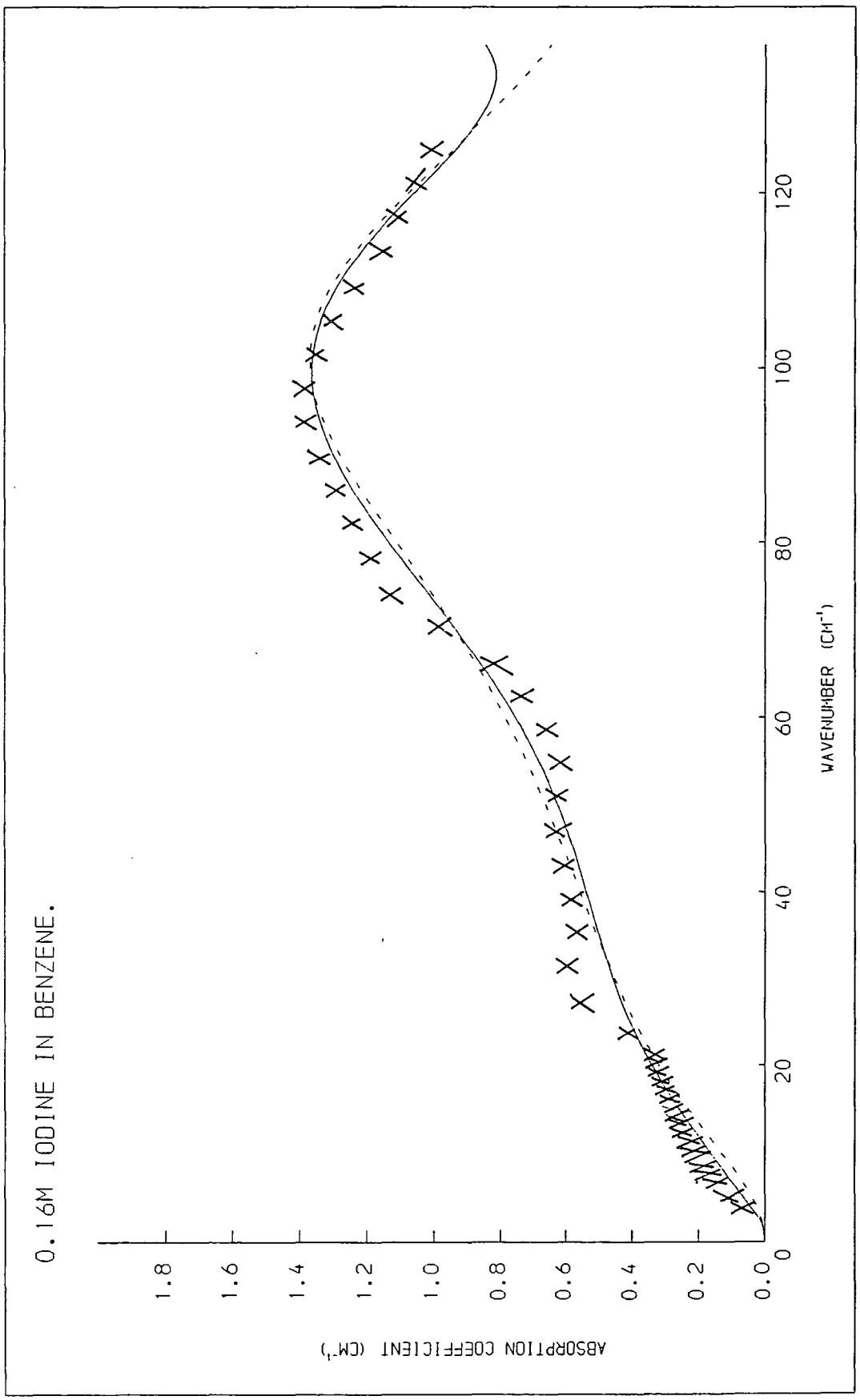
0.16M IODINE IN BENZENE.
ABSORPTION COEFFICIENT (CM⁻¹)
0.0
0.2
0.4
0.6
0.8
1.0
1.2
1.4
1.6
1.8
0
20
40
60
80
100
120
WAVENUMBER (CM⁻¹)

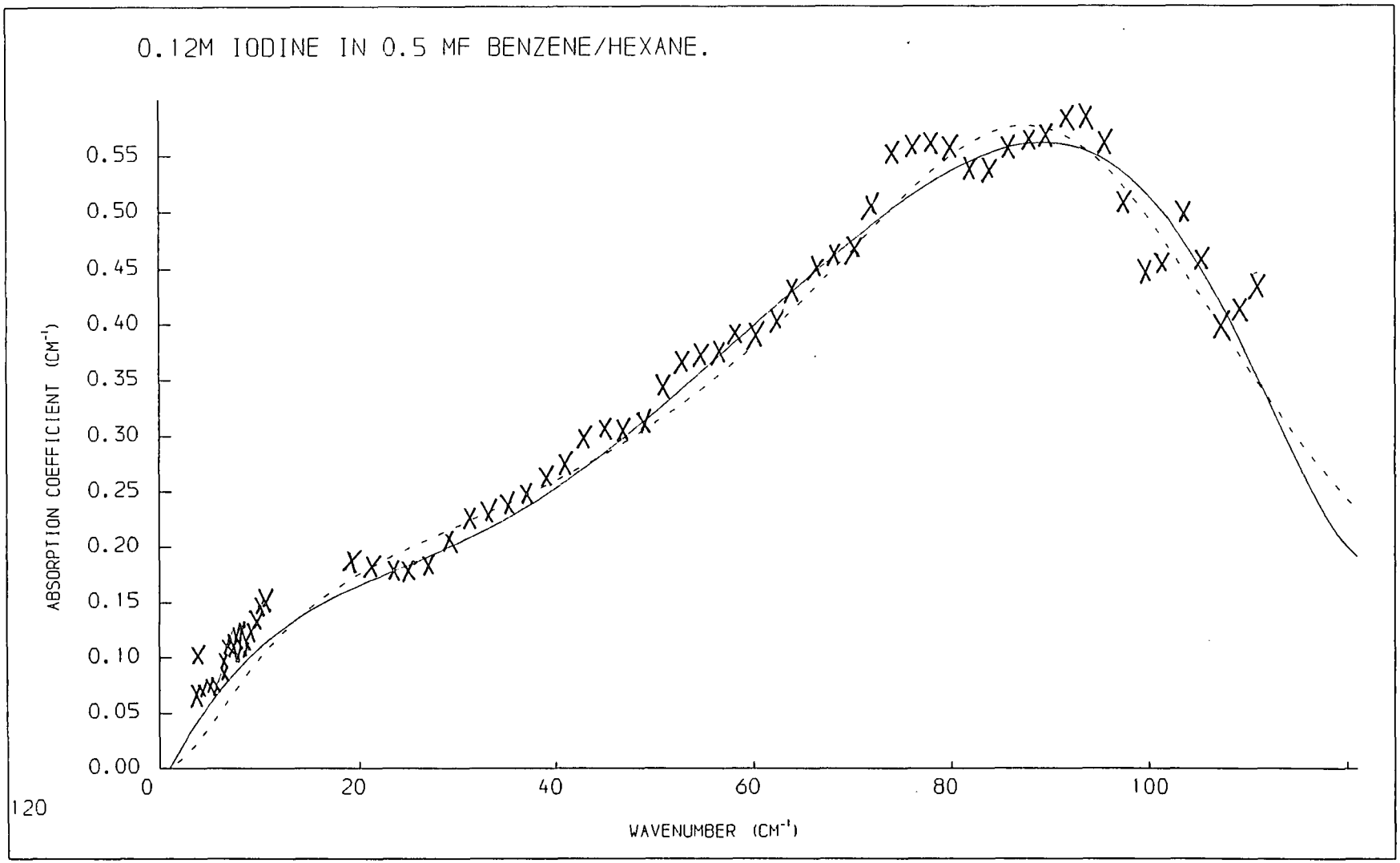
0.12M IODINE IN 0.5 MF BENZENE/HEXANE.
ABSORPTION COEFFICIENT (CM⁻¹)
0.00
0.05
0.10
0.15
0.20
0.25
0.30
0.35
0.40
0.45
0.50
0.55
0
20
40
60
80
100
WAVENUMBER (CM⁻¹)

Fig.6.4.9

Fig. 6.50

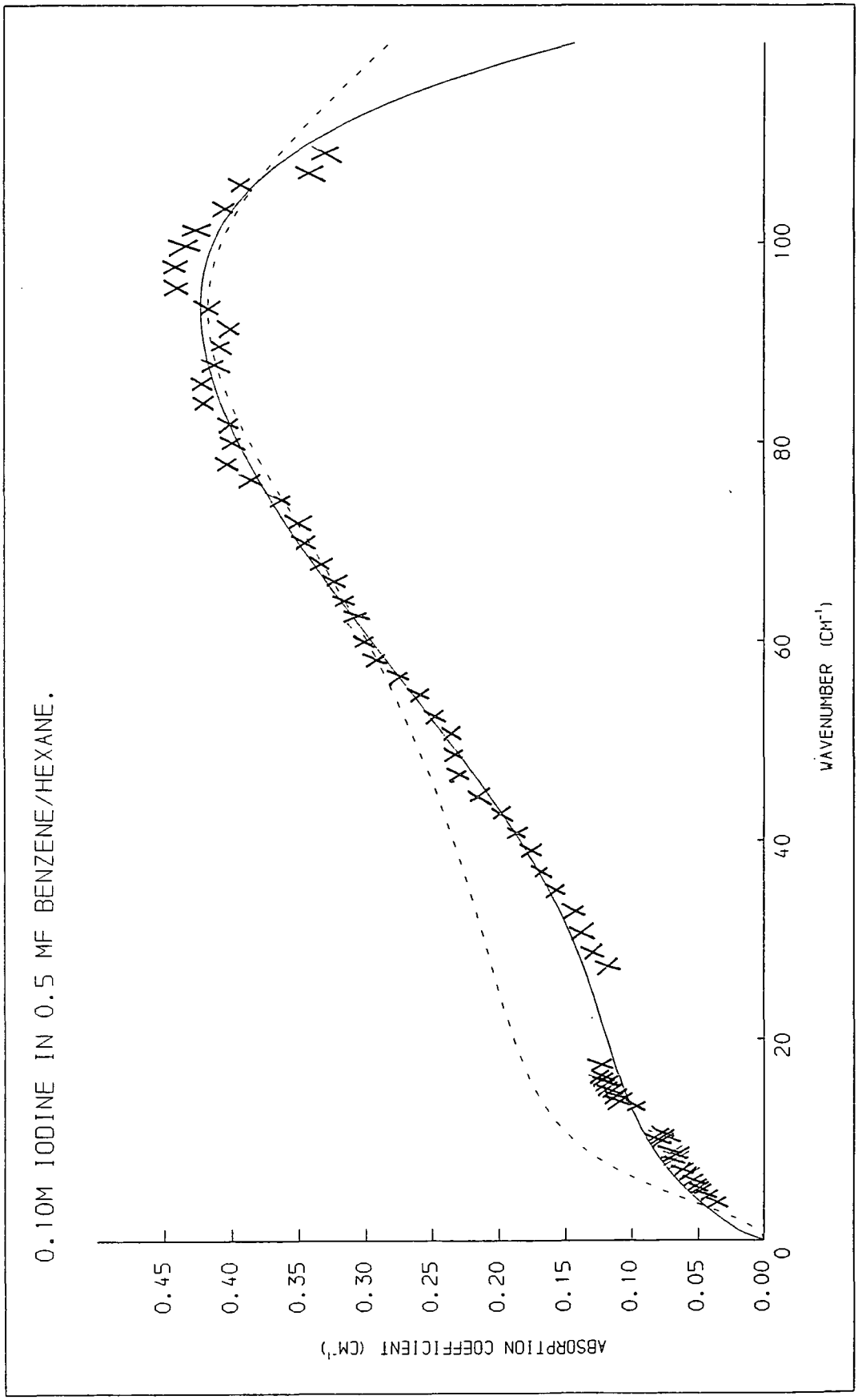
0.10M IODINE IN 0.5 MF BENZENE/HEXANE.
ABSORPTION COEFFICIENT (CM⁻¹)
0.00
0.05
0.10
0.15
0.20
0.25
0.30
0.35
0.40
0.45
0
20
40
60
80
100
WAVENUMBER (CM⁻¹)

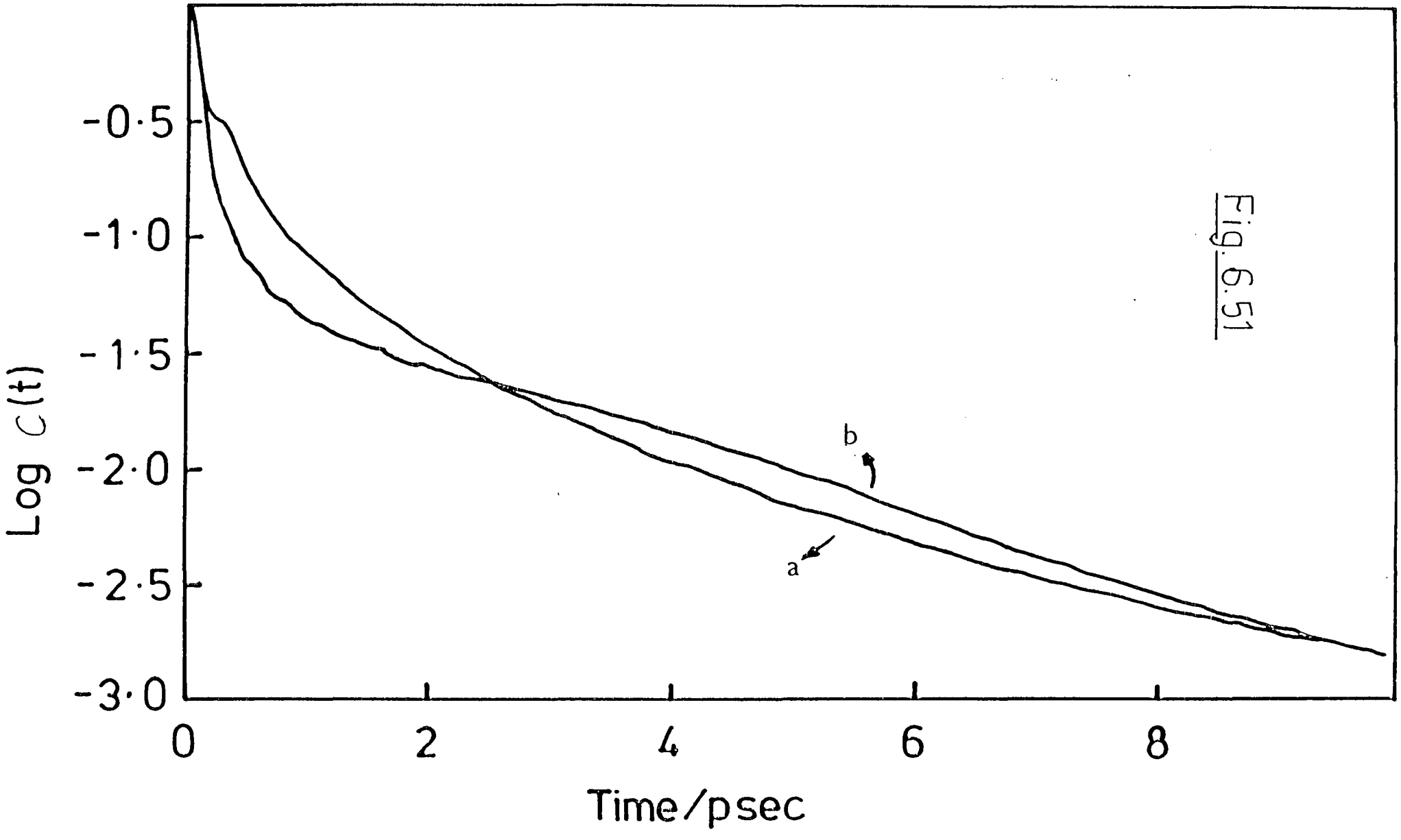

Fig. 6.51

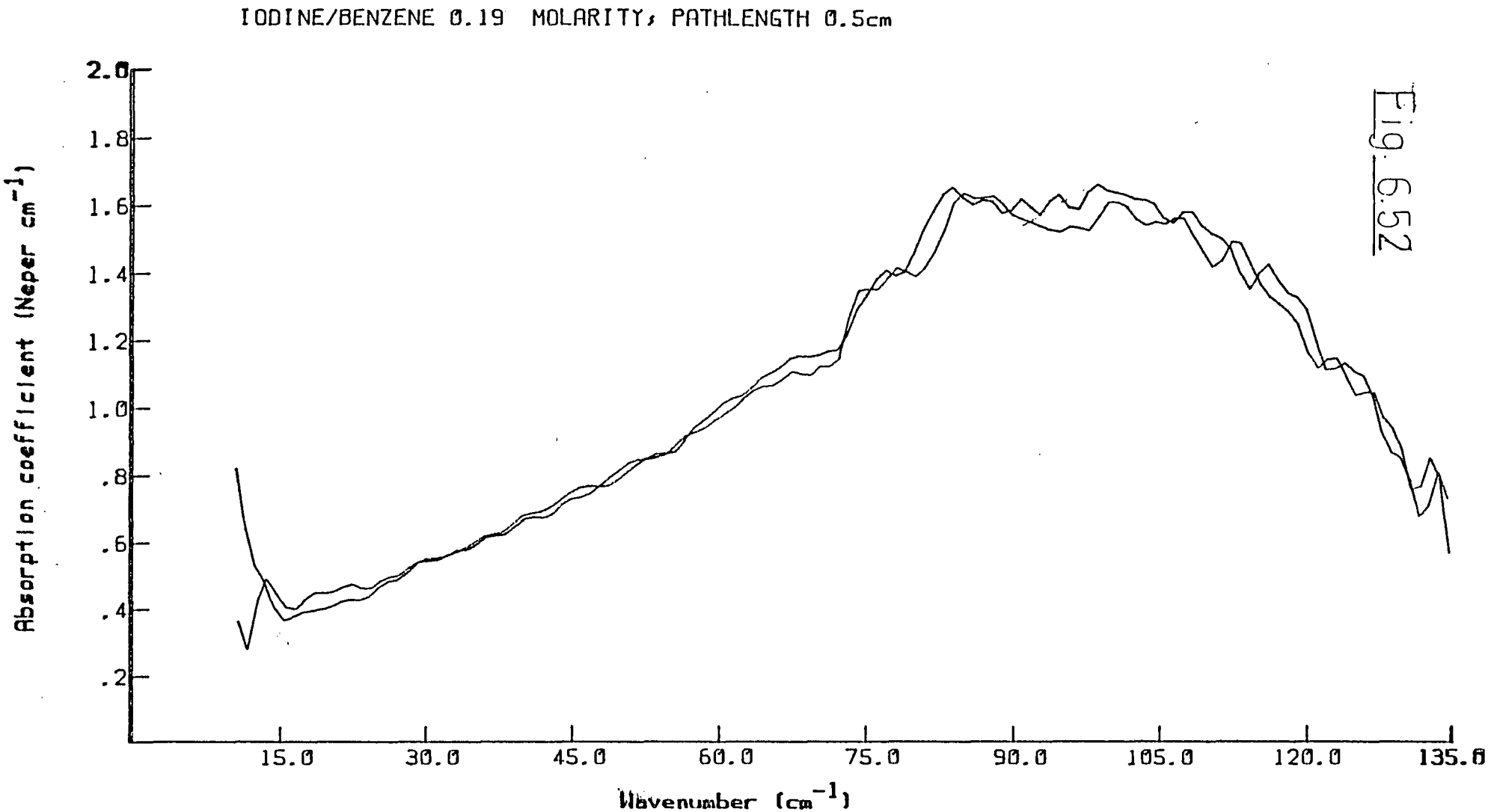
IODINE/BENZENE 0.19 MOLARITY; PATHLENGTH 0.5cm
Absorption coefficient (Neper cm^{-1})
2.0
1.8
1.6
1.4
1.2
1.0
.8
.6
.4
.2
15.0
30.0
45.0
60.0
75.0
90.0
105.0
120.0
135.0
Wavenumber (cm^{-1})

Fig. 6.52

spectrum due to iodine-benzene interactions. Thus the contribution to spectrum b from benzene-benzene interactions is more dominant at lower frequencies than higher frequencies. This fact could point to different time-scales of interaction for two benzene molecules as compared to a benzene molecule with an iodine molecule.

The intensity of the iodine-benzene absorption bands obtained in this work are slightly greater than those obtained elsewhere [92]. This is likely to be due to differences in the residual water content of the benzene solvent after drying.

The spectra for the iodine-benzene interactions alone appear to have a low frequency shoulder which, at first sight, might be attributed to the superposition of a separate band, so that the full spectrum is a combination of two induced absorption bands. It is worth considering the possibility of there being two separate collision-induced processes which would give rise to two such bands.

Firstly, if we were to assume that iodine exists in the solvent as an equilibrium between 'complexed' and 'non-complexed' iodine, then the collision-induced interactions for the iodine molecules in the two cases with solvent benzene might be expected to occur on different time scales. This would lead to a shift in frequency between the 'complexed' and 'non-complexed' forms. However, no evidence for the validity of such an assumption can be resolved for the ν_{I_2} band which is sensitive to much shorter

time-scales. Thus the observation of formation of a complex at such low frequencies through resolving separate bands can be ruled out.

Alternatively, the proposed two band structure could be interpreted as resulting from the separation in the spectral domain of contributions to the collision-induced absorption from an induced-dipole on benzene caused by the iodine molecule quadrupole moment, and an induced-dipole on iodine due to the benzene quadrupole moment. However, from an intensity consideration this could not be the case. Since there are relatively few iodine molecules compared to benzene molecules, the intensity of one would have to be much greater than the other. This is obviously not the case. Furthermore, it would be difficult to envisage how the time-scale of the two bands could be different seeing as they arise from the same interaction.

It is probably more feasible to treat the spectrum as one band describing the fluctuating induced dipoles on both molecules. The appearance of the shoulder must then be accounted for by a complex time dependence of the relaxation processes and would be best studied in the temporal domain by means of the correlation functions.

6.4.2 Interpretation of Correlation Functions

A correlation function describes the time evolution of the relaxation processes; the rate at which a molecule

losses its memory of previous events. At very short times the correlation function tends towards the limit of a free rotor; that is, the times are short compared to the time between collisions. For a perfect free rotor (no collisions) the correlation function is exponential. Thus, if a molecule is rotating freely at short times, the log plot of the correlation function should be a straight line over these times.

At long times, the molecules are expected to have reached their rotational diffusional limit, since the times are now long compared to the time between collisions and the orientation of the molecule is much less correlated with its previous orientations.

A relaxation time, τ, can be measured from the slope of the correlation function over a particular time period. A different relaxation time can be measured from the area under the correlation function. The two times will only be the same for the case of a free rotor. The relaxation time used here is defined by

$$\tau = -t \,/_{\ell n\, c(t)} \tag{6.30}$$

For a real liquid the correlation functions are complicated and difficult to interpret because they not only reflect the reorientational characteristics of the single molecule, i.e.

$$c(t) = \sum_{i=i} M_i(t)\, M_i\,(0) \tag{6.31}$$

but the correlation between different molecules, including the many-body correlations discussed in section 6.1.2.

It is difficult to separate the different contributions to the correlation functions, but some progress can be made by attempting to assess the relative importance of the different contributions through comparison of correlation functions obtained in different experiments.

For the case of iodine in benzene, a number of comparisons can be made. The shapes of the correlation functions for the spectra derived from ratioing iodine/benzene against a different pathlength of iodine/benzene (procedure b) and those obtained from ratioing iodine/benzene against benzene (procedure a) are obviously different. If we denote the total induced moment of an interacting pair as M_{ij}, equation 6.13. for these two correlation functions reads:

procedure b $$c(t) = \Sigma\, M_{BB}(t) M_{BB}(o) + \Sigma\, M_{IB}(t)\, M_{IB}(o) + \Sigma\, M_{IB}(t)\, M_{IB'}(o) + \ldots \quad (6.32)$$

procedure a $$c(t) = \Sigma\, M_{IB}(t)\, M_{IB}(o) + \Sigma\, M_{IB}(t)\, M_{IB'}(o) + \ldots \quad (6.33)$$

Correlation functions derived by these procedures for a 0.2M solution of iodine in benzene are compared in figure 6.49. As expected, the function obtained using procedure a is less complicated since the effects of benzene-benzene interactions have been removed and they can be described by

assuming two relaxation processes, neither of which is exponential. The correlation function for the iodine/benzene versus iodine/benzene case probably involves more than two relaxation processes.

The relaxation times measured at the short and long time limits for different concentrations of iodine in benzene are listed in table 6.4. Comparing those obtained with procedure a and procedure b for the 0.2M iodine solution reveals that the iodine-benzene interactions relax on a relatively slow time scale compared to the benzene-benzene interactions. This would suggest that the iodine-benzene interaction is fairly long-ranged, in agreement with a quadrupole induced dipole mechanism.

Further comparison of these two correlation functions reveals that the one derived through procedure a has a 'kink' at approximately 0.3 psec which is not present in the correlation function for procedure b. The same feature is visible in the same region for an 0.16M concentration of iodine in benzene also recorded using procedure a (figure 6.41). This feature corresponds to approximately $20cm^{-1}$ in the frequency domain, i.e. the position of the apparent shoulder on the low frequency side of the far infrared band.

The interpretation of this 'kink' in the correlation functions, which is also present for the iodine in benzene/hexane mixture system, is unclear but likely to represent the complicated time-evolution of the collision-induced dynamics.

When interpreting the correlation functions, it is important to note that, with the exception of the case of 0.2M iodine in benzene, the correlation functions above about 1 psec. are unreliable since data was not collected at very low frequencies ($< 5cm^{-1}$). In the absence of microwave data, the long-time part of the correlation functions were obtained from an extrapolation of the absorption coefficient data to zero in the frequency domain. As such, only the short-time part of the correlation functions will be discussed. The correlation functions are all plotted out to long-times, however, in order to facilitate comparison with figures 6.25 and 6.27 for which microwave data [91] have been included.

As can be seen from table 6.4 the relaxation times for the short-time part of the correlation functions get progressively shorter as the concentration of iodine is reduced. this suggests that the rate of collisions increases as the iodine concentration is reduced, thus causing the molecules to lose their memory of previous events in a shorter period of time.

The correlation function for the 0.06M iodine solution in benzene has a very different appearance to the others. This, however, is probably due to the effects of noise in the spectrum. As can be seen from figure 6.42 the absorption band has noise spikes superimposed on it and, when Fourier transformed, these produce sinusoidal oscillations in the correlation function.

The correlation functions for iodine is an 0.5 mole fraction of benzene in hexane are presented in figures 6.33 to 6.37. The relaxation times, table 6.4, do not follow a regular pattern as do those for the iodine in benzene case, but the data for the solvent mixture are less reliable for the reasons discussed earlier (section 6.2.1). Comparing the correlation functions for iodine in benzene/hexane with those for iodine in benzene, the very short-time part (<0.5ps) is similar for the two cases. Between approximately 0.5ps to 1.0ps, however, the correlation functions for iodine in benzene/hexane show a relaxation time which is much slower. This may be due in some part to the many body terms discussed earlier in this section.

6.4.3 Intensity and Moment Analysis

For a 0.2M solution of iodine in benzene, theoretical values have been obtained [92,118] for spectral moments using equations 6.24 and 6.25. They are quoted as $32cm^{-2}$ for the zeroth moment (intensity) and $1.6 \times 10^4\ cm^{-3}$ for the second moment. These values compare very well with experimental values obtained using the data reported here in equations 6.27 and 6.28. The experimental intensity and second moment were found to be $21cm^{-2}$ and $2.6 \times 10^4 cm^{-3}$ respectively; an agreement which is probably fortuitous to some extent. Nevertheless, the fact that the correct order of magnitude for these quantities has been predicted gives

some credence to the model proposed by Besnard [92].

Thus, the low frequency far infrared band is well described using a classical description of induced interactions via a quadrupole induced dipole mechanism. There is no evidence from the moment analysis in this spectral range that short-ranged donor-acceptor forces are of any importance.

Theoretical values for other concentrations of iodine in benzene or benzene/hexane mixtures have not been reported. The experimental values are listed in table 6.2.

6.4.4 Fitting to Band Shape Models

The two models outlined in sections 4.2.4 and 4.2.5 that have been used as a solution to the generalised Langevin equation to model our absorption data are essentially equivalent [119] and differ only in the methodology applied to solving the master equation. The application of both approaches is intended to be a useful check of our data and of the two approaches. Although, as mentioned before, the absolute values of the parameters used in the fitting do not have a well defined physical meaning, it is hoped that changes in the parameters with concentration or dilution will yield some information on the systems studied.

Both models fit the data reasonably well, including the low frequency shoulder on the spectrum of iodine-benzene interactions. This particular feature of the spectrum is represented particularly well using the Oxtoby model and is expected to represent the longer-ranged potentials in the system where the shape of the molecules is less important in defining the interaction potential. This shows that the far infrared band may be modelled by considering the induced dipole fluctuations of a single entity in the presence of the surrounding molecules. This lends support to the conclusions drawn in section 6.4.1 where it was thought that one absorption band describes the complex time dependence of the induced dipoles on both molecules.

The fitting parameters used in both approaches for modelling solutions of iodine in benzene and iodine in a 0.5 mole fraction of benzene in hexane are listed in table 6.3. The parameters obtained using the Mori fit to the data presented here for pure benzene agree well with those quoted in the literature [120]. Comparing these values of the Mori parameters for pure benzene to those for the 0.2M iodine in benzene solution (ratioed against iodine in benzene), the value for $K_o(0)$ remains essentially static. The value of $K_1(0)$, however, decreases on addition of iodine. This could be interpreted as being indicative of weaker overall interactions. For the same solution of iodine in benzene with benzene-benzene interactions removed, $K_o(0)$ is still very similar but $K_1(0)$ is now larger than for the pure

benzene case. This might suggest that the iodine-benzene interactions are stronger than the benzene-benzene interactions. If this were the case then to explain the lower value of $K_1(0)$ for iodine in benzene versus iodine in benzene compared with pure benzene, a weakening of benzene-benzene interactions on addition of iodine would have to be envisaged.

As we move from pure benzene interactions, to benzene-benzene plus iodine-benzene interactions, through to iodine-benzene interactions alone, there is a trend in the Mori torque correlation time ($1/\gamma$) to longer times. Thus relaxation is occurring on a longer time scale, in agreement with conclusions drawn from the correlation functions in section 6.4.2.

The Oxtoby approach leads to similar conclusions. The harmonic frequency, ω_o, within the cage changes very little on replacing benzene-benzene interactions with iodine-benzene interactions, and neither does the mean squared fluctuating forces, ω_1. The damping parameter, γ, however decreases significantly on addition of iodine and therefore the damping gets slower in agreement with the results from the Mori approach. The ratio of ω_1 to ω_o gives an indication of the strength of the interaction as discussed in section 4.2.5. As ω_1/ω_o decreases, the strength of the interaction increases, and table 6.3 shows that iodine-benzene interactions are stronger than the benzene-benzene interactions.

As we move to more dilute solutions of iodine in benzene the Mori $K_1(0)$ parameter decreases as would be expected since there is less hinderance to motion. The torque relaxation times, $1/\gamma$, show an increase with concentration for both approaches in contradiction to conclusions drawn from the correlation functions for these solutions.

All other parameters, i.e. $K_o(0)$ for the Mori approach, and ω_o and ω_1 for the Oxtoby approach show little change with concentration. The anomalous value of $K_o(0)$ for the 0.06M iodine solution is likely to be due to poor fitting.

For the dilution studies with hexane the parameters are probably less reliable due to noise in the spectra. The trends observed in the concentration effect on the fitting parameters for the iodine/benzene case appear to be reversed. This was also noted for the relaxation times measured from the correlation functions. This is more likely to be due to poor data than to the effects of cancellation in the many-body terms. The values of ω_1/ω_o, however, in the Oxtoby fit seem to be quite significant and suggest that the interactions are weaker. Another significant difference arising through dilution with hexane is the large fall in the value of the Mori $K_o(0)$ parameter, although $K_1(0)$ does not experience the same extent of drop. This fall in $K_o(0)$ is probably due to an increase in the translational freedom of the system on dilution, as would be expected.

6.5 Conclusions

From the studies on the iodine-benzene system undertaken here it is clear that the interaction of benzene with iodine leads to a different induced far infrared spectrum from that due to benzene-benzene interactions. The correlation functions reveal that the time evolution of the relaxation processes is complicated, but both long and short time processes are discernable. The iodine-benzene interactions are found to relax on a slower time scale than benzene-benzene interactions since their correlation times are longer. Relaxation times taken from fitting of the Langevin equation by two approaches support this conclusion. However, the modelling fails to describe the concentration dependence of the rates of relaxation at short-times. The correlation functions show clearly that relaxation occurs faster as the concentration of iodine is reduced. The fitted parameter, $1/\gamma$, in both the Mori approach and the Oxtoby approach shows the opposite trend.

Comparing the values of the second moments obtained experimentally and through the Mori parameter $K_o(0)$, the agreement in the trends is very good. In table 6.5 the experimental second moment and Mori $K_o(0)$ parameter are compared for each solution after having weighted all the $K_o(0)$ values by the factor which is necessary to make that for pure benzene equal to the experimental value. From this

TABLE 6.5

COMPARISON OF SECOND MOMENTS AND MORI $K_o(0)$ PARAMETER

	M_2/M_o	$K_o(0) \times \frac{3.6}{20.6}$
Pure benzene	3.6	3.6
0.2M I_2/benz (vs. I_2/benz)	3.8	3.6
0.2M I_2/benz	3.2	3.3
0.16M I_2/benz	4.0	3.8
0.06M I_2/benz	10.6	6.6
0.12M I_2/benz/hex	2.5	2.1
0.10 I_2/benz/hex	1.2	1.3

it is evident that the Mori model accounts for the second moment very well for this system.

In general, however, although the models fit the data very well, it is not always clear what the fitted parameters actually mean and, as such, it is difficult to draw valid conclusions from the fitting.

The model of Besnard and Lascombe [92] gives an absolute value of the intensity and second moment for this system which is close to that measured experimentally in this work. The model is based on a quadrupole induced dipole mechanism of interaction and does not include any contributions from short-ranged donor-acceptor attractive potentials. It is concluded that within the limitations of this model it is unnecessary to include any forces other than purely electrostatic ones to describe the iodine-benzene system.

However, the limitations of the model are quite severe, particularly through describing the polarisabilities of iodine and benzene as being isotropic. Much more work is required on different systems and as a function of temperature and presssure to further our understanding of the types of interaction and the relaxation processes involved.

A major contribution to providing new models, or improving existing ones, could be made if a reliable method of inluding effects from the many body terms could be found. The experiments made in this work by dilution studies with

hexane have proved inconclusive, due probably to the limited range of iodine concentrations available that provide spectra with reasonable signal to noise ratio. The greatest difference observed on dilution lies in the Mori fitting parameter $K_o(0)$ which is related to the second moment. This points to a greater degree of translational freedom of the iodine and benzene molecules, which give rise to the induced spectrum, on dilution.

The relaxation times measured from the correlation functions and taken from the fitting procedures show a different trend with iodine concentration when hexane is introduced to the iodine/benzene system. Further dilution work is required in order to discover whether or not this is a real effect. The theory of Lascombe and Besnard [92] predicts a spectral intensity which does not follow Beer's law for different concentrations of hexane or other inert solvent. This is because the three body contribution to the correlation function is not linear with benzene concentration, equation 6.21. Further work on the iodine/benzene/solvent system holding the iodine concentration constant and varying the mole fraction of benzene would be a powerful test of the theory. If the three body contribution has been correctly included in the expression, then a plot of the calculated first and second moments against benzene concentration would not give a straight line, and therefore Beer's law would not be obeyed.

CHAPTER 7

INFRARED ANALYSIS OF LANGMUIR BLODGETT FILMS

7.1 Introduction

A Langmuir-Blodgett film consists of ordered layers of molecules deposited onto a substrate. They are produced by 'dipping' the substrate into a solvent, usually water, which has a monolayer of organic material floating on the surface - the so called Langmuir film. This technique is described in the next section.

The remarkable properties of oil in spreading over a large surface area of water has been recognised since early times. The phenomenon was put to use for its 'stilling' effect on the surface for such diverse applications as oyster-spotting, where oil was placed on the water to reduce the surface-ripples which refracted the light, and for seal-hunting; the fishermen being able to locate the seals because of the stillness of the water above them when they were feeding on oily fish.

Evidence for the strange properties of oil on water, such as the afore-mentioned, where collected by the American statesman Benjamin Franklin and published in 1774 together with his own observations [121].

It was left to Lord Rayleigh, however, to calculate

that the layer of oil could be as small as a monolayer [122]. The research into such films began to be more formalised when Langmuir introduced his 'trough' in which films could be formed and studied in laboratory conditions [123]. Using this he showed how it was possible to study the sizes and shapes of molecules and their orientation at the liquid-air interface. The transfer of these floating monolayers on to a substrate to build up several organic layers was described by Blodgett [124].

Most of the original research and much of the research today involves long-chain fatty acids. These molecules are amphiphilic, i.e. they consist of a long oleophilic hydrocarbon 'tail' and a highly polar hydrophilic acid 'head' at one end. They lie on the surface of the water as illustrated in figure 7.1a.

Since the early pioneering work of Langmuir and Blodgett, there has been a great and varied effort worldwide in research related to the structure and application of these remarkable films. Indeed, it is a subject area which has caught the attention of several notable people including an American Statesman [121] an English Lord [122] and a British Prime Minister [125]. The major advances in this field have been reviewed in several recent papers [126-129].

The applications proposed for these types of film (see section 7.3) depend upon them having well-defined, uniform and homogeneous layers which can be reproduced on a large scale. Infrared spectroscopy can be used as a

Fig. 7.1

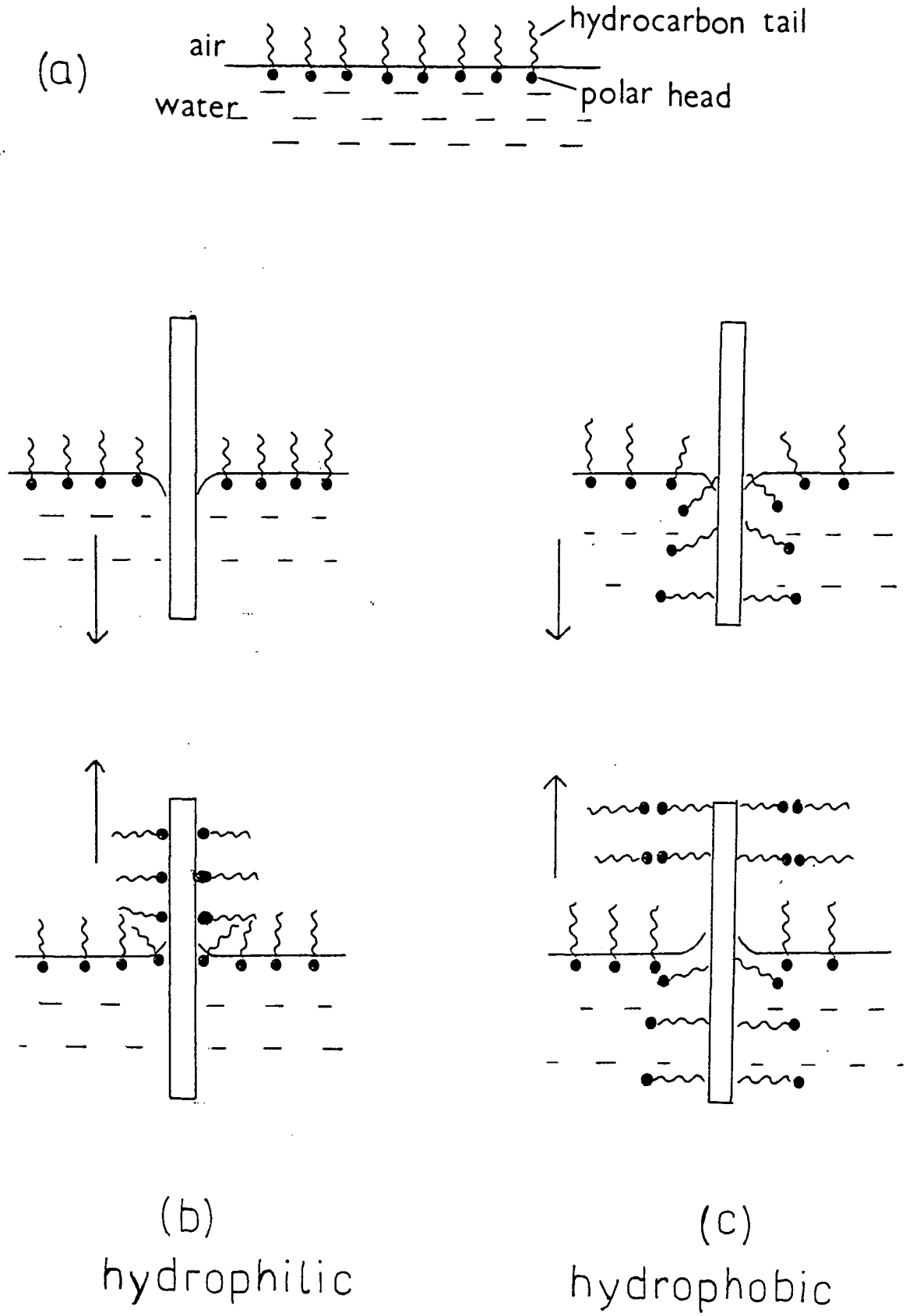
(a)
air
water
hydrocarbon tail
polar head
(b)
hydrophilic
(c)
hydrophobic

Fig. 7.2

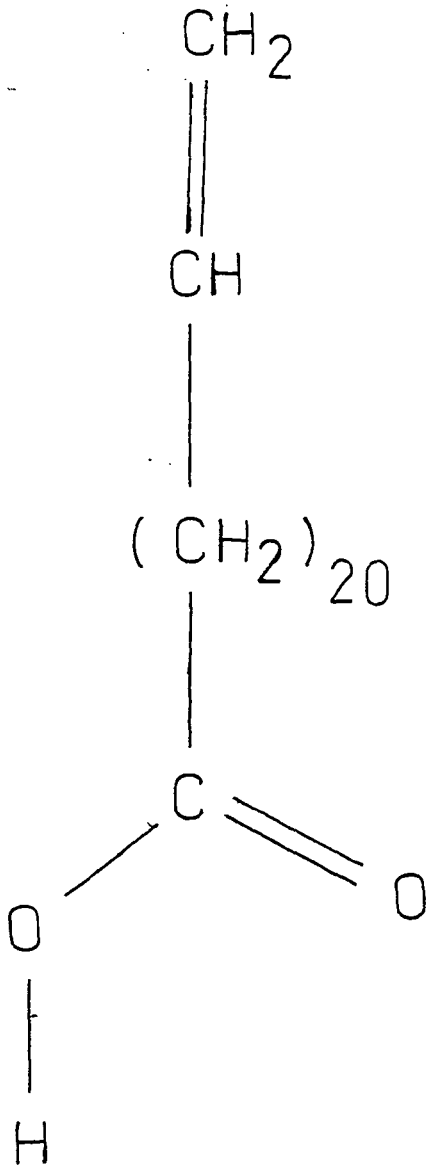

ω – Tricosenoic acid

non-destructive probe to examine the detailed molecular structure of Langmuir-Blodgett films. In this work, the infrared spectrum of ω-tricosenoic acid (figure 7.2) on a silicon substrate has been studied as a function of numbers of layers in order to investigate the structural aspects of the system.

7.2 Production of Langmuir-Blodgett films

There are basically three stages involved in the production of Langmuir-Blodgett films: the formation of a monolayer on the surface of the subphase; the compression of this monolayer to produce a homogeneous film, and the deposition of the film onto a substrate.

7.2.1 Formation of a monolayer

For any controlled experiment on Langmuir Blodgett films it is important to be able to guarantee a good reproducibility of uniform layers. It is essential to work in a clean environment with hyper-pure trough water, and to monitor closely all the conditions such as surface tension and pH.

A small amount of the material dissolved in a suitable volatile organic solvent is introduced to the subphase in the Langmuir trough, figure 7.3, such that, when the solvent evaporates, there is sufficient material to form a monolayer

Fig. 7.3

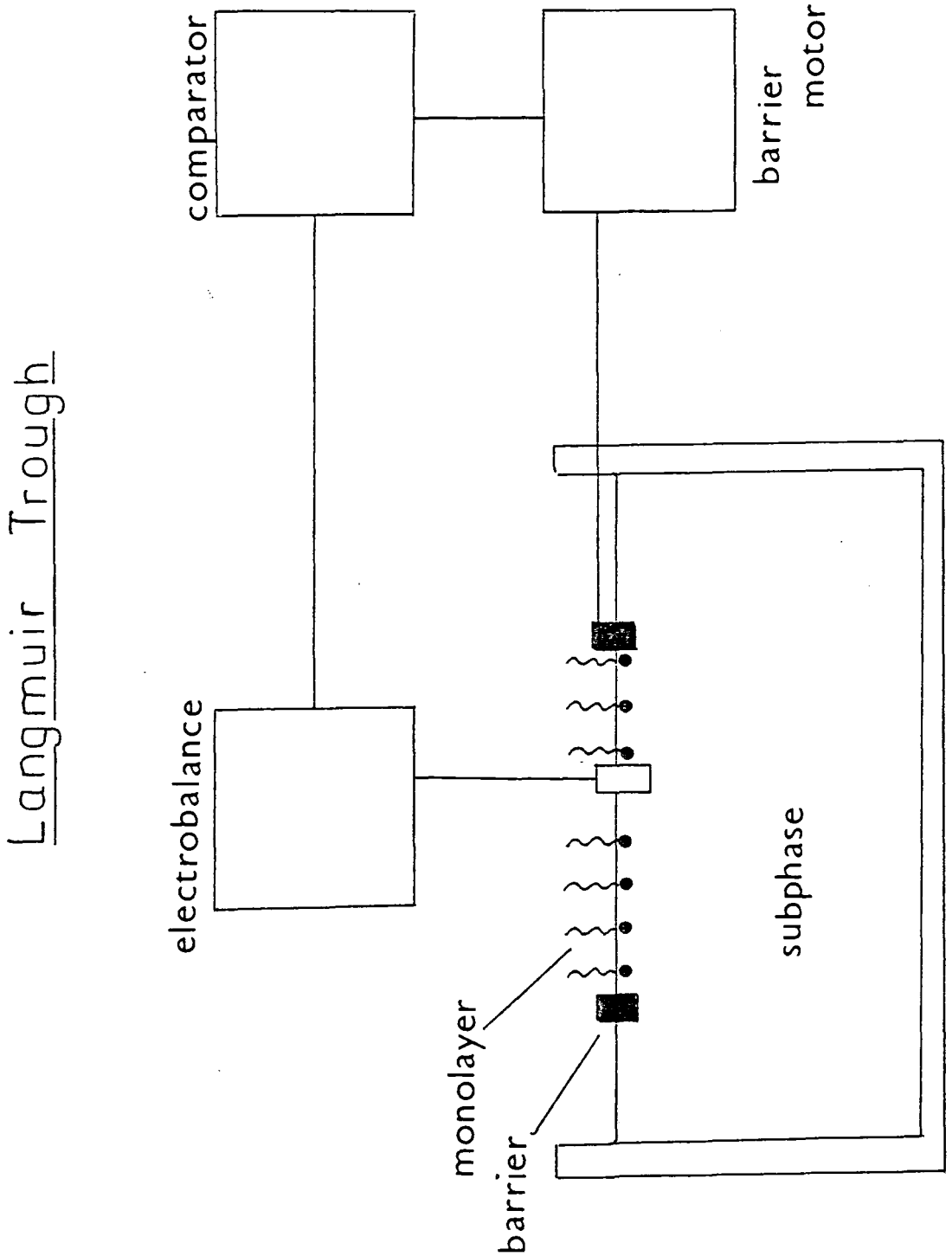
Langmuir Trough
comparator
barrier motor
electrobalance
subphase
monolayer
barrier

only. Chloroform was used as solvent for the ω-tricosenoic samples. The pH can be varied by addition of hydrochloric acid or ammonium hydroxide and, for an organic acid monolayer, will affect the equilibrium between the acid and its salt.

7.2.2 Compression of the Monolayer

In order to produce a homogeneous film, the monolayer must be compressed parallel to the surface in order to bring the molecules close together in an approximately vertical orientation. If the film is not compressed sufficiently then holes will be incorporated into it; if it is over-compressed then it will buckle and the monolayer will be destroyed. This has been achieved using a plastic-coated glass-fibre barrier coupled to a microbalance which continually monitors the surface pressure by means of a Wilhelm sensor [130] at the liquid surface.

As the film is compressed, the surface tension reduces and this can be plotted out as an isotherm of surface pressure versus surface area. By means of this feedback arrangement, the surface tension may be maintained at a constant level as molecules are removed in dipping. This is of vital importance in producing a uniform Langmuir-Blodgett film.

The integrity and purity of the monolayer can be checked before dipping by producing an isotherm over a range

Langmuir Isotherm

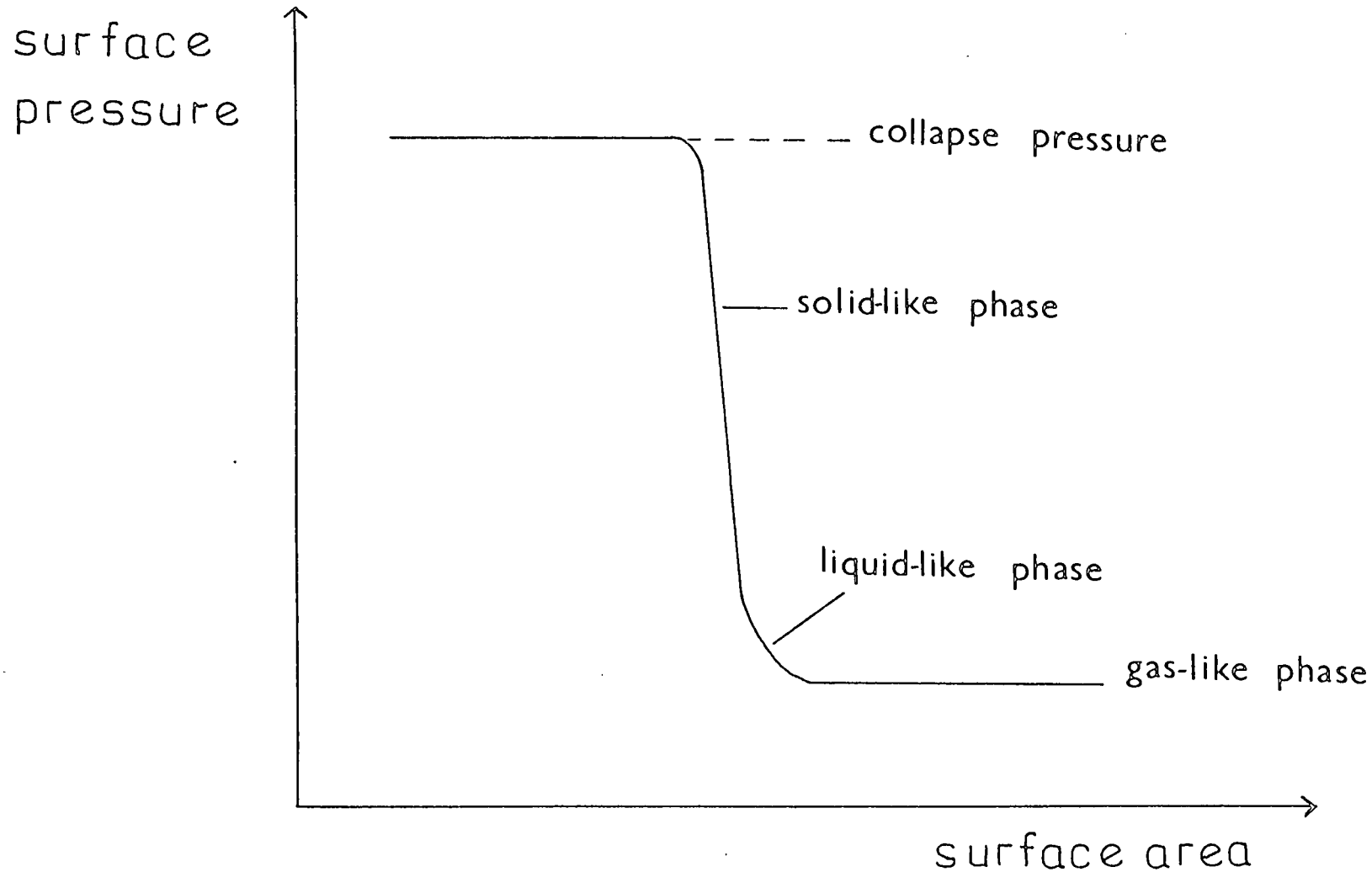

Fig. 7.4

of surface area. A typical isotherm has three distinct regions and is illustrated in figure 7.4.

Dipping is carried out at a pressure corresponding to the solid-like phase.

7.2.3 Deposition on to a Substrate

A monolayer may be lifted off the surface by moving a suitable substrate through it. For a substrate with a hydrophobic surface there is no pick up on the first immersion but, otherwise, a monolayer is deposited at each traverse through the liquid-air interface. This is illustrated for the case of a hydrophilic and a hydrophobic surface in figures 7.1(b) and 7.1(c).

The integrity of the films depend critically on the speed of dipping, and this may be controlled by means of a motor powered micrometer screw system.

Silicon is naturally hydrophilic due to its surface oxide layer and so will pick up only odd numbers of layers after surface grease has been removed by refluxing with e.g. 1,1,1-trichlorethane for half an hour. Removing the oxide layer leaves a hydrophobic layer which picks up even numbers of layers. The oxide layer may be removed by standing the silicon substrate in $Si(CH_3)_2Cl_2$ vapour for several hours. Note that for the two cases, different ends of the first molecule are up against the substrate, figure 7.5.

Fig. 7.5

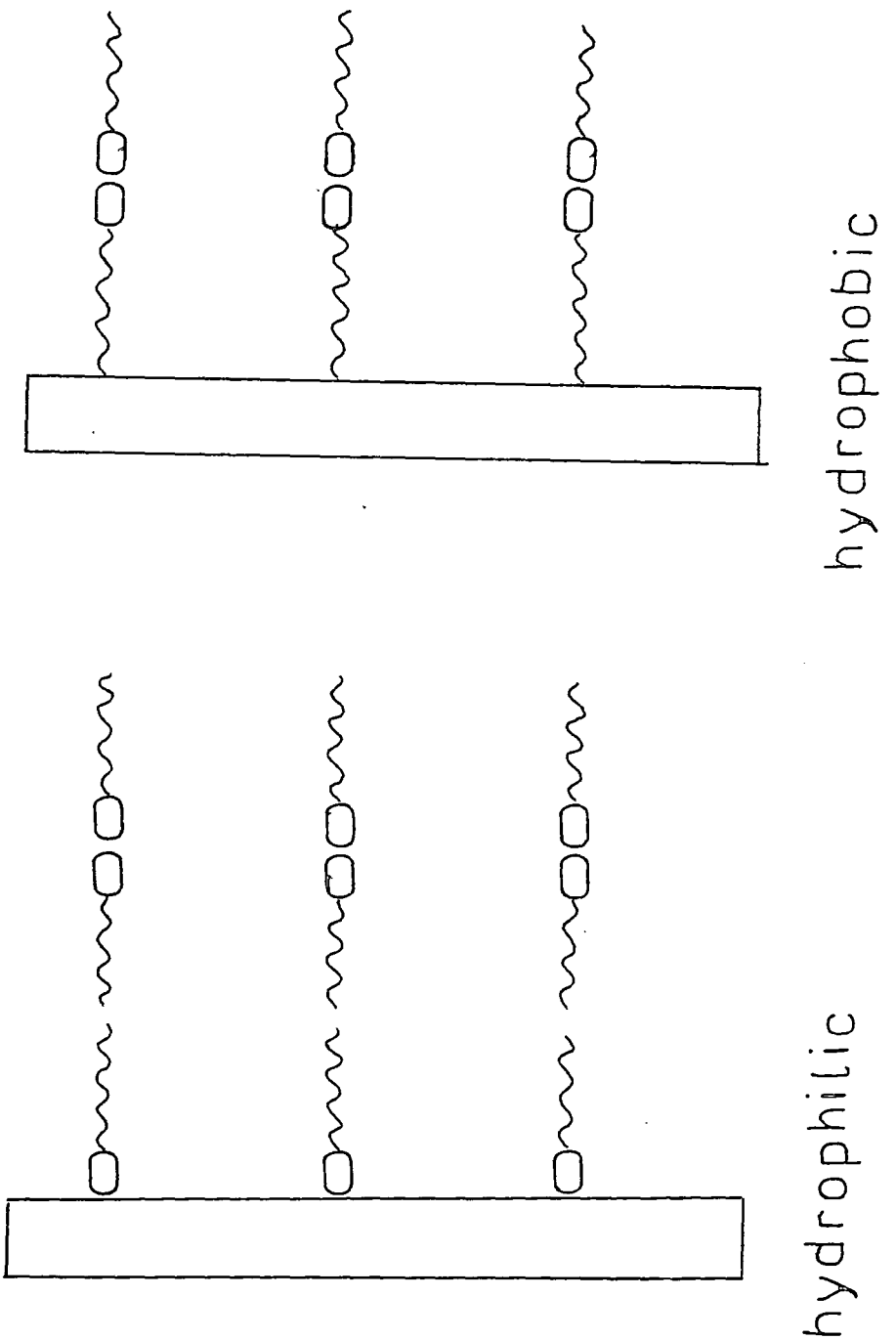

7.3 Application of Langmuir-Blodgett films

Many potential applications for Langmuir Blodgett films have been suggested, and only a few shall be described here. However the main conclusion to be drawn from a discussion of any of these suggestions is that much more work is required in order to increase our understanding of the systems and enable more suitable and better characterised structures to be produced.

The main advantage of Langmuir Blodgett films is that their thickness, d, may be controlled to an extremely high precision. Also, through using different molecules and varying the pH of the subphase, the refractive index, n, may be varied. This immediately suggests an applicability to integrated optics, since the optical properties of thin films are highly dependent on n and d. The propagation characteristics of electromagnetic waves can thus be tailored with a high degree of control using Langmuir Blodgett films, which may therefore be useful as waveguides. As yet, the films have proved too fragile for practical use [131].

Aother potential use for the films is as high impedance metal-insulator-metal cells, e.g. a capacitor microphone. This is such that its sensitivity depends upon the inverse square of the plate separation. With Langmuir-Blodgett film technology enabling deposition of single molecular layers onto a substrate, this sensitivity can be expected to be

very high.

Another important application as an insulator would be in modifying the charge distribution at semiconductor surfaces, particularly where the semiconductor oxide has inadequate insulating properties. Considering the general trend in the size and reduction of electronic components over the last few decades, the high degree of control, on a molecular scale, of the structure of Langmuir-Blodgett films could bring such structures to the forefront of technology [134].

Further applications include uses in simulating biological membranes [132], solar cells [133], biosensors and tunneling devices. These, and others, are described in detail in the reviews referenced in Section 7.1.

7.4 Structural studies of Langmuir Blodgett films by Infrared Spectroscopy

7.4.1 Introduction

Although a dispersive infrared instrument may be used to study Langmuir Blodgett films, it is restricted to measurements of many-layered films. The detailed analysis of films incorporating low numbers of layers, or even just a monolayer, is more suited to a Fourier Transform instrument with its associated advantages (see section 1.2).

Since the molecules constituting the films are highly

orientated it is necessary to take into account certain considerations which would not apply to the bulk materials. The electric field vector associated with an electromagnetic wave is perpendicular to the direction of propagation of that wave. Thus in a standard transmission experiment on a Langmuir Blodgett film, the electric field vector is parallel to the substrate surface (figure 7.6a) and only those molecular groups posessing a component of their transition dipole moment parallel to the surface will contribute to the infrared absorption spectrum. Those groups whose transition dipole moment is perpendicular to the surface will not be seen by normal transmission.

A technique called grazing incidence reflection involves reflecting the infrared beam at an angle of approximately 86° to the surface normal (figure 7.6b). In this case a component of the electric field vector is perpendicular to the surface and thus groups with a transition dipole moment in this direction may be studied using this method. A combination of grazing incidence and transmission infrared allows a detailed description of group orientation by a comparison of relative intensities measured by the two techniques [135].

The absorbance depends on the relative orientation of the infrared electric field, E, and the dipolar transition moment, μ.

These, and other relevant vectors, are illustrated in figure 7.7 for a transmission experiment. If polarised

Fig. 7.6

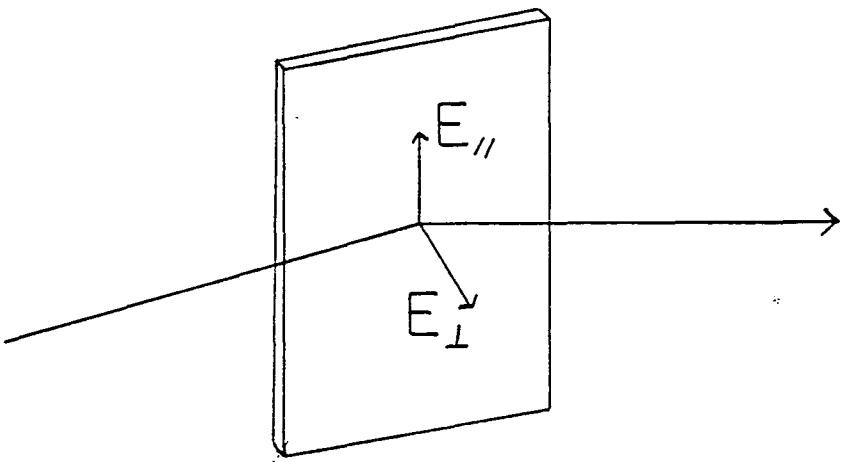

(b) grazing incidence

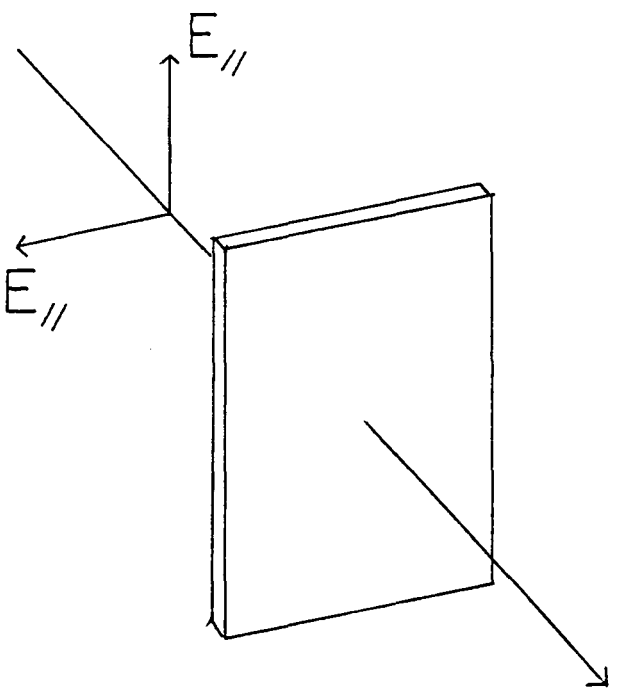

(a) normal incidence

Fig. 7.7

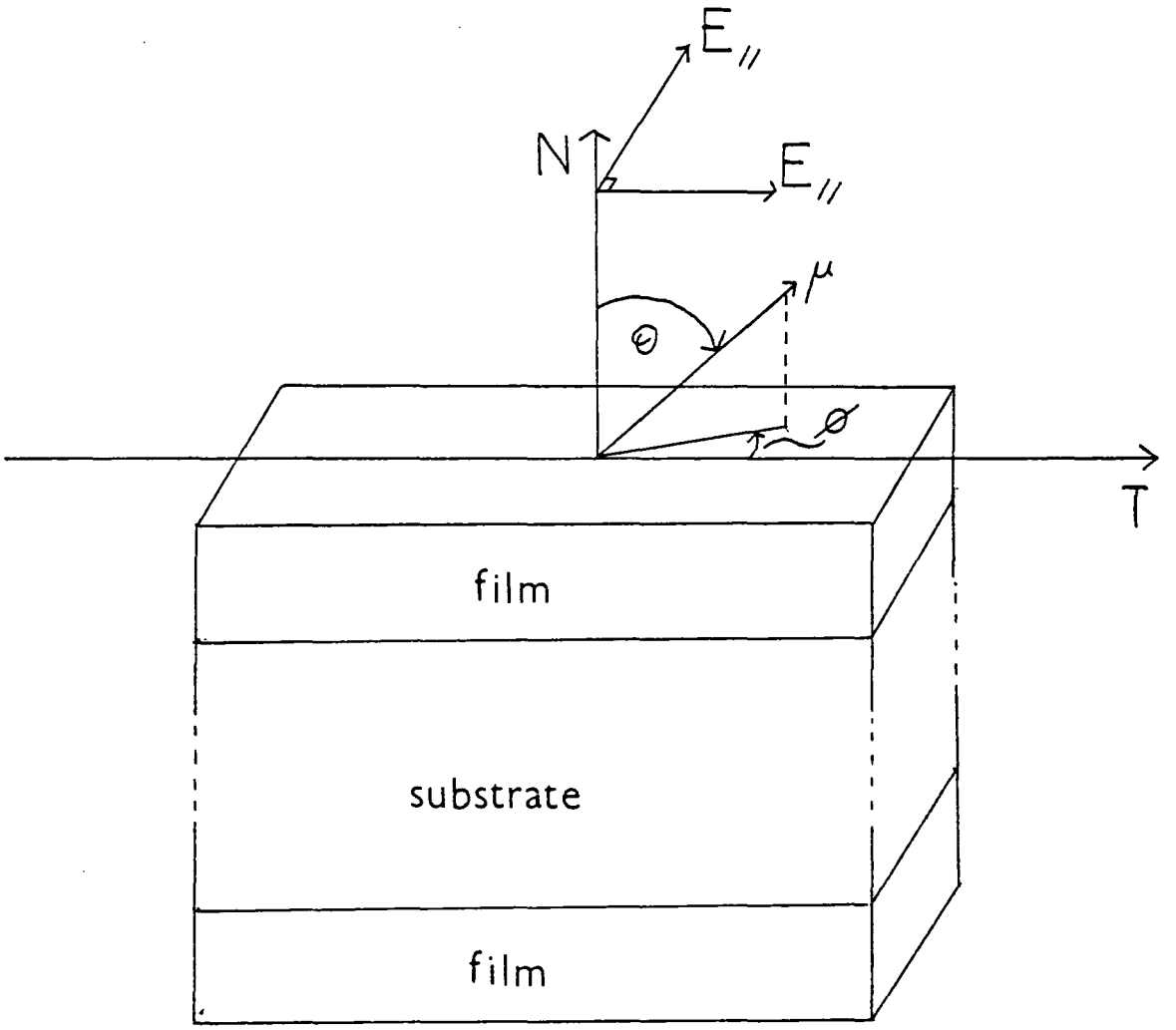

N - normal

T - transfer direction

radiation is used then only one component of $E_{\parallel}$ will be operative, and differences in absorbance spectra for vertically and horizontally polarised light can provide important information on the orientation of certain groups.

7.4.2 Orientation of films on the substrate

The fatty acid layers, once deposited on the substrate, form crystalline regions [136-138] as distinct from the hexagonal close-packed arrangement they exhibit on the subphase [138]. These crystal phases may be orthorhombic, monoclinic or triclinic in character and they each lead to different orientations of the hydrocarbon chain relative to the substrate.

Many fatty acids and their salts have been studied on different substrates by infrared spectroscopy, the earlier studies typically being done on many-layer structures. More recent studies, hwever, have concentrated on the structures of the first few layers deposited onto the substrate. A typical example is stearic acid which was studied as a many-layer assembly [139] in which the hydrocarbon chains of the acid molecules were found to be orientated away from the normal in the direction of transfer, T. A more recent study [140] using attenuated total reflection (ATR) on between one and nine layers of stearic acid on germanium has shown, by examination of the CH_2 scissoring band (δCH_2), that the first layer deposited

exhibits orthorhombic packing, perpendicular to the surface, and subsequent layers crystallise in the monoclinic form with the chain axes at an angle of approximately 30° to the normal.

A similar ATR study of calcium arachidate on glass plates [141] showed that these acid salts stand with their hydrocarbon chains perpendicular to the substrate surface. This was later confirmed [142] by monitoring the carbonyl band intensity through a combination of grazing incidence reflection and normal transmission experiments.

Previous infrared studies of ω-tricosenoic acid [142,144] have been performed on forty one layers of the acid on a calcium fluoride substrate. normal incidence and variable angle incidence geometries were employed, as well as polarised incident radiation. It was concluded that the films were orientated at approximately 18° to the normal, along the transfer direction, such that the crystals were in the monoclinic form. The tilt towards the direction of transfer was attributed to hydrodynamic flow (figure 7.8) in the sub-phase at the point of deposition. It was shown further that the orientation was related to film compressibility in the sub-phase, and does not occur if the film is in a solid compact state. Such a state was shown to be not possible for ω-tricosenoic acid, but possible at sufficient surface pressure for its saturated analogue, behenic acid.

A more recent infrared study of one, three and nine

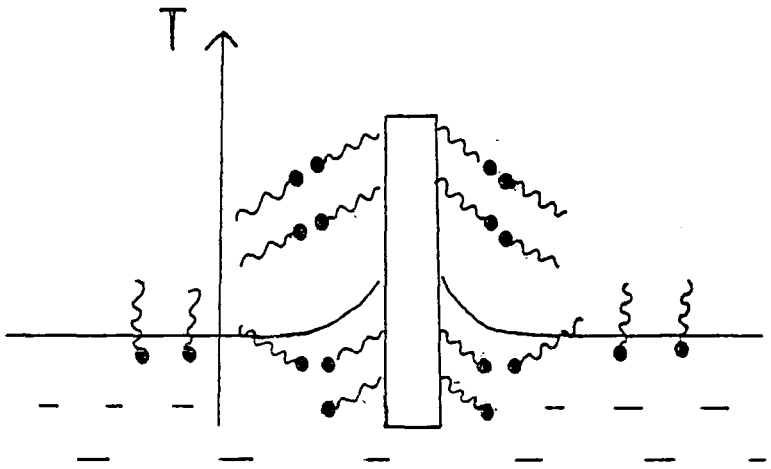

Fig. 7.8

Fig. 7.9

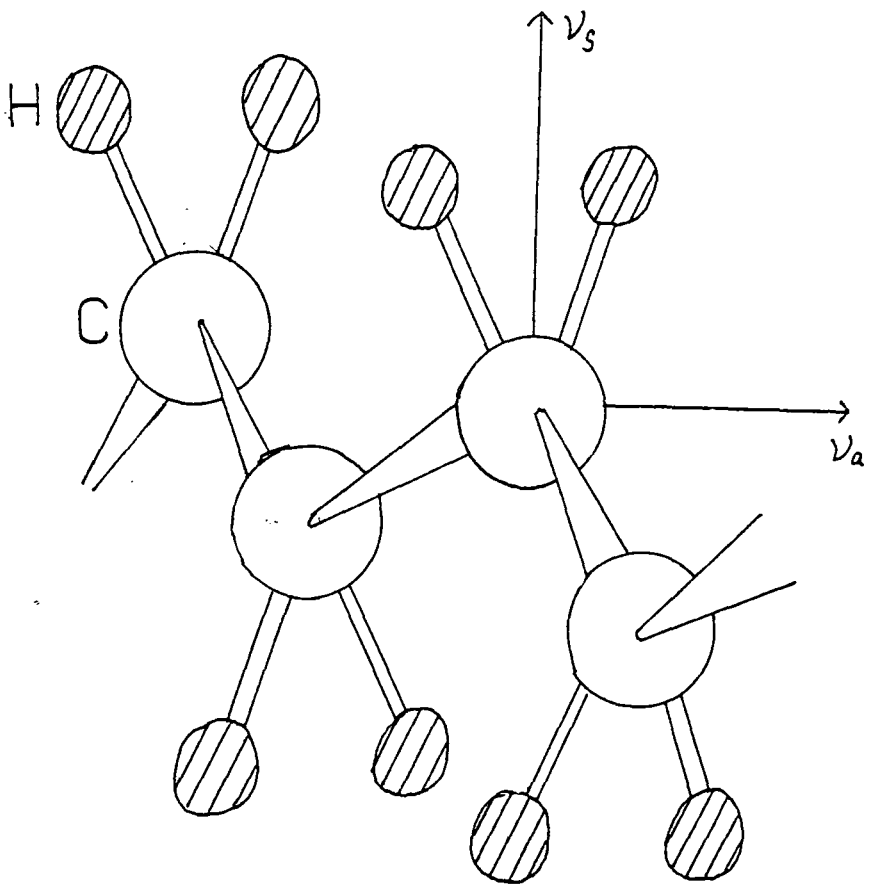

layers of ω-triceosenoic acid on an aluminium substrate [145] has provided evidence that the first layer is orthorhombic, with molecular chains perpendicular to the substrate, and increasing layers tilt progressively towards 18° to the normal in the direction of transfer.

7.4.3 Band assignments

Assignments of the major bands for Langmuir Blodgett films quoted in the literature and obtained in this work are presented in table 7.1.

The δCH_2 scissoring mode is split due to the crystal field as is characteristic of n-alkanes [148]. The relative intensities of these two modes depend strongly on the angle of incidence of radiation [143].

The symmetric and asymmetric, ν_s and ν_a, stretching vibrations of the CH_2 groups have transition dipole moments perpendicular to the chain axis, as shown in figure 7.9. As they are mutually perpendicular their relative intensities are sensitive to the polarisation of incoming radiation [140].

The acid dimer band should be split into a doublet depending on the position of the C_β carbon atom [147] (see figure 7.10) which can be cis or trans to the carbonyl group. When cations are present in the sub-phase, no bands due to acid dimers are present in the spectrum [142]. Studies of stearic acid on germanium [140] revealed that

TABLE 7.1

MODE	LITERATURE ASSIGNMENTS	THIS WORK
ν_a CH_2	3086cm^{-1} [a], 2919cm^{-1} [b]	2920cm^{-1}
ν CH	3000cm^{-1} [a]	3074cm^{-1}
ν_s CH_2	2980cm^{-1} [a], 2850cm^{-1} [b]	2850cm^{-1}
ν C=O (free acid)	1745cm^{-1}	
ν_{cis} C=O (acid dimer)	1709cm^{-1} [c], $\sim$ 1710cm^{-1} [d]	1698cm^{-1}
ν_{trans} C=O (acid dimer)	1699cm^{-1} [c]	
ν C=C	1644cm^{-1} [a]	1641cm^{-1}
ν_a CO_2^- (salt)	1590cm^{-1} [a], 1542cm^{-1} [b]	
δ" CH_2	1474cm^{-1} [b], 1472cm^{-1} [d]	1473cm^{-1}
δ' CH_2	1462cm^{-1} [b], 1462cm^{-1} [d]	1465cm^{-1}
ν_s CO_2^- (salt)	1472cm^{-1} [a], 1432cm^{-1} [b]	

a $CH_2CH(CH_2)_{19}CO_2H$ on oxidised aluminium [146]

b $CH_3(CH_2)_{18}COO^-$ on silver [142]

c $CH_3(CH_2)_{10}COOH$ bulk [147]

d $CH_2CH(CH_2)_{20}CO_2H$ on C_aF_2 [144]

Fig. 7.10

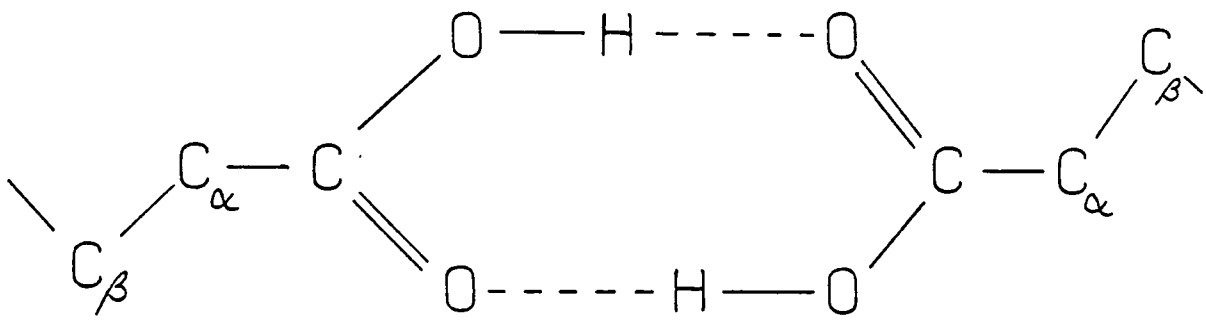

Cis

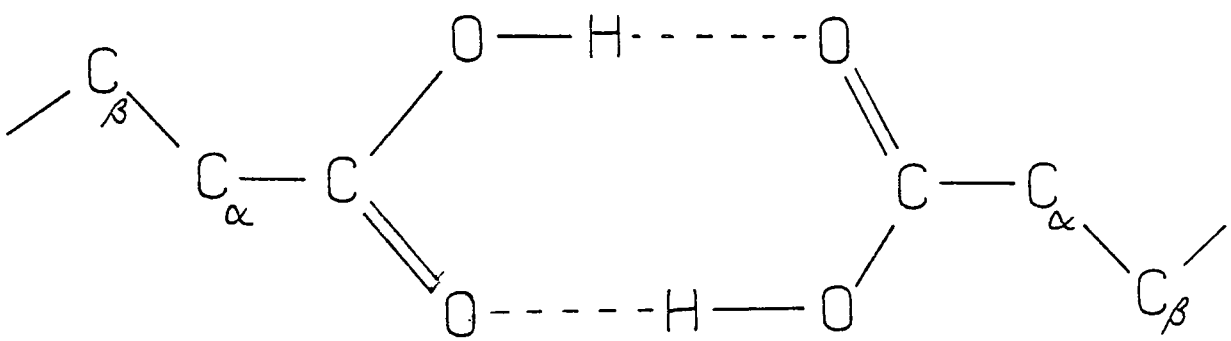

Trans

this acid is in the cis configuration for the first monolayer but in the trans configuratin for subsequent layers.

7.4.4 Band Intensities

Previous infrared analyses of Langmuir Blodgett films have shown that there are generally no frequency shifts or line-width changes with respect to the numbers of layers [140,149]. A study of calcium arachidate on a silver substrate [149] showed a linear plot of $\nu_s(CO_2^-)$ versus number of layers between four and ten layers. Below this number the intensity was less than expected, and this was interpreted as evidence for patches in the first few films. A similar plot for $\nu(CH_2)$ revealed a straight line of a different slope. A separate study of one to nine layers of stearic acid on germanium [140] showed linear plots of intensity versus number of layers for the carbonyl band and the $\nu(CH_2)$ bands. The slopes were approximately parallel. An interesting feature of this study was the lack of observation of any carbonyl intensity at monolayer coverage.

7.5 Experimental Details

The Langmuir-Blodgett films used in this work were prepared in the department of Applied Physics in the

University of Durham. The silicon substrate was 2Ω resistance cut in the <100> plane. Each substrate measured 6cm by 2cm and was half blank and half covered with ω-tricosenoic acid. In this way, the same piece of silicon wafer could be used for both sample and background runs simply by sliding along a holder built especially for the purpose.

The samples were stored at all times in an inert atmosphere (dry nitrogen or vacuum) and in the dark. They were handled carefully with tweezers to avoid contact with skin and possible transfer of grease to the films. The sample compartment of the spectrometer was well purged with dry nitrogen before and during the experiment.

Large numbers of scans were required to achieve a reasonable signal-to-noise ratio, particularly for films with very few layers at acid. The maximum number of scans used for one run was 41000, equivalent to a run-time of over five hours.

7.6 Results and Discussion

Spectra of 1,2,3,4,5,6,7,8,11 and 12 layers of ω-tricosenoic acid on silicon substrate are presented in figures 7.11 to 7.30. Spectra covering the region 1900 cm^{-1} to 1300 cm^{-1} have been smoothed.

Many of the spectra have a large water-band centred at approximately 3300 cm^{-1}. This is due to a recurring problem

of the detector window icing up during the course of an experiment. The water-band is not evidence for water in the film since this band can change dramatically between different runs for the same film. Compare for example, figure 7.31 with figure 7.21.

A notable feature of the spectra is that the quality is very variable and does not, as expected, increase with the number of layers. This may point to a difference in the quality of the films themselves. The spectrum of three layers (figure 7.16) has a clearly discernable well-defined carbonyl band whereas that for four layers (figure 7.18) or that for eleven layers (figure 7.28) is very poor.

The band shapes and positions (table 7.1) do not vary throughout the spectra.

Band intensities were measured from the integrated area where the signal to noise level was good or, otherwise, from peak heights. The intensity of the CH_2 stretching bands and the dimer C=O band as a function of number of layers are shown in figures 7.32 and 7.33. The plot for the CH_2 groups lies on a straight line which may be extrapolated to zero for no coverage. However, the carbonyl band exhibits a zig-zagging rise in intensity with increasing layer deposition with odd layers lying above the mean slope. Although this phenomenon has been predicted [149] its observation has not been reported in the literature.

An identical experiment was performed [150] using the same Langmuir Blodgett structures, and a similar zig-zagging

plot was observed for the carbonyl band intensities. In this case, however, the alternation in intensity with successive layers occurred in the opposite manner (odd layers below the mean slope). The only difference between the experiments was that a different Fourier Transform spectrometer was used to collect the data. This, however, provides an explanation of the discrepancies between the two sets of data.

As a consequence of the beamsplitter material and orientation, the radiation incident on the sample is partially polarised in a vertical direction [20]. The set of data presented in figures 7.11 to 7.31 were recorded with the Nicolet 60SX spectrometer whereas the second set of data [150] were recorded with a Mattson Sirius. The mirrors labelled M8 and MF5 in the illustration of the Nicolet optics (figure 3.14) cause the polarisation of light to be rotated through 90°. There is no such rotation of polarisation for the Mattson optics. Thus in one experiment the beam is partially horizontally polarised, and in the other experiment it is partially vertically polarised. Now since oriented groups are very sensitive to the beam polarisation they will produce different intensities for different polarisations.

The fact that a different type of alternation is seen between the two experiments must point to the presence of a difference in orientation of one layer relative to the previous one, at least for the first few layers. For

conclusive corroboration of these results it would be useful to repeat the experiments with fully polarised light.

Support is leant to these conclusions by a recent study [151] on the same ω-tricosenoic acid-silicon system by reflection high energy electron diffraction (RHEED). A seven layer sample from this study was shown to be tilted at an angle of 20° to the normal along the transfer direction. However, for one, three and five layers the direction of tilt was found to be random. Layers comprising of two and four layers (hydrocarbon chain up against the silicon) were found to be orientated in the transfer direction.

For odd numbers of layers the carbonyl group is against the substrate. There is evidence that a strong bond is formed between the two [152] and although its choice of orientation is random, once chosen this orientation remains fixed regardless of the orientation of further deposited layers. However, further deposited layers become more and more susceptible to influence by hydrodynamic flow until, by the seventh layer, all subsequent molecules are oriented in the transfer direction.

Even numbers of layers have their hydrocarbon chain end in contact with the substrate and this is not expected to form a strongly orientated physical or chemical bond and is thus more readily influenced by hydrodynamic flow. The second layer must adopt the same orientation as the first to maximise the delocalisation energy of the acid dimer by maintaining planarity.

Thus the structure in the first few monolayers is critically dependent on the chemical nature of the substrate surface and the orientation of these layers is determined to a large extent by the orientation of the first layer. This epitaxial development in molecules of ω-tricosenoic acid on silicon has been observed elsewhere [153] where it was also noted that the presence of cations in the subphase tends to inhibit the process.

The presence of a dimer carboxylate band in the spectrum of the monolayer may be indicative of the fact that several molecules are actually lying parallel to the surface. This has been observed elsewhere [153]. An alternative explanation is that there is an interaction between adjacent carbonyl groups along the surface of the substrate to form a delocalised system as illustrated in figure 7.42. In such a case, the carbonyl stretching bands are expected to occur in the same region as the dimer bands.

Since the fatty acid films are deposited from an aqueous subphase, water molecules are likely to be incorporated into the overall structure. This may have important consequences on the properties of the Langmuir-Blodgett films. Furthermore, the extent and effect of water-vapour uptake from the atmosphere is largely unknown. As an attempt to investigate the extent of this water uptake and, at the same time, the ageing of the films, the structures with five and six layers were left open to

the atmosphere for a period of several weeks. The infrared spectrum was then taken and the results are presented in figures 7.34 and 7.37. These can then be compared to the spectra recorded on the fresh films, figures 7.19 to 7.22. Little change can be seen for the six layer sample, but the spectrum of the five layer sample has changed considerably, particularly in the $1900cm^{-1}$ to $1300cm^{-1}$ region. This appears to be due to degradation of the film. Further work is necessary to investigate whether this means that odd numbered layers are more susceptible to degradation than even numbered layers, or whether the dipping parameters have a bearing on the durability of the films.

In both samples there is a distinct change in the spectrum around $1525cm^{-1}$, and this appears to be due to uptake of impurities e.g. grease, since it can appear on the film (figure 7.37) or on the substrate (figure 7.35).

Any study of the uptake of water from the Langmuir trough or the atmosphere is hampered by the presence of ice on the detector window as mentioned earlier. However, the samples with five and six layers were placed in a dessicator which was pumped down to 10^{-5} torr for five hours. It was hoped that this would remove most of the water from the films. The spectra recorded after pumping are presented in figures 7.38 and 7.41. No distinct changes can be seen from the spectra shown in figures 7.34 to 7.37. The water band above $3100cm^{-1}$ seems to be dominated by the ice on the detector window.

7.7 Conclusions

Fourier transform infrared spectroscopy provides a powerful non-destructive tool for the study of Langmuir-Blodgett films, even down to a monolayer. The CH_2 stretching bands show an intensity varying linearly with numbers of layers deposited. The carbonyl stretching bands, at low numbers of layers, show a zig-zagging pattern which is interpreted as a change in the orientation of successive layers, in agreement with other recent studies [151].

The observation of this zig-zagging of the carbonyl intensities is thought to be made possible by the partially polarised nature of the incident infrared beam. Future studies of the detailed structure of these films would be considerably enhanced by comparing results from normal incidence and grazing incidence spectroscopies and studies with fully polarised incident radiation. Attenuated total reflection spectroscopy shows great promise for the study of films down to monolayer coverage.

The orientation of the first few layers is thought to be critically dependent on the chemical nature of the substrate surface. The orientation of the first layer seems to determine the orientation of successive layers. Hydrodynamic flow at the liquid-air interface of the Langmuir trough may play an important role in determining the structure of these films.

Studies on the ageing properties of these films, and on incorporation of water have proved somewhat inconclusive. Further investigations of this nature need to be done on a greater variety of layer-numbers and as a function of dipping parameters. A severe problem arises from the presence of ice on the detector window, and this must be eliminated before meaningful studies of water incorporation can be carried out.

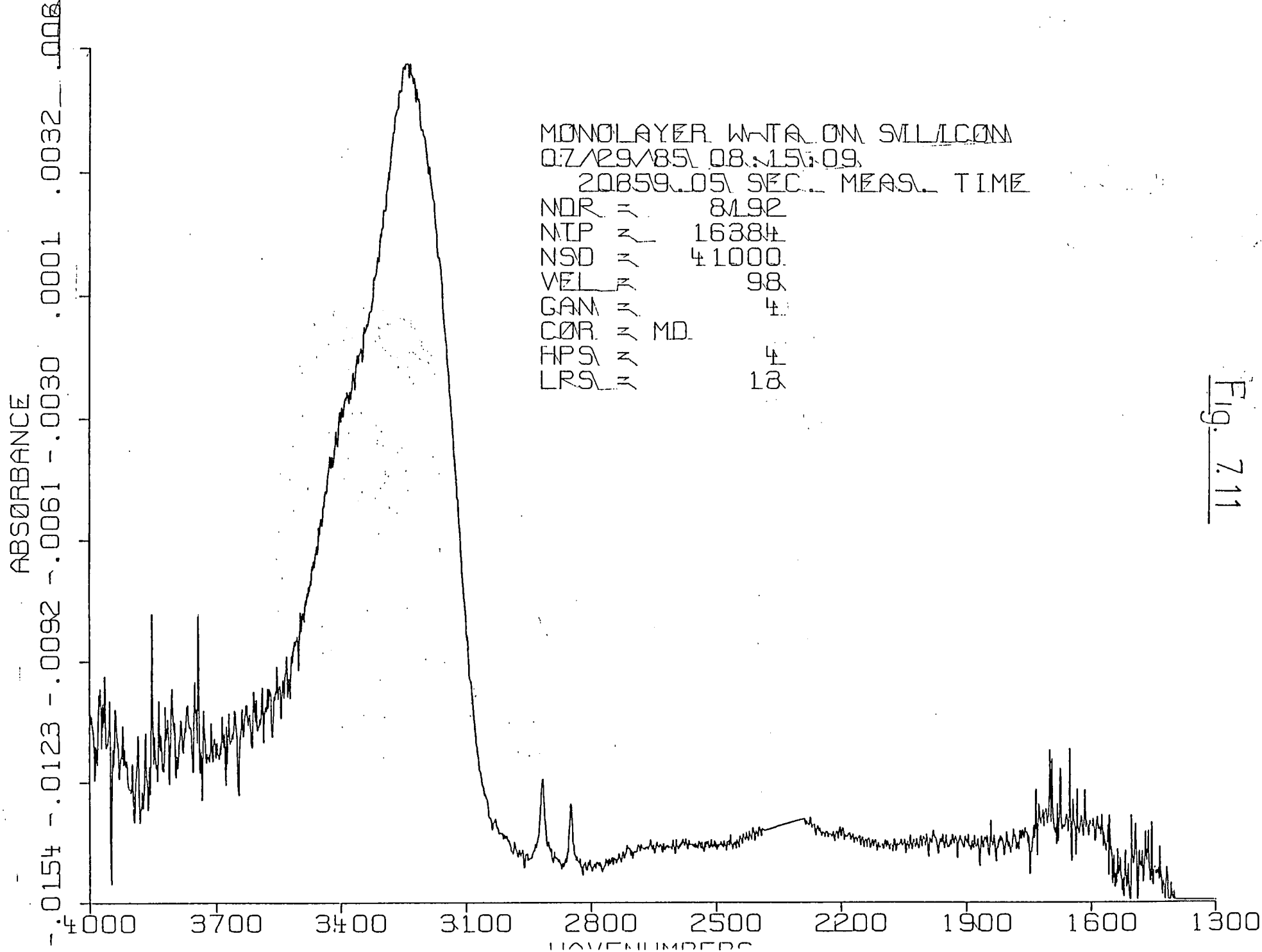
MONOLAYER WATER ON SILICON
07/29/85 08:15:09
20859.05 SEC. MEAS. TIME
NDR = 8192
NTP = 16384
NSD = 41000.
VEL = 98
GAN = 4
COR = MD
HPS = 4
LRS = 12
ABSORBANCE
-.0154 -.0123 -.0092 -.0061 -.0030 .0001 .0032
4000 3700 3400 3100 2800 2500 2200 1900 1600 1300

Fig. 7.11

ABSORBANCE
-.01753
.01715
.01677
.01639
.01601
.01563
.01525
1900
1825
1750
1675
1600
1525
1450
1375
1300
1886.251
1870.013
1840.649
1794.718
1695.305
1675.118
1647.025
1621.746
1579.793
1567.690
1560.168
1535.485
1514.724
1499.221
1463.284
1421.603
1402.777
1390.982
1369.373
monolayer

Fig. 7.12

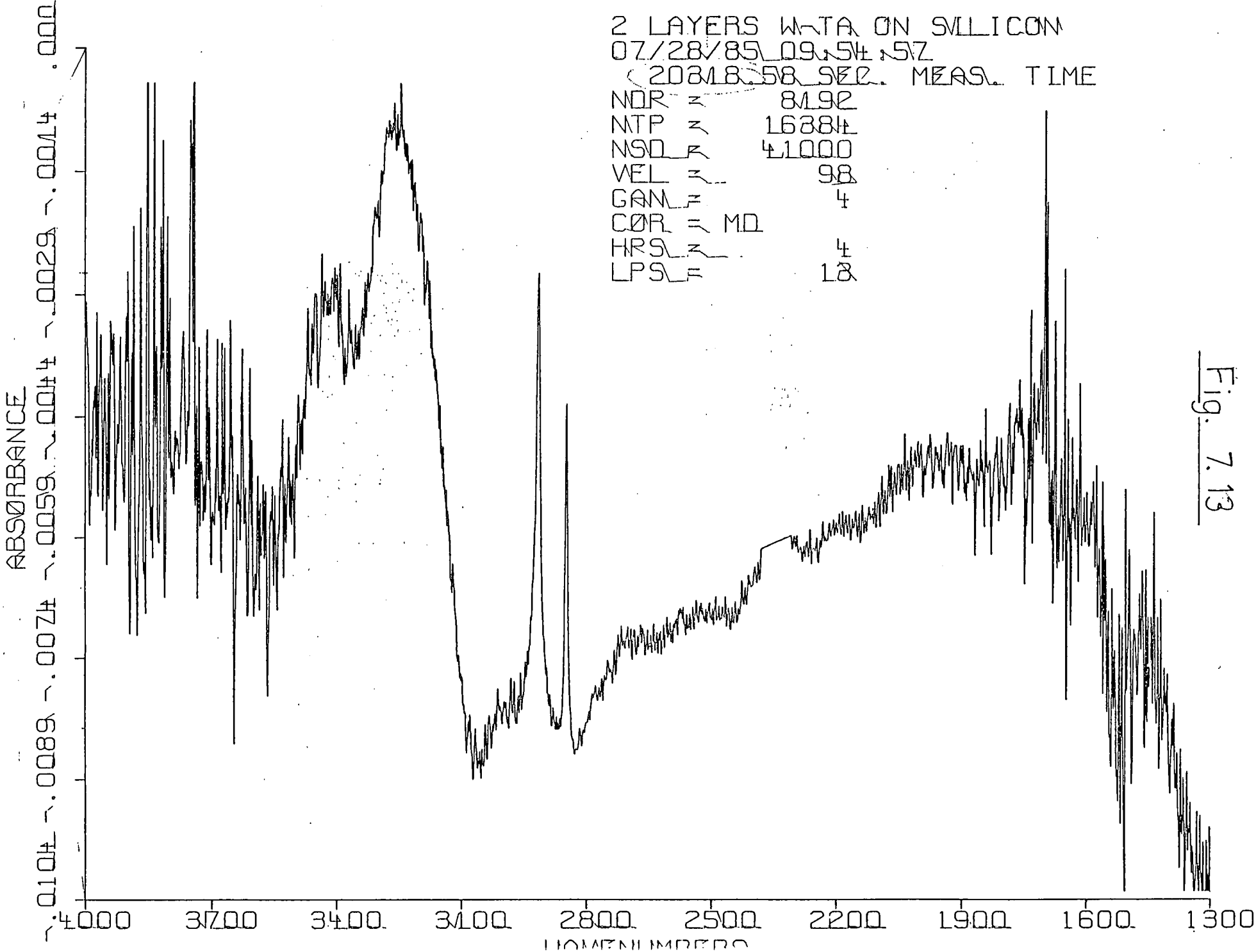
2 LAYERS WATA ON SILICON
07/28/85 09:54:57
20818.58 SEC. MEAS. TIME
NDR = 8192
NTP = 16384
NSD = 41000
VEL = 98
GAN = 4
COR = MD
HRS = 4
LPS = 18
ABSORBANCE
-.0104 -.0089 -.0074 -.0059 -.0044 -.0029 -.0014 .000
4000 3700 3400 3100 2800 2500 2200 1900 1600 1300

Fig. 7.13

Fig. 7.14

2 layers
ABSORBANCE
-.010k
-.0089
-.007k
-.0059
-.004k
-.0029
-.001k
.000
1900
1825
1750
1675
1600
1525
1450
1375
1300

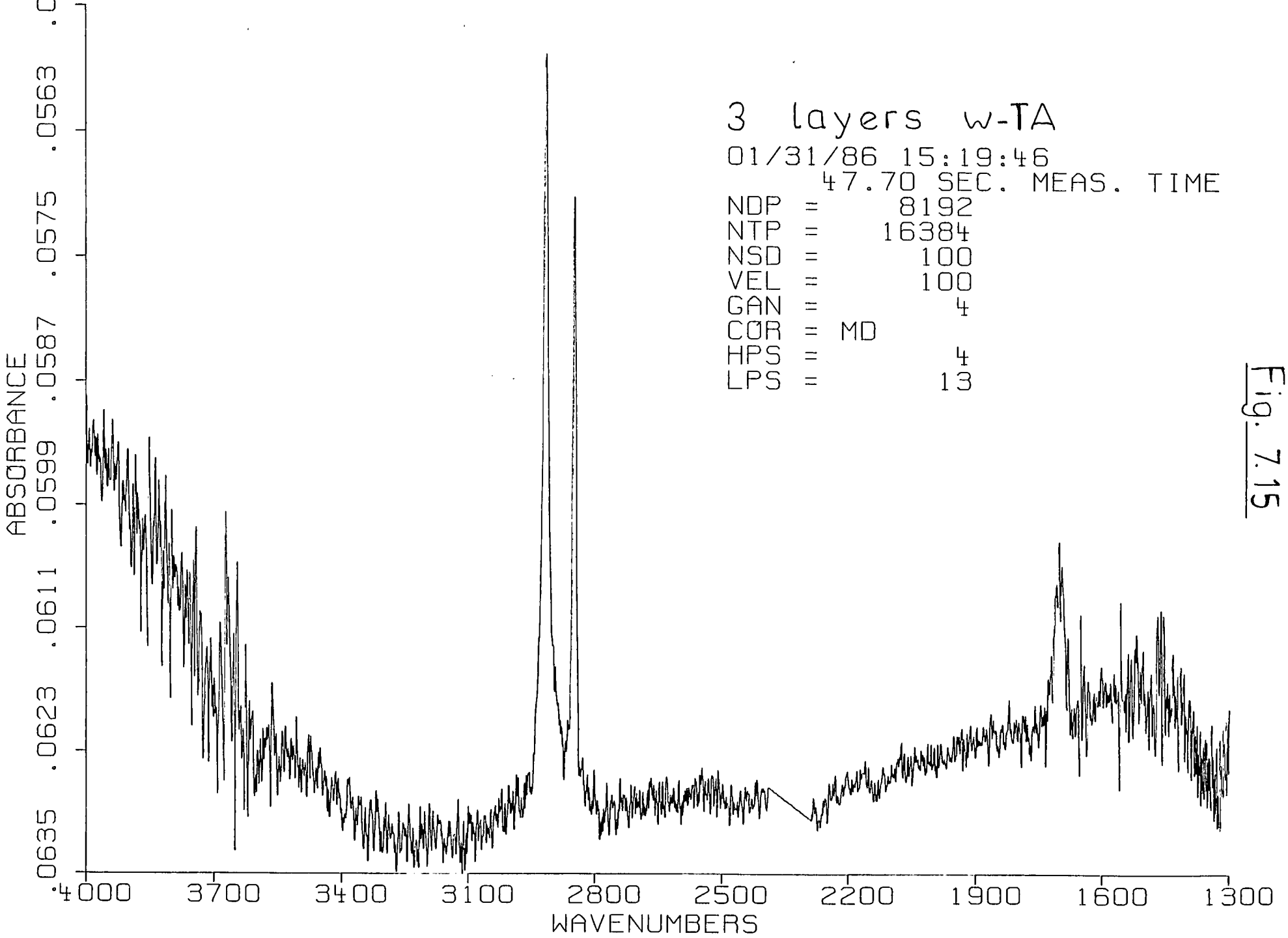
3 layers w-TA
01/31/86 15:19:46
47.70 SEC. MEAS. TIME
NDP = 8192
NTP = 16384
NSD = 100
VEL = 100
GAN = 4
COR = MD
HPS = 4
LPS = 13
ABSORBANCE
.0635 .0623 .0611 .0599 .0587 .0575 .0563
4000 3700 3400 3100 2800 2500 2200 1900 1600 1300
WAVENUMBERS

Fig. 7.15

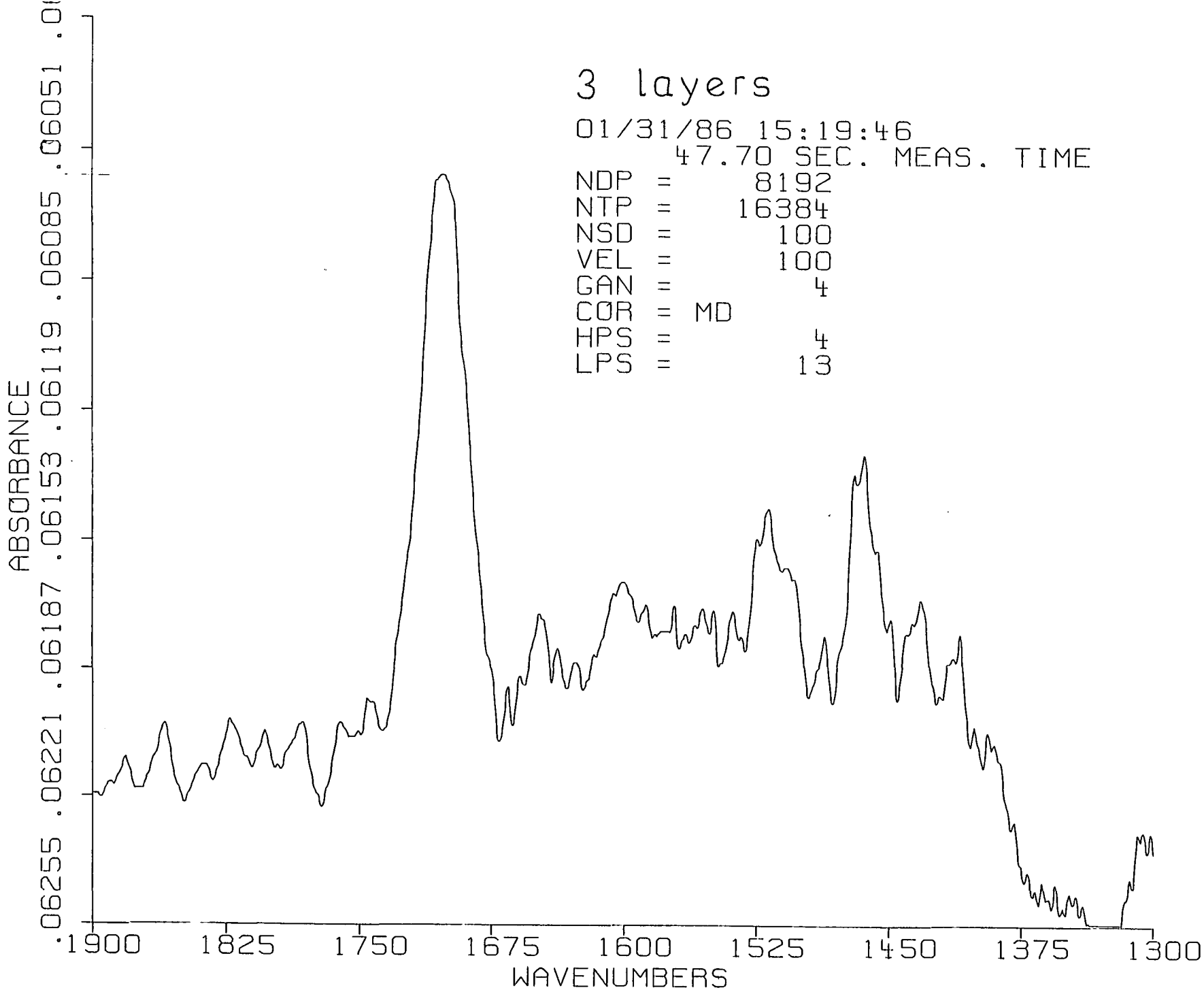
3 layers
01/31/86 15:19:46
47.70 SEC. MEAS. TIME
NDP = 8192
NTP = 16384
NSD = 100
VEL = 100
GAN = 4
COR = MD
HPS = 4
LPS = 13
ABSORBANCE
.06255 .06221 .06187 .06153 .06119 .06085 .06051
1900 1825 1750 1675 1600 1525 1450 1375 1300
WAVENUMBERS

Fig. 7.16

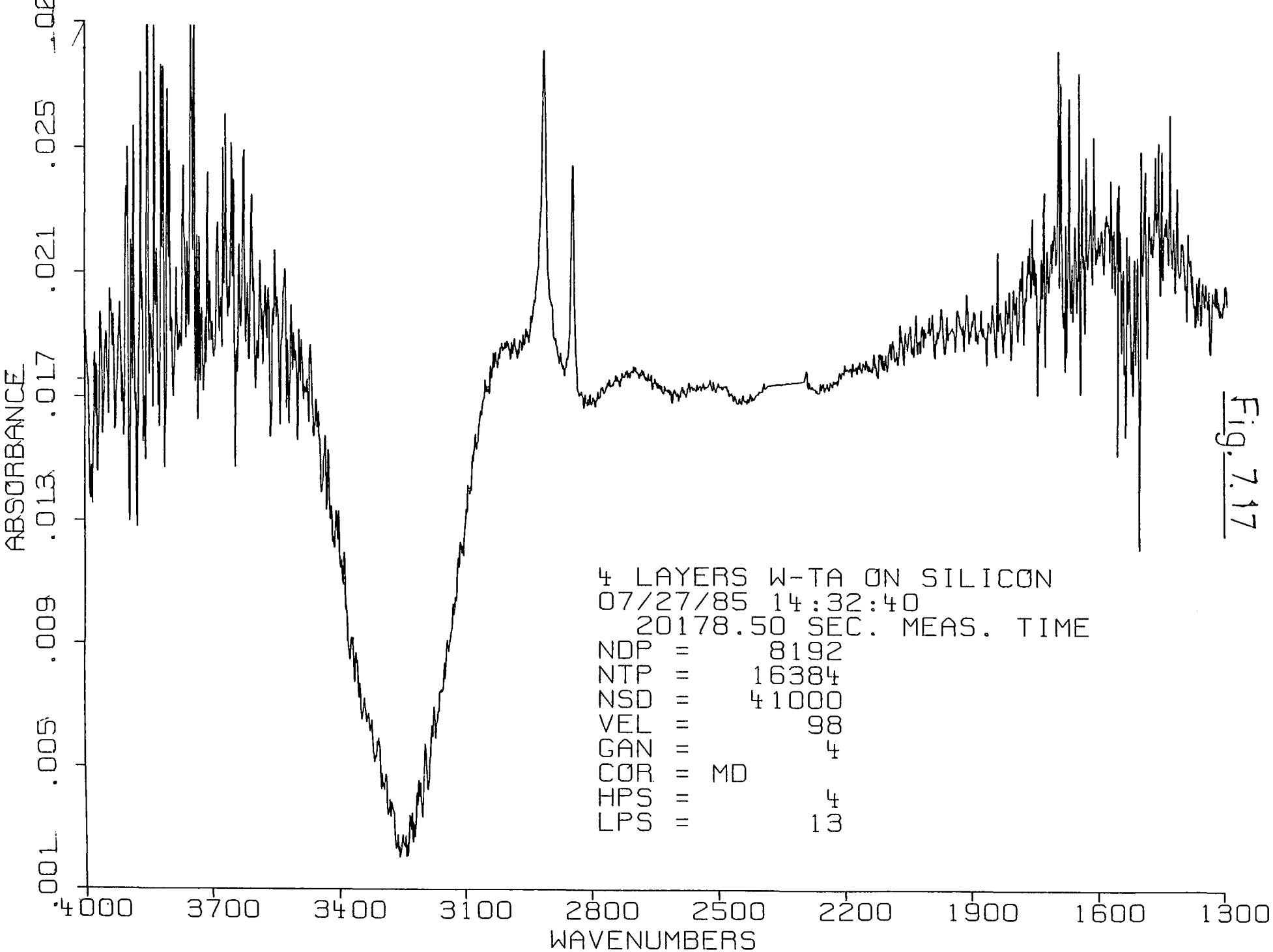
ABSORBANCE
.001
.005
.009
.013
.017
.021
.025
4000
3700
3400
3100
2800
2500
2200
1900
1600
1300
WAVENUMBERS
4 LAYERS W-TA ON SILICON
07/27/85 14:32:40
20178.50 SEC. MEAS. TIME
NDP = 8192
NTP = 16384
NSD = 41000
VEL = 98
GAN = 4
COR = MD
HPS = 4
LPS = 13

Fig. 7.17

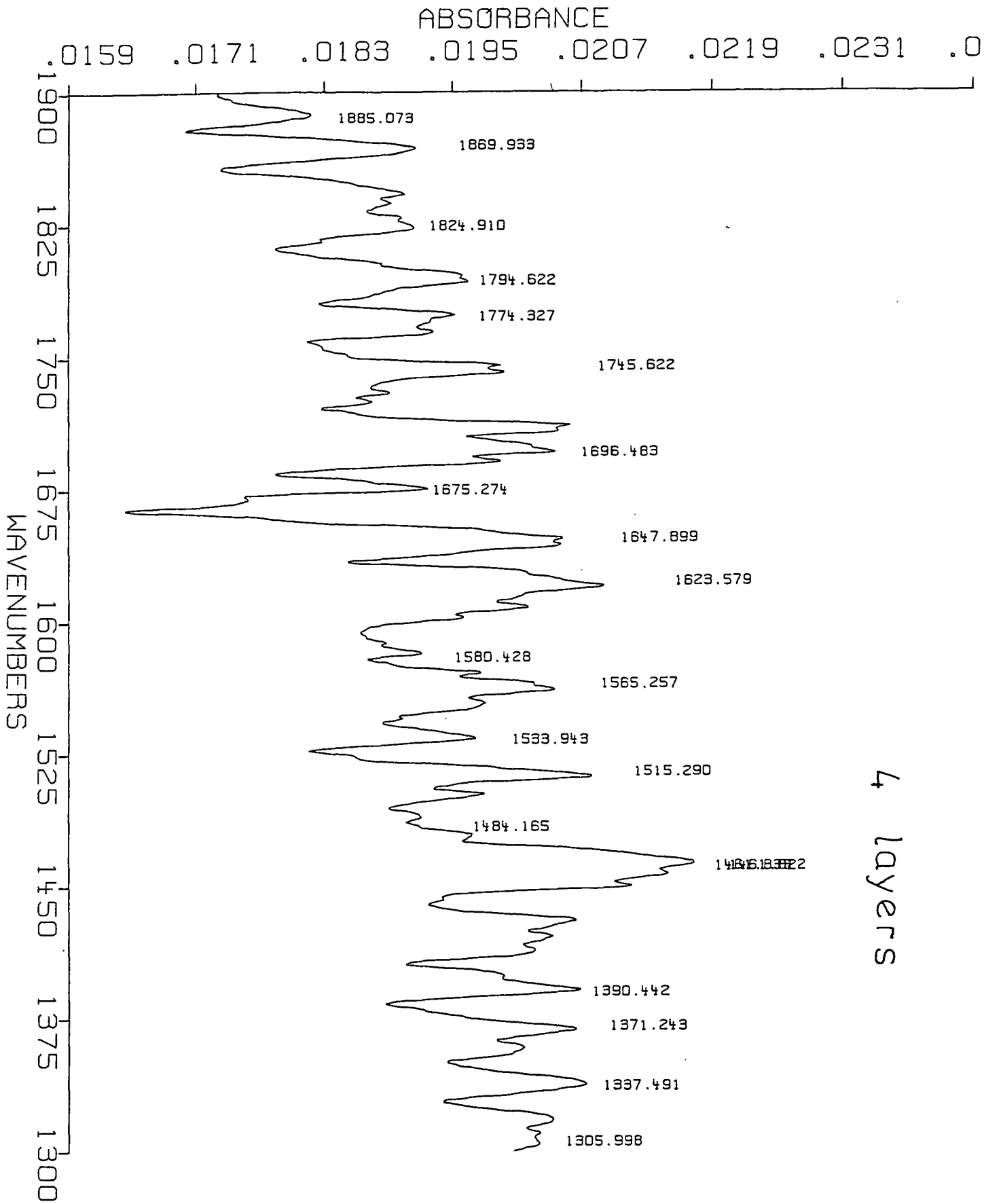
ABSORBANCE
.0159
.0171
.0183
.0195
.0207
.0219
.0231
WAVENUMBERS
1900
1825
1750
1675
1600
1525
1450
1375
1300
1885.073
1869.933
1824.910
1794.622
1774.327
1745.622
1696.483
1675.274
1647.899
1623.579
1580.428
1565.257
1533.943
1515.290
1484.165
1390.442
1371.243
1337.491
1305.998
4 layers

Fig. 7.18

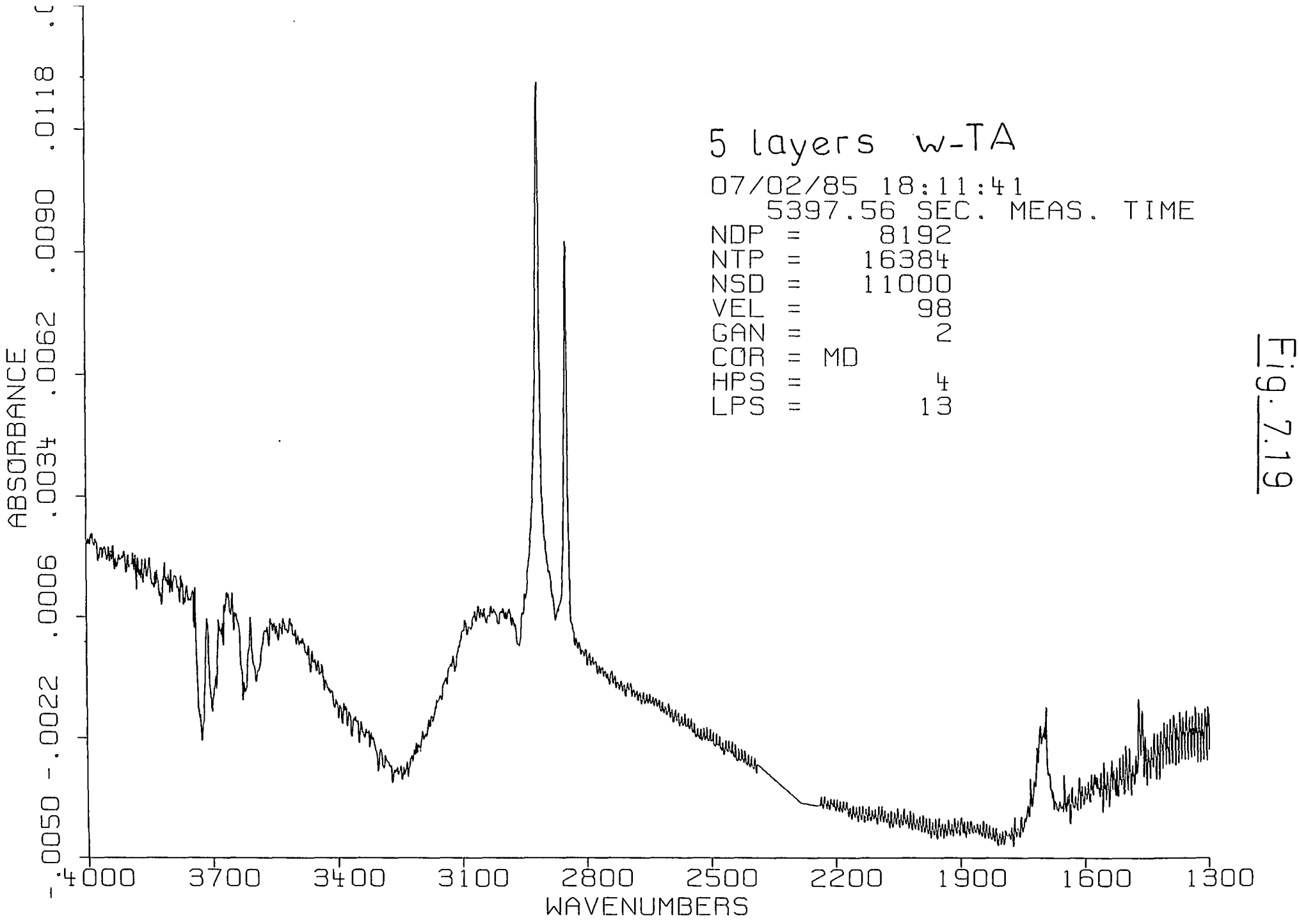
5 layers w-TA
07/02/85 18:11:41
5397.56 SEC. MEAS. TIME
NDP = 8192
NTP = 16384
NSD = 11000
VEL = 98
GAN = 2
COR = MD
HPS = 4
LPS = 13
ABSORBANCE
.0118
.0090
.0062
.0034
.0006
-.0022
-.0050
4000
3700
3400
3100
2800
2500
2200
1900
1600
1300
WAVENUMBERS

Fig. 7.19

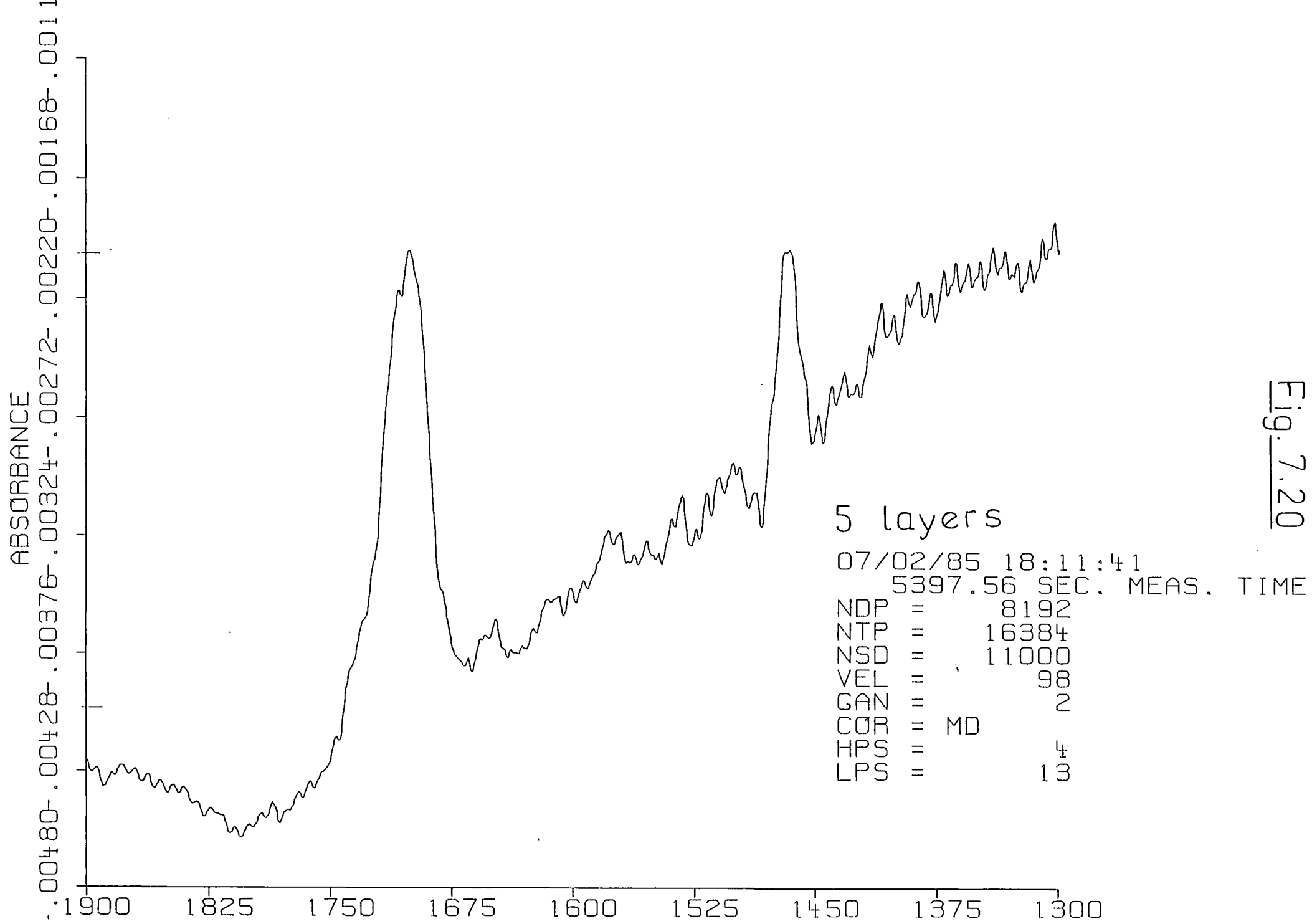
ABSORBANCE
.00480
.00428
.00376
.00324
.00272
.00220
.00168
.00116
1900
1825
1750
1675
1600
1525
1450
1375
1300
5 layers
07/02/85 18:11:41
5397.56 SEC. MEAS. TIME
NDP = 8192
NTP = 16384
NSD = 11000
VEL = 98
GAN = 2
COR = MD
HPS = 4
LPS = 13

Fig. 7.20

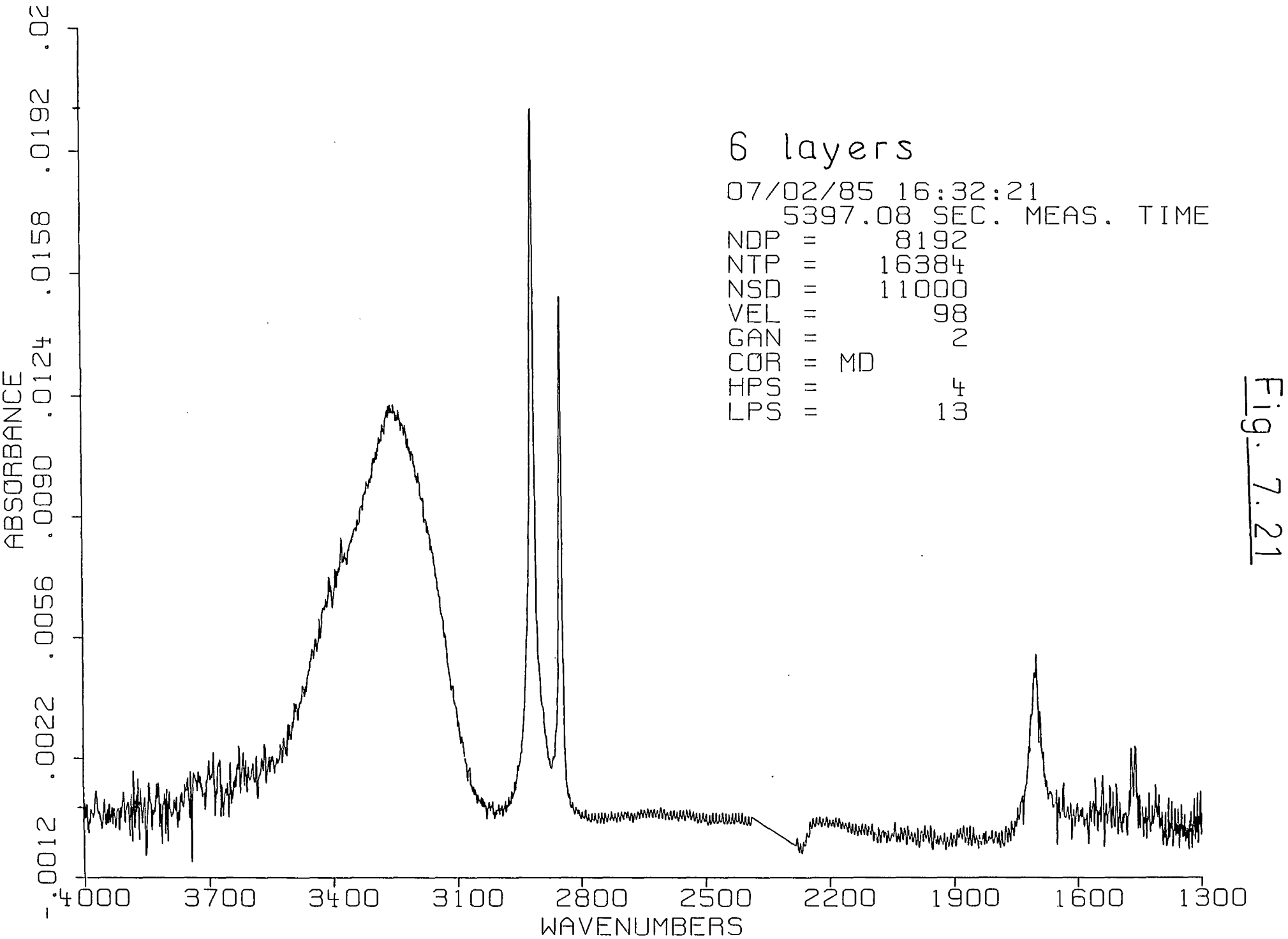
6 layers
07/02/85 16:32:21
5397.08 SEC. MEAS. TIME
NDP = 8192
NTP = 16384
NSD = 11000
VEL = 98
GAN = 2
COR = MD
HPS = 4
LPS = 13
ABSORBANCE
-.0012
.0022
.0056
.0090
.0124
.0158
.0192
.02
4000
3700
3400
3100
2800
2500
2200
1900
1600
1300
WAVENUMBERS

Fig. 7.21

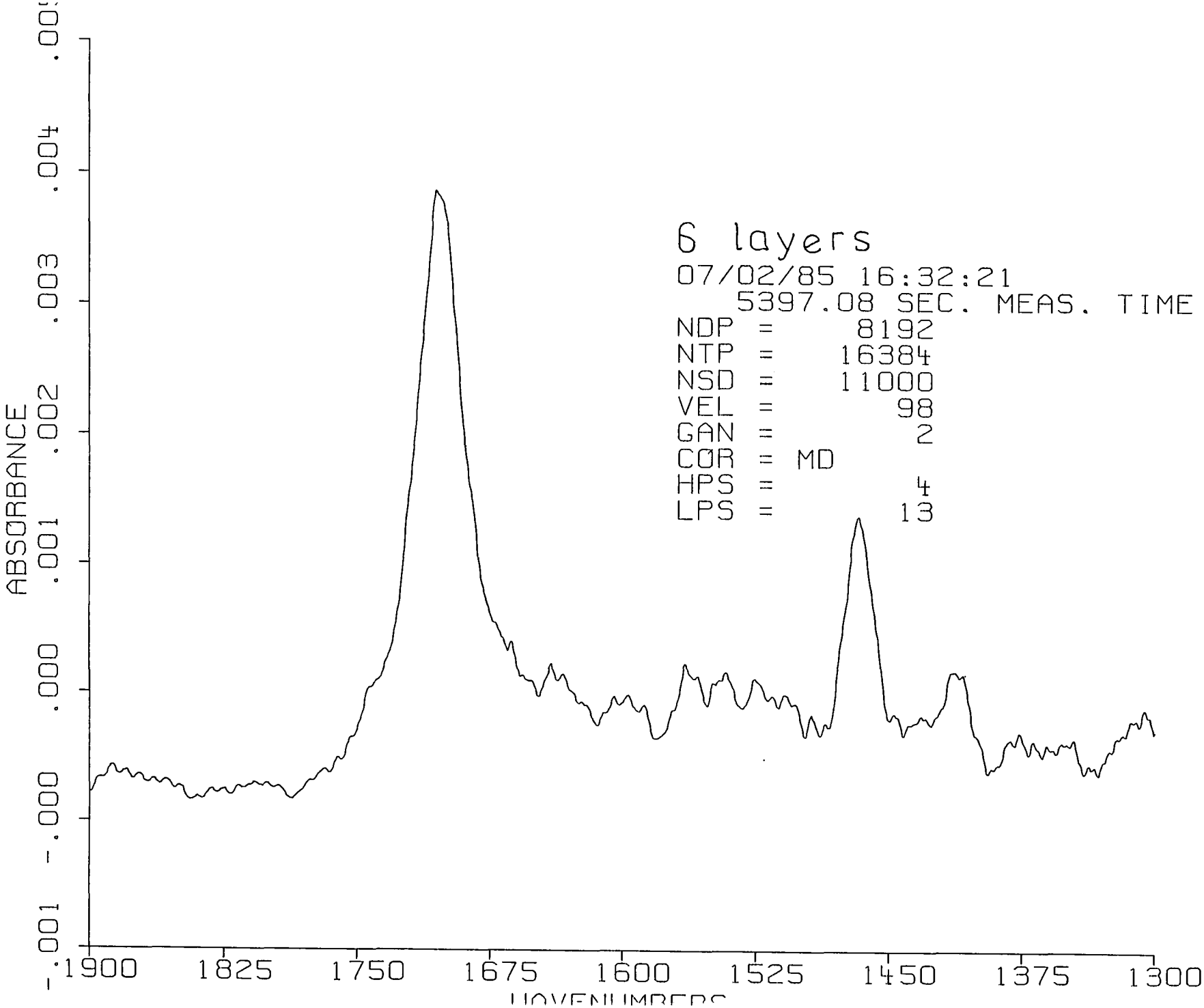
6 layers
07/02/85 16:32:21
5397.08 SEC. MEAS. TIME
NDP = 8192
NTP = 16384
NSD = 11000
VEL = 98
GAN = 2
COR = MD
HPS = 4
LPS = 13
ABSORBANCE
.005
.004
.003
.002
.001
.000
-.000
-.001
1900
1825
1750
1675
1600
1525
1450
1375
1300

Fig. 7.22

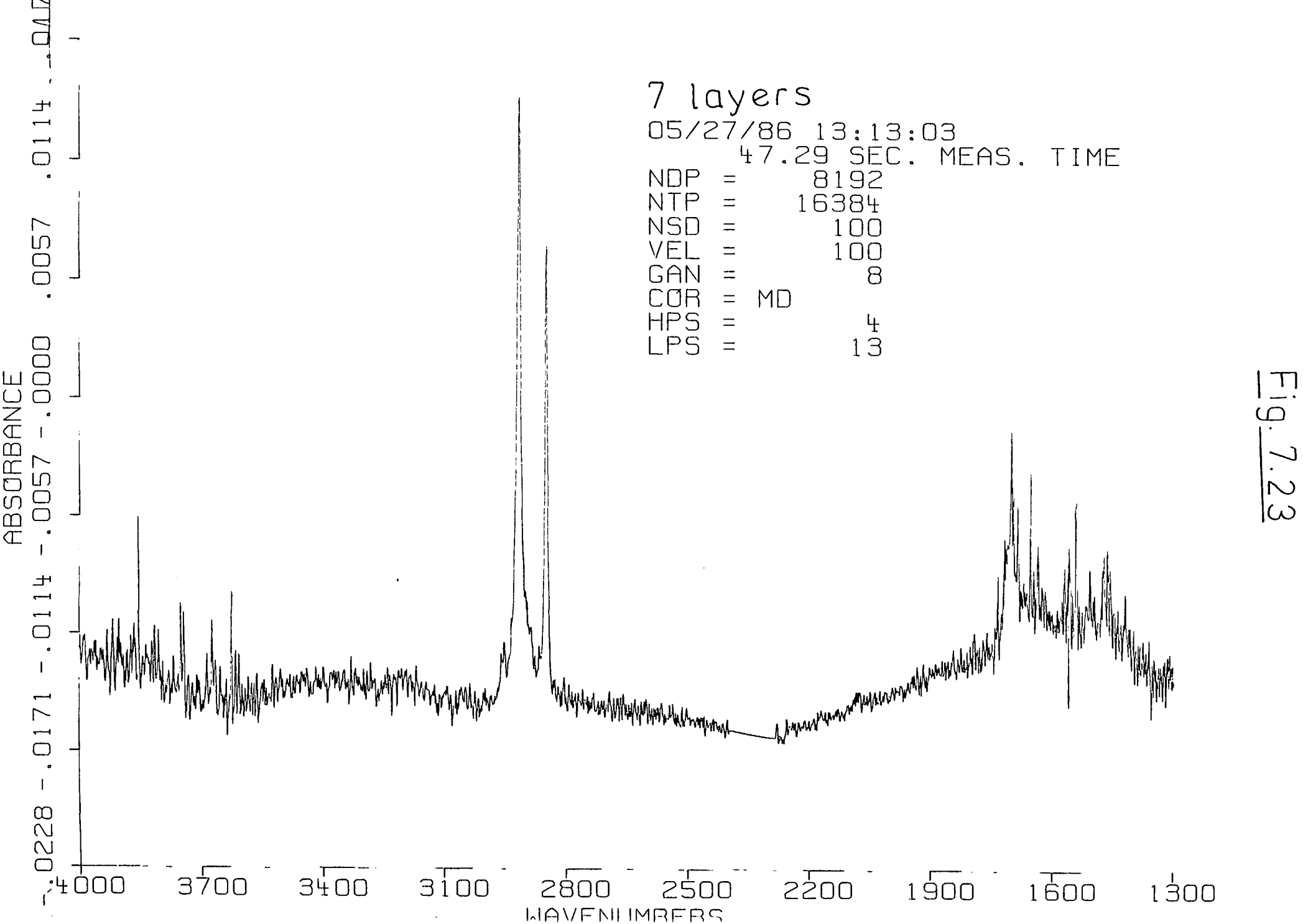
7 layers
05/27/86 13:13:03
47.29 SEC. MEAS. TIME
NDP = 8192
NTP = 16384
NSD = 100
VEL = 100
GAN = 8
COR = MD
HPS = 4
LPS = 13
ABSORBANCE
.0228
-.0171
-.0114
-.0057
-.0000
.0057
.0114
4000
3700
3400
3100
2800
2500
2200
1900
1600
1300
WAVENUMBERS

Fig. 7.23

Fig. 7.24

7 layers
ABSORBANCE
-.0138
-.0119
-.0100
-.0081
-.0062
-.0043
-.0024
1900
1825
1750
1675
1600
1525
1450
1375
1300

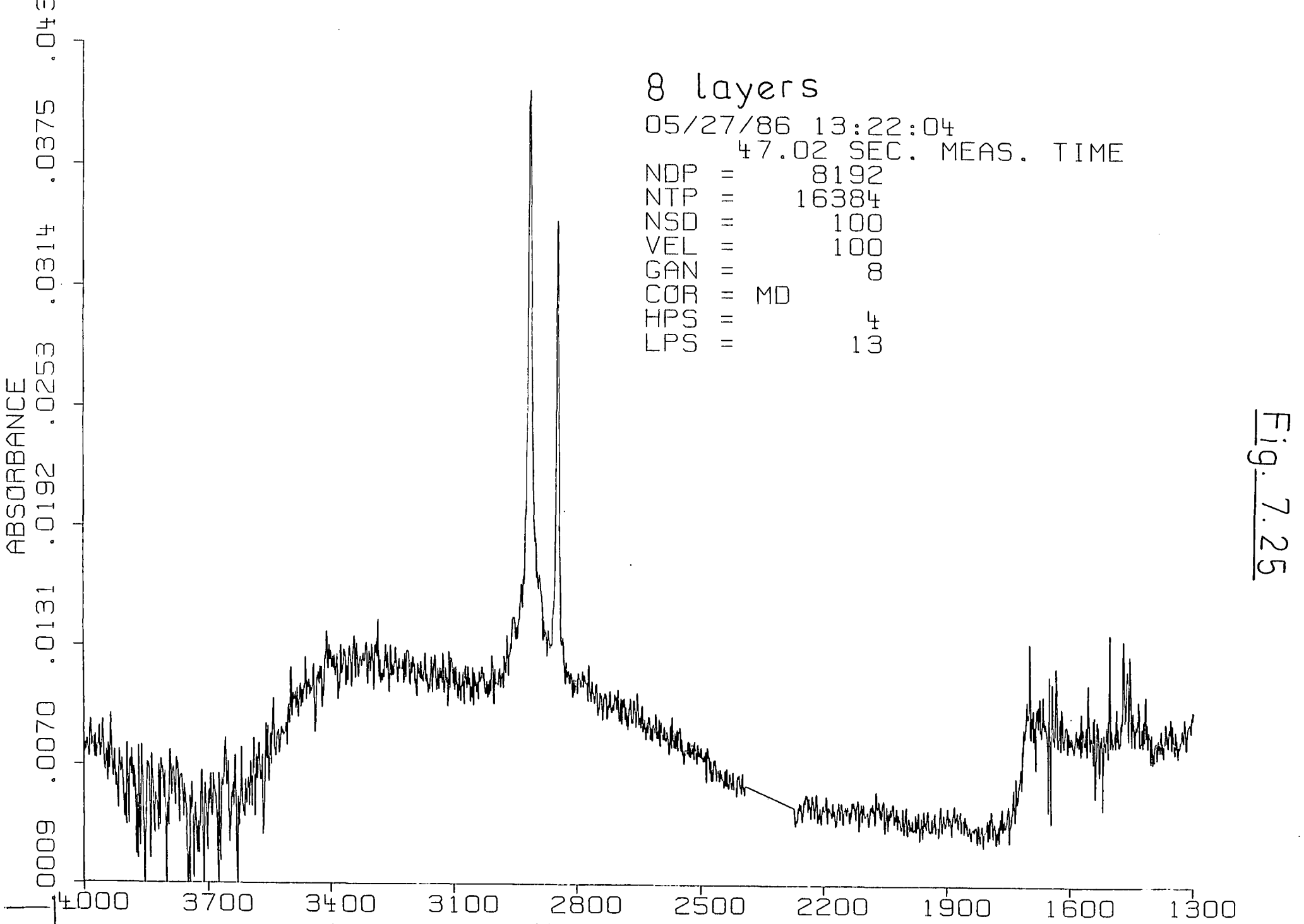
8 layers
05/27/86 13:22:04
47.02 SEC. MEAS. TIME
NDP = 8192
NTP = 16384
NSD = 100
VEL = 100
GAN = 8
COR = MD
HPS = 4
LPS = 13
ABSORBANCE
.0009
.0070
.0131
.0192
.0253
.0314
.0375
.043
4000
3700
3400
3100
2800
2500
2200
1900
1600
1300

Fig. 7.25

Fig. 7.26

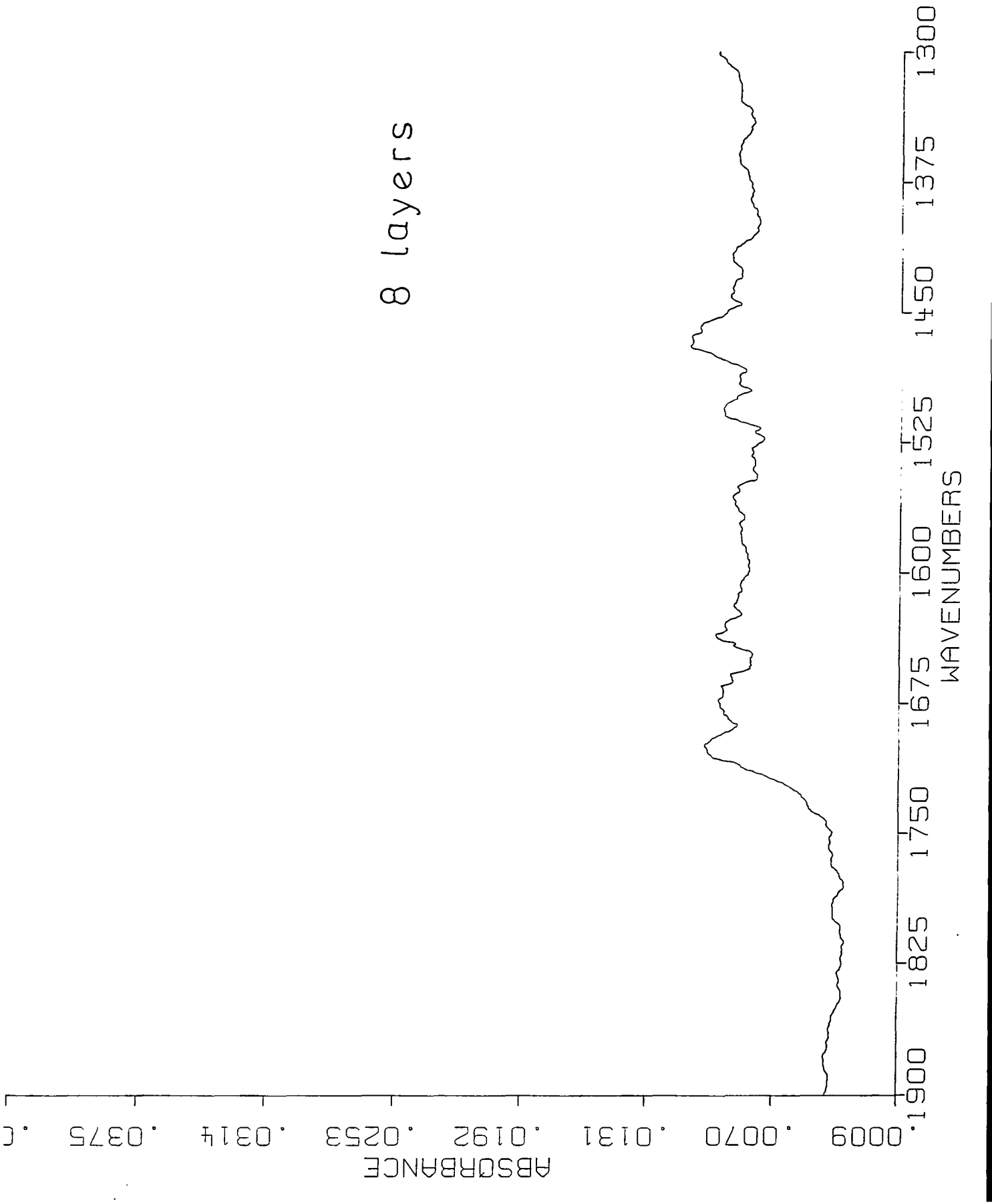
8 layers
ABSORBANCE
.0009
.0070
.0131
.0192
.0253
.0314
.0375
1900
1825
1750
1675
1600
1525
1450
1375
1300
WAVENUMBERS

Fig. 7.27

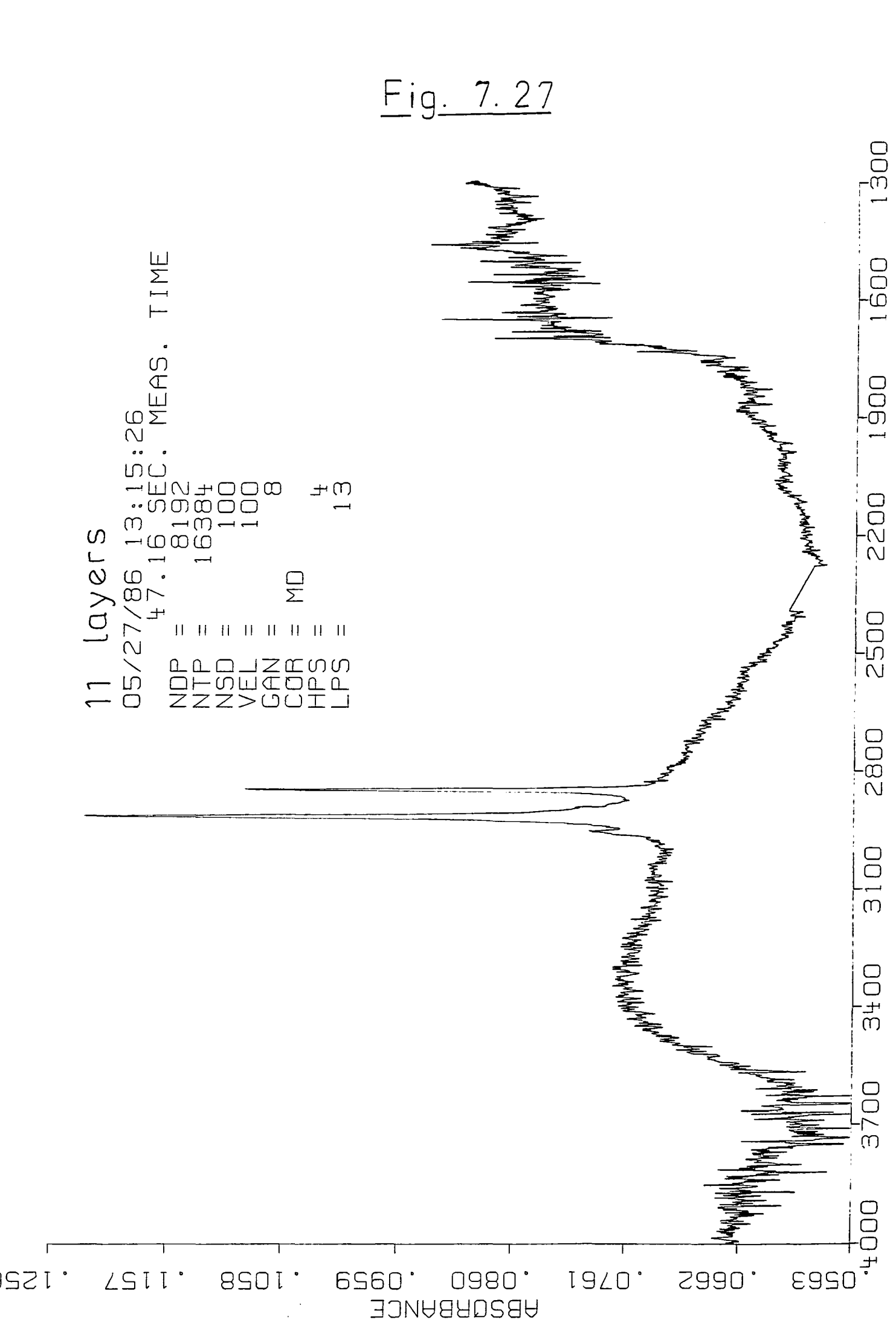
11 layers
05/27/86 13:15:26
47.16 SEC. MEAS. TIME
NDP = 8192
NTP = 16384
NSD = 100
VEL = 100
GAN = 8
COR = MD
HPS = 4
LPS = 13
ABSORBANCE
.0563
.0662
.0761
.0860
.0959
.1058
.1157
.1256
4000
3700
3400
3100
2800
2500
2200
1900
1600
1300

Fig. 7.28

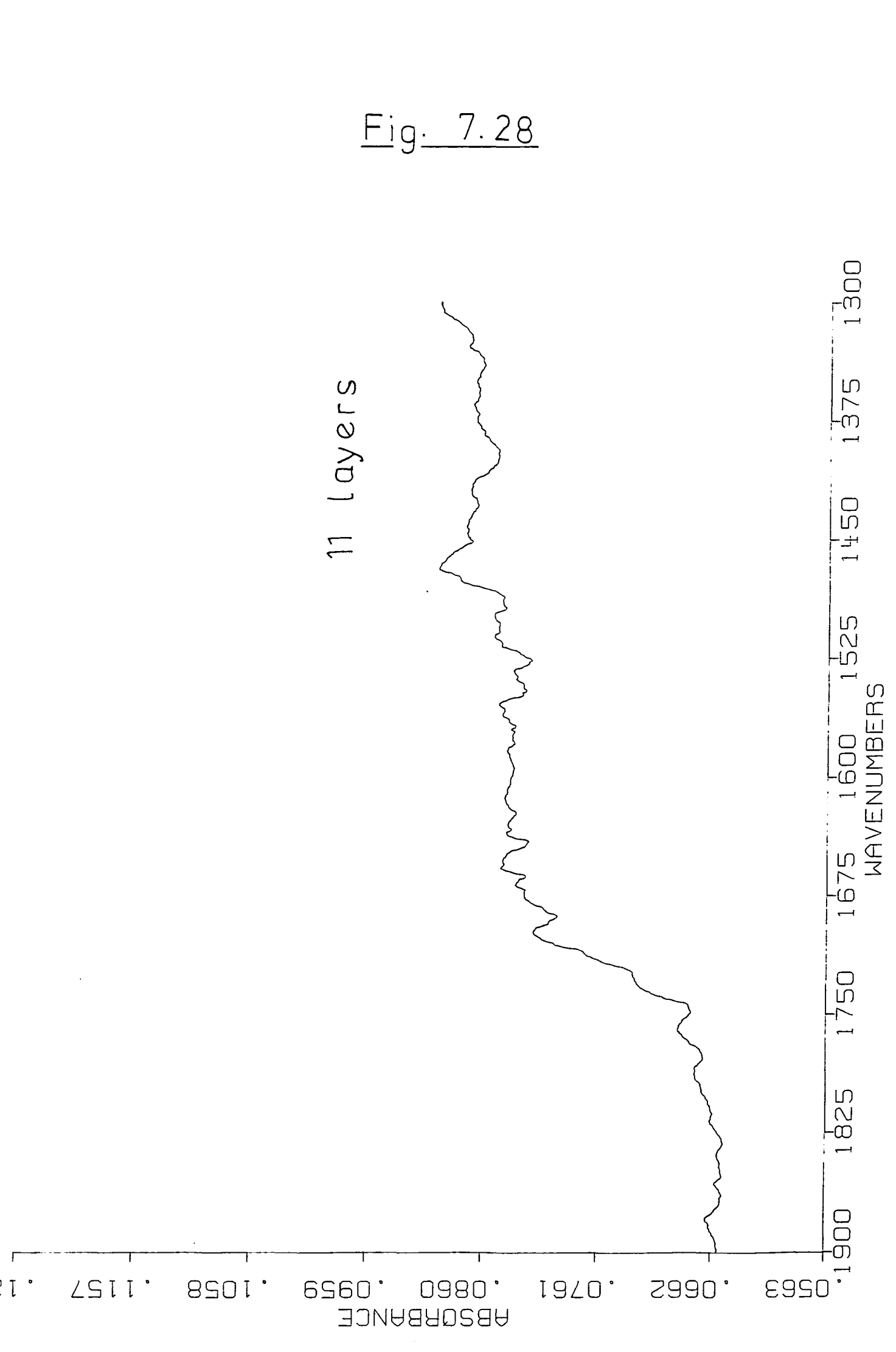
11 layers
ABSORBANCE
.0563
.0662
.0761
.0860
.0959
.1058
.1157
WAVENUMBERS
1900
1825
1750
1675
1600
1525
1450
1375
1300

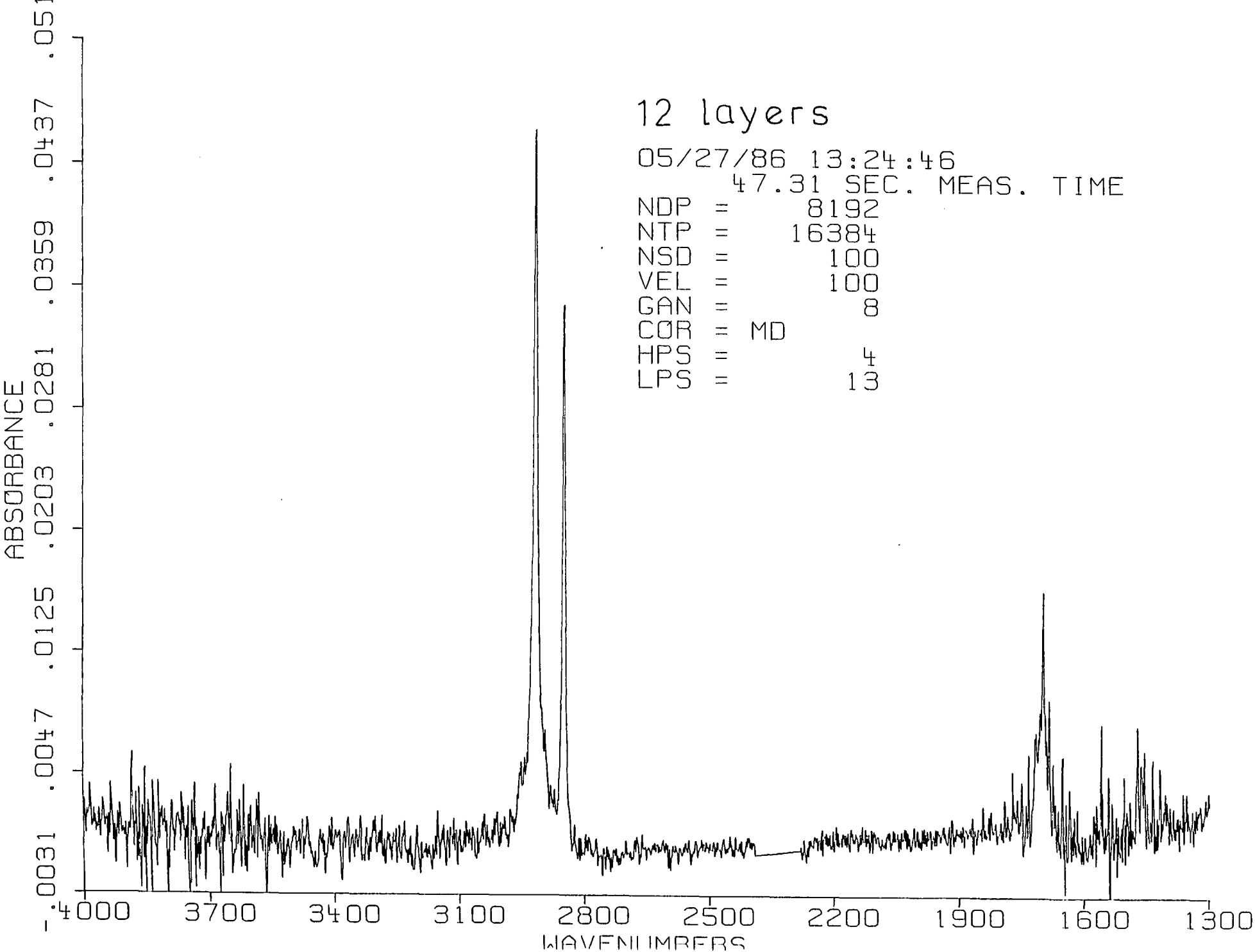
12 layers
05/27/86 13:24:46
47.31 SEC. MEAS. TIME
NDP = 8192
NTP = 16384
NSD = 100
VEL = 100
GAN = 8
COR = MD
HPS = 4
LPS = 13
ABSORBANCE
.0516
.0437
.0359
.0281
.0203
.0125
.0047
-.0031
4000
3700
3400
3100
2800
2500
2200
1900
1600
1300
WAVENUMBERS

Fig. 7.29

Fig. 7.30

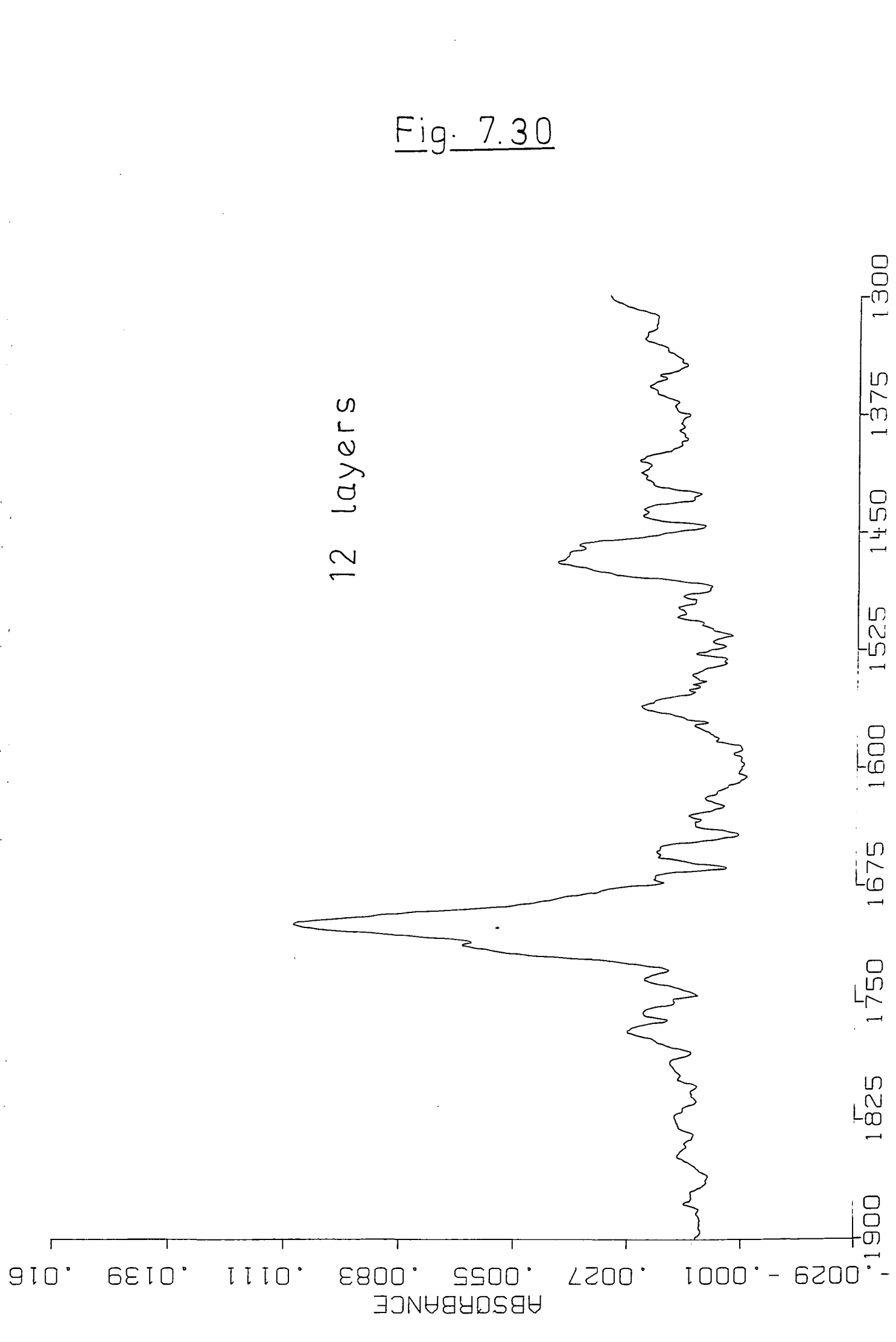
12 layers
ABSORBANCE
-.0029
-.0001
.0027
.0055
.0083
.0111
.0139
.016
1900
1825
1750
1675
1600
1525
1450
1375
1300

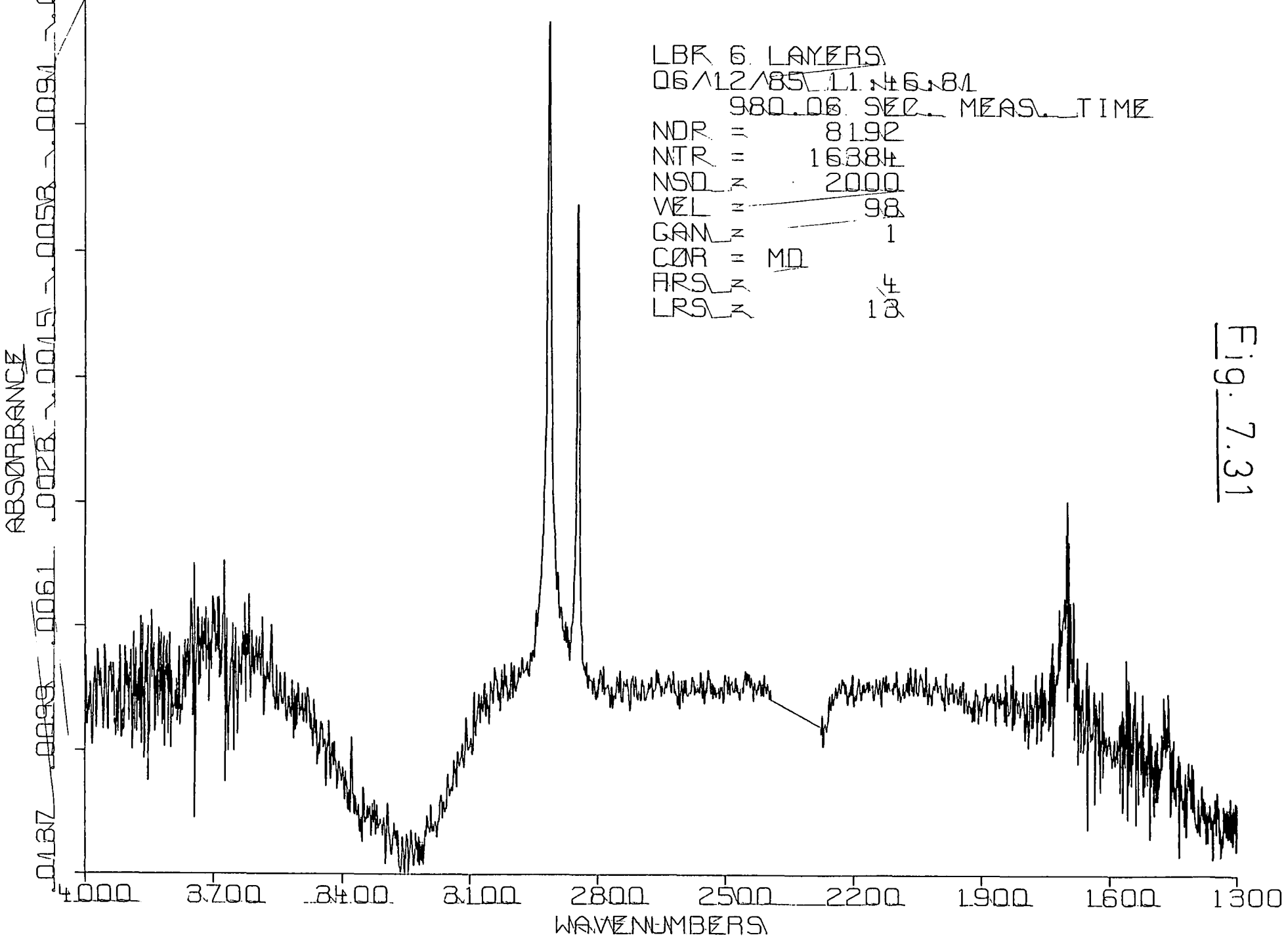
LBR 6 LAYERS
06/12/85 11:46:81
980.06 SEC. MEAS. TIME
NDR = 8192
NTR = 16384
NSD = 2000
VEL = 98
GAN = 1
COR = MD
FRS = 4
LRS = 18
ABSORBANCE
.0137
.0099
.0061
.0023
-.0015
-.0053
-.0091
4000
3700
3400
3100
2800
2500
2200
1900
1600
1300
WAVENUMBERS

Fig. 7.31

Fig. 7.32

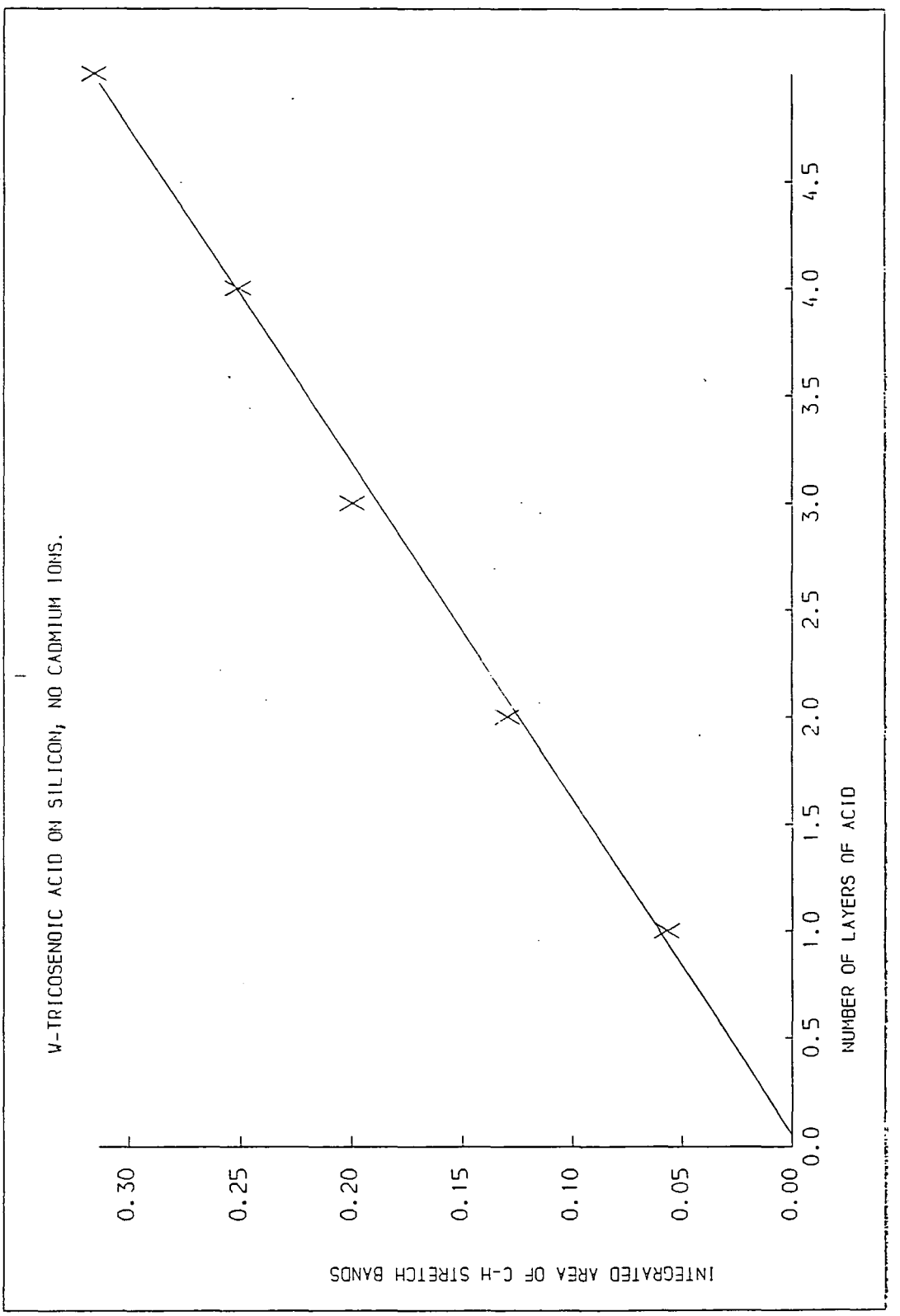
W-TRICOSENOIC ACID ON SILICON, NO CADMIUM IONS.
INTEGRATED AREA OF C-H STRETCH BANDS
0.00
0.05
0.10
0.15
0.20
0.25
0.30
0.0
0.5
1.0
1.5
2.0
2.5
3.0
3.5
4.0
4.5
NUMBER OF LAYERS OF ACID

Fig. 7.33

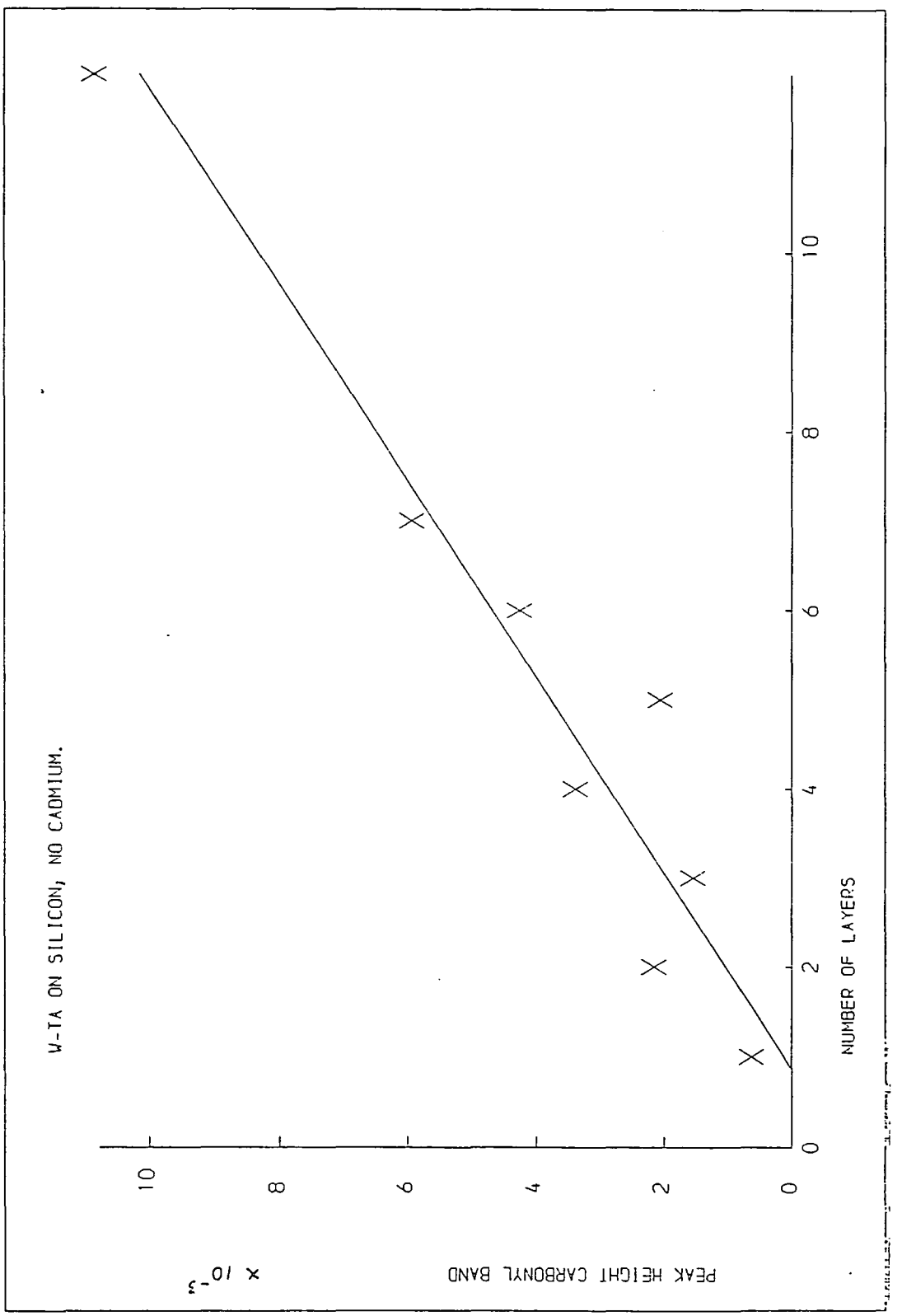
W-TA ON SILICON, NO CADMIUM.
PEAK HEIGHT CARBONYL BAND
x 10⁻³
0
2
4
6
8
10
NUMBER OF LAYERS

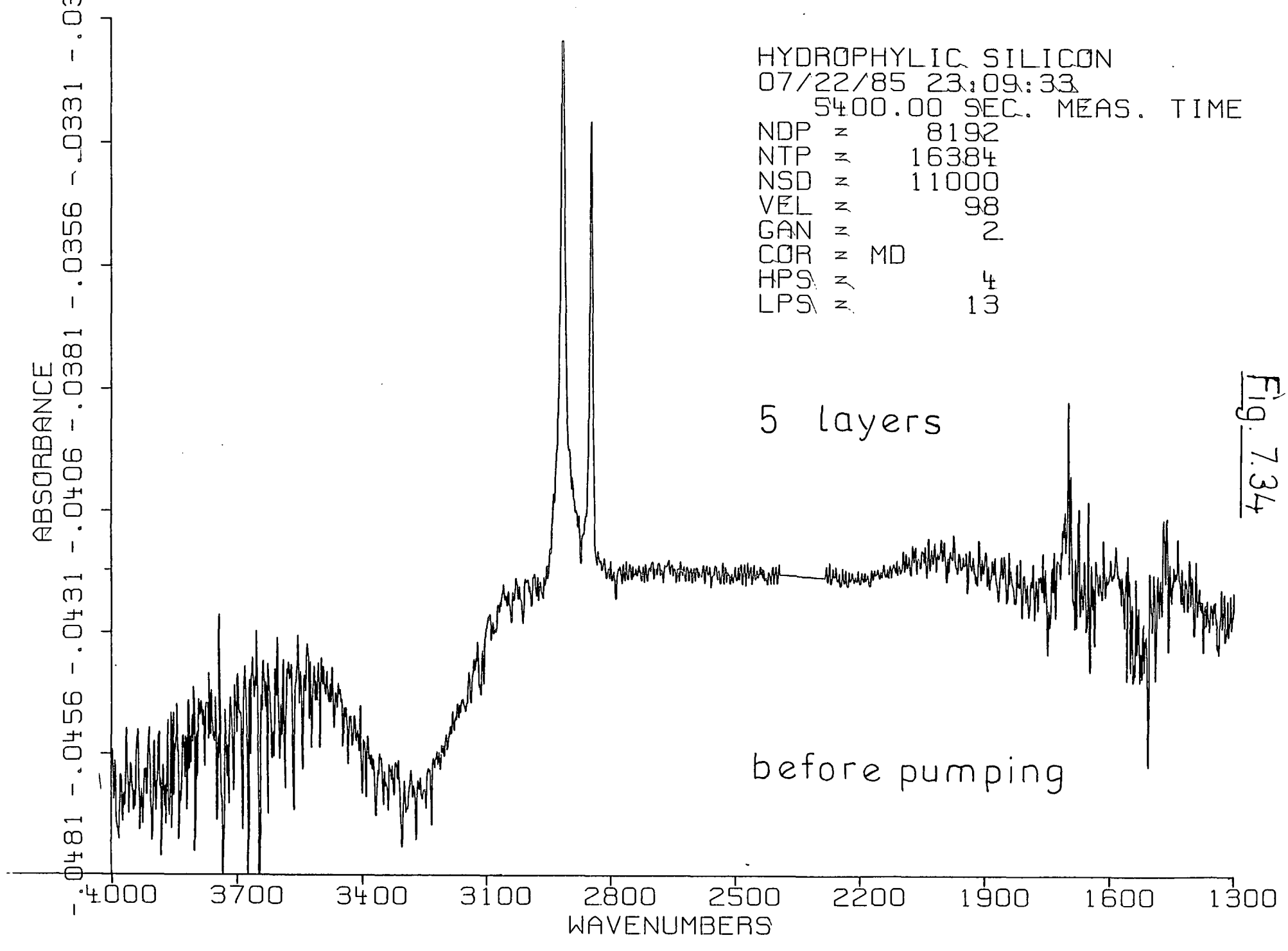
HYDROPHYLIC SILICON
07/22/85 23:09:33
5400.00 SEC. MEAS. TIME
NDP = 8192
NTP = 16384
NSD = 11000
VEL = 98
GAN = 2
COR = MD
HPS = 4
LPS = 13
5 layers
before pumping
ABSORBANCE
-.0481 -.0456 -.0431 -.0406 -.0381 -.0356 -.0331 -.03
4000 3700 3400 3100 2800 2500 2200 1900 1600 1300
WAVENUMBERS

Fig. 7.34

Fig. 7.35

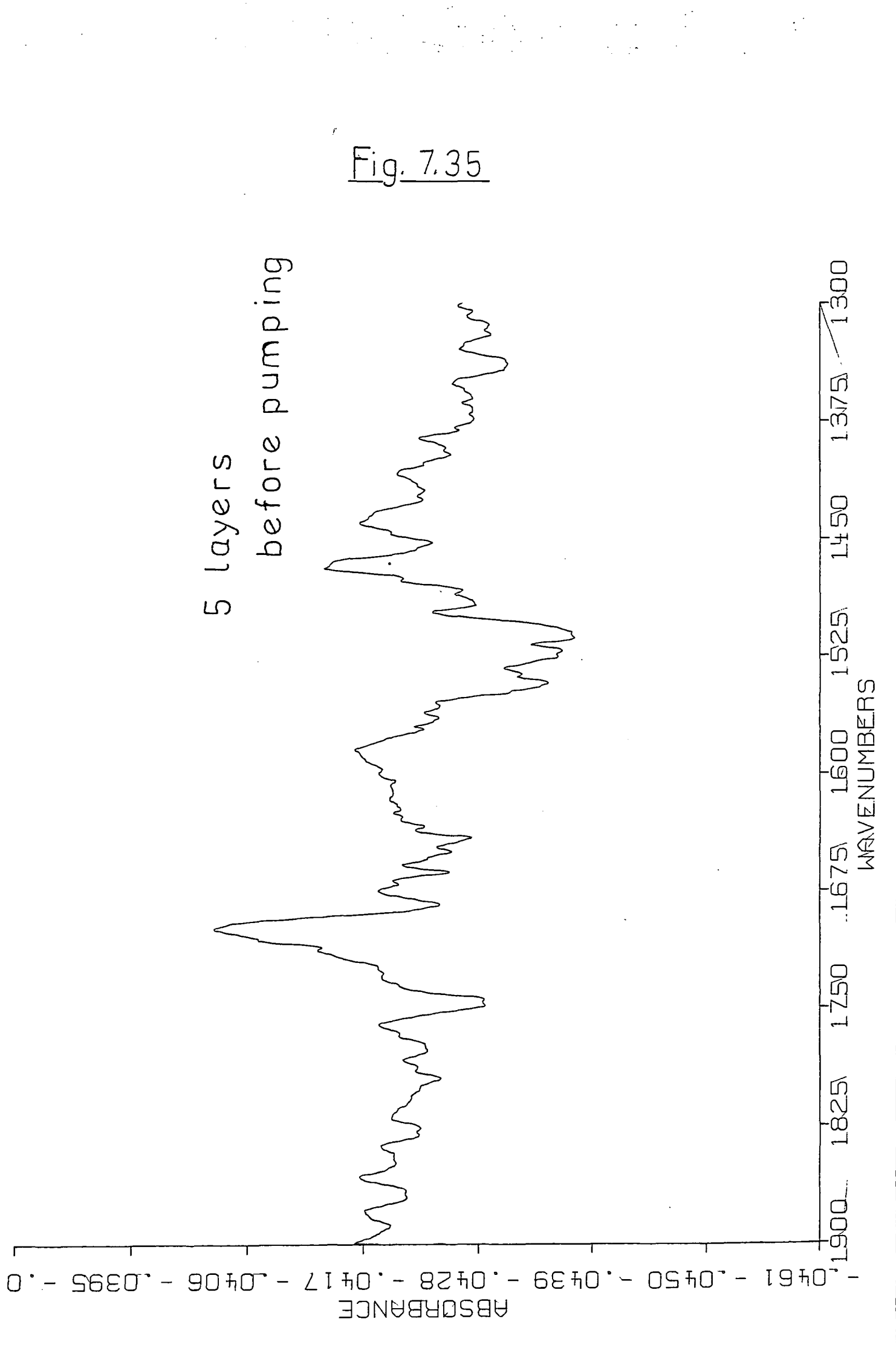
5 layers
before pumping
ABSORBANCE
-.0461
-.0450
-.0439
-.0428
-.0417
-.0406
-.0395
-.0
1900
1825
1750
1675
1600
1525
1450
1375
1300
WAVENUMBERS

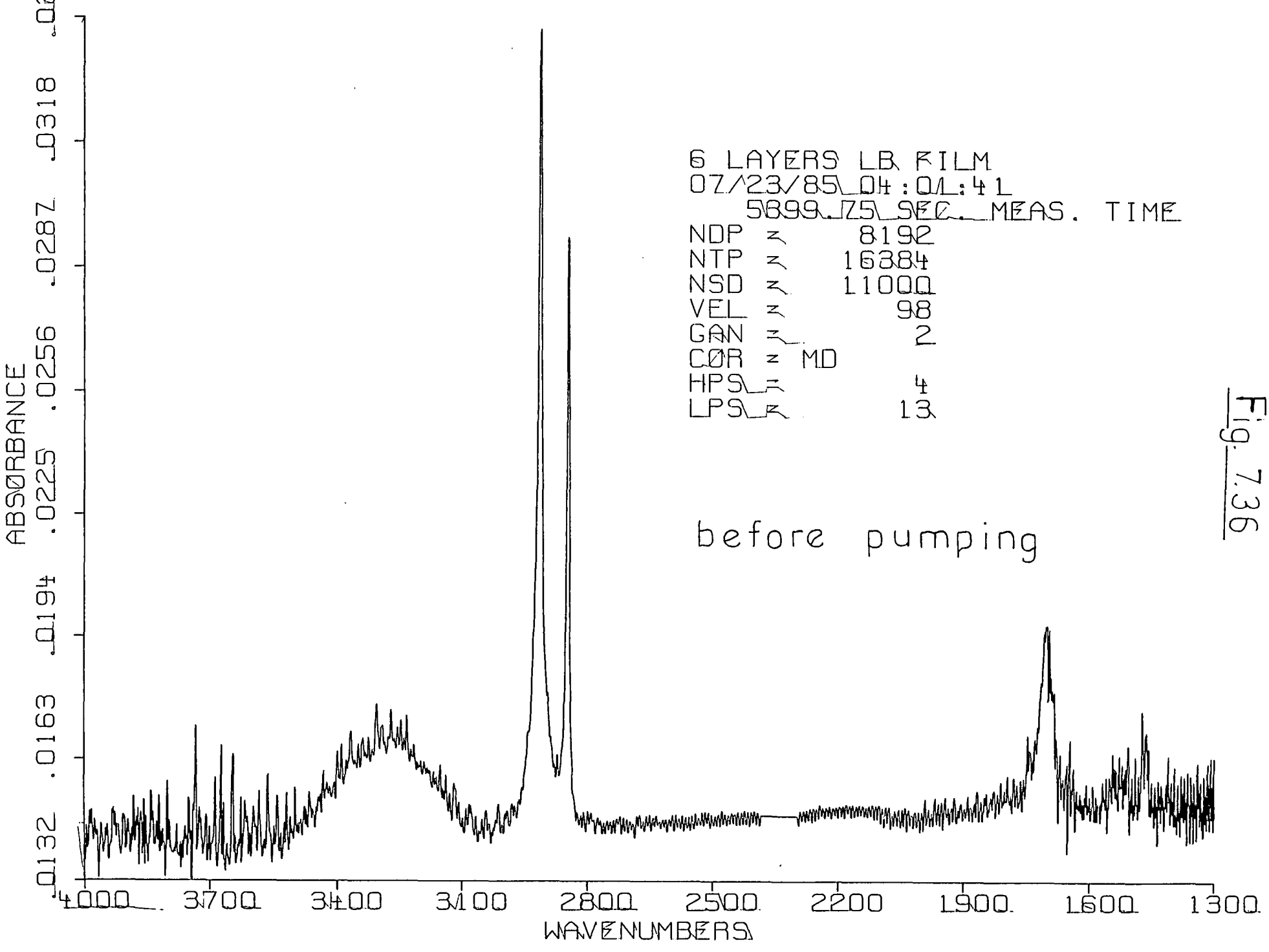
6 LAYERS LB FILM
07/23/85 04:01:41
5899.75 SEC. MEAS. TIME
NDP = 8192
NTP = 16384
NSD = 11000
VEL = 98
GAN = 2
COR = MD
HPS = 4
LPS = 13
before pumping
ABSORBANCE
.0132
.0163
.0194
.0225
.0256
.0287
.0318
4000
3700
3400
3100
2800
2500
2200
1900
1600
1300
WAVENUMBERS

Fig. 7.36

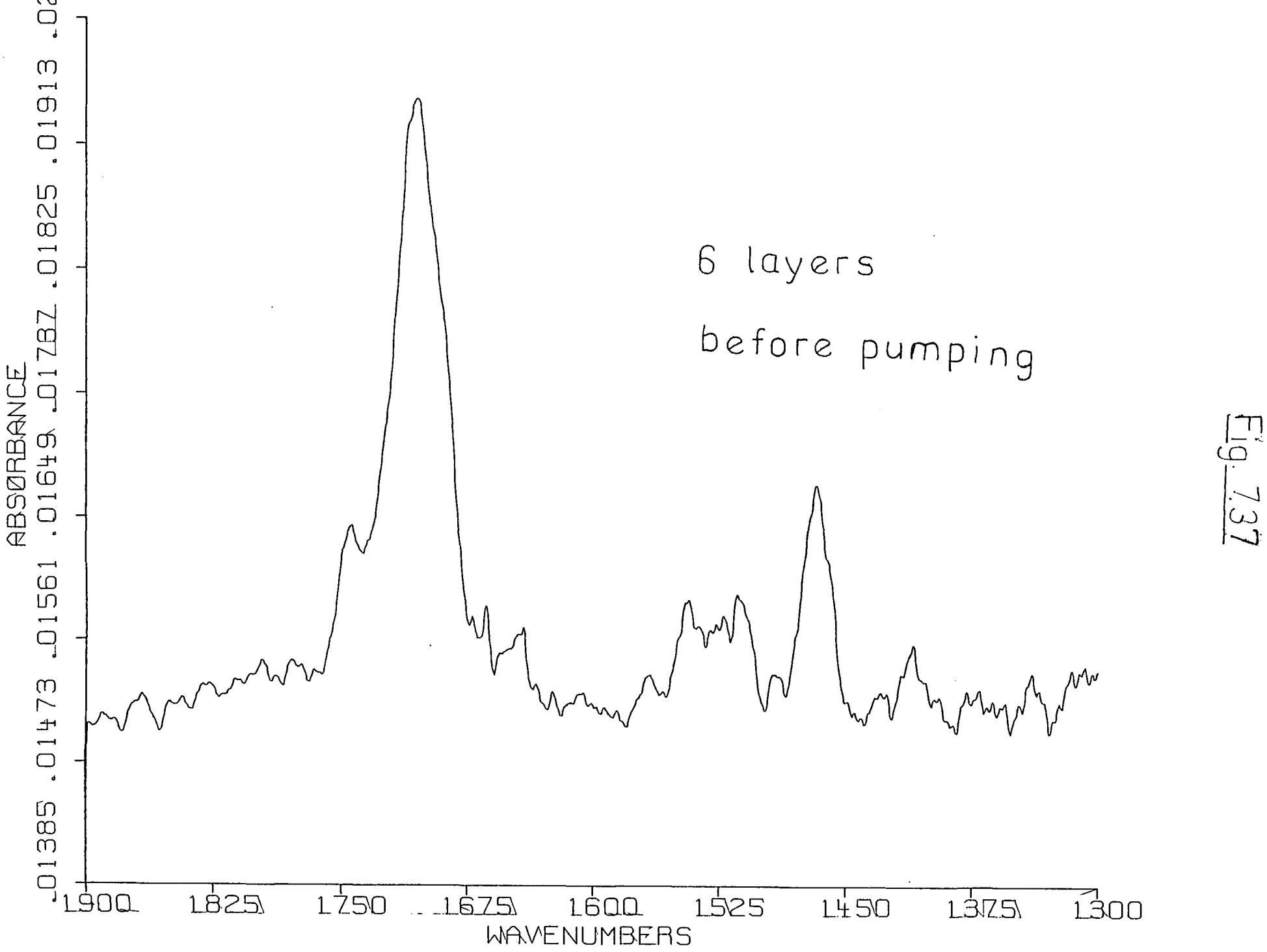
6 layers
before pumping
ABSORBANCE
.01385 .01473 .01561 .01649 .01737 .01825 .01913
1900 1825 1750 1675 1600 1525 1450 1375 1300
WAVENUMBERS

Fig. 7.37

Fig. 7.38

5 layers on
SILICON AFTER PUMPING
07/24/85 28:29:17
5398.82 SEC. MEAS. TIME
NDP = 8192
NTP = 16384
NSD = 11000
VEL = 98
GAN = 2
COR = MD
HPSL = 4
LPSL = 13
ABSORBANCE
.0022
.0006
.0034
.0062
.0090
.0118
.0146
.0174
3700
3600
3500
3400
3300
3200
3100
3000
2900
2800
2700
2600
2500
2400
2300
2200
2100
2000
1900
1800
1700
1600
1500
1400
1300
1200
1100
1000

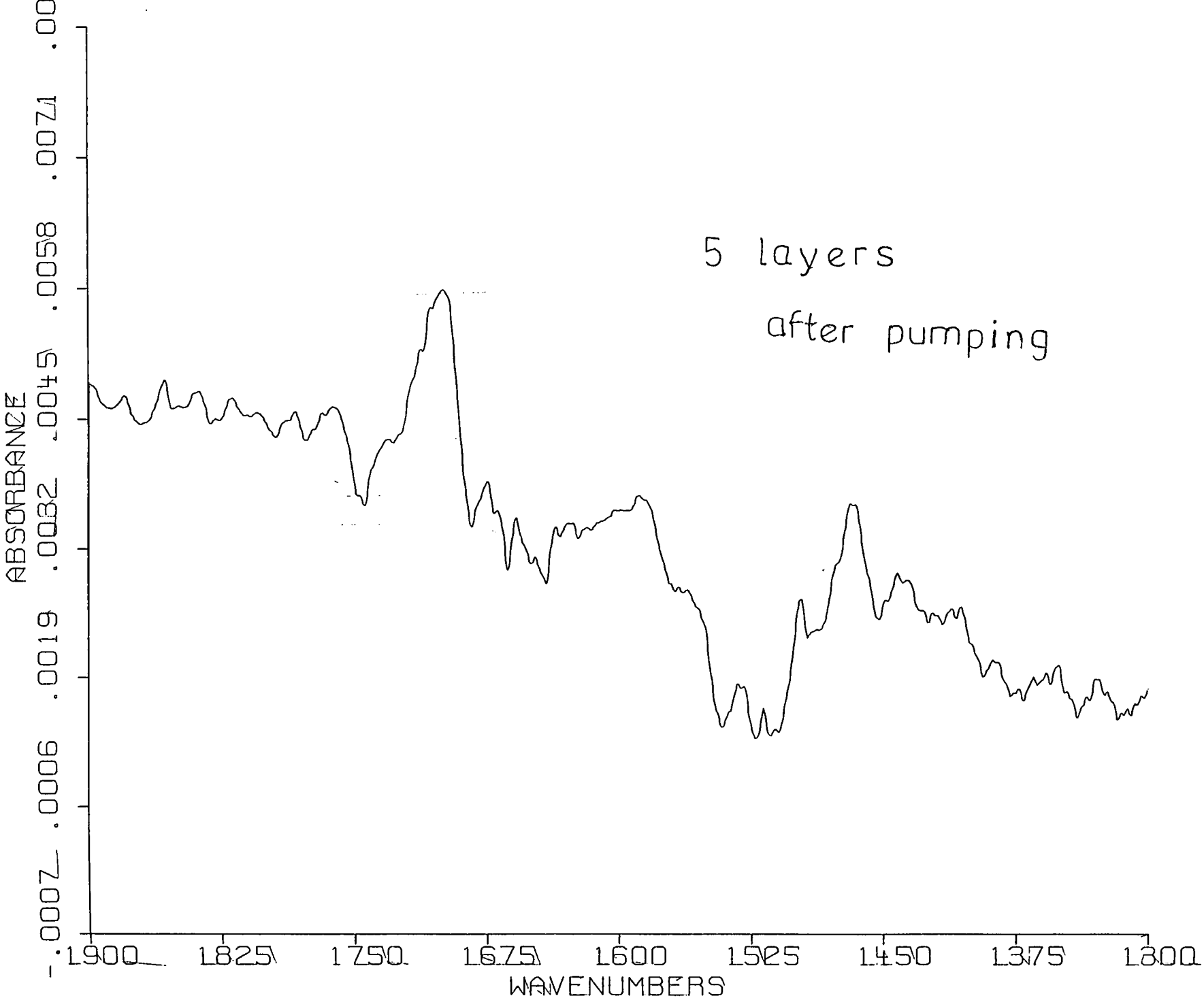
5 layers
after pumping
ABSORBANCE
-.0007
.0006
.0019
.0032
.0045
.0058
.0071
.00
1900
1825
1750
1675
1600
1525
1450
1375
1300
WAVENUMBERS

Fig. 7.39

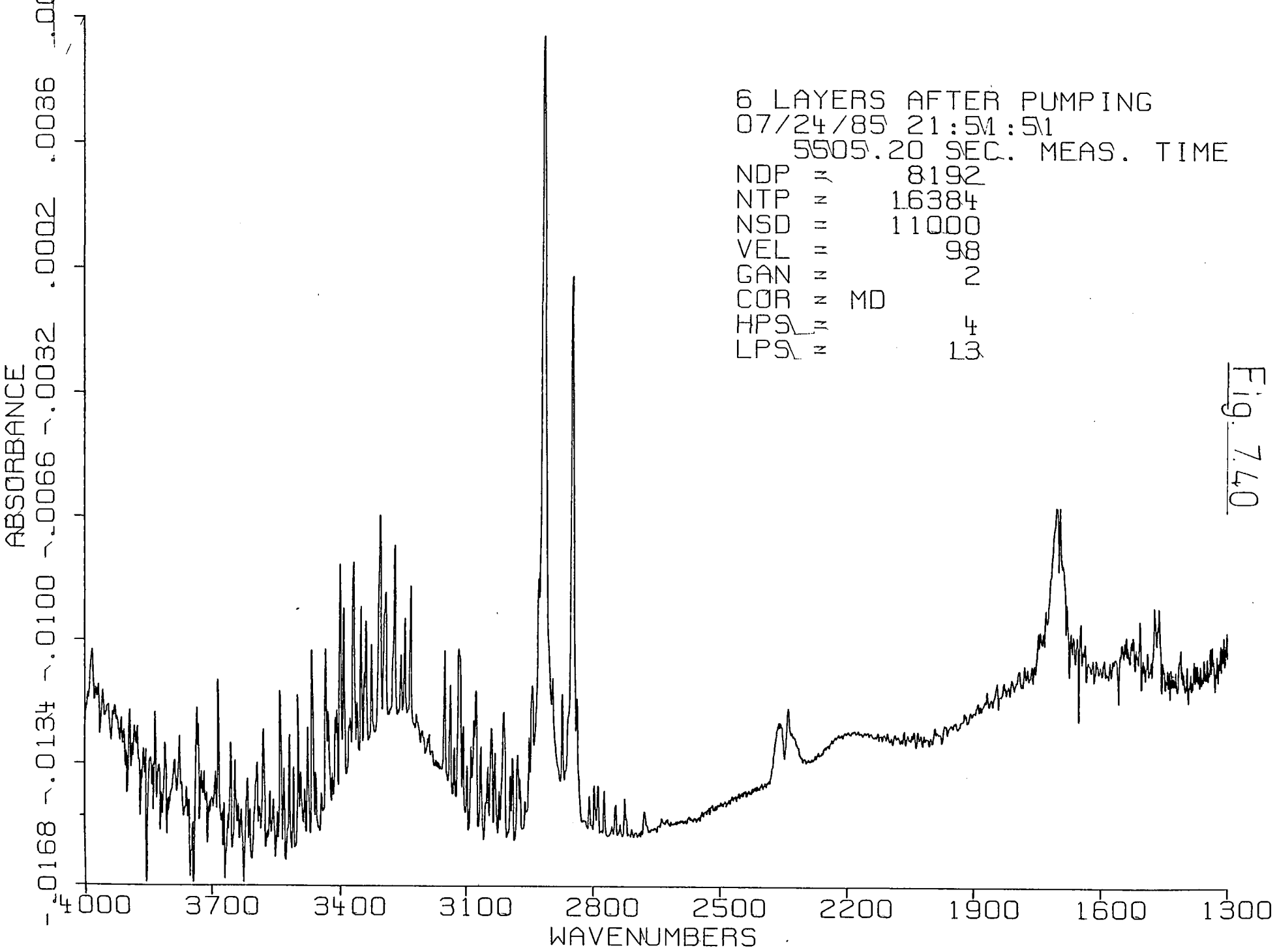
6 LAYERS AFTER PUMPING
07/24/85 21:51:51
5505.20 SEC. MEAS. TIME
NDP = 8192
NTP = 16384
NSD = 11000
VEL = 98
GAN = 2
COR = MD
HPS = 4
LPS = 13
ABSORBANCE
-.0168
-.0134
-.0100
-.0066
-.0032
.0002
.0036
4000
3700
3400
3100
2800
2500
2200
1900
1600
1300
WAVENUMBERS

Fig. 7.40

Fig 7.41

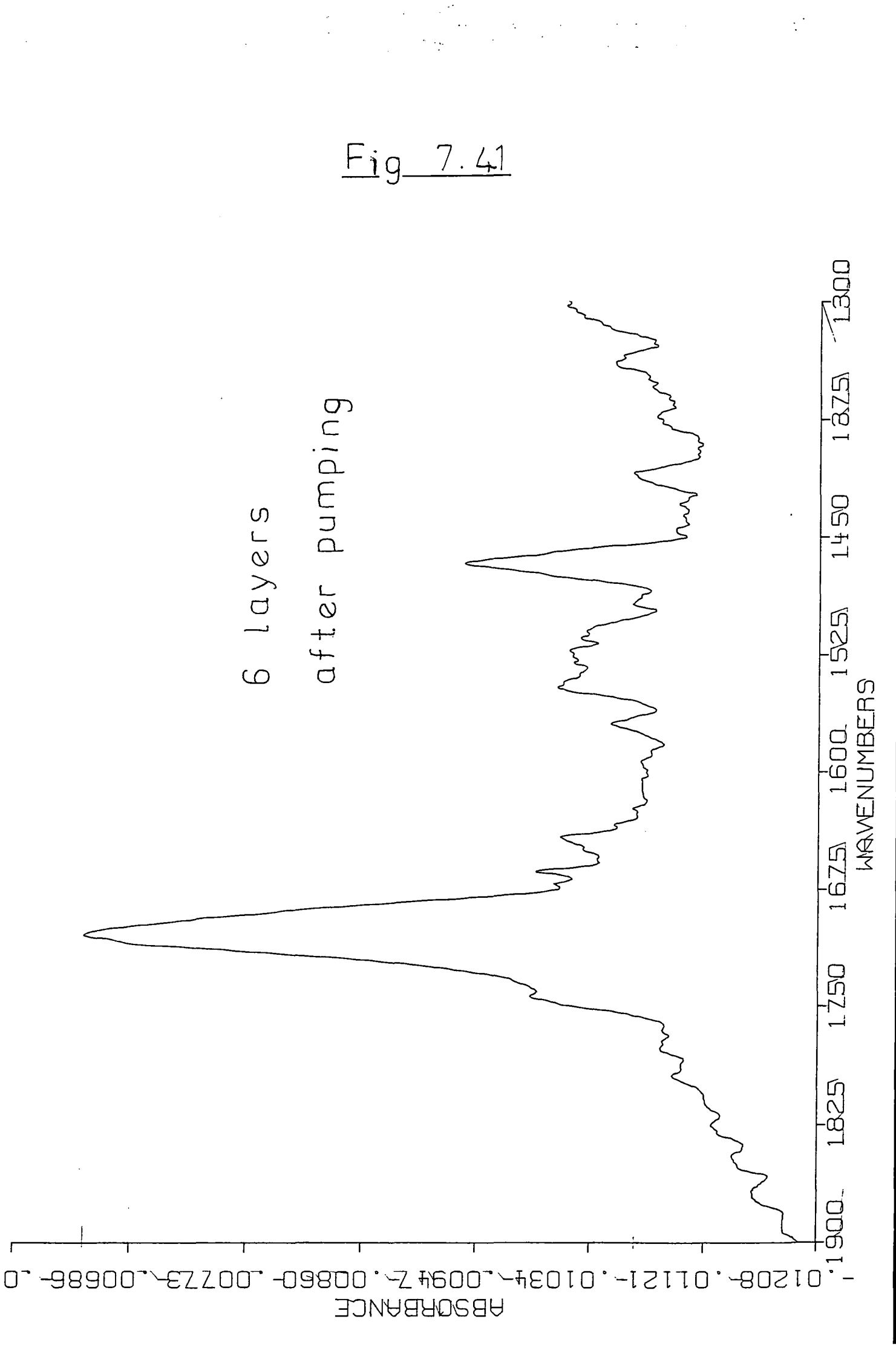
6 layers
after pumping
ABSORBANCE
-.01208 -.01121 -.01034 -.00947 -.00860 -.00773 -.00686 -.0
1900 1825 1750 1675 1600 1525 1450 1375 1300
WAVENUMBERS

Fig. 7.42

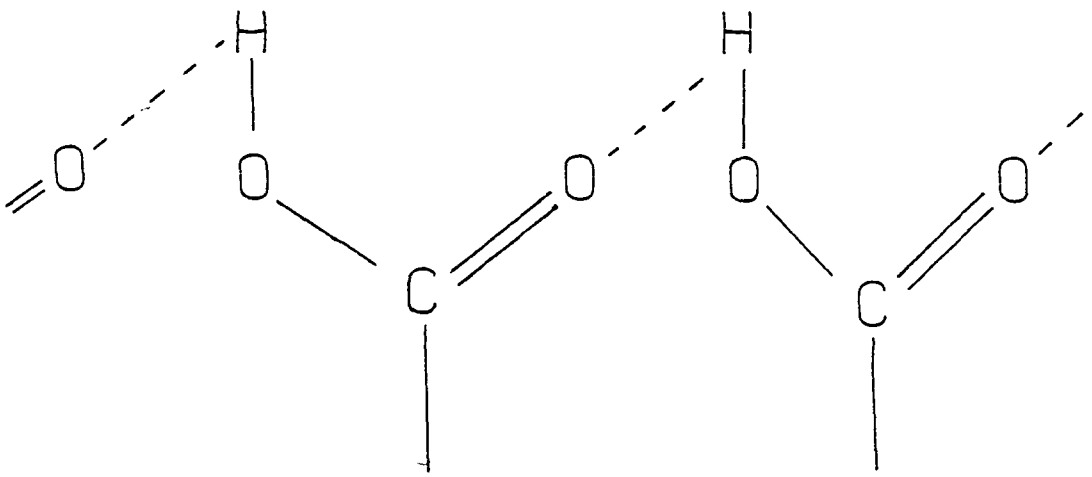

APPENDIX I

RESEARCH COLLOQUIA, SEMINARS, AND LECTURES

The Board of Studies in Chemistry requires that each postgraduate research thesis contains an appendix, listing:

(a) all research colloquia, research seminars and lectures arranged by the Department of Chemistry during the period of the author's residence as a postgraduate student;

(b) lectures organised by Durham University Chemical Society;

(c) all research conferences and meetings attended and papers presented by the author during the period when research for the thesis was carried out;

(d) details of the postgraduate induction course.

(a) LECTURES ORGANISED BY DURHAM UNIVERSITY 1983 - 1986

5.10.83 Prof. J.P. Maier (Basel, Switzerland)
"Recent approaches to spectroscopic characterization of cations".

12.10.83 Dr. C.W. McLeland (Port Elizabeth, Australia),
"Cyclization of aryl alcohols through the intermediacy of alkoxy radicals and aryl radical cations".

19.10.83 Dr. N.W. Alcock (Warwick),
"Aryl tellurium (IV) compounds, patterns of primary and secondary bonding".

26.10.83 Dr. R.H. Friend (Cavendish, Cambridge).
"Electronic properties of conjugated polymers".

30.11.83 Prof. I.M.G. Cowie (Stirling),
"Molecular interpretation of non-relaxation processes in polymer glasses".

2.12.83 Dr. G.M. Brooke (Durham),
"The fate of the ortho-fluorine in 3,3-sigmatropic reactions involving polyfluoro-aryl and -hetero-aryl systems".

14.12.83 Prof. R.J. Donovan (Edinburgh),
"Chemical and physical processes involving the ion-pair states of the halogen molecules".

10. 1.84 Prof. R. Hester (York)
"Nanosecond Laser Spectroscopy of Reaction Intermediates".

18. 1.84 Prof. R.K. Harris (UEA)
"Multi-nuclear solid state magnetic resonance".

8. 2.84 Dr. B.T. Heaton (Kent),
"Multi-nuclear NMR studies".

15. 2.84 Dr. R.M. Paton (Edinburgh)
"Heterocyclic Syntheses using Nitrile Sulphides".

7. 3.84 Dr. R.T. Walker (Birmingham),
"Synthesis and Biological Properties of some 5-substituted Uracic Derivatives; yet another example of serendipity in Anti-viral Chemotherapy".

21. 3.84 Dr. P. Sherwood (Newcastle)
"X-ray photoelectron spectroscopic studies of electrode and other surfaces".

21. 3.84 Dr. G. Beamson (Durham/Kratos)
"EXAFS: General Principles and Applications.

23. 3.84 Dr. A. Ceulemans (Leuven)
"The Development of Field-Type models of the Bonding in Molecular Clusters".

2. 4.84 Prof. K. O'Driscoll (Waterloo)
"Chain Ending reactions in Free Radical Polymerisation".

3. 4.84 Prof. C.H. Rochester (Dundee).
"Infrared Studies of adsorption at the Solid-Liquid Interface".

25. 4.84 Dr. R.M. Acheson (Biochemistry, Oxford)
"Some Heterocyclic Detective Stories".

27. 4.84 Dr. T. Albright (Houston, U.S.A.)
"Sigmatropic Rearrangements in Organometallic Chemistry".

14. 5.84 Prof. W.R. Dolbier (Florida, U.S.A.).
"Cycloaddition Reactions of Fluorinated Allenes".

16. 5.84 Dr. P.J. Garratt (UCL)
"Synthesis with Dilithiated Vicinal Diesters and Carboximides".

22. 5.84 Prof. F.C. de Schryver (Leuven)
"The use of Luminescence in the study of micellar aggregates" and
"Configurational and Conformational control in excited state complex formation".

23. 5.84 Prof. M. Tada (Waseda, Japan)
"Photochemistry of Dicyanopyrazine Derivatives".

31. 5.84 Dr. A. Haaland (Oslo)
"Electron Diffraction Studies of some organometallic compounds.

11. 6.84 Dr. J.B. Street (IBM, California)
"Conducting Polymers derived from Pyrroles".

19. 9.84 Dr. C. Brown (IBM, California)
"New Superbase reactions with organic compounds".

21. 9.84 Dr. H.W. Gibson (Signal UOP, Illinois)
"Isomerization of Polyacetylene".

19.10.84 Dr. A. Germain (Languedoc, Montpellier)
"Anodic Oxidation of Perfluoro Organic Compounds in Perfluoroalkane Sulphonic Acids".

24.10.84 Prof. R.K. Harris (Durham)
"N.M.R. of Solid Polymers".

28.10.84 Dr. R. Snaith (Strathclyde)
"Exploring Lithium Chemistry: Novel Structures, Bonding and Reagents".

7.11.84 Prof. W.W. Porterfield (Hampden-Sydney College, USA)
"There is no Borane Chemistry (only Geometry)".

7.11.84 Dr. H.S. Munro (Durham)
"New Information from ESCA Data".

21.11.84 Mr. N. Everall (Durham)
"Picosecond Pulsed Laser Raman Spectroscopy".

27.11.84 Dr. W.J. Feast (Durham)
"A Plain Man's Guide to Polymeric Organic Metals".

28.11.84 Dr. T.A. Stephenson (Edinburgh)
"Some recent studies in Platinum Metal Chemistry".

12.12.84 Dr. K.B. Dillon (Durham)
"31p N.M.R. Studies of some Anionic Phosphorus Complexes".

11. 1.85 Emeritus Prof. H. Suschitzky (Salford)
"Fruitful Fissons of Benzofuroxanes and Isobenzimic azoles (umpolung of o-phenylenediamine)".

13. 2.85 Dr. G.W.J. Fleet (Oxford)
"Synthesis of some Alkaloids from Carbohydrates".

19. 2.85 Dr. D.J. Mincher (Durham)
"Stereoselective Synthesis of some novel Anthracyclinones related to the anti-cancer drug Adriamy and to the Steffimycin Antibiotics".

27. 2.85 Dr. r. Mulvey (Durham)
"Some unusual Lithium Complexes".

6. 3.85 Dr. P.J. Kocienski (Leeds)
"Some Synthetic Applications of Silicon-Mediated Annulation Reactions".

7. 3.85 Dr. P.J. Rodgers (I.C.I. plc. Agricultural Division, Billingham)
"Industrial Polymers from Bacteria".

12. 3.85 Prof. K.J. Packer (B.P. Ltd./East Anglia)
"N.M.R. Investigations of the Structure of Solid Polymers".

14. 3.85 Prof. A.R. Katritzky F.R.S. (Florida)
"Some Adventures in Heterocyclic Chemistry".

20. 3.85 Dr. M. Poliakoff (Nottingham)
"New Methods for detecting Organometallic Intermediates in Solution".

28. 3.85 Prof. H. Ringsdorf (Mainz)
"Polymeric Liposomes as Models for Biomembranes and Cells?".

24. 4.85 Dr. M.C. Grossel (Bedford College, London)
"Hydroxypyridone dyes - Bleachable one-dimensional metals?".

25. 4.85 Major S.A. Shackelford (U.S. Air Force)
"In Situ Mechanistic Studies on Cendensed Phase Thermochemical Reaction Processes: Deuterium Isotope Effects in HMX Decomposition, Explosives and Combustion".

1. 5.85 Dr. D. Parker (I.C.I. plc. Petrochemical and Plastics Division, Wilton)
"Applications of Radioisotopes in Industrial Research".

7. 5.85 Prof. G.E. Coates (formerly of University of Wymoning, USA)
"Chemical Education in England and America: Successes and Deficiencies".

8. 5.85 Prof. D. Tuck (Windsor, Ontario)
"Lower Oxidation State Chemistry of Indium".

8. 5.85 Prof. G. Williams (U.C.W. Aberystwyth)
"Liquid Crystalline Polymers".

9. 5.85 Prof. R.K. Harris (Durham)
"Chemistry in a Spin: Nuclear Magnetic Resonance".

14. 5.85 Prof. J. Passmore (New Brunswick, U.S,A.)
"The Synthesis and Characterisation of some Novel Selenium-Iodine Cations, aided by Se N.M.R. Spectroscopy".

15. 5.85 Dr. J.E. Packer (Auckland, New Zealand)
"Studies of Free Radical Reactions in aqueous solution using Ionising Radiation".

17. 5.85 Prof. I.D. Brown (McMaster University, Canada)
"Bond Valence as a Model for Inorganic Chemistry".

21. 5.85 Dr. D.L.H. Williams (Durham)
"Chemistry in colour".

22. 5.85 Dr. M. Hudlicky (Blacksburg, USA)
"Preferential Elimination of Hydrogen Fluoride from Vicinal Bromofluorocompounds".

22. 5.85 Dr. R. Grimmett (Otago, New Zealand)
"Some Aspects of Nucleophilic Substituton in Imidazoles".

4. 6.85 Dr. P.S. Belton (Food Research Institute, Norwich)
"Analytical Photoacoustic Spectroscopy".

13. 6.85 Dr. D. Woolins (Imperial College, London)
"Metal -Sulphur - Nitrogen Complexes".

14. 6.85 Prof. Z. Rappoport (Hebrew University, Jerusalem)
"The Rich Mechanistic World of Nucleophilic Cinylic Substitution".

19. 6.85 Dr. R.N. Mitchell (Dortmund)
"Some Synthetic and NMR - Spectroscopic Studies of Organotin Compounds".

26. 6.85 Prof. G. Shaw (Bradford)
"Synthetic Studies on Imidazole Nucleosides and the Antibiotic Coformycin".

12. 7.85 Dr. K. Laali (Hydrocarbon Research Institute, University of Southern Californa)
"Recent Developments in Superacid Chemistry and Mechanistic Considerations in Electrophilic Aromatic Substitutions: A Progress Report".

13. 9.95 Dr. V.S. Parmar (University of Delhi),
"Enzyme Assisted ERC Synthesis".

30.10.85 Dr. S.N. Whittleton (University of Durham),
"An Investigation of a Reaction Window".

5.11.85 Prof. M.J. O'Donnell (Indiana-Purdue University),
"New Methodology for the Synthesis of Amino acids".

20.11.85 Dr. J.A.H. MacBride (Sunderland Polytechnic).
"A Heterocyclic Tour on a Distorted Tricycle-Biphenylene".

28.11.85 Prof. D.J. Waddington (University of York),
"Resources for the Chemistry Teacher".

15. 1.86 Prof. N. Sheppard (University of East Anglia),
"Vibrational and Spectroscopic Determinations of the Structures of Molecules Chemisorbed on Metal Surfaces".

29. 1.86 Dr. J.H. Clark (University of York),
"Novel Fluoride Ion Reagents".

12. 2.86 Prof. O.S. Tee (Concordia University, Montreal),
"Bromination of Phenols".

12. 2.86 Dr. J. Yarwood (University of Durham),
"The Structure of Water in Liquid Crystals".

19, 2.86 Prof. G. Procter (University of Salford),
"Approaches to the Synthesis of some Natural Products".

26. 2.86 Miss C. Till (University of Durham),
"ESCA and Optical Emission Studies of the Plasma Polymerisation of Perfluoroaromatics".

5. 3.86 Dr. D. Hathway (University of Durham), "Herbicide Selectivity".

5. 3.86 Dr. M. Schroder (University of Edinburgh), "Studies on Macrocycle Complexes".

12. 3.86 Dr. J.M. Brown (University of Oxford), "Chelate Control in Homogeneous Catalysis".

14. 5.86 Dr. P.R.R. Langridge-Smith (University of Edinburgh), "Naked Metal Clusters - Synthesis, Characterisation and Chemistry".

9. 6.86 Prof. R. Schmutzler (University of Braunschweig), "Mixed Valence Diphosphorous Compounds".

23. 6.86 Prof. R.E. Wilde (Texas Technical University), "Molecular Dynamic Processes from Vibrational Bandshapes".

(b) LECTURES ORGANISED BY DURHAM UNIVERSITY CHEMICAL SOCIETY DURING THE PERIOD 1983 - 1986

20.10.83 Prof. R.B. Cundall (Salford) "Explosives".

3.11.83 Dr. G. Richards (Oxford) "Quantum Pharmacology".

10.11.83 Prof. J.H. Ridd (U.C.L.) "Ipso-Attack in Electrophilic Aromatic Substitution".

17.11.83 Dr. J. Harrison (Sterling Organic), "Applied Chemistry and the Pharmaceutical Industry" (Joint Lecture with the Society of Chemical Industry).

24.11.83 Prof. D.A. King (Liverpool) "Chemistry in 2-Dimensions".

1.12.83 Dr. J.D. Coyle (The Open University), "The Problem with Sunshine".

26. 1.84 Prof. T.L. Blundell (Birkbeck College, London). "Biological Recognition: Interactions of Macromolecular Surfaces".

2. 2.84 Prof. N.B.H. Jonathan (Southampton),
"Photoelectron Spectroscopy - A Radical Approach".

16. 2.84 Prof. D. Phillips (The Royal Institution),
"Luminescence and Photochemistry - a Light Entertainment".

23. 2.84 Prof. F.G.A. Stone F.R.S. (Bristol),
"The Use of Carbene and Carbyne Groups to Synthesise Metal Clusters"
(The Waddington Memorial Lecture).

1. 3.84 Prof. A.J. Leadbetter (Rutherford Appleton Labs.),
"Liquid Crystals".

8. 3.84 Prof. D. Chapman (Royal Free Hospital School of Medicine, London)
"Phospholipids and Biomembranes: Basic Science and Future Techniques".

28. 3.84 Prof. H. Schmidbaur (Munich, F.R.G.),
"Ylides in Coordination Sphere of Metal: Synthetic, Structural and Theoretical Aspects"
(R.S.C. Centenary lecture).

18.10.84 Dr. N. Logan (Nottingham),
"N O and Rocket Fuels".

23.10.84 Dr. W.J. Feast (Durham),
"Syntheses of Conjugated Polymers. How and Why?".

8.11.84 Prof. B.J. Aylett (Queen Mary College, London),
"Silicon - Dead Common or Refined?".

15.11.84 Prof. B.T. Golding (Newcastle-upon-Tyne),
"The Vitamin B Mystery".

22.11.84 Prof. D.T. Clark (I.C.I. New Science Group),
"Structure, Bonding, Reactivity and Synthesis as revealed by ESCA".
(R.S.C. Tilden lecture).

29.11.84 Prof. C.J.M. Stirling (University College of North Wales)
"Molecules taking the Strain".

6.12.84 Prof. R.D. Chambers (Durham),
"The Unusual World of Fluorine".

24. 1.85 Dr. A.K. Covington (Newcastle-upon-Tyne),
"Chemistry with Chips".

31. 1.85 Dr. M.L.H. Green (Oxford),
"Naked Atoms and Negligee Ligands".

7. 2.85 Prof. A. Ledwith (Pilkington Bros.),
"Glass as a High Technology Material"
(Joint Lecture with the Society of Chemical Industry).

14. 2.85 Dr. J.A. Salthouse (Manchester),
"Son et Lumiere".

21. 2.85 Prof. P.M. Maitlis, F.R.S. (Sheffield)
"What Use is Rhodium?".

7. 3.85 Dr. P.W. Atkins (Oxford),
"Magnetic Reactions".

17.10.85 Dr. C.J. Ludman (University of Durham)
"Some Thermochemical aspects of Explosions".
(A Demonstration Lecture).

24.10.85 Dr. J. Dewing (U.M.I.S.T.),
"Zeolites - Small Holes, Big Opportunities".

31.10.85 Dr. P. L. Timms, (University of Bristol),
"Some Chemistry of Fireworks"
(A Demonstration Lecture).

7.11.85 Prof. G. Ertl, (University of Munich),
"Heterogeneous Catalysis",
(R.S.C. Centenary lecture).

14.11.85 Dr. S.G. Davies (University of Oxford),
"Chirality Control and Molecular Recognition".

21.11.85 Prof. K.H. Jack, F.R.S. (University of Newcastle-upon-Tyne),
"Chemistry of Si-Al-O-N Engineering Ceramics"
(Joint Lecture with the Society of Chemical Industry).

28.11.85 Dr. B.A.J. Clark (Research Division, Kodak ltd.)
"Chemistry and Principles of Colour Photography".

23. 1.85 Prof. Sir Jack Lewis, F.R.S. (University of Cambridge),
"Some More Recent Aspects in the Cluster Chemistry of Ruthenium and Osmium Carbonyls"
(The Waddington Memorial Lecture).

30. 1.86 Dr. N.J. Phillips (University of Technology, Loughborough)
"Laser Holography".

13. 2.86 Prof. R. Grigg (Queen's University, Belfast),
"Thermal Generation of 1,3-Dipoles".
(R.S.C. Tilden lecture).

20. 2.86 Dr. C.J.F. Barnard, (Johnson Matthey Group Research),
"Platinum Anti-Cancer Drug Development - From Serendipity to Science".

27. 2.86 Prof. R.K. Harris, (University of Durham),
"The Magic of Solid State NMR".

6. 3.86 Dr. B. Iddon (University of Salford),
"The Magic of Chemistry"
(A Demonstration lecture).

APPENDIX II

CONFERENCES ATTENDED DURING THE PERIOD OCTOBER 1983 AND SEPTEMBER 1986

1. 1983 International Conference on Fourier Transform Spectroscopy, Durham University, September 1983.

2. European Molecular Liquids Group, "Beyond the One Molecule Approach", Nice, France, September 1984.

3. Millimetre Wave Loss Processes and Phenomena, a workshop, Durham University, July 1985.

4. Infrared Discussion group, University of Durham, July, 1986.

Appendix III

MACRO COMMANDS ON CHN9

ALPHACAL {dat1} {dat2}	CALCULATES ABSORPION COEFFICIENT FROM BACKGROUND AND SAMPLE INTERFEROGRAMS. PARAMETER FILES REQUIRED: FTPAR FFTARPAR
COMP {prog}	COMPILES FORTRAN PROGRAM prog.s AND LOADS OBJECT CODE INTO prog.o
IF {prog.s}	RUNS THE INTERACTIVE FORTRAN PACKAGE, COMPILES prog.s AND LOADS THE NAG, GHOST AND IG LIBRARIES.
FULLINT {dat1} {dat2} {windat}	SOLVES FOR ABSORPTION COEFFICIENT AND REFRACTIVE INDEX USING THE FULL INTERFEROGRAM METHOD. dat1 - FIRST INTERFEROGRAM dat2 - SECOND INTERFEROGRAM windat - WINDOW INTERFEROGRAM PARAMETER FILES REQUIRED: FTPAR ITRPAR WNPAR
LASERPLOT {plotfile}	OBTAINS PLOT USING THE LASER PLOTTER, SCALING TO 0.8.
MORI {data}	FITS THE MORI CONTINUED FRACTION TO N AND ALPHA DATA. PARAMETER FILES REQUIRED: NEWPAR
NANDALPH {dat1} {dat2}	TRANSFORMS AND ANALYSES DISPERSIVE INTERFEROGRAMS TO GIVE N AND ALPHA. dat1 IS THE SMALLER PATHLENGTH. PARAMETER FILES REQUIRED: FTPAR & NAPAR
TIDY {PROG.S}	TIDIES A FORTRAN PROGRAM.

DESCRIPTION OF PROGRAMS ON CHN9.

ABSMOL CONVERTS ABSORPTION COEFFICIENT FROM CM-1 TO CM-1 MOLES/LITRE. AND PLOTS OUT BOTH FOR SEVERAL SPECTRA.
E.G. £RUN ABSMOL.O+*GHOST 7=alpha 9=-plot

ALPHPLOT PLOTS THREE ABSORPTION COEFFICIENT SPECTRA ON THE SAME PLOT AND THEN PLOTS THEM NORMALISED TO 1.0. READS IN DATA FROM CONV.S. WRITTEN TO PLOT BENZENE; I2/BZ vs. I2/BZ; I2/BZ vs. BENZENE.
E.G. £RUN ALPHPLOT.O+*GHOST 7=-alpha 9=-plot

AREA CALCULATES THE AREA UNDER A CURVE USING THE TRAPEZOIDAL RULE.

BANAL A BAND-SHAPE ANALYSIS PLOTTING PROGRAM. PLOTS ABSORPTION COEFFICIENT AND ITS LOG; ABSORPTION CROSS-SECTION AND ITS LOG.
E.G. £RUN BANAL.O+*GHOST 7=specdata 8=-results 9=-plot

CONV CONVERTS OUTPUT FROM FFTAR TO ABSORPTION COEFFICIENT, IN ORDER TO BE READ IN BY OXTOBY, ALPHPLOT OR LSTSQPOLY.
E.G. £RUN CONV.O+*GHOST 5=-abs 6=-alpha

DEBYE CALCULATES VALUES OF N & ALPHA FROM THE DEBYE EQUATION BETWEEN ANY FREQUENCIES. PROMPTS FOR ALL PARAMETERS IN DEBYE EQUATION. PLOTS ALL CURVES.
E.G. £RUN DEBYE.O+*GHOST 7=output 9=plot

DEBPLOT CALCULATES VALUES OF N AND ALPHA FROM THE DEBYE EQUATION. PROMPTS FOR VALUES OF EO, Einfinity AND RELAXATION TIME. THEN CALCULATES THE COMPLEX INSERTION LOSS. PLOTS OUT ALL CURVES.
INPUT ON UNIT 1; OUTPUT ON UNITS 7 & 8
E.G. £RUN DEBPLOT.O+*GHOST 1=windowdata 7=alpha&n 8=insloss 9=plot

DRIFT CALCULATES A FRINGE SHIFT TERM, CORRECTED FOR INSTRUMENT INSTABILITY, FOR USE WITH DISPERSIVE REFLECTION MEASUREMENTS. THE RAW INTERFEROGRAMS ARE INPUT ON UNIT 7 IN THE ORDER BY WHICH THEY WERE RECORDED (MAX. OF 3); OUTPUT IS TO THE SCREEN. THE CORRECTED FRINGE SHIFT TERM CAN THEN BE USED IN PROGRAM 'REFOPCON'. GHOST ROUTINES ARE INCLUDED.
E.G. £RUN DRIFT.O+*GHOST 7=int1+int2+int3 9=-plot

EDIT REMOVES UNWANTED FRINGES OR NOISE SPIKES IN AN INTERFEROGRAM. PROGRAM IS RUN INTERACTIVELY AT A GRAPHICS TERMINAL AND PROMPTS WITH VISUAL AIDS AS TO WHICH PARTS ARE TO BE REMOVED.THE POINTS REMOVED ARE REPLACED WITH AVERAGE VALUES OF AN OPTIONAL NUMBER OF SURROUNDING POINTS.INPUT IS ON UNIT 7;OUTPUT ON UNIT 8.
E.G. £RUN EDIT.O+*IG+*GHOST 7=rawint 8=edint 99=-scrnplot

FFTPROG DEVELOPED FROM SSFFT SUCH THAT THE PROGRAM CAN NOW CHOOSE FOR ITSELF WHETHER TO TRANSFORM A DOUBLE-SIDED OR SINGLE-SIDED INTERFEROGRAM.

FSVPLOT PLOTS OUT THE STAGES IN PHASE CORRECTING A SINGLE-SIDED INTERFEROGRAM ACCORDING TO THE PROCEDURE OF FORMAN, STEELE & VANASSE. INPUT ON UNIT 4; OUTPUT TO PLOTTER.
E.G. £RUN FSVPLOT.O+*GHOST 4=-ints 9=-plot

FSVPLOT2 AS FSVPLOT BUT PLOTS WHOLE OF RAW & PHASE CORRECTED INTERFEROGRAMS RATHER THAN JUST CENTRAL PORTION.

FLINT ANALYSES THE FULL INTERFEROGRAM OBTAINED USING THE DISPERSIVE LIQUID CELL. THE SECANT METHOD IS USED IN ORDER TO ITERATE TOWARDS THE SOLUTION, IN N AND ALPHA, OF THE THEORETICAL COMPLEX INSERTION LOSS CONSTRUCTED USING FRESNEL'S EQUATIONS.
E.G. £RUN FULLINT.O 8=unit8 7=input 1=solution
UNIT7: The liquid pathlengths in cm.
The no. of reflectioins in sample & background.
Accuracies required in n & alpha.
Parameter for finding 2nd. limit for secant method from the guess.
UNIT8: No. of pts. in window spectra.
Waveno. limits and step.
Optical constants of window.
Title.
Liquid sin/cos data.

INTPLOT PLOTS RAW INTERFEROGRAM.
E.G. £RUN INTPLOT.O+*GHOST 7=int 9=-plot

ITPLOT PLOTS THE OUTPUT FROM FLINT.S
E.G. £RUN ITPLOT.O+*GHOST 7=int 9=-plot

LSTSQ PRODUCES A LEAST SQUARE FIT TO LINEAR PLOTS.
E.G. £RUN LSTSQ.O+*GHOST 9=-plot

LSTSQPOLY COMPUTES CHEBYSHEV COEFFICIENTS FOR A SET OF DATA UP TO ANY DEGREE AND UTILISES THESE TO FIT A CURVE TO THE DATA AND INTERPOLATE BETWEEN THE GIVEN POINTS.
E.G. £RUN LSTSQPOLY.O+*NAG+*GHOST 5=data 9=-plot

MEAN PLOTS THE AVERAGE VALUE OF UP TO 50 SPECTRA, TOGETHER WITH THE ERROR ON THE MEAN TO TWO STANDARD DEVIATIONS. SPECTRA MAY BE NORMALISED TO ANY VALUE AT A SELECTED FREQUENCY ELEMENT. INPUT ON UNIT 7; OUTPUT TO PLOTTER.
E.G. £RUN MEAN.O+*GHOST 7=data 9=-plot

OXTOBY FITS ABSORPTION COEFFICIENT DATA (FROM CONV) TO MODEL OF OXTOBY.
E.G. £RUN OXTOBY.O+*IG+*GHOST 7=alpha 9=-plot

OXTOBYFIT AS ABOVE BUT USES A LEAST SQUARES ROUTINE TO FIT THE DATA.
E.G. £RUN OXTOBYFIT.O+*NAG+*GHOST 7=alpha 9=-plot

SSFFT DERIVED FROM 'HIBRID'.TRANSFORMS, AVERAGES & RATIOS UP TO 3 BACKGROUND AND SAMPLE INTERFEROGRAMS, TREATING THEM AS SINGLE-SIDED. PHASE CORRECTION IS PERFORMED ACCORDING TO PROCEDURE OF FORMAN, STEELE & VANASSE.
E.G. £RUN SSFFT.O

Appendix IV

```
C        FLINT.S
C
C         DETERMINES THE LIQUID OPTICAL CONSTANTS FROM A DISPERSIVE
C         TRANSMISSION EXPERIMENT FOR ANY NUMBER OF INTERNAL
C         REFLECTIONS. THIS IS ACHIEVED BY AN ITERATIVE PROCEDURE
C         FOR SOLVING THE COMPLEX FRESNEL EQUATIONS CONSTRUCTED
C         FOR THE VARIOUS REFLECTION/PROPAGATION TERMS INVOLVED.
C
C         INPUT IS SIN/COS VALUES FOR TWO DIFFERENT LIQUID PATHLENGTHS
C         AND ALPHA/N VALUES FOR THE WINDOW.
C
C        BRENDAN CATLOW          FEBRUARY 1986
C
C
     DIMENSION AWN(512), AWA(512), SCS(1024), SCB(1024), TITLE(20),
    1          WN(512), ILEXPR(512), ILEXPI(512)
     REAL LN(512), LA(512), LA1, LA3, PI
     DOUBLE PRECISION ILTHR1, ILTHR2, ILTHR3, ILTHI1, ILTHI2, ILTHI3,
    1       RR1, RI1, DENOMR, DENOMI, RR2, RI2, RR3, RI3, NUMER, NUMEI,
    2       TR3, TI3, TR2, TI2, TR1, TI1, SC1, SC2, ILEXPR, ILEXPI,
    3       SCS, SCB, LN1, LN2, LN3, LK1, LK2, LK3, INC, INCR, INCI,
    4       DILR, DILI
C
C INPUT:
C        DS,DB             - LIQUID PATHLENGTHS FOR SAMPLE & BACKGROUND
C        NRS,NRB           - NO. OF (1,1) FRINGES     "        "
C        STRTS,STRTB       - MIRROR START POSITIONS   "        "
C        ACCR,ACCI         - ACCURACY REQUIRED IN REAL & IMAGINARY PARTS
C                            OF THE COMPLEX INSERTION LOSS
C        INC               - INCREMENT REQUIRED IN DETERMINING NEXT
C                            VALUE OF GUESS IN ITERATIVE ROUTINE
C        WNSTRT,WNEND      - FIRST & LAST WAVENUMBER REQUIRED IN FINAL
C                            SPECTRUM.
C        GF                - GAIN FACTOR (ratio of gain for first pathlength
C                                         to that for second pathlength)
C
     READ (8,100) DS, DB, NRS, NRB, STRTS, STRTB, GF
     READ (8,110) ACCR, ACCI, INC
     READ (8,120) WNSTRT, WNEND
     READ (8,200) LN1, LA1
     READ (7,160)
     READ (7,130) NS, SI, NPTS, WNLOW, WNHIGH, WS
     READ (7,140) (AWN(J),J=1,NPTS)
     READ (7,150) (AWA(J),J=1,NPTS)
     READ (7,160) (TITLE(I),I=1,20)
     READ (7,170) NP, ZPDS
     READ (7,180) (SCS(J),J=1,NP)
     READ (7,160)
     READ (7,170) NP, ZPDB
     READ (7,180) (SCB(J),J=1,NP)
C
     PI = 3.14159
     FS = ((STRTS - STRTB) + (ZPDS - ZPDB) * SI / 2000.0) / (DS - DB)
C
C           SET UP WAVENUMBER ARRAY
C
     WN(1) = WNLOW
     L = 1
     LL = 1
     DO 20 J = 2, NPTS
       K = J - 1
       WN(J) = WN(K) + WS
```

```
      IF (WN(J) .GT. WNSTRT) GO TO 10
      L = J + 1
      GO TO 20
   10 IF (WN(J) .LT. WNEND) GO TO 20
      LL = J
      GO TO 30
   20 CONTINUE
C
C         COMPUTE THE EXPERIMENTAL INSERTION LOSS
C
   30 DO 40 J = L, LL
      K = NP - J + 1
      CALL DIVCN(SCS(J), SCS(K), SCB(J), SCB(K), ILEXPR(J), ILEXPI(J))
   40 CONTINUE
      WRITE (6,190) WNSTRT
   45 LK1 = LA1 / (4.0*PI*WN(L))
      LN1 = LN1 - FS
C
C     THE FOLLOWING IS A SECANT ITERATIVE PROCEDURE FOR FINDING
C     THE THEORETICAL COMPLEX INSERTION LOSS
C
      WRITE (6,210)
      WRITE (6,220)
      DO 70 J = L, LL
        NIT = 1
   50   CALL ILLC(AWN(J), AWA(J), WN(J), DS, DB, LN1, LK1, NRS, NRB,
     1       ILTHR1, ILTHI1)
        CALL MULTCN(LN1, LK1, INC, 0.0D0, INCR, INCI)
        CALL ADDCN(LN1, LK1, INCR, INCI, LN2, LK2)
        CALL ILLC(AWN(J), AWA(J), WN(J), DS, DB, LN2, LK2, NRS, NRB,
     1       ILTHR2, ILTHI2)
        CALL DIVCN(ILTHR1, ILTHI1, ILTHR2, ILTHI2, RR1, RI1)
        CALL SUBCN(RR1, RI1, 1.0D0, 0.0D0, DENOMR, DENOMI)
        CALL DIVCN(ILEXPR(J), ILEXPI(J), ILTHR2, ILTHI2, RR2, RI2)
        CALL SUBCN(RR2, RI2, 1.0D0, 0.0D0, TR1, TI1)
        CALL SUBCN(LN1, LK1, LN2, LK2, TR2, TI2)
        CALL MULTCN(TR2, TI2, TR1, TI1, NUMER, NUMEI)
        CALL DIVCN(NUMER, NUMEI, DENOMR, DENOMI, TR3, TI3)
        CALL ADDCN(LN2, LK2, TR3, TI3, LN3, LK3)
        CALL ILLC(AWN(J), AWA(J), WN(J), DS, DB, LN3, LK3, NRS, NRB,
     1       ILTHR3, ILTHI3)
        CALL SUBCN(ILTHR3, ILTHI3, ILEXPR(J), ILEXPI(J), DILR, DILI)
        ADILR = DABS(DILR)
        ADILI = DABS(DILI)
        LA3 = LK3 * 4.0 * PI * WN(J)
        LN1 = LN3
        LK1 = LK3
        LN3 = LN3 + FS
        WRITE (6,230) WN(J), NIT, LN3, LA3, ADILR, ADILI
        IF (ADILR .GT. ACCR) GO TO 60
        IF (ADILI .GT. ACCI) GO TO 60
        LN(J) = LN3
        LA(J) = LA3 + ALOG(GF)
        GO TO 70
   60   NIT = NIT + 1
        IF (NIT .GT. 40) GO TO 80
        GO TO 50
   70 CONTINUE
      WRITE (1,160) (TITLE(I),I=1,20)
      NPTS = LL - L
```

```
      NSETS = 1
      WRITE (1,135) NSETS, L, NPTS, WNSTRT, WNEND, WS
      WRITE (1,140) (LN(J),J=L,LL)
      WRITE (1,150) (LA(J),J=L,LL)
      GO TO 240
   80 WRITE (6,90) WN(J)
      WRITE (6,95)
      READ (5,200) LN1, LA1
      IF (LN1 .LT. 0.0) GO TO 240
      L = J
      GO TO 45
   90 FORMAT (' ', 'STOP AT WAVENUMBER', F10.6, '- FAILED TO CONVERGE WI
     1THIN 40 ITERATIVE STEPS')
   95 FORMAT (' ','ENTER NEW ESTIMATES AT THIS WAVENUMBER (OR -1 TO QUIT
     1)')
  100 FORMAT (2F8.5, 2I2, 3F8.5)
  110 FORMAT (2F12.6, F12.6)
  120 FORMAT (2F12.6)
  130 FORMAT (I4,F4.0,I4,3F12.6)
  135 FORMAT (3I4,3F12.6)
  140 FORMAT (10F10.6)
  150 FORMAT (10F10.4)
  160 FORMAT (20A4)
  170 FORMAT (I4, F5.0)
  180 FORMAT (10E16.5)
  190 FORMAT (' ', 'ENTER ESTIMATES OF LIQUID N & ALPHA AT WAVENUMBER
     1  ', F8.5)
  200 FORMAT (F10.6, F10.4)
  210 FORMAT (' ', 'WAVENUMBER', 4X, 'NO. OF', 6X, 'N', 8X, 'ALPHA', 5X,
     1       'ACCURACY IN COMPLEX INSERTION LOSS')
  220 FORMAT (' ', 12X, 'ITERATIONS', 28X, 'REAL', 6X, 'IMAGINARY')
  230 FORMAT (F12.6, 5X, I2, 3X, F10.6, 1X, F10.4, 4X, 2F12.8)
  240 STOP
      END
C
C          THE FOLLOWING SUBROUTINES PERFORM COMPLEX
C          ARITHMETIC.
C
      SUBROUTINE MULTCN(A, B, C, D, E, F)
      DOUBLE PRECISION A, B, C, D, E, F
      E = (A*C) - (B*D)
      F = (B*C) + (D*A)
      RETURN
      END
      SUBROUTINE DIVCN(A, B, C, D, E, F)
      DOUBLE PRECISION A, B, C, D, E, F
      G = (C*C) + (D*D)
      E = ((A*C) + (B*D)) / G
      F = ((B*C) - (A*D)) / G
      RETURN
      END
      SUBROUTINE SUBCN(A, B, C, D, E, F)
      DOUBLE PRECISION A, B, C, D, E, F
      E = A - C
      F = B - D
      RETURN
      END
      SUBROUTINE ADDCN(A, B, C, D, E, F)
      DOUBLE PRECISION A, B, C, D, E, F
      E = A + C
```

```
      F = B + D
      RETURN
      END
      SUBROUTINE SQUCN(A, B, C, D)
      DOUBLE PRECISION A, B, C, D
      C = (A*A) - (B*B)
      D = (B*A) + (B*A)
      RETURN
      END
C
      SUBROUTINE ILLC(ANW, AAW, WN, D1, D2, ANT, AAT, NR1, NR2, ILR,
     1           ILI)
C
C         SUBROUTINE FOR CONSTRUCTING THE THEORETICAL COMPLEX
C         INSERTION LOSS FOR THE CASE OF THE SPECIAL LIQUID
C         DISPERSIVE CELL.
C
      DOUBLE PRECISION ANLR, ANLI, ANWR, ANWI, AR, AI, BR, BI, R21R,
     1       R21I, AR1, AI1, AR2, AI2, ILR, ILI, R23R, R23I, A2R1, A2I1,
     2       A2R2, A2I2, S11R2, S11I1, S11R1, S11I2, S12R1, S12I1,
     3       S12R2, S12I2, ANT, AAT
      R23R = -1.0
      R23I = 0.0
      ANLR = ANT
      ANLI = AAT
      ANWR = ANW
      ANWI = AAW / (4.0*3.14159*WN)
      CALL SUBCN(ANLR, ANLI, ANWR, ANWI, AR, AI)
      CALL ADDCN(ANLR, ANLI, ANWR, ANWI, BR, BI)
      CALL DIVCN(AR, AI, BR, BI, R21R, R21I)
      AR = -(2.0*WN*3.14159*AAT*D1)
      AR = DEXP(AR)
      AI = 2.0 * 3.14159 * ANLR * WN * D1
      BR = DCOS(AI)
      BI = DSIN(AI)
      A2R1 = AR * BR
      A2I1 = AR * BI
      AR = -(2.0*WN*3.14159*AAT*D2)
      AR = DEXP(AR)
      AI = 2.0 * 3.14159 * ANLR * WN * D2
      BR = DCOS(AI)
      BI = DSIN(AI)
      A2R2 = AR * BR
      A2I2 = AR * BI
      CALL SQUCN(A2R1, A2I1, AR, AI)
      CALL MULTCN(AR, AI, R23R, R23I, S11R1, S11I1)
      CALL SQUCN(A2R2, A2I2, BR, BI)
      CALL MULTCN(BR, BI, R23R, R23I, S11R2, S11I2)
      AR1 = S11R1
      AI1 = S11I1
      AR2 = S11R2
      AI2 = S11I2
      ON = 1
      NR = NR1
   10 NR = NR - 1
      IF (NR .EQ. 0) GO TO 20
      ON = ON + 1
      CALL REFL(R23R, R23I, R21R, R21I, A2R1, A2I1, ON, S12R1, S12I1)
      CALL ADDCN(AR1, AI1, S12R1, S12I1, AR1, AI1)
      GO TO 10
```

```
   20 NR = NR2
      ON = 1
   30 NR = NR - 1
      IF (NR .EQ. 0) GO TO 40
      ON = ON + 1
      CALL REFL(R23R, R23I, R21R, R21I, A2R2, A2I2, ON, S12R2, S12I2)
      CALL ADDCN(AR2, AI2, S12R2, S12I2, AR2, AI2)
      GO TO 30
   40 CALL DIVCN(AR1, AI1, AR2, AI2, ILR, ILI)
      RETURN
      END
C
      SUBROUTINE REFL(R23R, R23I, R21R, R21I, A2R, A2I, ON, RFR, RFI)
C
C             SUBROUTINE FOR PRODUCING THE REFLECTION COEFFICIENT
C             AT AN INTERFACE.
C
      DOUBLE PRECISION R21R, R21I, R23R, R23I, A2R, A2I, CR, CI, AR, AI,
     1       BR, BI, RFR, RFI
      N = ON - 1
      CALL MULTCN(R23R, R23I, R23R, R23I, AR, AI)
   10 N = N - 1
      IF (N .EQ. 0) GO TO 20
      CALL MULTCN(R23R, R23I, AR, AI, AR, AI)
      GO TO 10
   20 N = ON - 1
      IF (N .LT. 2) GO TO 40
      N = N - 1
      CALL MULTCN(R21R, R21I, R21R, R21I, BR, BI)
   30 N = N - 1
      IF (N .EQ. 0) GO TO 50
      CALL MULTCN(R21R, R21I, BR, BI, BR, BI)
      GO TO 30
   40 BR = R21R
      BI = R21I
   50 N = (ON*2) - 1
      CALL MULTCN(A2R, A2I, A2R, A2I, CR, CI)
   60 N = N - 1
      IF (N .EQ. 0) GO TO 70
      CALL MULTCN(A2R, A2I, CR, CI, CR, CI)
      GO TO 60
   70 CALL MULTCN(AR, AI, BR, BI, RFR, RFI)
      CALL MULTCN(RFR, RFI, CR, CI, RFR, RFI)
      RETURN
      END
```

```
MACRO FULLINT DAT1 DAT2 WINDAT
 $EMPTY -MP1 !
 $EMPTY -MP2 !
 $EMPTY -ANW !
 $EMPTY -SC1 !
 $EMPTY -SC2 !
 $SC FTPAR
 $R GPONFFT.O 5={WINDAT} 8=FTPAR 7=-MP1
 $SC FTPAR
 $R GPONFFT.O 5={WINDAT} 8=FTPAR 7=-MP2
 $R FIWIN.O 5=-MP1+-MP2 8=WNPAR 7=-ANW 6=-6
 $SC FTPAR
 $R GPONFFT.O 5={DAT1} 8=FTPAR 7=-SC1
 $R GPONFFT.O 5={DAT2} 8=FTPAR 7=-SC2
 $COPY -ANW+-SC1+-SC2 -INPUT
 $CRE NALPHA
 $R FLINT.O 7=-INPUT 8=ITRPAR 1=NALPHA
 $CRE PLOT
 $R ITPLOT.O+*GHOST 5=NALPHA 9=PLOT
ENDMACRO
```

Appendix V

UPPER BOUNDS FOR DISCRETE FEATURES IN THE FAR-INFRARED SPECTRUM OF LIQUID ACETONITRILE

J.R. BIRCH, Kong Fan PING [1]

Division of Electrical Science, National Physical Laboratory, Teddington, Middlesex TW11 0LW, UK

S.K. HUSAIN

Department of Physics, Birkbeck College, Malet Street, London WC1E 7HX, UK

J. YARWOOD and B. CATLOW

Department of Chemistry, Science Laboratories, University of Durham, South Road, Durham DH1 3LE, UK

Received 3 October 1984; in final form 24 April 1985

Experimental results are presented that allow upper bounds to be placed on the intensity of any discrete structure that may be superimposed on the generally accepted form of the broad far-infrared absorption profile of liquid acetonitrile. These bounds are considerably less than the intensities of features that have been discussed in previous publications.

1. Introduction

In recent publications Evans [1–3] has presented the results of far-infrared power transmission measurements on acetonitrile (CH_3CN) and other liquids in the spectral region between 30 and 250 cm^{-1}. The data were interpreted as presenting evidence for the presence of discrete spectral features superimposed upon the normal broad and featureless far-infrared absorption band which is due to roto-translational motion of the molecular dipole. This spectral detail was discussed in terms of strong cooperative reorientation of molecular "clusters" or "aggregates" in the liquid. Such an observation of a significant cooperative contribution to the far-infrared dielectric response would, if correct, be of considerable importance and would require drastic reassessment and modification of current models of the microscopic dynamics of the liquid state.

In view of the potential importance of such effects the present study was initiated to provide an independent determination of the absorption spectrum of liquid acetonitrile between 30 and 150 cm^{-1}, the region of observation of the proposed structure in Evans' work. In order to establish whether or not such spectral features are "real" two different measurement strategies were adopted. The first was an attempt to duplicate the transmission results of Evans using the techniques of conventional Fourier transform spectroscopy. The second was to determine the complex refraction spectrum of the liquid by the completely different measurement technique of dispersive Fourier transform spectrometry (DFTS) [4] used in reflection.

Since the molecule has a very high dipole moment its absorption coefficient is very high and transmission measurements are difficult because the detected signal level, and therefore the signal-to-noise ratio, are necessarily low. Furthermore, these are lowest at the band centre, the region where much of the proposed structure is observed. Thus not only is sensitivity to the presence of small features low, but susceptibility to random and systematic errors is at its greatest. Nevertheless, it is possible to make good transmission mea-

[1] On leave of absence from the Shanghai Institute of Technical Physics, Shanghai, People's Republic of China.

surements on such a liquid using a liquid-helium-cooled bolometer as detector.

The dispersive reflection technique [4] involves the direct determination of the spectral variation of both the attenuation and phase shift imposed on an electromagnetic wave on reflection at an interface between a transparent solid (silicon) and the liquid of interest. This method has several advantages for higher absorbing liquids. Firstly it gives the full dielectric response without the use of approximations or assumptions. This is extremely valuable for comparison with models for molecular rotation [5]. Secondly, the detected signal levels are considerably higher because the radiation is not required to traverse an optically opaque material. Thirdly, the transmission method necessarily requires work with very thin liquid layers (of the order of 25–50 μm). This leads to severe problems with layer uniformity and reproducibility, especially if polymeric windows are used, as was the case in Evans' work. The reflection techique does not rely at all on specimen thickness. Furthermore, since the two techniques are susceptible to completely different sources of error, one might reasonably have confidence in the presence of any discrete features found to be common to *both* experiments.

2. Experimental

The DFTS measurements were made with an interferometer of modular construction [6] in which the upper surface of the window of the liquid cell [5] formed the fixed mirror of the interferometer. The detector used was a quartz window Golay cell. Measurements were made in the spectral region between 30 and 150 cm^{-1} at a resolution of 2 cm^{-1} and at a temperature of 293 ± 1 K. Fifteen independent measurements were made using four specimens of liquid CH_3CN (BDH Chemicals Ltd., Special for Spectroscopy).

The power transmission measurements were performed on a Beckman RIIC FS720 Michelson interferometer. The detector was either a QMC Ltd liquid-helium-cooled Ge bolometer or a diamond-window Golay cell. The two interferometer arms were carefully thermostatted to avoid instabilities introduced by temperature changes. The transmission cell was of a standard demountable design with wedged silicon windows separated by PTFE spacers. Its temperature was controlled to 298 ± 2 K. The measurements were made at an apodised resolution of ≈2 cm^{-1}. A total of over 30 independent measurements were made using Eastman Kodak Spectroscopic Grade CH_3CN which had been thoroughly dried over type 4A molecular sieves.

3. Results and discussions

Figs. 1 and 2 show the absorption and refraction spectra determined by the DFTS measurement. In each graph two spectra are shown. The upper spectra, plotted as crosses, represent the average absorption and refraction spectra obtained from the fifteen measurements. The lower plots represent the standard deviations of the fifteen component spectra at each spectral element. There are several points of comparison between these spectra and those of Evans. First, although the two absorption spectra have similar large-scale spectral variations the overall value is about twice that of Evans. Furthermore, the spectrum is in good quantitative agreement not only with that determined in other power transmission measurements by Arnold et al. [7], but also with calculations based on simulation studies by Edwards and Madden [8]. This difference in level can probably be attributed to uncertainties in determining the effective optical thickness of the specimen used in the transmission measurements of Evans, as has been discussed above. Second, although there is small-scale structure superimposed on the absorption profile determined in the present work, it does not correspond in position with the structure reported by Evans, and it is generally of the order of, or less than, the standard deviation of the data set. There is *no* clear evidence for well defined discrete features in these spectra. Similarly, the refraction spectrum has no discrete structure at a level significantly above its standard deviation.

The potential difficulties of low signal levels in transmission measurements on acetonitrile have been discussed in the introduction. This is illustrated in fig. 3 which shows typical modulus spectra recorded in the present transmission measurements. Spectrum (a) is the background spectrum of the intrument with no liquid present, spectra (b), (c) and (d) are the corresponding spectra recorded through 25, 40 and 100 μm thicknesses of acetonitrile. The transmission results

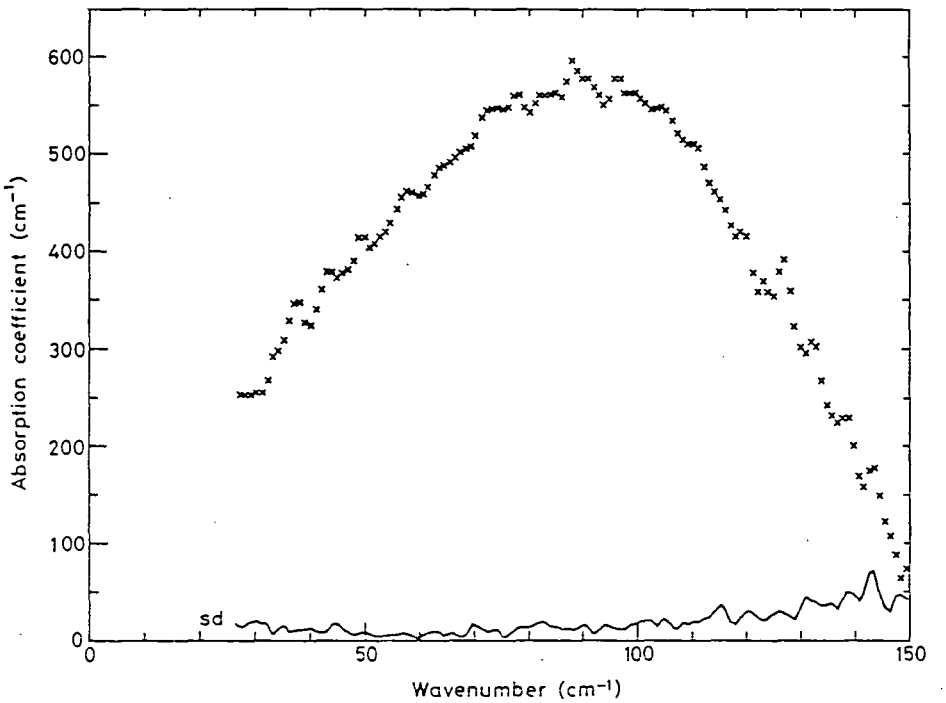

Fig. 1. The absorption spectrum of acetonitrile at 293 K determined by dispersive Fourier transform spectroscopy in reflection between 20 and 150 cm^{-1}. The crosses represent the mean of fifteen independent determinations, while the continuous curve represents the standard deviation of the fifteen individual spectra at each spectral element.

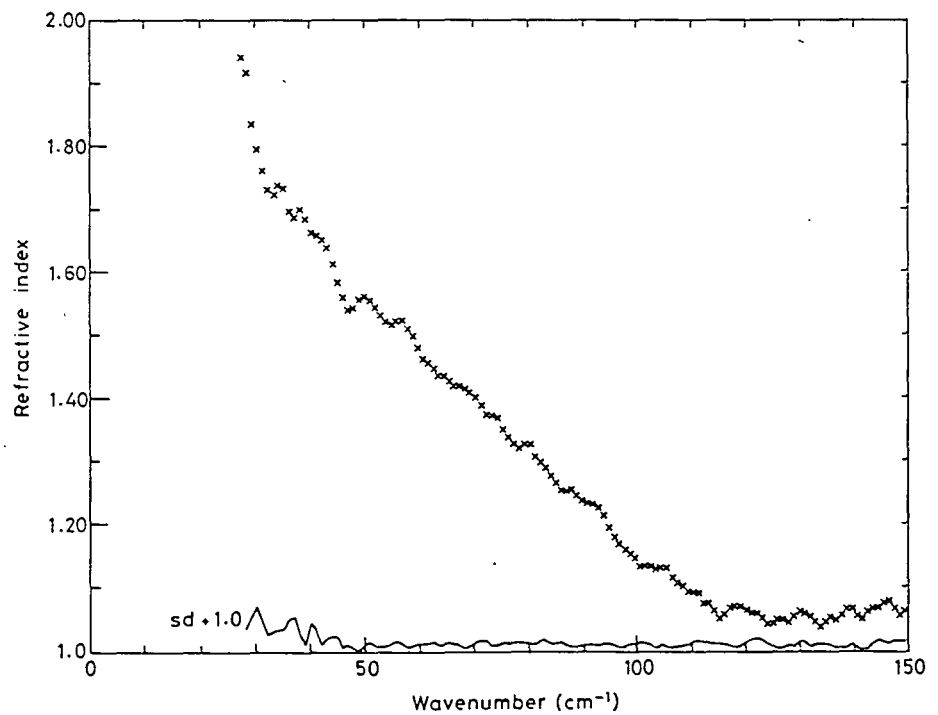

Fig. 2. The refraction spectrum of acetonitrile at 293 K determined by dispersive Fourier transform spectroscopy in reflection between 20 and 150 cm^{-1}. The data are plotted as in fig. 1.

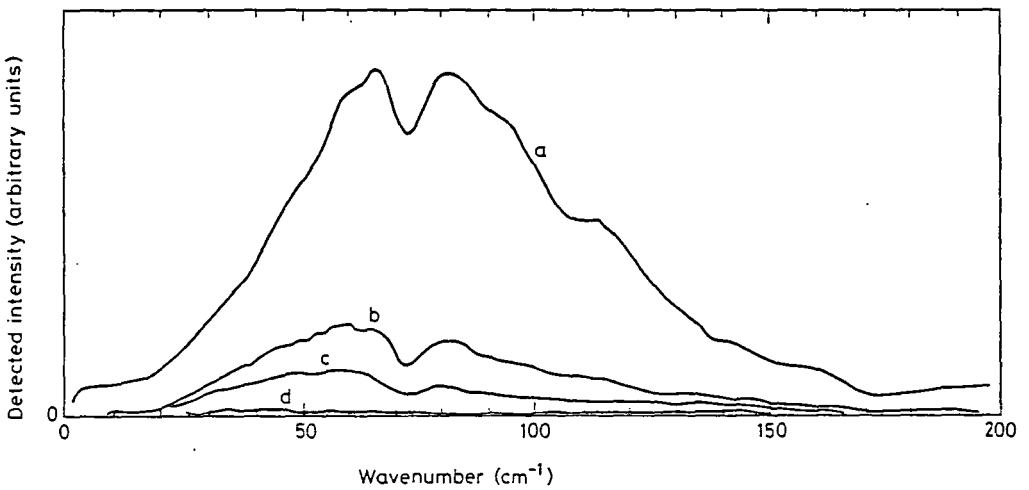

Fig. 3. Typical modulus spectra recorded in transmission measurements. (a) Background instrumental spectrum with no liquid present, (b), (c) and (d) are the corresponding spectra recorded through 25, 40 and 100 μm of acetonitrile, respectively.

to be referred to next were all recorded through acetonitrile thicknesses between 15 and 50 μm. Thus, the raw data of the present work, the liquid modulus spectra, were at signal levels that were well above the limiting random-signal level of the measurement (closely approached by spectrum (d) in fig. 3). Fig. 4 shows the power transmission data obtained with the Ge bolometer (fig. 4a) and the Golay cell (fig. 4b) and include the standard deviation data. The overall level of these is slightly above that of the DFTS results of fig. 1. Again, this can be attributed to a small uncertainty in the measured value of the cell thickness. However, there is again no evidence of any structure outside the levels implied by the standard deviations.

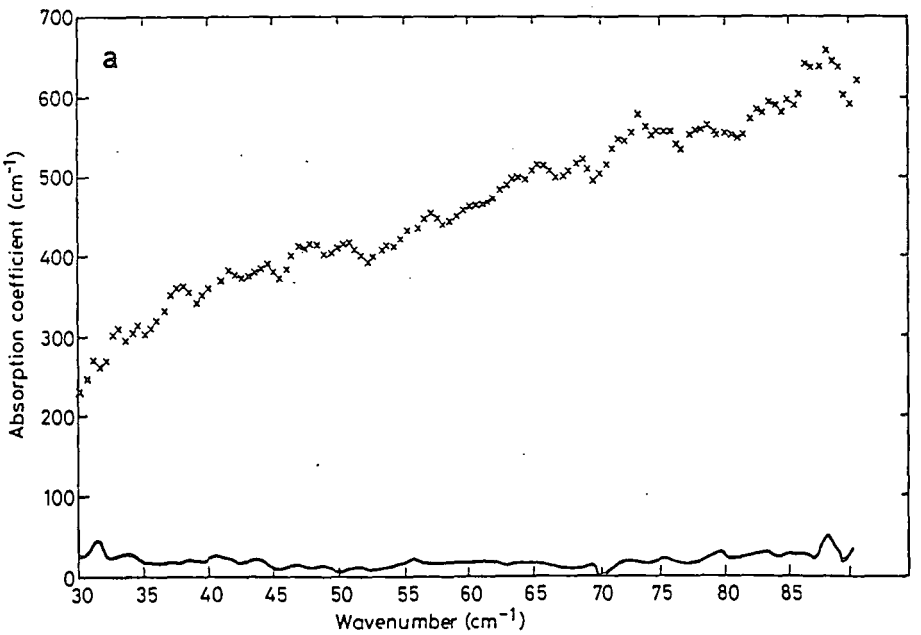

Fig. 4a

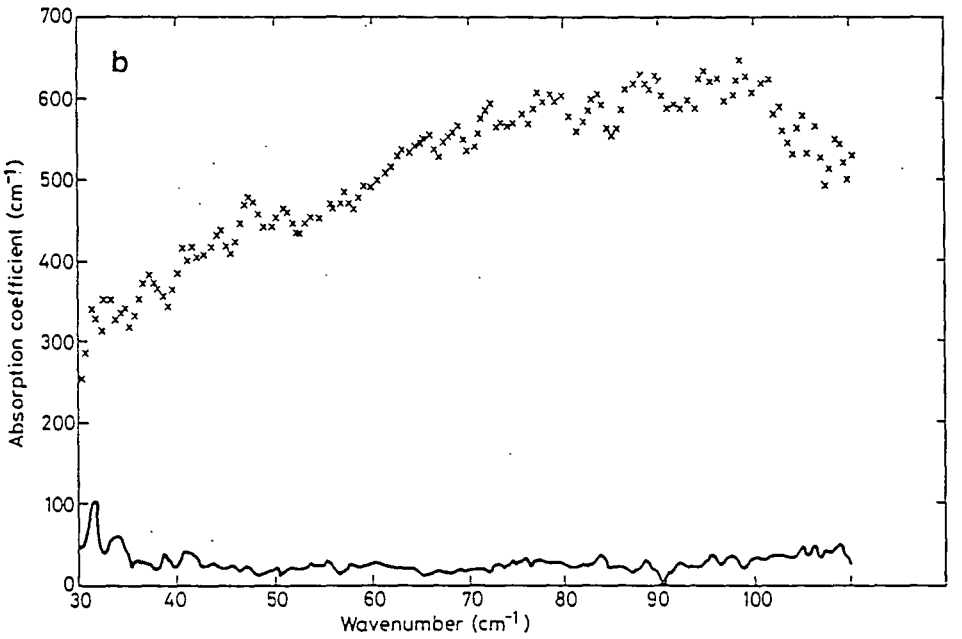

Fig. 4b

Fig. 4. (a) The absorption spectrum of acetonitrile at 298 K determined by power transmission spectroscopy between 30 and 90 cm^{-1} using a germanium bolometer. The crosses represent the mean of thirty independent determinations taken at several liquid thicknesses in the range 15–50 μm, while the continuous curve represents the standard deviation of the thirty individual spectra at each spectral element. (b) The absorption spectrum of acetonitrile at 298 K determined by power transmission spectroscopy between 30 and 110 cm^{-1} using a Golay cell. The data are plotted as in (a).

There is one main conclusion that can be drawn from these studies of the optical constants of acetonitrile. If there *are* any discrete features superimposed on the far-infrared absorption profile of this liquid, their intensities must be less than levels implied by the standard deviation of the present spectra. In particular, if one calculates the product of the standard error of the mean of the data set (in figs. 1 and 2) and the value of Student's t appropriate to the 99% confidence level [9], one finds that the confidence interval at this confidence level is 1.6 times the standard deviation. Thus, there is a high level of confidence that any discrete structure must be of such intensity as to lie within ±0.8 times the standard deviation of the mean absorption spectrum. This also applies to structure that may be only partially resolved at 2 cm^{-1} resolution. There is one condition under which discrete features having intensities above the standard deviation levels could be present, but not resolved. This would be if they were regularly spaced in wavenumber. They would then not be resolved until the interferogram delay was such as to include their first interference signature. The present results imply that if such features are present they must be more closely spaced than 2 cm^{-1}.

One can summarise the results of the present study as puting the following upper bounds on the presence of discrete features in the far-infrared spectrum of liquid acetonitrile. First, at the 99% confidence level the intensities of such features must fall within the levels implied by the spectra of fig. 1. These levels are less than the intensities of the features presented in the work of Evans. Second, the present measurements would not have revealed the presence of such features if they were regularly and more closely spaced in wavenumber than 2 cm^{-1}.

References

[1] G.J. Evans, J. Chem. Soc. Faraday Trans. II 79 (1983) 547.
[2] G.J. Evans, Chem. Phys. Letters 99 (1983) 173.
[3] G.J. Evans, J. Mol. Liquids 29 (1984) 263.

[4] J.R. Birch and M. Bennouna, Infrared Phys. 21 (1981) 229.
[5] J.R. Birch, G.P. O'Neill, J. Yarwood and M. Bennouna, J. Phys. E15 (1982) 684.
[6] G.W. Chantry, H.M. Evans, J. Chamberlain and H.A. Gebbie, Infrared Phys. 9 (1969) 85.
[7] K.E. Arnold, J. Yarwood and A.H. Price, Mol. Phys. 48 (1983) 451.
[8] D.M.F. Edwards and P.A. Madden, Mol. Phys. 51 (1984) 1163.
[9] P.J. Campion, J.E. Burns and A. Williams, A code of practice for the detailed statement of accuracy (HMSO, London, 1973).

Appendix VI

Journal of Molecular Structure (Theochem), 135 (1986) 415—422
Elsevier Science Publishers B.V., Amsterdam — Printed in The Netherlands

INTERACTION-INDUCED FAR-INFRARED SPECTRA OF THE HALOGENS*

B. CATLOW and J. YARWOOD

Department of Chemistry, University of Durham, Durham City, DH1 3LE (Great Britain)

(Received 11 July 1985)

ABSTRACT

Infrared, $\nu(X—X)$, spectra are presented for Cl_2, Br_2 and I_2 dissolved in liquid benzene, and for I_2 dissolved in different solvents. An attempt is made to interpret the band profiles using the available theories of intermolecular spectroscopy. The $I(\nu)$ results for Br_2 and Cl_2 appear to fit a two slope line shape indicating both short and long range interactions. The relationship between the $\nu(I—I)$ band intensities found in this work and the solvent polarisability and quadrupole moments agree well with that expected from the theory of Madden and Cox [1, 2]. The data demonstrate that interpretation in terms of short-range, donor—acceptor forces alone is inadequate.

INTRODUCTION

It is now recognised [1—3] that the study of intermolecular fluctuations and interactions in liquids is best attempted using spectral response functions which are (in the isolated molecular approximation) dipole or polarisability "forbidden". This ensures that the relevant correlation functions (and therefore spectral profiles) are those whose variables depend directly on the intermolecular coordinates, rather than being composite functions of both "self" and "distinct" parts [4]. Accordingly, there have recently been a number of quite detailed experimental spectral investigations of simple liquid systems. These include studies on H_2 [5, 6], N_2 [7—10], CO_2 [9, 10], CS_2 [1, 2], CH_4 [11, 12], CCl_4 [12—14], C_2H_4 [14, 15], C_2H_6 [3], SF_6 [16] and other non-polar liquids [14, 17, 18].

However, the detailed interpretation of such data in such a way as to cast light on the relevant intermolecular potentials (a major goal of liquid state physics and chemistry) has been found difficult. Both the theories and the experiments involved are very much in the process of development and much more careful work is needed along both directions. Our aim in this work was to provide some reliable band profiles and to try to make contact with the theories of intermolecular spectroscopy [1—3, 9, 17, 19] which are available.

Interaction induced spectra of the halogens (X_2, X = Cl, Br, I) have been known for nearly 50 years [20] and there is much data [21—25] on the

*Dedicated to Professor Robert S. Mulliken.

0166-1280/86/$03.50

infrared spectra of halogens dissolved in "complexing" solvents. It is appropriate here that much of the work was (and still is) inspired by the pioneering theoretical work of Professor Robert Mulliken and by the associated careful experimental work of Professor Willis Person [20]. However, little of the data on halogens has been interpreted in the light of the most modern ideas, despite the early recognition [26] that information on both short (charge transfer) and long range potentials could, in principle at least, be extracted. Except for the recent calculations of electrostatic interaction energies [22], the molecular dynamics simulation of liquid Cl_2 [23, 27] we know of no other band shape work of this kind on halogen molecules.

THEORETICAL BACKGROUND

The most comprehensive theoretical approach to the interpretation of interaction-induced spectra is that of Cox and Madden [1, 2]. We extract, here, the parts of that theoretical framework necessary to make the connection with our experimental data. Two types of interaction-induced spectra of the halogen may be observed.

(i) The Σ_g^+ ν(X—X) intramolecular stretching mode of the halogen which, in $D_{\infty h}$, is dipole "forbidden" (see first table in the appendix of ref. 1). For the ν(X—X) normal coordinate (q^i) the observed intensity depends on the vibrationally modulated total dipole moment (M).

$$\sum_i q^i_{X_2} \cdot \frac{\partial M}{\partial q^i} = \frac{1}{3} \sum_{i \neq j} \left[q^i_{X_2} \left(\frac{\partial \alpha_{X_2}}{\partial q_{X_2}} \right)^i T^{(3)}(r_{ij})\, \theta^j_{Bz} + \alpha^j_{Bz} \cdot T^{(3)}(r_{ji}) q^i_{X_2} \left(\frac{\partial \theta_{X_2}}{\partial q_{X_2}} \right)^j \right] \quad (1)$$

This expression gives the two first non zero terms in the total dipole moment derivative expansion. Both terms depend on the dipole—quadrupole tensor

$$T^{(3)}_{\alpha\beta\gamma}(r_{ij}) = (4\pi\epsilon_0)^{-1} \Delta_\alpha \Delta_\beta \Delta_\gamma (r_{ij}^{-1}) \quad (2)$$

$$= (4\pi\epsilon_0)^{-1}\ 3(5 r_\alpha r_\beta r_\gamma - r^2 (r_\alpha \delta_{\beta\gamma} + r_\beta \delta_{\alpha\gamma} + r_\gamma \delta_{\alpha\beta}) r^{-7}$$

where i and j refer to individual molecules (halogen and benzene, respectively) and where α, β, γ refer to cartesian directions in a laboratory frame. The main assumptions involved include the neglect of orbital overlap and dispersion terms, and the treatment of the molecular polarisability as though it were concentrated at a point. From eqn. (1) it is seen that the band intensity should follow the solvent polarisability and quadrupole moment and the Raman intensity of the ν(X—X) vibrational band (through $\partial\alpha/\partial q_i$). Previous intensity measurements have been related to the extent of charge transfer [20] although electrostatic interactions have also been considered [20—23].

(ii) For the far-infrared band (5—100 cm^{-1}), usually attributed to interaction-induced dipole fluctuations [29], Madden [1] gives the static induced dipole moment for a linear centrosymmetric molecule as

$$M^i = \sum_{ij} \alpha^i_{X_2} T^{(3)}(r^{ij}) \theta^j_{Bz} \quad (3)$$

this being the halogen molecule moment induced (in dilute solution) by the surrounding solvent quadrupoles. M^i clearly varies from one solvent to another or from one halogen to another in the same solvent. Since spectra in the 5—100 cm^{-1} region are rather difficult to obtain reliably for halogen-containing systems attention is concentrated here on the ν(X—X) band. We intend to follow up the very far-infrared region at a later date since eqn. (3) is easier to handle than eqn. (1). It is worth noting, however, that, since solutions of halogens in solvents such as cyclohexane also show broad bands in the far-infrared [28], eqn. (3) may not give the complete picture.

EXPERIMENTAL

These measurements were all carried out using Analar grade materials and "Spectral" grade solvents which had been thoroughly dried over molecular sieves. The work on Cl_2 and Br_2 was carried out, as far as possible, with protection from UV light. The instruments used were a Perkin-Elmer 580B (in the case of work between 250 and 600 cm^{-1}) and a Beckman RIIC FS720 (interferometer) between 10 and 250 cm^{-1}. Solvent spectra at the same pathlength were subtracted in all cases. (This is particularly important for considerations in the very far-infrared where even non-polar liquids have significant absorption [29.)

RESULTS AND DISCUSSION

Figures 1—3 show the ν(X—X) spectra of halogens Cl_2, Br_2 and I_2, respectively, dissolved in liquid benzene. Figures 4 and 5 show the spectra of iodine in different solvents while Fig. 6 shows the complete I_2 spectrum in benzene

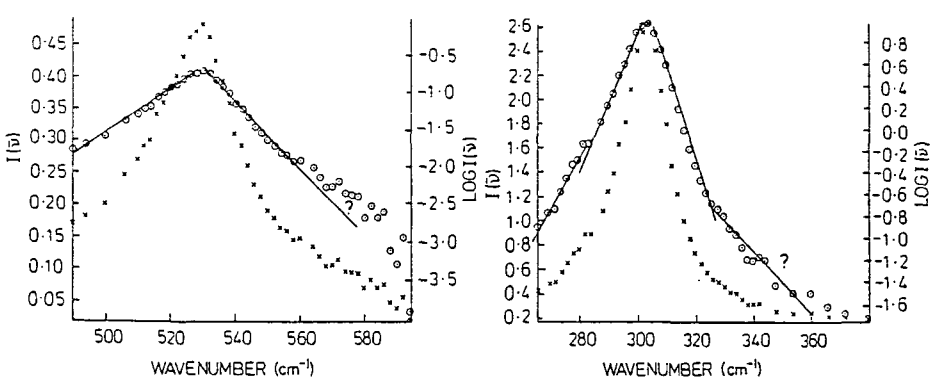

Fig. 1. Spectrum of ν(Cl—Cl) band for a saturated solution of Cl_2 in benzene, T = 300 K; conc. ≈ 3.6 M.

Fig. 2. Spectrum of ν(Br—Br) band for a solution of Br_2 in benzene T = 300 K; conc. ≈ 2.4 M.

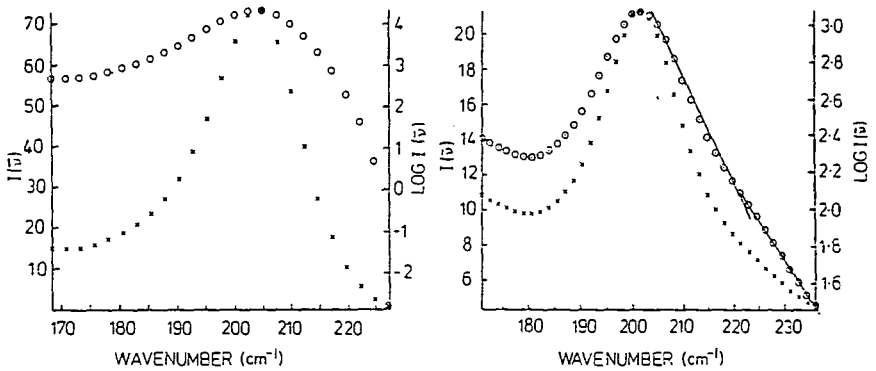

Fig. 3. Spectrum of ν(I—I) band for a solution of I_2 in benzene, T = 340 K; conc. ≈0.2 M.

Fig. 4. Spectrum of ν(I—I) band for a solution of I_2 in carbon disulphide, T = 300 K; conc. ≈0.2 M.

from 40—220 cm^{-1}. In each case, a solvent background spectrum has been removed. Tables 1 and 2 summarise measurements made in this work (and in some previous studies) and some of the parameters needed for the interpretation of our data.

Most previous intensity studies on these bands have been interpreted in

TABLE 1

Summary of spectral parameters for halogens dissolved in benzene and other solvents[a]

	Solvent	$\tilde{\nu}_{X-X}$ (cm^{-1})	$\Delta\tilde{\nu}_{1/2}$ (cm^{-1})	$10^{-3}\,B_i$[b] (cm mol^{-1})	Ref.
Cl_2	Gas	558(R)			e
	CCl_4	545	87.6		b
	Bz	527/531	40.9/28	—/153	b, f
	p-dioxan	520			d
	Bz	530	32	14.9	this work
Br_2	Gas	318(R)			e
	Bz	304/305(R)	16	416	g, f
	Cs_2	308/307(R)	16	108	g, f
	Bz	304	22	77.5	this work
I_2	Gas	213(R)			f
	Bz	205	12	160	c
	Bz	205	20	199.4	this work
	CS_2	203		78.6	this work
	p-dioxan	205			this work
	p-dioxan	206	6.0	680	c

[a]Intensity differences between workers is due to differences in the effective halogen concentrations used. (R) refers to Raman data. [b]Ref. 22. [c]Ref. 37. [d]Ref. 21. [e]Ref. 38. [f]Ref. 39. [g]Ref. 24.

TABLE 2

Band shape parameters for $\nu(X_2)$ band in benzene[a]

	$\tilde{\nu}_{max}$[a] (cm^{-1})	$\Delta\tilde{\nu}_{1/2}$ (cm^{-1})	α_{max}[c] ($cm^2\ mol^{-1}$)	$10^{-3}\ B_i$ ($cm\ mol^{-1}$)	γ^{-1} (cm^{-1})	$10^{25}\ \alpha^{\parallel}$ (cm^3)	$q_{X_2}(\partial\alpha/\partial Q)_{X_2}$[d]
Cl_2	530 556^{g}(R) 548^{sl}(R)	32	550	14.9	29	66	1.192
Br_2	304 317^{g}(R) 312^{sl}(R)	22	900	77.5	15	99.5	1.138
I_2	205 213^{g}(R) 207^{sl}(R)	20(12)[b]	10 000	199.4	(non-linear?)	175	2.158

[a](R) indicates Raman data, (g) gas phase, (sl) solution phase. [b]Ref. 37. [c]$\alpha_{max} = 1/cl \log_e(I_0/I)$ at $\tilde{\nu}_{max}$. [d]Ref. 40.

terms of the extent of charge transfer in a 1:1 molecular complex [20]. However, there have also been attempts to discuss electrostatic effects on the band intensity (ref. 21 Chap. 1) [20, 22, 23, 26, 27] and attempts were made to average the quadrupole-induced interactions over all relative orientations of the binary pair of molecules involved in a "collision". It was found [22] that between 40 and 100% of the observed intensity of the ν(Cl—Cl) band in benzene could be attributed to electrostatic interactions brought about by binary collisions. It therefore seems quite likely that the leading terms in the interaction tensor represented by eqn. (1) may be able to explain these electrostatic contributions. It is thus relevant to consider the changes of shape, width and intensity of the bands for the different halogens in the light of what is expected from eqn. (1). It has often been predicted [19, 30—32] that for collision-induced spectra the band shapes are expon-

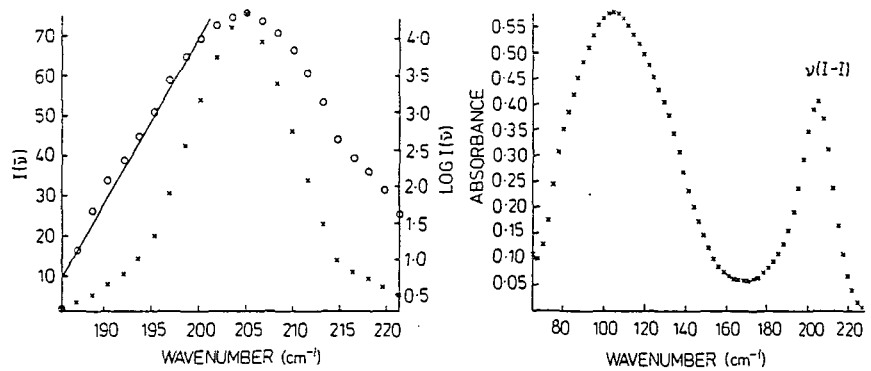

Fig. 5. Spectrum of ν(I—I) band for a solution of I_2 in a cyclohexane/dioxan mixture, T = 300 K; conc. ≈0.2 M.

Fig. 6. Far-infrared spectrum of iodine in benzene showing both ν(I—I) and the interaction-induced dipole fluctuation band at ca. 100 cm^{-1}. T = 340 K; conc. ≈0.2 M.

ential and $\log I(\bar{\nu})$ vs. $\bar{\nu}$ plots are linear i.e.

$$\log I(\nu) \propto \exp(-\gamma\bar{\nu}) \tag{4}$$

where γ is a parameter related to the Lennard—Jones interaction potential parameters [19], σ, the collision diameter and, ϵ, the potential well-depth. It has sometimes been found [19, 30, 32, 33] that the $I(\bar{\nu})$ data for a given band fits a two slope line shape (with two separate γ values). Figures 1 and 2 show that this may also be the case for Cl_2 and Br_2 in benzene, better data in the wings being needed to confirm the point. However, for I_2 in benzene (Fig. 3). the line shape does not appear to be exponential at all. The two slope line shapes have been interpreted [19, 32] in terms of a short range (high frequency) repulsive interaction combined with a long range (low frequency) DID interaction. For the halogen—benzene interaction one might envisage both donor—acceptor (short range) and classical electrostatic (longer range) interactions so the observation of two possible values is not unreasonable. However, the reason for different behaviour in the case of I_2—benzene is unclear. Equation (4) was, of course, derived for binary collisions in simple liquids. For the dense, complicated systems considered here γ is unlikely to be more than an empirical parameter which appears (Table 2) to follow the inverse band width. It is noticeable that the rate of vibrational phase relaxation gets slower (band narrows) in passing from Cl_2 to I_2. This is worth investigating further but, if the band width is mainly controlled by inhomogeneous broadening [34] (i.e., by a distribution of molecular environments in the liquid), the implication is that the I_2 interacts most strongly with benzene and is subject to a narrower range of interaction potentials. Turning now to the use of eqn. (1) for interpretation purposes we see that the band intensities for ν(X—X) band in a given solvent should follow the modulated polarisability $(\partial\alpha/\partial q)_{X_2}$ and the modulated quadrupole moment $(\partial\theta/\partial q)_{X_2}$ of the halogen. The available data [24] for $(\partial\alpha/\partial q)_{X_2}$ are given in Table 2 along with the peak height intensity data. It is clear that there is a monotonic increase in the intensity (based on total halogen) while this is not the case for $q_{X_2}(\partial\alpha/\partial q)_{X_2}$. Since $(\partial\theta/\partial q)_{X_2}$ is not known we cannot be certain that the second term in eqn. (1) is important. However, it was found to be so for ν_1 of CS_2 [1, 2] and there is no reason to believe that it may be ignored here. For the same halogen in different solvents the intensity should depend on the solvent polarisability and quadrupole moment. The ratio of solvent polarisabilities and quadrupole moments for benzene and carbon disulphide are 2:1 and 3:1, respectively [29, 35]. The ratio of ν(I—I) band intensity in these two solvents is $\approx$3:1 (Table 1) so this is not unreasonable by comparison with that predicted by eqn. (1). It is clear that more work is required to characterise more fully these band shapes (and the band at very low frequency) and compare them with models for interaction-induced absorption, including new ones which are now becoming available [36]. Nevertheless, the data collected so far are, at least, not inconsistent with eqn. (1) and they demonstrate convincingly

that interpretation in terms of the short range donor—acceptor forces alone is inadequate.

ACKNOWLEDGEMENTS

One of us (J. Y.) wishes to record his thanks to Professor Willis B. Person for first stimulating his interest in these systems. S.E.R.C. are thanked for equipment grants and a studentship (to B. C.) Some of this work was performed with the technical help of Mr. R. Green and interpreted with the help of discussions with Dr. P. A. Madden and Dr. G. Birnbaum. We record sincere thanks to all three.

REFERENCES

1 T. I. Cox and P. A. Madden, Mol. Phys., 39 (1980) 1487.
2 T. I. Cox and P. A. Madden, Mol. Phys., 43 (1981) 287, 307.
3 F. G. Baglin, V. Zimmerman and H. Versmold, Mol. Phys., 52 (1984) 877.
4 J. Yarwood, Ann. Rep. R. Soc. Chem., C (1982) 157.
5 U. Buontempo, S. Consulo, P. Dore and L. Nencini, Can. J. Phys., 60 (1982) 1422.
6 M. Moraldi, A. Borysow and L. Frommhold, Chem. Phys., 86 (1984) 339.
7 U. Buontempo, J. Chem. Phys., 63 (1975) 2570.
8 A. De Santis and M. Sampoli, Mol. Phys., 51 (1984) 97.
9 W. A. Steele and G. Birnbaum, J. Chem. Phys., 72 (1980) 2250.
10 C. I. Manzanares, A. Munoz and D. Hidalgo, Chem. Phys., 87 (1983) 363.
11 T. Nanba, J. Phys. Soc. Jpn., 44 (1978) 1755.
12 H. P. Posch, Mol. Phys., 37 (1979) 1059, 40 (1980) 1137.
13 Y. Le Duff and A. Gharbi, Opt. Commun., 30 (1979) 369; Mol. Phys., 40 (1980) 545.
14 H. Arning, K. Tibulski and T. Dorfmüller, Ber. Bunsenges. Phys. Chem., 85 (1981) 1068.
15 C. Chapados and T. K. Bose, J. Chem. Phys., 69 (1978) 1069.
16 A. Rosenberg and G. Birnbaum, J. Chem. Phys., 52 (1970) 683.
17 G. C. Tabisz, in D. A. Long, Barrow and Sheridan (Eds.), Molecular Spectroscopy, Specialist Periodical Reports, Vol. 6, The Chemical Society, London, 1978, p. 136.
18 K. Fujiwara, Bull. Chem. Soc. Jpn., 52 (1979) 227.
19 G. Birnbaum, B. Guillot and S. Bratos, Adv. Chem. Phys., 51 (1982) 49.
20 R. S. Mulliken and W. B. Person, Molecular Complexes, Wiley, New York; 1969, and references therein.
21 For a review up to 1973 see: J. Yarwood in Structure and Spectroscopy of Molecular Complexes, Plenum, London, 1973, Chaps. 2 and 4.
22 T. Jao and W. B. Person, J. Phys. Chem., 83 (1979) 1181.
23 C. S. Murty, K. Singer, D. Steele, J. J. Tindle and R. Vallauri, Chem. Phys. Lett., 90 (1982) 95.
24 J. Put, G. Maes and P. Huyskens, Spectrochim. Acta, 37 (1981) 699.
25 G. Maes, J. Mol. Struct., 61 (1980) 95; Adv. Mol. Relaxation Interact. Processes, 16 (1980) 209.
26 M. W. Hanna, J. Am. Chem. Soc., 90 (1968) 285; J. Am. Chem. Soc., 90 (1968) 5358.
27 R. Vallauri, Proceedings of the NATO Advanced Workshop on Phenomena Induced by Intermolecular Interactions, Chateau de Bonas, 1983, in press.
28 J. Yarwood, unpublished data.
29 M. M. Davies, in J. Lascombe (Ed.), Molecular Motions in Liquids, Reidel, 1974, p. 615 and references therein.

30 J. A. Buccaro and T. A. Litovitz, J. Chem. Phys., 54 (1971) 3846.
31 R. A. Stuckart, C. J. Montrose and T. A. Litovitz, Faraday Symp. Chem. Soc., 11 (1977) 4.
32 W. M. Gelbart, Adv. Chem. Phys., 26 (1974) 1.
33 D. P. Shelton, M. S. Mathur and G. C. Tabisz, Phys. Rev. A: 11 (1975) 834.
34 W. G. Rothschild, Dynamics of Molecular Liquids, Wiley, New York, 1984, Chap. 3.
35 M. P. Bogaard, A. D. Buckingham, R. K. Pierens, A. H. White, J. Chem. Soc., Faraday Trans. 1: 74 (1978) 3008.
36 D. W. Oxtoby, Proceedings of NATO Advanced Workshop on Phenomena Induced by Intermolecular Interactions, Chateau de Bonas, 1983, in press.
37 J. Yarwood and W. B. Person, J. Am. Chem. Soc., 90 (1968) 594.
38 H. Stammreich, R. Forneris and Y. Tavares, Spectrochim. Acta, 17 (1961) 775, 1173.
39 W. B. Person, R. E. Erickson and R. E. Buckles, J. Am. Chem. Soc., 82 (1960) 29.
40 C. F. Merlevede and G. Maes, Adv. Mol. Relaxation Interact. Processes, 16 (1980) 111.

Appendix VII

Far-Infrared Interaction-Induced Spectra of the Halogens

by Jack Yarwood and Brendan Catlow

Department of Chemistry, University of Durham,

South Road, Durham DH1 3LE, U.K.

Short title: Far-infrared spectra of I_2 in benzene.

Proofs to Dr. J. Yarwood at above address.

Abstract

We have investigated the far-infrared spectrum (3-125 cm^{-1}) of iodine in benzene solutions over a range of concentrations. The data have been successfully analysed in terms of a quadrupole-polarisability interaction mechanism [7] which leads to fluctuating dipoles when the molecules rotate and translate relative to one another. Band shape analysis, via the corresponding correlation functions, indicates that at least two relaxation times are involved in the description of the interaction processes. These times appear to get slower when Bz-Bz interactions are replaced by Bz-I_2 interactions. This analysis is supported by fitting the data to two different solutions of the generalised Langevin equation (GLE). These show up changes in interaction dynamics very well, but are less good at predicting the extent of the intermolecular forces. This may be due to the relative inaccuracy of the measured higher spectral moments. It is found that the rate of torque fluctuations for Bz-I_2 interactions is slower than that in the Bz-Bz case, probably reflecting more specifically directed and stronger forces between the molecules. There is little evidence from these data that the short-ranged potentials contain any significant 'donor-acceptor' contribution.

I. INTRODUCTION

It is now accepted [1-3] that in order to have the best chance of elucidating the nature of interaction-induced dynamic processes in dense fluid systems, one needs to study spectra which, in the isolated molecule approximation, are 'forbidden'. The difficulties involved [4] in the deconvolution of molecular and intermolecular (induced) contributions are such that little progress has so far been made with 'allowed' spectra. Current theories [1-7] of interaction induced processes are limited by simplifications and approximations involved, for example, in neglecting many body interactions. Nevertheless, considerable progress has been made in the detailed interpretation of forbidden bands of molecules such as N_2 [1,8], CS_2 [2] and CO_2 [1,9]. The basic theoretical tools are therefore available, but they can only be tested and developed with the aid of a range of reliable data for a range of experimental systems. One important set of such systems which has been studied only recently [7,10] in this context is that consisting of mixtures of the halogen molecules with solvents forming so-called charge-transfer or donor-acceptor complexes [11,12]. The interaction potentials for such 'complexes' were originally thought [13] to be dominated by short-ranged electron donor-acceptor stabilizing forces even though there was evidence [14,15] that electrostatic (coulombic and polarisation) (long-ranged) forces might be equally important. We have recently shown [10] that the effects of long and short ranged forces may be distinguished using detailed band shape analyses. It has also been shown, for example, [7] how the time scales of different interaction induced (spectral) contributions may be used to provide information about the possible temporal and spatial domains within

which interaction is taking place.

The main objectives of the present paper are (a) to report much more extensive work on the benzene-iodine system in the far-infrared region (b) to show how such spectra are to be interpreted in terms of current theories [1,2,4,5-7,16] of interaction-induced band intensities, and band shapes. We hope to point the way forward in the study of mixtures of interacting molecules which can provide much information about intermolecular potentials in fluids.

II. THEORETICAL BACKGROUND

Any theory of interaction-induced absorption in mixtures of iodine with organic ('donor'?) solvents such as benzene must ultimately be able to explain the intensities and band shapes of the two features in the observed spectra (such as those shown in fig. 1). The band at about 205 cm^{-1} is, of course, due to the internal mode of the I_2 molecule [11] but its' shape and intensity must be controlled by molecular interactions since the ν_{II} vibration is (symmetry) forbidden in the isolated molecule approximation. The band centred near 100 cm^{-1} does not involve a vibrational mode. It arises mainly through fluctuations of the intermolecular potential (and hence of the induced dipole) as the molecules rotate and translate relative to one another on a psec time scale. The question then arises [7] whether the same interaction-induced absorption component may be employed to describe each of the two features or whether different parts of the (rather complex) intermolecular potential (which is a priori, unknown) dominate the high and low frequency (short and long time) parts of the spectrum. Since our colleagues [7] have made a detailed study of the far-infrared and Raman spectra of the $\bar{\nu}_{II}$ mode we concentrate in this paper on a discussion of the low frequency band. There are two basic theoretical

approaches to the elucidation of interaction-induced spectral bandshapes.

(1) Attempts can be made [1-7] to deduce analytical expressions for the band intensities or associated time correlation functions in terms of molecular properties (terms in the multiple expansion of the total dipole moment). The difficulty with this approach is that some of the properties needed; for example the polarisability and quadrupole moment derivatives with respect to normal coordinate are unknown for this (relatively) complicated system. Furthermore, it is not obvious how to include the effects of many body interactions [3,4,7].

(2) The observed band shapes may be 'modelled' using analytical (approximate) solutions to the generalised Langevin equation for roto-translational motion [17,18]. The difficulty with this approach is that the number of model parameters needs to be kept low - in order to ensure a meaningful fit to the data. Furthermore, it is not always obvious what the parameters mean physically, and so relating the model parameters to the nature of the intermolecular potential is not easy.

An examination of the two different approaches is well worthwhile since there are points of contact between the two approaches which may therefore be mutually beneficial.

The spectrum which needs to be modelled is,

$$\alpha(\omega) = \frac{4\pi^2}{3\hbar c V n(\omega)} \omega(1-e^{-h\omega/kT}) I(\omega) \qquad (1)$$

where $\alpha(w)$ is the measured absorbance. In practical units,

$$\alpha(\bar{\nu}) = \frac{1}{\ell c'} \log_e(T_o/T)_{\bar{\nu}} \qquad (2)$$

where ℓ and c' are the pathlength and molar concentration, and where $I(\bar{\nu})$ is related to the correlation function of the total dipole moment,

$$I(\bar{\nu}) = c \int_{-\infty}^{+\infty} \langle \bar{M}_T(o)\bar{M}_T(t)\rangle \exp(-i2\pi c\bar{\nu}t) \qquad (3)$$

The function $\langle \bar{M}_T(o).\bar{M}_T(t)\rangle$ which in principle includes all contributions to the dipole density [19] is thus obtained by the Fourier transform of the function,

$$I(\bar{\nu}) = \frac{\alpha(\bar{\nu})n(\bar{\nu})}{\bar{\nu}[1-\exp(-h\bar{\nu}c/kT)]} \qquad (4)$$

The first approach to the interpretation of the spectra represented by eqn. 1 and shown in fig. 1 is to make certain assumptions about the origin of the time dependent dipole density $\bar{M}_T(t)$. The most important of these is that the predominant interaction is a quadrupole-polarisability interaction (the molecules having no permanent dipoles). For benzene-iodine pairs (in dilute solutions of iodine in benzene) the induced dipole is then,

$$\vec{\mu}_i = \sum_j \frac{1}{3}\underline{\underline{\alpha}}_i . T^{(3)}(r_{ij}) : \underline{\underline{Q}}_j \qquad (5)$$

$\underline{\underline{\alpha}}_i$ is polarisability tensor of molecule i which experiences the electric field produced by quadrupoles on molecules j ($\underline{\underline{Q}}_j$ being the traceless tensor associated with these molecules). If the polarisability anisotropy is ignored then

$$\underline{\underline{\alpha}}_i = \alpha \underline{\underline{I}} \qquad (6)$$

where α is the mean (scalar) polarisability and orientational contributions will be observed only through the reorientation of the $\underline{\underline{Q}}_j$ components on B_z and I_2 molecules. The polarisability and quadrupole components are of course, dependent upon vibrational displacement. However, for simplicity, the benzene molecule is treated as a rigid entity (no vibrational coordinates are involved in the spectral domain of interest) and the leading terms in the relevant Taylor expansion in normal coordinate q_{II} are

$$\alpha_{I_2} = \alpha_{I_2}^{o} + \left[\frac{\partial \alpha}{\partial q_{II}}\right]_{q=q_o} q_{II} \tag{7}$$

and

$$\underline{\underline{Q}}_I = \underline{\underline{Q}}_I^{o} + \left[\frac{\partial \underline{\underline{Q}}_I}{\partial q_{II}}\right]_{q=q_o} q_{II} \tag{8}$$

(where superscripts o refer to equilibrium properties).

Lascombe and Besnard [7] have shown that the induced dipole correlation function is then given by,

$$\langle \mu(o).\mu(t)\rangle = A(t) + B(t)\langle q_{II}(o).q_{II}(t)\rangle (\equiv C(t)) \tag{9}$$

where $\langle q_{II}(o).q_{II}(t)\rangle$ is the vibrational correlation function [ ] of the ν(I-I) vibrational mode. It was assumed that Bz-Bz and Bz-I_2 orientational correlations could be ignored and also that motions associated with vibrational, rotational and translational motions are statistically uncorrelated. In each equation the first term represents the combined benzene and iodine rotational, and two body mutual translational contributions. The second term represents 3 body contributions. It is clear that in equation (9) the A(t) term models the low frequency band (at 100 cm^{-1}) while the B(t) term takes account of the ν(I-I)-high frequency band at 205 cm^{-1} (not considered in detail here).

In order to compare the experimental data with these equations it is convenient to use moments [ ] since these are readily compared with measured band areas. Ignoring the 3 body contributions, the integrated intensity is related to the zeroth moment [ ], given for the low frequency band by,

$$M_o = A(o) = 12N_I N_{Bz}\left\{(\alpha_I \eta_{Bz})^2 + (\alpha_{Bz}\eta_I)^2\right\}\langle r_{BzI}^{-8}\rangle \tag{10}$$

where,

$$M_o = \frac{3\hbar cV}{4\pi^2}\int \frac{\alpha(\bar{\nu})n(\bar{\nu})d\bar{\nu}}{\bar{\nu}[1-\exp(-h\bar{\nu}c/kT)]} \tag{11}$$

The second moment is defined by,

$$M_2 = -\ddot{A}(o) = -\left\langle \left[\frac{\partial^2 C(t)}{\partial t^2}\right]_{t=o} \right\rangle \equiv \int_o^\infty \bar{\nu}^2 I(\bar{\nu}) d\bar{\nu} \qquad (12)$$

Using equations (1) and (4) this gives,

$$M_2 = \frac{3\hbar eV}{4\pi^2} \int_o^\infty \frac{\bar{\nu}\alpha(\bar{\nu})n(\bar{\nu})}{[1-\exp(-h\bar{\nu}c/kT)]} \qquad (13)$$

For the low frequency band this has been shown [7] to be given by,

$$M_2 = -\ddot{A}(o) = 12N_I N_{Bz}\left\{(\alpha_I \eta_{Bz})^2 \frac{6kT}{I_{Bz}} + (\alpha_{Bz}\eta_I)^2 \frac{6kT}{I_I}\right\} \langle r_{BzI}^{-8}\rangle + 336N_I N_{Bz}\left\{(\alpha_I\eta_{Bz})^2 + (\alpha_{Bz}\eta_I)^2\right\} \frac{kT}{M_{BzI}} \langle r_{BzI}^{-10}\rangle \qquad (14)$$

where M_{BzI} is the reduced mass of the Bz-I pair and I_x the principal moment of inertia along the main symmetry axis of each molecule.

It should be noted that expressions (10), (11) and (14) depend on use of an isotropic potential [20] (such as the Lennard-Jones model) between benzene and iodine molecules. This assumption results in the $\langle r^{-8}\rangle$ and $\langle r^{-10}\rangle$ distance dependences derived from the form of the interaction tensor given in equation (5). For the low frequency band it is possible to calculate the normalised 2nd moment. Equations (10) and (14), when combined, give

$$\frac{M_2}{M_o} = \frac{(\alpha_I^o \eta_{Bz})^2 \frac{6kT}{I_{Bz}} + (\alpha_{Bz}\eta_I)^2 \frac{6kT}{I_I}}{(\alpha_I^o\eta_{Bz})^2 + (\alpha_{Bz}\eta_I)^2} \text{ (rotational)} + 28 \frac{kT}{M_{BzI}} \frac{\langle r_{BzI}^{-10}\rangle}{\langle r_{BzI}^{-8}\rangle} \text{ (translational)} \qquad (15)$$

Provided one knows the parameters α and η for both molecules, valuable information may then be derived about the relative contributions to the measured intensity and shape of the observed low frequency band profile [21].

The second approach to modelling of the observed spectra considered in this paper is based on solutions to the generalised Langevin equation [17,18] (GLE) for roto-translational motion of interacting molecules

$$\frac{d(G(t))}{dt} = -i\Omega_o G(t) - \int_o^t K_o(\tau)G(t-\tau)d\tau \qquad (16)$$

where G(t) is, in general, a translational-rotational correction function and where $K_o(t)$ is a memory function matrix proportional to the autocorrelation function of the random force, which incorporates the non-Markovian behaviour of the dynamic interactions in dense phases. Ω_o is a frequency matrix whose (diagonal) components are the slow variables of the system. There are two approaches to the solution of equation (16).

(i) The first method involves using the Mori approach to the solution of the GLE written in a form which emphasises the existence of a hierarchy of memory functions, $K_n(t)$. viz:

$$\frac{dK_{n-1}(t)}{dt} = -i\Omega_o K_{n-1}(t) - \int_o^t K_n(\tau)K_{n-1}(t-\tau)d\tau \qquad (17)$$

The solution may be written as a continued fraction, [ ],

$$\hat{G}(\omega) = \cfrac{G_{tr}(o)}{i(\omega-\Omega_o) + \cfrac{K_o(o)}{i(\omega-\Omega_o) + \cfrac{K_{n-1}(o)}{i(\omega-\Omega_n) + \tilde{K}_n(\omega)}}} \qquad (18)$$

where $\hat{G}(\omega)$ is the Fourier-Laplace transform of $G_r(t)$. The continued fraction must be truncated at some order n in order to achieve a closed relation for the spectral density. Some authors [22] have used,

$$K_n(t) = 2K_n\delta(t)$$

which is the equivalent of assuming diffusional motion of the particles (K'(t) changing very rapidly compared with G(t)). The observed far-infrared spectrum is known not to conform to such a model since diffusional motion [23] leads to an exponential time decay and a Lorentzian band shape. One commonly used truncation employed for the interpretation of far-infrared spectra of non-polar liquids is

$$K_2(t) = K_2(o)\exp(-\gamma t) \qquad (19)$$

in which case

$$\hat{G}(-i\omega) = \frac{[(-i\omega)^2 - i\omega\gamma + K_2(o)]}{(-i\omega)^3 + (-i\omega)^2\gamma + i\omega[K_2(o) + K_1(o)] + \gamma K_1(o)} \qquad (20)$$

where $K_1(o)$ and $K_2(o)$ are related to the 2nd and 4th spectral moments - see below and $\frac{1}{\gamma}$ is an effective correlation time for the intermolecular torques. The spectral density is,

$$\alpha(\omega) = \frac{N\omega[1-\exp(-h\omega/kT)]\ \mathrm{Re}[\tilde{G}_{tr}(-i\omega)]}{n(\omega)} \qquad (21)$$

(cf. eqn. 1)

So

$$\alpha(\omega) = \frac{N\omega[1-\exp(-h\omega/kT)]\ K_1(o)K_2(o)\gamma}{n(\omega)\ \gamma^2[K_1(o)-\omega^2]^2 + \omega^2[\omega^2-(K_1(o)+K_2(o))]^2} \qquad (22)$$

The 'constant' N includes [23] the $\epsilon_o-\epsilon_\infty$ term which is a measure of the total dielectric loss between static frequency and the far-infrared. This factor may be kept fixed - if ϵ_o and ϵ_∞ are known but may otherwise be used as a parameter. This procedure is, of course, independent of assumptions about the nature of the intermolecular potential. By the same token it is more difficult to know precisely what the parameters mean physically. However, since

$$K_1(o) \equiv 2kT/I_{BzI} \qquad (23a)$$

and

$$K_2(o) = \frac{kT}{I_{BzI}}\left[2 + \frac{\langle N^2\rangle}{2(kT)^2}\right] \qquad (23b)$$

one does get some measure of the intermolecular potentials $\langle N^2\rangle$ through the mean squared torque which although not an absolute measure for one set of conditions may be useful for comparisons between different environments (for example for different I_2 concentrations, temperatures or for dilution in other solvents - see section IV).

(ii) The alternative approach is to approach the solution of eqn. (16) using the multivariable method of successive approximation published by Keyes and Kivelson [17]. Oxtoby [16] has used this approach in his

'cell' model which may be applied to solutions of benzene containing iodine. In this model the I_2 molecule is allowed to translate in a spherical cell of surrounding benzene molecules (fig. 2). The intermolecular potential is assumed to be isotropic (L.J. potential) and it is a function of the displacement R of the I_2 molecule from the centre of the cell. The potential has in principle both attractive and repulsive parts including the effects of charge transfer but, being isotropic, contains only 2 and 3 body terms. The dynamics of the iodine molecule in the solvent 'cell' are treated through the variation of R with time. This relative motion ensures that the pair dipole moment $\mu(r)$ where

$$\vec{\mu}(r) = \vec{r}\,\epsilon(r) \tag{24}$$

where $\epsilon(r)$ is an effective charge separation, is time dependent. Of course, this dipole moment is modulated by the ν_{II} vibrational motion but we consider here only the low frequency band shape. The slow variables then introduced are

$$A_1 = M_R\,R(t) \tag{25a}$$

$$A_2 = \dot{A}_1 = P(t) \tag{25b}$$

$$A_3 = \dot{A}_2 = F(t) \tag{25c}$$

where P(t) and F(t) are the momentum and force variables corresponding to R(t). M_R is the reduced mass of the interacting pair. The P(t) variable is included to allow for damped motion in a harmonic well and F(t) is necessary for the treatment of cell potential anharmonicities and fluctuations in the forces. The equation

$$\frac{d}{dt}\vec{A}(t) = [i\underline{\underline{\Omega}}-\underline{\underline{K}}].\vec{A}(t) + \vec{f}(t) \tag{26}$$

(cf equation 18 - f(t) is a vector of random forces)

is then solved using the projection operator method [ ] and one gets

$$i\underline{\underline{\Omega}} - \underline{\underline{K}} = \begin{bmatrix} 0 & 1 & 0 \\ -\omega_o^2 & 0 & 1 \\ 0 & \frac{\omega_1^4}{\omega_o^2} & -\gamma \end{bmatrix} \tag{27}$$

where

$$\omega_o^2 = \frac{\langle A_2 . A_2 \rangle}{\langle A_1 . A_1 \rangle} = \frac{\langle P^2 \rangle}{M_R^2 \langle R^2 \rangle} \tag{28a}$$

$$\omega_1^4 = \frac{\langle A_3 . A_3 \rangle}{\langle A_1 . A_1 \rangle} = \frac{\langle (\delta F)^2 \rangle}{M_R^2 \langle R^2 \rangle} \tag{28b}$$

and

$$\gamma = \frac{\alpha}{w_1^4} \tag{28c}$$

The calculated spectral intensity of equation (1) is given [16] by,

$$I(\omega) = \frac{2\omega_1^4/\gamma\omega_o^4}{[1-\omega^2/\omega_o^2]^2 + \omega^2/\gamma^2[\omega^2/\omega_o^2 - \omega_1^4/\omega_o^4 - 1]^2} \tag{29}$$

from which $\alpha(\omega)$ may be calculated. The parameter ω_o is related to the average harmonic frequency of relative translational motion within the cell potential, $V_c(R)$; ω_1 depends on the anharmonic motions and the force fluctuations and γ (through α) gives a relaxation scale for these force fluctuations. Notice that the effects of relative rotational motions are neglected in this model. Birnbaum et al [22] have shown that these model parameters may be written in terms of the variations of induced dipoles with varying intermolecular potential. They are therefore impossible to calculate unless a detailed potential is assumed. However, they may be useful in efforts to discern what happens as a function of concentration and temperature.

III. EXPERIMENTAL

Benzene (and the other solvents) were purchased from the Aldrich Chemical Co. Ltd. and the iodine from BDH Chemicals Ltd. The benzene was dried over molecular sieves but otherwise the materials were used without further purification. Solutions were made up by weight in graduated flasks immediately prior to use. Far-infrared cells with polyethylene windows were employed for non-dispersive measurements. Path lengths between 1 and 2.5 mm were needed. For dispersive work a special refractive index cell [24] was used in conjunction with a modified Beckmann-RIIC FS720 interferometer. Measurements were made down to ~ 3 cm^{-1} using this instrument and a QMC Industrial Research Ltd. helium cooled germanium bolometer.

IV RESULTS AND DISCUSSION

(i) Overview of Experimental Data

Figures 3, 4 and 5 illustrate the general nature and quality of spectra which are obtained in the 3-125 cm^{-1} region. It is instructive to examine in detail the intensity and shape behaviour as a function of concentration and subtraction procedure. In fig. 3(a) we show the spectra of three different concentrations of iodine in benzene (with the same pathlength of pure benzene subtracted). In fig. 3(b) they have been normalised to remove the effect of iodine concentration. It is clear that within the experimental error, Beer's law is obeyed for these solutions. This is expected if the induced spectra arise from Bz-I_2 interactions (since the benzene concentration is, in effect, constant). However, even in mixtures, where both components are varied in concentration [25], the leading intensity term is linear in concentration [1]. These spectra also show that the removal of an 'equal' pathlength of benzene from a solution containing benzene and

iodine is accurate, at least to a first approximation. Figure 4 shows the low frequency part of the 100 cm^{-1} band, again as a function of iodine concentration but now with a shorter pathlength of the mixture removed as a background. Again Beer's law is obeyed but it is noticeable also that the low frequency part of this band is now a different shape. This is emphasised in figure 5 which shows a direct comparison of a spectrum containing both the effects of Bz-Bz and Bz-I_2 FIGS. 3, 4, 5 interactions (B) with that containing only Bz-I_2 interactions (C). This clearly implies that Bz-Bz interactions contribute more to the low frequency part of the total spectrum, without prejudice to further division of the Bz-I_2 spectrum into Bz-induced and I_2-induced contributions [21]. It should be noted that the intensity level of our spectra in the 100 cm^{-1} region are different from those of Lascombe and Besnard [7]. This may be due to different degrees of drying of the benzene.

(ii) Band Shapes and Intensities

In order to assess that nature and time scale of the dynamic processes involved in the observed spectrum, it is appropriate to transform our spectral data into the time domain. Equation 4 shows that we need $\alpha(\bar{\nu})$ and $n(\bar{\nu})$ over the whole frequency range from zero until the function $I(\bar{\nu})$ becomes negligible (>50 cm^{-1} in this case). For a 0.2 M solution of I_2 in Bz we have combined our data with the microwave data of Kettle and Price [26] to provide a complete absorption spectrum over the required range. This has been used to compute the refractive index $n(\bar{\nu})$ in the region of interest using a Kramers/Kronig analysis [27]. The results are compared with our experimental data in fig. 6 while the absorption cross sections $I(\bar{\nu})$ and the corresponding correlation functions are shown in figs. 7 and 8.

As may be seen the shapes of the two correlation functions are quite different, reflecting the different interactions and their time scales. In the solution containing both Bz-Bz and Bz-I_2 interactions, relaxation seems to occur on (at least!) two different scales, neither

FIGS. 6, 7 and 8

of which is exponential in time (figure 8(A)). The approximate corresponding correlation times are ~0.4 and ~3 psec. The correlation function obtained for benzene-I_2 interactions (fig. 8(B)) also shows evidence of two relaxation processes. Both appear to have longer relaxation times - probably near to ~0.7 and ~6 psec. The situation is clearly complicated, but in a general sense the functions reflect, correctly, the less complicated nature of the interaction dynamics when the effects of Bz-Bz interactions in the 20-80 cm^{-1} region are removed. This change in absorption in the intermediate frequency range is clearly reflected in the 1-5 psec time range. However, the fact that the Bz-I_2 interactions relax in a relatively slow time scale lends strong support to the (relatively long-ranged) quadrupole induced dipole mechanism proposed by Lascombe and Besnard [7]. On the other hand, there is some evidence of a very short time process (fig. 8(B)) which might be associated with repulsive or short ranged attractive forces.

One other way of checking that absorption is due primarily to such a mechanism is our intensity and moment analysis since theoretical values have been obtained [7] from eqns. 10 and 14. Our absorption coefficient data have been shown [21] to agree very well with those obtained at Bordeaux, at least at low wave numbers. Our intensities and second moments obtained from the experimental data (equations 10 and 12) are 21 cm^{-2} and 2.6×10^4 cm^{-3} respectively, which are somewhat smaller than those reported by Lascombe and Besnard. The theoretical

values are 32 cm^{-2} and 1.6 x 10^4 cm^{-3} respectively, [7,21). We agree that the quality of agreement is probably fortuitous, but it is pleasing nevertheless, that the model predicts at least the correct orders of magnitude. It is concluded along with others [14,15,28] that the effects of donor-acceptor short-ranged forces are unimportant in this spectral range.

(iii) Fitting to Band Shape Models

In section II we have outlined two approaches to the solution of the generalised Langevin equation (eqn. 15). These approaches use the same starting point and differ only in the method used to solve the master equation. They should therefore be equivalent. It is therefore a good test of our data and the modelto seek out any differences between fits to equations (22) and (29) in terms of parameter changes with concentration or dilution, etc. In figs. 9 and 10 we show typical fits to these two equations and in table 1 we have tabulated the parameters. As pointed out in section II the physical meaning of these parameters is not too clear so their absolute values may not be too meaningful. But we may at least be able to get information about the systems studied from changes in parameters. The far-infrared region provides a stringent test of such models since spectra observed there are extremely sensitive to the psec and sub-psec dynamics.

First of all, from figures 9 and 10 it is clear that the spectra are reasonably well-represented by both equations (22) and (29) - both with and without subtraction of a benzene background. In particular, the 'shoulder' on the spectra of Bz-I_2 interactions in the 10-40 cm^{-1} region (figs. 9 and 10, A and B) is well reproduced by the model. The

FIGS. 9 and 10

Oxtoby approach is rather better in this region, which in all probability represents the region controlled by long-ranged potentials

(and possibly affected more by translational motion). At the shortest times both approaches give good results - again with the 'cell' model approach being somewhat better. Comparison of fitted parameters for the different solutions (table 1) shows significant changes on going,

TABLE 1

for example, from pure benzene (where our data agree well with those in the literature [29], to iodine in benzene (with pure benzene removed). Considering the Mori truncated fraction approach first, it is seen that although the 2nd moment ($K_0(o)$) changes little, the torque parameter (proportional to the 4th moment, $K_1(o)$) increases somewhat on going from Bz-Bz interactions to the Bz-I_2 spectrum. This may be indicative of stronger interactions as might be expected, since the polarisability of I_2 is higher [7]. The torque correlation time ($\frac{1}{\gamma}$) gets bigger so relaxation occurs on a marginally longer time scale. (This agrees with our previous analysis based on the observed short time parts of the correlation functions in fig. 8). Fitting to the cell model we find that the harmonic frequency (ω_o) within the cage does not change very much, nor indeed does the mean squared fluctuating forces (ω_1). But the force damping rate, γ, changes significantly. Indeed, the ratio γ/ω_o changes by a factor of two on going from Bz-Bz spectra to Bz-I_2 spectra. Again $\frac{1}{\gamma}$ gets larger so the damping (or force fluctuation) ate gets slower on replacing Bz-Bz interactions with Bz-I_2 interactions. The ratio ω_1/ω_o is >1, the condition for a weak interaction [16]. It would appear that the 'cell' model is less able to detect changes in the extent of fluctuating forces on the molecules due to interactions, although both approaches easily show up chages in the interaction dynamics.

V. CONCLUSIONS

To summarise our main conclusions, it would appear from the

studies so far carried out in our laboratory that,

(a) The interaction of Bz and I_2 leads to quite a different induced far-infrared spectrum from that due to Bz-Bz interactions. However, in both cases, both short and long time relaxation processes are discernable from the corresponding correlation functions. Both long and short ranged potentials are needed to describe the interactions.

(b) Beer's Law is quite accurately obeyed over the limited range of iodine concentrations available in benzene.

(c) The quadrupole-polarisability model seems to be reasonably good at predicting observed intensities and second moments. There is no need to include significant contributions from short ranged (DA) attractive potentials.

(d) Band shaping models derived by solving the generalised Langevin equation for roto-translational motion fit the data quite well with parameters which would indicate that the random forces fluctuate rather more slowly when Bz-Bz interactions are replaced by Bz-I_2 interactions.

(e) Much more work is required at different temperatures, and in different solvents before the behaviour of these potentials can be further characterised.

Acknowledgements

Support from SERC in the form of equipment grants and a studentship (to BC) are gratefully acknowledged. We also owe sincere thanks to Prof. J. Lascombe and Dr. M. Besnard who sent us their data prior to publication.

References

1. W.A. Steele and G. Birnbaum, J. Chem. Phys., 1980, 72, 2250.
2. T.I. Cox and P.A. Madden, Mol. Phys., 1980, 39, 1487; ibid. 1981, 43, 287, 307.
3. F.G. Baglin, V. Zimmerman and H. Versmold, Mol. Phys., 1984, 52, 877
4. P.A. Madden in Molecular Liquids - Dynamics and Interactions, (Eds. A.J. Barnes, W.J. Orville-Thomas and J. Yarwood), Reidel, Dordrecht, 1984, pp. 431-474 (and references therein).
5. G. Birnbaum, B. Guillot and S. Bratos, Adv. Chem. Phys., 1982, 51, 49.
6. G. Birnbaum in 'Vibrational Spectroscopy of Molecular Liquids and Solids', (Ed. S. Bratos and R.M. Pick), Plenum, New York, 1980, p. 147.
7. J. Lascombe and M. Besnard, Mol. Phys., 1986, 58, 573..
8. A. De Samtis and M. Sanpoli, Mol. Phys., 1984, 51, 97.
9. C.J. Manzanares, A. Munoz and D. Hidalgo, Chem. Phys., 1983, 87, 363.
10. B. Catlow and J. Yarwood, J. Mol. Structure, 1986, 135, 415.
11. J. Yarwood and M. Tamres in 'Spectroscopy and Structure of Molecular Complexes', Plenum, 1973, Chapters 2 and 3.
12. G. Maes, J. Mol. Structure, 1980, 61, 95; J. Put, G. Maes and P. Huyskens, Spectrochim. Acta, 1981, 37, 699.
13. W.B. Person and R.S. Mulliken, Molecular Complexes, Wiley, New York (1969).
14. M.W. Hanna, J. Amer. Chem. Soc., 1968, 90, 285, 5358.

15. C.S. Murty, K. Singer, D. Steele, J.J. Tindle and R. Vallauri, Chem. Phys. Lett., 1982, 90, 95.

16. D.W. Oxtoby in Proc. NATO Advanced Workshop on 'Phenomena Induced by Intermolecular Interactions' (Ed. G. Birnbaum), Plenum, 1984, pp.715-726.

17. T. Keyes and D. Kivelson, J. Chem. Phys., 1972, 57, 4599.

18. W.A. Steele, ref. 4 pp.

19. D.M.F. Edwards and P.A. Madden, Mol. Phys., 1984, 51, 1141, 1163.

20. C.G. Joslin, C.G. Gray and Z. Gburski, Mol. Phys., 1984, 53, 203.

21. J. Lascombe and M. Besnard, personal communication of unpublished results.

22. B. Guillot, S. Bratos and G. Birnbaum, Phys. Rev. A. 1982, 25, 773.

23. M.W. Evans, G.J. Evans, J. Yarwood, P.L. James and R. Arndt, Mol. Phys., 1979, 38, 699.

24. J.R. Birch, G.P. O'Neill, J. Yarwood and M. Bennouna, J. Phys. E. Sci. Instruments, 1982, 15, 684.

25. L. Potthast, J. Sammios and T. Dorfmüller, Chem. Phys., 1986, 102, 147.

26. J.P. Kettle and A.H. Price, J. Chem. Soc., Faraday Trans. II, 1972, 68, 1306.

27. D.A. McQuarrie, Statistical Mechanics, Harper and Row, 1973, p.498-9.

28. T. Jao and W.B. Person, J. Phys. Chem., 1979, 83, 1181.

29. M.W. Evans, G.J. Evans, W.J. Coffey and P. Grigolini in Molecular Dynamics, Wiley-Interscience, New York, 1983, p.748.

Figure Captions

Fig. 1. Far-infrared spectrum of iodine in benzene (with benzene (with benzene spectrum removed) 0.2 Molar, 340 K.

Fig. 2. The Oxtoby 'cell' model for iodine translating in a 'cage' of benzene molecules.

Fig.3. (a) Far-infrared spectra of iodine in benzene at (A) 0.2 M (B) 0.16 M (C) 0.06 M (291 K) ratioed against an equal pathlength of pure benzene

(b) as in 3A except that the spectra have been divided by $[I_2]$.

Fig. 4. (a) Far-infrared spectra of iodine in benzene (A) 0.2 M (B) 0.16 M (C) 0.13 M (D) 0.08 M (291 K) ratioed against a shorter pathlength of benzene/I_2 at the same I_2 concentration.

(b) as in 4A except that the spectra have been divided by $[I_2]$.

Fig. 5. (A) pure benzene spectrum 291 K (B) 0.2 M I_2 in Bz ratioed against a shorter pathlength (C) 0.2 MI_2 in Bz ratioed against pure benzene.

Fig. 6. Comparison of measured (B) and calculated (A) refractive index (0.2 M I_2 in Bz, 291 K).

Fig. 7. Computed cross sections, $I(\bar{\nu})$ for I_2 in benzene (0.2 M at 291 K). A. with benzene absorption removed (R.H. scale), B. without benzene spectrum removed (L.H. scale).

Fig. 8. Correlation functions obtained for 0.2 M I_2 in benzene (291 K). A. without benzene absorption removed. B. with benzene spectrum removed.

Fig. 9. The Mori truncated fraction approach. Comparison of observed and fitted far-infrared spectra of iodine in benzene. A and D. Observed and fitted spectra (respectively) with benzene spectra subtracted (L.H. scale). C and B. Observed and fitted spectra without benzene spectrum subtracted (R.H. scale).

Fig. 10. The Oxtoby 'cell' model approach. Comparison of observed and fitted far-infrared spectra of iodine in benzene. A and B. Observed and fitted spectra with benzene absorption removed (L.H. scale). C and D. Observed and fitted spectra without benzene absorption removed (R.H. scale).

Table 1. Model parameters for the far-infrared spectra of benzene and iodine in benzene (all at 291 K).

Mori truncated fraction[a]	$K_o(o)$	$K_1(o)$	γ	$\epsilon_o-\epsilon_\infty$
	22.5	118.6	14.8	0.036
Benzene liquid (291 K	20.6	114.9	13.9	-
(Lit. data - ref. 29)	20.8	110.6	12.8	0.023
0.2 M I_2 in Bz - (I_2 in Bz)	20.7	105.2	12.1	-
0.2 M I_2 in Bz - (Bz)	18.9	121.2	10.3	-

Oxtoby 'cell' model[b]	ω_o	ω_1	γ	ω_1/ω_o	γ/ω_o
Benzene liquid (291 K)	52.8	80.3	174.5	1.53	3.28
0.2 M I_2 in Bz - (I_2 in Bz)	51.8	77.2	141.9	1.49	2.73
0.2 M I_2 in Bz - (Bz)	54.0	75.3	97.9	1.39	1.81

(a) the parameters are weighted by I/2kT in order to render them dimensionless.

(b) all the parameters are in $psec^{-1}$ (see ref. 16).

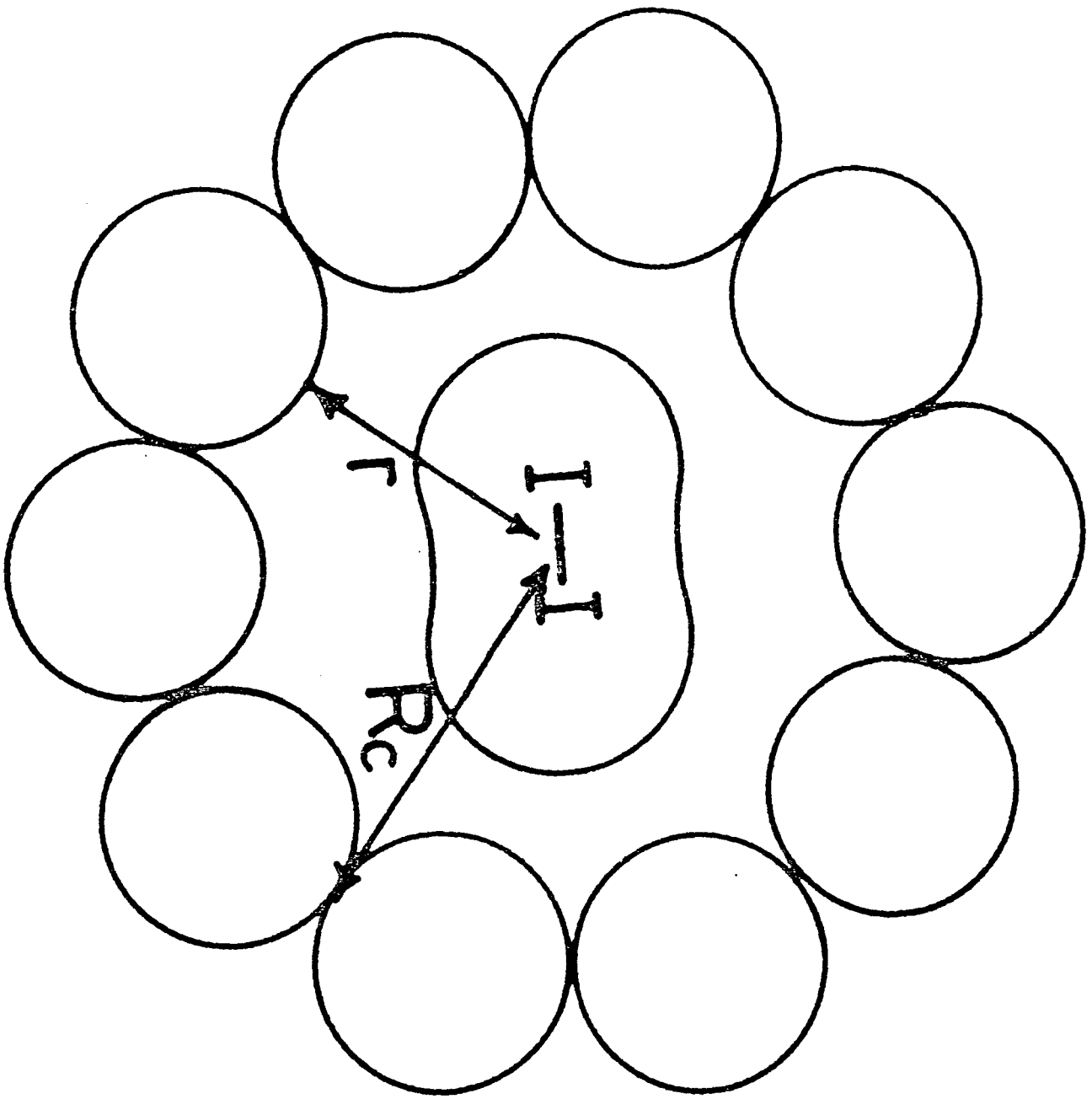
r
L
Rc

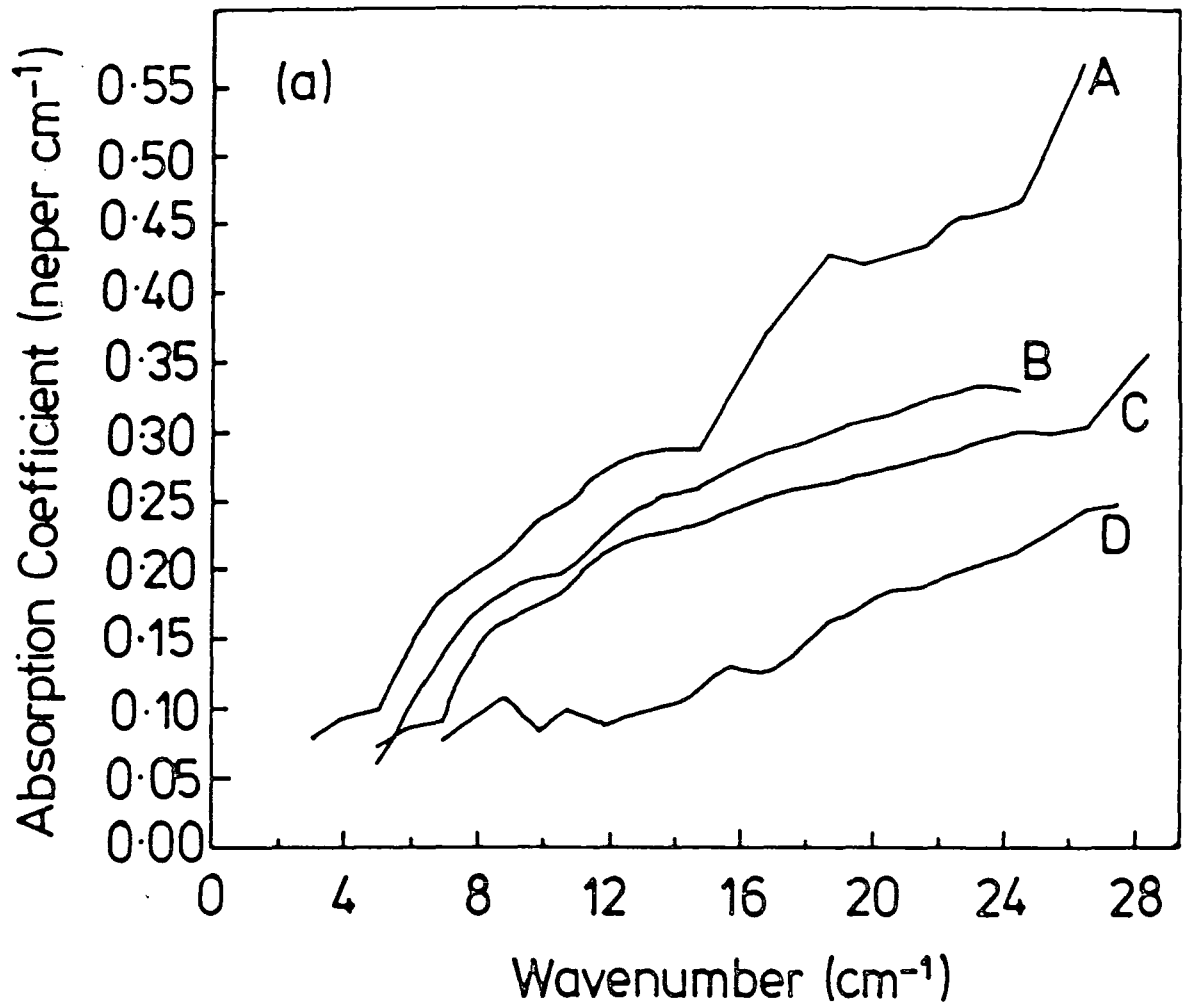
(a)
A
B
C
D
Absorption Coefficient (neper cm⁻¹)
0·55
0·50
0·45
0·40
0·35
0·30
0·25
0·20
0·15
0·10
0·05
0·00
0
4
8
12
16
20
24
28
Wavenumber (cm⁻¹)

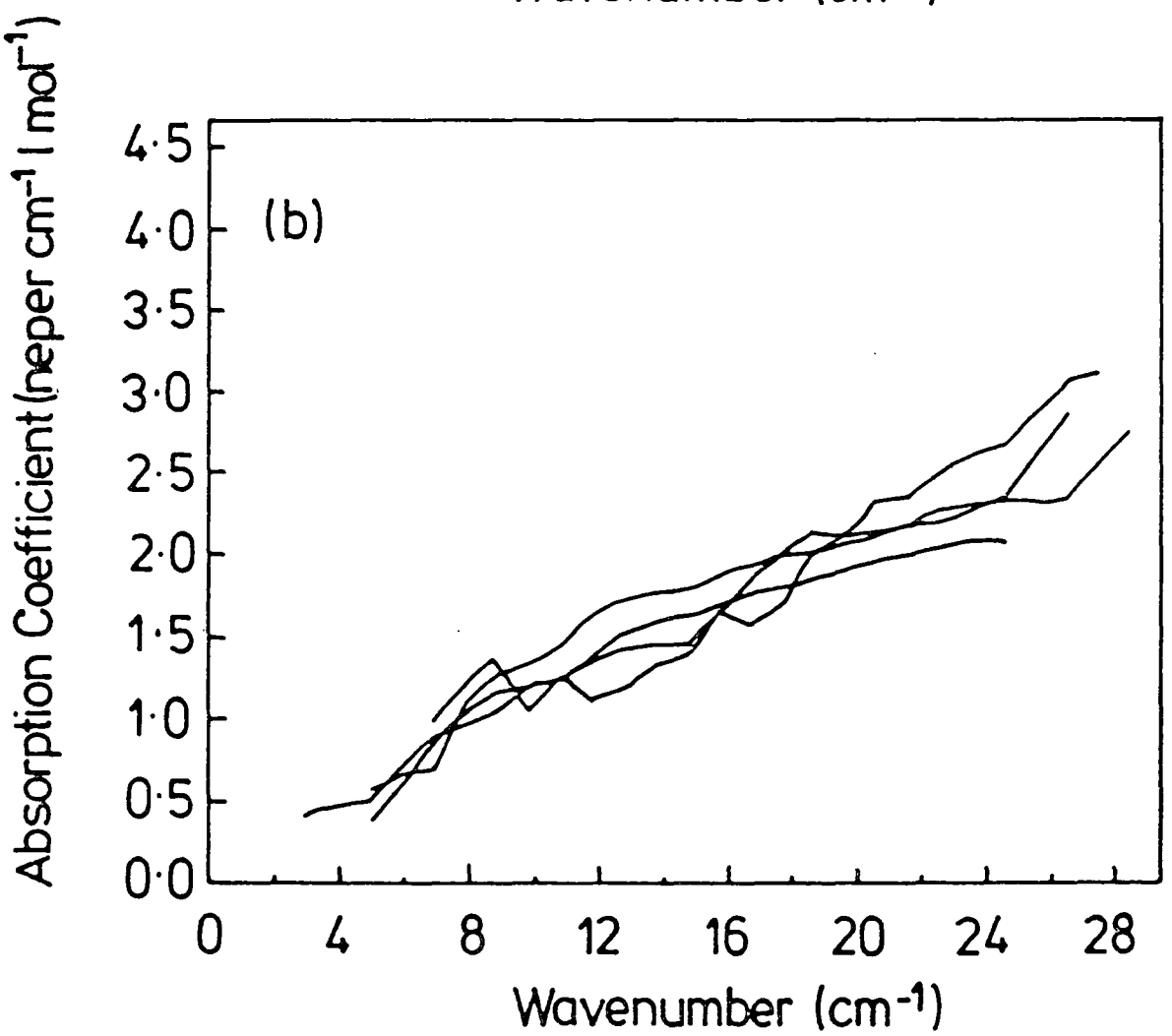
(b)
Absorption Coefficient (neper cm⁻¹ l mol⁻¹)
4·5
4·0
3·5
3·0
2·5
2·0
1·5
1·0
0·5
0·0
0
4
8
12
16
20
24
28
Wavenumber (cm⁻¹)

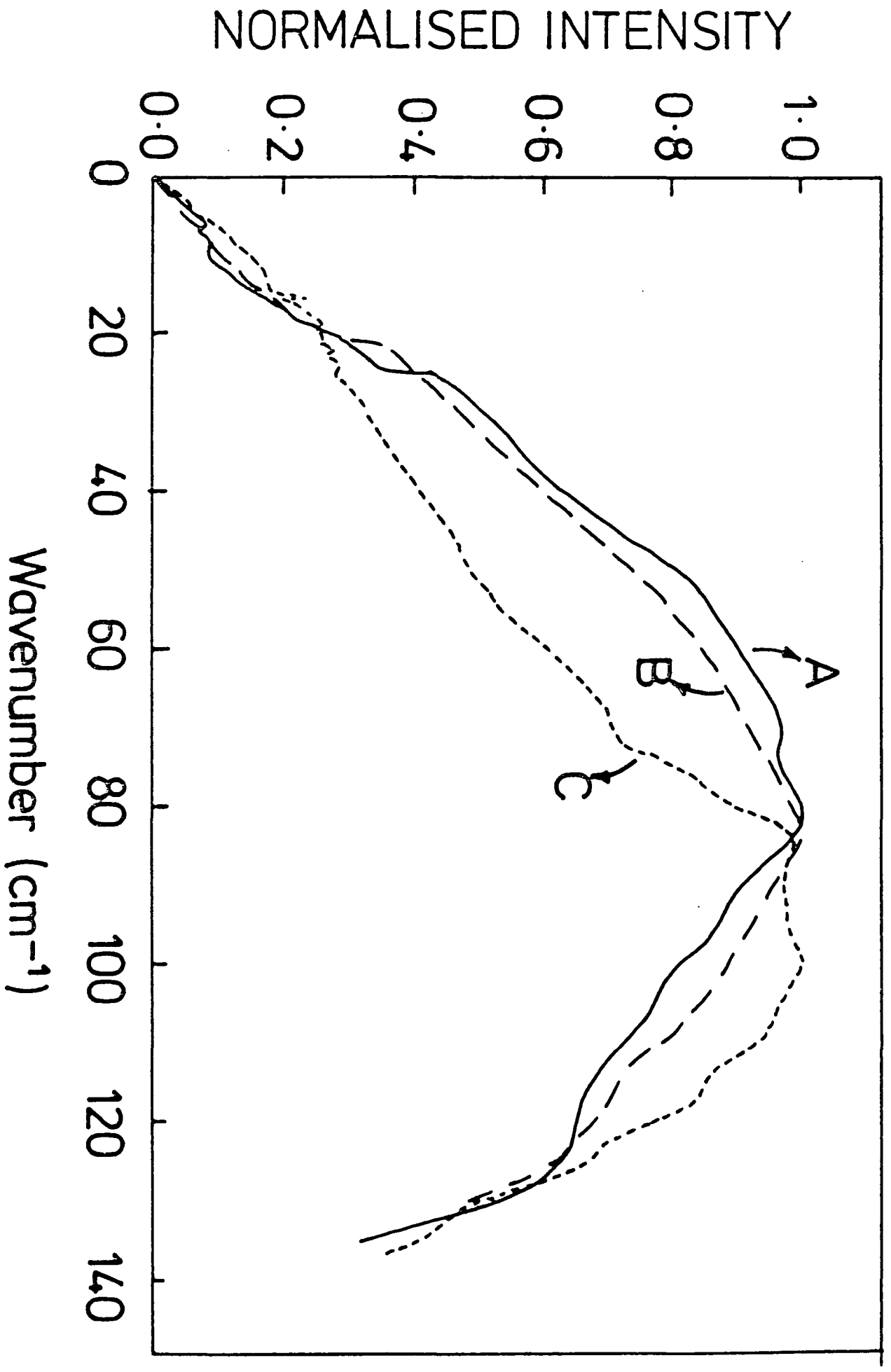
NORMALISED INTENSITY
0·0
0·2
0·4
0·6
0·8
1·0
0
20
40
60
80
100
120
140
Wavenumber (cm⁻¹)
A
B
C

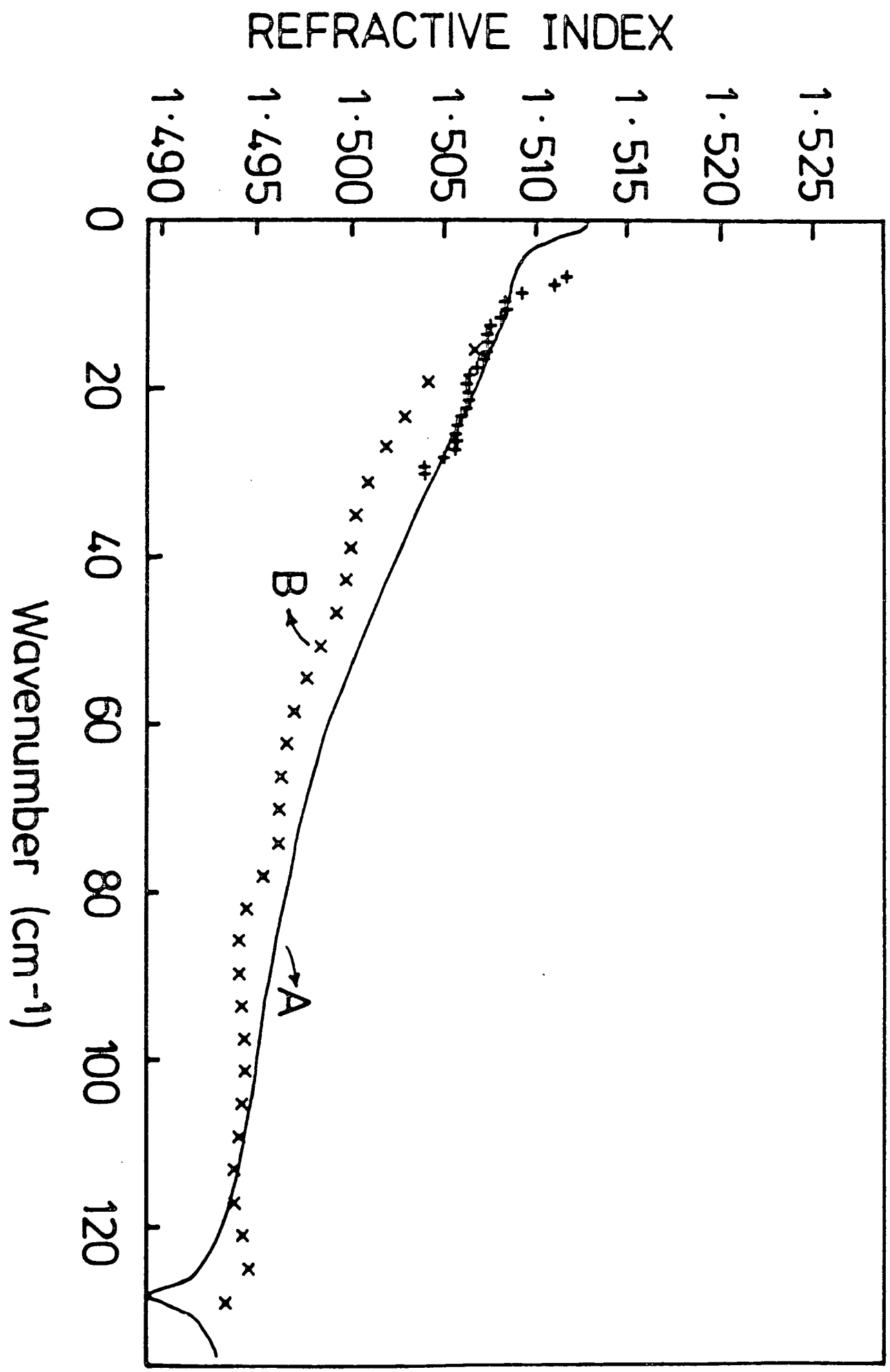
REFRACTIVE INDEX
1.490
1.495
1.500
1.505
1.510
1.515
1.520
1.525
0
20
40
60
80
100
120
Wavenumber (cm-1)
B
A

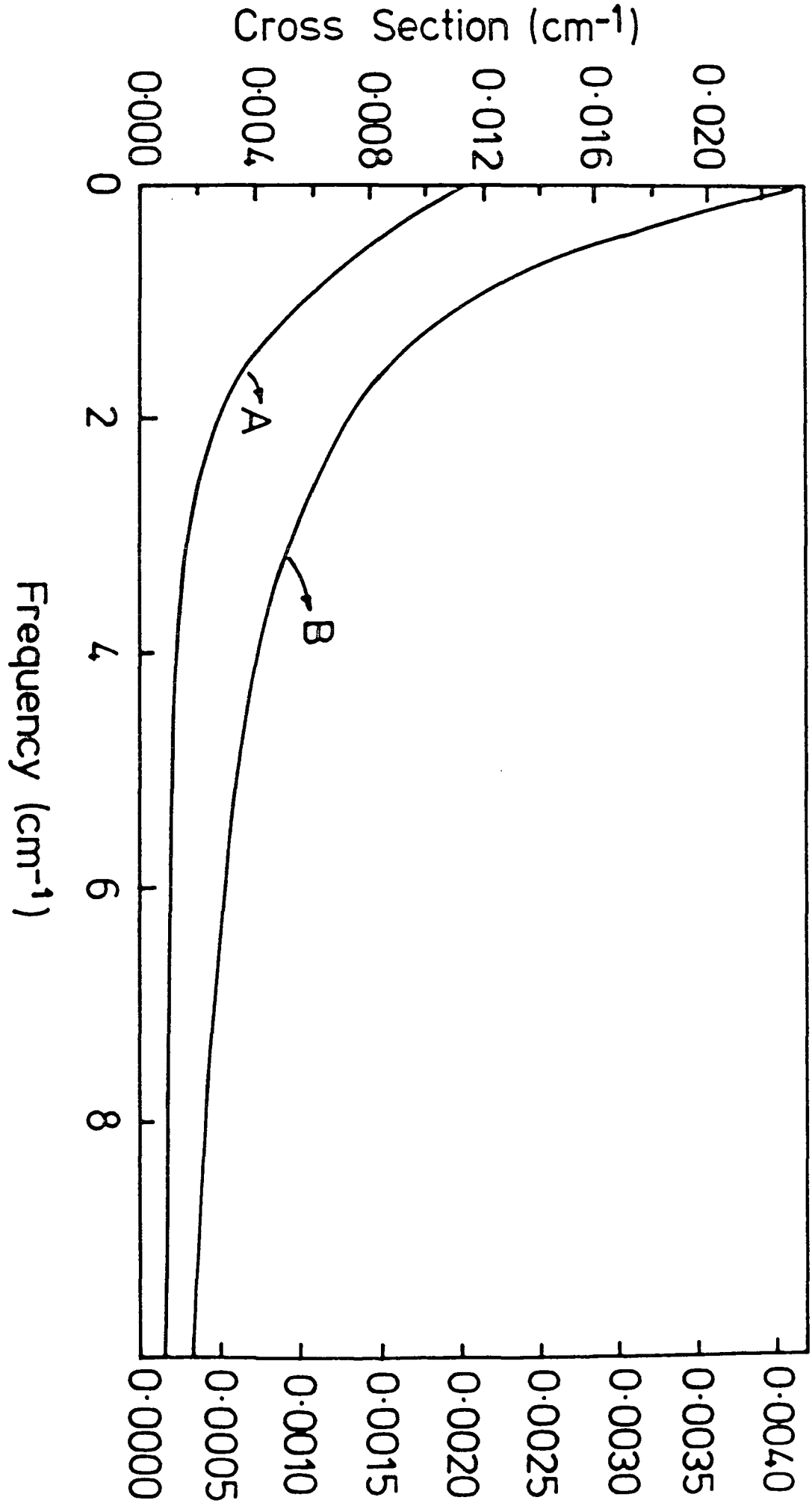
Cross Section (cm-1)
0·000
0·004
0·008
0·012
0·016
0·020
0
2
4
6
8
Frequency (cm-1)
A
B
0·0000
0·0005
0·0010
0·0015
0·0020
0·0025
0·0030
0·0035
0·0040

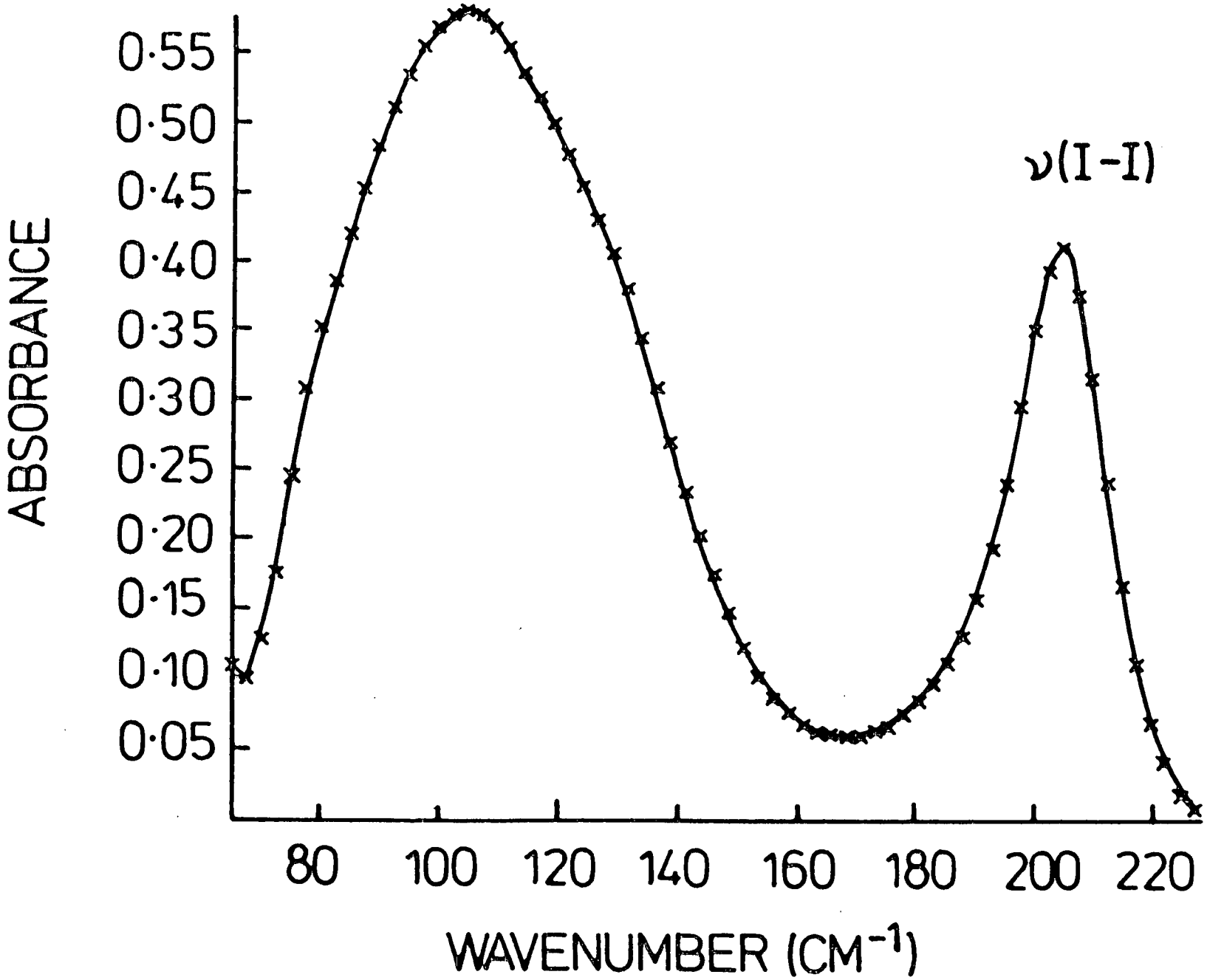
ABSORBANCE
0·55
0·50
0·45
0·40
0·35
0·30
0·25
0·20
0·15
0·10
0·05
ν(I-I)
80
100
120
140
160
180
200
220
WAVENUMBER (CM⁻¹)

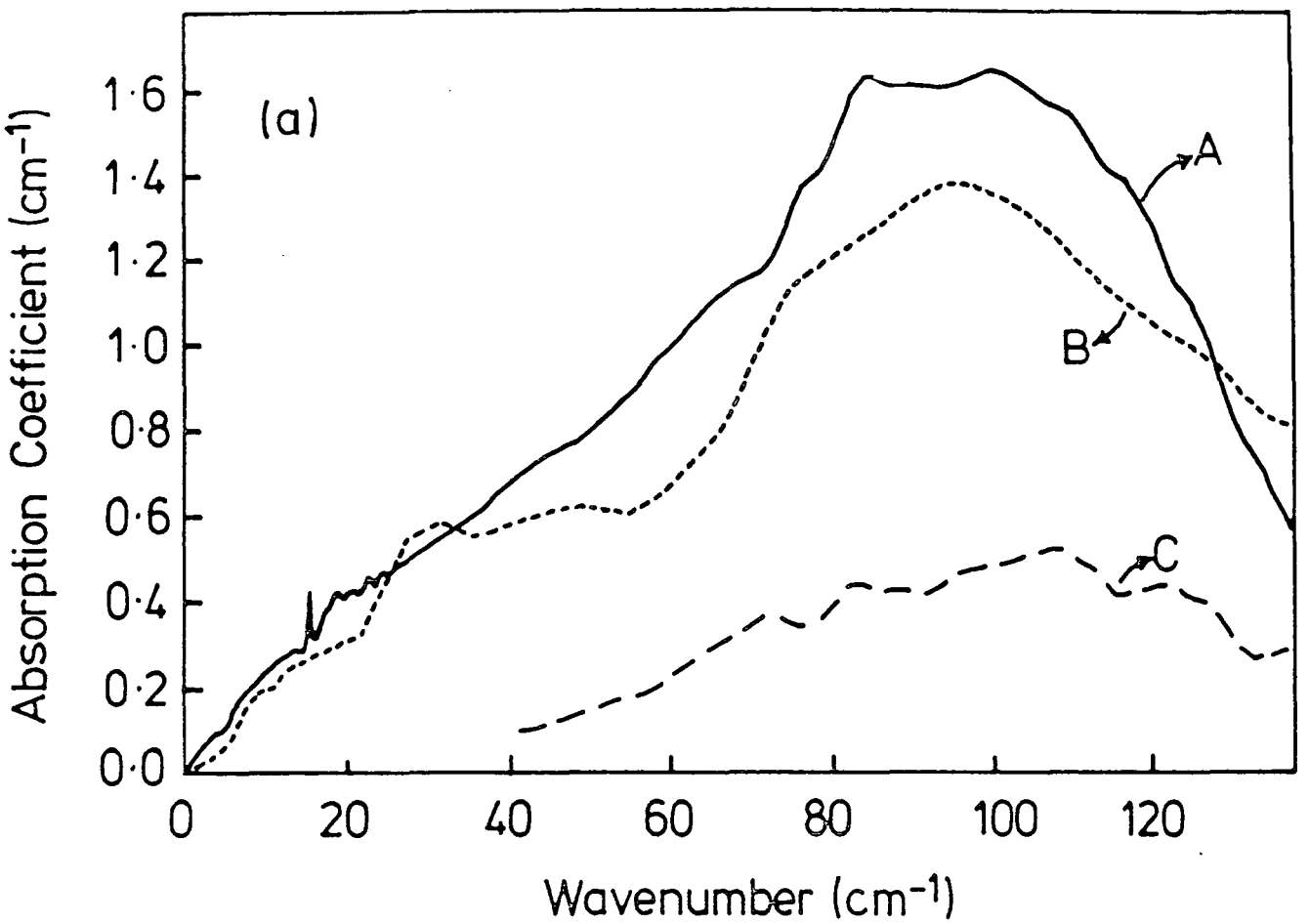
(a)
Absorption Coefficient (cm⁻¹)
1·6
1·4
1·2
1·0
0·8
0·6
0·4
0·2
0·0
A
B
C
0
20
40
60
80
100
120
Wavenumber (cm⁻¹)

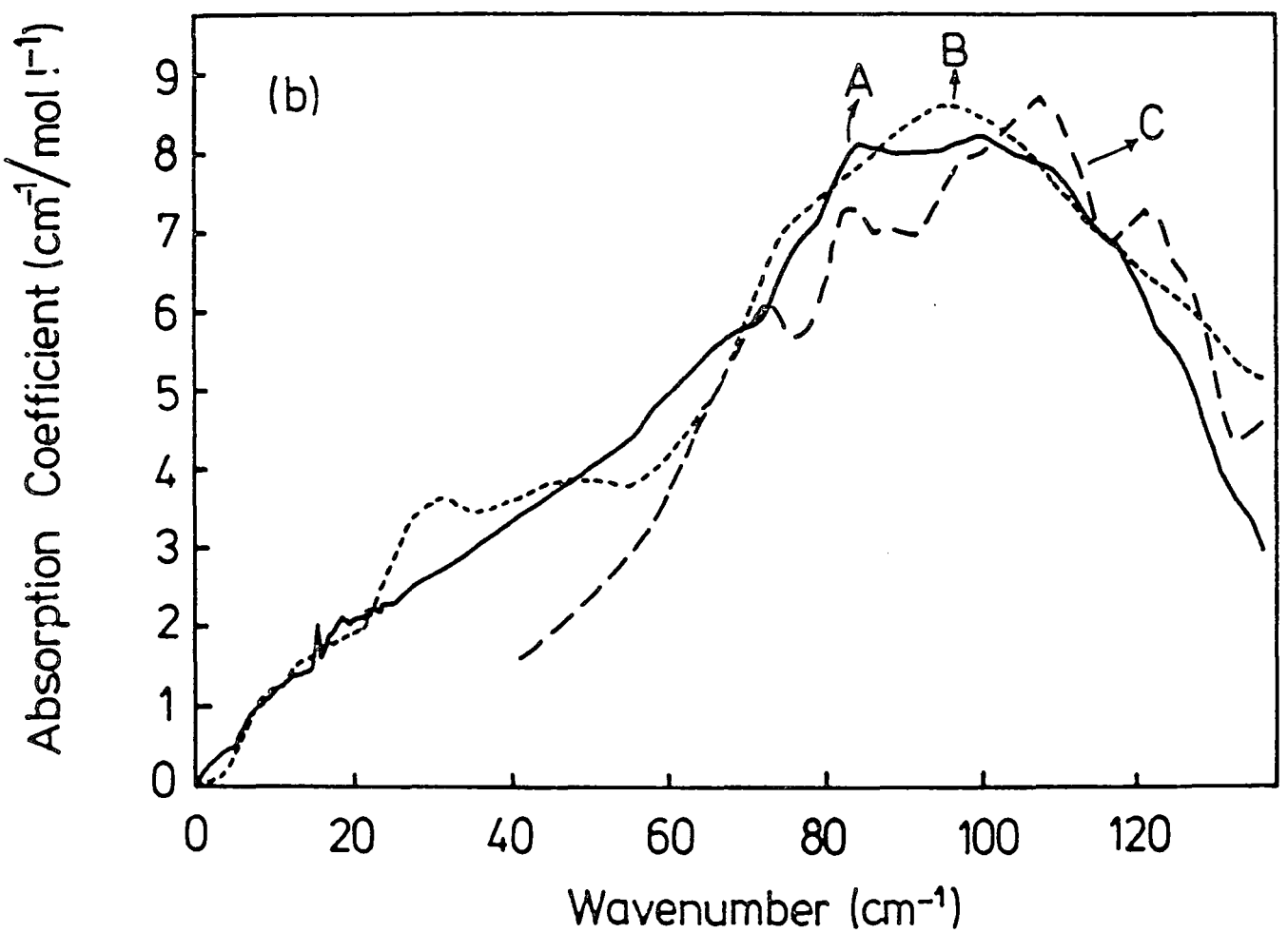
(b)
Absorption Coefficient (cm⁻¹/mol l⁻¹)
9
8
7
6
5
4
3
2
1
0
A
B
C
0
20
40
60
80
100
120
Wavenumber (cm⁻¹)

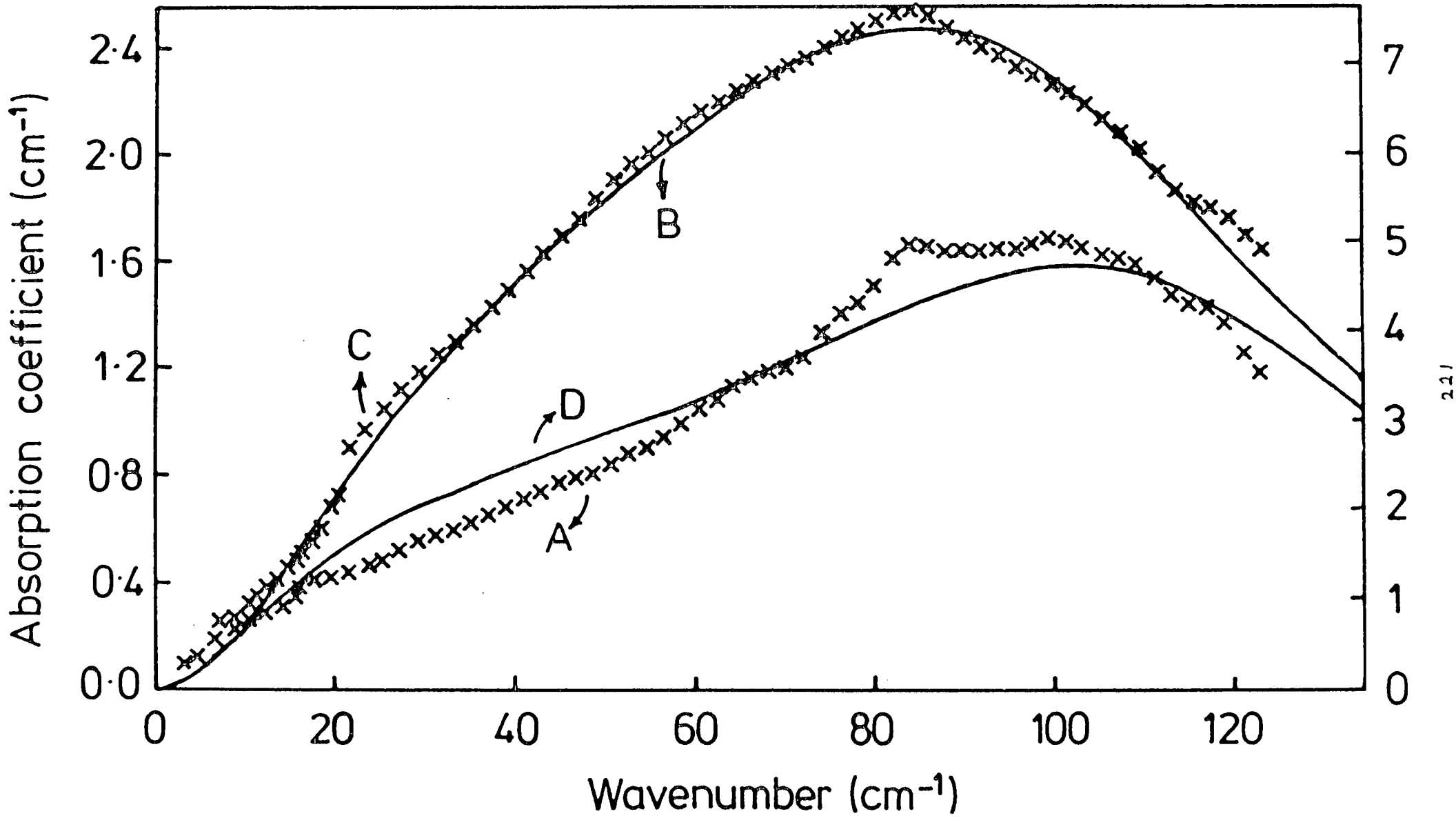
Absorption coefficient (cm⁻¹)
2·4
2·0
1·6
1·2
0·8
0·4
0·0
0
20
40
60
80
100
120
Wavenumber (cm⁻¹)
7
6
5
4
3
2
1
0
A
B
C
D

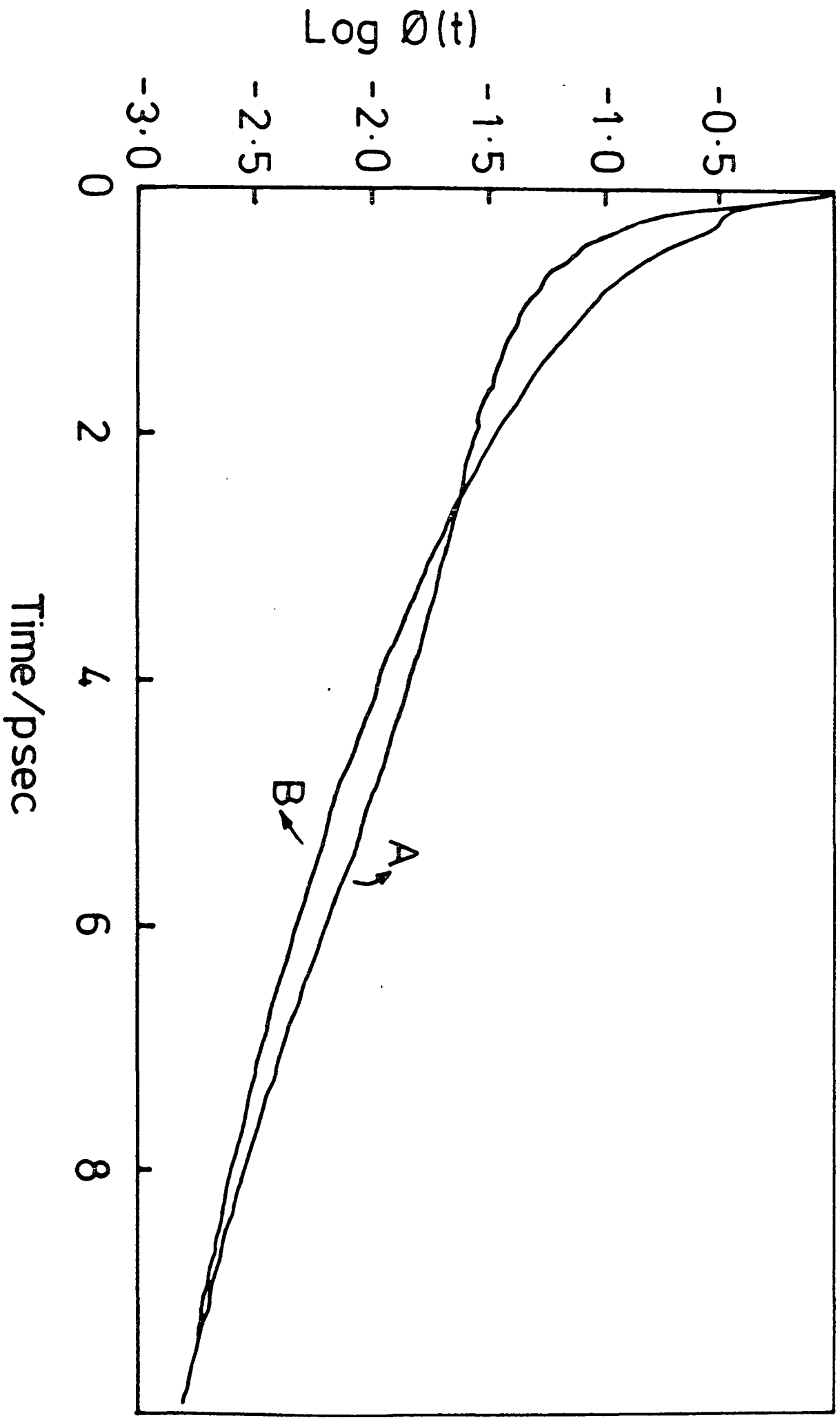
Log Ø(t)
-3.0
-2.5
-2.0
-1.5
-1.0
-0.5
0
2
4
6
8
Time/psec
B
A

REFERENCES

1. Chamberlain, J. 'The Principles of Interferometric Spectroscopy' Wiley (1979)

2. Bell, R. J. 'Introductory Fourier Transform Spectroscopy' Academic Press (London) (1972)

3. Griffiths, P. R. 'Chemical Infrared Fourier Transform Spectroscopy' Wiley (1975)

4. Bracewell, R. N. 'The Fourier Transform and its Applications' McGraw-Hill (1978)

5. Chantry, G. W. 'Long Wave Optics' Vol. 1. Academic Press (1984)

6. Martin, D. H. 'Spectroscopic Techniques for Far Infrared, Submillimetre and Millimetre Waves' North-Holland Publishing Co. Amsterdam (1967)

7. Martin, D. H.; Puplett, E. Infrared Physics, 10, 105 (1969)

8. Strong, J. Vanasse, G. A. J. Opt. Soc. Amer. 50, 1960 (1960)

9. Formān, M. L.; Steele, W. H.; Vanasse, G. A. J. Opt. Soc. Amer. 56, 59 (1966)

10. Felgett, P. B. J. Phys. Radium 19, 187 (1958)

11. Felgett, P. B. Infrared Physics 24, 95 (1984)

12. Jacquinot, P. J. Opt. Soc. Amer. 44, 761 (1954)

13. Bell, E. E. Infrared Physics 6, 57 (1966)

14. Chantry, G. W. 'Submillimetre Spectroscopy' Academic Press (1971)

15. Chamberlain, J. Infrared Physics 11, 25 (1971)

16. Chamberlain, J.; Gebbie, H. A. Infrared Physics 11, 57 (1971)

17. Fleming, J. W.; Gibson, M. J. J. Mol Structure 63, 326 (1976)

18. Rao, K. N.; de Vore, R. V.; Plyler, E. K. J. Research Nat. Bur. Stand. 67A, 351 (1963)

19. Slater, J. C.; Frank, N. H. 'Electromagnetism' McGraw-Hill (1947)

20. Heavens, O. C. 'Optical Properties of Thin Solid Films' Dover NY (1965)

21. Fleming, J. W.; Chantry, G. W. IEEE IM 23, 473 (1974)

22. Birch, J. R.; Parker, T. J. Ch. 3 'Infrared and Millimetre Waves' Vol. 2 Ed. Button, K. J. Academic Press (1979)

23. Genzel, L.; Kremer, F. Phys. Rev. B. 29, 4595 (1984)

24. Birch, J. R.; Parker, T. J. Infrared Physics 19, 103 (1979)

25. Birch, J. R.; Bulleid, C. E. Infrared Physics 17, 279 (1979)

26. Afsar, M. N.; Chantry, G. W. IEEE MIT 25, 509 (1977)

27. Appendix 2 of reference 5.

28. Birch, J. R.; O'Neill, G. P.; Yarwood, J.; Bennouna, M. J. Phys. E.: Sci. Instrum. 15, 684 (1982)

29. Honijk, D. D.; Passchier, W. F.; Mandel, M.; Afsar, M. N. Infrared Physics 17, 9 (1977)

30. Birch, J. R.; Bennouna, M. Infrared Physics 21, 229 (1981)

31. Birch, J. R. Infrared Physics 18, 613 (1978)

32. O'Neill, G. P. Ph.D. Thesis, Univ. of Durham (1986)

33. Vandergraft, J. S. 'Introduction to Numerical Computations' Academic Press (1978)

34. Afsar, M. N. Proc. IEEE 67, 1460 (1979)

35. Guillaume, F. Personal communication

36. Birch, J. R.; Kong Fan Ping Infrared Physics 24, 309 (1984)

37. Birch, J. R,; Dromey, J. D.; Lesurf, J. Infrared Physics 21, 225 (1981)

38. Russell, E. E.; Bell, E. E. Appl. Optics 5, 393 (1966)

39. Chantry, G. W.; Chamberlain, J. Ch. 20 'Polymer Science' Ed. Jenkins, A. D. North Holland (1972)

40. Montaner, A.; Galtier, M.; Benoit, C.; Aldissi, M. Physica Solidi 66, 267 (1981)

41. Chaing, C. K.; Fincher, C. R. Phys. Rev. Lett. 33, 1098 (1977)

42. Lux, P. J. Ph.D. Thesis, Univ. of Durham (1986)

43. Davies, G. J.; Evans, M. J. Chem. Soc. Farad. II 7, 1194 (1976)

44. Potthast, L.; Samois, D.; Dorfmueller, T. Chem Phys. 102, 147 (1986)

45. Michielson, J.; Ketelaar, J. Mol. Phys. 24, 1181 (1972)

46. Cox, T. I.; Madden, P. A. Mol. Phys. 39, 1487 (1980)

47. Cox, T. I.; Madden, P. A. Mol. Phys. 43, 287,307 (1981)

48. Davies, G. J.; Chamberlain, J.; Davies, M. J. Chem. Soc. Farad. II 8, 1223 (1973)

49. Dagg, I. R.; Read, L.; Smith, W. Can. J. Phys. 60, 1431 (1982)

50. Pringle, W. C.; Jacobs, S. M.; Rosenblatt, D. M. Mol. Phys. 50, 205 (1983)

51. Buontempo, U.; Maselli, P. J. Mol. Liquids 32, 161 (1986)

52. Birnbaum, G. 'Vibrational Spectroscopy of Molecular Liquids and Solids' Eds. Bratos, S.; Pick, R. M. Plenum NY (1980)

53. Edwards, D. M. F.; Madden, P. A.; McDonald, I. R. Mol. Phys. 51, 1141 (1984)

54. Edwards, D. M. F.; Madden, P. A. Mol. Phys. 51, 1163 (1984)

55. Madden, P. A. 'Raman Spectroscopy Linear and Non-Linear' p. 307 eds. Lascombe, J.; Huong, P. V. Wiley (1982)

56. Steele, W. A.; Birnbaum, G. J. Chem. Phys. 72, 2250 (1980)

57. Baglin, F. G.; Zimmerman, V.; Versmold, M. Mol. Phys. 52, 877 (1984)

58. Catlow, B.; Yarwood, J. J. Mol. Structure 135, 415 (1986)

59. Posch, H. A. Mol. Phys. 37, 1059 (1979)

60. Fromhold, L. Adv. Chem. Phys. 46, 1 (1981)

61. Langevin, P. J. Phys. 4, 678 (1905)

62. Evans, M. W.; Evans, G. J.; Coffey, W. T.; Grigolini, P. 'Molecular Dynamics' Wiley-Interscience, NY (1983)

63. Bottcher, C. J. F.; Borderwijk, P. 'Theory of Electric Polarisation' Elsevier Scientific (1978)

64. Rocard, Y. J. Phys. Radium 4, 247 (1933)

65. Powles, J. G. Trans. Farad Soc. 44, 802 (1948)

66. Poley, J. J. Chem. Phys. 23, 405 (1955)

67. Gerschel, A.; Darmon, I.; Brot, C. Mol. Phys. 23, 317 (1972)

68. Hill, N. E. Proc. Phys. Soc. 82, 723 (1963)

69. Chantry, G. W.; Gebbie, H. A. Nature 208, 378 (1965)

70. Kellar, B.; Kneubuhl, F. Helv, Phys, Acta 45, 1127 (1972)

71. Costines, M. E.; Marsault-Herail, F.; Levi, G. Mol. Phys. 38, 1035 (1979)

72. Lynden-Bell, R. M.; Steele, W. A. J. Phys. Chem. 88, 6514 (1984)

73. Oxtoby, D. W. in Proc. Nato Adv. Workshop on 'Phenomena Induced by Intermolecular Interactions' Ed. Birnbaum, G. Plenum NY (1984)

74. Coffey, W. T. Chem. Phys. Lett. 123, 416 (1986)

75. Evans, G. J.; Evans, M. W. J. Chem. Soc. Farad. II 7, 1170 (1976)

76. Berne, B. J.; Harp, D. J. Adv. Chem. Phys. 17, 100 (1970)

70. Kubo, R. J. Phys. Soc. Japan 12, 570 (1957)

78. Gordon, R. G. J. Chem. Phys. 44, 1830 (1966)

79. Gordon, R. G. J. Chem. Phys. 43, 1307 (1965)

80. Evans, M.; Davies, G. J. J. Chem. Soc. Farad. II 7 1206 (1976)

81. Hertfeld, K. F.; Litovitz, T. A. 'Absorption and Dispersion of Ultrasonic Waves' Academic Press, NY (1959)

82. Buckingham, A. D. Adv. Chem. Phys. 12, 107 (1967)

83. Evans, G. J. J. Chem. Soc. Farad. II 2, 547 (1983)

84. Evans, G. J. Chem. Phys. Letters 99, 173 (1983)

85. Evans, G. J. Personal communication

86. Arnold, K. E.; Yarwood, J.; Price, A. H. Mol. Phys. 48, 451 (1983)

87. Birch, J. R.; Ping, K. F.; Husain, S. K.; Yarwood, J.; Catlow, B. Chem. Phys. Letters 117, 197 (1985)

88. Yarwood, J.; Person, W. B. J. Amer. Chem. Soc. 90, 594 (1968)

89. Mulliken, R. S.; Person, W. B. J. Amer. Chem. Soc. 91, 3409 (1969)

90. Bhowmik, B. B. Spectrochim. Acta 27A, 321 (1971)

91. Kettle, J. P.; Price, A. H. J. Chem. Soc. Farad. II 68, 1306 (1972)

92. Lascombe, J.; Besnard, M. Mol. Phys. 58, 573 (1986)

93. Madden, P. A. Mol. Phys. 39, 1487 (1980)

94. Baglin, F. G.; Zimmerman, V.; Versmold, H. Mol. Phys. 52, 877 (1984)

95. Yarwood, J. (Ed.) 'Spectroscopy and Structure of Molecular Complexes' Plenum, London (1973)

96. Jacobsen, R. J.; Brasch, J. W. Spectrochim. Acta 21, 1753 (1965)

97. Schuster, P.; Zundel, G.; Sandorfy, C. 'The Hydrogen Bond' North-Holland Publishing Co. Amsterdam (1976)

98. Mulliken, R. S. J. Amer. Chem. Soc. 72, 600 (1950)

99. Mulliken, R. S. J. Amer. Chem. Soc. 74, 811 (1952)

100. Mulliken, R. S. J. Phys. Chem. 56, 801 (1952)

101. Mulliken, R. S.; Person, W. B. 'Molecular Complexes' Wiley NY (1969)

102. Hanna, M. W. J. Amer. Chem. Soc. 90, 5358 (1968)

103. Hanna, M. W. J. Amer. Chem. Soc. 90, 285 (1968)

104. Hanna, M. W. J. Amer. Chem. Soc. 91, 4035 (1969)

105. Jao, T.; Person, W. B. J. Phys. Chem. 83, 1181 (1979)

106. Klaboe, P. J. Amer. Chem. Soc. 89, 3667 (1967)

107. Rosen, H.; Shen, Y. R.; Stenman, F. Mol. Phys. 22, 33 (1971)

108. Put, J.; Moses, G.; Huyskens, P. Spectrochim. Acta 37, 699 (1981)

109. Lake, R. F.; Thompson, H. W.; Proc. Roy. Soc. A297, 440 (1967)

110. Paatero, M.; Eskola, S.; Stenman, F. in Proceedings of the 10th Int. Conf. Raman Spectroscopy Ed. Peticolas, W. L.; Hudson, B. (1986)

111. Buontempo, U.; Codastefano, P.; Cunsolo, S.; Dore, P.; Maselli, P. Can. J. Phys. 61, 156 (1983)

112. Buontempo, U.; Maselli, P. J. Mol. Liquids 32, 161 (1986)

113. Buontempo, U.; Cunsolo, S.; Dore, P.; Maselli, P. Mol. Phys. 38, 2111 (1979)

114. Birnbaum, G.; Steele, W. A. J. Chem. Phys. 72, 2250 (1980)

115. Buontempo, U.; Maselli, P.; Nencini, L. Can. J. Phys. 61, 1498 (1983)

116. Buontempo, U.; Cunsolo, S.; Jacucci, G.; Weiss, J. J. J. Chem. Phys.

63, 2570 (1975)

117. Yarwood, J. in 'Molecular Liquids - Dynamics and Interactions' Ed. Barnes, A. J. Reidel Publishing Co.(1984)

118. Lascombe, J.; Besnard, M. Personal communication

119. Oxtoby, D. W. Personal communication

120. page 748 reference 62

121. Franklin, B. Phil. Trans. Royal Soc. 64, 445 (1774)

122. Lord Rayleigh Phil. Magazine 48, 321 (1899)

123. Langmuir, I. J. Amer. Chem. Soc. 39, 1848 (1917)

124. Blodgett, K. B. J. Amer. Chem. Soc. 57, 1007 (1935)

125. The Rt. Hon. M. Thatcher M.P. Personal communication.

126. Roberts, G. G. Sensors and Activators 4, 131 (1983)

127. Roberts, G. G. Contemporary Phys. 25, 109 (1984)

128. Roberts, G. G. Adv. Phys. 34, 475 (1985)

129. Peterson, I. R.; Girling, I. R. Science Progress 69, 533 (1985)

130. Gaines, G. L. 'Insoluble Monolayers at Liquid - Gas Interfaces' Wiley Interscience (1966)

131. Grunfeld, F.; Pitt, C. W. Thin Solid Films 99, 249 (1983)

132. Heckmann, K.; Strobl, Ch.; Bauer, S. Thin Solid Films 99, 265 (1983)

133. Roberts, G. G.; Petty, M. C.; Dharmadasa, M. Proc. IEE Solid State and Electron Devices 128, 197 (1981)

134. Munn, R. W. Chemistry in Britain 20, 518 (1984)

135. Chollet, P. A. Thin Solid Films 68, 13 (1980)

136. Knoll, W.; Philpott, M. R.; Golden, W. G. J. Chem. Phys. 77, 219 (1982)

137. Staromlynska, J.; Saunders, F. C.; Harrison, K. J.; Tandy, D. Mol. Cryst. Liq. Cryst 102, 175 (1984)

138. Peterson, I. R.; Russell, G. J. Brit. Polymer J. 17, 364 (1985)

139. Koyama, Y. et al. J. Coll. Int. Sci. 61, 438 (1971)

140. Kimura, F.; Umemura, J.; Takenaka, T. Langmuir 2, 96 (1986)

141. Ohnisha, T. et al. J. Phys. Chem. 82, 1989 (1978)

142. Rabolt, J. F.; Burns, F. C.; Schlotter, N. E.; Swalen, J. D. J. Chem. Phys. 78, 946 (1983)

143. Chollet, P. A.; Messier, J. Chem. Phys. 73, 235 (1982)

144. Chollet, P. A.; Messier, J. Thin Solid Films 99, 197 (1983)

145. Chollet, P. A.; Frisby, H.; Hoclet, M. Chem. Phys. 97, 365 (1985)

146. Allara, D. L.; Nuzzo, R. G. Langmuir 1, 1 (1985)

147. Hayashi, S.; Umemuro, J. J. Chem. Phys. 63, 1732 (1975)

148. Snyder, R. G.; Schachtschneider, J. H. Spectrochim. Acat 19, 85 (1960)

149. Allara, D. L.; Swalen, J. D. J. Phys. Chem. 86, 2700 (1982)

150. Davies G. H. Personal communication of unpublished results

151. Jones, C. A.; Russell, G. J.; Petty, M. C.; Roberts, G. G.

Phil. Mag. in press.

152. Golden, W. G.; Snyder, C. D.; Smith, B. J. Phys. Chem. 86, 4675 (1982)

153. Peterson, I. R.; Russell, G. J. Brit. Polymer J. 17, 364 (1985)